ELECTRO-OPTIC-WAVEGUIDE FREQUENCY-TRANSLATORS IN LITHIUM NIOBATE FABRICATED BY TITANIUM INDIFFUSION AND PROTON EXCHANGE

A Thesis

Submitted to the Faculty of Engineering

of The University of Glasgow

for the degree of

Doctor of Philosophy

by

Ka Kha Wong, B.Sc.(Electronics & Electrical Engineering)

1989

ProQuest LLC.
789 East Eisenhower Parkway
P.O. Box 1346
Ann Arbor, MI 48106 – 1346

ACKNOWLEDGEMENTS

I would like to express my sincere thanks to Professor J. Lamb for his encouragement, supervision, and enthusiasm in this project and also for the provision of the excellent research facilities and materials in the Department of Electronics and Electrical Engineering.

I am greatly indebted to Professor Richard M. De La Rue for his close supervision and constant encouragement in my 2nd and 3rd year of this project. His advice and help in preparing this thesis is also gratefully acknowledged.

It is of great pleasure to express my sincere thanks to Dr Steve Wright for his constant help, advice, and encouragement during the 1st year of this work.

Useful discussions with various members of the Integrated and Guided-Wave Optics Team is also gratefully acknowledged, in particular, Professor Peter J.R. Laybourn, Mr R. Hutchins, Dr R. Dunsmuir, Professor C.D.W. Wilkinson, and Dr G. Stewart.

The excellent and enthusiastic technical advice and support from Mr G. Boyle, Mr T. Wright, Mr K. Piechowiak, Mrs L. Hobbs, Mr J. Clark, Mr J. Crichton, Mr J. Young, Mr R. Harkins, Mr D.N. Thomson, and Mr H. Anderson and his staff in the Mechanical Workshop is greatly appreciated.

I would also wish to express many thanks to Dr I. Andonovic, Dr B. Bjortorp, Dr E.Y.B. Pun, Dr Alfredo Yi-Yan and Dr R. Steele for many useful discussions.

It is also of great pleasure to thank Dr D.F. Clark and Dr A.C.G. Nutt for collaborative work on the characterization of proton-exchange slab waveguides in $LiNbO_3$. The help and advice from Dr B. Bjortorp in obtaining the frequency response plots for the phase modulators is gratefully acknowledged.

The collaborative work with Dr J. Winfield in the Department of Chemistry of the University of Glasgow on the chemistry of the proton-exchange process in $LiNbO_3$ is much appreciated. The advice from Professor S. Thomson and Dr K. Tyler is gratefully acknowledged.

I would like to thank the Scholarship Committee of the University of Glasgow and the Committee of Vice-Chancellors and Principals of the Universities (U.K.) for their financial assistance throughout the three years of this work.

It is also my pleasure to thank Mr Nick Parsons and Mr Steve Gratze of GEC Research Ltd., Marconi Research Centre for support and encouragement in the dilute melt proton exchange (DMPE) work and also for allowing me to include the experimental results in this thesis. In addition I would like to thank the other partners of the JOERS $LiNbO_3$ Technology consortium (STC Technology Ltd., Plessey Research Caswell Ltd., Glasgow University, University College London, and Surrey University) for their permission to allow the DMPE work to be published in this thesis.

This project has been supported by a grant from the Science and Engineering Research Council (S.E.R.C.), U.K. The work on DMPE in $LiNbO_3$ was supported by GEC Research Ltd. and The Department of Trade and Industry, UK.

In addition I would like to thank Dr Herman van de Vaart of Allied-Signal, Inc. for his constant encouragement and support in my completion of the thesis. The constant encouragement from Dr S. Sriram of Battelle Columbus Laboratories to complete the thesis is also greatly appreciated.

Finally, I would like to express my very sincere thanks to my wife, Sau Chi for her love, patience, continual support, and encouragement throughout the length of this project and the eventual completion of this thesis. To her I owe the very painful days that she has to spend alone while I completed this.

Dedicated To:

Sau Chi, Dad, Mum, and Seng-Chung

With All My Love

TABLE OF CONTENTS

		Page No.
ACKNOWLEDGEMENTS		i
TABLE OF CONTENTS		iii
SUMMARY		xi
CHAPTER 1	INTRODUCTION	
	1.1 Optical Communications, Integrated Optics, And Integrated Optical Sensor Technology: an Outlook	1
	1.2 Progress on Active Lithium Niobate Devices	4
	1.3 Objectives of this Investigation	7
	1.4 Organisation of the Thesis	8
	References	10
CHAPTER 2	REVIEW OF OPTICAL FREQUENCY TRANSLATION TECHNIQUES USING GUIDED-WAVE OPTICS TECHNOLOGY	
	2.1 Introduction	17
	2.1.1 Microwave Frequency Translation	18
	2.1.2 Optical Frequency Translation using Bulk Optical Devices	19
	2.1.3 Optical Frequency Translation using Guided-Wave Optics Technology	21
	2.2 Integrated Optics Acousto-Optic (Bragg) Interactions for Optical Frequency Translation	24
	2.2.1 Integrated Optical Waveguide X-Junction Frequency Shifter (Tsai et al)	25
	2.2.2 Integrated Optical Waveguide X-Junction Frequency Shifter (Von Helmolt et al)	27
	2.2.3 Integrated Optic Frequency Shifters with SAWs (Schaffer and Peterman)	29
	2.2.4 Discussions of Optical Frequency Translators Realised by Acousto-Optic (Bragg) Interactions	31

2.3 Integrated Optical Electro-Optic Frequency-Translators 32

2.3.1 Quadrature Method of Frequency Translation 32
2.3.1.1 Proposal by Culshaw And Wilson 33
2.3.1.2 Demonstrations by John And Wilson 35
2.3.1.3 Demonstration by Izutsu et al 36
2.3.1.4 Discussions of Optical Frequency-Translators Realised by the Quadrature Method 37
2.3.2 Electro-Optical Bragg Array Optical Frequency-Translator 38
2.3.3 Electro-Optical Frequency-Translator by Heismann And Ulrich 40
2.3.4 Integrated-Optical Channel-Waveguide Frequency-Translator by Johnson et al 42
2.3.5 Serrodyne Optical Frequency-Translators 43
2.3.6 Discussions of Optical Frequency-Translators Realised by Electro-Optic Methods 44

2.4 Single-Mode Optical Fibre Frequency-Translators 45

2.4.1 Acousto-Optic Realisation 46
2.4.2 Serrodyne Realisation 47

2.5 Summary 47

References 49

CHAPTER 3 THEORY OF 'SERRODYNE' METHOD OF OPTICAL FREQUENCY TRANSLATION

3.1 Introduction 55

3.2 Optical Frequency Translation by Phase-Modulation 55

3.3 Optical Frequency Translation by Sawtooth Phase-Modulation 57

3.4 Analysis of Serrodyne Performance 58

3.4.1 Introduction 58
3.4.2 Effect of Non-Zero Flyback/Fall-time 60
3.4.3 Effect of Non-Optimum Sawtooth Amplitude 62
3.4.4 Effect of Non-Linear Sawtooth Phase Variation 63
3.4.5 Effect of Non-Optimum Operation Over 63

a Band/Range of Frequencies using a Constant Sawtooth Amplitude
3.4.6 Effects of the Presence of Amplitude Modulation in an Electro-Optic Phase Modulator 65

3.5 Examples of the Use of Optical Frequency-Translators in Fibre-Optic and Integrated Optical Sensor Systems 67

3.5.1 Introduction 67
3.5.2 Fibre-Optic Hydrophone 67
3.5.3 Fibre-Optic Gyroscope 69
3.5.4 Fibre-Optic Laser Doppler Velocimeter 72

3.6 Summary 74

Appendix 3.1 75

A3.1.1 Fourier Series - Recap 75
A3.1.2 Output Waveform Analysis for Stepped Phase Function 75
A3.1.2.1 Ideal N-Step Case 77
A3.1.2.2 Ideal 3-Step Case 83

Appendix 3.2 84

A3.2.1 Perfect Sawtooth Waveform 84
A3.2.2 Effect of Finite Flyback Time T_f 86

Appendix 3.3 89

A3.3.1 Sawtooth Waveform with 2nd Order Polynomial Non-Linearities and with Zero Flyback Time 89
A3.3.2 Sawtooth Waveform with 2nd Order Polynomial Non-Linearities and Finite Flyback Time T_f 91

References 94

CHAPTER 4 WAVEGUIDE FABRICATION TECHNIQUES

4.1 Introduction 96

4.2 Fabrication of Ti:$LiNbO_3$ Active Devices 96

4.2.1 Introduction 96
4.2.2 Mask Making 97
4.2.3 Substrate Preparation 98
4.2.4 Waveguide Pattern Preparation 101
4.2.5 Waveguide Formation 101
4.2.6 Titanium Indiffusion 103
4.2.7 Electrode Formation 106
4.2.8 End Polishing 107

4.2.9 Mounting the Samples 109
4.2.10 Summary on the Fabrication of Ti:$LiNbO_3$ Active Devices 110

4.3 Fabrication of Proton-Exchanged $LiNbO_3$ Slab, Stripe and Active Devices 111

4.3.1 Proton-Exchange Technique for $LiNbO_3$ Waveguide Fabrication - a Review 111
4.3.1.1 Introduction 111
4.3.1.2 What is the Proton Exchange Technique? 111
4.3.1.3 Mechanisms of the Process, Structural and Optical Characterization 112
4.3.1.4 Passive and Active Integrated Optical Devices 114
4.3.1.5 Problems with the Proton-Exchange Process for Optical Waveguide Formation 117
4.3.1.6 Summary on the Proton-Exchange Method of Optical Waveguide Formation in $LiNbO_3$ 118
4.3.2 Apparatus used for Proton-Exchange Experiments 119
4.3.3 Slab Waveguide, Stripe Waveguide, and Active Device Fabrication 121
4.3.3.1 Introduction 121
4.3.3.2 Fabrication of PE Slab Optical Waveguides by using Concentrated Benzoic Acid Melts 121
4.3.3.3 Fabrication of PE Slab Optical Waveguides by using Diluted Benzoic Acid Melts 124
4.3.3.4 Realisation of Active PE Devices 126
4.3.4 Summary - Realisations of Waveguides and Devices in $LiNbO_3$ by the Proton-Exchange Process 129

4.4 Overall Summary 129

Appendix 4.1 131

References 133

CHAPTER 5 THEORETICAL ANALYSIS AND EXPERIMENTAL EVALUATION OF SLAB AND STRIPE OPTICAL WAVEGUIDES WITH STUDIES OF ELECTRO-OPTIC ACTIVITY

5.1 Introduction 142

5.2 Theory of Planar Dielectric Optical Waveguides 143

5.2.1 Introduction 143
5.2.2 Step Index Waveguides 143
5.2.2.1 Ray Optics Treatment of Optical Waveguides 143
5.2.2.2 Electromagnetic Theory Treatment of Optical Waveguides 146
5.2.2.3 Comments on Step Index Waveguide Analysis 147
5.2.3 Treatment of Normalised Waveguide Dispersion Equations by Kolgenik and Ramaswamy 148
5.2.4 The IWKB Method of Waveguide Refractive Index Profile Determination 150

5.3 Theory of Stripe (Two Dimensional) Dielectric Optical Waveguides 153

5.3.1 Introduction 153
5.3.2 Summary of Published Analyses used in this Thesis 153
5.3.3 Marcatili's Analytical Solution 154
5.3.4 The Knox and Toulios Solution (Effective Index Method) 156

5.4 Techniques for Studying Slab and Stripe Optical Waveguide 158

5.4.1 Introduction 158
5.4.2 The Prism Coupler Technique 159
5.4.3 The End-Fire Coupling Technique 163

5.5 Ti:$LiNbO_3$ Slab Waveguide Measurements 164

5.6 Measurements on Slab Waveguides Formed by Proton-Exchange using Concentrated Benzoic Acid Melts 166

5.6.1 Measurement at λ= 632.8 nm (for X- and Z-cut Waveguides) 166
5.6.2 Measurement at λ= 1150 nm (for X-cut Waveguides) 169
5.6.3 Propagation Loss Measurements 169
5.6.3.1 Introduction 169
5.6.3.2 Intermodal Scattering 171
5.6.3.3 Out-of-Plane Scattering 172
5.6.3.4 In-Plane Scattering 174

5.7 Measurements on Slab Waveguides Formed by Proton-Exchange using Diluted Benzoic Acid Melts 175

5.7.1 Waveguide Refractive Index 175

Measurements
5.7.2 Waveguide Stability Study 177
5.7.3 Propagation Loss Measurements 177
5.7.4 Optical Damage Effects 178
5.7.5 Annealing Experiments 179
5.7.6 In-Plane and Intermodal Scattering Measurements 179
5.7.7 Electro-Optic Activity Study using Mach-Zehnder Interferometers 180

5.8 Summary 182

References 185

CHAPTER 6 EXPERIMENTAL RESULTS OF THE OPTICAL SERRODYNE FREQUENCY-TRANSLATORS

6.1 Introduction 189

6.2 Design of the Optical Phase-Modulators 189

6.2.1 Introduction 189
6.2.2 The Electro-Optic Effect 190
6.2.3 Theoretical Performance of q Lumped Electrode Type Optical Phase-Modulator 194
6.2.3.1 Phase-Modulator Voltage Requirements 194
6.2.3.2 Design of Lumped Electrodes for Phase-Modulator 196
6.2.4 Choice of Single-Mode Stripe Optical Waveguides 199
6.2.5 Design of Electrode Structures 200

6.3 Test Equipment and Experimental Techniques 202

6.3.1 Introduction 202
6.3.2 Self Heterodyne Experimental Arrangement 202
6.3.2.1 Main Experimental Setup 202
6.3.2.2 RF Radiation Problems 203
6.3.2.3 Optical Detectors and Detection Principles 204
6.3.3 Theoretical Calculation of the Self Heterodyne Detection Process 205

6.4 Evaluation of Optical Serrodyne Frequency-Translators 207

6.4.1 Introduction 207
6.4.2 Optical Evaluations of Phase-Modulators 207
6.4.2.1 Ti:$LiNbO_3$ Phase-Modulators 207
6.4.2.2 Proton Exchange $LiNbO_3$ 209

Phase-Modulators
6.4.3 Electrical Frequency Response of Phase-Modulators 213
6.4.4 Experimental Results for Titanium-Indiffused Phase-Modulators Driven by Sawtooth Electrical Waveforms 213
6.4.4.1 Determination of $V_{2\pi}$ Values 213
6.4.4.2 Effect of Non-Zero Flyback/Fall-Time 215
6.4.4.3 Effect of Non-Optimum Sawtooth Amplitude 217
6.4.4.4 Effect of Non-Optimum Operation Over a Band/Range of Frequencies using a Constant Sawtooth Amplitude 218
6.4.4.5 Presence of Amplitude Modulation in an Electro-Optic Phase-Modulator and its Effects 219
6.4.5 Experimental Results for Proton-Exchange Phase-Modulators Driven by Sawtooth Electrical Waveforms 221
6.4.5.1 Determination of $V_{2\pi}$ Values 221
6.4.5.2 Effect of Non-Zero Flyback/Fall-Time 223
6.4.5.3 Effect of Non-Optimum Sawtooth Amplitude 224
6.4.5.4 Effect of Non-Optimum Operation Over a Band/Range of Frequencies using a Constant Sawtooth Amplitude 225
6.4.5.5 Presence of Amplitude Modulation in an Electro-Optic Phase-Modulator and its Effects 226

6.5 Summary 227

Appendix 6.1 230

Appendix 6.2 232

A6.2.1 Background Theory 232
A6.2.2 Example of a Calculation to Obtain the Value of k 232

References 234

CHAPTER 7 CONCLUSIONS AND RECOMMENDATIONS

7.1 Introduction 237

7.2 The Use of Integrated Optics Technology for Fibre-Optic Communication and 238

Fibre-Optic Sensor Systems

7.3 Optical Frequency-Translators and Their Potential Use in Fibre-Optic Sensors 239

7.4 The Serrodyne Method of Frequency Translation 240

7.5 Optical Waveguide Fabrication Techniques 241

7.6 Optical Waveguide Analysis and Evaluations 243

7.7 Optical Serrodyne Frequency-Translators 247

7.8 Proposals for Future Work 251

7.8.1 Improvements to the Fabrication of Serrodyne Frequency-Translators 251

7.8.2 Improvements to the Evaluation Techniques for the Serrodyne Frequency-Translators 252

7.8.3 A Proposal for an Optical Frequency-Translator 253

7.9 Concluding Remarks 254

References 255

LIST OF PUBLICATIONS 256

SUMMARY

The work described in this thesis arose as a result of the need for an optical frequency translator in fibre and integrated optical sensors that employ heterodyne detection techniques. The devices were realised in X- and Y-cut $LiNbO_3$ using proton exchange and titanium indiffusion respectively.

Chapter 1 provides an outlook in the areas of optical communications, integrated optics and integrated optical sensor technology. The rapid advancement in the state of the art of integrated optical components in $LiNbO_3$ is reviewed with implications to the future development of fibre and integrated optical sensors.

A review of all known frequency translation methods using microwave, bulk optics and guided wave optics components was carried out and reported in Chapter 2. This was necessary to establish the performances, advantages and disadvantages of all the known methods. In performing the above review of frequency translators, it was found that the use of the serrodyne (or commonly known as sawtooth) method, which is the main subject of this thesis, is one of two attractive ways to realise a simple, low frequency (a few MHz) and high performance device. The integrated optical device used in this technique was the phase modulator. The other method is the use of the quadrature method in conjunction with an integrated optical Mach-Zehnder interferometer which is capable of generating frequency translations in the GHz regime.

Chapter 3 provides the necessary theoretical background to the understanding of the serrodyne technique for frequency translation. The Fourier analysis of the sawtooth waveform with respect to a number of non-ideal situations was carried out to predict sideband suppression levels. Examples of three uses of serrodyne frequency translators in fibre and integrated optical sensors are described.

Chapter 4 describes in detail the fabrication procedures for the realisation of titanium indiffused phase modulators in Y-cut $LiNbO_3$. A review of the proton exchange technique for realisation of passive and active devices in $LiNbO_3$ was carried out. Problems with waveguides and devices realised by concentrated benzoic acid melts were identified. A possible solution to all the above problems is to realise the waveguides using diluted benzoic acid melts (lithium benzoate being the dilutant used in all the experiments reported in this thesis). A complete fabrication procedure for the realisation of a proton exchange phase modulator is described in detail.

The use of various slab and stripe optical waveguide analysis models is described in Chapter 5. Special attention was given to the analysis of slab and stripe proton exchange waveguides. Techniques that were used extensively to characterise the optical performances of the slab and stripe optical waveguides are also described in detail. The experimental evaluations (at 633 nm) of optical waveguides realised by the proton exchange method (both by concentrated and diluted benzoic acid melts) are given in detail. The improved optical waveguide and device performances realised by diluted benzoic acid melts are stated.

Chapter 6 outlines the complete design procedures for the optical phase modulators used in this thesis. The test equipment and experimental techniques that were used to evaluate the phase modulators as serrodyne frequency translators are described. The evaluations of the serrodyne frequency translators using commercially available sawtooth waveform generators are presented. The various problems that resulted in the limited performance of the frequency translators are discussed and supported by experimental verifications. The experimental results were compared to the theoretically predicted results. Hence this establishes the main limiting factors for a high performance serrodyne frequency translator.

The main results of this work are summarized in Chapter 7. In addition proposals for improving the test procedures and the performances of serrodyne optical frequency translators are stated. Other possible candidates for use as optical frequency translators are discussed with descriptions on their implementations using integrated optical components.

CHAPTER 1 INTRODUCTION

1.1	Optical Communications, Integrated Optics, And Integrated Optical Sensor Technology: an Outlook	1
1.2	Progress on Active Lithium Niobate Devices	4
1.3	Objectives of this Investigation	7
1.4	Organisation of the Thesis	8
	References	10

CHAPTER 1

INTRODUCTION

1.1 Optical Communications, Integrated Optics, and Integrated Optical Sensor Technology: an Outlook

The first demonstration of the basic principle of optical communication using sunlight as the carrier was reported by A.G. Bell in 1880 [1.1]. In the present century, the invention of the laser in the early sixties [1.2] stimulated work in the entire field of optics and rekindled interest in optical communications.

The use of glass optical fibres in light-wave communication systems was first suggested by Kao and Hockham [1.3] in 1966. Since then, intense research in fabricating low-loss glass optical fibres, suitable sources and detectors has developed. The losses in optical fibres have been reduced from 20 dB/km [1.4] in 1970 at 632.8 nm to as low as 0.2 dB/km [1.5] at 1550 nm.

Advantages of using optical fibre communication systems include high bandwidth (i.e. high speed), small size, isolation from electromagnetic disturbances and low loss (i.e. possibly, long-distance communication links without any repeaters). Presently both multimode and single-mode optical communication systems are employed in local area networks and trunk links in Australia, France, Germany, Italy, Japan, U.K. and U.S.A.

One of the new areas of optics that has generated a tremendous amount of interest and activity is "integrated optics". The term "integrated optics" was coined by S.E. Miller in 1969 [1.6]. Since that time, a large number of industrial, university and government research laboratories have become involved in this field. Like integrated electronics, the goals of integrated optics have been set out as miniaturisation and integration of optical devices and systems. These miniature optical circuits could then be used in optical

communication systems where direct optical signal processing such as signal regeneration, signal modulation and signal switching could be effectively performed.

In their simplest form, integrated optical devices consist of a thin transparent waveguide layer on top of a glass or a ferroelectric material (e.g. $LiNbO_3$ or $LiTaO_3$) or III-V semiconductor. The layer is typically not more than a few microns thick and its refractive index is higher than the substrate refractive index. Due to these small dimensional requirements, integrated optical devices can be extremely small and could contain several components providing various different functions on the same chip, e.g. a $LiNbO_3$ balanced receiver consisting of components that will perform phase modulation, optical mixing, polarisation control and frequency translation on the same chip [1.7, 1.8] or a number of similar components performing one specific function e.g. a $LiNbO_3$ 4x4 [1.9] or an 8x8 [1.10] non-blocking IO switch matrix chip utilising sixteen or sixty-four IO directional couplers respectively. Recently, Duthie [1.11] demonstrated a reduced 8x8 Ti:$LiNbO_3$ switch array that needed only twenty-eight IO directional couplers. With the latter method, it is possible to realise a 16x16 IO switch array on a 3" $LiNbO_3$ wafer.

Integrated optics can be divided into two general areas. The first is called passive integrated optics. This area includes coupling, guiding, and splitting of optical waves without the aid of external fields or acoustic waves. The second area is active integrated optical devices. Here an external electric field or magnetic field or acoustic wave is used to provide for the modulation, deflection, variable coupling, etc., of optical waves. Several excellent review articles [1.12-1.26] and some recent books [1.27-1.32] give detailed discussions of the concepts of optical waveguiding and integrated optics technology.

Integrated optics can also be divided between monolithic integration and hybrid integration. In monolithic integrated optical circuits, the aim is to integrate sources, modulators, detectors and accompanying conventional electronics on the same substrate chip, i.e. in practice by using III-V compound semiconductors. This area is currently under intense research with very promising partial monolithic integrated optical circuits already demonstrated, e.g. a laser diode with driver and feedback control electronics [1.33, 1.34], and photodetectors with integral low-noise amplifiers [1.35, 1.36]. This area of research has opened new avenues in growth technology using metalorganic chemical vapour deposition (MOCVD) [1.37] and molecular beam epitaxy (MBE) [1.38]. A variety of optical devices, passive or active may be made from either AlGaAs alloy compounds grown epitaxially on GaAs substrates (for 850 nm operation) or InGaAsP alloy compounds grown on InP substrates (for 1300 nm or 1550 nm operation). The use of semiconductor technology for optical devices and systems has resulted in better transistors, e.g. high speed and high gain transistors have been made from the GaAs/AlGaAs material system [1.39, 1.40]. The possibility of forming optical devices and transistors on a common substrate allows the smooth combination of optics with electronics in the form of an integrated optical electronic circuit (IOEC). This in turn opens up new possibilities and new applications to modern electronics.

In hybrid integrated optical circuits, different substrates (e.g. glass, silicon, GaAs, InP, $LiNbO_3$, $LiTaO_3$) can be used to form sources, modulators and detectors. These may be interconnected by optical fibres or butt coupled to realise useful optical systems such as the integrated optical spectrum analyser [1.41] or the integrated optical fibre laser Doppler velocimeter [1.42]. Very low-loss (0.05 dB/cm) optical waveguides [1.43] have been realised on glass substrates using the ion-exchange [1.44] and laser annealing techniques. These devices can be used in passive systems. For

forming active devices like modulators and switches, the ferroelectric material lithium niobate ($LiNbO_3$) has been shown to be possibly the most promising material. In some special applications, $LiTaO_3$ may prove to be a useful material since it has been reported that it can handle about two orders of magnitude more optical power than $LiNbO_3$ before the onset of photorefractive damage [1.45].

Recently, integrated optics technology (hybrid) has been used to realise laboratory optical sensors units to measure temperature [1.46], micro-displacement [1.47], pressure [1.48], electromagnetic fields [1.49], moving objects [1.42], and rotation [1.50]. This new and important area of application for integrated optics, in part, stimulated work reported in this thesis.

1.2 Progress on Active Lithium Niobate Devices

$LiNbO_3$ and $LiTaO_3$ are ferroelectric materials which have several physical properties that make them suitable substrate materials for forming passive and active devices [1.31]. Some of the special physical properties include large electro-optic coefficients, a large piezoelectric effect, low acoustic propagation loss and large non-linear optic coefficients. Of the two materials, $LiNbO_3$ is more popular. For integrated optics this is primarily due to its high Curie temperature, i.e. 1150°C which facilitates the indiffusion of various metals without any effects on the ferroelectric domain structure. Optical waveguides have been fabricated in $LiTaO_3$ by the indiffusion of such metals as niobium [1.51, 1.52], copper [1.53-1.55], titanium [1.56, 1.57], and more recently zinc [1.58]. However, recently optical waveguides and electrooptic devices have been demonstrated in $LiTaO_3$ by proton exchange (PE) [1.59-1.63]. The devices realised by the proton exchange technique did not have to be repoled since the fabrication temperature was around 235°C, i.e. below the Curie temperature of $LiTaO_3$ (650°C). More experiments on proton exchange in $LiTaO_3$ in the form of optical waveguide

characterisations and electro-optic active devices have to be carried out to demonstrate the usefulness of this method.

The main drawback in using $LiNbO_3$ and $LiTaO_3$ is that lasers or detectors cannot be readily fabricated on the same substrate. A Nd:$LiNbO_3$ laser has been reported [1.64]. It was pumped by a Krypton laser at 735 nm to give a lasing wavelength of 1085 nm. The lasing action only lasted for 10 minutes due to the photorefractive effect. This could be overcome by maintaining the Nd:$LiNbO_3$ substrate at around 165°C. Room temperature laser diode-pumped cw laser oscillation in Nd:MgO:$LiNbO_3$ was recently reported by Cordova-Plaza et al with exhibited pumping thresholds as low as 2 mW and at an absorbed pump power of 9 mW produced a cw output of 2 mW, with the electric field parallel to the c axis, at λ = 1.085 μm [1.65]. The authors also reported that the photorefractive effects were practically eliminated by the addition of MgO to $LiNbO_3$ and by pumping at wavelengths above 810 nm. Photodetectors realised using silicon material have been fabricated on $LiTaO_3$ [1.66]. This may open up new avenues whereby the PE devices can be integrated with the detectors and hence form a useful subsystem.

The first optical waveguides in $LiNbO_3$ were formed by the outdiffision of lithium from the crystal surface [1.67]. To date, the most common technique for forming optical waveguides in $LiNbO_3$ has been by titanium indiffusion [1.68]. Using photolithographic methods, high quality, low-loss slab and stripe optical waveguides can be produced [1.69]. Recently, the proton-exchange technique has been employed to form slab and stripe optical waveguides in $LiNbO_3$ [1.70]. This method of optical waveguide fabrication will be discussed in detail in Chapter 4 of this thesis.

A wide variety of active devices have been realised in Ti:$LiNbO_3$ using both slab and stripe waveguides. Slab optical waveguides are used mainly for acousto-optic devices such as beam-deflectors [1.71] and the integrated

optical spectrum analyser (IOSA) [1.72]. For most electro-optic devices, stripe optical waveguides are commonly used.

The simplest electro-optic device fabricated in $LiNbO_3$ is the optical phase modulator (Figure 1.1). As can be seen, it consists of a straight lithium indiffused stripe waveguide in $LiNbO_3$ with a pair of electrodes positioned according to the orientation of the crystal axes and the propagating optical mode (quasi-TE or quasi-TM). This device was extensively used in the study of electro-optic frequency shifting of light [1.73], which is the main portion of the thesis. By a variation in the design of the electrodes, low-voltage (typically 2 volts), high extinction ratio (typically 20 dB) and high frequency (typically 1.2 GHz) optical amplitude modulators have been demonstrated [1.74] with a similar configuration to that for the phase-modulator.

The Y-junction switch/modulator (Figure 1.2) has been studied extensively by several researchers [1.75-1.77]. Essentially this device together with two phase modulators can be used to form a balanced bridge modulator/Mach-Zehnder interferometer (Figure 1.3). This device has been the subject of rigorous study due to its efficiency as an amplitude modulator at low to high frequencies (17 GHz) [1.78-1.80].

Other electro-optic modulators that have been reported in the literature include Bragg diffraction modulators [1.81], Bragg reflection modulators [1.82], and Bragg deflection switches [1.83].

Another interesting switch/modulator device is based on the directional coupler [1.84] (Figure 1.4). This device has two stripe waveguides in close proximity. Light that is launched into one arm of the device can be transferred to the other arm via the evanescent field coupling effect. Proper design of the interaction/coupling length, interwaveguide distance and suitable electrode configuration can result in a high performance intensity modulator [1.85], high frequency switch/modulator [1.86, 1.87], TE-

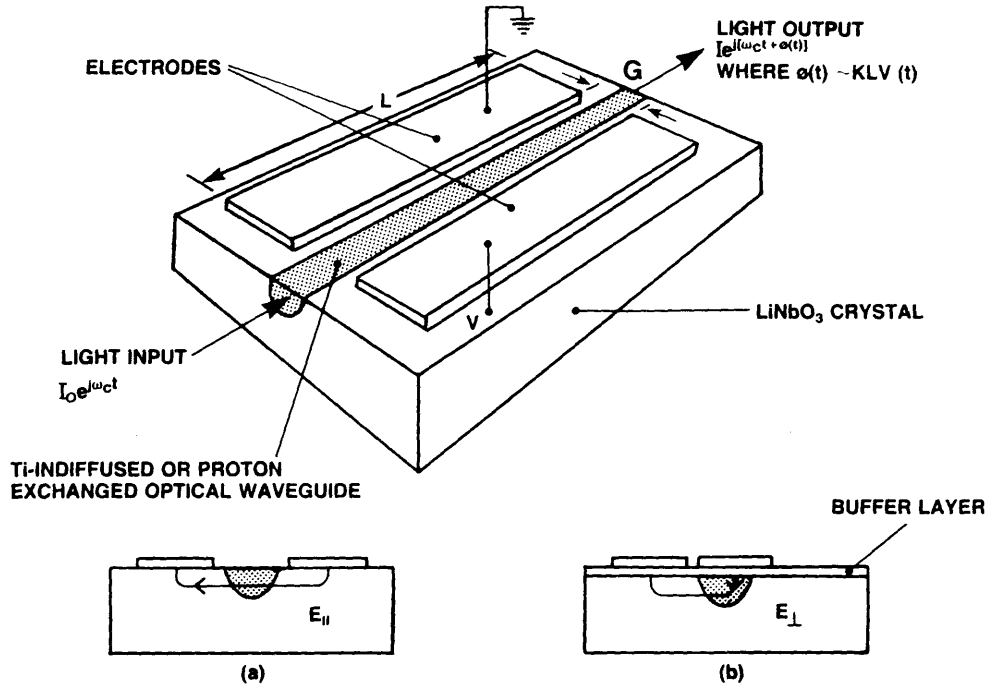

Figure 1.1 Schematic Of An Integrated Optical Phase Modulator

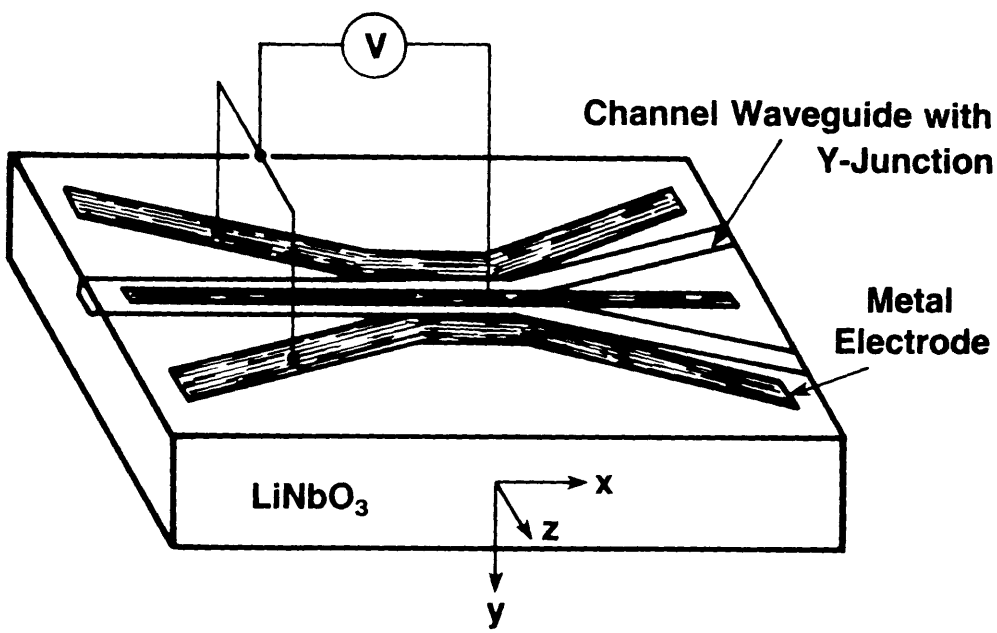

Figure 1.2 Schematic Of An Integrated Optical Y-Junction Switch/Modulator

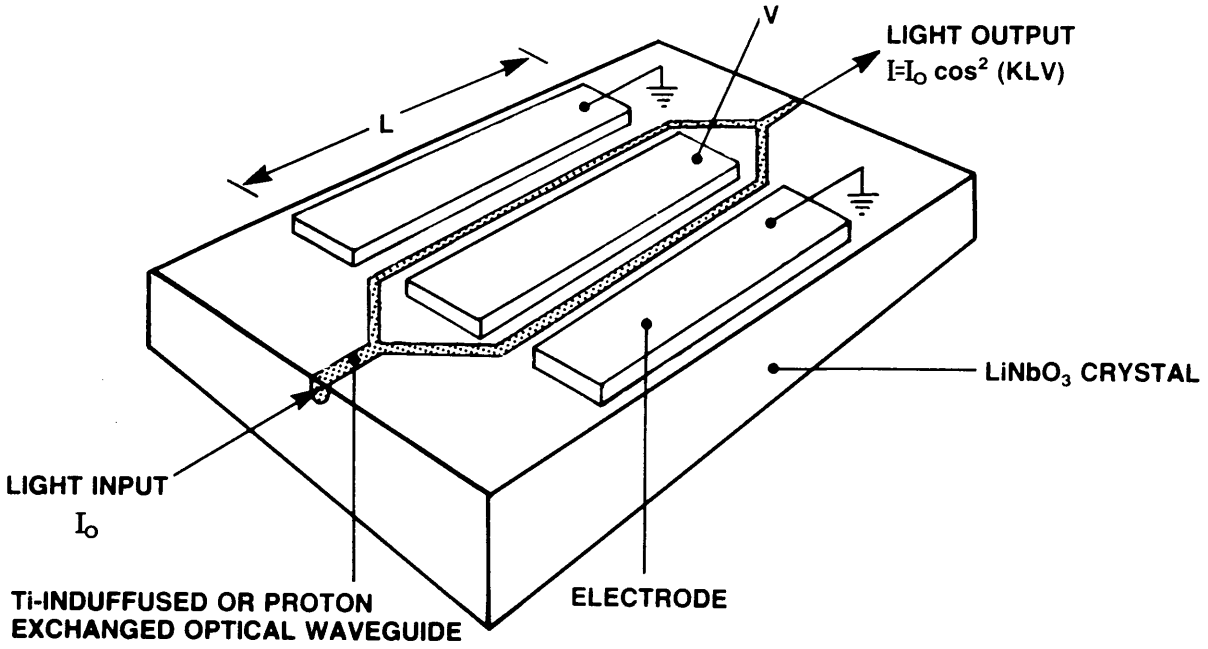

Figure 1.3 Schematic Of An Integrated Optical Mach-Zehnder Interferometer

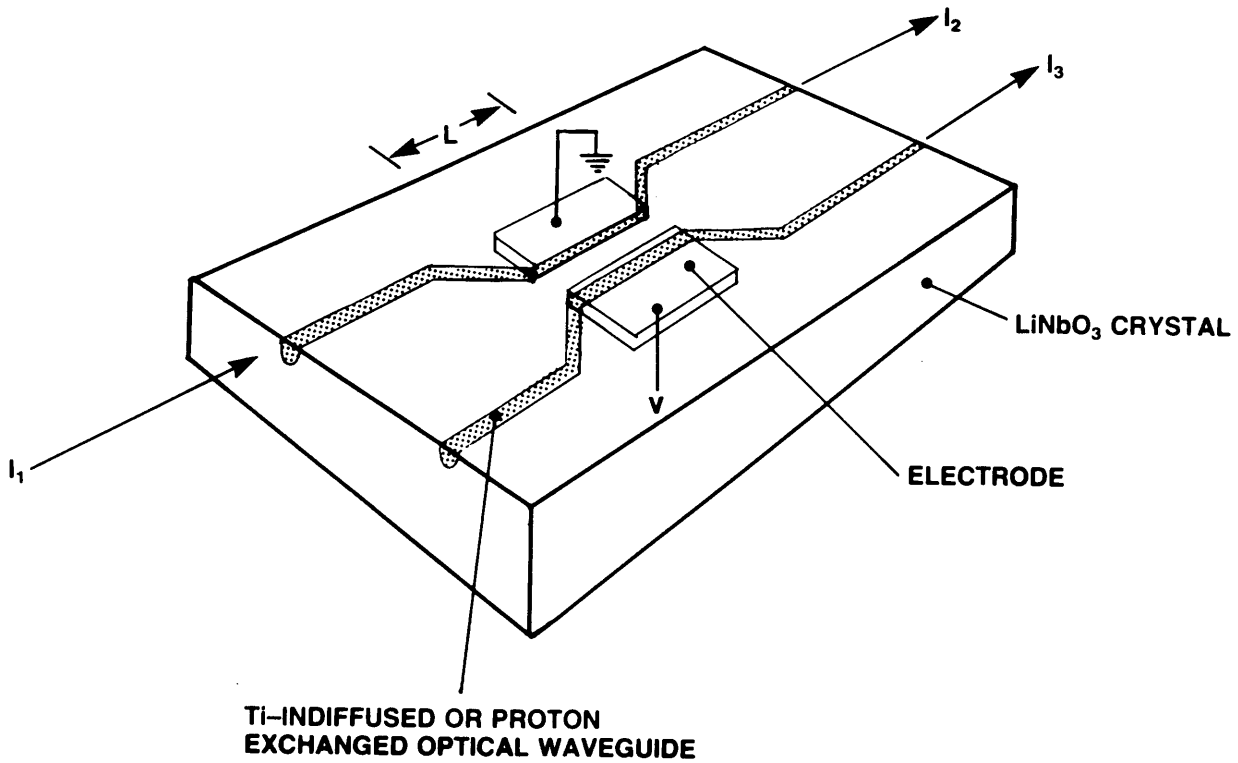

Figure 1.4 Schematic Of An Integrated Optical Directional Coupler Switch

TM mode controllers/converters [1.88] and polarisation independent filters [1.89]. Tapered velocity optical directional couplers showing 100% coupling have been realised and a computer analysis indicated that this type of directional coupler has greatly improved tolerance properties and does not, in particular, suffer from the severe tolerence restriction placed on velocity synchronism in conventional uniform directional couplers [1.90].

Recently the use of X-cut $LiNbO_3$ devices with the laser beam propagating in stripe waveguides along the Z-direction has received some attention. The main reason was that various researchers have found the waveguides to be resistant to optical damage effects [1.91, 1.92]. By propagating slightly off the Z-axis ($\cong 2°$) and having suitable electrode patterns, mode convertors without the need for a birefringence tuning voltage have also been demonstrated in X-cut, Ti:$LiNbO_3$ waveguides with propagation along the Z-axis [1.93].

The use of photodetection and electrical feedback to optical devices like the phase modulator and the Mach-Zehnder interferometer can result in bistable optical devices [1.94] and optical multivibrators [1.95] respectively.

Also, the large non-linear optical coefficients of the crystal have led to the demonstration of second harmonic generation [1.96] and parametric frequency generation [1.97]. More recently researchers are proposing the use of $KTiOPO_4$ (KTP) for non-linear optical applications such as SHG [1.98].

1.3 Objectives of this Investigation

The main aim of the work carried out for this thesis was to demonstrate an efficient optical frequency translator/shifter based on titanium-indiffused or proton-exchanged $LiNbO_3$ waveguide phase modulators at low frequencies (0-1 MHz) for future coherent integrated optical sensor systems. It is of prime importance to have an optical frequency translator that acts on light in a stripe optical waveguide. This device could well be an important

and integral part of an integrated optical sensor chip that employs heterodyne detection schemes for phase retrieval, for example in the optical fibre gyroscope [1.50].

In the search for a well confined optical waveguide mode for efficient phase modulation, the proton exchange (PE) technique of waveguide formation was investigated in detail for both X- and Z-cut $LiNbO_3$. Problems were identified with PE optical waveguides formed by concentrated benzoic acid. A possible solution to those problems identified was to realise the PE optical waveguide by diluting the benzoic acid with lithium benzoate. After the complete characterisation of PE slab waveguides formed by the above two methods, PE stripe optical phase modulators of the type shown in Figure 1.1 were fabricated using X-cut $LiNb0_3$. These devices were used and studied as optical frequency translators. In addition guided-wave Mach-Zehnder interferometers were fabricated by DMPE to enable the study of electrooptic activity.

1.4 Organisation of the Thesis

A completely up-to-date review of optical frequency translation techniques and practical demonstrations is presented in Chapter 2. The advantages and disadvantages of the various optical frequency shifting devices mentioned will be discussed in detail. Chapter 3 contains the basic theory of the "serrodyne" effect used for optical frequency translation presented in this thesis. The effects associated with a non-ideal sawtooth waveform are discussed. Other important problems like the amplitude modulation always present to some extent in optical phase modulators will also be discussed. Two waveguide fabrication techniques are presented in Chapter 4. The titanium indiffusion technique is described in the initial part of this chapter, while the latter part is concerned with the proton-exchange (PE) technique. As already mentioned, the PE experiments were divided into

two main activities, namely concentrated and diluted benzoic acid waveguide studies. An Appendix at the end of the chapter provides information on the important physical and chemical properties of $LiNbO_3$. The results of a detailed study of slab optical waveguiding on X-cut and Z-cut proton-exchanged waveguides using concentrated and diluted benzoic acid melts in $LiNbO_3$ are described in Chapter 5. Results of a theoretical and experimental study on stripe optical waveguides made by proton-exchange in $LiNbO_3$ are also described in the same chapter. In addition, results of the electrooptic behaviour of Mach-Zehnder interferometers formed by DMPE are presented at the end of Chapter 5. Experimental work on optical frequency translators (including the evaluation of the optical properties of stripe optical waveguides) employing the "serrodyne" effect using $Ti:LiNbO_3$ and $H^+:LiNbO_3$ phase modulators is presented in Chapter 6. Here the comparison of theoretical predictions and experimental results is made. Finally, Chapter 7 draws conclusions on the work performed and described in the thesis, with a few possible suggestions for future investigations towards the realisation of an efficient and high performance serrodyne frequency translator. In addition, a number of improved evaluation techniques for the optical translators are described.

REFERENCES

[1.1] A.G. Bell, "On the Production and Reproduction of Sound by Light", Proc. Am. Assn. Adv. Sci., Vol. 29, pp 115-136, 1880.

[1.2] A.L. Schawlow and C.H. Townes, "Infra-red and Optical Masers", Physical Rev., Vol. 112, No. 6, pp 1940-1949, 15 December 1958.

[1.3] K.C. Kao and G.A. Hockham, "Dielectric-Fibre Surface Waveguides for Optical Frequencies", Proc. IEE, Vol. 113, No. 7, pp 1151-1158, July 1966.

[1.4] F.P. Kapron, D.B. Keck and R.D. Maurer, "Radiation Losses in Glass Optical Waveguides", Appl. Phys. Lett., Vol 17, No. 10, pp 423-425, 15 November 1970.

[1.5] T. Miya, Y. Terunuma, T. Hosaka and T. Miyashita, "Ultimate Low-Loss Single-Mode Fibre at 1.55 μm", Electron. Lett., Vol. 15, No. 4, pp 106-108, 15 February 1979.

[1.6] S.E. Miller, "Integrated Optics: An Introduction", The Bell Syst. Tech. J., Vol. 48, No. 7, pp 2059-2069, September 1969.

[1.7] R.C. Booth, B.E. Daymond-John and P.G. Flavin, "Fabrication of $LiNbO_3$ Components for Coherent Optical Telecommunications", Colloquium on Integrated Optics, I.E.R.E. (U.K.), 12 June 1984

[1.8] R.C. Booth, "Private Communication", B.T.R.L., 1983.

[1.9] L. McCaughan and G.A. Bogert, "4x4 Ti:$LiNbO_3$ Integrated-Optical Crossbar Switch Array", Appl. Phys. Lett., Vol. 47, No. 4, pp 348-350, 15 August 1985.

[1.10] P. Granestrand, L. Thylen, B. Stoltz, K. Bergvall, W. Doldissen, H. Heindrich, and D. Hoffmann, "Strictly Non-Blocking 8x8 Integrated Optic Switch Matrix in $LiNbO_3$", Topical Meeting on Integrated & Guided-Wave Optics, Atlanta, Georgia, Paper WAA3, pp 4-5, 26-28 February 1986.

[1.11] P.J. Duthie, M.J. Wale, and I. Bennion, "A New Architecture for Large Integrated Optical Switch-Arrays", Topical Meeting on Photonic Switching, Incline Village, Nevada, pp ThD4-1 to ThD4-3, 18-20 March 1987.

[1.12] J.E. Goell, R.D. Standley and T. Li, "Optical Waveguides Bring Laser Communication Closer", Electronics, Vol. 43, No. 18, pp 60-67, 31 August 1970.

[1.13] J.E. Goell and R.D. Standley, "Integrated Optical Circuits", Proc. IEEEE, Vol. 58, No.10, pp 1504-1512, October 1970.

[1.14] S.E. Miller, "A Survey of Integrated Optics", IEEE J. Quantum Electron., Vol. QE-8, No. 2, pp 199-205, February 1972.

[1.15] R. Ulrich, "Thin Dielectric Films for Integrated Optics", J. Vac. Sci. Technol., Vol 11, No. 1, pp 156-162, January/February 1974.

[1.16] P.K. Tien, "Integrated Optics", Scientific America, Vol. 230, No. 4, pp 28-35, April 1974.

[1.17] H.F. Taylor and A. Yariv, "Guided Wave Optics", Proc. IEEE, Vol 62, No. 8, pp 1044-1060, August 1974.

[1.18] H. Kogelnik, "An Introduction to Integrated Optics", IEEE Trans. Microwave Theory and Techniques, Vol. MTT-23, No. 1, pp 2-16, January 1975.

[1.19] P.K. Tien and A.A. Ballman, "Research in Optical Films for the Applications of Integrated Optics", J. Vac. Sci. Technol., Vol. 12, No. 4, pp 892-904, July/August 1975.

[1.20] E.M. Conwell, "Integrated Optics", Physics Today, pp 48-59, May 1976.

[1.21] P.K. Tien, "Integrated Optics and New Wave Phenomena in Optical Waveguides", Rev. Mod. Phys., Vol. 49, No. 2, pp 361-420, April 1977.

[1.22] H. Kogelnik, "Review of Integrated Optics", Fibre and Integrated Optics, Vol. 1, No. 3, pp 227-241, July 1978.

[1.23] M.J. Brookfield, "Integrated Optics - A Future Technique In Communications", Commun. International, Vol. 5, No. 8, pp 21-27, August 1978.

[1.24] A Yariv, "Guided Wave Optics", Scientific America, Vol. 240, No. 1, pp 64-72, January 1979.

[1.25] P.K. Cheo, "Integrated Optical Devices and Applications", J. Phys. E: Sci. Instrum., Vol. 12, pp 2-12, 1979.

[1.26] P.J.R. Laybourn and J. Lamb, "Integrated Optics: A Tutorial Review", The Radio and Electronic Engineer, Vol. 51, No. 7/8, pp 397-413, July/August 1981.

[1.27] D. Marcuse, Ed., "Integrated Optics", IEEE Press, N.Y., 1973.

[1.28] D.B. Ostrowsky, Ed., "Fibre and Integrated Optics", Plenum Press, N.Y., 1979.

[1.29] T. Tamir, Ed., "Integrated Optics", Springer-Verlag, Heidelberg, 1979.

[1.30] R.G. Hunsperger, "Integrated Optics: Theory and Technology",Springer-Verlag, Berlin, 1982.

[1.31] S. Martellucci and A.N. Chester, Eds., "Integrated Optics: Physics and Applications", Plenum Press, N.Y., 1983.

[1.32] Lynn D. Hutcheson (Ed.), "Integrated Optical Circuits and Components - Design and Applications", Marcel Dekker, Inc., N.Y., 1987.

[1.33] N. Bar-Chaim, K.Y. Lau, I. Ury and A. Yariv, "Monolithic Opto-electronic Integration of a GaAlAs Laser, A Field-Effect Transistor and a Photodiode", Appl. Phys. Lett., Vol. 44, No. 190, pp 941-943, 15 May 1984.

[1.34] O. Wada, T. Sanada, H. Nobuhara, M. Kuno, M. Makiuchi, T. Fujii, and T. Sakurai, "Four-Channel AlGaAs/GaAs OEIC Transmitter Array for Optoelectronic Switch Application", ECOC, Barcelona, Spain, pp 159-162, 1986.

[1.35] K. Kasahara, J. Hayashi, K. Makita, K. Taguchi, A. Suzuki, H. Nomura, "Monolithically Integrated $In_{0.53}Ga_{0.47}As$ PIN/InP-MISFET Photoreceiver", Electron. Lett., Vol. 20, No. 8, pp 314-315, 12 April 1984.

[1.36] S. Hata, H. Yasaka, K. Nakashima, H. Asahi, and S. Uehara, "Monolithic Integration of a Schottky Photodiode and MESFET Using an InAlAs/InGaAs Heterostructure", ECOC, Barcelona, Spain, pp 123-126, 1986.

[1.37] J.P. Hirlz, M. Razeghi, M. Bonnet, and J.P. Duchemin, "$Ga_{0.47}In_{0.53}As$/InP and GaInAsP/InP Double Heterostructures Grown by Low-Pressure Metal-Organic Vapour Phase Epitaxy" in "GaInAsP Alloy Semi-Conductors" T.P. Pearsall, Ed., John Wiley and Sons, N.Y., 1982.

[1.38] C.E.C. Wood, "III-V Alloy Growth by Molecular-Beam Epitaxy" in "GaInAsP Alloy Semi-Conductors" T.P. Pearsall, Ed., John Wiley and Sons, N.Y., 1982.

[1.39] H. Ohno and J. Barnard, "Field-Effect Transistors" in "GaInAsP Alloy Semi-Conductors", T.P. Pearsall, Ed., John Wiley and Sons, N.Y., 1982.

[1.40] M.R. Stiglitz, "Will Gallium Arsenide Take Over Where Silicon Leaves Off", Microwave Journal, pp 24-34, August 1985.

[1.41] S.M. Al-Shukri, A. Dawar, R.M. De La Rue, G.F. Doughty, N. Finlayson, and J. Singh, "Integrated Optical Techniques For Acousto-Optic Receivers", in Advanced Signal Processing, Edited by D.J. Creasey, Peter Peregrinus Ltd., I.E.E., London, pp 62-71, 1985.

[1.42] H. Toda, M. Haruna, and H. Nishihara, "Optical Integrated Circuit for a Fibre Laser Doppler Velocimeter", J. Lightwave Tech., Vol. LT-5, No. 7, pp 901-905, July 1987.

[1.43] S. Dutta, H.E. Jackson and J.T. Boyd, "Use of Laser Annealing to Achieve Low Loss in Corning 7059 Glass, ZnO, Si_3N_4 , Nb_2O_5 , and Ta_2O_5 Optical Thin Film Waveguides", SPIE Vol. 321, Integrated Optics II, pp 23-28, 28-29 January 1982.

[1.44] G. Stewart, C.A. Millar, P.J.R. Laybourn, C.D.W. Wilkinson and R.M. De La Rue, "Planar Optical Waveguides Formed by Silver-Ion Migration in Glass", IEEE J. Quantum Electron., Vol. QE-13, No. 4, pp 192-200, April 1977.

[1.45] H.J. Levinstein, A.A. Ballman, R.T. Denton, A. Ashkin, and J.M. Dziedzic, "Reduction of the Susceptibility to Optically Induced Index Inhomogeneities in $LiNbO_3$ and $LiTaO_3$", J. Appl. Phys., Vol. 38, No. 8, pp 3101-3102, July 1967.

[1.46] L.M. Johnson, F.J. Leonberger and G.W. Pratt, "Integrated Optical Temperature Sensor", Appl. Phys. Lett., Vol. 41, No. 2, pp 134-136, 15 July 1982.

[1.47] M. Izutsu, A. Enokihara and T. Sueta, "Optical Waveguide Micro-Displacement Sensor", Electron. Lett., Vol. 18, No. 20, pp 867-868, 30 September 1982.

[1.48] M. Izutsu, A. Enokihara, N. Mekoda and T. Sueta, "Optical Waveguide Pressure Sensor", Second European Conf. on Integrated Optics, Florence, Italy, IEE Conf. No. 227, pp 144-147, 17-18 October 1983.

[1.49] C.H. Bulmer, W.K. Burns and R.P. Moeller, "Linear Interferometric Waveguide Modulator for Electromagnetic-Field Detection", Opt. Lett., Vol. 5, No. 5, pp 176 - 178, May 1980.

[1.50] D. Eberhard and E. Voges, "Fibre Gyroscope With Phase-Modulated Single-Sideband Detection", Opt. Lett., Vol. 9, No. 1, pp 22-24, January 1984.

[1.51] J.M. Hammer and W. Phillips, "Low-Loss Single-Mode Optical Waveguides And Efficient High Speed Modulators Of $LiNb_xTa_{1-x}O_3$ on $LiTaO_3$", Appl. Phys. Lett., Vol. 24, No. 11, pp 545-547, 1 June 1974.

[1.52] V. Ramaswamy and R.D. Standley, "Growth Strains And Losses In Nb-Diffused $LiTaO_3$ Optical Film Waveguides", Appl. Phys. Lett., Vol. 26, No. 1, pp 10-12, 1 January 1975.

[1.53] J. Noda, T. Saku, and N. Uchida, "Fabrication Of Optical Waveguiding Layer In $LiTaO_3$ By Cu Diffusion", Appl. Phys. Lett., Vol. 25, No. 5, pp 308-310, 1 September 1974.

[1.54] Y. Okamura, S. Yamamoto, and T. Makimoto, "Electro-Optic Guided-To-Radiation Mode Conversion In Cu-Diffused $LiTaO_3$ Waveguide With Periodic Electrodes", Appl. Phys. Lett., Vol. 32, No. 3, pp 161-163, 1 February 1978.

[1.55] S. Yamamoto, K. Shibata, and T. Makimoto, "Electrooptic Control Of Radiation Loss In Off-Axial Propagation In A $LiTaO_3$ Waveguide", Opt. Commun., Vol. 31, No. 2, pp 139-142, November 1979.

[1.56] S.K. Sheem, W.K. Burns, and A.F. Milton, "Leaky-Mode Propagation In Ti-Diffused $LiNbO_3$ And $LiTaO_3$ Waveguides", Opt. Lett., Vol. 3, No. 3, pp 76-78, September 1978.

[1.57] V.V. Atuchin, K.K. Ziling, and D.P. Shipilova, "Investigation Of Optical Waveguides Fabricated By Titanium Diffusion In $LiTaO_3$", Sov. J. Quantum Electron., Vol. 14, No. 5, pp 671-674, May 1984.

[1.58] D.W. Yoon and O. Eknoyan, "Characterization Of Vapor Diffused Zn:$LiTaO_3$ Optical Waveguides", J. Lightwave Technology, Vol. 6, No. 6, pp 877-880, June 1988.

[1.59] Yu. L. Kopylov, V.B. Kravchenko, E.N. Mirgorodskaya, and A.V. Bobylev, "Fabrication of Waveguides in Lithium Niobate and Tantalate by Proton Diffusion from a Benzoic Acid Solution", Sov. Tech. Phys. Lett., Vol. 9, No. 5, pp 259-260, May 1983.

[1.60] S.M. Al-Shukri, J.F. Duffy, R.M. De La Rue, G. Mazzi, A. Carnera, and M.N. Armenise, "Single-Mode Planar and Stripe Waveguides by Proton Exchange in Lithium Tantalate and Lithium Niobate", SPIE Vol. 651, Integrated Optical Circuit Engineering III, pp20-25, 16-18 April 1986.

[1.61] W.B. Spillman, Jr., N.A. Sanford, and R.A. Soref, "Optical Waveguides in $LiTa0_3$ Formed By Proton Exchange", Opt. Lett., Vol. 8, No. 9, pp497-498, September 1983.

[1.62] K.K. Wong, A.C. O'Donnell, I.A. Wood, and N.J. Parsons, "Integrated Optical Mach-Zehnder Interferometers in $LiTa0_3$ Fabricated By Proton

Exchange", Proc. of the Fourth European Conf. on Integrated Optics, Glasgow, Scotland, pp 123-126, 11-13 May 1987.

[1.63] K. Tada, T. Murai, T. Nakabayashi, T. Iwashima, and T. Ishikawa, "Fabrication of $LiTaO_3$ Optical Waveguide By H^+ Exchange Method", Jap. J. Appl. Phys., Vol. 26, No. 3, pp 503-504, March 1987.

[1.64] I.P. Kaminow and L.W. Stulz, "Nd:$LiNbO_3$ Laser", IEEE J. Quantum Electron., Vol. QE-11, No. 6, pp 306-308, June 1975.

[1.65] A. Cordova-Plaza, T.Y. Fan, M.J.F. Digonnet, R.L. Byer, and H.J. Shaw, "Nd:MgO:$LiNbO_3$ Continuous-Wave Laser pumped By A Laser Diode", Opt. Lett., Vol. 13, No. 3, pp 209-211, March 1988.

[1.66] R.E. Reedy and S.H. Lee, "Silicon Photodetector Integrated on a Lithium Tantalate Substrate", Appl. Phys. Lett., Vol. 44, No. 1, pp 19-21, 1 January 1984.

[1.67] I.P. Kaminov and J.R. Carruthers, "Optical Waveguiding Layers in $LiNbO_3$ and $LiTaO_3$", Appl. Phys. Lett., Vol. 22, No. 7, pp 326-328, 1 April 1983.

[1.68] R.V. Schmidt and I.P. Kaminow, "Metal-Diffused Optical Waveguides in $LiNbO_3$", Appl. Phys. Lett., Vol. 25, No. 8, pp 458-460, 15 October 1974.

[1.69] A.D. McLachlan, "Theoretical and Experimental Investigations of Titanium Diffused Lithium Niobate Optical Waveguides", PhD Thesis, University of Glasgow, Dept. of Electronics and Elect.Enging., January 1981.

[1.70] J.L. Jackel, C.E. Rice and J.J. Veselka, "Proton Exchange for High Index Waveguides in $LiNbO_3$", Digest of Topical Meeting on Integrated and Guided-Wave Optics, Pacific Groove, Post-Deadline Paper, PDP1-1 to PDP1-4, 6-8 January 1982.

[1.71] Y.K. Lee and S. Wang, "Electo-optic Bragg-Deflection Modulators: Theoretical and Experimental Studies", Appl. Opt., Vol. 15, No. 6, pp 1565-1572, June 1976.

[1.72] D. Mergerian, E.C. Malarkey, R.P. Pautienus, J.C. Bradley, G.E. Marx, L.D. Hutcheson and A.L. Kellner, "Operational Integrated Optical R.F. Spectrum Analyser", Appl. Opt., Vol. 19, No. 18, pp 3033-3034, 15 September 1980.

[1.73] K.K. Wong and S. Wright, "An Optical Serrodyne Frequency Translator", First European Conference on Integrated Optics, London, IEE Conf. Proc., No. 201, pp 63-65, 14-15 September 1981.

[1.74] B. Bjortorp, "Active and Passive Devices in Lithium Niobate by Single and Double Diffusion of Titanium", PhD Thesis, University of Glasgow, Dept. of Electronics and Electrical Engineering, August 1983.

[1.75] H. Sasaki and R.M. De La Rue, "Electro-Optic Y-junction Modulator/Switch", Electron. Lett., Vol. 12, No. 18, pp 459-460, 2 September 1976.

[1.76] H. Sasaki and I. Anderson, "Theoretical and Experimental Studies on Active Y-Junctions in Optical Waveguides", IEEE J. Quantum Electron., Vol. QE-14, No. 11, pp 883-892, November 1978.

[1.77] M. Izutsu, Y. Nakai and T. Sueta, "Operation Mechanism of the Single-Mode Optical-Waveguide Y-Junction", Opt. Lett., Vol. 7, No. 3, pp 136-138, March 1982.

[1.78] Y. Ohmachi and J. Noda, "Electro-Optic Light Modulator with Branched Ridge Waveguide", Appl. Phys. Lett., Vol. 27, No. 10, pp 544-546, 15 November 1975.

[1.79] F. Auracher and R. Keil, "Design Considerations and Performance of Mach-Zehnder Waveguide Interferometers", Wave Electron., Vol. 4, pp 129-140, 1980.

[1.80] C.M. Gee, G.D. Thurmond and H.W. Yen, "17 GHz Bandwidth Electro-Optic Modulator", Appl. Phys. Lett., Vol. 43, No. 11, pp 998-1000, 1 December 1983.

[1.81] G.L. Tangonan, D.L. Persechini, J.F. Lotspeich and M.K. Barnoski, "Electro-optic Diffraction Modulation in Ti-Diffused $LiTa0_3$", Appl. Opt., Vol. 17, No. 20, pp 3259-3263, 15 October 1978.

[1.82] J.C. An, Y. Cho and Y. Matsuo, "Electro-Optic Distributed Bragg-Reflection Modulators for Integrated Optics", IEEE J. Quantum Electron., Vol. QE-13, No. 4, pp 206-208, April 1977.

[1.83] B. Chen and C.M. Meijer, "Bragg Switch for Optical Channel Waveguides", Appl. Phys. Lett., Vol. 33, No. 1, pp 33-35, 1 July 1978.

[1.84] R.V. Schmidt and H. Kogelnik, "Electro-Optically Switched Coupler with Stepped $\Delta\beta$ Reversal using Ti-diffused $LiNb0_3$ Waveguides", Appl. Phys. Lett., Vol. 28, No. 9, pp 503-506, 1 May 1976.

[1.85] J.S. Wilkinson and M.G.F. Wilson, "Design and Performance Of a Low Crosstalk Directional Coupler Switch", IEE Proc., Vol. 131, Pt. H, No. 5, pp 304-308, October 1984.

[1.86] R.C. Alferness, C.H. Joyner, L.L. Buhl and S.K. Korotky, "High-Speed Travelling-Wave Directional Coupler Switch/Modulator for λ= 1.32 μm", IEEE J. Quantum Electron., Vol. QE-19, No. 9, pp 1339-1341, Sepetember 1983.

[1.87] S.K. Korotky, G. Eisenstein, R.S. Tucker, J.J. Veselka, and G. Raybon, "Optical Intensity Modulation to 40 GHz Using a Waveguide Electro-Optic Switch", Appl. Phys. Lett., Vol. 50, No. 23, pp 1631-1633, 8 June 1987.

[1.88] R.C. Alferness, and L.L. Buhl, "Electro-Optic Waveguide TE-TM Mode Converter with Low Drive Voltage", Opt. Lett., Vol. 5, No. 11, pp 473-475, November 1980.

[1.89] R.C. Alferness, and L.L. Buhl, "Polarisation Independent Optical Filter Using Interwaveguide TE/TM Conversion", Appl. Phys. Lett., Vol. 39, No. 2, pp 131-134, 15 July 1981.

[1.90] M.G.F. Wilson and G.A. Teh, "Tapered Optical Directional Coupler", IEEE Trans. on Microwave Theory and Techniques, Vol. MTT-23, No. 1, pp 85-92, January 1975.

[1.91] R.L. Holman, J.R. Busch, C.M. Verber, V.E. Wood, N.F. Hartman, and P.J. Cressman, "Z-Axis Propagation and the Avoidance of Optical Damage in Lithium Niobate Waveguides", Seventh Topical Meeting on Integrated & Guided-Wave Optics, Kissimmee, Florida, pp WC2-1 to WC2-4, 24-26 April 1986.

[1.92] S. Thaniyavarn, "Wavelength-Independent, Optical-Damage-Immune $LiNbO_3$ TE-TM Mode Convertor", Opt. Lett., Vol. 11, No. 1, pp 39-41, January 1986.

[1.93] A. Donaldson and K.K. Wong, "Phase-Matched Mode Converter in $LiNbO_3$ Using Near-Z-Axis Propagation", Electron. Lett., Vol. 23, No. 25, pp 1378-1379, 3 December 1987.

[1.94] P.W. Smith, I.P. Kaminow, P.J. Maloney and L.W. Stulz, "Integrated Bistable Optical Devices", Appl. Phys. Lett., Vol. 33, No. 1, pp 24-26, 1 July 1978

[1.95] A. Neyer and E. Voges, "Hybrid Electro-Optical Multivibrator Operating by Finite Feedback Delay", Electron. Lett., Vol. 18, No. 2, pp 59-60, 21 January 1982.

[1.96] N. Uesugi, K. Daikoku and K. Kubota, "Electric Field Tuning of Second-Harmonic Generation in a Three-Dimensional $LiNbO_3$ Optical Waveguide", Appl. Phys. Lett., Vol. 34, No. 1, pp 60-62, 1 January 1979.

[1.97] N. Uesugi, "Parametric Difference Frequency Generation in a Three-Dimensional $LiNbO_3$ Optical Waveguide", Appl. Phys. Lett., Vol. 36, No. 3, pp 178-180, 1 February 1980.

[1.98] J.D. Bierlein, A. Ferretti, L.H. Brixner, and W.Y. Hsu, "Fabrication and Characterization of Optical Waveguides in $KTiOPO_4$", Appl. Phys. Lett., Vol. 50, No. 18, pp 1216-1218, 4 May 1987.

CHAPTER 2 REVIEW OF OPTICAL FREQUENCY TRANSLATION TECHNIQUES USING GUIDED-WAVE OPTICS TECHNOLOGY

2.1 Introduction 17

2.1.1 Microwave Frequency Translation 18
2.1.2 Optical Frequency Translation using Bulk Optical Devices 19
2.1.3 Optical Frequency Translation using Guided-Wave Optics Technology 21

2.2 Integrated Optics Acousto-Optic (Bragg) Interactions for Optical Frequency Translation 24

2.2.1 Integrated Optical Waveguide X-Junction Frequency Shifter (Tsai et al) 25
2.2.2 Integrated Optical Waveguide X-Junction Frequency Shifter (Von Helmolt et al) 27
2.2.3 Integrated Optic Frequency Shifters with SAWs (Schaffer and Peterman) 29
2.2.4 Discussions of Optical Frequency Translators Realised by Acousto-Optic (Bragg) Interactions 31

2.3 Integrated Optical Electro-Optic Frequency-Translators 32

2.3.1 Quadrature Method of Frequency Translation 32
2.3.1.1 Proposal by Culshaw And Wilson 33
2.3.1.2 Demonstrations by John And Wilson 35
2.3.1.3 Demonstration by Izutsu et al 36
2.3.1.4 Discussions of Optical Frequency-Translators Realised by the Quadrature Method 37
2.3.2 Electro-Optical Bragg Array Optical Frequency-Translator 38
2.3.3 Electro-Optical Frequency-Translator by Heismann And Ulrich 40
2.3.4 Integrated-Optical Channel-Waveguide Frequency-Translator by Johnson et al 42
2.3.5 Serrodyne Optical Frequency-Translators 43
2.3.6 Discussions of Optical Frequency-Translators Realised by Electro-Optic Methods 44

2.4 Single-Mode Optical Fibre Frequency-Translators 45

2.4.1 Acousto-Optic Realisation 46

2.4.2 Serrodyne Realisation 47

2.5 Summary 47

References 49

CHAPTER 2

REVIEW OF OPTICAL FREQUENCY TRANSLATION TECHNIQUES USING GUIDED-WAVE OPTICS TECHNOLOGY

2.1 Introduction

In this chapter, the basic concept of frequency shifting or translation is introduced. The historical development and use of frequency translators for microwave systems applications is discussed. Frequency translators at optical wavelengths are introduced initially in terms of realisations using bulk optical devices. Then, taking account of the advances in integrated and guided-wave optics technology, currently proposed and demonstrated optical frequency shifters are discussed in detail and predicted and experimentally achieved performances will be given.

A frequency translator can be defined as a device that will act upon an input electrical signal (low frequency to microwave frequency) or an optical signal having a certain frequency so as to produce an output signal where frequency is shifted by some desired amount from that of the input. Ideally, this will be accomplished without loss of power and without the generation of unwanted frequencies.

Frequency translators operate on the principle that when an input signal of the form:

$$e_{in} = \sin(2\pi f_{in} t + \theta) \qquad (2.1)$$

is subjected to a modulating signal θ which varies linearly with time such as:

$$\theta = kt = (2\pi f_m)t \qquad (2.2)$$

the resultant output signal is:

$$e_{in} = \sin 2\pi(f_{in} + f_m)t \qquad (2.3)$$

Equation (2.3) illustrates an ideal frequency translation from an input frequency, f_{in}, to a new frequency $(f_{in} + f_m)$. Some often-used synonyms for the name frequency translator are frequency shifter, frequency converter, single-sideband modulator and synchrodyne.

As can be seen from Equation (2.1), practical frequency translation generally involves some form of modulation process that will result in the generation of upper and lower sidebands at frequencies differing from the carrier frequency by an integer multiple of the modulation frequency. The aim in a frequency translation device is to achieve a lossless frequency translation to the first sideband (i.e. the required shifted frequency) with complete suppression of the carrier, complete suppression of the first symmetrical sideband and suppression of all other sidebands as far as possible. It is also desirable to accomplish this with as low a modulation power as possible. Generally, and particularly at optical carrier frequencies, the translation frequency is only a small percentage of the carrier frequency [2.1, 2.2].

2.1.1 Microwave Frequency Translation

Many devices producing microwave and optical frequency translation have been reported in the literature but all fall short of the ideal situation in one respect or another. For microwave frequency translation, the two most common and widely used modulation techniques are linear [2.3] and serrodyne [2.4] phase modulation. The simplest concept is the continuous linear phase shifter first demonstrated by Fox in 1947 [2.3]. This was a rotating mechanical device with the frequency shift limited, at best, to a few kilohertz. Cachceris demonstrated an electronic version of the Fox

phase shifter in 1954 [2.5] giving frequency shifts of the order of ± 20 kHz, with carrier suppression greater than 20 dB and overall sideband suppression greater than 35 dB. In 1956, Soohoo published a description of the application of a sawtooth drive to a Faraday-rotation type phase shifter to effect frequency translation [2.4]. Cumming, in 1957, employed linear sawtooth modulation of transit time on a klystron to produce frequency shifts from sub-audio frequencies to 57 MHz, with at least 20 dB suppression of undesired components and a conversion loss of less than 1 dB [2.6].

Another approach to achieving frequency translation is based on the balanced modulator principle first described in the MIT Radiation Laboratory Series [2.7]. This principle was applied by Clavin in 1962 to demonstrate a microwave single-sideband modulator or microwave frequency shifter using ferrite devices as balanced modulators [2.8].

In the 1950's and 1960's, microwave frequency translators were used extensively in a wide variety of microwave applications [2.6] including Doppler simulation and correction for testing Doppler radars, frequency shifting in many RF microwave relay stations, reference wave generation in coherent moving target indicator (MTI) radar transmitters, electrical scanning of antennas and frequency off-setting for homodyne measurement of attenuation, phase-shift, reflection-coefficient, RF-leakage and antenna patterns.

2.1.2 Optical Frequency Translation using Bulk Optical Devices

The invention of the laser in the early sixties [2.9] prompted research in optical heterodyne detection [2.10] schemes for communications, heterodyne interferometers [2.2, 2.11, 2.12], laser Doppler techniques for velocity measurements [2.13], molecular spectroscopy [2.14] and infra-red radar [2.15]. In all the schemes, some method of performing optical frequency shifting has to be used. There are two major approaches to the

control of optical frequency. One is by changing the laser frequency [2.16] and the other is shifting the frequency by employing an external modulator of some kind. In the latter approach, generation of a continuous shift of useful magnitude (up to, say, a few MHz) with high efficiency, there are three practical methods available: (i) diffraction by a rotating grating [2.17], (ii) diffraction by an acousto-optic Bragg cell [2.18-2.20] and (iii) devices depending on electro-optic effects [2.21-2.24].

Of the three methods mentioned, frequency shifting by electro-optic devices has the following advantages: an absence of moving parts, accurate control of frequency, the possibility of obtaining rapid frequency changes if required, and a wide bandwidth.

There are several ways of producing an optical frequency shift which depend on the use of the electro-optic effect. In its simplest form, an electro-optic modulator produces a change in the optical path difference between the two perpendicular polarisation components of a light beam and this path difference can be controlled by an applied voltage.

There are two basic types of electro-optic effect, the linear (Pockels) effect and the quadratic (Kerr) effect. Most modern electro-optic devices use materials which exhibit a linear dependence of retardation on electric field. This so-called 'Pockels effect' is only possible in crystals having a structure that lacks a centre of symmetry. The most commonly used materials are ammonium dihydrogen phosphate (ADP), potassium dihydrogen phosphate (KDP) [2.21], potassium dideuterium phosphate (KD*P) and lithium niobate ($LiNb0_3$) [2.25].

In the 'Kerr effect', the relative retardation of waves polarised parallel to and perpendicular to a transverse electric field is proportional to the square of the field. This effect occurs to some extent in all transparent material (e.g. crystals, glasses and liquids). The liquid nitrobenzene exhibits

this effect to an unusually large extent and has been used for many years in electro-optic modulators.

Buhrer et al [2.21, 2.22] first proposed and demonstrated the possibility of performing optical frequency shifting by rotation of an applied electric field in a linear electro-optic crystal with a threefold axis. Figure 2.1 shows the arrangement for performing single-sideband suppressed carrier optical modulation. Incident light is passed first through a plane polariser and then a quarter-wave birefringent plate which acts as a right-hand circular polariser. The light continues through two KDP crystals, along their optic axes (or c-directions) as shown in Figure 2.1. After passing through the two electro-optic crystals, the light goes through a left-hand circular analyzer which is the mirror image of the first polariser. This left-hand analayzer allows only the left-hand component to pass, blocking the right-hand component. A modulating electric field is applied to each crystal along the c-axis. The modulation voltages are applied to the two crystals with a 90° phase difference Also, the two crystals have their b-axis at 45° to each other. The principle of the modulation technique is that a rotating birefringent plate will act upon a circularly polarised light beam to produce a separable component shifted in frequency. The system just described simulates the action of a rotating birefringent plate with the result that the output frequency is the sum of the input light frequency and the modulating frequency or, in effect, the upper sideband.

2.1.3 Optical Frequency Translation Using Guided-Wave Optics Technology

There is considerable interest at present in the use of optical fibres in sensors and transducers [2.26-2.28]. In these devices a length of optical fibre (often several hundred metres long) is used to convert a small velocity perturbation due to some external influence (e.g. acoustic, temperature,

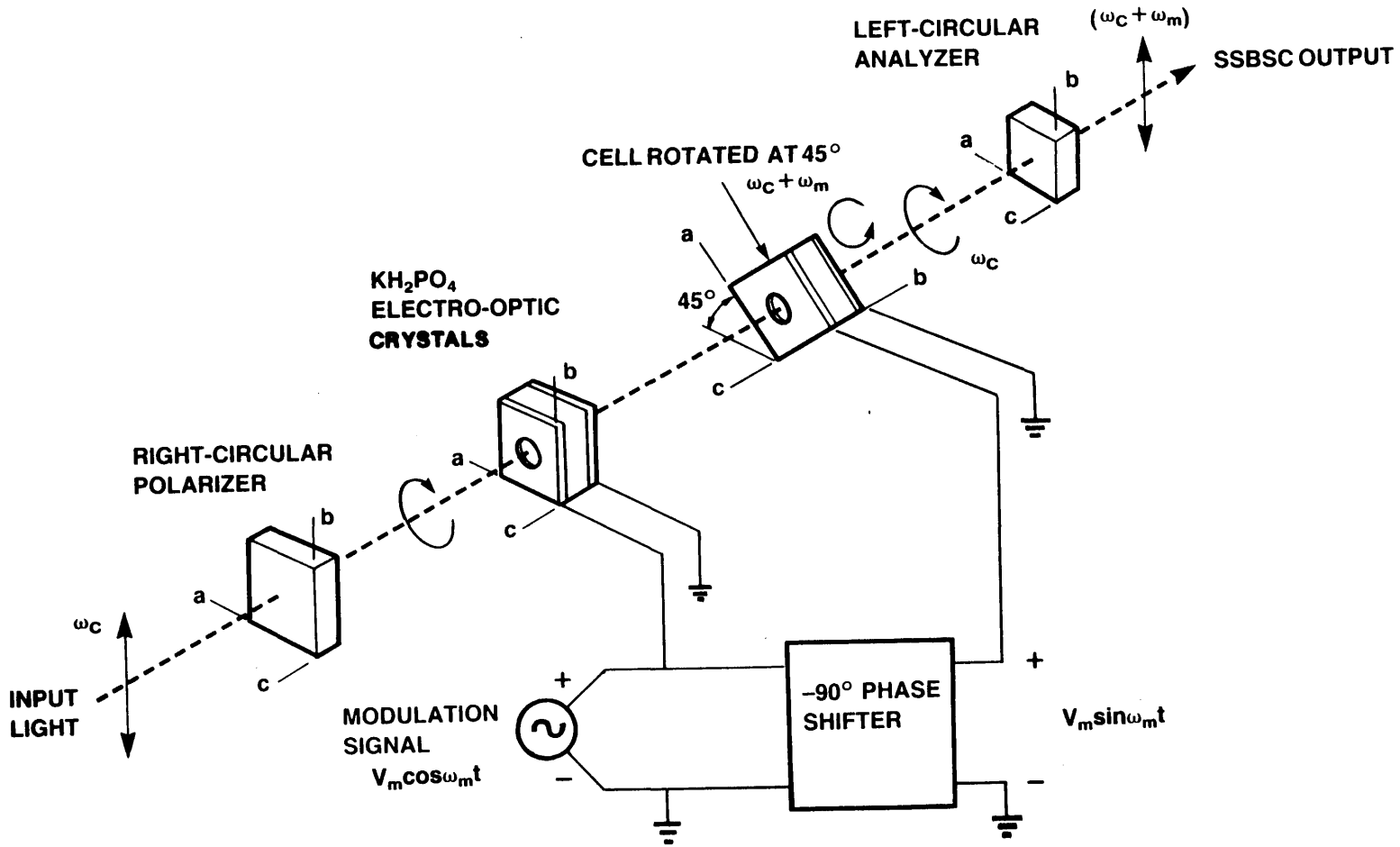

Figure 2.1 Single-Sideband Suppressed-Carrier Optical Modulation Scheme (After Ref. 2.21)

magnetic, rotation, etc.) into a measurable phase change. A variety of optical signal-processing schemes have been proposed for measuring this resultant phase change, generally using some form of interferometer (e.g. a Mach-Zehnder interferometer). A homodyne interferometer is often used to convert this velocity perturbation into an intensity change. However, there are considerable advantages in using heterodyne techniques to translate the phase change to some convenient intermediate frequency, including potentially greater sensitivity [2.29-2.37] and the availability of a digital output [2.38, 2.39].

In order to integrate any heterodyne scheme into a robust planar optical circuit, an optical frequency translator which operates upon light confined in a stripe waveguide is desirable. Several possible devices of this type are reviewed fully in later sections of this chapter.

One of the most common way to perform single-sideband (S.S.B.) generation or optical frequency shifting is by using acousto-optic Bragg interaction. The Bragg cell is most commonly used to realise optical frequency shifting, but realisation in an integrated optic form suitable for coupling to single-mode fibres is difficult. However, three independent groups have realised integrated optic frequency translators using Bragg interactions.

Tsai et al [2.40, 2.41] and von Helmolt et al [2.42] used X-junction channel waveguides and interdigital transducers to generate single-sideband (S.S.B.) on $LiNbO_3$ substrates. Recently Schaffer and Peterman [2.43] proposed and Schaffer [2.44] demonstrated an integrated optic Bragg-modulator consisting of tapered monomode waveguides and a SAW field in between the waveguides. Kingston et al [2.45] demonstrated a planar-type S.S.B. generator by producing a travelling index wave using an interdigitated electrode grating on a $Ti:LiNbO_3$ surface waveguide. This technique has been extended to stripe waveguides and can be useful. Nosu et

al [2.46] demonstrated an acousto-optic frequency shifter for single-mode fibres which could find useful application in an all-single-mode fibre-optic gyroscope [2.47]. All these methods will be examined in depth in Section 2.2.

The quadrature technique is a common method for S.S.B. generation in electronics and in microwave systems [2.48]. A realisation with a guided-wave integrated-optic interferometer on $LiNbO_3$ has been proposed by Culshaw and Wilson [2.49]. The device was recently demonstrated by John and Wilson [2.50]. A direct realisation of the quadrature technique employing a number of Mach-Zehnder interferometers and using amplitude modulation has been demonstrated by Izutsu [2.51]. These methods will be discussed fully in Section 2.3.

Heismann and Ulrich recently proposed [2.52] and demonstrated [2.53] a S.S.B. modulator and phase shifter using electro-optic interaction with a travelling electric wave in Ti:$LiNbO_3$ waveguides. Auracher and Keil [2.54] and recently Gee et al [2.55] demonstrated that a guided-wave Mach-Zehnder interferometer can be made to produce unsymmetrical sidebands about the carrier with a proper dc bias and a modulation signal. Heismann's optical frequency shifter will be discussed in more detail in Section 2.4.

At microwave frequencies, a common technique of single-sideband generation is by phase modulation using a sawtooth modulating waveform (known as serrodyne modulation). This technique has been discussed in Section 2.1.1 and is also of particular interest at optical frequencies since it can be realised easily by means of integrated electro-optic phase modulation [2.56-2.59]. An optical fibre serrodyne shifter was demonstrated using a simple piezoelectrically strained fibre [2.60]. More detailed descriptions of the integrated optical and fibre optic serrodyne frequency translators are found in Sections 2.3.4 and 2.4 respectively. In Chapters 3 and 6, the serrodyne modulation method of frequency translation at optical

frequencies with its realisation by integrated optic phase modulators will be discussed in detail.

2.2 Integrated Optics Acousto-Optic (Bragg) Interactions for Optical Frequency Translation

The acousto-optic interaction has been extensively employed in planar optical waveguides to realise wideband Bragg cells [2.61-2.63]. The Bragg cell is one of the most common way to perform frequency shifting on a laser beam.

Figure 2.2 shows a simple planar acousto-optic modulator. For the modulator to operate in the Bragg regime [2.64], the interaction length (L) between the optical and acoustic beams must be relatively long so that multiple diffraction can occur. This condition can be expressed as follows:

$$L >> \Lambda^2 n_{eff}/\lambda_o \qquad (2.4)$$

where λ_o is the optical wavelength in free space,

Λ is the wavelength of the acoustic waves and

n_{eff} is the effective refractive index of the guided optical mode.

The angular condition for Bragg diffraction to occur is given by:

$$\sin \theta_B = \lambda_o/(2\Lambda n_{eff}) \qquad (2.5)$$

where θ_B is the Bragg angle defined within the medium of interaction.

It should be noted that the diffracted (or 1st order) output beam will emerge at an angle of $2\theta_B$ with respect to the undiffracted (or 0th order) beam. The efficiency of the Bragg diffraction (η) [2.64] defined by the ratio of the power in the diffracted beam (I_1) to the power in the incident beam (I_o) is given by:

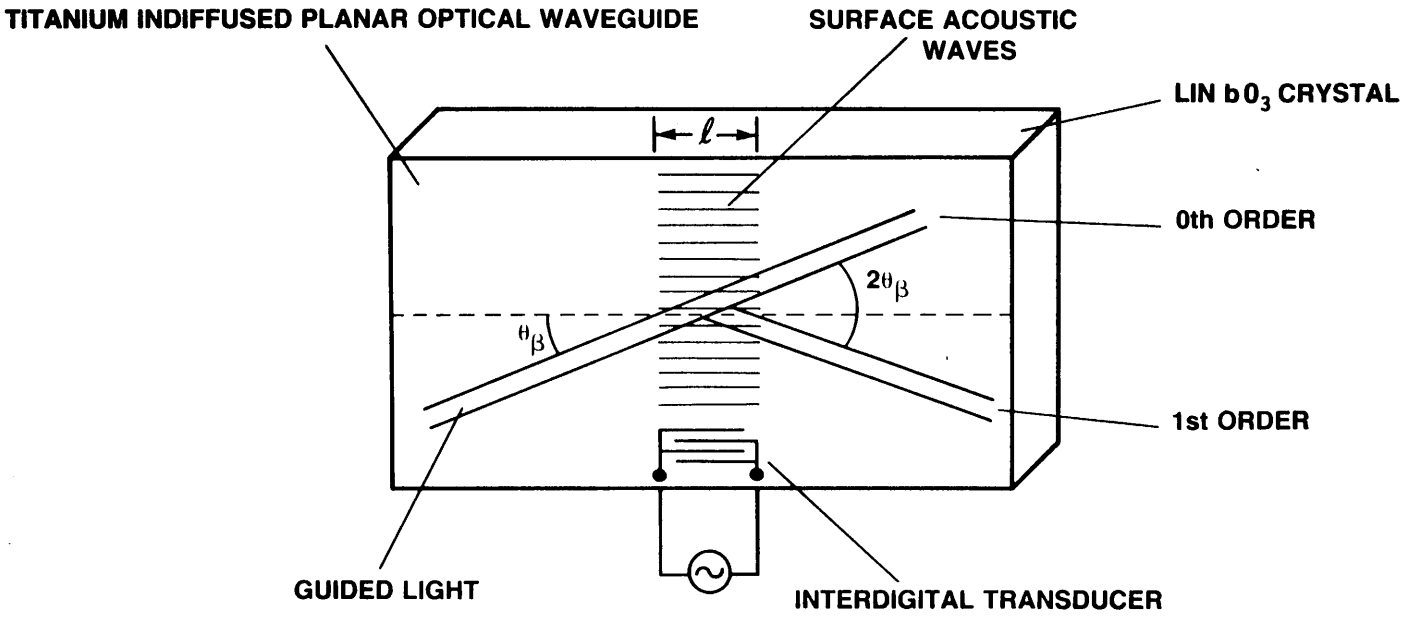

Figure 2.2 A Ti:LiNbO$_3$ Planar Acousto-Optic Bragg Modulator

$$\eta = I_1/I_0 = \sin^2 \{[(\pi L n_{eff})/(\lambda_0\sqrt{2})]\sqrt{(MP_s)}\} \qquad (2.6)$$

where M is the Figure of Merit of the material, and

P_s is the acoustic power density (Watt/m^2).

With the emergence of single-mode optical fibre systems, it became desirable to realise a channel acousto-optic Bragg cell which could be easily interfaced with the fibre system. In 1980, Tsai et al [2.40] reported the first, multimode, Bragg channel optical frequency shifter.

Recently, two groups have independently demonstrated single-mode waveguide X-junction Bragg frequency shifters. These will be described in detail in Sections 2.2.1 and 2.2.2. In Section 2.2.3, an integrated optic Bragg frequency shifter employing tilted and tapered monomode waveguides is described.

2.2.1 Integrated Optical Waveguide X-junction Frequency Shifter (Tsai et al)

The use of acousto-optic interactions in channel waveguides was first described in 1980 by Tsai et al [2.40]. The motivation behind this study was that comparable cross-sections of optical channel waveguides and optical fibres would enable the efficient interfacing of acousto-optic devices to fibre optic systems.

In the 1980 demonstration, Tsai et al used a crossed pair of channel waveguides (i.e. an X-junction) in which a laser beam (at 632.8 nm) in one input waveguide was diffracted and at the same time frequency shifted by a surface acoustic wave (SAW) propagating in the crossover region and deflected into the other waveguide. This device consisted of Y-cut Ti:$LiNbO_3$ stripe waveguides of width 20 μm. It was multimoded but did result in a diffraction efficiency of 40%. The peak rf power for this diffraction

efficiency was measured to be 600 mW. Tsai et al however did not mention the optical power level of the unshifted signal. The centre frequency of the SAW was 634 MHz, appropriate for the 3.0° intersection angle between the two channel waveguides. Ten finger pairs of 0.77 mm aperture were used in the transducer. The frequency response, namely, the diffracted power versus the acoustic frequency, measured at a fixed rf drive power of 500 mW indicated that a -3 dB deflector bandwidth of 71 MHz was demonstrated by Tsai et al [2.40]. Tsai et al [2.40] concluded that the deflector bandwidth was limited by the transducer bandwidth.

The above study was extended recently to a single-mode waveguide X-junction of 10 μm channel width [2.41]. Figure 2.3 shows the complete device geometry. As before, the channel waveguides were fabricated by titanium indiffusion in Y-cut $LiNbO_3$ substrates. The interdigital transducer was symmetrically located so that the SAW generated would propagate across the X-intersection region. The crossing-point of the two channel waveguides, shown by shaded lines was of the '2 Δn-type', i.e. the refractive index change in the cross-over region was twice that of the other sections of the channel waveguides. The reason for this given by Tsai et al was that this provides tighter waveguide mode confinement in the cross-over region. Because of this tighter confinement, the authors claimed that the crosstalk between the two output waveguides (i.e. "3" and "4") should be considerably smaller than in the 'Δn-type' crossover region, resulting in a higher suppression of the carrier with respect to the frequency shifted signal.

The operation of this A.O. X-junction frequency shifter can be explained as follows. If an optical wave is incident at waveguide "1", then it will be Bragg-diffracted by the moving optical grating induced by the SAW, and part of the incident light will be deflected to waveguide "3". In this case, the frequency of this deflected light will be up-shifted by an amount equal to the acoustic frequency. Similarly, an optical wave that is incident at

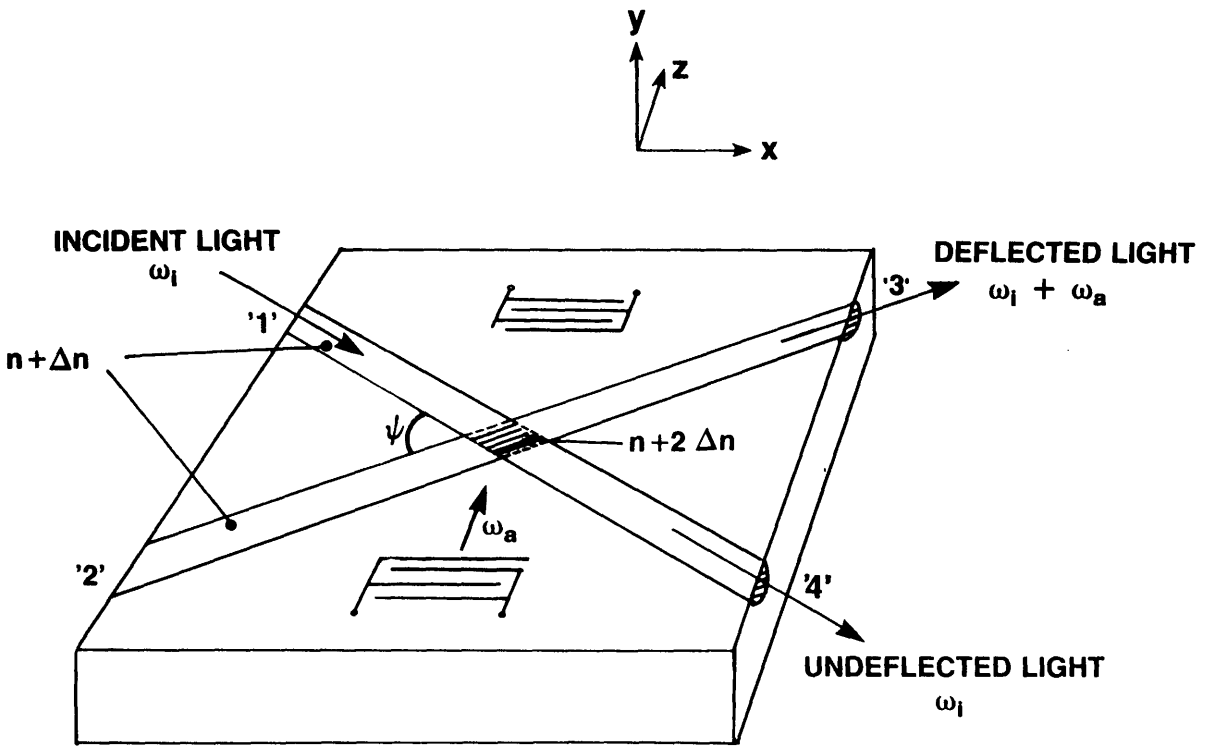

Figure 2.3 An Optical Frequency Translator Using X-Junction Waveguides And Acousto-Optic Interactions (After Reference 2.41)

waveguide "2" will have a portion of its light intensity deflected to waveguide "4". The frequency of the deflected light in this case will be down-shifted by the same amount as in the up-shift case.

The device (with the branching angle, $\psi = 1.5°$) was tested at $\lambda = 632.8$ nm. The A.O. interaction region was calculated to be of dimensions 382 μm by 382 μm. Both prism and end-fire coupling were employed to excite the fundamental TE_{11} mode of the channel waveguides. It was observed experimentally that a diffraction efficiency of 50% was attained by applying an RF drive power of 400 mW (≅ 130 mW of acoustic drive power). To match the above choice of Bragg angle, the centre frequency of the SAW-IDT was 320 MHz with 30 finger pairs. The 3 dB bandwidth of this device was found to be 13.4 MHz. This was limited by the design of the IDT.

A single-mode AO X-junction frequency shifter has, therefore, been demonstrated by Tsai et al with very encouraging performance. The experiment indicated that an integrated optic frequency shifter module with a equal power split and a tunable frequency offset is realisable.

2.2.2 Integrated Optical Waveguide X-junction Frequency Shifter (Von Helmolt et al)

The integrated optical frequency translator demonstrated by von Helmolt et al [2.42] was similar to that discussed by Tsai et al [2.41]. There are, however, several differences between the two devices. These will be outlined in the later part of this discussion.

Figure 2.4 shows the schematic of the integrated optic Bragg type S.S.B. modulator demonstrated by von Helmolt. It consists of two crossed single-mode waveguides "1" and "2" (X-junction) and an interdigital transducer (IDT) of width L. The SAW generated by the IDT propagates along the Y-direction of the Z-cut $LiNbO_3$ substrate.

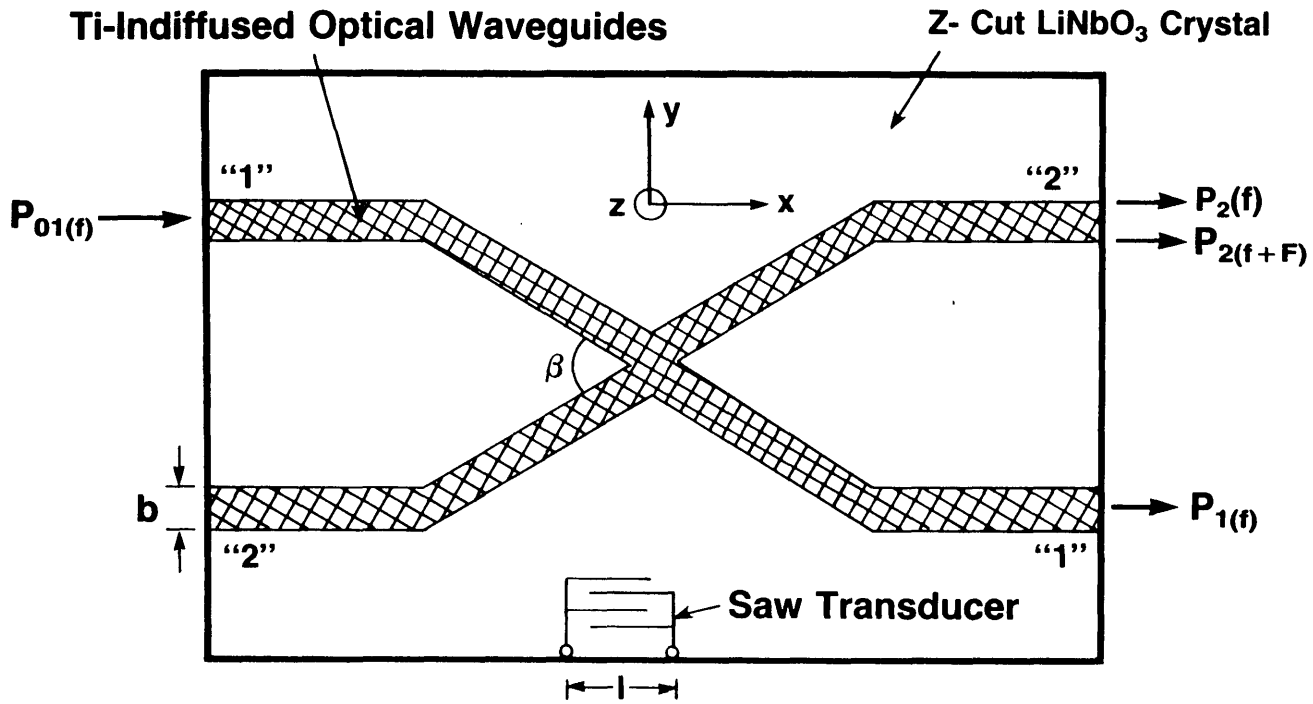

Figure 2.4 An Integrated Optic Bragg Type S.S.B. Modulator Demonstrated By von Helmolt (After Reference 2.42)

For high diffraction efficiency, von Helmolt et al have realised L = L_{ao}, where L_{ao} is the acousto-optic (AO) interaction length, given by:

$$L_{ao} = \frac{b}{\sin(\beta/2)}, \qquad (2.7)$$

where b is the width of the optical waveguide, and

β is the crossing angle of the two channel waveguides "1" and "2".(β is equal to two times the Bragg angle.)

Again, if an optical wave of frequency f is incident in waveguide "1", then it will be deflected to waveguide "2" at the crossover of the X-junction. This is due to the presence of a moving phase grating generated by a SAW at frequency f. The deflected light in waveguide "2" will be up-shifted by f. Similarly, if the optical wave is incident in waveguide "2", it will be deflected to "1" and at the same time down-shifted in frequency by an amount f.

The device described by von Helmolt et al was fabricated using a Z-cut $LiNbO_3$ substrate. The light propagated along the X-direction whilst the SAW travelled along the Y-direction. The waveguide X-junction was formed by titanium indiffusion. The width of the channel waveguides was 3 μm and the device was operated at λ= 850 nm using a Hitachi HLP 1400 semiconductor laser. One of the most important parameters studied was the variation of static cross-talk between waveguides "1" and "2" in relation to the crossing angle β. The static cross-talk C was defined as follows:

$$C = 10 \log [P_2/(P_1 + P_2)] \text{ dB} \qquad (2.8)$$

where P_1 and P_2 were the optical powers in waveguides "1" and "2" respectively. Two types of polarisation (i.e. TE and TM) were used in the study of the static cross-talk. It was found, in both cases, that there is a linear dependence between C and β for $\beta \geq 1.5°$. However, the value of the

static cross-talk was reduced for light with TE polarisation. At $\beta = 3°$, the measured values of C for TE and TM polarisations quoted by von Helmolt et al are -23 dB and -9.5 dB respectively. Thus, for their experimental demonstration a value of $\beta = 3.5°$ and TE polarisation were chosen to enable better results to be obtained.

By using an IDT, L = 120 μm, with a centre frequency of 629 MHz and driving it with 1.4 W electrical power, a 10:90 split in the input light power was observed. A 16 dB carrier suppression had been attained experimentally by von Helmolt et al.

In summary, von Helmolt et al has demonstrated an integrated optical Bragg S.S.B. modulator similar to that described by Tsai et al. The differences between the two are:-

(i) There is no special increase in the refractive index of the crossover region in the waveguide X-junction realised by von Helmolt, compared to the device desribed by Tsai et al,

(ii) The devices were fabricated on a different cut of $LiNbO_3$ substrates, and

(iii) The operation wavelength of the devices was different.

2.2.3 Integrated Optic Frequency Shifters with SAWs (Schaffer and Petermann)

Recently Schaffer and Petermann [2.43] proposed an integrated optical frequency shifter which employed a pair of tilted and tapered monomode waveguides with a region of acoustooptic (AO) interaction between them. The schematic of the proposed device is shown in Figure 2.5. As indicated by Equation 2.5 (the Bragg condition), if the incident laser beam is close to the Bragg angle θ_b at the AO interaction area, then the beam will be deflected from taper 1 into taper 2.

A simulation performed by the researchers indicated that the contours of the tapered waveguide regions should be parabolic. This

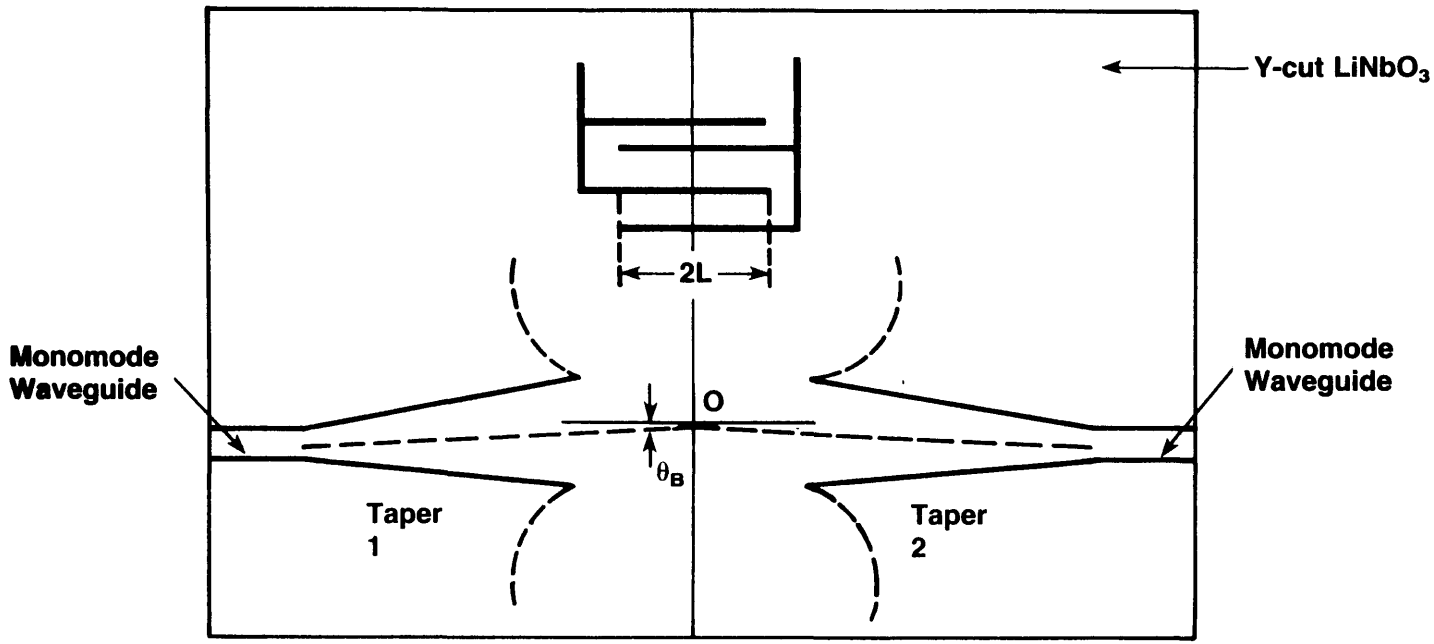

Figure 2.5 Schematic Arrangement Of The Bragg-Modulator Proposed By Schaffer And Petermann And Demonstrated By Schaffer

configuration yielded minimal coupling between the fundamental and the higher order modes in the waveguide transition areas. A SAW frequency of 200 MHz yielded a deflection angle of about 0.56° for YZ-$LiNbO_3$. In this particular case, the waveguide width at the end of the taper was 80 μm to ensure that a narrow lobe was achieved in the far field. This yielded a crosstalk between the tilted tapers of about 40 dB without any SAW interactions. The width of the AO interaction region between the two tapers was 4 mm (i.e. 2L). The researchers simulated the interaction with a Gaussian beam input and found that, the suppression of all unwanted sidebands was better than 60 dB below the required shifted signal. With more realistic input optical field distributions the results indicated that the suppression of all unwanted sidebands was between 20 and 30 dB below the shifted signal.

The frequency shifter shown in Figure 2.5 was recently demonstrated by Schaffer [2.44]. The device was fabricated in Y-cut $LiNbO_3$ using the titanium indiffusion method of waveguide formation. The laser beam and the SAW was propagated along the X- and Z-direction of the crystal respectively. The stripe waveguide was 5 μm in width and were operated in the single mode regime at a wavelength of 780 nm using a suitable waveguide fabrication recipe (50 nm thick titanium films, Diffused for 5 hours at 1000°C in flowing oxygen with water vapour to suppress outdiffusion). The waveguide width at the end of the taper was 80 μm with the length of the parabolic contoured taper to be 9 mm. The electrodes of the interdigital transducer were 4 mm long and consisted of 200-300 nm thick aluminium. The completed frequency shifters were 28 mm long. The frequency shifter was evaluated in a bulk Mach-Zehnder interferometer and a Bragg cell was employed to facilitate display of the positive and negative sidebands on the spectrum analyser. Overall suppression of unwanted frequencies of better than 30 dB (TM) and 20 dB (TE) were measured. A

deflection efficiency of about 40% was measured by using fibre coupling at the input and output of the device. The electrical power required was 500 mW. The acoustic power in the interaction region was deduced by Schaffer to be approximately 125 mW [2.44].

2.2.4 Discussions of Optical Frequency Translators Realised by Acousto-Optic (Bragg) Interactions

An important feature of the two Bragg waveguide X-junction frequency shifters is that, once the device has been fabricated, it will only function at a particular centre frequency with a limited frequency excursion in either direction. The reason for this is that when the centre frequency of the modulating signal is varied, the acoustical wavelength of the SAW will vary accordingly and this will change the Bragg angle as described by Equation (2.5). This in turn will also increase the cross-talk level between the two output waveguides and therefore is a significant negative feature.

The use of a '2Δn-type' crossover region by Tsai et al could be a good idea since they claimed cross-talk levels between the two output waveguides could be reduced by better confinement in that region of the waveguide X-junction. Recent theoretical studies of X-junction structures of the '2Δn-type' by Neyer et al [2.65] using the beam propagation method (BPM) indicated that the crosstalk levels are extremely dependant on the waveguide unsymmetries. In consequence, they proposed and realised three X-type structures with symmetric input and output waveguides. They demonstrated experimentally that X-junction with cross-over regions with extra titanium resulted in the best crosstalk levels [2.65].

The final device described did not offer any better features except for an improvement in the suppression of unwanted sidebands of 4 dB and, in fact, it poses more problems for researchers trying to realise the device. It

will be especially difficult to ensure that the optical waveguides, in particular the tapered regions, are single moded.

In conclusion, the three devices just described are limited in bandwidth (about 10 MHz mentioned by Tsai et al). They are also limited in the dynamic range because of the cross-talk between the two output waveguides. (A 16 dB carrier suppression was obtained experimentally by von Helmolt et al.). Another disadvantage of the two devices is the high electrical power ($\geq$ 1 Watt) needed to perform the Bragg diffraction.

2.3 Integrated Optical Electro-Optic Frequency Translators

In this section several methods of optical frequency translation using the electro-optic effect in $LiNbO_3$ will be discussed. A detailed description of the electro-optic effect in $LiNbO_3$ will be given in Chapter 6, Section 6.2.2. In short, the electro-optic effect is the change in the refractive index of a material (e.g. $LiNbO_3$, $LiTaO_3$, KDP, etc.) due to the application of an electric field. This will in turn affect the phase of the propagating guided waveguide mode.

2.3.1 Quadrature Method of Frequency Translation

A well known method of generating single-sideband suppressed carrier (S.S.B.S.C) signals, as mentioned earlier, is based on the phase shift or quadrature method shown in Figure 2.6. This technique operates by the cancellation of one sideband when introducing proper phase shifts (i.e. 90°) between the two arms of the bridge and between the multiplying signals.

Assume that the input signal $f_c(t)$ and the modulating signal $f_m(t)$ are $\cos(\omega_c t)$ and $\sin(\omega_m t)$ respectively. Then the outputs of balanced modulators A and B are $[\sin(\omega_c t)\cos(\omega_m t)]$ and $[\cos(\omega_c t)\sin(\omega_m t)]$ respectively. By appropriately combining these two output signals, an up-shift or a down-

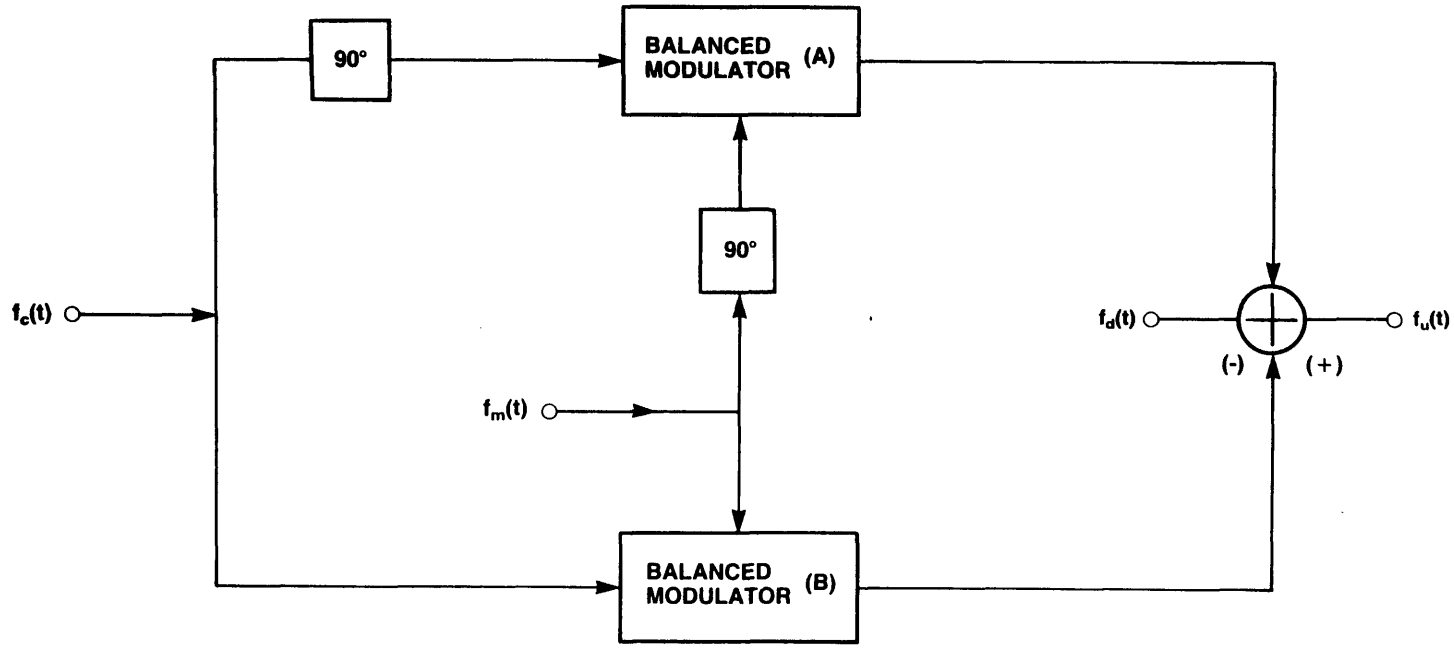

Figure 2.6 Quadrature/Phase Shift Method of S.S.B.S.C. Generation

shift in frequency can be obtained, i.e. up-shift signal, $f_u(t) = \sin(\omega_c+\omega_m)t$ and down-shift signal, $f_d(t) = \sin(\omega_c-\omega_m)t$.

Sections 2.3.1.1, 2.3.1.2, and 2.3.1.3 will describe a proposal, a demonstration, and another demonstration of optical frequency shifting using the quadrature technique by Culshaw [2.49], John [2.50], and Izutsu [2.51] respectively.

2.3.1.1 Proposal by Culshaw and Wilson

The first proposal for a broadband optical frequency shifter (dc to several GHz), based on the quadrature method of S.S.B.S.C. generation, was that by Culshaw and Wilson [2.49]. Figure 2.7 shows the schematic representation for this proposed optical frequency shifter. The balanced modulators were not realised by using I.O. Mach-Zehnder interferometers. Instead, I.O. phase modulators driven in phase quadrature by square waves f(t) and f'(t) were proposed, where:

$$f(t) = \sum_{n=1}^{\infty} 4/[(2n-1)\pi]\ \sin(2n-1)\omega_m t, \text{ and} \qquad (2.9)$$

$$f'(t) = \sum_{n=1}^{\infty} \{[4(-1)^{n-1}]/[(2n-1)\pi]\}\ \cos(2n-1)\omega_m t. \qquad (2.10)$$

In the analysis described by Culshaw, Giles and Wilson [2.66] it was assumed that the input carrier signal is of the form $(\sqrt{2})\cos(\omega_c t)$, the modulated components in the upper and lower arms will be given by:

$$f(t)\ \sin\omega_c t = \sum_{n=1}^{\infty} \{[2(-1)^{n-1}]/[(2n-1)\pi]\}\ \{\sin[\omega_c + (2n-1)\omega_m]t +$$

$$\sin[\omega_c - (2n-1)\omega_m]t\}, \text{ and} \qquad (2.11)$$

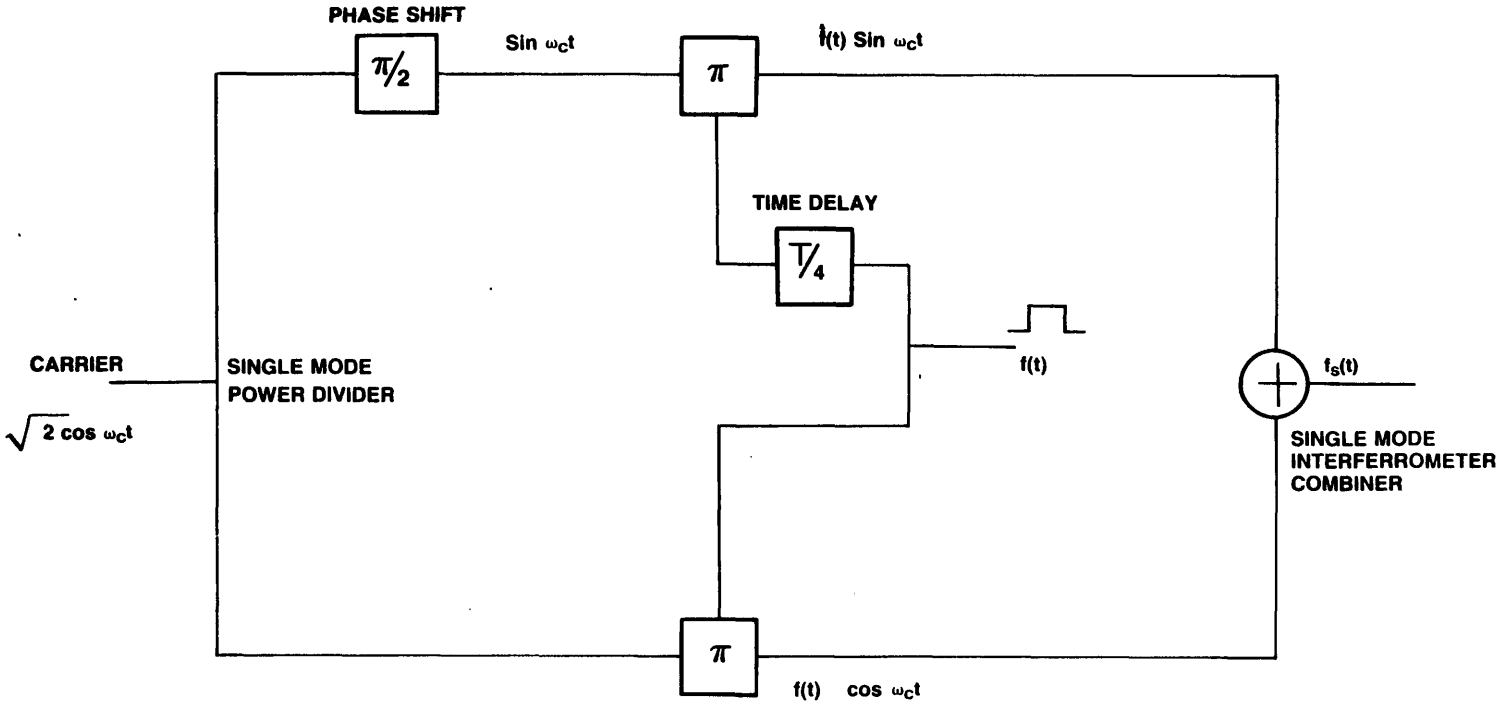

Figure 2.7 Schematic Representation Of The Proposed Optical Frequency Translator (After Reference 2.46)

$$f(t)\ \cos\omega_c t = \sum_{n=1}^{\infty} \{2/[(2n-1)\pi]\}\ \{\sin[\omega_c + (2n-1)\omega_m]t -$$

$$\sin[\omega_c - (2n-1)\omega_m]t\}. \qquad (2.12)$$

respectively.

These two modulated optical components (Equations 2.11 and 2.12) then interfere in a waveguide Y-junction. All in-phase components at each frequency will be added in power and thus the output of the waveguide $f_s(t)$ is:

$$f_s(t) = (2\sqrt{2}/\pi)\ \{\sin(\omega_c + \omega_m)t - (1/3)\sin(\omega_c - 3\omega_m)t +$$

$$(1/5)\ \sin(\omega_c + 5\omega_m)t + ...\}. \qquad (2.13)$$

This implies that the final spectrum (From Equation 2.13) contains a mixture of upper and lower sidebands spaced at four times the fundamental modulation frequency with the carrier completely suppressed. The theoretical conversion efficiency is -3.9 dB (or 41%).

Figure 2.8 illustrates the complete layout of the propose integrated optic (I.O) frequency shifter with all the necessary monitoring and detection facilities to produce error signals. It would be based on a single-mode stripe waveguide Mach-Zehnder interferometer with one static phase shifter and two phase modulators. Also, the use of an optical directional coupler is proposed for implementing a closed-loop error control system.

An optical detector with necessary amplification was proposed for monitoring the output from the side arm of the optical directional coupler. The optical phase shifter is very sensitive to variations in the applied voltages, photorefractive effects, and may also drift due to temperature changes. From their analysis, any errors due to variations in static phase

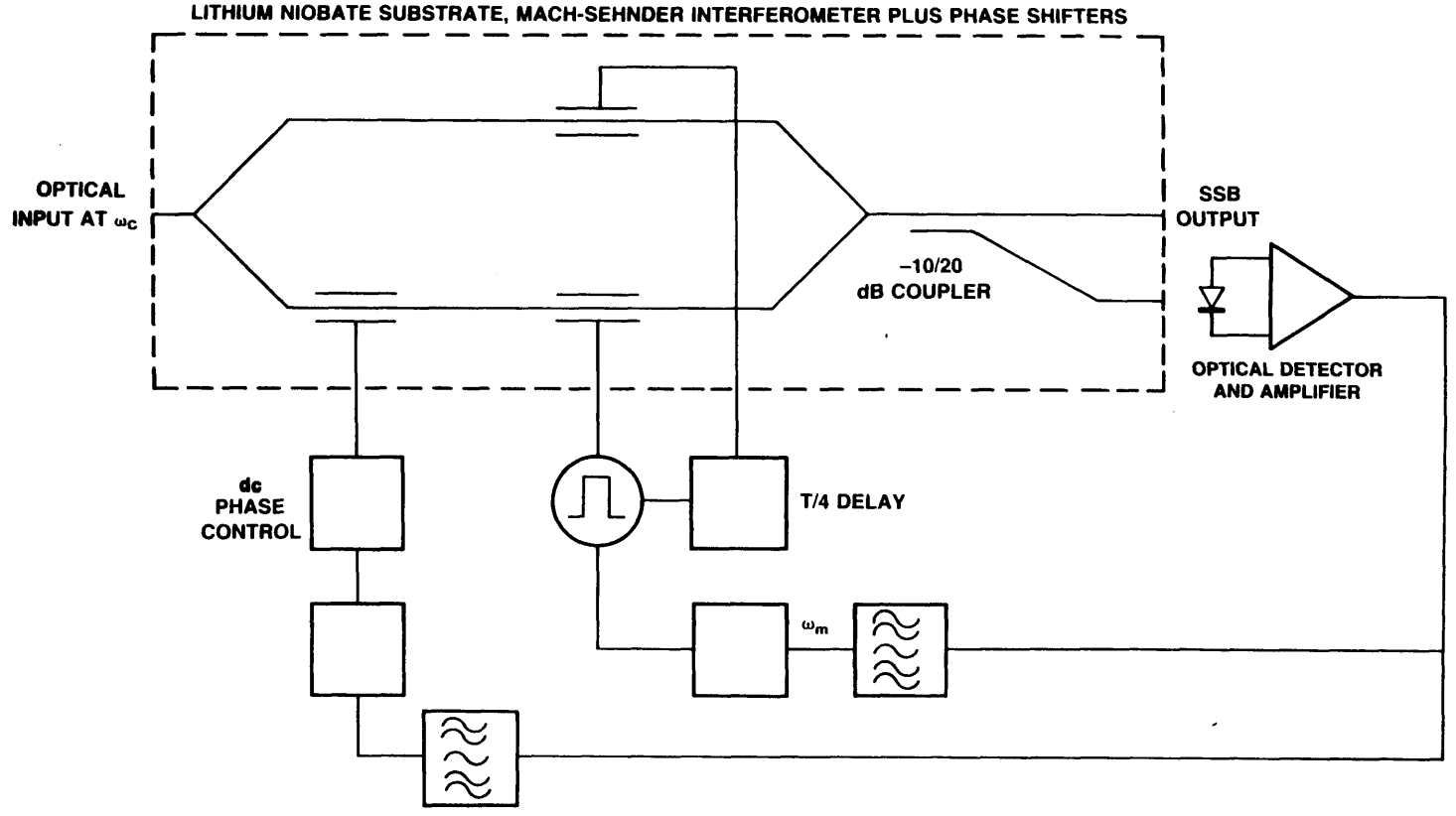

Figure 2.8 Complete Schematic Layout Of The Proposed IO Frequency Translator With All Necessary Facilities To Produce Feedback Error Signals (After Reference 2.46)

settings can be monitored by the presence of the 2nd harmonic signal on the photodetector. As for errors due to the phase modulators, the presence of the fundamental modulating frequency on the monitoring detector can be used as an error-correction signal.

In summary, a broadband integrated optic frequency shifter with error-correction to the spectrum has been proposed. All the electronics needed to drive this device can be derived from conventional digital circuitry. A theoretical conversion efficiency of -3.9 dB (41%) has been quoted. The proposed frequency shifter could be realised using Ti:$LiNbO_3$ waveguides. Such a device might find applications in integrated optic sensor and FSK optical communication systems in which there are requirements for a wideband (dc - 10 GHz) frequency shifter.

2.3.1.2 Demonstration by John and Wilson [2.50]

The device proposed in the above section was partially demonstrated and implemented using a titanium indiffused Mach-Zehnder interferometer in X-cut $LiNbO_3$ with the necessary electrode pattern (Figure 2.9). The device was operated at 633 nm using single mode waveguides of width 4 μm. The experimental setup shown in Figure 2.10 was used to evaluate the optical frequency shifter. The device was tested from dc to 20 MHz. With ECL implementation of the digital driving electronic circuitary, it is possible to drive the frequency shifter at higher frequencies. It was found to have carrier to image sideband suppression of around 30 dB and had a conversion efficiency of about 40.5% (-3.9 dB). As can be seen from Figure 2.10, correction signals were available to ensure continuously maintained high suppression levels between the shifted and the image sidebands. In conclusion the demonstration of device performance reported by John and Wilson was good and compared favourably with other techniques of optical frequency shifting already described and those to be described. An

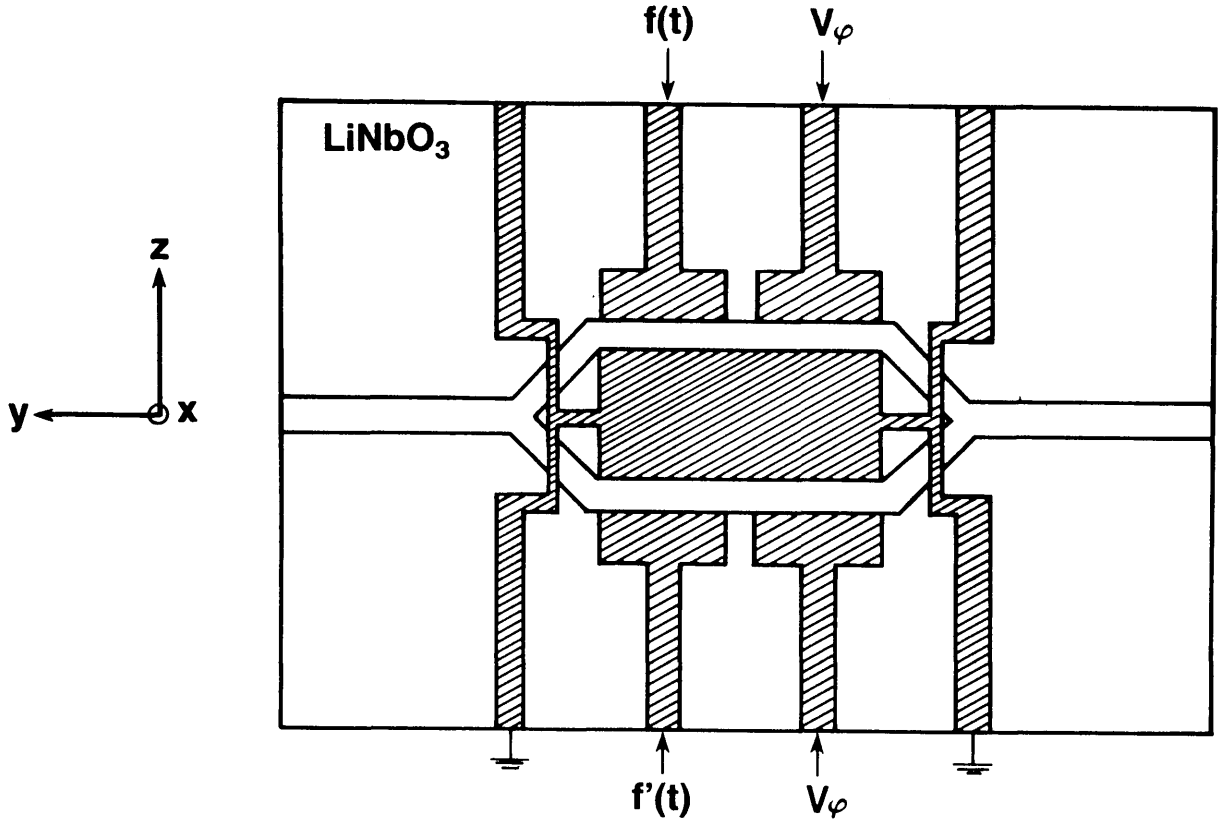

Figure 2.9 Schematic Representation Of The Integrated Optic S.S.B. Generator (After Reference 2.47)

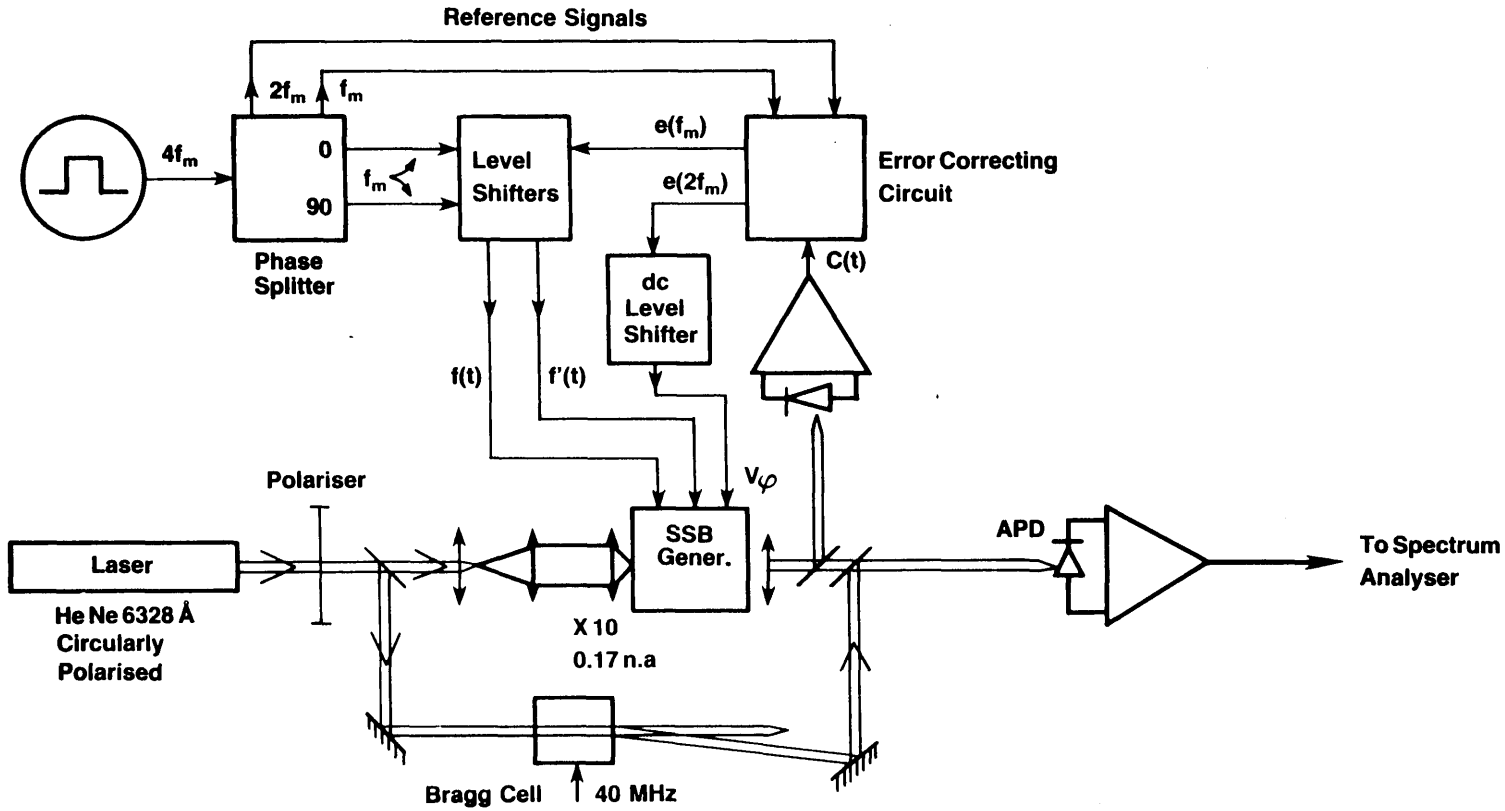

Figure 2.10 Schematic Of The Experimental Arrangement Used To Test The IO S.S.B. Generator (After Reference 2.47)

important feature of this demonstration is the use of the feedback control circuitry to maintain good suppression levels as illustrated in Figure 2.10.

2.3.1.3 Demonstration By Izutsu et al

This was the first practical demonstration of optical frequency shifting by the quadrature technique [2.51], representing a direct interpretation of Figure 2.6. The operation was confirmed by constructing and testing the device using titanium indiffused waveguides in Z-cut $LiNbO_3$ substrates. A conversion efficiency of -5 dB (or 31.6%) was attained experimentally with an input drive power of 730 mW. The optical frequency shifting was demonstrated at 2 GHz.

Figure 2.11 illustrates a schematic diagram of the integrated optic S.S.B. frequency shifter. The integrated optic Mach-Zehnder interferometers were used as balanced modulators and two static phase shifters were employed to ensure a 90° phase shift after the laser light was divided by a 3 dB Y-junction. The outputs from the two balanced modulators were then combined using another 3 dB Y-junction.

Figure 2.12 shows the theoretical optical spectra at several points in Figure 2.13. Here ω_c and ω_m represents the angular frequencies of the input laser light and the modulating signals. In the final optical spectrum, the sidebands were spaced at four times the modulating frequency. The first 3 sidebands are given by:

Fundamental: $AJ_1(\phi_m)\ \exp[j(\omega_c + \omega_m)t$

3rd Order: $AJ_{-3}(\phi_m)\ \exp[j(\omega_c - 3\omega_m)t]$

5th Order: $AJ_5(\phi_m)\ \exp[j(\omega_c + 5\omega_m)t]$

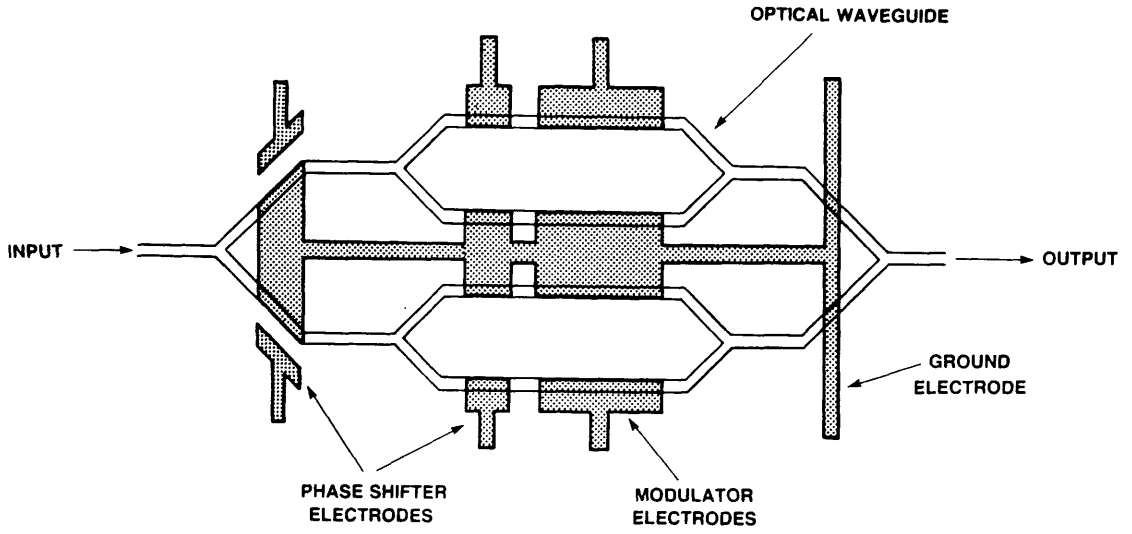

Figure 2.11 Layout Of The Optical Waveguides And Electrodes For The IO SSB Frequency Translator (After Reference 2.48)

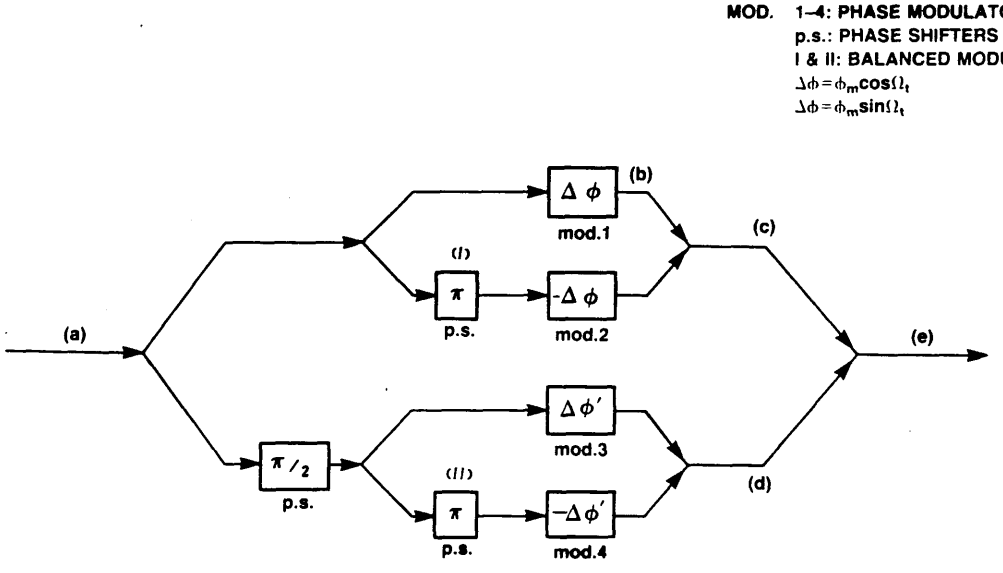

Figure 2.12 Schematic Diagram Of The IO SSB Modulator/Frequency Shifter (After Reference 2.48)

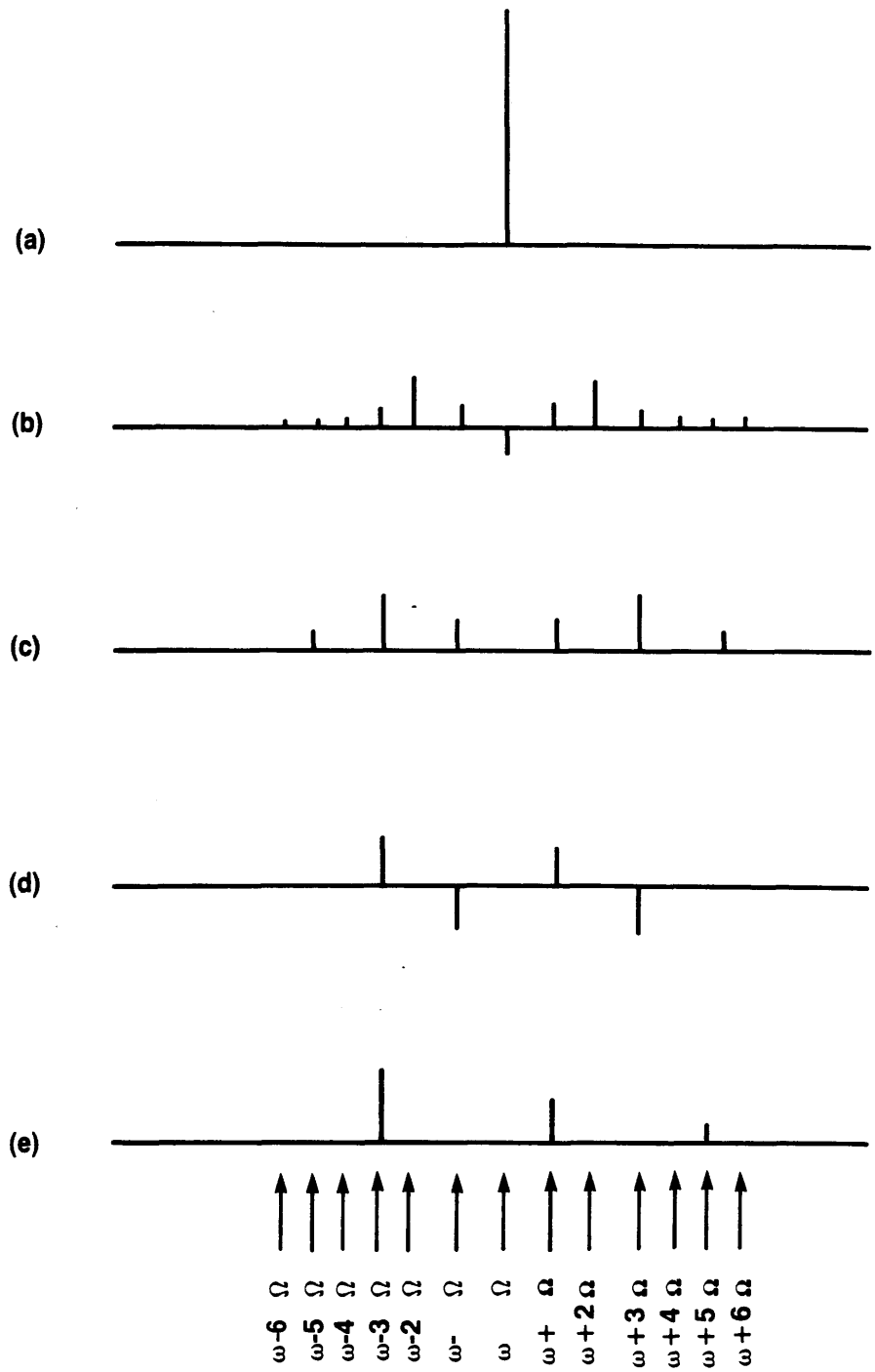

Figure 2.13 Expected Optical Frequency Spectra At Various Points In Figure 2.12 (After Reference 2.48)

where A is the amplitude of the input laser beam and ϕ_m is the amplitude of the phase retardation applied to the four phase modulators (mod. 1-4).

The maximum fundamental output [at $(\omega_c - \omega_m)$] should be obtained when ϕ_m = 1.8 rad. An expected conversion efficiency of -4.7 dB (33.9%) and a harmonic distortion of less than -20 dB referred to the incident optical carrier intensity had been predicted theoretically.

The device was realised using optical waveguides of 5 μm width. By changing and adjusting the relative phase shifts of the phase modulators, balanced modulation and upper and lower S.S.B. modulation were demonstrated. There was no mention of the discrimination between the carrier and the required sideband in the above demonstration. The measured half-wave voltage for the push-pull modulator was 5.3 V. The quoted optical insertion loss (which includes the input and output microscope objectives) was in the range of -20 dB to -30 dB.

2.3.1.4 Discussions of Optical Frequency Translators Realised by the Quadrature Method

In the quadrature method of performing optical frequency shifting, the cancellation of the sidebands in the interferometer arrangements is sensitive to parameter variations, for example, the optical phase shifter is sensitive to variations in the applied voltages and to photorefractive effects [2.50] and may also drift due to temperature changes.

In the optical frequency shifter proposed by Culshaw and Wilson [2.49] and demonstrated by John and Wilson [2.50], the effect of these errors was considered and a feedback system was employed to correct these errors. However, in the device demonstrated by Izutsu et al [2.51], no such considerations appear to have been made.

The device proposed by Culshaw and Wilson and demonstrated by John and Wilson is also superior to the device reported by Izutsu et al since it

requires fewer waveguide branches and phase shifters. This implies that the overall insertion loss will be lower and less sensitive to parameter variations since there are fewer optical phase shifters to control electrically.

The devices described by Culshaw and Wilson, John and Wilson, and Izutsu et al are in principle broadband, i.e. they can operate from dc to a few GHz. The devices seemed to have theoretically acceptable conversion efficiency of $\cong$ 40%. There was no mention of image sideband suppression in the device reported by Izutsu et al, thus making the evaluation of that device in a fibre-optic sensor system difficult. Initial results reported by John and Wilson on their optical frequency shifter indicated that with the use of electrical feedback control, they have achieved around 30 dB suppression of shifted signal to image signal with an experimental conversion efficiency of around 40.5% [2.50]. More experimental work has to be performed on the above two devices in order that they can be considered seriously for use in any fibre-optic sensor or communication system.

2.3.2 Electro-Optical Bragg Array Optical Frequency Translator

Integrated optical Bragg deflectors in planar waveguides have already been realised. [2.61-2.63]. In all these devices, the frequency shift is limited to tens of megahertz. The reason for this is that the diffraction efficiency decreases with long acoustic wavelengths.

Recently, Kingston et al [2.45] proposed and demonstrated a broadband planar guided-wave optical frequency translator using an electro-optical Bragg array. This device utilised the Bragg diffraction from a travelling index wave which was produced by an interdigital electrode grating on a titanium diffused waveguide in X-cut $LiNbO_3$ substrate. A novel feature of the device was that the grating electrodes were driven by a three-phase electrical signal. This resulted in a unidirectional wave with a fixed

Bragg angle determined by the electrode spacing. Thus, this device will always be operating in the Bragg or thick grating regime.

Figure 2.14 shows a Bragg array optical frequency translator with a much simplified grating electrode pattern with only 6 electrodes drawn and also a section view showing the index wave. The actual device has 120 electrodes fabricated on it. The electrode array is 5.8 mm long, 0.72 mm wide and the electrodes are spread 2 μm apart with a pitch of 6 μm. This implies that the wavelength of the index wave is 18 μm.

For their experimental study, a He-Ne laser operating at λ_0= 633 nm was used to excite the fundamental TE mode of the Ti:$LiNbO_3$ planar waveguide. This was carried out by coupling the laser beam into the LHS of the device. The diffracted beams were imaged on the RHS of the device. Given an array period of 18 μm, the Bragg angle (exterior) is $\cong$ 1.0° By aperturing off the undiffracted beam, the output optical spectra of the diffracted (frequency shifted) beam was measured using a scanning confocal Fabry-Perot interferometer. Instead of using 3 voltage sources at 120° relative phase, two equal voltage sources at a 60° relative phase angle and grounding one phase of the array could equally well be used.

Experimental measurements of S.S.B.S.C. operation were performed at 10 MHz and 100 MHz. These yielded a carrier-to-sideband conversion efficiency of 90% (-0.46 dB) with a suppression of the carrier and unwanted sideband of 100:1 (20 dB). The experiments were performed at frequencies up to 400 MHz. Kingston et al [2.44] indicated that the full expected carrier-to-sideband conversion efficiency was not achieved due to the problems of lead inductance and ohmic losses in the electrodes. In order to operate this device in the GHz region, one would require a careful microwave design with modified packaging and electrode configuration to take account of the high capacitance at such frequencies.

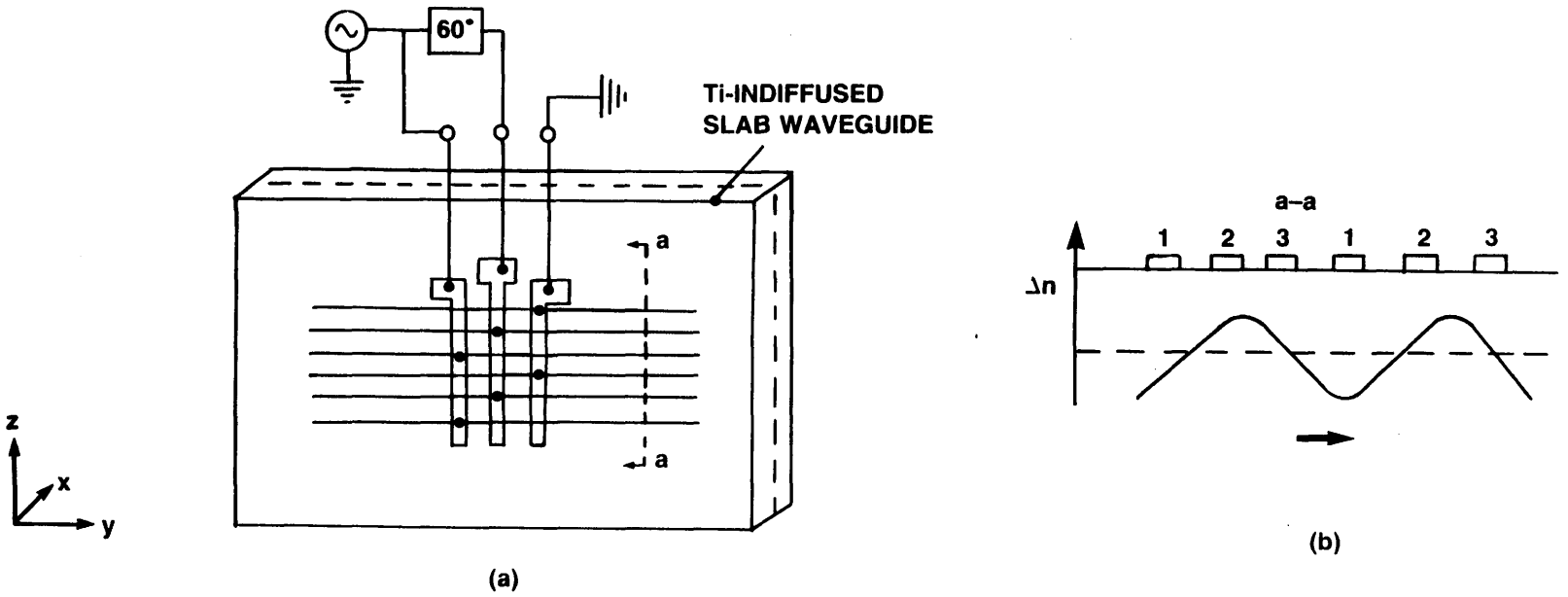

Figure 2.14 Schematic Of (a) A Bragg Array Optical Frequency Translator And (b) A Section View Of The Refractive Index Wave (After Reference 2.44)

In conclusion, a potentially wideband (dc to several GHz) guided-wave planar optical frequency translator using an electro-optical Bragg array has been demonstrated with some encouraging results.

2.3.3 Electro-Optical Frequency Translator by Heismann and Ulrich

Heismann and Ulrich have proposed and demonstrated an optical frequency translator using an electro-optic interaction [2.67, 2.68] with a travelling electric wave [2.52, 2.53] for TE-TM mode conversion combined with optical frequency shifting.

This optical frequency shifter is based on spatially weighted coupling between two nonsynchronous waves. These could, for instance, be the TE and TM modes of a stripe waveguide. Here the "weights" are realised by pairs of electrodes forming an electro-optically induced periodic coupling structure that can be moved at variable speeds forward and backward along the optical stripe waveguide.

Figure 2.15 shows a schematic of an integrated electro-optic frequency shifter based on the above principle. Let the period of the two sets of interdigital electrodes be Λ and the phase constants of the two propagating modes be β_1 and β_2; then

$$\Delta\beta = (\beta_1 - \beta_2) = 2\pi/\Lambda \qquad (2.14)$$

If the driving voltages, V_1 and V_2, of the two sets of electrodes are proportional to cos μ and sin μ, then the emerging wave optical will propagate as $\exp i(\mu - x\Delta\beta)$. By operating this proposed device with a time-linear phase shift, i.e. $\mu = \Omega t$, the emerging wave will propagate as $\exp i(\Omega t - x\Delta\beta)$. Therefore, it can be seen that a frequency translation Ω is attained using the travelling wave interaction.

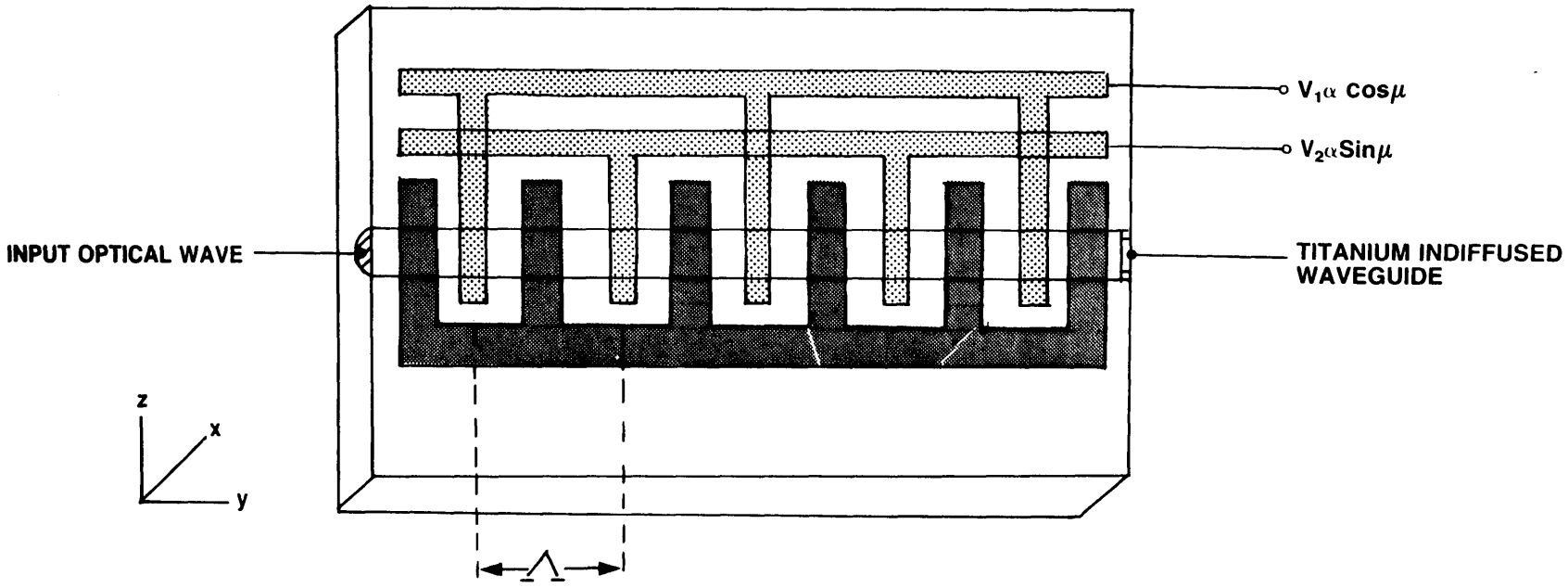

Figure 2.15 Schematic Of An IO Frequency Shifter (After Reference 2.49)

In contrast to the Bragg interaction technique for optical frequency translation, the electro-optic implementation enables the optical signal to be shifted from $-\Omega_{max}$ to $+\Omega_{max}$. Here the frequency limit of Ω is dictated by the electronic driving circuitry and the design of the electrodes. This device potentially will enable S.S.B. modulation to be performed from zero up to 1 GHz.

The device was designed for an operating wavelength of 730 nm. From the published value of birefringence for $LiNbO_3$, a beat length Λ = 9 mm was calculated. Therefore the gaps and widths of the electrodes were of equal values of 2.25 μm. With 960 such electrodes, arranged in 16 sections of 15 finger pairs in each of the two systems, a voltage of 27 V was needed for full transfer of power to the output beam. Therefore the total interaction length of the frequency translator was 4.464 mm.

The optical frequency translator described above was realised using a single-mode Ti:$LiNbO_3$ stripe waveguide on a Y-cut substrate. The device was tested with a tunable dye laser with the laser beam propagating along the X-direction and found to operate efficiently at λ= 723 nm. This implied that there was a discrepancy in the value of the birefringence of the $LiNbO_3$ device and the published value. The device was tested between -1 MHz and +1 MHz while driven by two phase-quadrature voltages of about 27 V at the offset frequency. In this case, the optical carrier and undesired sidebands were suppressed by better than 30 dB, using polarisers. The conversion efficiency was estimated to be $\geq$ 70%. The actual total device length was 4.5 mm and butt coupling of optical fibres to the device is clearly possible. The projected bandwidth of the device is a few GHz but it is anticipated that this will be very difficult to achieve because of electrical quadrature requirements.

The main drawbacks of the above device are:

(1) Its performance is dependent on the birefringence of the $LiNbO_3$ crystal since the electrode pattern is designed for a specific birefringence value, and

(2) The need for polarisers to filter off the carrier.

2.3.4 Integrated-Optical Channel-Waveguide Frequency Translator by Johnson et al

The optical frequency translator proposed and demonstrated by Johnson et al [2.69] is similar to that reported in Section 2.3.3. In the approach taken by Johnson et al, the interdigitated electrode structure was driven with a three-phase electrical signal to generate the refractive index perturbation so that phase-matching and therefore high conversion efficiency could be achieved from dc to several GHz. The use of the three-phase-drive interdigitated electrode system is similar in concept to the earlier reported paper on wide-band slab-waveguide Bragg-diffraction frequency translator [2.45] as described in Section 2.3.2.

The schematic of the device is illustrated in Figure 2.16. The basic operation of the device is similar to that of the device reported in Section 2.3.3. The format for generating the travelling refractive index wave using an interdigitated electrode array is shown in Figure 2.16. Here the relative phases of the electrical drive signal can be selected to achieve single sideband frequency translation to $-\omega_s$ or $+\omega_s$. For this device the upper frequency limit is determined by the capacitance of the electrode array. It is predicted that this device can operate up to several GHz. However at these higher operating frequencies, the design of the travelling wave electrode is critical and may be the major problem to its successful implementation.

The device was fabricated in X-cut $LiNbO_3$ with the optical waveguides oriented parallel to the Y-axis so that the r_{51} electrooptic coefficient could be utilised for TE/TM mode conversion. There were 201

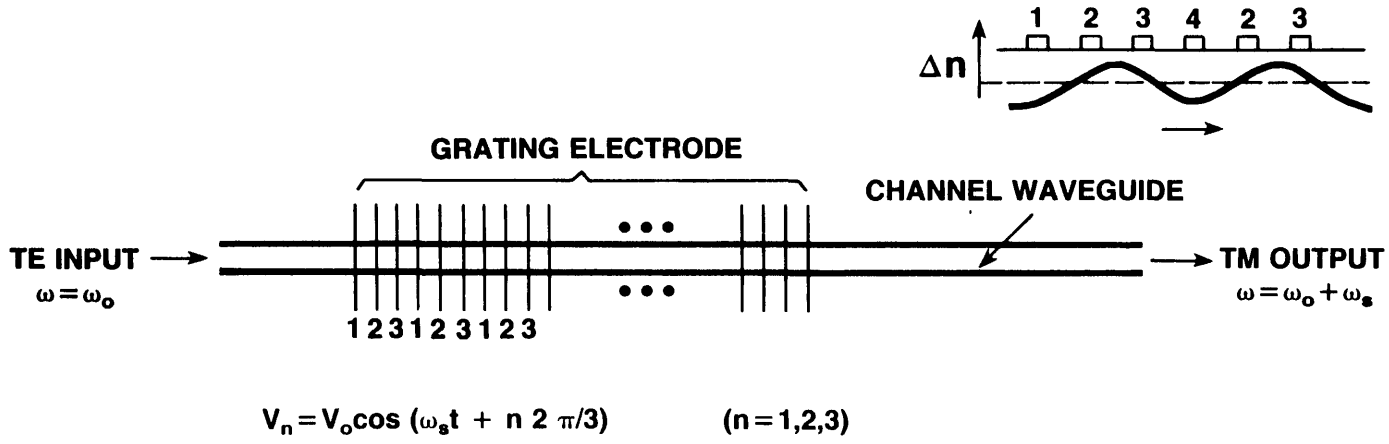

Figure 2.16 Schematic Of The Channel Waveguide Frequency Shifter. (A Sketch Of The Fundamental Component Of The Refractive Index Wave Generated Beneath The Three-Phase-Drive Electrode Structure Is Also Shown) (After Reference 2.66)

electrodes in the fabricated grating which corresponded to 67 rf wavelengths and the refractive index wave spatial period varied across the waveguide array from 13.8 μm to 20.1 μm. The experimental structure shown in Figure 2.17 consisted of an array of 32 straight waveguides intersecting a fanned-out electrode grating. The reason for this was to ensure that at least one device would be at or near the phase matched period.

The devices were tested at an operating wavelength of 1.15 μm by coupling TE polarised light into the optical waveguides and monitoring the TM polarised light output. Again, as described in Section 2.3.2, the electrode grating was driven with the equivalent of a three-phase-drive by grounding one phase and driving the other phases with equal voltages at a 60° relative phase angle [2.45]. The device was operated at 90 MHz with a peak-to-peak driving voltage of 10 V. The optimum electrode spacing was determined to be 5.1 μm which implied a birefringence value of 0.08 which is within the range of published birefringence values for $LiNbO_3$. For the reported device, a 10% conversion efficiency was measured. No mention of the suppression of the required sideband to the spurious sidebands was given. However Johnson et al did report the observation of lower and upper sidebands by unbalancing the drive voltages.

Again as in Section 2.3.3, the main drawbacks of this device are the dependence on the value of the birefringence of the $LiNbO_3$ substrate, broadband operation problems and the need for external or integral optical polarisers to ensure correct operation of the devices making this device unattractive for fibre sensors and optical communication systems applications.

2.3.5 Serrodyne Optical Frequency Translators

The serrodyne optical frequency translator can be classed as the simplest of all the optical frequency translators proposed and demonstrated

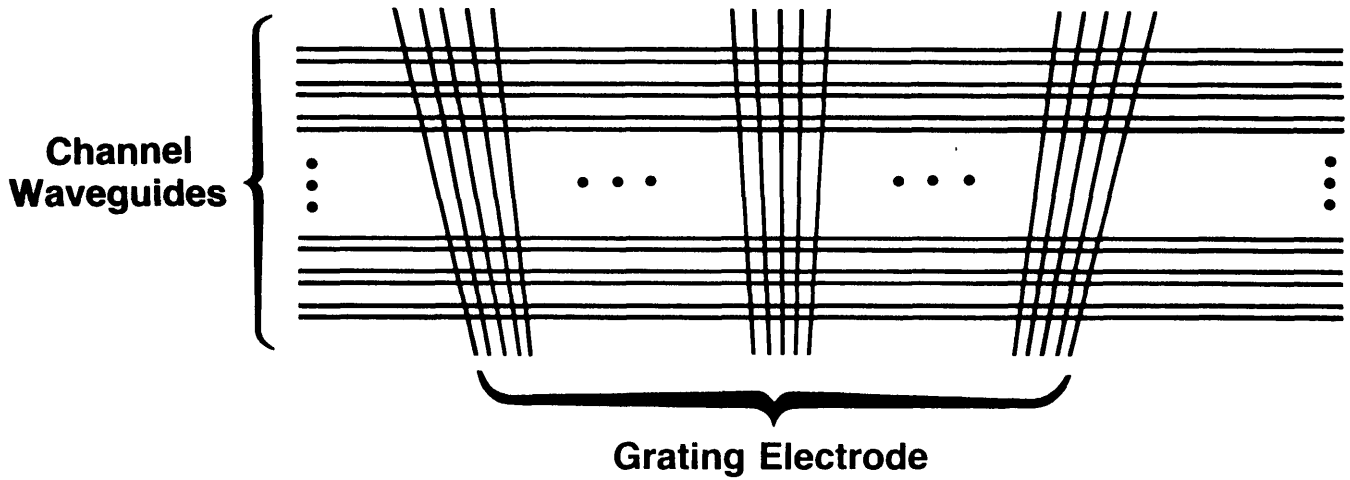

Figure 2.17 Schematic Of The Experimental Structure Showing A Portion Of Both The Waveguide Array And The Fanned-Out Grating Electrode (After Reference 2.66)

to this day. It consists of an integrated optical phase modulator and optical frequency translation is achieved by driving it with a sawtooth waveform. The device was first demonstrated by Wong and Wright [2.56] and later by Johnson and Cox [2.58] at operating wavelengths of 633 nm and 830 nm.respectively. Thylen et al [2.57] and Johnstone [2.70] later operated serrodyne modulators at a wavelength of 1.3 μm.

The serrodyne modulator was considered for use in the fibre optic gyroscope by Kay [2.59]. He considered the behaviour of the device in a closed-loop fibre-optic gyroscope. It was concluded that a non-ideal sawtooth waveform driven phase modulator can affect the scale factor of the gyro and its linearity. In order to reduce the errors to acceptable levels it is necessary to control the peak phase and also to minimise the flyback time of the sawtooth waveform. The value of the flyback time must be known in order to provide the necessary compensation in a closed loop gyro. Toda et al [2.71] employed a serrodyne frequency translator in their optical integrated circuit for realisation of a fibre based laser doppler velocimeter. The use of the serrodyne device was necessary in their self heterodyne detection scheme. The easy implementation and the good performance of the serrodyne device prompted its use in the optical signal processing chip.

The principle of operation and the various realisations of the serrodyne frequency translator are described in detail in Chapters 3 and 6 of this thesis respectively.

2.3.6 Discussions of Optical Frequency Translators Realised by Electro-Optic Methods

Of all the IO electro-optic frequency translators described, the two most useful types are the quadrature type devices proposed and demonstrated by Culshaw and Wilson [2.49] and John and Wilson [2.50] respectively and the serrodyne device [2.56]. All the others can be considered primarily as

interesting demonstrations. The device reported by Izutsu et al [2.51] is not practical due to the very high insertion loss and the requirement of many bias signals. Devices proposed and demonstrated by Kingston, Heismann, and Johnson, are not practically attractive since performance depends strongly on the birefringence of the $LiNbO_3$ crystal for optimum operation. In addition, these devices require polarisers to implement frequency translation and serious electrical matching problems exist for broadband high frequency operation. Hence the devices can be considered to be too complex and demanding (in tolerance terms) to use in actual system implementations..

2.4 Single-Mode Optical Fibre Frequency Translators

The use of an all-single-mode fibre optic system (e.g. in rotation sensors [2.47, 2.72]) is attractive since there may be a reduction in coupling problems compared to that encountered in coupling between single-mode fibres and single-mode channel waveguides in $LiNbO_3$ substrates. Also, the processing of the guided light could all be done within the fibre. Recently, all-single-mode fibre optic devices like, for example, directional couplers [2.73], polarisation controllers [2.74], polarisers [2.75], tunable couplers [2.76] and phase modulators [2.77] have all been demonstrated.

Optical fibre frequency translators using suitable optical fibres and suitable acousto-optic transducers appropriately located on the fibre have been proposed and demonstrated by various researchers [2.46, 2.78, 2.79, 2.80]. Optical fibre frequency translators based on the serrodyne method have also been demonstrated [2.60]. Examples of these devices are reported in the following sections.

2.4.1 Acousto-Optic Realisation

Nosu et al reported the first demonstration of an acousto-optic (AO) frequency translator using single-mode optical fibre [2.46]. Figure 2.18 illustrates the schematic of the device. It consisted of two PZT phase shifters with a highly birefringent fibre (in this case with a beat length, L_p = 3.4 cm). The distance between the centres of the phase shifters should be an odd multiple of a quarter beat length of the fibre. The jacket of the highly birefringent fibre was removed. The fibre was then placed in a capillary tube filled with mineral oil. The capillary tube with the fibre in it was then suitably placed through the two PZT cylinders, filled with mineral oil and held in place with teflon end caps. The principle is that a standing pressure wave (set-up when the PZT cylinders are driven with an RF source) will cause elastooptic coupling between the polarisation modes of the highly birefringent fibre.

When one of the PZT cylinders is driven by an RF signal, upper and lower sidebands will be generated on either side of the carrier. For the other cylinder, the same result will occur. If one of the cylinders is driven 90° out of phase with respect to the other, single-sideband generation will result. All these effects were observed experimentally. S.S.B.S.C. generation was performed at 5 MHz with a 20 dB discrimination between the upper and lower sidebands. There were no spurious sidebands observed at higher frequencies.

In summary, a simple single-mode AO frequency translator has been proposed and demonstrated using highly birefringent single-mode fibres. The device works up to 5 MHz with a suppression of 20 dB in the image sideband. Both up-shift and down-shift in frequency can be achieved by appropriately reversing the phase delay on the cylinders.

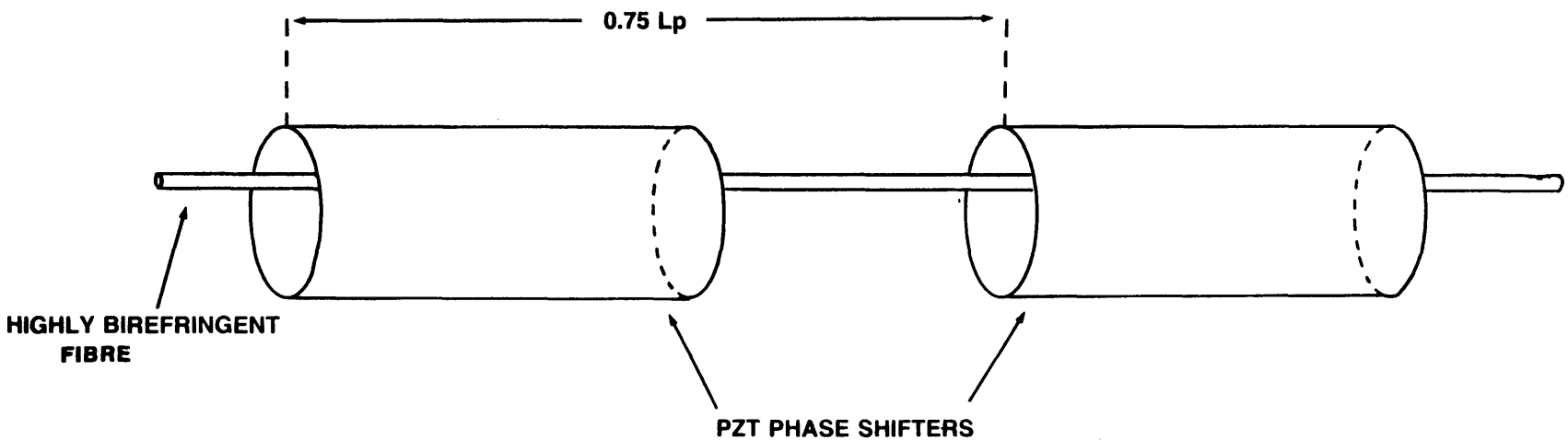

Figure 2.18 Schematic Of A Single-Mode Fibre Acousto-Optic Frequency Shifter (After Reference 2.53)

2.4.2 Serrodyne Realisation

Instead of an integrated optic phase-modulator, a simple optical-fibre phase-shifter was used by Dakin et al in their optical fibre serrodyne frequency translator experiments [2.60]. The optical fibre phase shifter consisted of several turns of optical fibre on a small hollow PZT cylinder of diameter 25.4 mm, length 25.4 mm, and wall thickness of 3.2 mm. The optical fibre (single-mode communication type) was bonded to the cylinder to ensure good mechanical coupling. The device was tested by driving it with a sawtooth waveform. However a number of problems were observed. Resonances were observed and these were therefore damped by the use of plasticine and eventually the device was packed into a metal box filled with a plastic damping compound. In addition, in order to ensure that the response of the PZT cylinder to sawtooth waveforms was improved, an electronic feedback method was used. No actual results on the optical frequency translation performance were reported. Therefore at this time this device cannot be compared to optical fibre translators realised by acousto-optic techniques.

2.5 Summary

Three main methods of optical frequency shifting/translation, i.e. acousto-optic/Bragg interaction with a surface acoustic wave, the quadrature method and the use of electro-optic interaction have all been discussed. Implementation to date by various configurations using integrated and guided-wave optics technology have all been examined. The serrodyne method of performing optical frequency translation by phase modulation with the application of sawtooth waveforms will be discussed fully in the Chapters 3 and 6. It can be concluded from this review of optical frequency

translators that the two most promising and practical methods that can be implemented for fibre systems are:-

(1) The serrodyne technique [2.56]: This method is useful when the range of frequency translation is from dc to tens of MHz but is limited at this time by the driving electronics, and

(2) The quadrature method (Culshaw and Wilson) [2.49]: This method is potentially useful for optical frequency translations of up to several GigaHertz.

REFERENCES

[2.1] M.A. Duguay, L.E. Hargrove and K.B. Jefferts, "Optical Frequency Translation of Mode-Locked Laser Pulses", Appl. Phys. Lett., Vol. 9, No. 8, pp 287-290, 15th October 1966.

[2.2] R. Crane, "Interference Phase Measurement", Appl. Opt., Vol. 8, No. 3, pp 538-542, March 1969.

[2.3] A.G. Fox, "An Adustable Waveguide Phase Changer", Proc. IRE, Vol. 35, pp 1489-1498, December 1947.

[2.4] R.F. Soohoo, "Ferrite Microwave Phase Shifters", IRE Conv. Rec., Pt. 5, pp 84-98, 1956.

[2.5] J. Cacheris, "Microwave Single-Sideband Modulator Using Ferrites", Proc. IRE, Vol. 42, pp 1242-1247, August 1954.

[2.6] R.C. Cumming, "The Serrodyne Frequency Translator", Proc. IRE, Vol. 45, pp 175-186, February 1957.

[2.7] C. Montgomery, "Techniques of Microwave Measurements", Vol. 11, MIT Radiation Laboratory Series, McGraw-Hill, N.Y., 1947, pp 331.

[2.8] A. Clavin, "A Microwave Ferrite Single-Sideband Modulator", IRE Trans. on Microwave Theory and Techniques, Vol. MTT-10, pp 98-102, March 1962.

[2.9] A.L. Schawlow and C.H. Townes, "Infra-red and Optical Masers", Phys. Rev., Vol. 112, No. 6, pp 1940-1949, 15th December 1958.

[2.10] C.F. Buhrer, L.R. Bloom and D.H. Baird, "Electro-Optic Modulation with Cubic Crystals, Appl. Opt., Vol. 2, pp 839-846, August 1963.

[2.11] R.N. Shagam and J.C. Wyant, "Optical Frequency Shifter for Heterodyne Interferometers using Multiple Rotating Polarisation Retarders", Appl. Opt., Vol. 17, No. 19, pp 3034-3035, 1st October 1978.

[2.12] G.E. Sammargren, "Up/Down Frequency Shifter for Optical Heterodyne Interferometer", J. Opt. Soc. Am., Vol. 65, No. 8, pp 960-961, August 1975.

[2.13] Y. Yeh and H.Z. Cummins, "Localised Fluid Flow Measurements with an He-Ne Laser Spectrometer", Appl. Phys. Lett., Vol. 4, No. 10, pp 176-178, 15th May 1964.

[2.14] G. Magerl and E. Bonek, "A 2.75 GHz Tunable $C0_2$-Laser Infra-red Source", J. Appl. Phys., Vol. 47, No. 11, pp 4901-4903, November 1976.

[2.15] W.E. Bicknell, L.R. Tomasetta and R.H. Kingston, "10.6 μm FM-Chirp Radar using Narrow-Band Correlation Detection", IEEE J. Quantum Electron., Vol. QE-11, No. 6, pp 308-311, June 1975.

[2.16] C. Yeh, "A Proposed Method of Shifting the Frequency of Light Waves", Appl. Phys. Lett., Vol. 9, No. 5, pp 184-185, 1st September 1966.

[2.17] W.H. Stevenson, "Optical Frequency Shifting by Means of a Rotating Diffraction Grating", Appl. Opt., Vol. 9, No. 3, pp. 649-652, March 1970.

[2.18] H. Cummins, N. Knable, L. Gampel and Y. Yeh, "Frequency Shifts in Light Diffracted by Ultrasonic Waves in Liquid Media", Appl. Phys. Lett., Vol. 2, No. 3, pp 62-64, 1st February 1963.

[2.19] H.Z. Cummins and N. Knable, "Single-Sideband Modulation of Coherent Light by Bragg Reflection from Acoustical Waves", Proc. IEEE, Vol. 51, pp 1246, September 1963.

[2.20] J.B. Abbiss and W.T. Mayo, Jr., "Deviation-Free Bragg Cell Frequency Shifting", Appl. Opt., Vol. 20, No. 4, pp 588-590, 15th February 1981.

[2.21] C.F. Buhrer, V.J. Fowler and L.R. Bloom, "Single-Sideband Suppressed-Carrier Modulation of Coherent Light Beams", Proc. IRE, Vol. 50, pp 1827-1828, August 1962.

[2.22] C.F. Buhrer, D. Baird and E.M. Conwell, "Optical Frequency Shifting by Electro-Optic Effect", Appl. Phys. Let., Vol. 1, No. 2, pp 46-49, 1st October 1962.

[2.23] T. Tudor, A. Dumitrica and D. Apostol, "Optical Frequency Translator using Two KDP Crystals in Tandem", Analele Universitatii Bucuresti, Fizic" XXIX, pp 31-35, 1980.

[2.24] A. Dumitrica and T. Tudor, "Single-Sideband Suppressed Carrier Electro-Optic Modulator", Rev. Roum. Phys., Tame 26, No. 2, pp 183-189, 1981.

[2.25] J.P. Campbell and W.H. Steier, "Rotating-Waveplate Optical Frequency Shifting in Lithium Niobate", IEEE J. Quantum Electron., Vol. QE-7, No. 9, pp 450-457, September 1971.

[2.26] D.E.N. Davies, "Making Measurements with Light", IEE Proc., Vol. 129, Pt A, No. 1, pp 16-23, January 1982.

[2.27] B. Culshaw, "Optical Fibre Transducers", The Radio and Electronic Engineer, Vol. 52, No.6 , pp 283-290 , June 1982.

[2.28] T.G. Giallorenzi, J.A. Bucaro, A. Dandridge, G.H. Sigel, Jr., J.H. Cole, S.C. Rashleigh and R.G. Priest, "Optical Fibre Sensor Technology", IEEE J. Quantum Electronics, Vol. QE-18, No. 4, pp 626-665, April 1982.

[2.29] M.J. Lavan, G.E. Van Damme and W.K. Cadwallender, "Possible Use of the Mach-Zehnder Heterodyne Interferometer as a Gyroscope", Opt. Enging., Vol. 16, No. 3, pp 313-314, May-June 1977.

[2.30] M.A. Nokes, B.C. Hill and A.E. Barell, "Fibre Optic Heterodyne Interferometer for Vibration Measurements in Biological Systems", Rev. Sci. Instrum., Vol. 49, No. 6, pp 722-728, June 1978.

[2.31] T.J. Hall, "High Performance Multimode Optical Fibre Acoustic Sensor Utilising Heterodyne Detection", IEE Proc., Vol. 127, Pt. H, No. 4, pp 193-200, August 1980.

[2.32] D.A. Jackson, "A Prototype Digital Phase Tracker for the Fibre Interferometer", J. Phys. E: Sci. Instrum., Vol. 14, pp 1274-1278, 1981.

[2.33] S.C. Lin and T.G. Giallorenzi, "Sensitivity Analysis of the Sagnac-effect Optical-Fibre Ring Interferometer", Appl. Opt., Vol. 18, No. 6, pp 915-931, 15th March 1981.

[2.34] B. Culshaw and I.P. Giles, "Frequency Modulated Heterodyne Optical Fibre Sagnac Inteferometer", IEEE J. Quantum Electron., Vol. QE-18, No. 4, pp 690-693, April 1982.

[2.35] M.L. Hemming, S.W. Thornton, R. Carpenter, W.J. Stewart, J.P. Dakin and C.A. Wade, "Optical Fibre Hydrophones with Down Lead Insensitivity", First International Conference on Optical Fibre Sensors, IEE Conf. Proc. No. 221, pp 23-27, 26-28 April 1983.

[2.36] D. Eberhard and E. Voges, "Optical Single-Sideband Detection Applied to Fibre-Optic Sensors", Second European Conference on Integrated Optics, Florence, 17-18 October 1983.

[2.37] N.A. Massie, R.D. Nelson and S. Holly, "High-performance Real-time Heterodyne Interferometry", Appl. Opt., Vol. 18, No. 11, pp 1797-1803, 1st June 1979.

[2.38] R.G. Cahill and E. Udd, "Phase-Nulling Fibre-Optic Laser Gyro", Opt. Lett., Vol. 4, No. 3, pp 93-95, March 1979.

[2.39] K. Hotate, N. Okuma, M. Higashiguchi and N. Niwa, "Rotation Detection by Optical Heterodyne Fibre Gyro with Frequency Output", Opt. Lett., Vol. 7, No. 7, pp 331-333, July 1982.

[2.40] C.S. Tsai, C.L. Chang , C.C. Lee and K.Y. Liao, "Acousto-Optic Bragg Deflection in Channel Optical Waveguides", Topical Meeting on Integrated and Guided-Wave Optics, Technical Digest of Post-Deadline Papers, pp PD7-1 to PD7-4, 1980.

[2.41] C.S. Tsai, C.T. Lee and C.C. Lee, "Efficient Acousto-Optic Diffraction in Crossed Channel Waveguide and Resultant Integrated Optic Module", Ultrasonics Symposium, IEEE, pp 422-425, 1982.

[2.42] C.H. von Helmolt, R.T. Kersten, W. Auch and W. Steudle, "Bragg Switch/S.S.B. Modulator with Integrated Optic Single-Mode Waveguides", Second European Conf. on Integrated Optics, Florence, 17-18 October 1983.

[2.43] C. Schaffer and K. Petermann, "Integrated Optic Frequency Shifters With SAWs", Proc. SPIE on "Integrated Optical Circuit Engineering III", Vol. 651, Innsbruck, Austria, pp 203-206, 16-18 April 1986.

[2.44] C. Schaffer, "Integrated-Optical Single-Sideband Bragg Modulator With Tapered Waveguides", Electron. Lett., Vol. 24, No. 10, pp 606-608, 12 May 1988.

[2.45] R.H. Kingston, R.A. Becker and F.J. Leonberger, "Broadband Guided-Wave Optical Frequency Translator using an Electro-Optical Bragg Array", Appl. Phys. Lett., Vol. 42, No. 9, pp 759-761, 1st May 1983.

[2.46] K. Nosu, S.C. Rashleigh, H.F. Taylor, and J.F. Weller, "Acousto-Optic Frequency Shifter for Single-Mode Fibres", Electron. Lett., Vol. 19, No. 20, pp 816-818, 29 September 1983.

[2.47] R.A. Bergh, H.C. Lefevre and H.J. Shaw, "All-Single-Mode Fibre-Optic Gyroscope", Opt. Lett., Vol. 6, No. 4, pp 198-200, April 1981.

[2.48] R.J. King, "Microwave Homodyne Systems", Peter Peregrinus Limited, 1978.

[2.49] B. Culshaw and M.G.F. Wilson, "Integrated Optic Frequency Shifter Modulator", Electron. Lett., Vol. 17, No. 3, pp 135-136, 5th February 1981.

[2.50] D. John and M.G.F. Wilson, "Experimental Demonstration of a Square Wave Driven Integrated Optical Frequency Shifter", Proc. of the Fourth European Conference on Integrated Optics, ECIO 87, Editors: C.D.W. Wilkinson and J. Lamb, Glasgow, Scotland, pp 107-110, 11-13 May 1987.

[2.51] M. Izutsu, S. Shikama and T. Sueta, "Integrated Optical S.S.B. Modulator/Frequency Shifter", IEEE J. Quantum Electron., Vol. QE-17, No. 11, pp 2225-2227, November 1981.

[2.52] F. Heismann and R. Ulrich, "Integrated-Optical Single-Sideband Modulator and Phase Shifter", IEEE J. Quantum Electron., Vol. QE-18, No. 4, pp 767-771, April 1982.

[2.53] F. Heismann and R. Ulrich, "Integrated-Optical Frequency Translator With Stripe Waveguide", Appl. Phys. Lett., Vol. 45, No. 5, pp 490-492, 1 September 1984.

[2.54] F. Auracher and R. Keil, "Method for Measuring the RF Modulation Characteristics of Mach-Zehnder Type Modulators", Appl. Phys. Lett., Vol. 36, No. 8, pp 626-629, 15th April 1980.

[2.55] C.M. Gee, G.D. Thurmond and H.W. Yen, "Travelling-Wave Electro-Optic Modulator", Appl. Opt., Vol. 22, No. 13, pp 2034-2037, 1st July 1983.

[2.56] K.K. Wong and S. Wright, "An Optical Serrodyne Frequency Translator", First European Conf. on Integrated Optics, London, IEE Conf. Proc. No. 201, pp 63-65, 14-15 September 1981.

[2.57] L. Thylen, P. Sjoberg, and G.E. Lindqvist, "Electro-Optical Serrodyne Frequency Translator for $\lambda = 1.3\ \mu m$", Proc. IEE, Pt. J, Vol. 132, No. 2, pp 119-121, April 1985.

[2.58] L.M. Johnson and C.H. Cox III, "Lithium Niobate Serrodyne Frequency Translator for Fibre-Optic Gyroscope", Proc. SPIE on "Fibre Optic Gyros - 10th Anniversary Conference", Vol. 719, pp 141-145, 24-26 September 1986.

[2.59] C.J. Kay, "Serrodyne Modulator in a Fibre-Optic Gyroscope", IEE Proc., Pt. J, Vol. 132, No. 5, pp 259-264, October 1985.

[2.60] J.P. Dakin, C.A. Wade, and C. Haji-Michael, "A Fibre Optic Serrodyne Frequency Translator Based on a Piezoelectrically-Strained Fibre Phase Shifter", IEE Proc., Pt. J, Vol. 132, No. 5, pp 287-290, October 1985.

[2.61] Y. Ohmachi, "Acousto-Optical Light Diffraction in Thin Films", J. Appl. Phys., Vol. 44, No. 9, pp 3928-3933, September 1973.

[2.62] R.V. Schmidt, "Acousto-Optic Interactions Between Guided Optical Waves and Surface Acoustic Waves", IEEE Trans. Sonics and Ultrasonics, Vol. SU-23, No. 1, pp 22-33, January 1976.

[2.63] C.S. Tsai, M.A. Alhaider, L.T. Nguyen and B. Kim, "Wideband Guided-Wave Acousto-Optic Bragg Diffraction and Devices using Multiple Tilted Surface Acoustic Waves", Proc. IEEE, Vol. 64, No. 3, pp 318-328, March 1976.

[2.64] R. Adler, "Interaction Between Light and Sound", IEEE Spectrum, Vol. 55, No. 5, pp. 42-54, May 1967.

[2.65] A. Neyer, W. Mevenkamp, and B. Kretzschmann, "Optimization Of X-Switches For Integrated Optical Switching Networks", Proc. 5th International Conference On Integrated Optics And Optical Fibre Communication and 11th European Conference On Optical Communication, Venezia, Italy, pp 369-372, 1-4 October 1985.

[2.66] B. Culshaw, I.P. Giles, and M.G.F. Wilson, "Integrated Optic Frequency Shifter", IEE Conference on Communications Equipment and Systems, Birmingham Metropole Hotel, pp 272-275, 20-22 April 1982.

[2.67] D. Marcuse, "Electro-optic Coupling Between TE and TM Modes in Anisotropic Slabs", IEEE J. Quantum Electron., Vol. QE-11, No. 9, pp 759-767, September 1975.

[2.68] R.C. Alferness and L.L. Buhl, "Electro-Optic Waveguide TE↔TM Mode Converter with Low Drive Voltage", Opt. Lett., Vol. 5, No. 11, pp 473-475, November 1980.

[2.69] L.M. Johnson, R.A. Becker, and R.H. Kingston, "Integrated-Optical Channel-Waveguide Frequency Shifter", Seventh Topical Meeting on Integrated and Guided-Wave Optics, Kissimmee, Orlando, pp WD4-1 to WD4-4, 24-26 April 1984.

[2.70] W. Johnstone, I. Andonovic, M.S. Ner, and D.N. MacFadyen, "Integrated Optical Frequency Translators", Colloquium on "Advances in Coherent Optic Devices and Technologies", London, 2/1-2/6, 26 March 1985.

[2.71] H. Toda, M. Haruna, and H. Nishihara, "Optical Integrated Circuit for a Fibre Laser Doppler Velocimeter", J. Lightwave Tech., Vol. LT-5, No. 7, pp 901-905, July 1987.

[2.72] S.K. Sheem, "Fibre-Optic Gyroscope with [3 x 3] Directional Coupler", Appl. Phys. Lett., Vol. 37, No. 10, pp 869-871, 15th November 1980.

[2.73] R.A. Bergh, G. Kotler and H.J. Shaw, "Single-Mode Fibre-Optic Directional Coupler", Electron. Lett., Vol. 16, No. 7, pp 260-261, 27th March 1980.

[2.74] H.C. Lefevre, "Single-Mode Fibre Fractional Wave Devices and Polarisation Controllers", Electron. Lett., Vol. 16, pp 778-780, 25th September 1980.

[2.75] R.A. Bergh, H.C. Lefevre and H.J. Shaw, "Single-Mode Fibre-Optic Polariser", Opt. Lett., Vol. 5, No. 11, pp 479-481, November 1980.

[2.76] M.J.F. Digonnet and H.J. Shaw, "Analysis of a Tunable Single Mode Optical Fibre Coupler", IEEE J. Quantum Electron., Vol. QE-18, No. 4, pp 746-754, April 1982.

[2.77] K. Nosu, H.F. Taylor, S.C. Rashleigh and J.F. Weller, "Acousto-Optic Phase Modulator for Single-Mode Fibres", 4th IOOC, Tokyo, Main Conference, Paper 28C3-5, pp 316-317, 27-30 June 1983.

[2.78] W.P. Risk and G.S. Kino, "Acousto-Optic Fibre-Optic Frequency Shifter Using Periodic Contact With a Copropagating Surface Acoustic Wave", Opt. Lett., Vol. 11, No. 5, pp 336-338, May 1986.

[2.79] H.F. Taylor, "Acoustooptic Phase and Frequency Shifters for Single Mode Fibers", Proc. SPIE on "Fibre Optic Gyros - 10th Anniversary Conference", Vol. 719, pp 87-91, 24-26 September 1986.

[2.80] J.N. Blake, B.Y. Kim, H.E. Engan, and H.J. Shaw, "All-Fiber Acousto-Optic Frequency Shifter Using Two-Mode Fiber", Proc. SPIE on "Fibre Optic Gyros - 10th Anniversary Conference", Vol. 719, pp 92-100, 24-26 September 1986.

CHAPTER 3 THEORY OF 'SERRODYNE' METHOD OF OPTICAL FREQUENCY TRANSLATION

3.1 Introduction 55

3.2 Optical Frequency Translation by Phase-Modulation 55

3.3 Optical Frequency Translation by Sawtooth Phase-Modulation 57

3.4 Analysis of Serrodyne Performance 58

3.4.1 Introduction 58
3.4.2 Effect of Non-Zero Flyback/Fall-time 60
3.4.3 Effect of Non-Optimum Sawtooth Amplitude 62
3.4.4 Effect of Non-Linear Sawtooth Phase Variation 63
3.4.5 Effect of Non-Optimum Operation Over a Band/Range of Frequencies using a Constant Sawtooth Amplitude 63
3.4.6 Effects of the Presence of Amplitude Modulation in an Electro-Optic Phase Modulator 65

3.5 Examples of the Use of Optical Frequency-Translators in Fibre-Optic and Integrated Optical Sensor Systems 67

3.5.1 Introduction 67
3.5.2 Fibre-Optic Hydrophone 67
3.5.3 Fibre-Optic Gyroscope 69
3.5.4 Fibre-Optic Laser Doppler Velocimeter 72

3.6 Summary 74

Appendix 3.1 75

A3.1.1 Fourier Series - Recap 75
A3.1.2 Output Waveform Analysis for Stepped Phase Function 75
A3.1.2.1 Ideal N-Step Case 77
A3.1.2.2 Ideal 3-Step Case 83

Appendix 3.2 84

A3.2.1 Perfect Sawtooth Waveform 84
A3.2.2 Effect of Finite Flyback Time T_f 86

Appendix 3.3 89

A3.3.1 Sawtooth Waveform with 2nd Order Polynomial Non-Linearities and with Zero Flyback Time 89
A3.3.2 Sawtooth Waveform with 2nd Order 91

References

CHAPTER 3

THEORY OF "SERRODYNE" METHOD OF OPTICAL FREQUENCY TRANSLATION

3.1 Introduction

In this chapter optical frequency translation by the phase-modulation technique using a periodic sawtooth waveform is discussed in detail. The effects of various imperfections in waveform parameters are considered. Finally, possible applications of optical frequency-translators in various fibre-optic systems are discussed briefly.

3.2 Optical Frequency Translation by Phase-Modulation

The need to measure accurately the optical phase changes due to an external stimulus in some optical fibre-sensor system has led to interest in optical frequency-translators based on phase-modulation techniques [3.1-3.5]. Clearly such optical frequency-translators can be realised by using integrated optical electro-optic phase modulators [3.6-3.11].

An ideal optical frequency-shift/translation can be achieved by applying a continuous linear phase deviation as shown in Figure 3.1(a) to an integrated electro-optic phase modulator. For an optical input waveform of unit amplitude and frequency f_c with applied phase-modulation function $\varnothing(t)$, the output waveform is expressed as:

$$e_o = \sin [2\pi f_c t + \varnothing(t)] \qquad (3.1)$$

For the case of the continuous phase function, i.e. $\varnothing(t) = 2\pi f_m t$, where f_m is the modulation frequency,

$$e_o = \sin (2\pi f_c t + 2\pi f_m t)$$

$$= \sin [(\omega_c + \omega_m)t] \qquad (3.2)$$

where $\omega_c = 2\pi f_c$ and $\omega_m = 2\pi f_m$

Equation (3.2) implies that the frequency translation is ideal. In practice, a continuous linear phase function is impossible to obtain, However, this function can also be produced by an ideal sawtooth phase function with a zero fall-time, as illustrated in Figure 3.1(b). This approach is discussed in detail in Section 3.3 of this chapter.

Alternatively, the continuous linear phase function can be approximated by a series of steps of phase (linear staircase) deviation, as shown in Figure 3.1(c). It will be shown in Appendix 3.1 that three is the minimum number of phase steps required to achieve frequency translation with significant suppression of the carrier and the first lower sideband and with a non-zero first upper sideband [3.12]. The phase function for this case becomes

$$\left.\begin{array}{ll} \varnothing(t) = 0 & \text{for } 0 \le t \le +T/3 \\ \varnothing(t) = \pi & \text{for } +T/3 \le t \le +2T/3 \\ \varnothing(t) = 2\pi & \text{for } +2T/3 \le t \le +T \end{array}\right\} \qquad (3.3)$$

where $T = 1/f_m$, is the modulation period.

The Fourier analysis (Appendix 3.1) for this ideal three-step phase function generates spectral lines only at every third modulating frequency interval with the intervening spectral lines going to zero. The amplitudes of

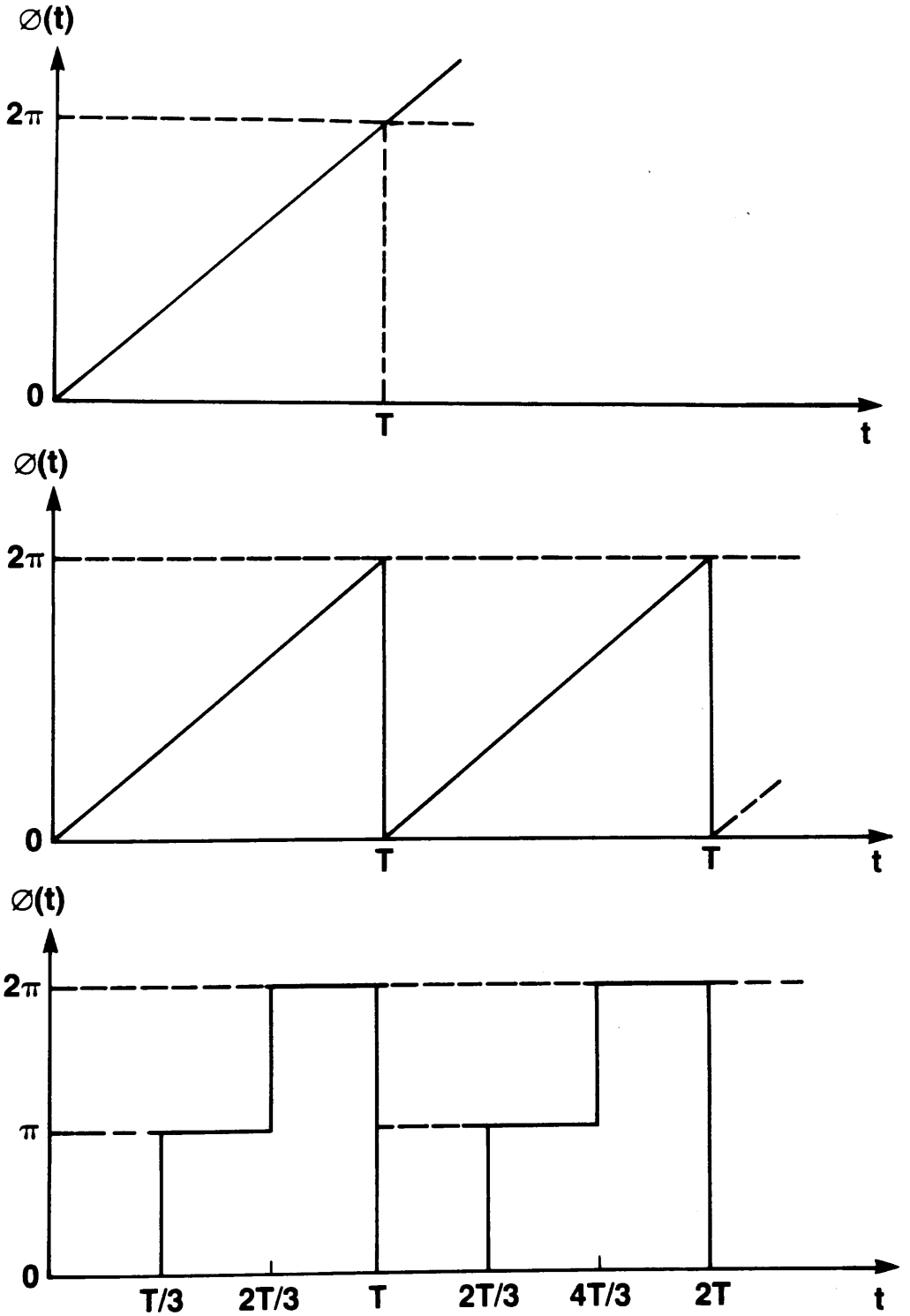

Figure 3.1 Phase Functions For
(a) Linear Continuous Type
(b) Ideal Sawtooth Type
(c) Ideal Three-Step Type

the remaining spectral lines relative to the unmodulated carrier can be shown to be (Appendix 3.1)

$$\left.\begin{aligned} |E_{n+}| &= K_o/n \quad \text{for } n = 1, 4, 7, 10 \ldots \\ |E_{n-}| &= K_o/n \quad \text{for } n = 2, 5, 8, 11 \ldots \end{aligned}\right\} \qquad (3.4)$$

where $K_o = (3\sqrt{3})/2\pi$ and $|E_{n\pm}|$ is the magnitude of the spectral line at $(f_c \pm nf_m)$. A plot of this spectrum is shown in Figure 3.2.

A more general Fourier analysis of an n-step phase function is also given in Appendix 3.1. In the final chapter of this thesis, a proposed optical frequency-translator (using multiple electrodes) based on this idea will be presented.

3.3 Optical Frequency Translation By Sawtooth Phase-Modulation

The serrodyne (the name serrodyne was derived from the Latin word "serra" meaning "saw" or sawtooth".) method approximates the continuous linear phase deviation [shown in Figure 3.1(a)] by increasing the phase of an optical signal continuously and linearly over the full period (T) of the modulation frequency (f_m) and returning instantaneously to the starting phase (i.e. a linear sawtooth waveform with zero fall-time).

From Figure 3.1(b), it can be seen that $\varnothing(t) = (2\pi/T)t = 2\pi f_m t$. Substituting this value of $\varnothing(t)$ into Equation 3.1 gives Equation 3.2 again is implying perfect frequency translation. Using Equation 3.2, it can be deduced that an upshift or a downshift in frequency can be obtained by applying a sawtooth waveform with positive or negative slope. However, in practice, it is not possible to generate a linear sawtooth with zero flyback-time/fall-time. In consequence, any description of a practical linear sawtooth waveform has to

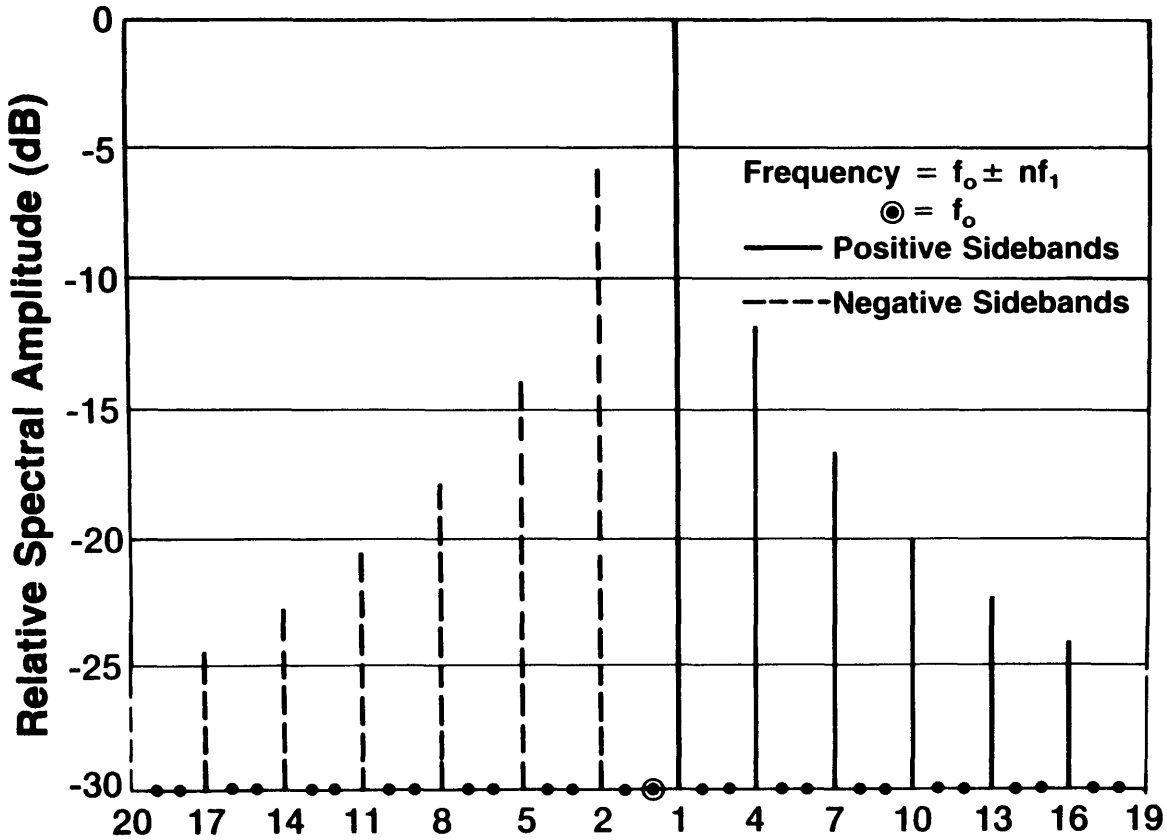

Figure 3.2 Ideal Spectral Response Of A Three–Step Phase Function

include a finite fall-time. The effect of this non-ideal property of a sawtooth waveform will be discussed in later sections of this chapter.

3.4 Analysis of Serrodyne Performance

3.4.1 Introduction

The performance of a serrodyne frequency-translator is evaluated quantitatively in terms of its output spectrum. For convenience, only up-conversion in frequency is considered since down-conversion is given by a mere change in sign in relevent terms.

To recap, the output spectrum of an ideal serrodyne up-frequency-translator is a single frequency, $(f_c + f_m)$, given by Equation 3.2. In practice, total conversion to a single sideband frequency (or perfect frequency translation) cannot be achieved. This means that the spectrum will contain frequencies given by:

$$f_c \pm nf_m \tag{3.5}$$

where n is any integer or zero. Equation 3.5 applies in general for a perfectly periodic waveform and is independent of the waveform and amplitude of the modulation signal.

The relative strengths or levels of the output frequency components could be used to define (when the modulation signal is applied), quantitatively, measures of serrodyne performance, which are:

$$S = 20\ \mathrm{Log}_{10}\left[\frac{\text{Output SA at the desired output frequency}}{\text{Output SA at the highest undesired frequency}}\right] \tag{3.6}$$

where SA is the signal amplitude which is proportional to optical field strength, and

$$L = 20\ \mathrm{Log}_{10}\left[\frac{\text{Output SA when the translator is unmodulated}}{\text{Output SA when the translator is modulated}}\right] \qquad (3.7)$$

where SA is again the signal amplitude, S is defined as the decibel (dB) suppression of a particular undesired frequency component and L is the dB translation loss or relative conversion efficiency. Hence, good performance corresponds to a large value of suppression of unwanted sidebands (S) and a small value of relative conversion loss (L).

The identified predominant factors limiting the performance of a serrodyne frequency-translator, in particular an integrated electro-optic phase modulator that is driven by a sawtooth waveform are:

(a) Non-zero flyback/fall-time,

(b) Non-optimum sawtooth amplitude,

(c) Non-linear sawtooth phase variation,

(d) Non-optimum operation over a band/range of frequencies using a constant sawtooth amplitude, and

(e) Amplitude modulation inherent in an electro-optic phase modulator (due to cut-off modulation as an extreme case of amplitude modulation effect or photoconductive effects [3.13]),

Although in practice a number of limiting factors would be competing, each will be treated separately and the combined effects discussed subsequently. It may well be that only one effect/problem dominates in determining performance of a serrodyne device. However, in a situation where two effects produce the same value of suppression in unwanted

sidebands, the two effects acting at the same time will give a suppression of typically 3 dB less than predicted by either of the effects separately assuming linear superposition and non-coherence of the two effects [3.14].

3.4.2 Effect of Non-Zero Flyback/Fall-Time

The inability of practical drive electronics to generate a perfect sawtooth waveform implies that the reset time or fall-time or flyback time of the waveform has some finite value. Figure 3.3 illustrates a sawtooth waveform with period T and finite fall-time T_f. The derivations of the Fourier amplitudes, C_n, for a perfect (with zero fall-time) (Figure 3.4) and a non perfect (with finite fall-time T_f) sawtooth are given in Appendix 3.2.

The harmonic amplitudes, C_n, for an upshift in frequency ω (where $\omega = 2\pi/T$) when a sawtooth waveform of peak-to-peak amplitude $\varnothing_p$ and finite fall-time T_f is used, are given by Equation A3.2.2.6 (Appendix 3.2), i.e.:

$$C_n = \left\{ \frac{(T - T_f)/T}{[\varnothing_p - 2\pi n(T-T_f)/T]} + \frac{T_f/T}{(\varnothing_p - 2\pi n T_f/T} \right\} * \sin[\varnothing_p - 2\pi n(T-T_f)/T] \qquad (3.8)$$

where n = 0, ±1, ±2, ...

In this analysis, due to the finite fall-time of the sawtooth waveform, the most difficult sidebands to be suppressed are C_0, C_{-1}, C_2, C_{-2}, and C_3 assuming an upshift in frequency at C_1. As can be seen from Equation 3.8, the two main parameters that affect the values of the generated sidebands as a result of frequency translation are the values of $\varnothing_p$ and T_f. Theoretical curves of sideband suppression with respect to variation of phase value about the peak-to-peak value $\varnothing_p$ and T_f/T for an upshift in frequency were studied.

Let's assume that the optimum peak-to-peak phase value is $\varnothing_0$. In this analysis,

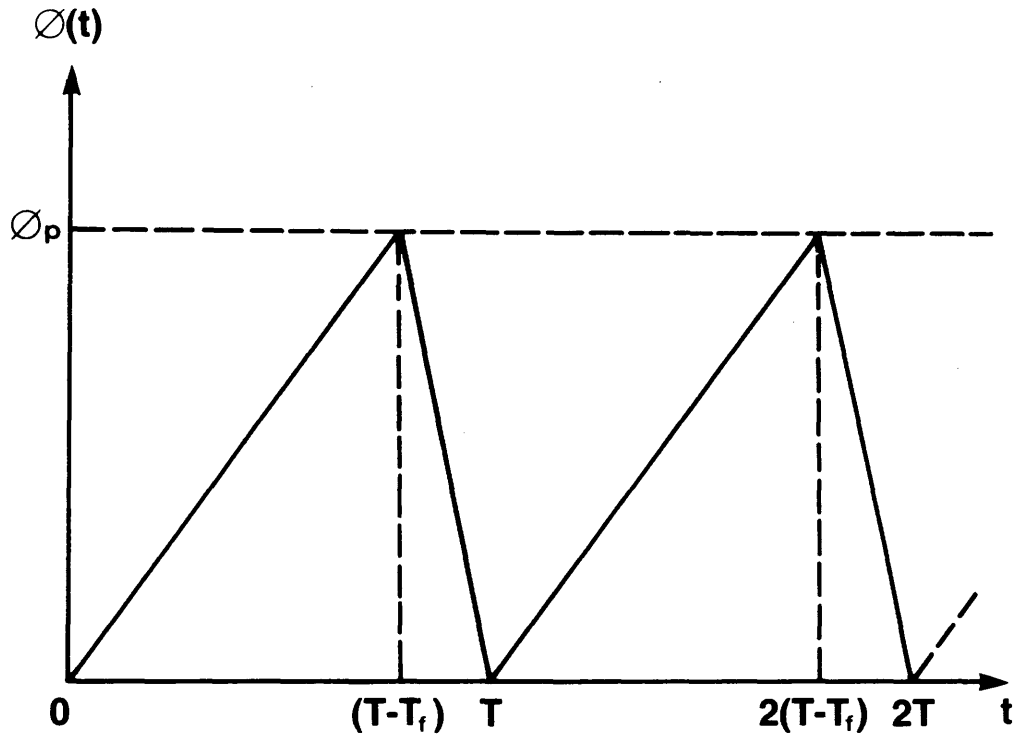

Figure 3.3 A Non–Ideal Sawtooth Waveform With Period T And A Finite Fall–Time T_f

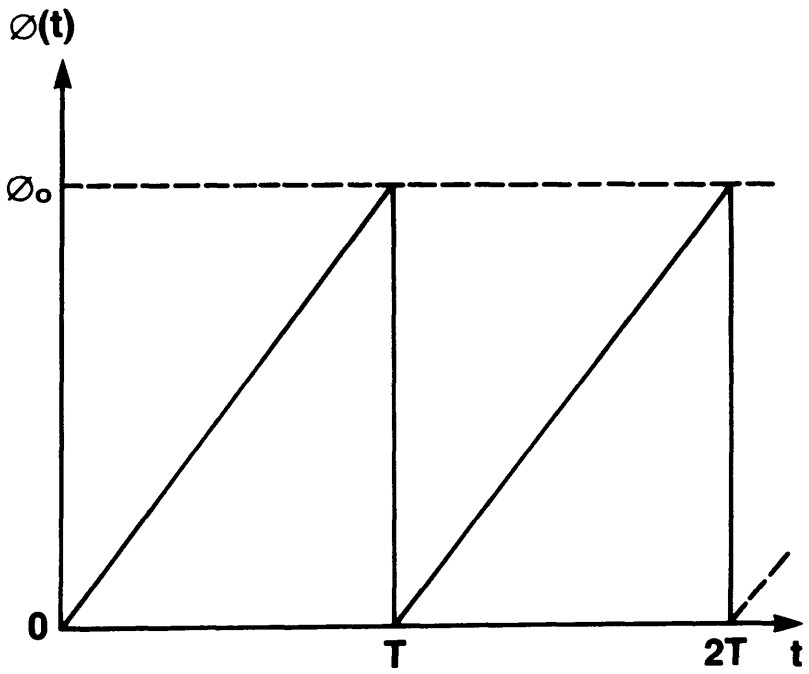

Figure 3.4 A Perfect Sawtooth Waveform With Period T

$$\varnothing_0 = \varnothing_p = 2\pi(1+d), \tag{3.9}$$

where d is a very small phase value deviation generally of the order of T_f/T. By substituting Equation 3.9 into Equation 3.8 and assuming $d << 1$, the approximated sideband values are:

$$\left.\begin{aligned} C_1 &= 1, \\ C_0 &= d, \\ C_{-1} &= (d - T_f/T)/2, \\ C_2 &= (-d - 2T_f/T), \\ C_{-2} &= (d - 2T_f/T)/3, \text{ and} \\ C_3 &= -(d + 3T_f/T)/2 \end{aligned}\right\} \tag{3.10}$$

A theoretical plot (Figure 3.5) of $|C_n|$ versus d, where $d = (\varnothing_0 - 2\pi)/2\pi$ was generated using Equation 3.10. Two important conclusions can be drawn from Figure 3.5. They are: (1) All the spurious sidebands are optimally suppressed when:

$$d = -(T_f/T) \tag{3.11}$$

Therefore from Figure 3.5, the overall suppression S_o of spurious sidebands relative to the required shifted sideband is given by:

$$S_o = 20 \log_{10} (T_f/T) \text{ dB}, \tag{3.12}$$

and (2) The image sideband is completely suppressed when:

$$d = (T_f/T) \tag{3.13}$$

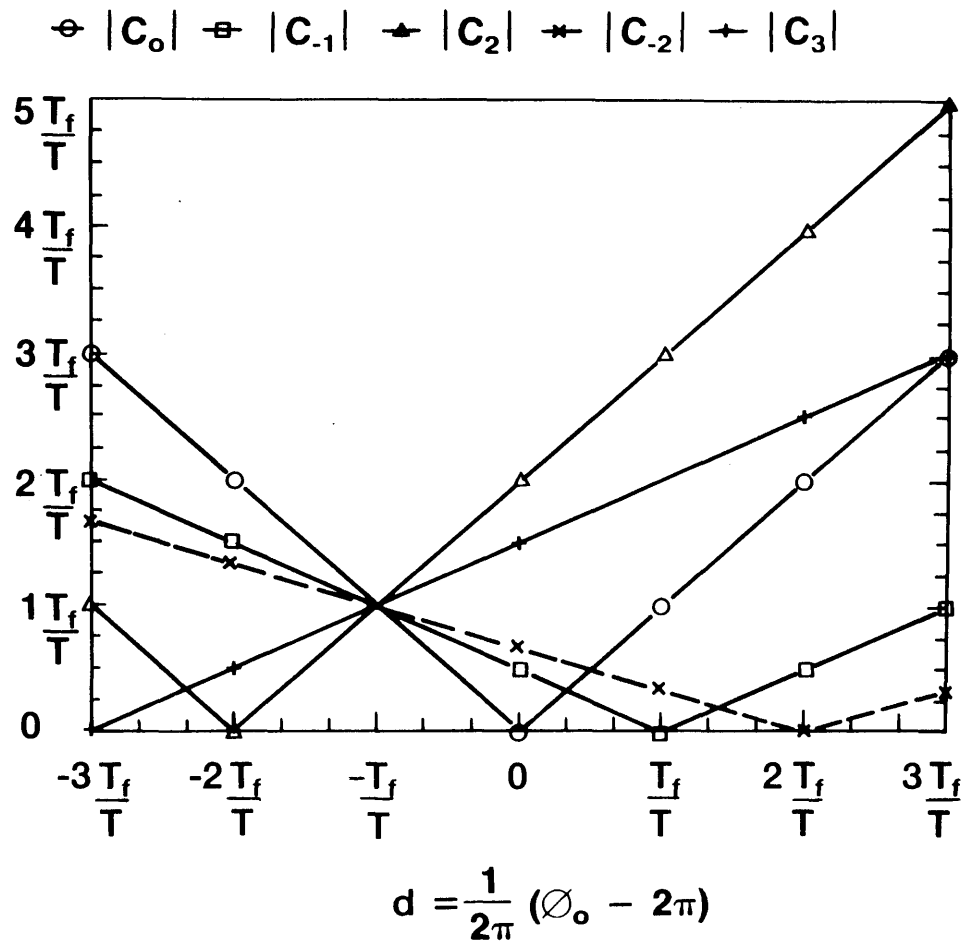

Figure 3.5 A Theoretical Plot Of $|C_n|$ Against A Very Small Phase Value Deviation d

Figure 3.6 shows a theoretical plot of S_o versus (T_f/T). As can be seen from this plot it is critical that the value of (T_f/T) is a minimum. Therefore, in order to achieve an overall serrodyne sideband suppression of for example 40 dB, the fall-time must be 1% of the period of the sawtooth signal. This implies that the bandwidth of the optical phase modulator and the function generator must be at least 100 times larger than the actual desired optical frequency translation. This bandwidth requirement is the primary practical limitation governing the maximum frequency translation which can be accomplished by the serrodyne method. Detailed discussions of this bandwidth limitation is given in Chapter 6.

3.4.3 Effect of Non-Optimum Sawtooth Amplitude

The presence of the finite fall-time T_f shown in Figure 3.7 also implies that the applied phase change for optimum spurious sideband suppression, $\varnothing_0$, is given by:

$$\tan\theta = \varnothing_p / T \qquad \text{and also} \qquad \tan\theta = (\varnothing_p - \varnothing_0) / T_f$$

$$\therefore \varnothing_0 = \varnothing_p\,[1-(T_f/T)] \tag{3.14}$$

where $\varnothing_p$ is the required appropriate 2π phase change. This treatment of the optimum phase change required for best overall spurious sideband suppressions can be confirmed by Figure 3.5.

Serrodyne frequency translators for use in closed-loop fibre-optic gyroscope [3.24] have to have best resultant overall (S_{or}) spurious sideband suppressions since this value will determine the linear dynamic range of the fibre-optic gyroscope. Table 3.1 and Figure 3.8 shows a table and plot of resultant overall spurious sideband suppression S_{or} in dB against d

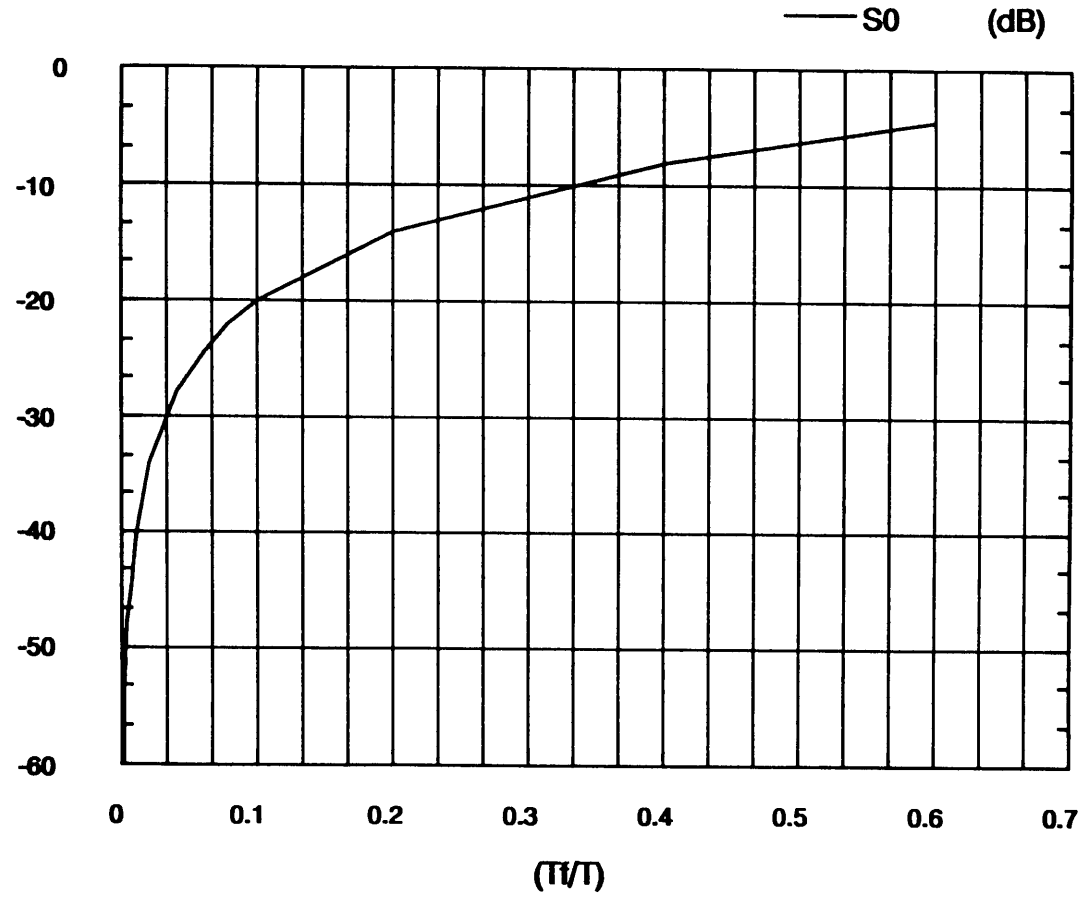

Figure 3.6 A Theoretical Plot Of Overall Spurious Sideband Suppression S_0 Against (T_f / T)

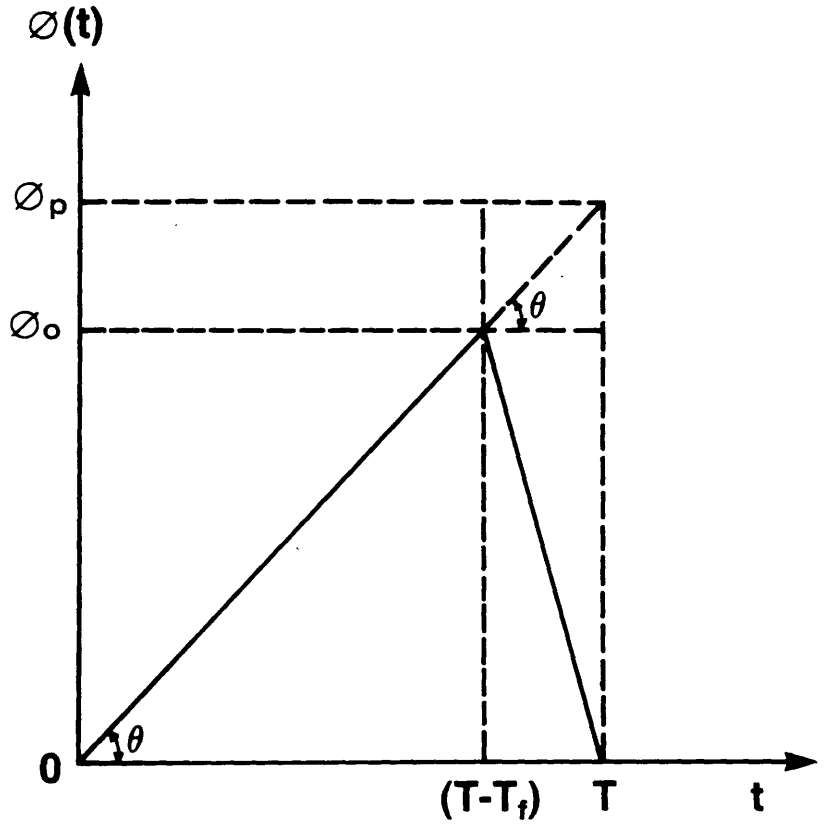

Figure 3.7 An Imperfect Sawtooth Waveform Used For Optimum Phase Value Calculation For Best Overall Spurious Sideband Suppression

Table 3.1 Results For Best Resultant Spurious Sideband Suppression With Respect To Variation In The Small Phase Value d

d	S_{or}
$(-T_f/T)$	S_0
0	S_0-6.02
(T_f/T)	S_0-9.54
$(-2T_f/T)$	S_0-6.02
$(2T_f/T)$	S_0-12.04
$(-3T_f/T)$	S_0-9.54
$(3T_f/T)$	S_0-13.98

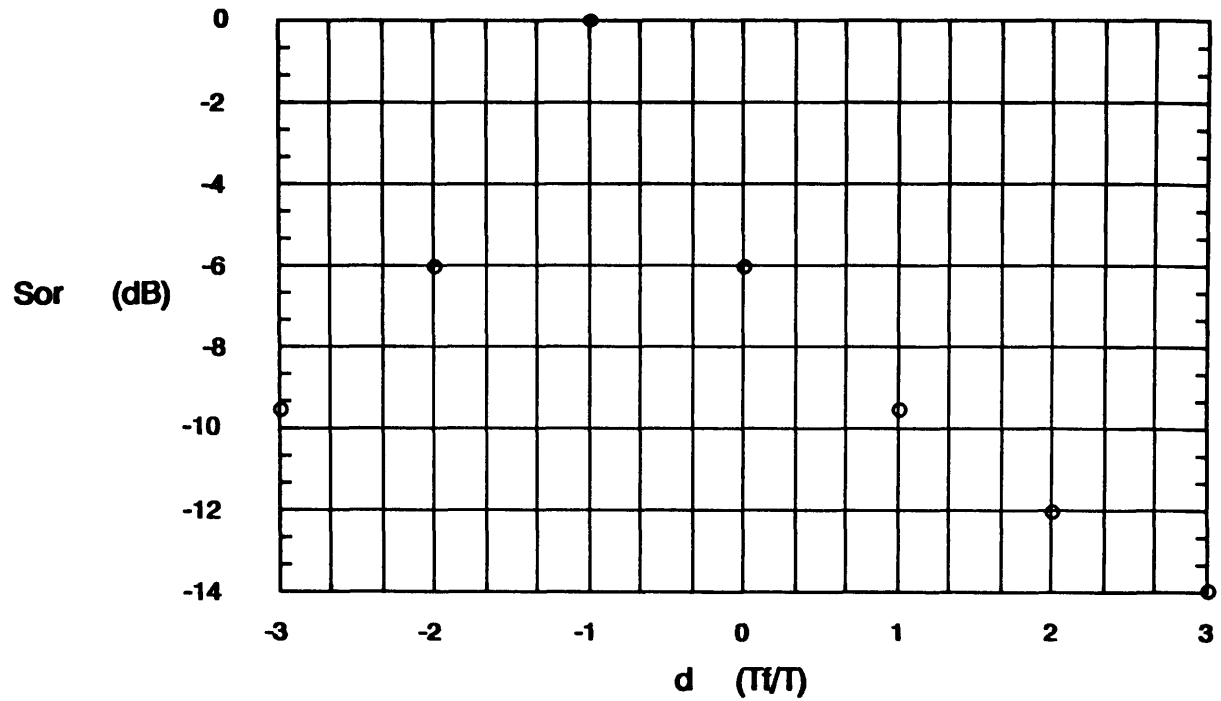

Figure 3.8 A Theoretical Plot Of Resultant Overall Spurious Sideband Suppression S_{0r} Against d

respectively. Numerical results to these theoretical studies are given in Chapter 6.

3.4.4 Effect of Non-Linear Sawtooth Phase Variation

Another possible source of spurious sideband generation is the non-linearity of the ramp section of a non-ideal sawtooth waveform. The analysis of the nonlinearity in the sawtooth waveform involves the assumption that the ramp section is a second order polynomial. Appendix 3.3 describes two analyses where firstly a study was carried out using a sawtooth with zero fall-time (Figure 3.9) and secondly a study was carried out using a sawtooth waveform with finite fall-time T_f (Figure 3.10). The result of the second analysis, i.e. involving a sawtooth with finite fall-time is given by Equation A3.2.2.4. Using Equation 3.9 and assuming that $d << 1$, C_1 can be approximated to $(T_f/T)(d - T_f/T)$. When compared to Equation 3.10, this indicated that there is degradation in the translated signal.

3.4.5 Effect of Non-Optimum Operation Over a Band/Range of Frequencies using a Constant Sawtooth Amplitude

The frequency response of the optical phase modulator may limit the performance of the serrodyne frequency-translator by limiting the achievable overall spurious sideband suppression. The phase modulator behaves like a low pass filter when the equivalent circuit of the device is considered. Here the electrode capacitance, C, of the device and any parasitic resistance, inductance, and/or capacitance in the electrical interfacing of the drive electronics to the electrodes of the optical device will contribute to the low-pass filter behaviour and also some resonances. The net result is the creation of a particular phase modulator voltage impulse response, h(t). In many electrical interfacing of the drive electronics to the electrodes of the phase modulator the inductive effects are generally negligible. By

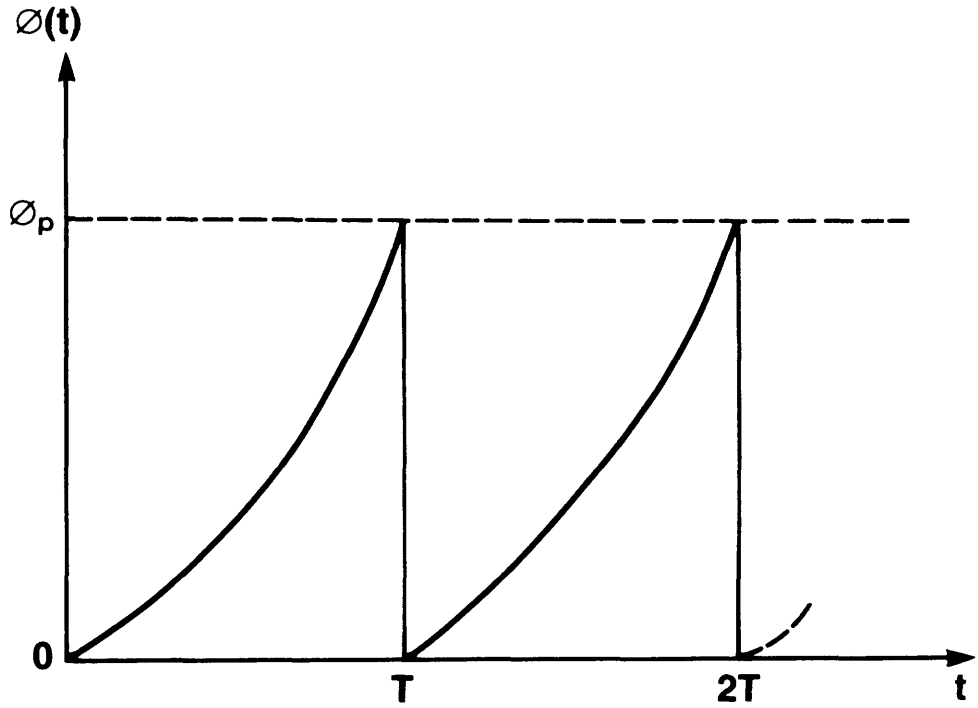

Figure 3.9 A Sawtooth Waveform With 2nd Order Polynomial Nonlinearities And Zero Flyback Time

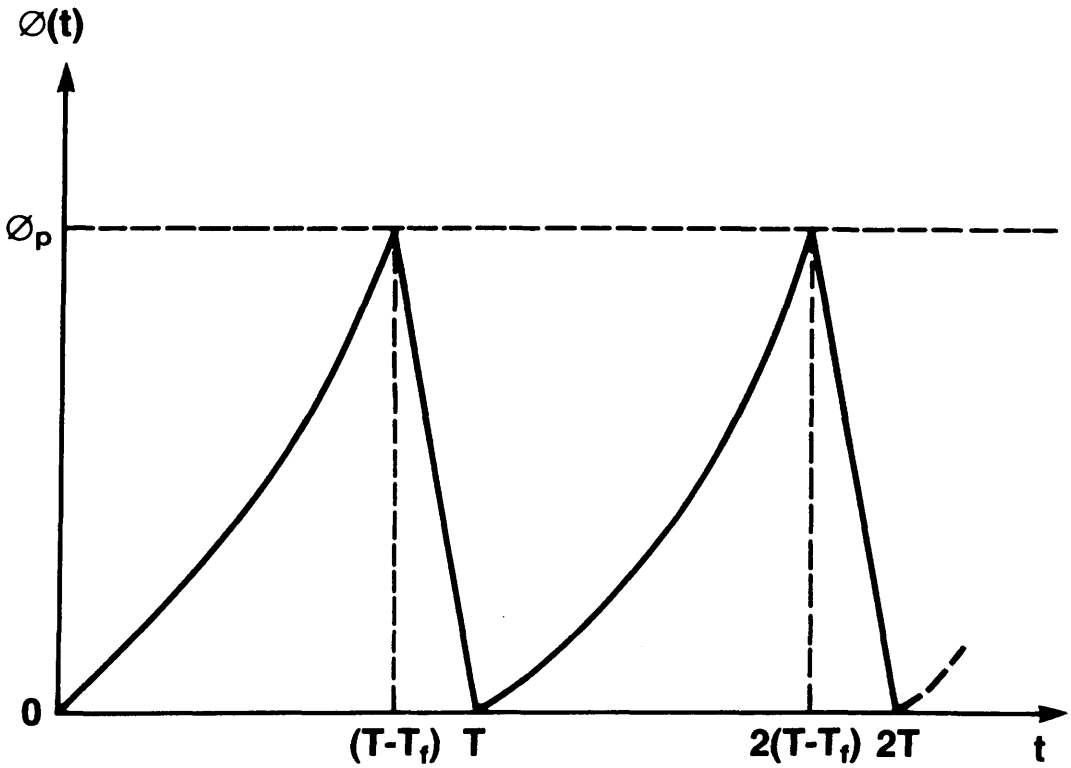

Figure 3.10 A Sawtooth Waveform With 2nd Order Polynomial Nonlinearities And A Finite Flyback Time Of T_f

performing the convolution of the sawtooth waveform with h(t), the delayed reset time T_{nf} is given by:

$$T_{nf} = T_f + RC \ln \{[(T-T_f)/T_f][1-\exp(-T_f/RC)]\} \quad (3.17)$$

where R is the effective resistance of the equivalent low pass filter circuit and the product RC is the response time of the device. From the theoretical analysis in Section 3.4.2, the new overall suppression S_{no} of spurious sidebands to the required translated signal is given by:

$$S_{no} = 20 \log_{10} (T_{nf}/T) \quad dB, \quad (3.18)$$

Therefore, the resultant degradation in the overall spurious suppression of sidebands is given as:

$$S_{do} = (S_{no} - S_o) \quad dB,$$

i.e. $$S_{do} = 20 \log_{10} (T_{nf}/T_f) \quad dB, \quad (3.19)$$

Figure 3.11 illustrates a plot of S_{do} for $1 < (T_{nf}/T_f) < 3$. Typically, for optical phase modulators used in the serrodyne experiments of this project, they have (T_{nf}/T_f) values of about 1.04 to 1.36 which correspond to 0.34 dB to 2.67 dB in degradation of overall spurious sideband suppressions.

In general the frequency response limitation is not a problem since most lumped electrode based phase modulators can be designed to have electrical bandwidths of up to 1 GHz and the optical phase modulators are driven with sawtooth waveform frequencies of less than a few MHz.

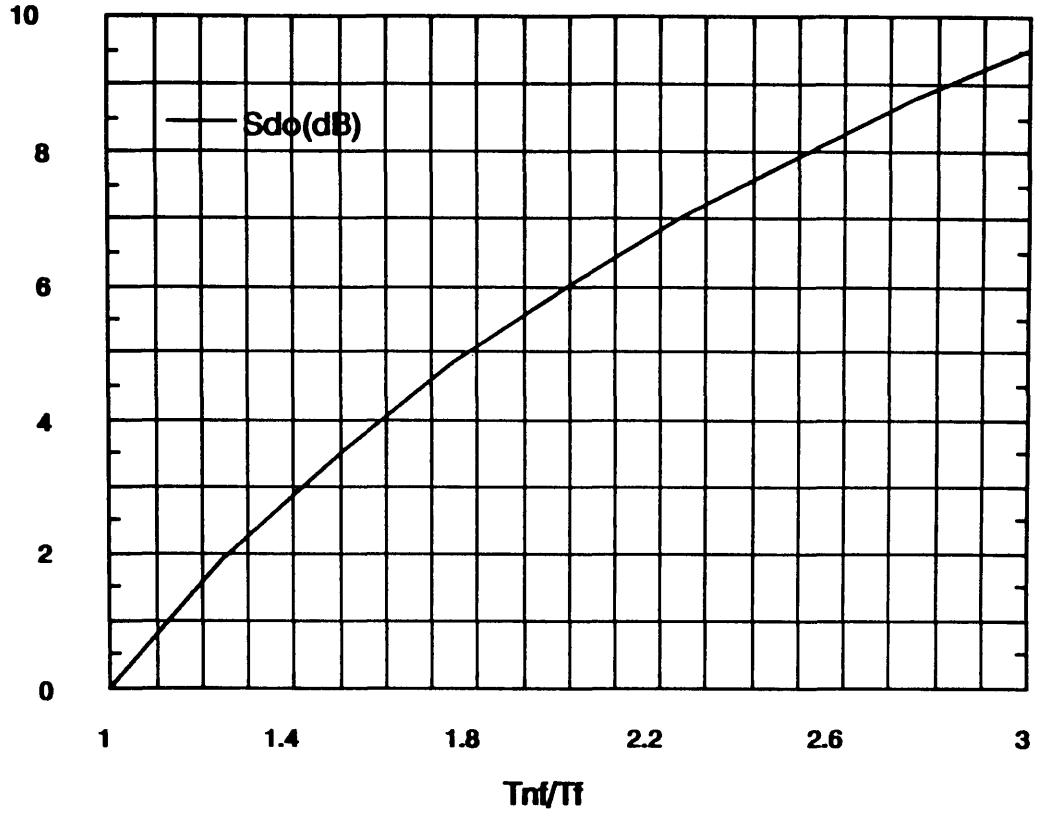

Figure 3.11 Plot Of The Resultant Degradation In Overall Spurious Suppression Of Sidebands With Respect To (T_{nf} / T_f)

3.4.6 Effects of the Presence of Amplitude Modulation in an Electro-Optic Phase Modulator

The presence of amplitude modulation in an optical phase modulator can limit the performance of the serrodyne device by severely affecting the image sideband suppression capability of the serrodyne device. The amplitude modulation effects may be due to one or more of the following effects:

(i) Perturbations to the refractive index of the optical waveguides due to the metallic electrodes,

(ii) Cut-off modulation, and

(iii) Fabry Perot effects.

Of the above three effects, (i) and (ii) are the most common with the last effect typically occurring in devices with parallel polished end faces. The effect of amplitude modulation on serrodyne device performance was analysed by Voges et al [3.15]. The suppression of the image sideband compared to the frequency translated signal is given by:

$$S_{im} = 20*\log_{10}(AM) \quad dB \tag{3.20}$$

where AM is the measured percentage amplitude modulation of the phase modulator under evaluation. The cut-off property of the stripe optical waveguides was found to be the key contributing factor to the level of measured amplitude modulation. Amplitude modulation levels of as high as 30% were measured which gave a S_{im} value of about 10 dB. Figure 3.12 shows a calculated plot of S_{im} (dB) at various amplitude modulation levels. In such weakly confined stripe waveguides, it is possible that additional amplitude modulation effects due to the metallic electrodes can arise. The solution is to

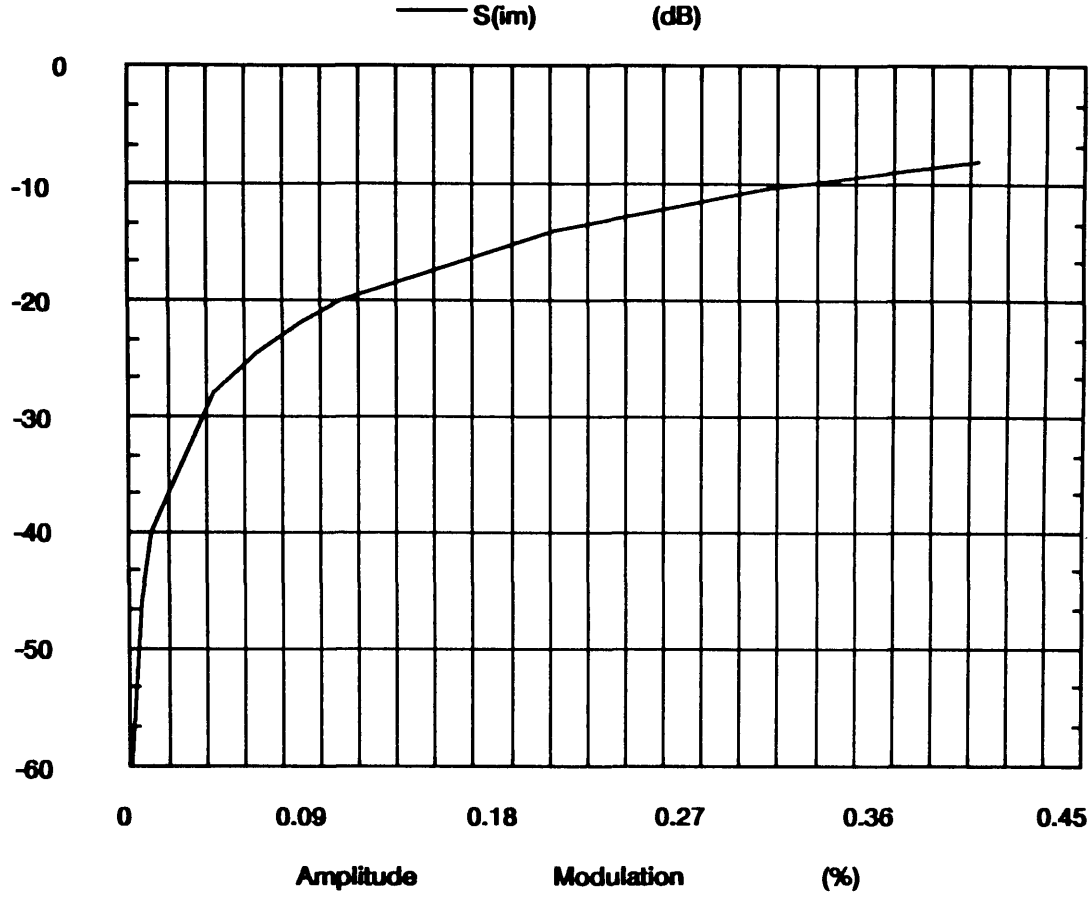

Figure 3.12 Plot Of The Ratio Of Shifted Sideband To Image Sideband At Various Amplitude Modulation Levels

ensure that the stripe waveguide is far away from cut-off and also a dielectric buffer layer such as SiO_2 can be deposited on the surface of the phase modulator to minimise the effects of the metal on the optical signal.

The Fabry Perot effect in a single mode stripe optical waveguide can be significant if the two end faces are parallel and have no anti-reflection coatings. The reflections from the end faces of the phase modulator will cause amplitude modulation in the photodetected output signal. The ratio of the maximum (I_{max}) and the minimum (I_{min}) photodetected current is given by:

$$I_{max}/I_{min} = [T_{max}/(1-R)^2]*\{1/[1 + F*\sin^2 [2\pi L(n + \Delta n)/\lambda]]\} \qquad (3.21)$$

where

T_{max} is the maximum transmittance,

$F = 4R/(1-R)^2$,

$R = R_0 e^{-\alpha L}$,

Δn = change in the refractive index of the waveguide due to the applied electric field,

λ = the optical wavelength of operation,

α = stripe waveguide propagation loss value (nepers/cm),

R_0 = the reflection coefficient of the end faces of the device, and

L is the length of the device.

The phase modulators used in the experiments reported in Chapter 6 did not have parallel end faces because they were trimmed using a diamond impregnated chain saw. Therefore, amplitude modulation effect due to Fabry Perot effects is minimial i.e. less than 1% which implies a S_{im} value of better than 40 dB.

3.5 Examples of the Use of Optical Frequency-Translators in Fibre-Optic and Integrated Optical Sensor Systems

3.5.1 Introduction

The use of optical frequency-translators in fibre and integrated optical sensor systems has been proposed and demonstrated by a number of research groups [3.3, 3.4, 3.5, 3.16]. For example, the phase-shift induced by an external perturbation within the single-mode fibre-sensor of Figure 3.13 is usually detected as an amplitude change. In a configuration without the optical frequency-shifter/translator, it is subject to the influence of amplitude variations. However by the use of an optical frequency-translator, the optical phase-shift is converted into a low-frequency electrical phase-shift (by using an appropriate photodetection scheme) which can be measured without the influence of amplitude changes [3.17]. In the rest of this section, three examples of applications where the use of optical frequency-translators has been proposed and demonstrated will be described.

3.5.2 Fibre-Optic Hydrophone

The first possible application is in a fibre-optic hydrophone. The fibre-optic hydrophone has been found to be a potentially superior tool for the measurement of acoustic fields. Both multimode [3.18, 3.19] and single-mode fibres [3.20] have been used as optical waveguides in hydrophone applications. The basic configuration of a fibre-optic hydrophone can be represented by Figure 3.13 with the acoustic fields as external perturbations. In this arrangement, the laser beam is split equally into two different paths; one of which transmits through a reference optical-fibre which is isolated from the acoustic field to be measured, and the other of which passes through a specially coated sensing optical-fibre (for extra sensitivity) which

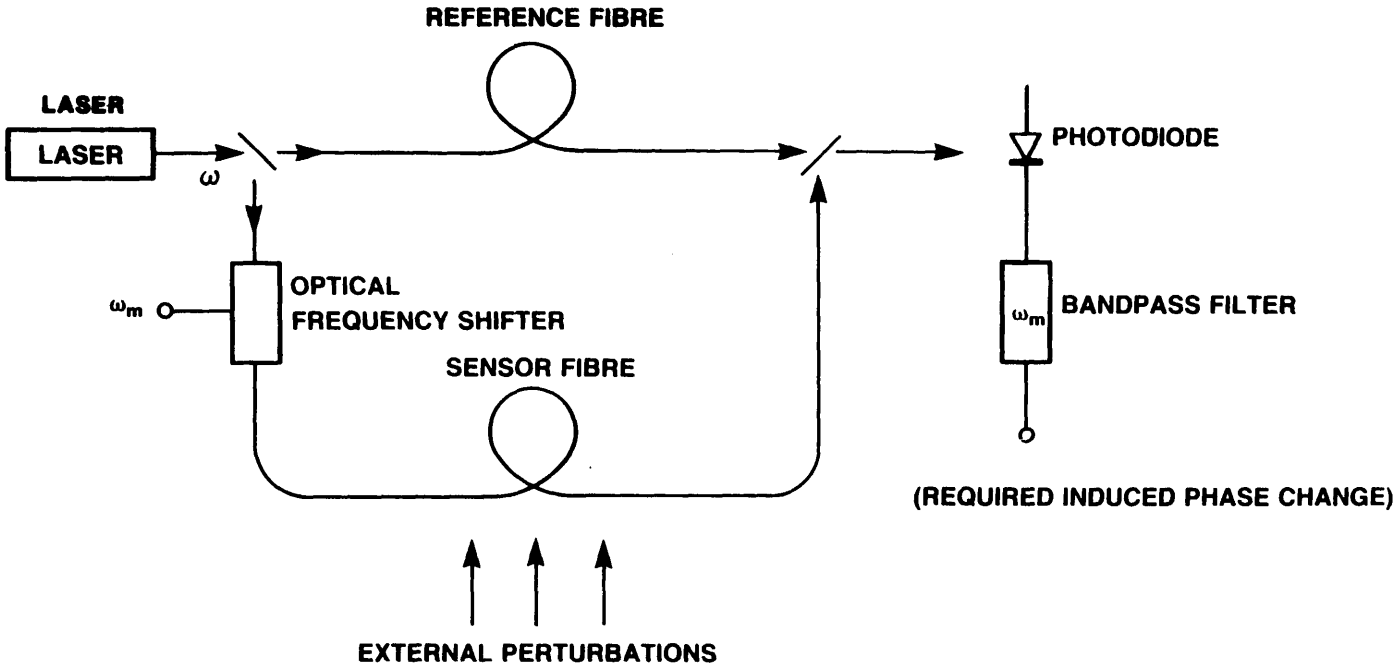

Figure 3.13 Application Of An Integrated Optical Frequency–Translator In A General Single Mode Fibre–Optic Sensor System

is exposed to the acoustic field [3.21, 3.22]. In general some form of modulation technique such as frequency-shift or phase-modulation is applied on the reference optical-fibre. The two optical beams are finally recombined and detected on the photodetector.

A possible implementation of the scheme shown in Figure 3.13 using integrated optical components is illustrated in Figure 3.14. The proposed chip consists of a 3 dB optical directional coupler with a phase modulator on one of the arms of the directional coupler. In this configuration, the output (A) from a semiconductor laser source operating at 830 nm or 1300 nm (given by $\cos \omega_c t$) is coupled to one of the input arms of the directional coupler. This optical beam is then split up equally by the appropriate application of a voltage to the directional coupler. The output from the lower arm of the directional coupler is connected optically to the sensing optical-fibre. The optical signal at the end of the sensing optical-fibre is given by $(A/2)\cos (\omega_c t+\Delta\phi)$. On the other output arm, a phase modulator is integrated and operated as a serrodyne optical frequency-translator (giving a frequency shift of ω_m). This arm is optically connected to the reference optical-fibre. The optical signal at the end of the reference optical-fibre is given by $(A/2)\cos [(\omega_c+\omega_m)t]$. The two optical outputs from the fibres are recombined using the help of another 3 dB directional coupler. The signal from one of the output ports of the directional coupler is then connected to the photodetector. The total optical field on the detector is given by:

$$F_t(t) \propto [\cos (\omega_c t+\Delta\phi) + \cos (\omega_c+\omega_m)t] \qquad (3.22)$$

The photodetector current $i_t(t)$ can then be expressed as:

$$i_t(t) \propto [F_t(t)]^2$$

$$\propto [\cos^2(\omega_c+\omega_m)t + \cos^2(\omega_c t+\Delta\phi) + \cos (\omega_m t-\Delta\phi) +$$

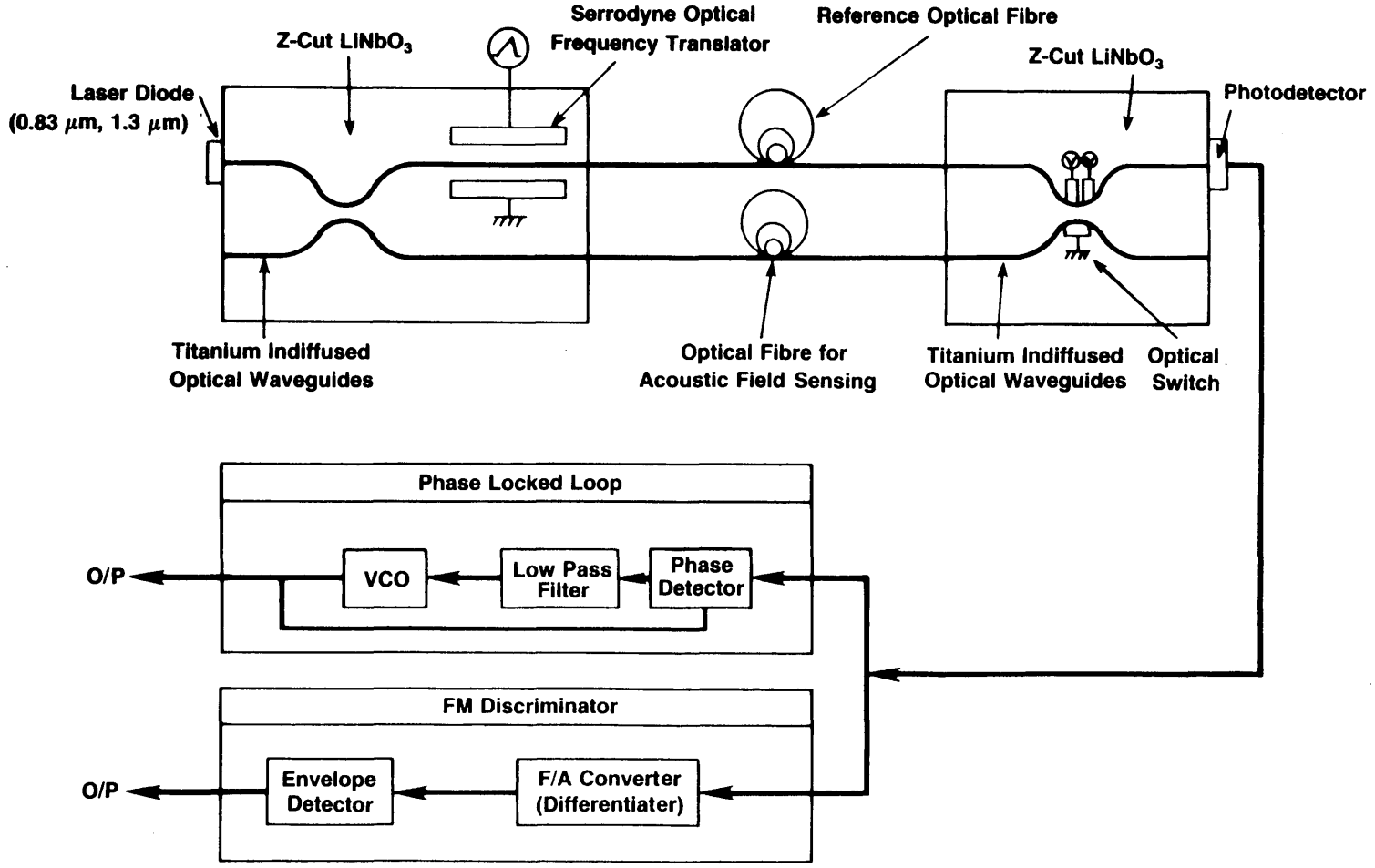

Figure 3.14 Proposed Fibre–Optic Hydrophone Using Integrated Optical Components

$$\cos (2\omega_c t+\omega_m t+\Delta\phi)] \qquad (3.23)$$

Due to the finite response time of the photodetector, the actual signal generated is:

$$i_t(t) \propto \cos (\omega_m t-\Delta\phi) \qquad (3.24)$$

This signal (Equation 3.24) can be detected electronically, for example, by means of a phase-locked loop or an FM discriminator. The phase-locked loop consists of a phase detector, a low pass filter, and a voltage controlled oscillator (VCO). The FM discriminator consists of a differentiator (phase-to-amplitude converter) and an envelope detector.

The main advantages of using integrated optics, in particular a serrodyne optical frequency-translator, are:

(a) The overall hydrophone is potentially more compact,
(b) The optical circuits can be mass produced using standard photolithographic methods, and
(c) The use of the frequency-translator makes heterodyne detection easier.

3.5.3 Fibre-Optic Gyroscope

Fibre-optic gyroscopes have great potential to replace the mechanical and the ring laser gyroscopes. One of the biggest uses of gyroscopes is in the area of navigation and guidance. The fibre-optic gyroscope is based on the Sagnac effect [3.23]. Although George Sagnac demonstrated in 1913 that the rotation of a closed optical path about an axis normal to its plane changes the interference pattern of the two light beams travelling the loop in opposite directions, fibre-optic gyroscopes have not been considered seriously until the demonstration of low loss single-mode optical-fibres in 1976. Although

both multimode and monomode optical fibres have been used in optical communication systems, only single-mode fibres can be used in practical fibre-optic gyroscopes. This is because different modes have effectively different propagation velocities and path lengths. Numerous single-mode fibre-optic gyroscopes have been demonstrated by a large number of research groups over the last 10 years [3.24].

The minimum configuration for a Sagnac fibre-optic gyroscope is shown in Figure 3.15. The laser beam after the first 3 dB coupler is passed through an optical polariser. Next the output from the polariser is divided equally by another 3 dB coupler and propagates in opposite directions around the optical-fibre loop. The two beams are recombined by the two couplers and detected by a photodetector. The optical intensity I at the photodetector (Figure 3.16) is given by:

$$I \cong P_0(1 + \cos\Delta\phi_s) \tag{3.25}$$

where P_0 is the optical power coupled into the first 3 dB coupler. The Sagnac phase-shift $\Delta\phi_s$ is related to the rotation rate Ω by:

$$\Delta\phi_s = [(2\pi LD)\Omega]/(c\lambda) \tag{3.26}$$

where L = The length of the optical-fibre coil,

D = The diameter of the optical-fibre coil,

λ = The wavelength of the laser source, and

c = The velocity of light in vacuum.

There are two principal ways in which signal processing can be used to recover the rotation rate. The first method is by using an open loop system whereby the optical intensity I is measured. By solving the inverse of Equation 3.25 using I, the Sagnac phase-shift can be determined. The second

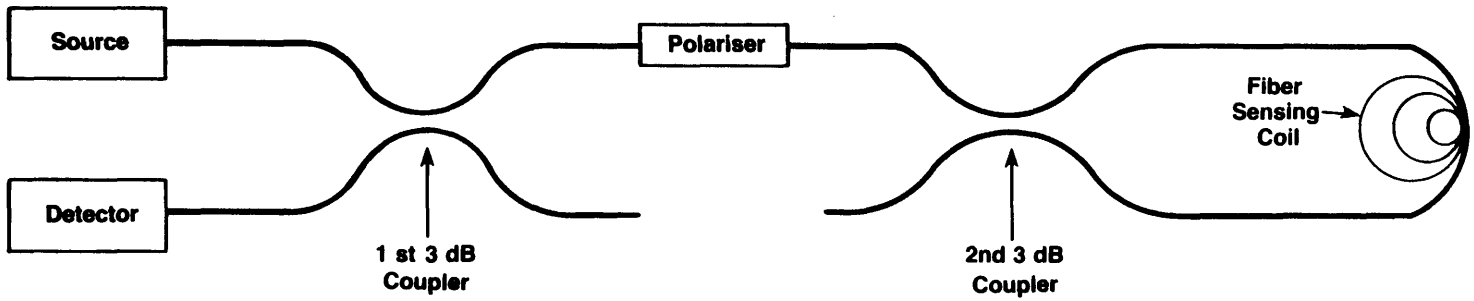

Figure 3.15 The 'Minimum Configuration' Of A Fibre–Optic Gyroscope

technique is by the use of a closed-loop system in which a nonreciprocal phase modulator is inserted into the optical path. This modulator generates a phase-shift which is equal in magnitude but opposite in sign to the Sagnac phase-shift $\Delta\phi_S$. The phase modulator is controlled by a feedback loop in such a way that the intensity I remains constant. The control signal used provides a measure of the rotation rate Ω. In the next paragraph, the use of an optical frequency-translator in the closed-loop system of an fibre-optic gyroscope is discussed. However a number of fibre-optic gyroscopes employing the open loop and other closed-loop methods for establishing the rotation rate have been reported and these can be found in Reference 3.24.

A nonreciprocal phase-shift $\Delta\phi$ can be achieved by introducing a frequency difference $\Delta\omega$ between the two counterpropagating beams. This is related to the transit time τ through the fibre coil by:

$$\Delta\phi = \Delta\omega\,\tau \tag{3.27}$$

This phase difference can be used to compensate the Sagnac phase-shift. In this case the frequency $\Delta\omega$ is proportional to the rotation rate Ω. In this situation a digital output with a large dynamic range is possible. This frequency difference can be generated by placing an optical frequency-translator in the optical path of the fibre gyroscope. The main problem to date in trying to implement the frequency-shift scheme is the realisation of a suitable optical frequency-translator. A review of optical frequency translation techniques and actual demonstrations using optical-fibres and integrated optical components has been given in Chapter 2 of this thesis.

The following properties are desired for such an optical frequency-translator [3.4, 3.10, 3.22, 3.24]:

(a) Realisation in a guided-wave optic form (using optical fibres or integrated optical components),

(b) High conversion efficiency,

(c) Low optical insertion loss,

(d) Suppression of carrier and image sideband by more than 60 dB, and

(e) A tuning range of: - 1 MHz < Δf < ± 1 MHz.

In order to satisfy the above requirements for an optical frequency-translator in the fibre-optic gyroscope, there are three potential candidates. They are:

(i) Integrated Optical Bragg frequency shifters,

(ii) Frequency shifters using the quadrature phase-shift method, and

(iii) Serrodyne optical frequency-translators.

A proposed configuration for a fibre-optic gyroscope using two integrated optical serrodyne frequency-translators is shown in Figure 3.16. The two frequency-translators are located symmetrically at both optical-fibre ends. The reason for using two frequency-translators is the need to overcome the problem of the large phase bias produced (which leads to large drift due to a high centre frequency) when only one frequency-translator is used [3.16].

In conclusion, the use of optical frequency-translators in fibre-optic gyroscopes has the advantages of small size, avoidance of 1/f noise, ruggedness, implementation of closed-loop schemes, and being producible in volume.

3.5.4 Fibre-Optic Laser Doppler Velocimeter

The use of a serrodyne optical frequency-translator in an optical chip to perform laser Doppler velocimetry has been successfully demonstrated [3.5]. A fibre laser Doppler velocimeter (LDV) using bulk optics and a heterodyne detection scheme was demonstrated by the same researchers.

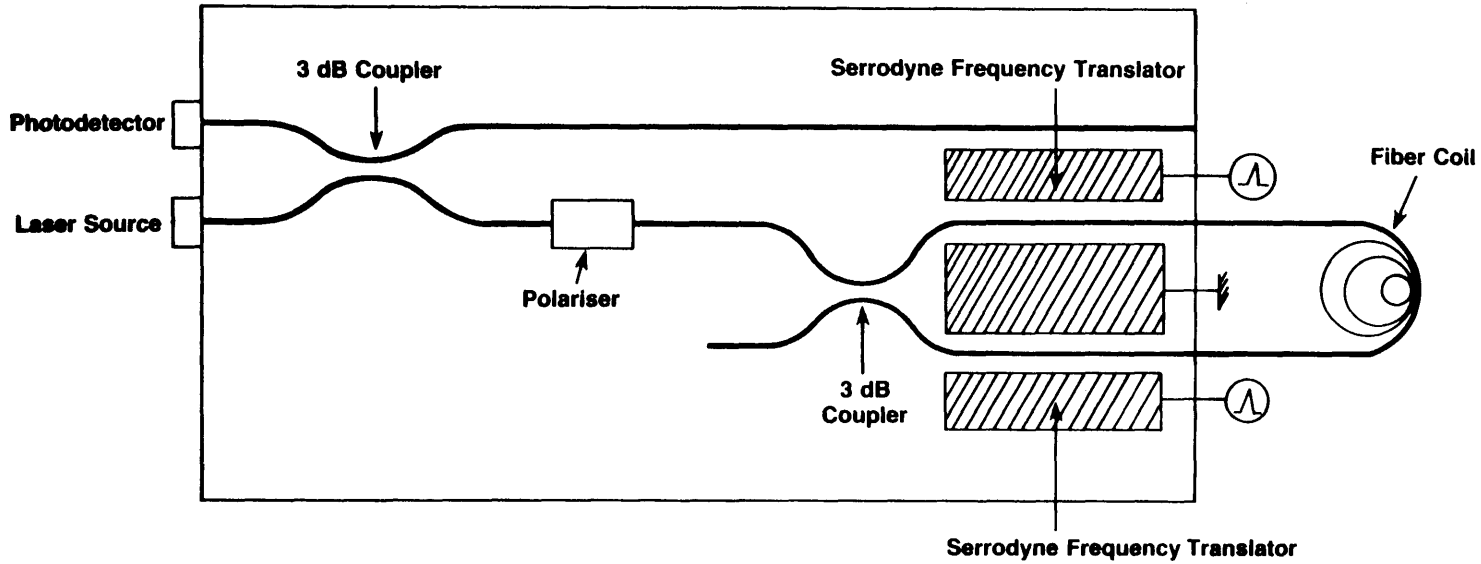

Figure 3.16 An Integrated Optical Gyro Chip Utilising Two Serrodyne Frequency–Translators Operating At Different Frequencies

The bulk optics LDV was basically a bulk Mach-Zehnder interferometer arrangement with a multimode optical-fibre to pick up the Doppler shifted signal. A Bragg cell was used as a frequency-translator in one arm of the interferometer to provide the necessary reference light level for heterodyne detection. In this device the dynamic range is determined by the amount of frequency translation of the reference light beam. The whole LDV was assembled by using the necessary bulk optical components on a 30 cm x 30 cm optical bench and was, therefore, quite bulky and needed careful optical alignment.

The motivations behind the use of integrated optical components for the fibre-optic LDV described above are reasonably obvious, i.e. that, the unit becomes more compact and rugged and does not require continuous optical realignment. The integrated optical chip for the fibre laser Doppler velocimeter consists of a waveguide interferometer (formed by the connection of two Y-junction single-mode waveguides) and a serrodyne optical frequency-translator. The entire optical chip was realised in an X-cut Ti:$LiNbO_3$ substrate, with the laser light being propagated in waveguides that were parallel to the Z-axis of the crystal (Figure 3.17). A single-mode optical-fibre was pigtailed to the optical chip to pick up the Doppler shifted signal. In this demonstration a signal to noise ratio of 30 dB was achieved.

In conclusion, the use of integrated optics technology has resulted in the successful realisation of a compact and rugged fibre LDV which can be easily implemented practically provided that the HeNe laser is replaced by a semiconductor laser with a linewidth value which is equivalent or smaller than the actual frequency translation value used. The key component used in this experiment was the serrodyne optical frequency-translator. The reason for it being chosen as the translator is the simplicity of the component and also the range of frequency translation needed in this

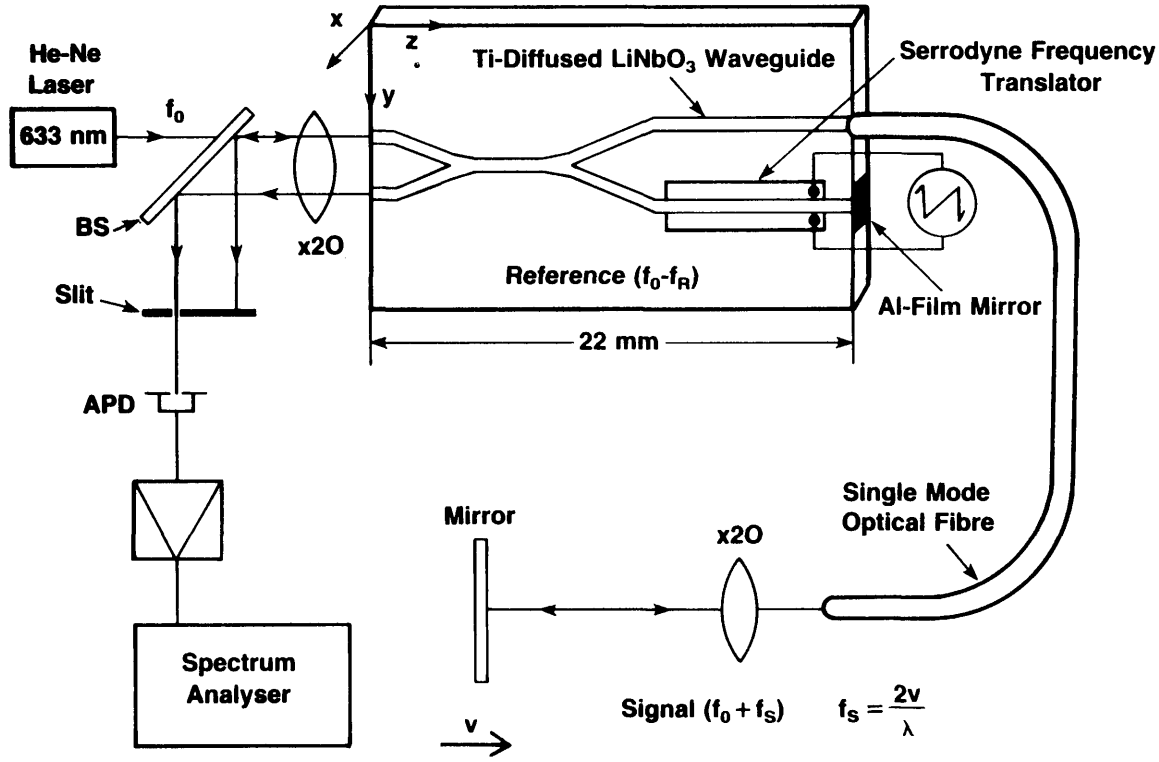

Figure 3.17 A Fibre Laser Doppler Velocimeter Realised Using Integrated Optics Technology – Y Junctions And A Phase Modulator (After Reference 3.5)

application (i.e. 100 kHz to 1 MHz) is well within the performance capability of this type of optical frequency-translator.

3.6 Summary

The use of the phase-modulation technique for optical frequency translation was discussed. The continuous linear phase function can be approximated by a staircase waveform or by a sawtooth waveform also known as serrodyne modulation. Fourier analysis for a 3-step and an n-step staircase waveform have been carried out.

An investigation into the factors limiting serrodyne device performance has been given. An optical phase modulator driven by a non-perfect sawtooth has been considered throughout the discussions. A number of problems affecting serrodyne modulation performance were identified and associated both with the driving waveform and with the detailed characteristics of the device.

The electrical limiting factors affecting overall sideband suppression include a non-zero fall-time, serrodyne voltage error (i,e, control of the 2π voltage), non-linear ramp section in the sawtooth waveform and frequency response limitation of the phase modulator. The optical limiting factor affecting sideband suppression is the presence of amplitude modulation (AM) effects. The presence of AM in a phase modulator may be attributed to mode perturbation of the guided wave due to the metallic electrodes, cut-off modulation effects and Fabry Perot modulations.

The use of optical frequency-translators in fibre-optic and integrated optical sensors has been discussed, in particular the use of such components in the fibre-optic hydrophone, fibre-optic gyroscope, and fibre-optic laser Doppler velocimeter has been described.

APPENDIX 3.1

SPECTRAL ANALYSIS OF STEPPED PHASE SHIFT

A3.1.1 Fourier Series - Recap

Let f(t) be a periodic function defined in the interval (-T/2, T/2)

$$f(t) = a_0/2 + \sum_{n=1}^{\infty} [\, a_n \cos(n\pi t/T) + b_n \sin(n\pi t/T)]$$

The Fourier coefficients of f(t) are given by:

$$a_n = 2/T \int_{-T/2}^{T/2} [f(t) \cos(n\pi t/T)]\, dt$$

$$= 2/T \int_{\alpha}^{\alpha+T} [f(t) \cos(n\pi t/T)]\, dt$$

(where n = 0, 1, 2, ...)

$$b_n = 2/T \int_{-T/2}^{T/2} [f(t) \sin(n\pi t/T)]\, dt$$

$$= 2/T \int_{\alpha}^{\alpha+T} [f(t) \sin(n\pi t/T)]\, dt$$

(where n = 0, 1, 2, ...)

Note that $\alpha, T \geq 0$ are constants.

A3.1.2 Output Waveform Analysis for Stepped Phase Function

Let the output waveform be expressed as:

$$E = e(t) \sin[\omega_c t + \theta(t)] \qquad \text{(A3.1.1)}$$

where e(t) is the signal amplitude. For our device, the loss is nearly independent of the phase. Therefore e(t) can be replaced by E_o,

ω_c is the carrier radian frequency, and

$\theta(t)$ is the periodic phase modulation.

Expanding Equation A3.1.1 yields:

$$E = E_o [\sin \omega_c t \cos \theta(t) + \sin \theta(t) \cos \omega_c t] \qquad \text{(A3.1.2)}$$

Since cos $\theta(t)$ and sin $\theta(t)$ are periodic over the time interval T, $\omega = 2\pi/T$, then applying A3.1.1 gives:

$$\sin \theta(t) = a_o/2 + \sum_{n=1}^{\infty} [a_n \cos n\omega t + b_n \sin n\omega t] \qquad \text{(A3.1.3)}$$

$$\cos \theta(t) = c_o/2 + \sum_{n=1}^{\infty} [c_n \cos n\omega t + d_n \sin n\omega t] \qquad \text{(A3.1.4)}$$

$$E = a_o/2 \cos \omega_c t + c_o/2 \sin \omega_c t +$$

$$1/2 \sum_{n=1}^{\infty} [(a_n - d_n) \cos (\omega_c + n\omega)t + (c_n + b_n) \sin (\omega_c + n\omega)t +$$

$$(a_n + d_n) \cos (\omega_c - n\omega)t + (c_n - b_n) \sin (\omega_c - n\omega)t] \qquad \text{(A3.1.5)}$$

$$\text{with } a_o = 2/T \int_{-T/2}^{T/2} \sin \theta(t)\, dt \qquad \text{(A3.1.6)}$$

$$c_o = 2/T \int_{-T/2}^{T/2} \cos \theta(t)\, dt \qquad \text{(A3.1.7)}$$

$$a_n = 2/T \int_{-T/2}^{T/2} \sin \theta(t) \cos n\omega t \, dt \qquad \text{(A3.1.8)}$$

$$b_n = 2/T \int_{-T/2}^{T/2} \sin \theta(t) \cos n\omega t \, dt \qquad \text{(A3.1.9)}$$

$$c_n = 2/T \int_{-T/2}^{T/2} \cos \theta(t) \cos n\omega t \, dt \qquad \text{(A3.1.10)}$$

$$\text{and } d_n = 2/T \int_{-T/2}^{T/2} \cos \theta(t) \sin n\omega t \, dt \qquad \text{(A3.1.11)}$$

A3.1.2.1 Ideal N-Step Case

For the ideal device $\theta(t)$ is an odd function. Therefore sin $\theta(t)$ is an odd function and cos $\theta(t)$ is an even function. (Note $\Delta\theta = 2\pi$ for $\Delta t = T$.)

Hence $a_o = a_n = c_o = d_n = 0$.

Therefore Equations A3.1.3 and A3.1.4 reduces to:

$$\sin \theta(t) = \sum_{n=1}^{\infty} b_n \sin n\omega t \qquad \text{(A3.1.12)}$$

$$\cos \theta(t) = \sum_{n=1}^{\infty} c_n \cos n\omega t \qquad \text{(A3.1.13)}$$

Substitution of Equations A3.1.12 and A3.1.13 into A3.1.2 gives:

$$E = E_o \left[\sin \omega_c t \sum_{n=1}^{\infty} c_n \cos n\omega t + \cos \omega_c t \sum_{n=1}^{\infty} b_n \sin n\omega t \right]$$

$$= E_o \left[(c_n + b_n) \sum_{n=1}^{\infty} \sin (\omega_c + n\omega)t \right]$$

$$\therefore E = E_o/2 \sum_{n=1}^{\infty} \left[(c_n + b_n) \sin (\omega_c + n\omega)t \right.$$

$$\left. + (c_n - b_n) \sin (\omega_c - n\omega)t \right] \qquad \text{(A3.1.14)}$$

Equation A3.1.13 implies the following:-

(i) The carrier is completely suppressed,

(ii) The amplitude of the upper sidebands (USB) is $E_o/2\ (c_n+b_n)$ at frequency $(\omega_c + n\omega)$, and

(iii) The amplitude of the lower sidebands (LSB) is $E_o/2\ (c_n-b_n)$ at frequency $(\omega_c - n\omega)$.

Figure 3.18 illustrates the N-stepped approximation to the continuous phase function. If the phase function $\theta(t)$ is divided into N-steps, then each phase step is equal to $2\ \pi/N$ in magnitude and the total excursion of the function is $(2\pi/N)(N-1)$ as the time varies between -T/2 and +T/2 in steps of T/N. If the reference is established as $\theta = 0$ at $T = 0$, then the function is odd and varies over the range

$$-(\pi/N)\ (N-1) \leq \theta \leq +(\pi/N)\ (N-1)$$

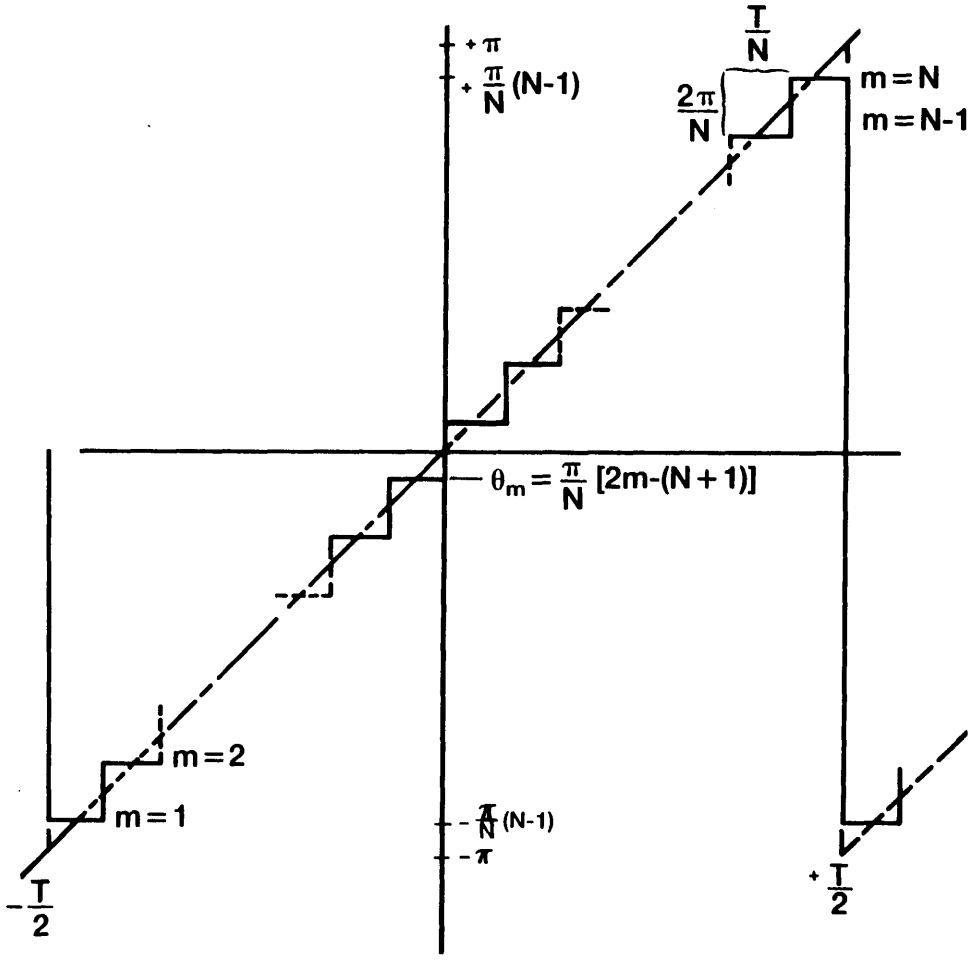

Figure 3.18 Phase Function Of An Ideal N–Step Sawtooth Waveform

For the mth step,

$$\theta_m = -(\pi/N)\ (N-1) + (2\pi/N)\ (m-1)$$

$$= (\pi/N)\ [2m - (N+1)] \qquad \text{(A3.1.15)}$$

and $-(T/2) + (m-1)\ (T/N) \leq t_n \leq -(T/2) + m\ (T/N)$

or $T/N\ [(m-1) - N/2\ ] \leq t_n \leq (T/N)\ [\ m - N/2]$ (A3.1.16)

Substituting Equations A3.1.15 and A3.1.16 into Equations A3.1.9 and A3.1.10 respectively, the expressions for b_n and c_n are:

$$b_n = 2/T \sum_{m=1}^{\infty} \int_{(T/N)[(m-1)-N/2]}^{(T/N)(m-N/2)} \sin(\pi/N)\ [2m - (N+1)]\ .\ \sin n\omega t\ dt \qquad \text{(A3.1.17)}$$

$$b_n = 2/T \sum_{m=1}^{\infty} \int_{(T/N)[(m-1)-N/2]}^{(T/N)(m-N/2)} \cos(\pi/N)\ [2m - (N+1)]\ .\ \cos n\omega t\ dt \qquad \text{(A3.1.18)}$$

Evaluating the integrals of Equations A3.1.17 and A3.1.18, and noting that $\omega T = 2\pi$ and $\sin [x + (n-1)\pi] = (-1)^{n+1} \sin x$,

$$E^+ = (E_o/2)\ [c_n + b_n] = \{[E_o(-1)^{n+1}]/[2\pi n] \sum_{m=1}^{N} \{\sin(\pi/N)\ [2m(n-1) + 1]$$

$$- \sin(\pi/N)\ [2m(n-1) - 2n+1]\ \} \qquad \text{(A3.1.19)}$$

$$E^- = (E_o/2)\ [c_n - b_n] = \{[E_o(-1)^{n+1}]/[2\pi n] \sum_{m=1}^{N} \{\sin(\pi/N)\ [2m(n+1) - 1]$$

$$- \sin(\pi/N)\ [2m(n+1) - 2n-1]\ \} \qquad \text{(A3.1.20)}$$

Further breaking down of sine functions into separate terms that contain m gives:

$$E^{+} = [E_0(-1)^{n+1}]/(2\pi n)\{ [\cos(\pi/N) - \cos(\pi/N)(1-2n)] * \sum_{m=1}^{N} \sin[2\pi m/N](n-1) + [\sin(\pi/N) - \sin(\pi/N)(1-2n)] * \sum_{m=1}^{N} \cos(2\pi m/N)(n-1) \} \quad \text{(A3.1.21)}$$

and $$E^{-} = [E_0(-1)^{n+1}]/(2\pi n)\{ [\cos(\pi/N) - \cos(\pi/N)(1+2n)] * \sum_{m=1}^{N} \sin[2\pi m/N](n+1) + [\sin(\pi/N) - \sin(\pi/N)(1+2n)] * \sum_{m=1}^{N} \cos(2\pi m/N)(n-1) \} \quad \text{(A3.1.22)}$$

Using the trigonometric series:

$$\cos x + \cos 2x + \ldots + \cos Nx = \{\sin[(2N+1)(x/2)]\}/[2\sin(x/2)] - (1/2) \quad \text{(A3.1.23)}$$

and $$\sin x + \sin 2x + \ldots + \sin Nx = [(1/2)\cot(x/2)] - \{\cos[(2N+1)(x/2)]\}/[2\sin(x/2)] \quad \text{(A3.1.24)}$$

In this case, $x = (2\pi)/[N(n-1)]$ for E^{+} and $x = (2\pi)/[N(n+1)]$ for E^{-}.

From Equation A3.1.23 it can be seen that:

$$\sum_{m=1}^{N} \sin\{[(2\pi m)/N](n-1)\} = \sum_{m=1}^{N} \sin\{[(2\pi m)/N](n+1)\} = 0$$

for all integer values of n. Therefore, Equations A3.1.21 and A3.1.2 reduce to:

$$E^{+} = \{[E_0(-1)^{n+1}]/(2\pi n)\}\{\sin(\pi/N) - \sin[(\pi/N)(1-2n)]\} \sum_{m=1}^{N} \cos\{[(2\pi m)/N](n-1)\}/N \quad \text{(A3.1.25)}$$

$$E^{-} = \{[E_0(-1)^{n+1}]/(2\pi n)\}\{\sin[(\pi/N)(1+2n)] - \sin(\pi/N)\} \sum_{m=1}^{N} \cos\{[(2\pi m)/N](n+1)\}/N \quad \text{(A3.1.26)}$$

For E^{+} and using the Equation A3.1.23,

$$\sum_{m=1}^{N} \cos\{[(2\pi m)/N](n-1)\} = \{[\sin(\pi/N)(n-1)]/[2\sin(\pi/N)(n-1)]\} - (1/2) \quad \text{(A3.1.27)}$$

If $(n-1)/N \neq k$, where k is any positive integer from 0 to $+\infty$, then from Equation A3.1.27, it can be deduced that $E^{+} = 0$. If however $(n-1)/N = k$, i.e. $n = (kN+1)$, and using Equation A3.1.25,

$$E^{+} = \{[E_0(-1)^{kN+2}]/[2\pi(kN+1)]\}[2\sin(\pi/N)]N \quad \text{(A3.1.28)}$$

$$or \quad |E^{+}| = [E_0/(kN+1)][\sin(\pi/N)/(\pi/N)] \qquad (A3.1.29)$$

Therefore the spectral lines appear at frequencies:

$$f_s = f_c + (kN+1)f \quad \Big|_{k=0}^{k=+\infty} \qquad (A3.1.30)$$

Now for E^{-}, we can deduce from Equation A3.1.23 that

$$\sum_{m=1}^{N} \cos\{[(2\pi m)/N]\,(n+1)\} = \{[\sin(\pi/N)(n+1)]/[2\sin(\pi/N)(n+1)]\} - (1/2) \qquad (A3.1.31)$$

If $(n+1)/N \neq k$, where k is any positive integer from +1 to $+\infty$, since n cannot take on negative values, then from Equation A3.1.31, we find that $E^{-} = 0$. If however $(n+1)/N = k$, i.e. $n = (kN-1)$, and using Equation A3.1.26, we find that:

$$E^{-} = \{[E_0(-1)^{kN}]/[2\pi(kN+1)]\}\,[-2\sin(\pi/N)]\,N \qquad (A3.1.32)$$

$$or \quad |E^{-}| = [E_0/(kN-1)][\sin(\pi/N)/(\pi/N)] \qquad (A3.1.33)$$

Now the spectral lines appear at frequencies:

$$f_s = f_c - (kN-1)f \quad \Big|_{k=+1}^{k=+\infty} \qquad (A3.1.34)$$

A3.1.2.2 Ideal 3-Step Case

For an ideal 3-step phase function (i.e, N = 3), the magnitude of the USB, E^+ is

$$E^+ = [(3\sqrt{3})/(2\pi)]\ [(E_0)/(3k+1)] \qquad \text{for } k = 0, 1, 2, \ldots$$

and the magnitude of the LSB, E^- is

$$E^- = [(3\sqrt{3})/(2\pi)]\ [(E_0)/(3k-1)] \qquad \text{for } k = 1, 2, 3, \ldots$$

APPENDIX 3.2

SPECTRAL ANALYSIS OF PERFECT AND NON-PERFECT SAWTOOTH WAVEFORMS

A3.2.1 Perfect Sawtooth Waveform

Let $\varnothing(t)$ be a perfect periodic sawtooth function defined in the interval (0, T)

$$\varnothing(t) = (\varnothing_p/T)\ t \qquad \text{for } 0 \leq t \leq T \qquad \text{(A3.2.1.1)}$$

where $\varnothing_p$ is the peak-to-peak phase value of the perfect sawtooth waveform as illustrated in Figure 3.4 (Chapter 3). In order to accomplish the serrodyne performance, the sawtooth waveform is applied to the electrodes of an optical phase modulator. The optical output signal will be proportional to:

$$\text{Re}\ \{e^{j[\omega_c t + \varnothing(t)]}\} \qquad \text{(A3.2.1.2)}$$

where ω_c is the circular frequency of the input unshifted optical wave and $\varnothing(t)$ is a function proportional to the modulating sawtooth. Since $\varnothing(t)$ is an odd function, the Fourier coefficients of $\varnothing(t)$ are given by:

$$A_n = 0,$$

and to obtain a frequency analysis of Equation 3.2.1.2, $e^{j\varnothing(t)}$ is written as a Fourier series:

$$e^{j\varnothing(t)} \cong \sum_{-\infty}^{+\infty} C_n e^{jn\omega t} \qquad \text{(A3.2.1.3)}$$

where $\omega = 2\pi/T$ and

$$C_n = (1/T) \int_0^T e^{j[\varnothing(t) - n\omega t]}\, dt \qquad \text{(A3.2.1.4)}$$

(where $n = 0, \pm 1, \pm 2, \ldots$)

Substituting Equation A3.2.1.1 into Equation A3.2.1.4 gives:

$$C_n = (1/T) \int_0^T e^{j(\varnothing_p/T - n\omega)t}\, dt$$

$$= \{1/[jT(\varnothing_p/T - n\omega)]\} * \{e^{j(\varnothing_p/T - n\omega)T} - 1\}$$

Therefore,

$$\text{Re}\ (C_n) = [\sin(\varnothing_p - 2\pi n)]/[\varnothing_p - 2\pi n] \qquad \text{(A3.2.1.5)}$$

A3.2.2 Effect of Finite Flyback Time T_f

Let $\varnothing(t)$ be a periodic sawtooth function with a finite fall-time T_f, defined in the interval (0, T):

$$\varnothing(t) = [(\varnothing_p)/(T - T_f)]\, t \qquad \text{for } 0 \le t < (T-T_f), \text{ and} \qquad \text{(A3.2.2.1)}$$

$$\varnothing(t) = [(\varnothing_p/(T_f)(T - t)]\, t \qquad \text{for } (T-T_f) < t \le T, \qquad \text{(A3.2.2.2)}$$

Since $\varnothing(t) = \varnothing(t + T)$ for periodic waveform, therefore Equation A3.2.2.2 can be rewritten as:

$$\varnothing(t + T) = [(\varnothing_p/(T_f)(- t)]\, t \qquad \text{for } -T_f < t \le 0, \qquad \text{(A3.2.2.3)}$$

where $\varnothing_p$ is the peak-to-peak phase value of the non-ideal sawtooth waveform as illustrated in Figure 3.3 (Chapter 3). Since $\varnothing(t)$ is an odd function, the Fourier coefficients of $\varnothing(t)$ are given by:

$$A_n = 0,$$

and to obtain a frequency analysis of Equation A3.2.1.2, $e^{j\varnothing(t)}$ is written as a Fourier series:

$$e^{j\varnothing(t)} \cong \sum_{-\infty}^{+\infty} C_n e^{jn\omega t} \qquad \text{(A3.2.2.4)}$$

where $\omega = 2\pi/T$ and

$$C_n = (1/T) \int_0^T e^{j(\varnothing(t) - n\omega t)}\, dt \qquad \text{(A3.2.2.5)}$$

(where $n = 0, \pm 1, \pm 2, \ldots$)

Substituting Equations A3.2.2.1 and A3.2.2.3 into Equation A3.2.2.5 gives:

$$C_n = (1/T) \int_0^{T-T_f} e^{j[(\varnothing_p)/(T-T_f) - n\omega]t}\, dt$$

$$+ (1/T) \int_0^{T_f} e^{j[(-\varnothing_p)/(T_f) - n\omega)]t}\, dt$$

$$= \{1/jT[\varnothing_p/(T-T_f) - n\omega]\} * \{e^{j[\varnothing_p/(T-T_f) - n\omega)(T-T_f)} - 1\}$$

$$+ \{1/jT[(-\varnothing_p/T_f) - n\omega]\} * \{e^{j[-\varnothing_p/T_f - n\omega)(T_f)} - 1\}$$

$$= \{[(T-T_f)/T]/j[\varnothing_p - 2\pi n(T-T_f)/T]\} * \{e^{j[\varnothing'_p - 2\pi n(T-T_f)/T]} - 1\}$$

$$+ [(T_f/T)/(\varnothing_p + 2\pi n T_f/T)] * \sin[\varnothing_p + 2\pi n T_f/T]$$

$$\text{Re}\,(C_n) = \{[(T-T_f)/T]/[\varnothing_p - 2\pi n(T-T_f)/T] * \sin[\varnothing_p - 2\pi n(T-T_f)/T\}$$

$$+ [(T_f/T)/(\varnothing_p + 2\pi n T_f/T)] * \sin[\varnothing_p - 2\pi n(T-T_f)/T + 2\pi n T/T]$$

Therefore,

$$C_n = \{[(T-T_f)/T]/[\varnothing_p - 2\pi n(T-T_f)/T] * \sin[\varnothing_p - 2\pi n(T-T_f)/T\}$$

$$+ \{[(T_f/T)/(\varnothing_p + 2\pi n T_f/T)] * \sin[\varnothing_p - 2\pi n(T-T_f)/T]\}$$

$$C_n = \left\{ \frac{(T - T_f)/T}{[\varnothing_p - 2\pi n(T-T_f)/T]} + \frac{T_f/T}{(\varnothing_p - 2\pi n T_f/T} \right\} * \sin[\varnothing_p - 2\pi n(T-T_f)/T]$$

(A3.2.2.6)

APPENDIX 3.3

SPECTRAL ANALYSIS OF PERFECT AND NON-PERFECT SAWTOOTH WAVEFORMS WITH 2ND ORDER POLYNOMIAL NON-LINEARITIES

A3.3.1 Sawtooth Waveform with 2nd Order Polynomial Non-Linearities and with Zero Flyback Time

Let $\varnothing(t)$ be a periodic sawtooth function with 2nd order polynomial non-linearitites and zero flyback time, defined in the interval (0, T):

$$\varnothing(t) = (\varnothing_p/2T^2)\, t^2 + (\varnothing_p/2T)\, t \qquad \text{for } 0 \le t \le T \qquad \text{(A3.3.1.1)}$$

where $\varnothing_p$ is the peak-to-peak value of the sawtooth waveform with 2nd order polynomial non-linearities as illustrated in Figure 3.9. Using the relationships:

$$e^{j\varnothing(t)} \cong \sum_{-\infty}^{+\infty} C_n e^{jn\omega t} \qquad \text{(A3.3.1.2)}$$

where $\omega = 2\pi/T$ and

$$C_n = (1/T) \int_0^T e^{j[\varnothing(t) - n\omega t]}\, dt \qquad \text{(A3.3.1.3)}$$

(where n = 0, ±1, ±2, ...)

Substituting Equation A3.3.1.1 into Equation A3.3.1.3 gives:

$$C_n = (1/T) \int_0^T e^{j[(\varnothing_p/2T^2)\, t^2 + (\varnothing_p/2T)\, t - n\omega t)]}\, dt$$

$$C_n \equiv \{1/[jT(\varnothing_p/2T - 2\pi n/T)]\} * \{e^{j(\varnothing_p/2T - 2\pi n/T)T} - 1\}$$

$$*(1/T) \int_0^T [1 + j\varnothing_p t^2/2T^2 - (\varnothing_p)^2 t^4/8T^4 - j(\varnothing_p)^3 t^6/48T^6 + (\varnothing_p)^4 t^8/384T^8]\, dt$$

$$C_n = [1/j(\varnothing_p/2 - 2\pi n)] * [1 + j\varnothing_p/6 - (\varnothing_p)^2/40 - j(\varnothing_p)^3/336$$

$$+ (\varnothing_p)^4/3456] * \{e^{j(\varnothing_p/2 - 2\pi n)} - 1\}$$

$$C_n = [1/j(\varnothing_p/2 - 2\pi n)] * [1 + j\varnothing_p/6 - (\varnothing_p)^2/40 - j(\varnothing_p)^3/336$$

$$+ (\varnothing_p)^4/3456] * \{[-1 + \cos(\varnothing_p/2 - 2\pi n)] + j\sin(\varnothing_p/2 - 2\pi n)\}$$

Therefore,

$$\mathrm{Re}\ (C_n) = \{\sin[(\varnothing_p/2 - 2\pi n)/(\varnothing_p/2 - 2\pi n)]\} * [1 - (\varnothing_p)^2/40$$

$$+ (\varnothing_p)^4/3456] + [\cos(\varnothing_p/2 - 2\pi n)/(\varnothing_p/2 - 2\pi n)] * [\varnothing_p/6 - (\varnothing_p)^3/336]$$

$$[1/(\varnothing_p/2 - 2\pi n)] * [(\varnothing_p)^3/336 - \varnothing_p/6] \qquad \text{(A3.3.1.4)}$$

A3.3.2 Sawtooth Waveform with 2nd Order Polynomial Non-Linearities and Finite Flyback Time T_f

Let $\varnothing(t)$ be a periodic sawtooth function with 2nd order polynomial non-linearities and a finite fall-time T_f, defined in the interval (0, T)

$$\varnothing(t) = [(\varnothing_p)/2(T-T_f)^2]\, t^2 + [(\varnothing_p)/2(T-T_f)]\, t$$

for $0 \le t < (T-T_f)$, and (A3.3.2.1)

$$\varnothing(t) = [(\varnothing_p/T_f)(T - t)] \quad \text{for } (T-T_f) < t \le T, \quad \text{(A3.3.2.2)}$$

Since $\varnothing(t) = \varnothing(t + T)$ for periodic waveform, therefore Equation A3.3.2.2 can be rewritten as:

$$\varnothing(t + T) = [(\varnothing_p/(T_f)(- t)] \quad \text{for } -T_f < t \le 0, \quad \text{(A3.3.2.3)}$$

where $\varnothing_p$ is the peak-to-peak value of the non-ideal sawtooth waveform as illustrated in Figure 3.10. Substituting Equations A3.3.2.1 and A3.3.2.3 into Equation A3.3.1.3 gives:

$$C_n = (1/T)\ \{ \int_0^{(T-T_f)} e^{j[(\varnothing_p/2(T-T_f)^2)\, t^2 + (\varnothing_p/2(T-T_f))\, t - n\omega t]}\, dt$$

$$+ \int_0^{T_f} e^{j[(-\varnothing_p/T_f)t - n\omega t]}\, dt$$

From previous analysis in Section A3.2.2,

$$\int_0^{T_f} e^{j[(-\varnothing_p/T_f)t - n\omega t]}\, dt = \{(T_f/T)/(\varnothing_p + 2\pi n T_f/T)\}$$

$$*\{\ \sin[\varnothing_p - 2\pi n(T-T_f)/T]\ \}$$

and,

$$(1/T) \int_0^{(T-T_f)} e^{j[(\varnothing_p/2(T-T_f)^2)\, t^2 + (\varnothing_p/2(T-T_f))\, t - n\omega t]}\, dt$$

$$\cong \{1/[jT(\varnothing_p/2(T-T_f) - 2\pi n/T)]\} * \{e^{j(\varnothing_p/2(T-T_f) - 2\pi n/T)(T-T_f)} - 1\}$$

$$*(1/T) \int_0^{(T-T_f)} [1 + j\varnothing_p t^2/2(T-T_f)^2 - (\varnothing_p)^2 t^4/8(T-T_f)^4$$

$$- j(\varnothing_p)^3 t^6/48(T-T_f)^6 + (\varnothing_p)^4 t^8/384(T-T_f)^8$$

$$= \{1/[jT(\varnothing_p/2(T-T_f) - 2\pi n/T)]\} * \{e^{j[\varnothing_p/2(T-T_f) - 2\pi n/T](T-T_f)} - 1\}$$

$$*[(T-T_f)/T] * [1 + j\varnothing_p/6 - (\varnothing_p)^2/40 - j(\varnothing_p)^3/336 + (\varnothing_p)^4/3456]$$

$$= \{[(T-T_f)^2/T^2]\ /[j(\varnothing_p/2 - 2\pi n(T-T_f)/T)]\}$$

$$*\{e^{j(\varnothing_p/2 - 2\pi n(T-T_f)/T)} - 1\}$$

$$*[1 + j\varnothing_p/6 - (\varnothing_p)^2/40 - j(\varnothing_p)^3/336 + (\varnothing_p)^4/3456]$$

Therefore,

$$\mathrm{Re}\ (C_n) = \{(T_f/T)/(\varnothing_p + 2\pi n T_f/T)\} * \{\ \sin[\varnothing_p - 2\pi n(T-T_f)/T]\ \}$$

$$+\ [(T-T_f)^2/T^2] * \{1 - [(\varnothing_p)^2/40] + [(\varnothing_p)^4/3456]\ \}$$

$$*[\sin(\varnothing_p/2 - 2\pi n(T-T_f)/T)/(\varnothing_p/2 - 2\pi n(T-T_f)/T)]$$

$$+\ [(T-T_f)^2/T^2] * \{(\varnothing_p)/6 - (\varnothing_p)^3/336\ \} *[\cos(\varnothing_p/2 - 2\pi n(T-T_f)/T)$$

$$/(\varnothing_p/2 - 2\pi n(T-T_f)/T)]$$

$$+\ [(T-T_f)^2/T^2]/[(\varnothing_p/2 - 2\pi n(T-T_f)/T)] * [\ (\varnothing_p)^3/336 - (\varnothing_p)/6\ ]$$

(A3.2.2.4)

REFERENCES

[3.1] R.F. Cahill and E. Udd, "Solid-State Phase-Nulling Optical Gyro", Appl. Opt., Vol. 19, No. 18, pp 3054-3056, 15th September 1980.

[3.2] J.L. Davis and S. Ezekiel, "Closed-Loop, Low-Noise Fibre-Optic Rotation Sensor", Opt. Lett., Vol. 6, No. 10, pp 505-507, October 1981.

[3.3] M.L. Henning, S.W. Thornton, R. Carpenter, W.J. Stewart, J.P. Dakin and C.A. Wade, "Optical Fibre Hydrophones with Down Lead Insensitivity", First International Conference on Optical Fibre Sensors, I.E.E. (U.K.), pp 23-27, 26-28th April 1983.

[3.4] C.J. Kay, "Serrodyne Modulator in a Fibre-Optic Gyroscope", IEE Proc., Vol. 132, Pt. J, No. 5, pp 259-264, October 1985.

[3.5] H. Toda, M. Haruna and H. Nishihara, "Integrated-Optic Device for a Fibre Laser Doppler Velocimeter", Electron. Lett., Vol. 22, No. 19, pp.982-984, 11th September 1986.

[3.6] K.K. Wong and S. Wright, "An Optical Serrodyne Frequency Translator", First European Conference on Integrated Optics, London, IEE Conf. Proc., No. 201, pp 63-65, 14-15th September 1981.

[3.7] K.K. Wong, S. Wright and R.M. De La Rue, "Performance of a Serrodyne Optical Frequency Translator", Topical Meeting on Integrated and Guided-Wave Optics, U.S.A, pp WA5-1 to WA5-5, 6-8th January 1982.

[3.8] K.K. Wong, R.M. De La Rue, and S. Wright, "Electro-Optic-Waveguide Frequency Translator in $LiNbO_3$ Fabricated by Proton Exchange", Opt. Lett., Vol. 7, No. 11, pp 546-548, November 1982.

[3.9] K.K. Wong and R.M. De La Rue, "An Improved Electro-Optic Waveguide Serrodyne Frequency Translator in X-Cut $LiNbO_3$ Using Proton-Exchange", First International Conference on Optical Fibre Sensors, I.E.E. (U.K.), pp 72-74, 26-28th April 1983.

[3.10] L.M.Johnson, "Integrated-Optic Fibre-Gyroscope Chip Components", Third International Conference on Optical Fibre Sensors, U.S.A, pp 120, 13-14th February 1985.

[3.11] L. Thylen, P. Sjoberg and G.E. Lindqvist, "Electro-Optical Serrodyne Frequency Translator for $\lambda = 1.3\ \mu m$", IEE Proc., Vol. 132, Pt. J, No. 2, pp 119-121, April 1985.

[3.12] J.S. Jaffe and R.C. Mackey, "Microwave Frequency Translator", IEEE Trans. on Microwave Theory and Techniques, Vol. MTT-13, No. 3, pp 371-378, May 1965.

[3.13] R.V. Schmidt, P.S. Cross and A.M. Glass, "Optically Induced Crosstalk In $LiNbO_3$ Waveguide Switches", J. Appl. Phys., Vol. 51, No. 1, pp 90-93, January 1980.

[3.14] R.C. Cumming, "Serrodyne Performance and Design", The Microwave Journal, Vol. 8, pp 84-87, September 1965.

[3.15] E. Voges, O. Ostwald, B. Schiek, and A. Neyer, "Optical Phase And Amplitude Measurement By Single Sideband Homodyne Detection", IEEE J. Quantum Electron., Vol. QE-18, No. 1, pp 124-129, January 1982.

[3.16] K. Bohm and K. Petermann, "Signal Processing Schemes For The Fibre-Optic Gyroscope", SPIE Vol. 719 Fibre Optic Gyroscopes: 10th Anniversary Conference, Cambridge, MA, pp 36-44, 24-26 September 1986.

[3.17] D.E.N. Davies, "Making Measurements With Light", IEE Proc., Vol. 129, Pt A, No. 1, pp 16-23, January 1982.

[3.18] J.H. Cole, R.L. Johnson, and P.G. Bhuta, "Fibre-Optic Detection Of Sound", J. Acoust. Soc. Am., Vol. 62, No. 5, pp 1136-1138, November 1977.

[3.19] J.A. Bucaro, H.D. Dardy, and E.F. Carome, "Fibre-Optic Hydrophone", J. Acoust. Soc. Am., Vol. 62, No. 5, pp 1302-1304, November 1977.

[3.20] P. Shajenko, "On The Feasibility Of Using Multimode Optical Fibres In Optical Hydrophones", J. Acoust. Soc. Am., Vol. 69, No. 6, pp 1829-1830, June 1981.

[3.21] D.H. McMahon, A.R. Nelson, and W.B. Spillman, "Fibre-Optic Transducers" IEEE Spectrum, Vol. 18, No. 12, pp 24-29, December 1981.

[3.22] T.G. Giallorenzi, J.A. Bucaro, A. Dandridge, G.H. Sigel, Jr., J.H. Cole, S.C. Rashleigh, and R.G. Priest, "Optical Fibre Sensor Technology", IEEE J. Quantum Electron., Vol. QE-18, No. 4, pp 626-665, April 1982.

[3.23] E.J. Post, "Sagnac Effect", Rev. Mod. Phys., Vol. 39, No. 2, pp 475-493, April 1967.

[3.24] E. Udd (Editor), Proceedings SPIE Vol. 719, "Fibre Optic Gyros: 10th Anniversary Conference", Cambridge, MA, 24-26 September 1986.

CHAPTER 4 WAVEGUIDE FABRICATION TECHNIQUES

4.1 Introduction 96

4.2 Fabrication of Ti:$LiNbO_3$ Active Devices 96

4.2.1 Introduction 96
4.2.2 Mask Making 97
4.2.3 Substrate Preparation 98
4.2.4 Waveguide Pattern Preparation 101
4.2.5 Waveguide Formation 101
4.2.6 Titanium Indiffusion 103
4.2.7 Electrode Formation 106
4.2.8 End Polishing 107
4.2.9 Mounting the Samples 109
4.2.10 Summary on the Fabrication of Ti:$LiNbO_3$ Active Devices 110

4.3 Fabrication of Proton-Exchanged $LiNbO_3$ Slab, Stripe and Active Devices 111

4.3.1 Proton-Exchange Technique for $LiNbO_3$ Waveguide Fabrication - a Review 111
4.3.1.1 Introduction 111
4.3.1.2 What is the Proton Exchange Technique? 111
4.3.1.3 Mechanisms of the Process, Structural and Optical Characterization 112
4.3.1.4 Passive and Active Integrated Optical Devices 114
4.3.1.5 Problems with the Proton-Exchange Process for Optical Waveguide Formation 117
4.3.1.6 Summary on the Proton-Exchange Method of Optical Waveguide Formation in $LiNbO_3$ 118
4.3.2 Apparatus used for Proton-Exchange Experiments 119
4.3.3 Slab Waveguide, Stripe Waveguide, and Active Device Fabrication 121
4.3.3.1 Introduction 121
4.3.3.2 Fabrication of PE Slab Optical Waveguides by using Concentrated Benzoic Acid Melts 121
4.3.3.3 Fabrication of PE Slab Optical Waveguides by using Diluted Benzoic Acid Melts 124
4.3.3.4 Realisation of Active PE Devices 126
4.3.4 Summary - Realisations of Waveguides and Devices in $LiNbO_3$ by the Proton-Exchange Process 129

4.4 Overall Summary 129

Appendix 4.1 131

References 133

CHAPTER 4

WAVEGUIDE FABRICATION TECHNIQUES

4.1 Introduction

In this chapter, detailed procedures for fabrication of optical waveguides in $LiNbO_3$ by titanium indiffusion and proton-exchange are described. An up-to-date review on the proton-exchange technique is described to provide a full understanding of the process.

Slab and stripe optical waveguides have been fabricated using titanium indiffusion and proton-exchange. It is important to control the manufacturing process so that devices with predictable operating characteristics can be realised. Rough waveguide edges and misaligned electrodes lead to lossy or inefficient optical waveguide devices. The preparation of the $LiNbO_3$ substrates is of utmost importance. Grease, wax, and dust particles (even on the order of a few microns) cause serious fabrication problems, such as poor adhesion of titanium films to the substrates or discontinuous waveguide patterns.

4.2 Fabrication of Ti:$LiNbO_3$ Active Devices

4.2.1 Introduction

Lithium Niobate ($LiNbO_3$) is a ferroelectric and electro-optic material of considerable potential importance in single-mode optical fibre communications systems [4.1], signal processing applications [4.2] and sensor applications [4.3]. A concise summary of the structure and other properties of $LiNbO_3$ is given in Appendix 4.1 of this chapter.

Optical waveguides in $LiNbO_3$ can be produced by:-

(a) an electro-optically induced increase in the surface refractive index [4.4], (b) outdiffusion of lithium [4.5], (c) indiffusion of transition metals

[4.6], (d) ion bombardment [4.7], (e) proton-exchange [4.8], (f) a combination of titanium indiffusion and ion bombardment [4.9] and (g) a combination of titanium indiffusion and proton-exchange [4.10].

The most common technique of optical waveguide formation is method (c), of which titanium is the most popular transition metal used. Ion bombardment in fact decreases the refractive index of $LiNbO_3$ whereas the other processes increase it. The proton-exchange technique for waveguide fabrication is described in detail in Section 4.3.1.

The fabrication of a Ti:$LiNbO_3$ active device (a phase modulator in this thesis) can be divided into six main stages. They are:-

(i) Original mask making

(ii) Substrate preparation

(iii) Waveguide pattern preparation

(iv) Waveguide formation

(v) Titanium indiffusion

(vi) Electrode fabrication

4.2.2 Mask Making

Before the optical waveguide can actually be fabricated, a photographic mask of the necessary pattern needs to be prepared. All the original masks used in the experimental work on phase modulators reported in the thesis were made in the Department of Electronics and Electrical Engineering, University of Glasgow [4.11]. It is very important to ensure that the original mask is of highest quality. Any variations in width along the length of a waveguide for example, can degrade the performance of a device since the propagation constant of the optical wave will vary. Also the presence of

rough edges along the waveguide pattern could result in higher propagation losses since more light will be scattered into the substrate.

For the work of this thesis, the patterns of both the waveguide and its appropriate electrode masks were cut from Rubylith (a transparent polyester base coated with an opaque thin film). The cutting was carried out on a flat-bed cutting table (Aristo Co-ordinatograph) and the dark or light field masks were fashioned by selective removal of the cut opaque layer. This master pattern was then placed on a vertical light table. First a X20 reduction was made on a high resolution emulsion type plate using an Ultra-Micro Nikkor lens. Using a projection printer equipped with a Micro Tropel lens, a final reduction of X4 was made onto a Balzer photoresist-coated low-reflectivity chrome plate. A minimum linewidth of 1.25 μm over an 18 mm dimension has been obtained with this system. The original masks employed in the experimental work were well within the capabilities of this system.

4.2.3 Substrate Preparation

The crystal substrates used in these experiments were acoustic (SAW) grade lithium niobate ($LiNbO_3$) purchased from Barr and Stroud (Glasgow) Limited. X-cut, Y-cut and Z-cut $LiNbO_3$ were used. The Y-cut $LiNbO_3$ was in the form of discs, 50 mm in diameter, 0.5 mm thick and had the Z-axis normal to a flat cut on one edge of the plate. The X-cut and Z-cut $LiNbO_3$ were obtained from a boule measuring 25 mm x 80 mm x 50 mm. Substrates of the appropriate crystal cut (i.e. X- or Z-) were sawn with 1 mm thicknesses. The waveguide surfaces of the $LiNbO_3$ substrates were nominally polished to a smooth finish. Figure 4.1 shows a typical surface roughness profile of a Y-cut $LiNbO_3$ substrate. Measurements yielded a surface roughness of less than 4 nanometers. The stylus tip used for the measurements was spherical in shape and approximately 2.5 μm in diameter.

The inner alumina tube of the diffusion furnace was 12.5 mm in diameter and thus the width of all the $LiNbO_3$ substrates was standardised at 10 mm. The required X- or Z-cut substrates were mounted on a glass plate (using dental wax) and cut with a diamond saw. The final size of all substrates was 20 mm x 10 mm x 0.5 mm (or 1.0 mm), i.e. the nominal size of $LiNbO_3$ substrates used in the experiments reported in this thesis. Figure 4.2 shows X-cut, Y-cut and Z-cut $LiNbO_3$ substrates with their direction of propagation as along the Y-axis, X-axis and Y-axis respectively.

Before titanium deposition, the $LiNbO_3$ surface was thoroughly cleaned since the process of dicing the slices introduced a lot of grease and wax. If the substrates were not properly degreased and free of dust particles, the following would result:-

(a) Any slab waveguides fabricated would be lossy, and

(b) The stripe waveguide titanium pattern formed could peel off from the substrate resulting in a discontinuous titanium stripe. This will result in a high insertion loss for the Ti:$LiNbO_3$ strip waveguide fabricated because at the discontinuities the light is scattered into the substrate.

It is well known that $LiNbO_3$ is a very difficult material to handle and to clean. Since it is a piezoelectric crystal with high resistivity, high static charge could be formed on the surface of the substrate. This would result in dust particles being attracted to the surface. To assist in cleaning, an anti-static gun (Zerostat - ASP21) was employed to null any charges formed on the surfaces of the substrates. It was found that the Z-cut $LiNbO_3$ proved most difficult to clean due to the pyroelectric effects as a result of temperature changes during the cleaning process.

The substrates were cleaned in a series of warm and room temperature solvents in a clean room (class 100). To minimise the problem of dust particles being attracted to the surface of the $LiNbO_3$, they were kept in the

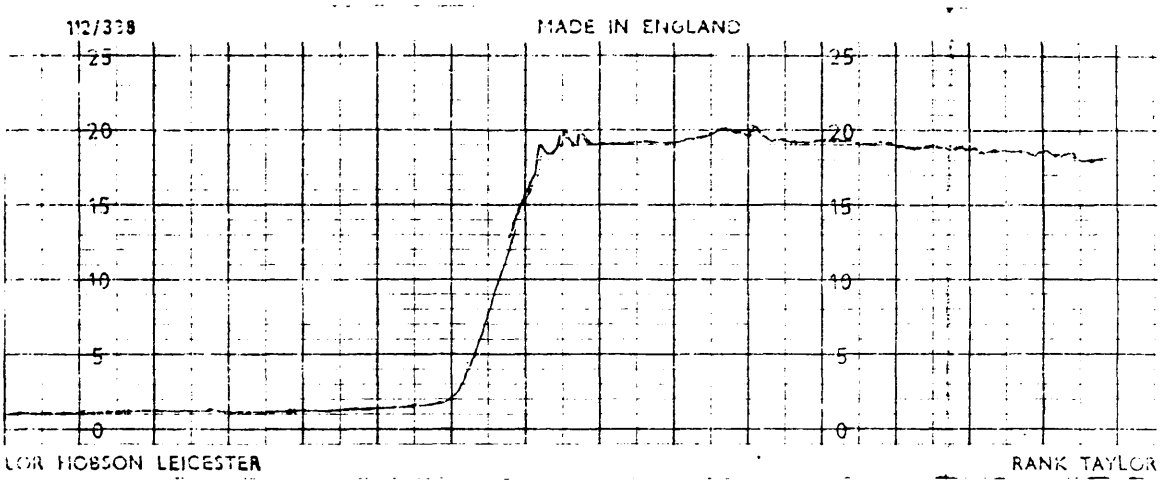

Figure 4.1 **A Typical Surface Roughness Profile Of A Y-Cut $LiNbO_3$ Substrate**

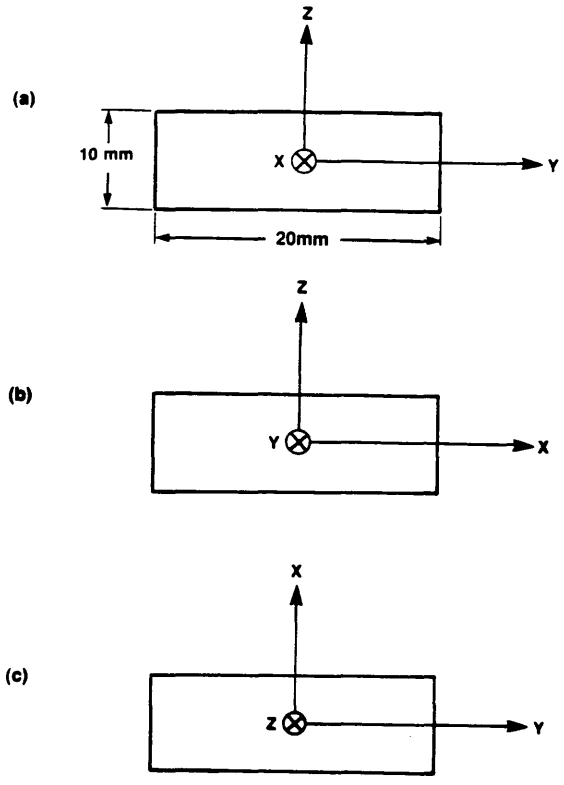

Figure 4.2 **Substrate Dimensions Of X-, Y-, And Z-Cut $LiNbO_3$ Used In All Experiments**

solutions all the time, i.e. they were never allowed to dry out. The following cleaning procedure for all $LiNbO_3$ substrates was adopted since it produced the best results:-

(i) All beakers and tweezers used in the cleaning process were cleaned ultrasonically in warm Trichloroethylene for 15 minutes. They were then cleaned ultrasonically in Acetone for another 15 minutes. The tweezers were then place in a beaker containing Iso-propyl alcohol (IPA). This was changed after 15 samples had been cleaned.

(ii) The $LiNbO_3$ substrates were first soaked in warm ($\cong$ 50°C) Trichloroethylene for 15 minutes and then agitated ultrasonically for another 15 minutes.

(iii) Ultrasonic agitation in Acetone (10 minutes), Methanol (10 minutes) and Iso-propyl alcohol (10 minutes) were carried out on the samples.

(iv) The samples were then soaked in a 10% Decon 90 solution for 12 hours.

(v) Rinsing with deionised water was carried out for 10 minutes.

(vi) The samples were then ultrasonically agitated in Acetone (10 minutes), Methanol (10 minutes) and finally Iso-propyl alcohol (10 minutes).

After stage (vi), the samples were blown dry with filtered oxygen-free nitrogen gas. They were kept in a pre-cleaned covered Pyrex dish until they were ready for waveguide pattern formation. It was noted that samples should always be spun with photoresist immediately after the solvent cleaning procedure. This was because any long delays ($\geq$ 1 hour) could result in poor photoresist adhesion to the substrates.

4.2.4 Waveguide Pattern Preparation

In all of the stripe waveguide pattern preparation, the positive resist Shipley AZ1350J was used. It was applied to the substrate by a filtered syringe (with 0.2 μm millipore type FGLP filter). The spinning was carried out on a standard vacuum semiconductor wafer spinner (Dage Precima or Hedway EC101) for 20 seconds at 4000 rpm. At this point, it was possible to assess the cleanliness of the substrates. Any problems (with small dust particles) were easily seen under a microscope and the samples cleaned again. The satisfactory photoresist covered samples were then baked in an oven (at 85°C-95°C) for 30 minutes to drive off the solvent from the photoresist.

The required waveguide pattern was formed by employing a chrome mask in either a U.V. quartz-halogen lamp contact printer arrangement (5 minutes exposure time) or by a Dage Precima mask aligner (20 seconds exposure time). Two to three exposures were made for each substrate. A 1:1 solution of deionised water and Shipley AZ developer was used to develop the exposed pattern for 20 seconds. The samples were rinsed in flowing deionised water for at least 2 minutes to remove all traces of the developer.

The samples were examined under a microscope unit for any defects. The most common problems included the presence of particles inside the waveguide opening. Ultrasonic agitation was employed to dislodge these particles. If this failed, the samples were processed right from the beginning again. Successful samples were now ready for titanium deposition.

4.2.5 Waveguide Formation

After preparation, the samples of $LiNbO_3$ were placed in a vacuum chamber so that a thin layer of titanium could be deposited on the surfaces.

The method employed for titanium deposition was electon-beam evaporation. The evaporation unit (Figure 4.3) consisted of a pumping system, an electron beam gun assembly and a quartz-crystal film-thickness monitoring device. The vacuum pump system was an Edwards 12E 6" silicone oil diffusion pump, backed out with a rotary pump. To avoid contaminating the deposition chamber with "backstreaming" diffusion pump oil, a liquid nitrogen cold trap is fitted. In the electron beam gun assembly, the titanium source discs (from Materials Research Corporation MARZ grade 99.97% pure titanium) were supported in a reactor grade graphite crucible and the power to the electron beam gun was supplied by a G.V. Planer power supply. A Speedivac quartz-crystal unit was used to monitor the titanium thickness during and after evaporation.

The electron beam evaporation process was initiated by pumping the pressure in the vacuum chamber down to around 10^{-6} Torr before power was applied to the electron beam gun. The power to the electron beam gun was slowly increased for the next 5 minutes during which time outgassing occurred and the pressure in the vacuum chamber rose to about $5x10^{-6}$ Torr. A shutter between the titanium target and the $LiNbO_3$ sample was kept closed until the target reached its melting point i.e. 1675°C. The power to the electron beam gun was set typically to around 160 W to 200 W (i.e. 4 kV at 40-50 mA). It was noted that at 1675°C the titanium target was white hot. At these values, the shutter was opened and the evaporation of the titanium began (at around 10^{-6} Torr). After the required amount of titanium had been deposited, the shutter was closed and by then the pressure in the vacuum chamber was around 5×10^{-7} Torr. After deposition, the electron beam unit was left to cool for 1.0 hour.

During the process of titanium evaporation, the film thickness of the titanium deposited was monitored with a Speedivac quartz crystal system. The resonant frequency of the quartz crystal changed as the titanium metal

was deposited. Also, for a given thickness, the frequency change is dependent on the particular material being deposited. Consequently, before the start of an evaporation run, the evaporation unit had to be calibrated. Several deposition runs were performed and the titanium films deposited on monitor glass slides were measured on a Taylor-Hobson talystep (accuracy of ± 20 Å at maximum sensitivity). Figure 4.4 shows a typical calibration graph for titanium deposition. Also, since the electron beam gun assembly is a cosine-type source, the uniformity of deposited titanium film could be improved by placing the substrate further from the source. In the system used, the substrate was about 35 cm from the titanium target. The limitation in height was due to the size of the bell-jar and also the presence of the quartz crystal unit.

The 'lift-off' process was employed to remove the unwanted titanium. The samples were soaked in acetone for about 15 minutes. By this time, the swelling of unwanted titanium film on either side of the regions required for stripe waveguide formation was visible to the human eyes and slight agitation of the samples resulted in the removal of most titanium. The samples were then ultrasonically agitated for about 2 minutes to ensure that all remnants of unwanted titanium were removed. The samples were examined under a microscope for defects. The most common problem was a broken titanium waveguide pattern. This may have been due to the presence of dust particles prior to titanium deposition. If the broken lines exceeded 20% of all lines present, the titanium pattern was removed in hydrofluoric acid (HF). The whole process of titanium waveguide pattern was repeated as before.

4.2.6 Titanium Indiffusion

The background knowledge for the required amount of titanium film for single-mode operation for a particular waveguide width and its

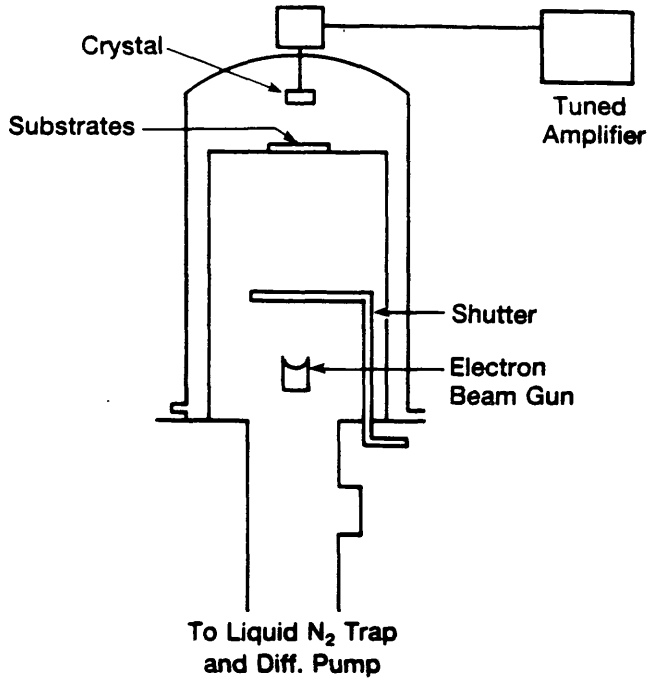

Figure 4.3 **Schematic Of The Electron-Beam Evaporation System**

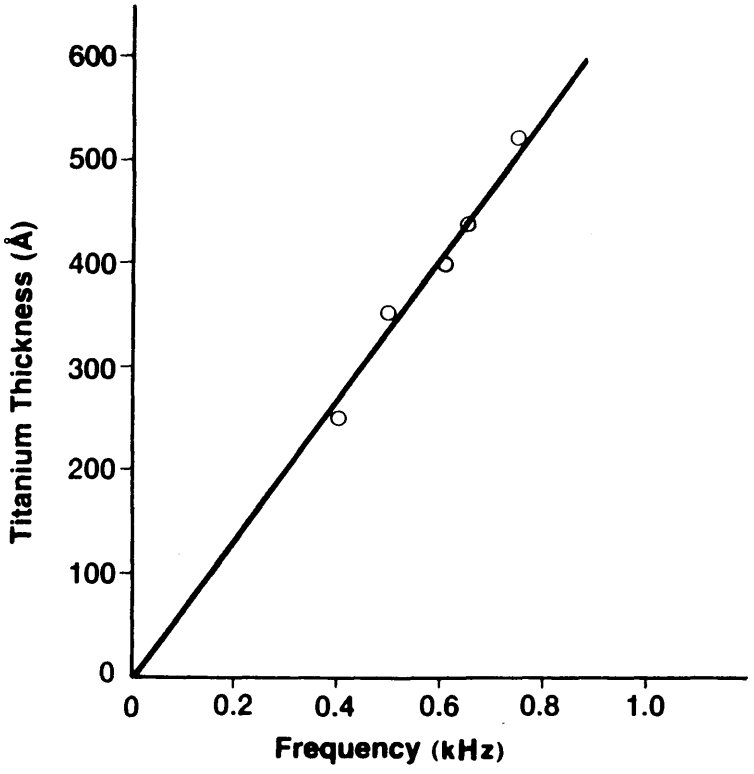

Figure 4.4 **A Typical Calibration Graph For The Titanium Deposition Process**

corresponding time of diffusion were taken from experimental data in the thesis of Esdaile [4.12] and McLachlan [4.13]. All the indiffusion of titanium into the $LiNbO_3$ substrates was performed at 1000°C in a horizontal tube furnace with a Morganite "Cruslite" heating element controlled by a West "Viscount" proportional controller. The temperature feedback to the controller from the furnace was provided by a Pt/Pt - 13% Rh thermocouple.

Using a Pt thermocouple, the flat hot zone of the furnace was located. Figure 4.5 shows the temperature profile of the diffusion that was used. The flat hot zone at 1000°C was estimated to be 30 mm. The reason for the abrupt drop in temperature as shown in Figure 4.5 is that both the ends of the furnace were open. It was found that the temperature in the flat hot zone was controlled to within ± 1°C of the temperature, i.e. 1000°C in this experimental work. The ramp-up time from room temperature to 1000°C was 1 hour and the furnace was always allow to cool down from 1000°C to room temperature.

The major problem that arises with the indiffusion of titanium in $LiNbO_3$ (congruent) is that of outdiffision [4.14]. Outdiffusion can be described simply as the dissociation of Li_2O from the $LiNbO_3$ at high temperatures (i.e. 980°C-1050°C). This produces a constant vapour pressure of Li_2O over the $LiNbO_3$ sample. Thus in an open diffusion system, where the Li_2O vapour can drift away, more Li_2O vapour will be produced to maintain a constant Li_2O vapour pressure over the sample. In so doing, the problem of outdiffusion is made worse.

From Appendix 4.1, it can be seen that the extraordinary refractive index of congruent $LiNbO_3$ is a function of lithium to niobium ratio. Any loss of lithium will result in a higher refractive index; creating a waveguiding region above the $LiNbO_3$ substrate [4.14]. For slab Ti:$LiNbO_3$ optical waveguides, the presence of an outdiffused layer implied that the number of modes, effective propagation indices and substrate cut-off index could be

modified. This change, however, need not seriously affect devices formed. In the case of stripe optical waveguides, the presence of an outdiffused layer has been shown by various researchers to affect seriously the performance of active devices[4.15]. Examples of these include the increase in cross-talk levels measured in optical Y-junction switches [4.16] and optical directional coupler switches.

Esdaile [4.17] performed experiments to prevent outdiffusion in Ti:$LiNbO_3$ waveguides using a closed chamber diffusion furnace (Figure 4.6). In this closed chamber, a small amount (about 0.5 g) of congruent $LiNbO_3$ powder was placed in the alumina tube holding the samples. The presence of congruent $LiNbO_3$ powder was to provide the equilibrium Li_2O vapour pressure over the samples, thus preventing the loss of any Li_2O from the $LiNbO_3$ surface. This technique was found by the author to suppress outdiffusion in approximately 60% of phase modulators fabricated. The failure to suppress outdiffusion on 40% of the diffused devices may possibly be attributable to occasional leakages in the closed tube setup (Figure 4.6).

Figure 4.7(a) shows a phase modulator output with an outdiffused layer. The phase modulator used Y-cut Ti:$LiNbO_3$ waveguide (400 Å initial titanium thickness, diffused at 1000°C for 6.0 hours in a closed tube diffusion unit). A HeNe laser beam (633 nm) propagating along the X-axis of the $LiNbO_3$ substrate was employed to excite the quasi-TE mode of the waveguide. When the quasi-TM mode of the waveguide was excited instead, the absence of the guided plane of laser light was evident [Figure 4.7(b)]. This confirmed the fact that outdiffusion only affected the extraordinary refractive index of the $LiNbO_3$.

Other researchers have also overcome the outdiffusion problem, using a variety of techniques [4.17-4.24]. The technique demonstrated by Jackel [4.22] using flowing wet argon or oxygen over the samples during the diffusion process seems to be a simple and widely used method for

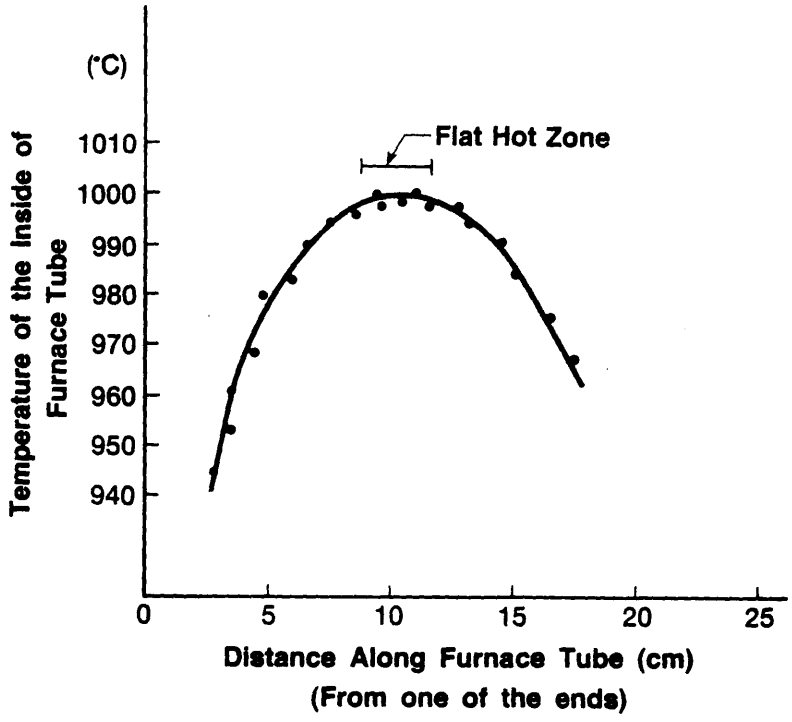

Figure 4.5 The Temperature Profile For The Diffusion Furnace

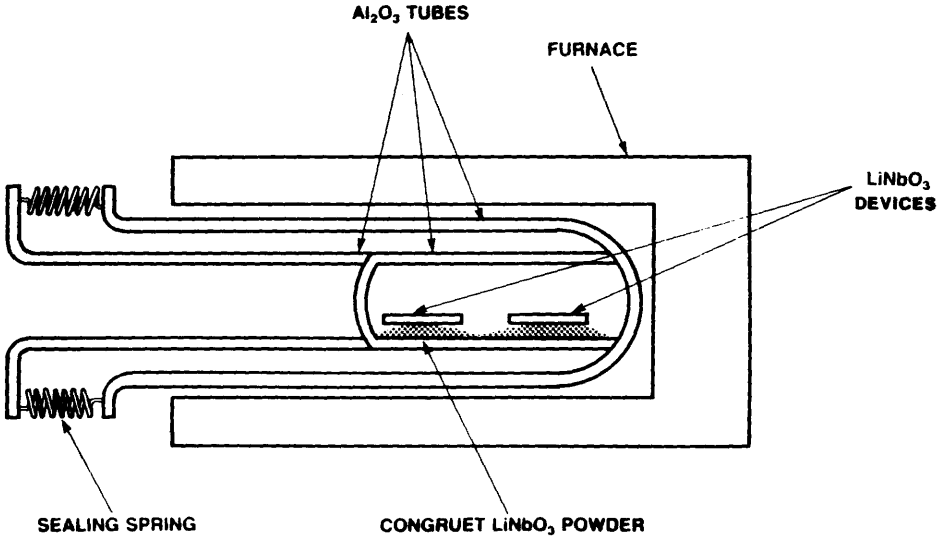

Figure 4.6 Closed-Tube Method For Out-Diffusion Suppression

Figure 4.7(a) Photograph Of A Phase Modulator Output With An Outdiffused Layer (Quasi-TE Mode Excited)

Figure 4.7(b) Photograph Of A Phase Modulator Output With An Outdiffused Layer (Quasi-TM Mode Excited)

outdiffusion suppression. The mechanism here is that the presence of hydrogen during the diffusion process reduces the mobility of lithium and, in so doing, hinders its readiness to dissociate from the $LiNbO_3$ substrate. This technique has been successfully employed by Andonovic [4.16] to fabricate Z-cut Ti:$LiNbO_3$ waveguides.

After the diffusion process (with complete cooling of the furnace to room temperature), the samples were ultrasonically cleaned in Trichloroethane (for 10 minutes), Methanol (for 10 minutes) and Acetone (for 10 minutes). The samples were now ready for electrode formation.

4.2.7 Electrode Formation

The formation of aluminium electrodes on the $LiNbO_3$ substrates represented the final stage in the production of all the active devices in the clean room. This was accomplished using an Edwards 12E deposition unit, a Dage Precima mask aligner and a suitable 'light-field' electrode mask. The use of this type of mask facilitated the alignment of the waveguides with the electrode pattern. The fabrication of this electrode mask was similar to the process described in Section 4.2.2. The only difference was that the pattern here was photographically reversed from negative to positive.

The cleaned samples were supported by glass slides approximately 20 cm from the heating coil element. About 10 cm of aluminium wire (99.99% pure - Goodfellows Metal) was used for each thermal evaporation run. It was found that to ensure excellent adhesion of the aluminium to $LiNbO_3$, not only had the $LiNbO_3$ samples to be thoroughly cleaned of any wax or grease, but the pressure in the vacuum chamber should be as low as possible (i.e. 10^{-6} Torr). The LT (low tension) was switched on and with the shutter closed, the current to the filament wire was increased slowly (15 seconds) to approximately 30 A. Once the outgassing had stopped, the shutter was opened and the current to the heating filament was maintained at around 30 A for 30

- 45 seconds. This resulted in aluminium film thicknesses of around 1500 - 2000 Å, as measured using the Taylor-Hobson Talystep on the monitor glass slides.

The samples were allowed to cool for 1 to 2 hours. After that, a layer of positive photoresist (AZ1350J) was spun on at 4000 rpm for 20 seconds using a Dage Precima standard vacuum semiconductor wafer spinner. The samples were then baked in an oven for 30 seconds at around 85°C.

The accurate X, Y, Z and θ movements on the Dage Precima mask aligner facilitated the alignment of the electrode mask with the waveguides. The job was made easy by the ridge effect of the titanium indiffused waveguides. A x200 split-field optical microscope was used continuously to monitor the complete alignment procedure. An alignment accuracy of about 1 μm was satisfactory since the waveguide width and electrode gap were around 4 μm and 6 μm respectively. This might well not be good enough if the widths and gaps were around 2 μm.

Once the alignment was complete, a quartz halogen lamp was used to expose the photoresist for 20 seconds. Development of the photoresist was performed using a Shipley AZ developer diluted to 1:1 with deionised water. Unwanted aluminium was etched away using phosphoric based aluminium etch. The situation here was monitored with extreme care to ensure that no over-etching occurred. The samples were thoroughly rinsed in flowing deionised water for 5 minutes. After inspection of the electrode pattern, if found to be satisfactory, the samples were ready for edge polishing. If the pattern was not right, the full process was repeated. Figure 4.8 shows a completed active Ti:$LiNbO_3$ device substrate.

4.2.8 End Polishing

The end-fire coupling technique [4.25] was employed in preference to the prism-coupling method [4.26] to test the active Ti:$LiNbO_3$ devices. The

main reason for doing so was that it was much more convenient since the devices were about 10 mm long and the electrode pattern could be of the same length. In addition it is more efficient to end-fire couple the laser beam into the stripe waveguides. Both techniques of coupling laser light into an optical waveguide are discussed in detail in Chapter 5.

The particular method of end polishing Ti:$LiNbO_3$ devices used was first developed at the University of Glasgow [4.27]. The samples to be polished were waxed on a brass plate with dental wax and both the ends were cut as close as possible to the waveguides, typically within about 0.5-1.0 mm, using a diamond saw. The sample was mounted on a Pyrex rod using Shellac since this material was found to be resistant to undercutting by the cleaning agents used and by Syton (used in the final polishing stage). The Shellac between the substrate and the Pyrex rod had to be as thin as possible. This was to reduce the chipping problem often experienced which could lead to longer times being needed for the end polishing of the substrate.

A jig developed by Piechowiak and Doughty [4.27] was used to hold up to six $LiNbO_3$ samples (i.e. with Pyrex rods) (Figure 4.9). A clock gauge was used to level all the samples and holders. The jig was then placed in a Logitech PM2 polishing machine where the samples were roughed down on a brass or cast iron plate using a mixture of water and 800 grit (12.5 μm) aluminium oxide (Aloxite) powder. The polishing was stopped once a good edge (i.e. an edge with no large or broken chips due to the diamond saw) could be seen using an optical microscope at x 100 magnification. This usually took 1/2 to 1 hour.

After the jig and the samples were cleaned of all the Aloxite, semi-polishing was performed on a solder top plate using diamond paste of 6 μm grit size. This intermediate polishing step, which lasted for about 1 hour, could possibly be left out. The reason for this intermediate step was to ensure

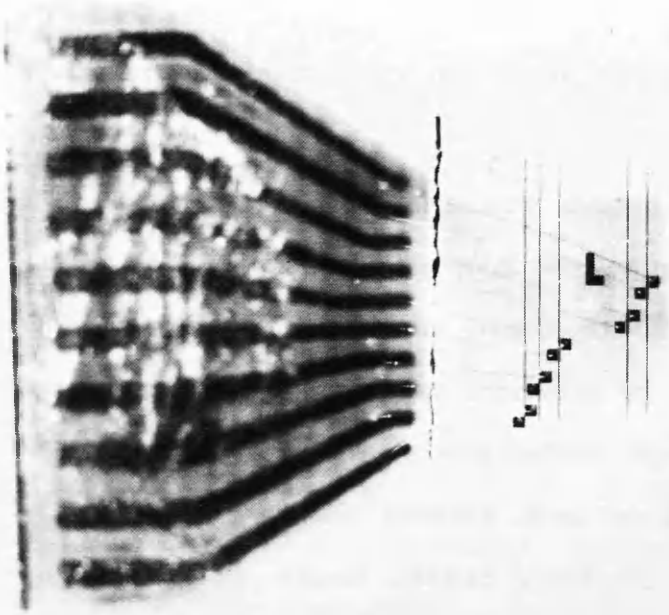

Figure 4.8 Photograph Of Completed Phase Modulators On A Y-Cut $LiNbO_3$ Substrate

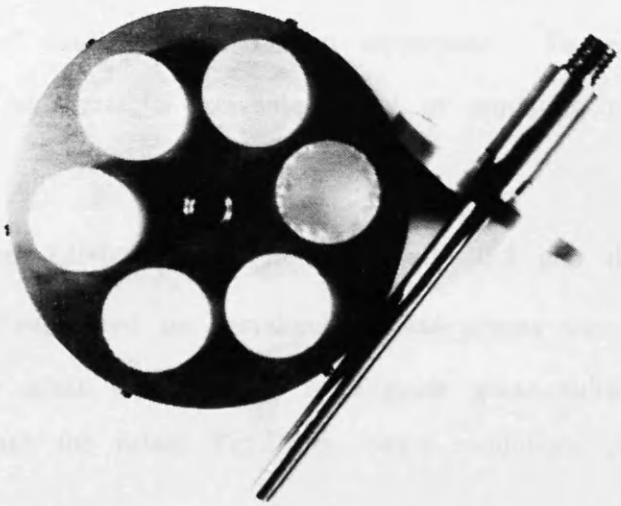

Figure 4.9 Photograph Of A Polishing Jig With Six $LiNbO_3$ Samples (Using Pyrex Rods)

that all remaining chippages due to the dicing of the $LiNbO_3$ were completely removed.

The jig and the samples were cleaned thoroughly before the final and longest (5-15 hours) polishing stage was started. A bowl type plate was used with an expanded polyurethane base into which Syton W15 (a colloidal silica) was poured. This stage was considered to be finished if, on inspection (at x400 magnification), a sharp well defined edge, free of chips, was achieved.

The samples were removed from the Pyrex holders by heating on a hotplate. Any excess Shellac could be removed completely by using methanol. Extreme care must be taken during the full polishing process so that no cross-contaminations and thermal shock could be experienced by the $LiNbO_3$ devices. This could lead to longer polishing times and broken samples respectively.

4.2.9 Mounting the Samples

After polishing, the Ti:$LiNbO_3$ devices were then tested optically by the end-fire technique for the number of guided modes and to ensure the problem of outdiffusion had been suppressed. To test all the five devices on the same substrate, a convenient way of mounting the device is that outlined below:-

(i) Since $LiNbO_3$ is fragile (especially 0.5 mm thick samples); the sample was first supported on rectangular glass pieces cut from an ordinary Chance laboratory glass slide. The rectangular glass substrates had to be slightly smaller than the actual Ti:$LiNbO_3$ phase modulator device.

(ii) The glass substrate (together with the active device) was then mounted on a printed circuit board with 10 defined copper tracks.

(iii) Finally, gold wires were bonded from the electrodes to the copper tracks.

Figure 4.10 shows an actual mounted, bonded active device ready for serrodyne modulation studies.

4.2.10 Summary on the Fabrication of Ti:$LiNbO_3$ Active Devices

Figure 4.11 summarises schematically the full fabrication stages of a Y-cut Ti:$LiNbO_3$ phase modulator. Throughout the fabrication procedure, extreme care was taken to ensure cleanliness of the highest quality was maintained. Failure to do so resulted in the failure of a particular fabrication stage. This meant a waste of processing effort and material and chemical wastage.

The production of straight lines with minimal irregularity, deposition of a required titanium thickness and control of the diffusion temperature meant that optical waveguides with the required number of modes (in this work normally only the single, fundamental, mode) and low losses were fabricated with ease. The mounting procedure outlined in the last section provided a cheap, quick and simple way of testing the active devices fabricated.

The overall production time required for an active Ti:$LiNbO_3$ device was approximately five full working days. This time does not include the end polishing of the sample. Comparison of the fabrication of active devices by titanium indiffusion and proton-exchange is made in Section 4.4.

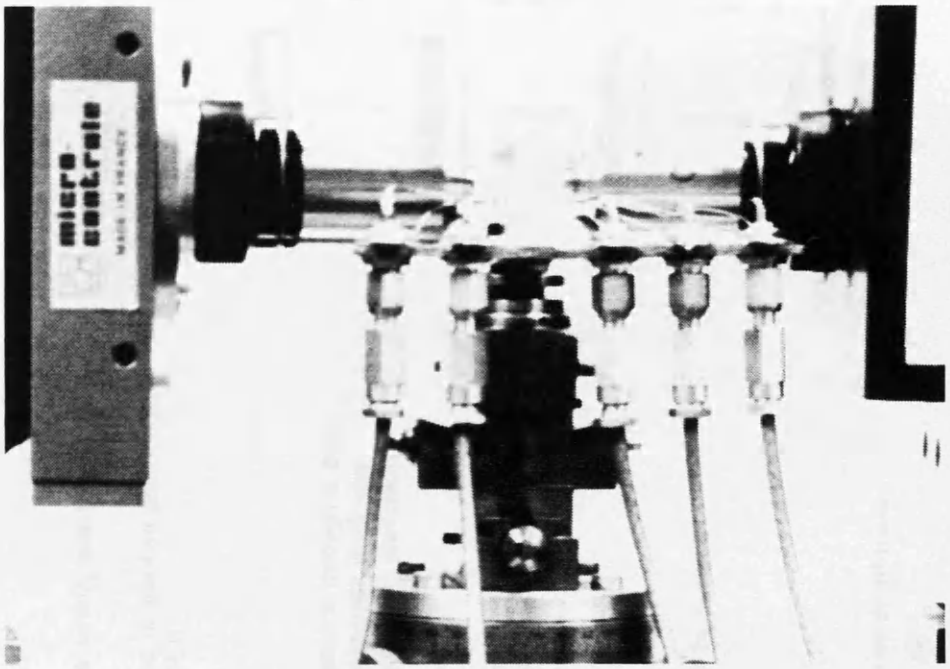

Figure 4.10 Photograph Of A Mounted And Bonded Phase Modulator Device (Ready To Be Tested)

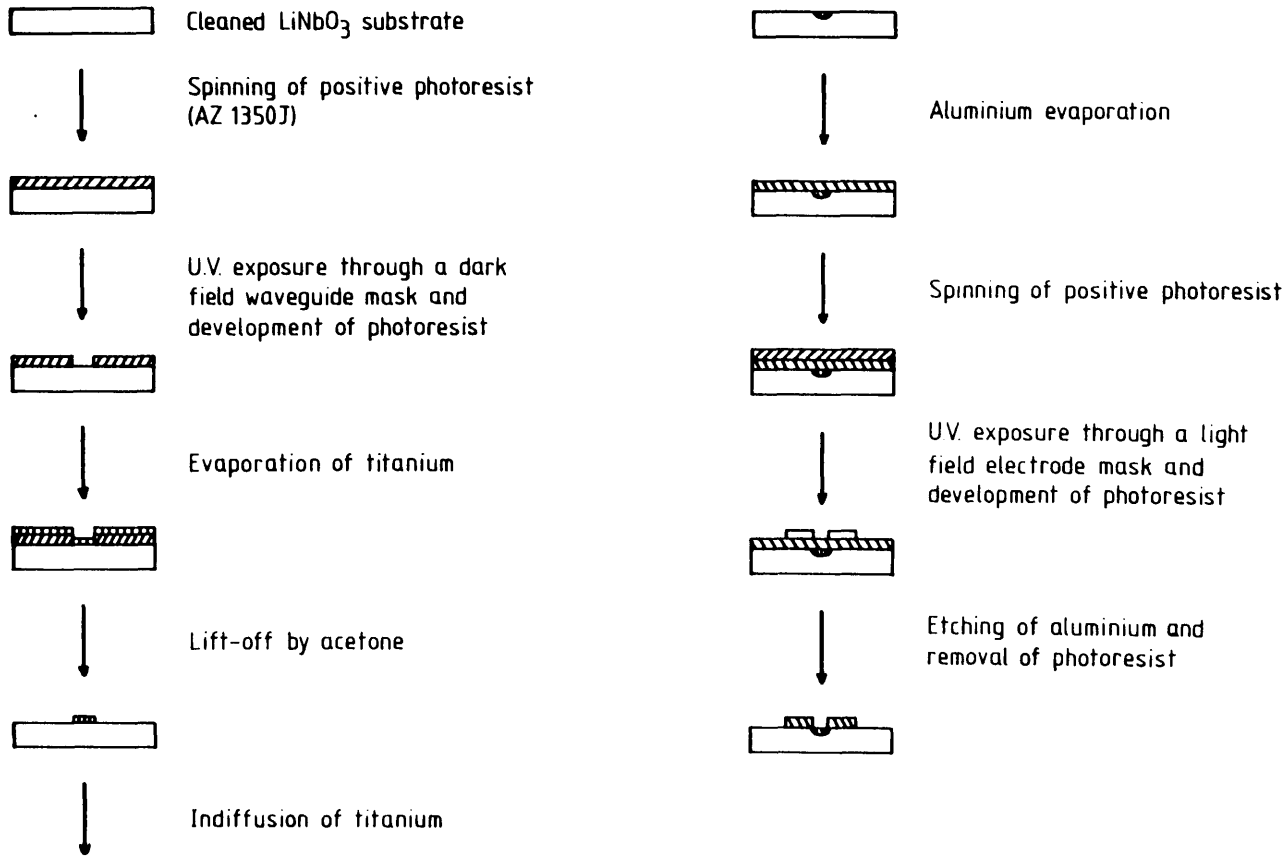

Figure 4.11 Summary Of The Full Fabrication Procedure For A Y–Cut Ti:$LiNbO_3$ Integrated Optical Phase Modulator

4.3 Fabrication of Proton-Exchanged $LiNbO_3$ Slab, Stripe, and Active Devices

4.3.1 Proton-Exchange Technique for $LiNbO_3$ Waveguide Fabrication - a Review

4.3.1.1 Introduction

In this section, a review of the proton-exchange technique for waveguide and device realisation in $LiNbO_3$ will be given. Various problems in the waveguides and devices fabricated by this method will be highlighted. The equipment and the fabrication techniques that were employed in this project to fabricate proton-exchanged (PE) waveguides and electro-optic PE phase modulators are described in detail.

4.3.1.2 What is the Proton Exchange Technique?

The proton exchange method was originally used as a means of preparing new cubic perovskites from $LiNbO_3$ and $LiTaO_3$ [4.28, 4.29]. It was realised that the technique could be employed to form optical waveguides in such materials, and this has subsequently been carried out in X- [4.30, 4.31], Y- [4.32, 4.33, 4.34], and Z- [4.35, 4.36] cut $LiNbO_3$ and X- [4.37-4.44] and Z-cut [4.43, 4.44] $LiTaO_3$, using molten benzoic acid as the protonic source.

The main advantage of the process is that fabrication of waveguides is quick and simple. The temperature required for the waveguide formation is low, between 160°C and 249°C [4.31]. The end result is a waveguide with a high index change of 0.12 (i.e. $\Delta n = 0.12$). However, the refractive index change is not isotropic as only the extraordinary refractive index is increased. There is a significant but smaller decrease in the ordinary refractive index [4.45]. This implies that only TE-modes are guided in proton-exchanged (PE) X- and Y-cut $LiNbO_3$ and TM-modes in PE Z-cut $LiNbO_3$.

Similarly, for $LiTaO_3$, only the TE-modes and the TM-modes are supported in the X- and Z-cut of this material respectively.

Another important advantage of proton-exchange waveguides in $LiNbO_3$ and more recently in $LiTaO_3$ is that they have been found to be more resistant to optical damage [4.46-4.48] than titanium-diffused waveguides. This will potentially be useful for satisfying a number of integrated optical component requirements at 830 nm [4.49].

The effects of optical waveguides formed in lithium-rich benzoic acid melts [4.50, 4.51, 4.52] and using titanium indiffusion followed by PE in $LiNbO_3$ [4.45, 4.53-4.56] in relation to the refractive index change and the refractive index profile have been studied. Also, recently, phosphoric acid has been employed to form optical waveguides with a Δn value of 0.15. [4.57, 4.58] The annealing of the PE waveguides has shown that the refractive index profile of the optical waveguide can be modified from an almost step-index profile to a graded-index profile [4.50, 4.59, 4.60]. The modification is dependent upon the annealing time, temperature, and atmosphere in which the process is carried out [4.61].

4.3.1.3 Mechanisms of the Process , Structural and Optical Characterization

The proton-exchange process in $LiNbO_3$ can be described broadly as the depletion of lithium and the replacement of hydrogen in the crystal. This occurs when the substrate is immersed in a protonic source, i.e., an acid (e.g. benzoic acid, palmitic acid, stearic acid, cinnamic acid, and mixtures) or a hydrate melt [e.g. $Mg(NO_3)_2.6H_2O$] , at the appropriate temperature. The exchange process can be complete, i.e. with all the lithium replaced [4.29], or it can be partial, depending on the acidity of the medium. However the effect of 'acidity' has by no means yet been fully and properly investigated. For optical waveguide fabrication, only partial exchange is of interest since total

exchange will cause the $LiNbO_3$ crystal to change from its hexagonal structure to a cubic perovskite. This volume change will result in the surface of the $LiNbO_3$ crystal to cracking. However, totally proton-exchanged layers cannot be obtained on large area $LiNbO_3$ single crystal substrates because the enormous stress introduced by this phase transformation does not allow any epitaxial adhesion of the new $HNbO_3$ phase on the substrate.

It has been established by some reasearchers that for the proton-exchange process to be useful for optical waveguide formation, the general composition of the exchanged regions is $(H_xLi_{1-x})NbO_3$ with $0.8 \geq x > 0$. One of the most commonly used protonic sources for partial exchange is benzoic acid [4.30] or diluted benzoic acid (dilution achieved by introducing an appropriate amount of lithium benzoate) [4.50-4.52]. In general the overall reaction between benzoic acid and $LiNbO_3$ can be described by Equation 4.1:

$$LiNbO_3 + (C_6H_5COOH)_x \longleftrightarrow Li_{1-x}H_xNbO_3 + (C_6H_5COOLi)_x \quad (4.1)$$

Several important problems (to be described in Section 4.3.1.6) have been found in optical waveguides and devices realised in $LiNbO_3$ by the proton-exchange technique. It is therefore important that a full understanding of the underlying materials science be carried out. Several researchers have employed Rutherford backscattering spectrometry (RBS), nuclear reactions, secondary ion mass spectrometry, scanning electron microscopy, and X-ray diffraction (by double crystal and topograph) to identify the structure, the thickness and the strain in the lattice of the exchanged layers [4.62, 4.63, 4.64, 4.65, 4.66]. The results from the above analytical study can be summarized below:-

(a) There was close agreement between optical waveguide thicknesses estimated from prism coupling measurements and estimates from resonant

nuclear interactions and RBS [4.62] From all the three measurements, it was found that the refractive index profile is step-like.for waveguides formed without annealing and

(b) The results from the X-ray diffractometry study indicated that the PE regions had undergone a positive lattice strain. For PE Z-cut $LiNbO_3$ crystals it was found that the strain was $\Delta c/c = 0.45\%$ (with $\Delta a/a$ being negligible) [4.62]. However researchers have also found that the extent of the lattice strain is also dependent on the $LiNbO_3$ substrate orientation [4.62].

Recent work reported by Loni et al employing hydrogen-isotopic effects in proton-exchanged and deuterium-exchanged $LiNbO_3$ may prove to be useful as an investigational tool in the understanding of the proton exchange process, in terms of the changes in the crystal stoichiometry, waveguide stability, and ionic conduction effects on acousto-optic and electro-optic device performance [4.68, 4.69, 4.70, 4.71].

The experimental characterization of the optical waveguides fabricated by concentrated and dilute melt molten benzoic acid melt in X- and Z-cut $LiNbO_3$ in this study will be measured by optical methods (in particular using the prism coupling and the end-fire coupling techniques). The full experimental procedures and analysis of the results are presented in Chapter 5.

4.3.1.4 Passive and Active Integrated Optical Devices

The high refractive index change that can be achieved with PE in $LiNbO_3$ suggests that this method can be used to realise high performance passive structures such as gratings and lens of various types. A 3 μm period grating with approximately 90% deflection efficiency was fabricated in X-cut $LiNbO_3$ by Pun et al [4.72]. This was then followed by a demonstration of a chirp grating lens by Warren et al [4.73]. Yu [4.74] demonstrated planar equivalents of aspheric bulk lens structures.

The use of PE regions as passive polarizing elements in conjunction with titanium-indiffused stripe waveguides has been demonstrated [4.75, 4.76, 4.77]. In these devices, both the TE and the TM modes are supported in the $Ti:LiNbO_3$ stripe waveguides. The PE insets however only support the TE or the TM modes, depending on the crystal cut used. High performance polarizers using appropriate lengths of PE inset have been demonstrated with TE/TM mode rejection ratios of as high as 50 dB and low optical excess insertion losses of the order of 1 dB [4.77, 4.78]. This result is better than results for the metal overlay/resonance absorption method [4.79]. In the latter polarizers, the ultimate device performance is very much dependent on the control of the thickness of the deposited dielectric layer between the metal overlay and the waveguide. Accurate control of this layer can be difficult and hence this type of polarizer is hard to realise with good repeatable performances. By tapering the overlay dielectric layer it is possible to realise a high performance polariser.

Other passive structures demonstrated to date include ring-resonators with a finesse of 6 [4.80, 4.81], and an interferometric temperature sensor in Z-cut $LiNbO_3$. In the latter structure, the large change in refractive index was used to realise low-loss waveguide bends and hence enable a large interferometer arm length difference to be realised in a compact structure [4.82]. This implies that highly sensitive temperature sensing applications can be accomplished, in this case, in Z-cut $LiNbO_3$ and could be digitised using several structures with different pathlength differences.

The use of PE optical waveguides in $LiNbO_3$ in non-linear optical interactions such as second harmonic generation (SHG) has also been demonstrated by a number of workers. SHG has been observed as a guided wave in $LiNbO_3$ waveguide at Nd:YAG laser wavelength, i.e. 1060 nm [4.83, 4.84]. Lim and co-workers recently reported on the second harmonic generation of blue and green light in periodically-poled titanium indiffused

and PE planar $LiNbO_3$ waveguides [4.85]. However, for the GaAs laser diode wavelength, i.e. 830 nm, phase matching to guided waves was not possible (e.g. without employing a periodic phase-matching strucuture) but it was possible to radiate plane waves into the $LiNbO_3$ substrate. This type of SHG radiation was observed in the form of Cerenkov radiation and in this case both the fundamental optical wave and the second harmonic wave were extraordinary waves [4.58, 4.86, 4.87]. The nonlinear coupling here is obtained via the nonlinear coefficient d_{33}, which is the largest in the case of $LiNbO_3$.

Electro-optic and acousto-optic devices have been demonstrated by various researchers [4.88-4.93]. Their results indicated variations in performance, with some indicating performance comparable with Ti:$LiNbO_3$ counterparts [4.88, 4.89, 4.91, 4.92] while others reported reductions in electro-optic [4.90, 4.93] and acousto-optic interaction strength of as much as three times.

In Chapter 6, experiments involving electro-optic phase modulators fabricated by titanium-indiffusion and proton-exchange are described in detail. It has been shown in those experiments that optical frequency translators made by PE had similar performance to Ti:$LiNbO_3$ frequency translators [4.88, 4.89]. However, the PE devices were found to be sensitive to non-zero d.c. voltage levels [4.89]. Work by Becker [4.90] on PE and titanium-indiffused Mach-Zehnder interferometers at 830 nm and 1300 nm concluded that the electro-optic activity was reduced by at least a factor of 2.7 in the case of the PE Mach-Zehnder interferometer devices. In contrast, work by Wong et al [4.91] on dilute melt PE MZI in X-cut $LiNbO_3$ indicated that the electro-optic efficiency is preserved. Work by Minakata and co-workers showed that the r_{33} electro-optic constant values in their PE Z-cut $LiNbO_3$ phase modulators were reduced to one-tenth of published r_{33} values for virgin crystals [4.93].

The use of PE X-, Y-, 128° rotated Y-, and Z-cut $LiNbO_3$ waveguides in acousto-optic (AO) devices has been investigated by a number of researchers [4.61, 4.94-4.104]. The general conclusions from all these were that there was a measured reduction in AO interaction efficiency, an increase in acoustic wave propagation losses, and substantial changes in the surface acoustic wave velocity. For example, Dawar and co-workers demonstrated that in reducing the in-plane scattering levels of the PE Y-cut $LiNbO_3$ waveguides, a drastic reduction in AO interaction efficiency was observed [4.61]. Recently, Burnett et al obtained SAW velocity values for X-, Y-, and Z-cut dilute melt PE regions in $LiNbO_3$ using scanning acoustic microscopy. Results obtained showed a substantial variation in their measured SAW velocity values with respect to the orientation of $LiNbO_3$ crystal used. Also another interesting result is that decreases in the propagation velocity were accompanied by an increase in the attenuation [4.105].

4.3.1.5 Problems with the Proton-Exchange Process for Optical Waveguide Formation

From the discussions in the two previous sections, it is evident that some important problems have been identified in PE waveguides fabricated using pure benzoic acid melts. The problems include:-

(a) The measured effective mode indices on a day-to-day basis reveal an oscillatory [4.106] and in some reports a general reduction in values [4.31]. This implies that the refractive index profile of the PE $LiNbO_3$ waveguides evolves with time after fabrication. Researchers have attributed these short and long term refractive index instabilities to continuous migration of protons within the thickness of the waveguiding layer [4.107], relaxation of the metastable structure ($H_xLi_{1-x}NbO_3$), and possibly a phase separated surface layer caused by dehydration of the PE regions.

(b) In electro-optic devices (phase modulators and Mach-Zehnder interferometers) it was found that the electro-optic activity was reduced in most device demonstrations [4.90]. Evidence exists where the r_{33} electro-optic coefficient of $LiNbO_3$ was found to be 10 times smaller in proton-exchange devices when compared to titanium-indiffused devices. However successful demonstrations of proton-exchange optical frequency translators with no measured reduction in electro-optic activity have been reported [4.88, 4.91]. The devices formed by pure PE however were sensitive to non-zero d.c. voltages [4.89]. On the other hand Mach-Zehnder interferometers formed by dilute melt PE were found to preserve the electro-optic coefficients and were not sensitive to dc voltages [4.91]. The details of the latter two experiments are reported in detail in Chapter 5 and 6 of this thesis.
(c) AO devices in proton-exchange waveguides have also been found to have reduced interaction efficiency. Variations in SAW velocities and increase in acoustic wave attenuations have been reported [4.105].

The body of evidence on the above problems associated with PE waveguides and devices is still far from complete or completely satisfactory.

4.3.1.6 Summary on the Proton-Exchange Method of Optical Waveguide Formation in $LiNbO_3$

PE optical waveguides in X-, Y-, and Z-cut $LiNbO_3$ have been extensively characterized by optical techniques. A number of problems have been found to be associated with PE waveguides and devices, such as index instability, d.c. extinction effects, reduced electro-optic activity and reduced acousto-optic interaction efficiency. Materials analysis techniques such as RBS, X-ray diffractometry, scanning & transmission electron microscopy, acoustic microscopy, SIMS, infra-red aborption (IRA), atomic absorption spectroscopy (AAS), and nuclear interactions provide a valuable basic understanding which should greatly assist in attaining ultimate objective of stable, high-

performance devices in $LiNbO_3$ realised by the proton-exchange process. It is clear that by employing all the above techniques, a better understanding of the structure of the PE regions will be known. This understanding can, in turn be used to help in the fabrication of low-loss (i.e. both in-plane and out-of-plane scatter losses) and efficient AO and EO devices in a repeatable manner.

It is the partial aim of this thesis to provide possible solutions to the problem of improving electro-optic device performance. In addition, a significant improvement in the optical quality of PE waveguides in X- and Z-cut $LiNbO_3$ has been demonstrated. The key for all these improvements is the fabrication of PE devices by dilute melt molten benzoic acid, the dilutant being lithium benzoate. The study for this work will be reported in Chapters 5 and 6 of this thesis. It is also noted that the process of annealing can be used in conjunction with the dilute melt proton-exchange process to realise optical waveguides and devices with specific properties.

4.3.2 Apparatus used for Proton-Exchange Experiments

The precise control of the set temperature of the molten benzoic acid (concentrated or diluted with lithium benzoate) is very crucial in the repeatable realisation of PE waveguides and devices. A number of options exist in the choice of a heating system. They include:-

(a) Precision, oil-filled, and stirred thermostatic baths,
(b) Horizontal or vertical type high temperature furnaces,
(c) Hot plates, and
(d) Fluidised alumina powder heating units.

After evaluation of the various options in terms of accuracy, cost, size, and ease of placing and operation in a fume hood, it was decided that option (a) was the most versatile (at least for application to proton-exchange).

Figure 4.12 shows an illustration of a Grant high temperature precision stirred thermostatic bath that was purchased and used in all the PE experiments described in this thesis. The crucial factor is the choice of the high temperature oil and this was Dow Corning 550 fluid which is rated for safe operation at temperatures up to 300°C. The Grant HE 10 bath has a specified range of operation range from 0 to 300°C and a temperature control accuracy of ±1.0°C when used with above mentioned high temperature oil.

The next step was to make an accessory plate just above the oil bath which would be capable of simultaneously holding four 250 ml stainless steel beakers. The purpose of this was to be able to fabricate PE waveguides in several different cuts of $LiNbO_3$ simultaneously. Figure 4.13 shows a detail schematic of the actual oil bath used in the PE waveguide study. Due to the irritating nature of the benzoic acid fumes, the PE oil bath was located in a fume hood. In addition, a precision scale (accurate to ± 0.001 gram) was used to weigh the lithium benzoate that was needed for the dilute-melt PE experiments.

The samples were mounted on PTFE holders (Figure 4.14) and the temperature of the molten benzoic acid was monitored by a digital thermometer with a chromel-aluminel thermocouple. The accuracy of the thermometer was ± 1.0°C.

As a final remark, it should be noted that other researchers have used sealed ampoules to carry out the PE process. In all the reported PE work in this thesis, the sealed ampoule approach was not used, since it can be time consuming and require additional equipment. The waveguides fabricated were found to be reproducible and no contamination problems were evident.

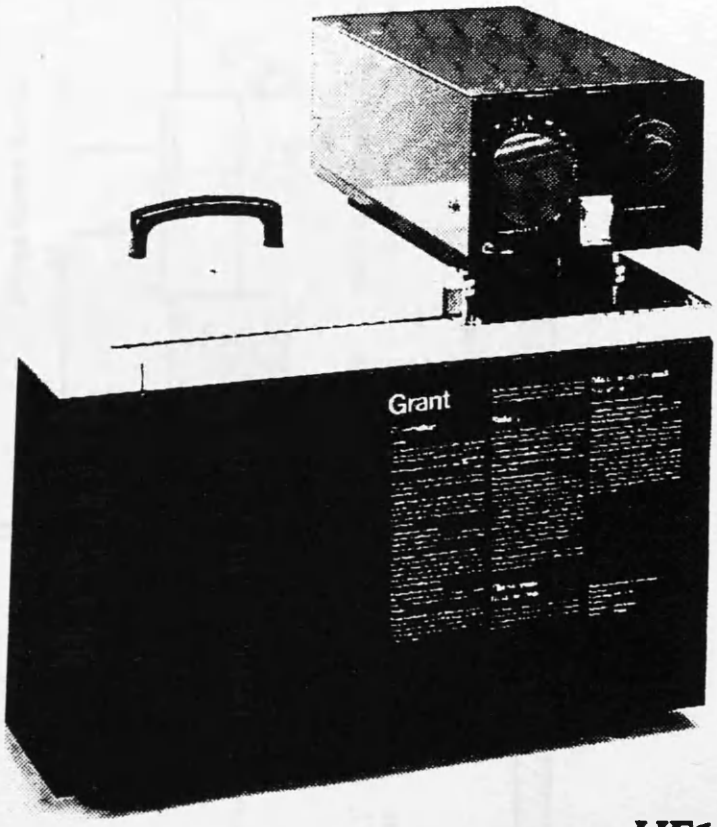

Figure 4.12 Photograph Of The Oil Bath Used For All The PE Experiments (Courtesy Of Grant Instruments, U.K.)

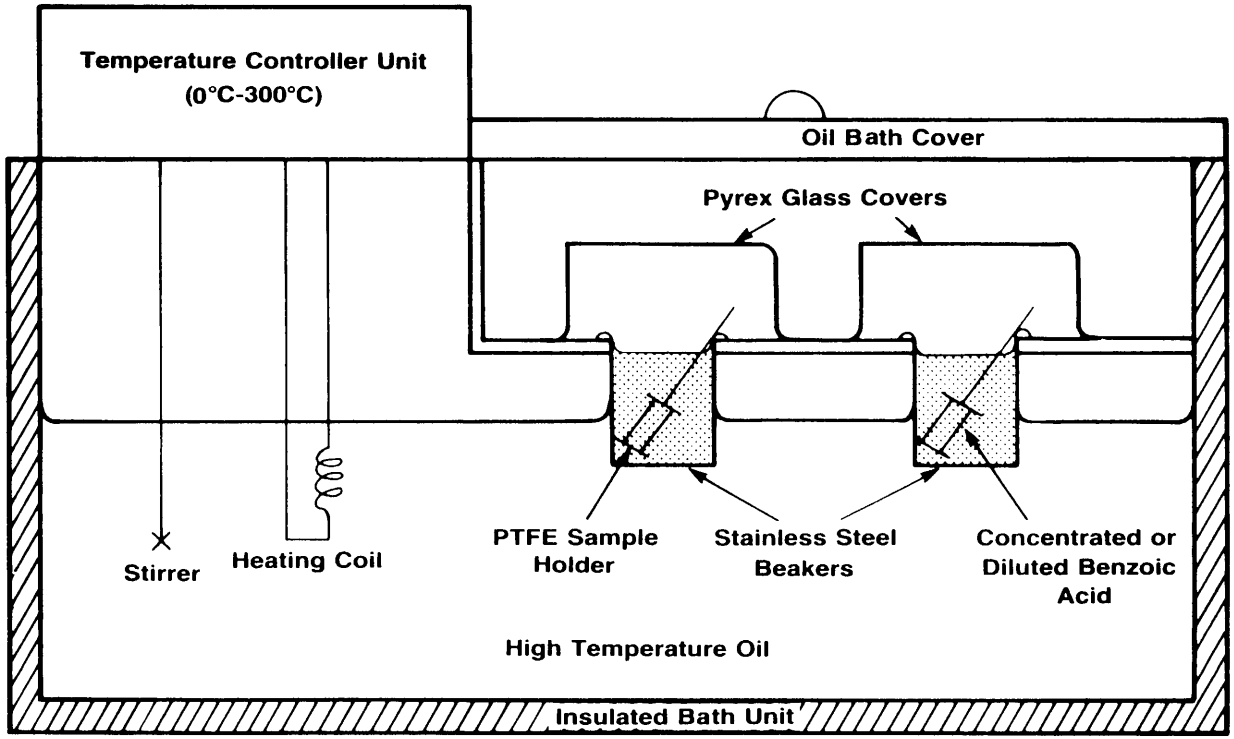

Figure 4.13 Schematic Of The Grant High Temperature Precision Stirred Thermostatic Bath Used For Proton Exchange

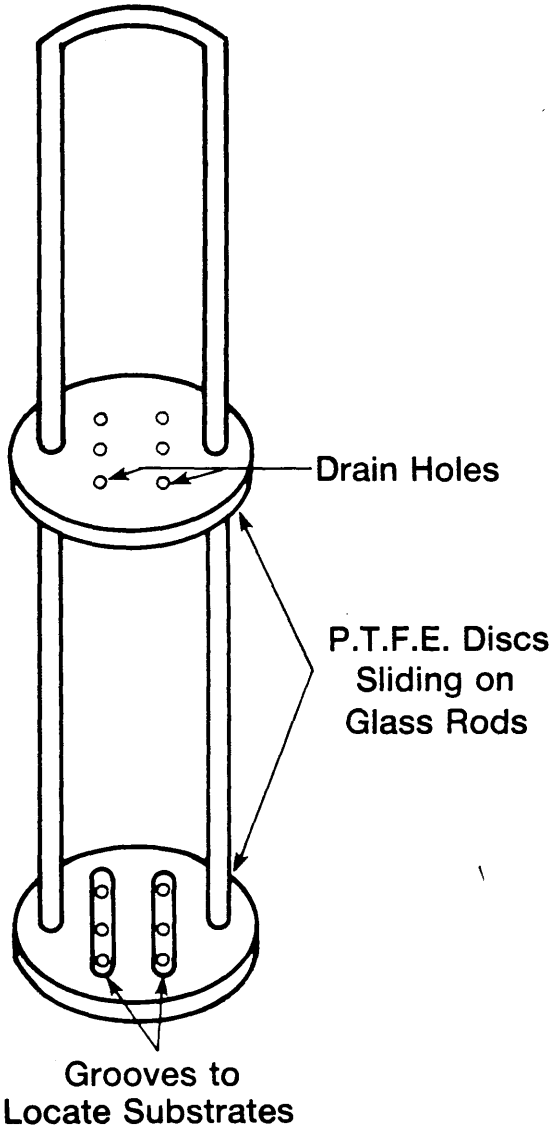

Figure 4.14 **PTFE Holder Used To Secure $LiNbO_3$ Substrates In The Molten Benzoic Acid Bath**

4.3.3 Slab Waveguides, Stripe Waveguides, and Active Device Fabrication

4.3.3.1 Introduction

The aim of this section is to describe the fabrication procedures used to realise the PE (dilute and concentrated benzoic acid melt) waveguides and devices reported throughout this thesis. All optical measurements and device performances are described in Chapters 5 and 6 respectively.

4.3.3.2 Fabrication of PE Slab Optical Waveguides by Using Concentrated Benzoic Acid Melts

AnalaR benzoic acid was used in all the PE experiments described in this thesis. The main reasons for the choice of benzoic acid are that it is cheap, non-poisonous, and has useful melting (122°C) and boiling points (249°C) [4.109].

X-, Y- and Z-cut $LiNbO_3$ substrates were cleaned ultrasonically and degreased thoroughly, as described in Section 4.2 of this chapter. The cleaned samples were then mounted in PTFE holders before being placed in approximately 230 ml of molten benzoic acid in a stainless steel beaker placed in the high temperature oil bath.

A number of Y-cut $LiNbO_3$ substrates were proton-exchanged in molten benzoic acid for 0.25 to 0.5 hour at 180°C. The result for all the PE Y-cut substrates was the formation of 'cracked' surfaces (Figure 4.15). This is due to the enormous strain associated with the PE process for this cut of the crystal. In view of this, no optical waveguide studies were carried out in Y-cut $LiNbO_3$.

X-cut $LiNbO_3$ was the main cut used in the PE waveguide device work described in this thesis and a detailed optical waveguide study was therefore carried out using this particular cut. However, slab waveguide studies of Z-cut $LiNbO_3$ were also performed to compare and contrast optical waveguide

Figure 4.15(a) Photomicrograph Of The Surface Of A Y-Cut PE $LiNbO_3$ Substrate (0.25 Hour, At 180°C, Mag. X 200)

Figure 4.15(b) Photomicrograph Of The Surface Of A Y-Cut PE $LiNbO_3$ Substrate (0.5 Hour, At 180°C, Mag. X 200)

characteristics, such as diffusion coefficients and propagation losses. This made it possible to identify if there were major differences between PE waveguides in X- and Z-cut $LiNbO_3$ so as to use the appropriate cut for a particular device application.

Prior to this, all necessary steps were taken to ensure that the temperature of the molten benzoic acid bath had stabilized at the predetermined temperature of exchange and thus to ensure that the results were valid and repeatable. In general it was found that the measured oil temperature value was about 5°C to 10°C higher than that measured in the benzoic acid beaker. In addition, it was necessary to allow the temperature of the benzoic acid beaker to stabilize to its preset value after the sample(s) and the holder were introduced into it. It was found that for most of the PE experiments an additional time of 10 to 15 minutes needed to be added to all the exchange times. Samples have to be pre-heated in an oven for the fabrication of single-mode PE stripe optical waveguides since relatively short exchange times are required, i.e. in some cases 5-10 minutes. The temperature of the benzoic acid beaker was monitored by a digital thermometer in all the PE waveguide fabrication experiments. (Note: The close monitoring of the temperature of the benzoic acid beaker is one of the most important steps in the successful realisation of repeatable PE passive and active devices in $LiNbO_3$ substrates)

Stainless steel beakers were used to ensure that excellent thermal contact between the benzoic acid and the high temperature oil could be achieved. The volume of the molten benzoic acid in the beaker was large enough to provide an effectively infinite source for PE. The beaker was also covered loosely to reduce the loss of benzoic acid and to provide a stable temperature environment. Generally, the benzoic acid was renewed after ten runs.

The preset exchange temperatures range between 160°C and 220°C. As explained earlier, the total exchange time was the time the sample was in the melt plus 10 minutes or 15 minutes depending on the number of samples in the benzoic acid melt. After the PE process and after the sample had cooled to room temperature, any remaining crystallized benzoic acid was removed using methanol. The samples were then cleaned in trichloroethylene. This was to ensure that any oil deposited during the process of removing the samples from the acid melt would be removed. The samples were then stored in a clean container and the slab waveguides were allowed to relax over a period of a few weeks before any optical waveguide characterization was carried out.

The PE X-cut $LiNbO_3$ process in molten benzoic acid leads to the formation of hydroxyl groups in the crystal lattice. The formation of these hydroxyl groups can be monitored by infrared (IR) spectroscopy in the OH-stretching region. Figure 4.16 shows a typical IR transmission spectrum from a virgin X-cut $LiNbO_3$ sample. It is well known from the literature that this peak is due to residual water in the $LiNbO_3$ crystal and is polarised perpendicular to the crystal axis [4.109]. Figure 4.17 shows the IR spectrum of a PE X-cut $LiNbO_3$ sample treated with benzoic acid at 180°C for two hours. Recent results by Loni et al [4.68-4.70] have confirmed that the lithium concentration (determined by AAS) present in molten benzoic acid after the PE reaction with Z-cut $LiNbO_3$ samples are in satisfactory agreement with estimates of hydrogen concentrations in the PE waveguide layer. Therefore it is very reasonable to monitor the extent of the PE process by monitoring the area under the OH peaks.

The spectra indicate that in the reaction at least two new OH groups are formed, which differ in their hydrogen bonding environment. The spectra of samples treated with benzoic acid show a large peak at 3506 cm^{-1}, polarised perpendicular to the crystal axis and of much greater intensity than the

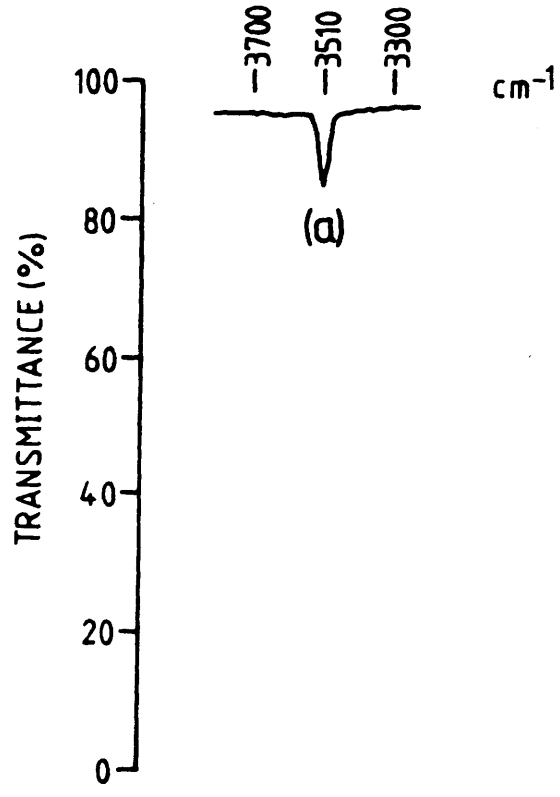

Figure 4.16 **A Typical IR Transmission Spectrum From A Virgin X-Cut $LiNbO_3$ Sample**

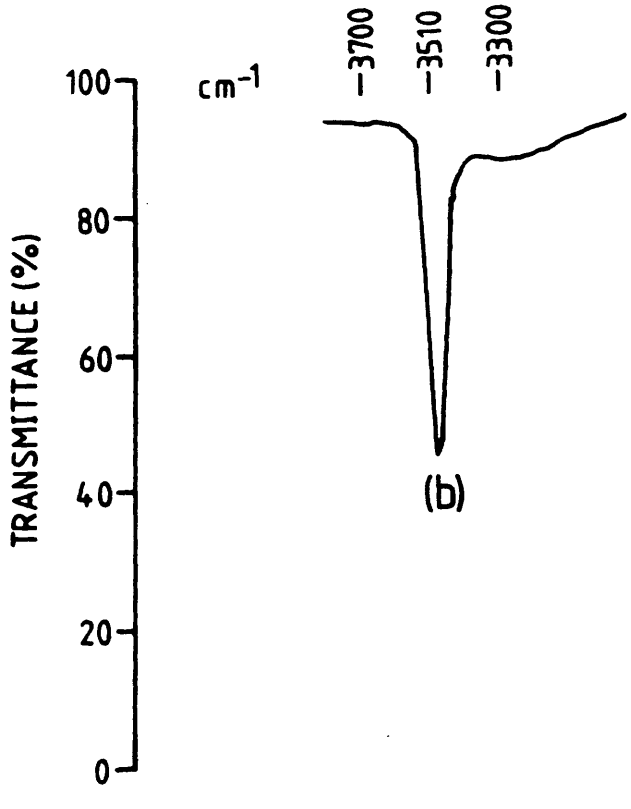

Figure 4.17 **IR Spectrum Of The PE X-Cut $LiNbO_3$ Sample (2 Hours, 180°C)**

original residual OH peak. This peak is asymmetric, and may arise from more than one type of OH group. A second peak, much weaker and broader than the peak at 3506 cm^{-1}, is observed at about 3280 cm^{-1}, and is unpolarised. Its position suggests that it is due to OH groups which participate in extensive hydrogen bonding. The spectra obtained appear to be very similar to those obtained from X-cut $LiNbO_3$ treated with a hydrate melt and nitric acid. In the latter work, the peak was attributed to the formation of a secondary phase, possibly cubic $HNbO_3$ [4.28].

Planar optical waveguides in X-cut $LiNbO_3$ were then formed in molten AnalaR benzoic acid with melt temperatures ranging from 160°C to 210°C and with exchange times ranging from 15 minutes to 7.0 hours. In the case of PE Z-cut $LiNbO_3$, waveguides were fabricated in melt temperatures ranging from 160°C to 220°C, with exchange times varying from 15 minutes to 5.0 hours (Note: The temperature quoted for all PE exchanges is the temperature of the molten benzoic acid melts.). The waveguides were evaluated immediately after they were fabricated to ensure that any changes in the effective refractive index values were noted. Waveguide measurements were carried out over a period of months until there were no detectable variations in the measured effective refractive index values within the range of measurement accuracy. The results of these measurements are presented in Section 5.6 of Chapter 5.

4.3.3.3 Fabrication of PE Slab Optical Waveguides by using Diluted Benzoic Acid Melts

A major reason for using the dilute melt proton-exchange (DMPE) process is to slow the exchange process, but it has also been found to give measurable improvements in the quality of the optical waveguide formed. Improvements such as lower propagation losses, lower in-plane scatter values, better control in realising single-moded stripe optical waveguides

and more reproducible electro-optic devices have been achieved. Results showing these improvements are fully described in Chapters 5 and 6.

Two factors that affect the overall rate of the PE process are:-

(a) The concentration of solvated protons available at the $LiNbO_3$ surface, and

(b) The outdiffusion rate of lithium ions.

In all the DMPE experiments, extra lithium ions were introduced into the protonic source. The diluted solutions used in all the experiments were prepared by mixing AnalaR lithium benzoate with AnalaR benzoic acid , in proportions defined by Equation 4.2.

$$X_d = (\text{Mole of Lithium Benzoate})/(\text{Mole of Benzoic Acid}) * 100\% \qquad (4.2)$$

where X_d was chosen to be either 0.5 or 1.0 for all the DMPE experiments of this thesis. Here, by defination, Mole of X = (Weight of X)/(Molecular Weight of X). The exchange process between the diluted benzoic acid and X- and Z-cut $LiNbO_3$ was carried out mostly at a temperature of 235°C, with some waveguides being fabricated at 245°C. It is noted that the melt dilution just described above involves small percentages of added lithium benzoate which is quite different to the melt dilution for sodium/silver ion exchange process where mostly sodium nitrate is used [4.110].

The mechanism of the DMPE process was monitored using IR spectroscopy. It was established that the exchange process can be monitored by measuring the increase in the formation of hydroxyl groups in the crystal lattice using IR spectroscopy. Figure 4.18(a) illustrates a typical infrared transmission spectrum from a virgin X-cut sample. Both the transmission faces have been optically polished to facilitate the measurements. Again it can be seen that there is residual water in the

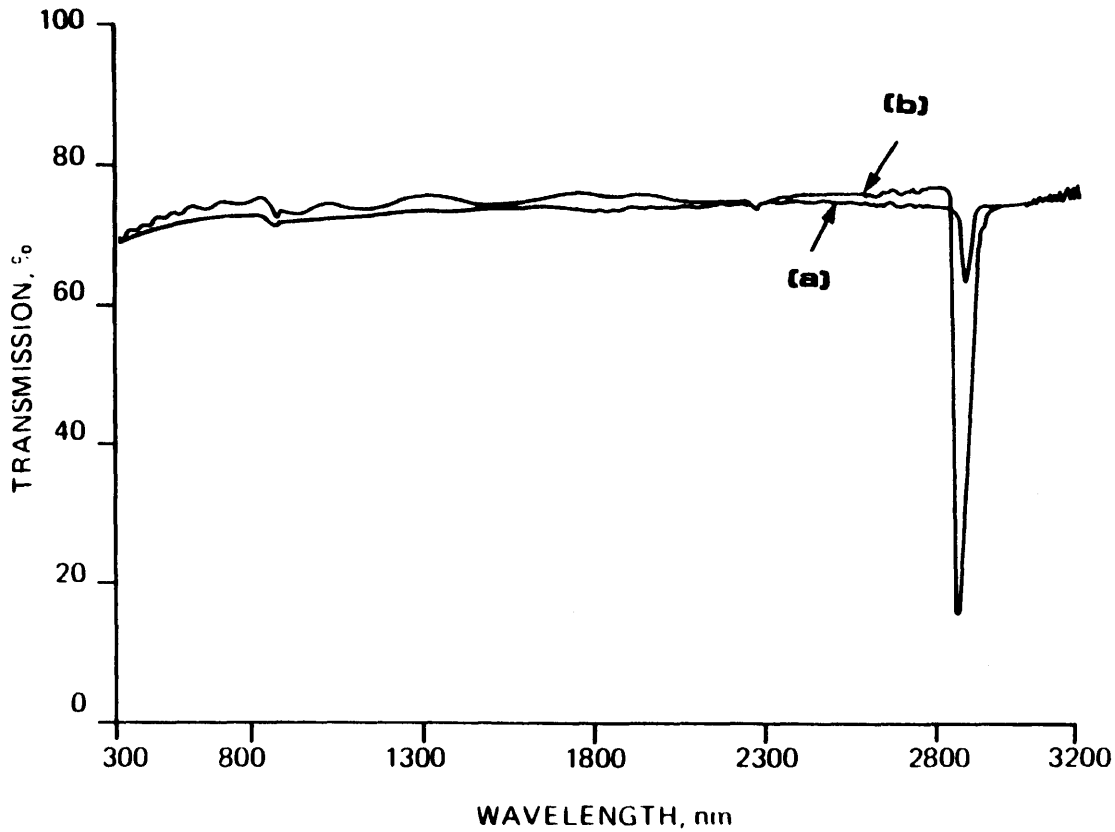

Figure 4.18 (a) A Typical IR Transmission Spectrum For A Virgin X–Cut $LiNbO_3$
(b) IR Spectrum Of The Same Sample But DMPE (1.0%)

crystal. Figure 4.18(b) is the IR spectrum of a dilute melt (1.0%) PE sample on the same piece of X-cut $LiNbO_3$ sample.

4.3.3.4 Realisation of Active PE Devices

The two electro-optic waveguide devices realised for the work of this thesis were phase modulators and Mach-Zehnder Interferometers. Both the phase modulators and the Mach-Zehnder interferometers were fabricated on X-cut $LiNbO_3$ sustrates. The substrate preparation has been described in Section 4.2.3. However, the phase modulator and the Mach-Zehnder interferometer were fabricated by using concentrated benzoic acid and diluted benzoic acid (diluted with lithium benzoate) respectively.

The PE phase modulator were operated as serrodyne optical frequency translators and their performance was then compared with that of Ti:$LiNbO_3$ counterparts and the results of this comparison are described in Chapter 6. On the other hand, the Mach-Zehnder interferometer were used in the study of the electro-optic activity of waveguides formed by DMPE and the results of this study are reported in Chapter 5.

The fabrication of PE electro-optic devices (phase modulator and Mach-Zehnder interferometer) can be divided into the following steps.

(a) Original mask-making:-

The mask set used to realise Ti:$LiNbO_3$ phase modulators was also used to realise PE phase modulators. The Mach-Zehnder interferometer mask set used for this study was generated by GEC Research, Hirst Research Centre [4.111]. In the latter case the devices were designed to operate at 830 nm [4.112].

(b) Substrate preparation:-

The procedure used here is the same as those described in Section 4.2.3.

(c) Diffusion waveguide mask pattern preparation:-

This part of the process is different from that used to realise Ti:$LiNbO_3$ devices. For stripe optical waveguide formation by proton-exchange, a thin layer of aluminium (about 1000 Å to 1500 Å) was deposited on the crystal substrate. Next the waveguide pattern was defined by photolithographic techniques using Shipley AZ1350J. The pattern was checked, and if found to be free of defects, the substrate was then immersed into an aluminium etch (phosphoric acid). After the appropriate etching time (about 5 minutes), the sample with the etched waveguide aluminium pattern was checked. The linewidths of the waveguide pattern were checked against a calibrated graticule under an optical microscope to ensure that they were similar to those found on the original waveguide mask. This is extremely important since, for example one micron in waveguide width variation can have significant effects on the modal properties of the waveguides and the overall performance of active devices (Chapter 6).

(d) PE waveguide formation:-

The next step was to perform proton-exchange on the devices. For the phase modulator, concentrated benzoic acid was used. In the case of the Mach-Zehnder interferometer devices, diluted benzoic acid melts were used (1% dilution). The choice of this dilution was based on the results of the DMPE slab waveguide study. The study indicated that the speed of waveguide formation was slowed to a speed where control of the modal properties of the stripe waveguides was acceptable; typically exchange times of 20 to 45 minutes. In both cases, the aluminium mask acted as an effective diffusion barrier for the proton-exchange process.

(e) Electrode fabrication:-

For the phase modulator, the aluminium masking layer used for waveguide defination could also be used for electrode fabrication. Therefore

it was very crucial that care should be taken in handling the aluminized sample before, during and after the PE-process. The rest of the fabrication procedures for the electrodes were as described in Section 4.2.7.

In the case of the Mach-Zehnder interferometer, the requirement of a SiO_2 buffer layer complicated the electrode formation process. The reason for the need of a buffer layer is to reduce the optical attenuation effect of the metallic electrodes on the optical mode since the gaps of the electrodes were comparable in width to that of the stripe waveguides. Since the proton-exchange stripe waveguides were impossible to see using the microscope of the mask aligner, a special procedure had to be introduced. All the aluminium masking layer was etched off except for the aluminized pattern of a Mach-Zehnder interferometer. This Mach-Zehnder interferometer pattern would provide the necessary alignment reference for the electrode mask pattern. Next an SiO_2 buffer layer of about 2000 Å was deposited using a Pyrox reactor. The SiO_2 is generated as a product from a reaction between silane and oxygen at the surface of a heated susceptor (at 400°C). The sample was then deposited with 1000 to 1500 Å of aluminium. The processing of the electrode from now onwards was similar to that found in Section 4.2.7. Figure 4.19 illustrates a photomicrograph of a section of a PE Mach-Zehnder interferometer. The illustration shows the alignment of the stripe waveguides with respect to the aluminium electrodes.

(f) Device completion:-

The fabricated phase modulator and Mach-Zehnder interferometer samples were then inspected under an optical microscope. The electrode gaps of the devices were measured to ensure that they were of the correct width. After this, the devices were polished (Section 4.2.8) and mounted for optical and electrical evaluation.

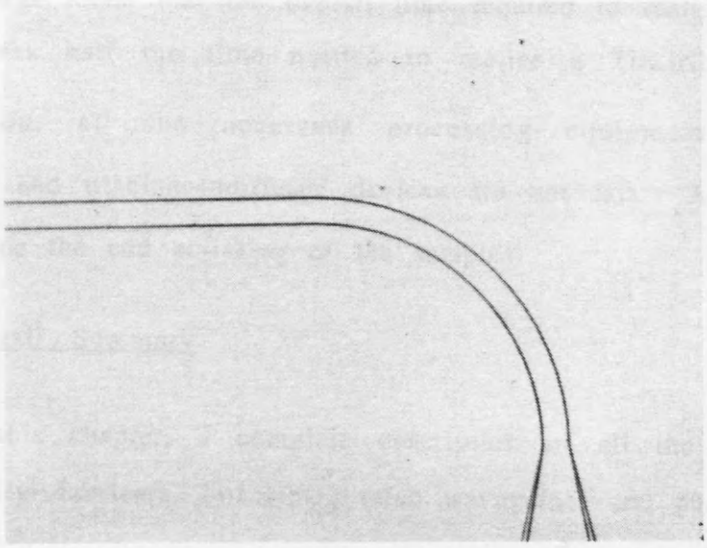

Figure 4.19 **Photomicrograph Of A Section Of A PE Mach-Zehnder Interferometer (In X-Cut $LiNbO_3$)**

4.3.4 Summary - Realisation of Waveguides and Devices in $LiNbO_3$ by the Proton-Exchange Process

Figures 4.20 and 4.21 summarise schematically the complete fabrication procedures of the phase modulator and the Mach-Zehnder interferometer respectively. As usual all the precautions taken in the realisation of a Ti:$LiNbO_3$ phase modulator were adhered to strictly. In addition, care must be taken in realising proton-exchange waveguides and devices since benzoic acid is an irritant on the human respiratory system.

It was found that the overall time required to realise a proton-exchange device was half the time needed to realise a Ti:$LiNbO_3$ device. In the comparison, all the necessary processing equipment for the proton-exchange and titanium-indiffused devices did not fail. Again this time does not include the end polishing of the samples.

4.4 Overall Summary

In this chapter, a complete description of all the necessary steps to successfully fabricate Ti:$LiNbO_3$ (slab waveguides and phase modulators) and proton-exchange devices (slab waveguides, phase modulators and Mach-Zehnder Interferometers) is outlined. The initial $LiNbO_3$ substrate preparation was found to be a critical step in realising high quality $LiNbO_3$ devices. An ultrasonic cleaning procedure involving the use of various heated halogenated and non-halogenated organic solvents was adhered to throughout the project. No major problems were encountered with the Ti:$LiNbO_3$ devices.

An overview of the proton-exchange technique for waveguide formation in $LiNbO_3$ has been given since this is a relatively new waveguide technology when compared to the titanium indiffusion method. A detailed description of the fabrication procedure for proton-exchange waveguides

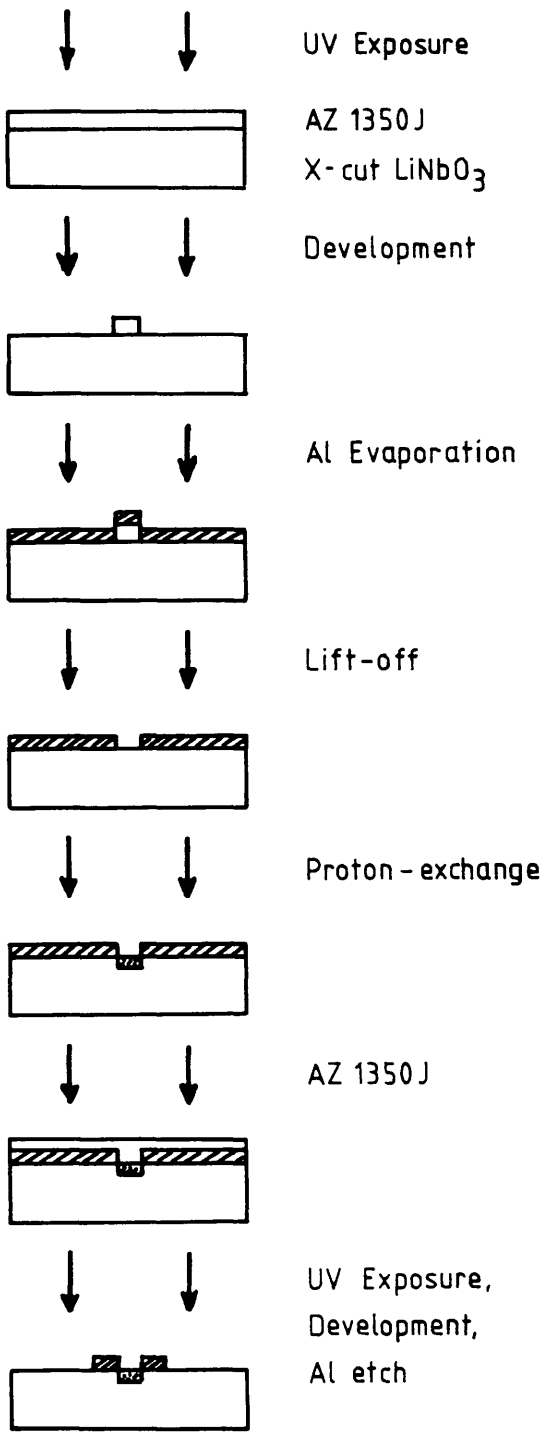

Figure 4.20 **Summary Of The Complete Fabrication Procedure For A PE Integrated Optical Phase Modulator**

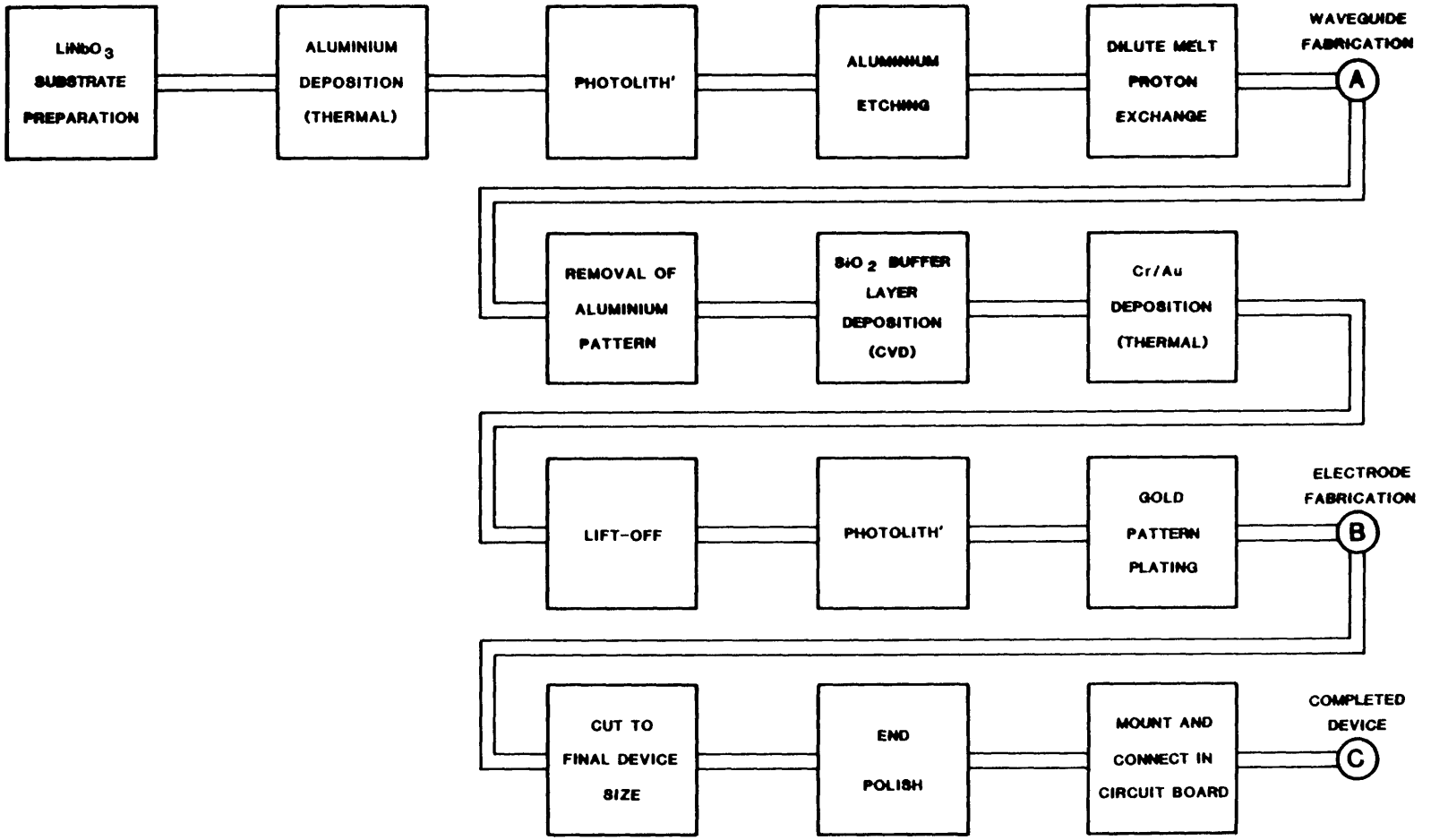

Figure 4.21 Summary Of The Complete Fabrication Procedure For A Dilute Melt Proton Exchanged Mach–Zehnder Interferometer

and devices using concentrated and diluted benzoic acid has been given. One of the important parameters that has to be accurately monitored is the actual exchange time in the proton-exchange process. Failure to do so can result in significant variations in optical properties of waveguides fabricated each time.

A number of problems were identified with waveguides fabricated using concentrated benzoic acid. A solution to some of the problems is to realise waveguides using diluted benzoic acid. The dilutant used in the experiment was lithium benzoate.

All the results of the study of optical waveguides and devices formed by titanium indiffusion, proton-exchange, and dilute melt proton-exchange are presented in Chapters 5 and 6.

Appendix 4.1

Structure and Properties of Lithium Niobate (Concise Summary)

(I) Structure of Lithium Niobate [4.109]

The lithium niobate lattice consists of a linear arrangement of cations, (in the order Li, Nb, Vacancy, Li), in the direction of the crystal axis, each surrounded by an octahedral array of oxygen atoms. The lithium niobate crystal has a three-fold axis of symmetry which places it in the trigonal (rhombohedral) point group 3m, space group R3c.

(II) Scalar Properties [4.109]

Density	4.64 g/cm^3	
Molecular Weight	147.85	
Melting Point	1253°C	
Curie Point	1150°C	
Moh Hardness	5	
Thermal Conductivity	10^{-12} cal/cm.s.°C	
Pyroelectric Coefficient	4 $nC/cm^2/°C$	(@ 300 K)
Resistivity	10^{13} Ω-cm	(@ 24°C)
	5 X 10^8 Ω-cm	(@ 400°C)
	140 Ω-cm	(@ 1200°C)

(III) Variation Of Ordinary And Extraordinary Refractive Indices [4.109]

Researchers have found that many crystal properties are dependent on the stoichiometry and these are shown in Table 4.1. Of those properties affected, the most important for optical waveguide propagation are the change in refractive index and birefringence. Figure 4.22 illustrates the variations of the ordinary and extraordinary refractive indices of $LiNbO_3$ as a function of the Li:Nb mole ratio measured at 633 nm. It can be seen from

	PROPERTY
STRONGLY DEPENDENT	Curie point Birefringence (Relative value) Phase-matching temperature for SHG NMR linewidth
SLIGHTLY DEPENDENT	Lattice parameters Density Dielectric constant Refractive indices EO coefficients NLO coefficients

Table 4.1 **Properties Of Lithium Niobate That Is Dependent On The Li/Nb Ratio**

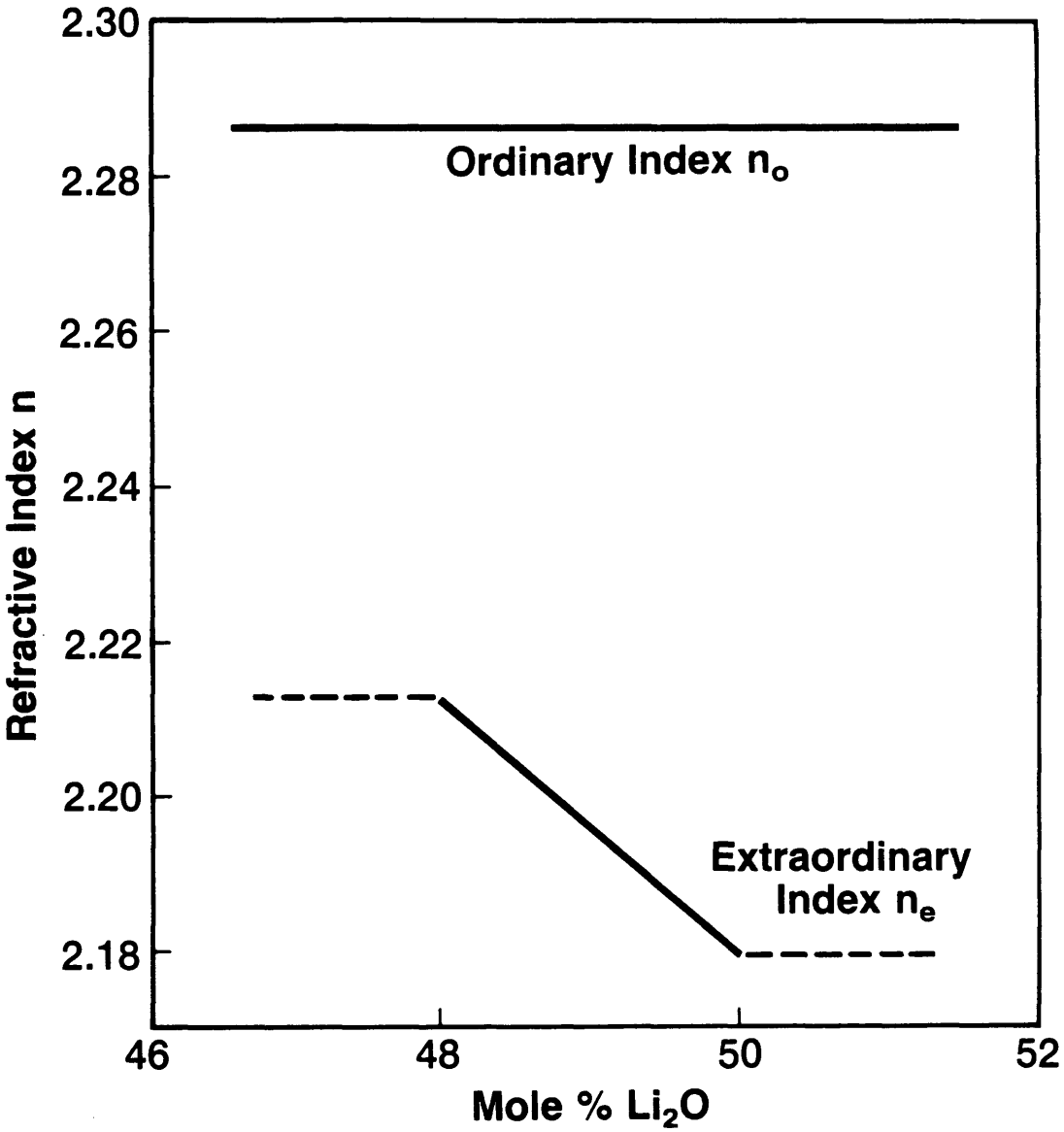

Figure 4.22 Refractive Index As A Function Of Composition (@ 633 nm)

Figure 4.22 that the extraordinary refractive index n_e is strongly dependent on the crystal composition (2.215-2.190) whereas the ordinary refractive index n_0 is not affected.

REFERENCES

[4.1] R.C. Alferness, "Guided-Wave Devices for Optical Communication", IEEE J. Quantum Electron., Vol. QE-17, No. 6, pp 946-959 June 1981.

[4.2] W.S.C. Chang, Chapter 8, "The Effects of Materials Technology and Fabrication Tolerance on Guided-Wave Optical Communication and Signal Processing", in VLSI Electronics: Microstructure Science, Vol. 3, Academic Press, 1982.

[4.3] O.G. Ramer, "Progress on Integrated Optic Waveguide Devices for Fibre Gyro Applications", in S. Ezekiel and H.J. Arditty, Eds. Fibre-Optic Rotation Sensors and Related Technologies, Proc. First International Conf., MIT, Cambridge, MA, USA, pp 124-129, 9-11 November 1981.

[4.4] I.T. Savatinova and S.C. Tonchev, "Electrically Induced Strip Waveguide Modulator", Second European Conf. on Integrated Optics, Florence, Italy, IEE Conf. Pub. No. 227, pp 126-128, 17-18 October 1983.

[4.5] I.P. Kaminow and J.R. Carruthers, "Optical Waveguiding Layers in $LiNbO_3$ and $LiTaO_3$", Appl. Phys. Lett., Vol. 22, No. 7, pp 326-328, 1 April 1973.

[4.6] R.V. Schmidt and I.P. Kaminow, "Metal-Diffused Optical Waveguides in $LiNbO_3$", Appl. Phys. Lett., Vol. 25, No. 8, pp 458-460, 15 October 1974.

[4.7] P.D. Townsend, "Ion Implantation and Integrated Optics", J. Phys. E: Sci. Instrum., Vol. 10, No. 3, pp 197-203, March 1977.

[4.8] J.L. Jackel, C.E. Rice and J.J. Veselka, "Proton-Exchange for High Index Waveguides in $LiNbO_3$", Digest of Topical Meeting on Integrated and Guided-Wave Optics, Pacific Groove, CA, Post-Deadline Paper, PDP1-4 to PDP1-4, 6-8 January 1982.

[4.9] J. Heibei and E. Voges, "Strip Waveguides in $LiNbO_3$ Fabricated by Combined Metal Diffusion and Ion Implantation", IEEE J. Quantum Electron., Vol. QE-18, No. 5, pp 820-825, May 1982.

[4.10] M. De Micheli, J. Botineau, P. Sibillot, D.B. Ostrowsky and M. Papuchon, "Fabrication and Characterisation of Titanium Indiffused Proton-Exchanged (TIPE) Waveguides in Lithium Niobate", Opt. Commun., Vol. 42, No. 2, pp 101-103, 15 June 1982.

[4.11] G. Boyle, Private Communication, University of Glasgow, Department of Electronics and Electrical Engineering, 1983.

[4.12] R.J. Esdaile, "Titanium Doped Lithium Niobate For Electro-Optic Devices", PhD Thesis, University of Glasgow, Department of Electronics and Electrical Engineering, April 1979.

[4.13] A.D. McClachlan, "Theoretical and Experimental Investigations of Titanium Diffused Lithium Niobate Optical Waveguides", PhD Thesis, University of Glasgow, Department of Electronics and Electrical Engineering, January 1981.

[4.14] J. Noda, "Ti-Diffused $LiNbO_3$ Waveguides and Modulators", J. Opt. Commun., Vol. 1, No. 2, pp 64-73, November 1980.

[4.15] T.R. Ranganath and S. Wang, "Ti-Diffused $LiNbO_3$ Branched Waveguide Modulators: Performance and Design", IEEE J. Quantum Electron., Vol. QE-13, No. 4, pp 290-295, April 1977.

[4.16] I. Andonovic, "Optical Waveguide Devices in Lithium Niobate", PhD Thesis, University of Strathclyde, Department of Electrical and Electronic Engineering, December 1982.

[4.17] R.J. Esdaile, "Closed-Tube Control of Outdiffusion During Fabrication of Optical Waveguides in $LiNbO_3$", Appl. Phys. Lett., Vol. 33, No. 8, pp 733-734, 15 October 1978.

[4.18] T.R. Ranganath and S. Wang, "Suppression of Li_2O Outdiffusion from Ti:diffused $LiNbO_3$ Optical Waveguides", Appl. Phys. Lett., Vol. 30, No. 8, pp 376-379, 15 April 1977.

[4.19] B.U. Chen and A.C. Pastor, "Elimination of Li_2O Outdiffusion Waveguide in $LiNbO_3$ and $LiTaO_3$", Appl. Phys. Lett., Vol. 30, No. 11, pp 570-571, 1 July 1977.

[4.20] S. Miyazawa, R. Guglielmi and A. Carenco, "A Simple Technique for Suppressing Li_2O Outdiffusion in Ti:$LiNbO_3$ Optical Waveguide", Appl. Phys. Lett., Vol. 31, No. 11, pp 742-744, 1 December 1977.

[4.21] W.K. Burns, C.H. Bulmer and E.J. West, "Application of Li_2O Compensation Techniques to Ti-Diffused $LiNbO_3$ Planar and Channel Waveguides", Appl. Phys. Lett., Vol. 33, No. 1, pp 70-72, 1 July 1978.

[4.22] J.L. Jackel, V. Ramaswamy and S.P. Lyman, "Elimination of Outdiffused Surface Guiding in Titanium-Diffused $LiNbO_3$", Appl. Phys. Lett., Vol. 38, No. 7, pp 509-511, 1 April 1981.

[4.23] M. Fakuma and J. Noda, "Li In-and-Out-Diffusion Processes in $LiNbO_3$, Jap. J. Appl. Phys., Vol. 20, No. 10, pp 1861-1865, October 1981.

[4.24] J.L. Jackel, "Suppression of Outdiffusion in Titanium Diffused $LiNbO_3$: A Review", J. Opt. Commun., Vol. 3, No. 3, pp 82-85, September 1982.

[4.25] W.K. Burns and G.B. Hocker, "End-Fire Coupling Between Optical Fibres and Diffused Channel Waveguides" Appl. Opt., Vol. 16, No. 8, pp 2048-2050, August 1977.

[4.26] P.K. Tein, R. Ulrich and R.J. Martin, "Modes of Propagating Light Waves in Thin Deposited Semiconductor Films", Appl. Phys. Lett., Vol. 14, No. 9, pp 291-294, 1 May 1969.

[4.27] Mr K. Piechowiak, Private Communication, University of Glasgow, Department of Electronics and Electrical Engineering, 1983.

[4.28] J.L. Jackel and C.E. Rice, "Topotactic $LiNbO_3$ to Cubic Perovskite Structural Transformation in $LiNbO_3$ and $LiTaO_3$", Ferroelectrics, Vol. 38, pp 801-804, 1981.

[4.29] C.E. Rice and J.L. Jackel, "$HNbO_3$ and $HTaO_3$: New Cubic Perovskites Prepared From $LiNbO_3$ and $LiTaO_3$ via Ion Exchange", J. Solid State Chem., Vol. 41, pp 308-314, 1982.

[4.30] J.L. Jackel, C.E. Rice, and J.J. Veselka, "Proton Exchange For High-Index Waveguides in $LiNbO_3$", Appl. Phys. Lett., Vol. 41, No. 7, pp 607-608, 1 October 1982.

[4.31] K.K. Wong, A.C.G. Nutt, D.F. Clark, P.J.R. Laybourn, and R.M. De La Rue, "Characterization of Proton-Exchange Slab Optical Waveguides in X-cut $LiNbO_3$", IEE Proc. Part J, Vol. 133, No.2, pp 113-117, April 1986.

[4.32] M. Goodwin and C. Stewart, "Proton-Exchanged Optical Waveguides in Y-cut Lithium Niobate", Electron. Lett., Vol. 19, No.6, pp 223-225, 17 March 1983.

[4.33] A. Campari, C. Ferrari, G. Mazzi, C. Summonte, S.M. Al-Shukri, A. Dawar, R.M. De La Rue, and A.C.G. Nutt, "Strain and Surface Damage Induced By Proton Exchange in Y-cut $LiNbO_3$", J. Appl. Phys., Vol. 58, No. 12, pp 4521-4524, 15 December 1985.

[4.34] N. Saiga and Y. Ichioka, "Acousto-Optic Interaction in Proton-Exchange 128° Rotated Y-cut $LiNbO_3$ Optical Waveguides", J. Appl. Phys., Vol. 61, No. 3, pp 1230-1233, 1 February 1987.

[4.35] A.C.G. Nutt, K.K. Wong, D.F. Clark, P.J.R. Laybourn, and R.M. De La Rue, "Proton-Exchange Lithium Niobate Slab and Stripe Waveguides: Characterization and Comparisons", Second European Conference on Integrated Optics, Florence, Italy, IEE Conf. Proc. No. 227, pp 53-56, 17-18 October 1983.

[4.36] D.F. Clark, A.C.G. Nutt, K.K. Wong, P.J.R. Laybourn, and R.M. De La Rue, "Characterization of Proton-Exchange Slab Optical Waveguides in Z-cut $LiNbO_3$", J. Appl. Phys., Vol. 54, No.11, pp 6218-6220, November 1983.

[4.37] Yu. L. Kopylov, V.B. Kravchenko, E.N. Mirgorodskaya, and A.V. Bobylev, "Fabrication of Waveguides in Lithium Niobate and Tantalate by Proton Diffusion from a Benzoic Acid Solution", Sov. Tech. Phys. Lett., Vol. 9, No. 5, pp 259-260, May 1983.

[4.38] S.M. Al-Shukri, J.F. Duffy, R.M. De La Rue, G. Mazzi, A. Camera, and M.N. Armenise, "Single-Mode Planar and Stripe Waveguides by Proton Exchange in Lithium Tantalate and Lithium Niobate", SPIE Vol. 651, Integrated Optical Circuit Engineering III, pp20-25, 16-18 April 1986.

[4.39] W.B. Spillman, Jr., N.A. Sanford, and R.A. Soref, "Optical Waveguides in $LiTaO_3$ Formed By Proton Exchange", Opt. Lett., Vol. 8, No. 9, pp497-498, September 1983.

[4.40] K.K. Wong, A.C. O'Donnell, I.A. Wood, and N.J. Parsons, "Integrated Optical Mach-Zehnder Interferometers in $LiTaO_3$ Fabricated By Proton Exchange", Proc. of the Fourth European Conf. on Integrated Optics, Glasgow, Scotland, pp 123-126, 11-13 May 1987.

[4.41] T. Findakly, P. Suchoski, and F. Leonberger, "High-Quality $LiTaO_3$ Integrated-Optical Waveguides and Devices Fabricated by the Annealed-Proton-Exchange Technique", Opt. Lett., Vol. 13, No. 9, pp 797-799, September 1988.

[4.42] T. Findakly, J. Farina, P. Suchoski, and F. Leonberger, "High Optical Power Performance of High-Quality $LiTaO_3$ Integrated Optical Waveguide Devices", Integrated and Guided-Wave Optics, 1989 Technical Digest Series, Vol. 4, Optical Society of America, pp WCC2-1 to WCC2-4, 6-8 February 1989.

[4.43] V.A. Ganshin, Yu. N. Korkishko, and T.V. Morozova, "Properties of Proton Exchanged Optical Waveguiding Layers in $LiNbO_3$ and $LiTaO_3$", Phys. Stat. Sol. (a), Vol. 110, No. 2, pp 397-402, 16 December 1988.

[4.44] K. Tada, T. Murai, T. Nakabayashi, T. Iwashima, and T. Ishikawa, "Fabrication of $LiTa0_3$ Optical Waveguide By H^+ Exchange Method", Jap. J. Appl. Phys., Vol. 26, No. 3, pp 503-504, March 1987.

[4.45] M. De Micheli, J. Botineau, P. Sibillot, D.B. Ostrowsky, and M. Papuchon, "Fabrication and Characterization of Titanium Indiffused Proton Exchanged (TIPE) Waveguides in Lithium Niobate", Opt. Commun., Vol. 42, No. 2, pp 101-103, 15 June 1982.

[4.46] K.K. Wong, "An Experimental Study of Dilute Melt Proton Exchange Waveguides in X- and Z-cut Lithium Niobate", GEC J. Research, Vol. 3, No. 4, pp 243-250, 1985.

[4.47] J.L. Jackel, A.M. Glass, G.E. Peterson, C.E. Rice, D.H. Olson, and J.J. Veselka, "Damage-Resistant $LiNb0_3$ Waveguides", J. Appl. Phys., Vol. 55, No. 1, pp 269-270, 1 January 1984.

[4.48] Y. Fujii and S. Tanikoshi, "Quantitative Measurement of High Resistivity to Optical Damage in Proton-Exchanged $LiNb0_3$ Optical Waveguides", Trans. IECE Japan, Vol. E-69, No. 2, pp 95-96, February 1986.

[4.49] N.J. Parsons, "Integrated Optical Components for Phased Arrays", GEC J. Research, Vol. 2, No. 2, pp 76-81, 1984.

[4.50] M. De Micheli, J. Botineau, S. Neveu, P. Sibillot, D.B. Ostrowsky, and M. Papuchon, "Independent Control of Index and Profiles in Proton-Exchanged Lithium Niobate Guides", Opt. Lett., Vol. 8, No. 2, pp 114-115, February 1983.

[4.51] J.L. Jackel, C.E. Rice, and J.J. Veselka, "Composition Control in Proton-Exchanged $LiNb0_3$", Electron. Lett., Vol. 19, No. 10, pp 387-388, 12 May 1983.

[4.52] K.K. Wong, N.J. Parsons, A.R. Oldroyd, and A.C. O'Donnell, "High Quality Optical Waveguides in $LiNb0_3$ By Dilute Melt Proton-Exchange", IOOC/ECOC'85, Venice, Italy, Vol. 1, pp 59-62, 1-4 October 1985.

[4.53] V. Hinkov and E. Ise, "Control of Birefringence in Ti:$LiNb0_3$ Optical Waveguides by Proton Exchange of Lithium Ions", J. Lightwave Tech., Vol. LT-4, No. 4, pp 444-448, April 1986.

[4.54] A.C.G. Nutt, E. Sudo, and K. Nishizawa, "Control of Ti-Diffused $LiNb0_3$ Waveguide Profile and Propagation Characteristics by The Proton Exchange of Lithium Ions", OFC/IOOC'87, Reno, Nevada, pp 64, 19-22 January 1987.

[4.55] A.L. Dawar, S.M. Al-Shukri, R.M. De La Rue, A.C.G. Nutt, and G. Stewart, "Fabrication and Characterisation of Titanium-Indiffused Proton-Exchanged Optical Waveguides in Y-cut $LiNbO_3$", Appl. Opt., Vol. 25, No. 9, pp 1495-1498, 1 May 1986.

[4.56] A.L. Dawar, S.M. Al-Shukri, R.M. De La Rue, A.C.G. Nutt, and G. Stewart, "Fabrication and Characterisation of Titanium-Indiffused Proton-Exchanged Optical Waveguides in Z-cut $LiNbO_3$", Opt. Commun., Vol. 61, No. 2, pp 100-104, 15 January 1987.

[4.57] K. Yamamoto and T. Taniuchi, "Proton-Exchanged $LiNbO_3$ Waveguides By New Protonic Source", First Optoelectronic Conference (OEC'86) Post-Deadline Papers Technical Digest, Paper B11-4, pp 16-17, July 1986.

[4.58] T. Taniuchi and K. Yamamoto, "Second Harmonic Generation By Cerenkov Radiation in Proton-Exchanged $LiNbO_3$ Optical Waveguide" Conference on Lasers and Electro-Optics, pp 230, 9-13 June 1986.

[4.59] S.M. Al-Shukri, A. Dawar, R.M. De La Rue, A.C.G. Nutt, M.R.S. Taylor, J.R. Tobin, G. Mazzi, A. Camera, and C. Summonte, "Analysis of Annealed Proton-Exchanged Waveguides on Lithium Niobate by Optical Waveguide Measurements and Microanalytical Techniques", Seventh Topical Meeting on Integrated and Guided-Wave Optics, Post-Deadline Papers, pp PD7-1 to PD7-4, 24-26 April 1984.

[4.60] K.K. Wong, "Integrated Optical Waveguides And Devices Fabricated By Proton Exchange: A Review", SPIE Vol. 993, Integrated Optical Circuit Engineering VI, pp 13-25, 1988.

[4.61] A. Dawar, S.M. Al-Shukri, and R.M. De La Rue, "Surface Acoustic Wave-Guides Optical Wave Interaction in Y-cut $LiNbO_3$ Annealed Proton-Exchanged Waveguides", IEEE International Workshop on Integrated Optical and Related Technologies For Signal Processing, 10-11 September 1984.

[4.62] C. Canali, A. Camera, G. Della Mea, R.M. De La Rue, A.C.G. Nutt, and J.R. Tobin, "Proton-Exchanged $LiNbO_3$ Waveguides: Material Analysis and Optical Characteristics", SPIE Vol. 460, Processing of Guided Wave Optoelectronic Materials, pp 49-55, 24-25 January 1984.

[4.63] A. Yi-Yan, J. Primot, J. Burgeat, and R. Guglielmi, "Proton Exchanged $LiNbO_3$ Waveguides : An X-Ray Analysis", Second European Conf. on Integrated Optics, Florence, Post-Deadline Papers, 17-18 October 1983.

[4.64] N.A. Sanford and W.C. Robinson, "Secondary-ion Mass Spectroscopy Characterisation of Proton-Exchanged $LiNbO_3$ Waveguides", Opt. Lett., Vol. 10, No. 4, pp 190-192, April 1985.

[4.65] C. Canali, A. Camera, G. Della Mea, P. Mazzoldi, S.M. Al-Shukri, A.C.G. Nutt, and R.M. De La Rue, "Structural Characterisation of Proton Exchanged $LiNbO_3$ Optical Waveguides", J. Appl. Phys., Vol. 59, No. 8, pp 2643-2649, 15 April 1986.

[4.66] W.E. Lee, N.A. Sanford, and A.H. Heuer, "Direct Observation of Structural Phase Changes in Proton-Exchanged $LiNbO_3$ Waveguides Using

Transmission Electron Microscopy", J. Appl. Phys., Vol. 59, No. 8, pp 2629-2633, 15 April 1986.

[4.67] M. Minakata, K. Kumagai, and S. Kawakami, "Lattice Constant Changes and Electro-Optic Effects in Proton-Exchanged $LiNbO_3$ Optical Waveguides", Appl. Phys. Lett., Vol. 49, No. 16, pp 992-994, 20 October 1986.

[4.68] A. Loni, R.M. De La Rue, and J.M. Winfield, "Proton-Exchanged, Lithium Niobate Planar-Optical Waveguides: Chemical and Optical Properties and Room-Temperature Hydrogen Isotopic Exchange Reactions", J. Appl. Phys., Vol. 61, No.1, pp 64-67, 1 January 1987.

[4.69] R.M. De La Rue, A. Loni, A. Lambert, J.F. Duffy, S.M. Al-Shukri, Y.L. Kopylov, and J.M. Winfield, "(Invited) Proton Exchange in Lithium Niobate and Lithium Tantalate", C.D.W. Wilkinson and J. Lamb (Editors), Proc. of the Fourth European Conference on Integrated Optics ECIO 87, Glasgow, pp 48-53, 11-13 May 1987.

[4.70] A. Loni, R.M. De La Rue, and J.M. Winfield, "Very Low-Loss Proton-Exchanged $LiNbO_3$ Waveguides With a Substantially Restored Electrooptic Effect", Presented in Topical Meeting on Integrated and Guided-Wave Optics, Santa Fe, New Mexico, pp MD3-1 to MD3-4, 28-30 March 1988.

[4.71] A. Loni, R.M. De La Rue, M.A. Foad, and J.M. Winfield, "Determination of the Extent of Reaction in Proton-Exchanged Lithium Niobate Optical Waveguides", Integrated and Guided-Wave Optics, 1989 Technical Digest Series, Vol. 4, Optical Society of America, pp WCC5-1 to WCC5-4, 6-8 February 1989.

[4.72] E.Y.B. Pun, K.K. Wong, I. Andonovic, P.J. R. Laybourn, and R.M. De La Rue, "Efficient Waveguide Bragg-Deflection Grating on $LiNbO_3$", Electron. Lett., Vol. 18, No. 17, pp 740-742, 19 August 1982.

[4.73] C. Warren, S. Forouhar, W.S.C. Chang, and S.K. Yao, "Double Ion Exchanged Chirp Grating Lens in Lithium Niobate Waveguides", Appl. Phys. Lett., Vol. 43, No.5, pp 424-426, 1 September 1983.

[4.74] Z.D. Yu, "Waveguide Optical Planar Lenses in $LiNbO_3$ - Theory and Experiments", Opt. Commun., Vol. 47, No. 4, pp 248-250, 15 September 1983.

[4.75] M. Papuchon and S. Vatoux, "Integrated Optical Polariser on $LiNbO_3$: Ti Channel Waveguides Using Proton Exchange", Electron. Lett., Vol. 19, No. 16, pp 612-613, 4 August 1983.

[4.76] T. Findakly and B. Chen, "Single-Mode Transmission Selective Integrated-Optical Polarisers in $LiNbO_3$", Electron. Lett., Vol. 20, No.3, pp 128-129, 2 February 1984.

[4.77] J.J. Veselka and G.A. Bogert, "Low-Loss TM-pass Polariser Fabricated By Proton Exchange For Z-cut Ti:$LiNbO_3$ Waveguides", Electron. Lett., Vol. 23, No. 1, pp 29-31, 2 January 1987.

[4.78] P.G. Suchoski, T.K. Findakly, and F.J. Leonberger, "Low-Loss High-Extinction Polarizers Fabricated in $LiNbO_3$ By Proton Exchange", Opt. Lett., Vol. 13, No. 2, pp 172-174, February 1988.

[4.79] J.P.G. Bristow, A.C.G. Nutt, and P.J.R. Laybourn, "Novel Integrated Optical Polarisers Using Surface Plasma Waves and Ion Milled Grooves in Lithium Niobate", Electron. Lett., Vol. 20, No. 25/26, pp 1047-1048, 6 December 1984.

[4.80] A. Mahapatra and W.C. Robinson, "Integrated-Optic Ring Resonators Made By Proton Exchange in Lithium Niobate", Appl. Opt., Vol. 24, No. 15, pp 2285-2286, 1 August 1985.

[4.81] A. Mahapatra and W.C. Robinson, "Proton Exchanged Ring Resonators in Lithium Niobate : Operation at 0.79 μm and 1.3 μm", SPIE Vol. 578, Integrated Optical Circuit Engineering II, pp 70-74, 17-19 September 1985.

[4.82] M. Haruna, H. Nakajima, and H. Nishihara, "Optical π-arc Waveguide Interferometer in Proton-Exchanged $LiNbO_3$ for Temperature Sensing", Appl. Opt., Vol. 24, No. 16, pp 2483-2484, 15 August 1985.

[4.83] M. De Micheli, J. Botineau, S. Neveu, P. Sibillot, D.B. Ostrowsky, and M. Papuchon, "Extension of Second-Harmonic Phase-Matching Range in Lithium Niobate Guides", Opt. Lett., Vol. 8, No. 2, pp 116-118, February 1983.

[4.84] S. Neveu, J.P. Barety, M. De Micheli, P. Sibillot, D.B. Ostrowsky, "Phase-Matched SHG Using the d_{33} Coefficient in Proton-Exchanged $LiNbO_3$ Guides", Seventh Topical Meeting on Integrated and Guided-Wave Optics, Post-Deadline Papers, pp PD6-1 to PD6-3, 24-26 April 1984.

[4.85] E.J. Lim, M.M. Fejer, and R.L. Byer, "Second Harmonic Generation of Blue and Green Light in Periodically-Poled Planar Lithium Niobate Waveguides", Topical Meeting on Nonlinear Guided-Wave Phenomena: Physics and Applications, Postdeadline Papers, Optical Society of America, pp PD3-1 to PD3-4, 2-4 February 1989.

[4.86] T.Taniuchi and K. Yamamoto, "Second Harmonic Generation With GaAs Laser Diode in Proton-Exchanged $LiNbO_3$ Waveguides", 12th European Conf. on Optical Commun., Barcelona, Spain, pp 171-174, 22-25 September 1986.

[4.87] G. Arvidsson, F. Laurell, B. Jaskorzynska, J. Webjorn, A. Loni, R.W. Keys, and R.M. De La Rue, "Influence of Annealing on the Conversion Efficiency for SHG by Cerenkov Radiation from Proton-Exchanged $LiNbO_3$ Waveguides", Topical Meeting on Nonlinear Guided-Wave Phenomena: Physics and Applications, 1989 Technical Digest Series, Vol. 2, Optical Society of America, pp THA3-1 to THA3-4, 2-4 February 1989.

[4.88] K.K. Wong, R.M. De La Rue, and S. Wright, "Electro-Optic-Waveguide Frequency Translator in $LiNbO_3$ Fabricated By Proton Exchange", Opt. Lett., Vol. 7, No.11, pp 546-548, November 1982.

[4.89] K.K. Wong and R.M. De La Rue, "An Improved Electro-Optic Waveguide Serrodyne Frequency Translator in X-cut $LiNbO_3$ Using Proton-Exchange", First International Conf. on Optical Fibre Sensors, London, IEE Conf., Proc. No. 221, pp 72-74, 26-28 April 1983.

[4.90] R.A. Becker, "Comparison of Guided-Wave Interferometric Modulators Fabricated on $LiNbO_3$ via Ti Indiffusion and Proton Exchange", Appl. Phys. Lett., Vol. 43, No.2, pp 131-133, 15 July 1983.

[4.91] K.K. Wong, "An Experimental Study of Dilute Melt Proton Exchange Waveguides in X- and Z-cut Lithium Niobate", GEC J. Research, Vol. 3, No. 4, pp 243-250, 1985.

[4.92] R. Chen and C.S. Tsai, "Thermally Annealed Single-Mode Proton-Exchanged Channel-Waveguide Cutoff Modulator", Opt. Lett., Vol. 11, No. 8, pp 546-548, August 1986.

[4.93] M. Minakata, K. Kumagai, and S. Kawakami, "Lattice Constant Changes and Electro-Optic Effects in Proton-Exchanged $LiNbO_3$ Optical Waveguides", Appl. Phys. Lett., Vol. 49, No. 16, pp 992-994, 20 October 1986.

[4.94] E.M. Korablev, Y. L. Kopylov, and V.V. Proklov, "Acousto-Optic Investigations of Proton-Exchanged Waveguides in $LiNbO_3$" IEEE International Workshop on Integrated Optical and Related Technologies For Signal Processing, 10-11 September 1984.

[4.95] R.L. Davis, "Acousto-Optic Bragg Diffraction in Proton Exchanged Waveguides", SPIE Vol. 517, Integrated Optical Circuit Engineering I, pp 74-81, 23-25 October 1984.

[4.96] A. Dawar, R.M. De La Rue, G.F. Doughty, N. Finlayson, S.M. Al-Shukri, and J. Singh, "Acouto-Optic Techniques in Integrated Optics", SPIE Vol. 517, Integrated Optical Circuit Engineering I, pp 64-73, 23-25 October 1984.

[4.97] V. Hinkov and E. Ise, "Surface Acoustic Waves Velocity Perturbation in $LiNbO_3$ by Proton Exchange", J. Phys. D : Appl. Phys., Vol. 18, pp L31-L34, 1985.

[4.98] V. Hinkov, E. Ise, and W. Sohler, "Low Frequency Collinear Acoustooptic TM_0-TE_0 Mode Conversion and Single Sideband Modulation in Proton-Exchanged $LiNbO_3$ Optical Waveguides", Proc. of The Third European Conf. on Integrated Optics, pp 169-173, 6-8 May 1985.

[4.99] M. Miyawaki and S. Ogura, "Efficient, Damage Resistant $LiNbO_3$ Acousto-Optic Waveguide Deflector", Appl. Phys. Lett., Vol. 47, No. 9, pp 918-920, 1 November 1985.

[4.100] A.L. Dawar, S.M. Al-Shukri, and R.M. De La Rue, "Guided-Wave Acousto-Optic Interaction in Proton-Exchanged Y-cut $LiNbO_3$", Appl. Phys. Lett., Vol. 48, No. 23, pp 1579-1581, 9 June 1986.

[4.101] C.S. Tsai, D.Y. Zang, and P. Le, "Acousto-Optic Bragg Diffraction in a $LiNbO_3$ Channel-Planar Composite Waveguide With Application to Optical Computing", Appl. Phys. Lett., Vol. 47, No. 6, pp 549-551, 15 September 1985.

[4.102] F.S. Hickernell, K.D. Ruehle, S.J. Joseph, G.M. Reese, and J.F. Weller, "The Surface Acoustic Wave Properties of Proton Exchanged YZ Lithium Niobate", IEEE Ultrasonics Symposium, pp 237-240, 1985.

[4.103] V. Hinkov, R. Optiz, and W. Sohler, "Ti:$H_xLi_{1-x}NbO_3$ Combined Optical and Acoustic Strip Waveguides For Efficient Collinear Acoustooptic Interactions", Proc. of the Fourth European Conf. on Integrated Optics, Glasgow, Scotland, pp 111-114, 11-13 May 1987.

[4.104] N. Saiga and Y. Ichioka, "Acousto-Optic Interaction in Proton-Exchange 128° Rotated Y-cut $LiNbO_3$ Optical Waveguides", J. Appl. Phys., Vol. 61, No. 3, pp 1230-1233, 1 February 1987.

[4.105] P.J. Burnett, G.A.D. Briggs, S.M. Al-Shukri, J.F. Duffy, and R.M. De La Rue, "Acoustic Properties of Proton-Exchanged $LiNbO_3$ Studied Using The Acoustic Microscopy V(Z) Technique", J. Appl. Phys., Vol. 60, No. 7, pp 2517-2522, 1 October 1986.

[4.106] A. Yi-Yan, "Index Instabilities in Proton-Exchanged $LiNbO_3$ Waveguides", Appl. Phys. Lett., Vol. 42, No. 8, pp 633-635, 15 April 1983.

[4.107] J.L. Jackel and C.E. Rice, "Short- and Long-Term Stability in Proton Exchanged Lithium Niobate Waveguides", SPIE Vol. 460, Processing of Guided Wave Optoelectronic Materials, pp 43-48, 24-25 January 1984.

[4.108] Data on Benzoic Acid, pp 1275-1276, Martindale-The Extra Pharmacopoeia, Twenty-Seventh Edition, The Pharmaceutical Press, London, 1979.

[4.109] A. Rauber, "Chemistry and Physics of Lithium Niobate", in E. Kaldis (Ed.), Current Topics In Material Science, Vol. 1, pp 495, 1978.

[4.110] G. Stewart and P.J.R. Laybourn, "Fabrication Of Ion-Exchanged Optical Waveguides From Dilute Silver Nitrate Melts", IEEE J. Quantum Electron., Vol. QE-14, No. 12, pp 930-934, December 1978.

[4.111] A. Magon, Private Communication, GEC Research, Hirst Research Centre, EBMF Group, 1984-1987.

[4.112] N.J. Parsons, Private Communication, GEC Research, Marconi Research Centre, Integrated Optics Group, 1985.

CHAPTER 5 THEORETICAL ANALYSIS AND EXPERIMENTAL EVALUATION OF SLAB AND STRIPE OPTICAL WAVEGUIDES WITH STUDIES OF ELECTRO-OPTIC ACTIVITY

5.1 Introduction 142

5.2 Theory of Planar Dielectric Optical Waveguides 143

5.2.1 Introduction 143
5.2.2 Step Index Waveguides 143
5.2.2.1 Ray Optics Treatment of Optical Waveguides 143
5.2.2.2 Electromagnetic Theory Treatment of Optical Waveguides 146
5.2.2.3 Comments on Step Index Waveguide Analysis 147
5.2.3 Treatment of Normalised Waveguide Dispersion Equations by Kolgenik and Ramaswamy 148
5.2.4 The IWKB Method of Waveguide Refractive Index Profile Determination 150

5.3 Theory of Stripe (Two Dimensional) Dielectric Optical Waveguides 153

5.3.1 Introduction 153
5.3.2 Summary of Published Analyses used in this Thesis 153
5.3.3 Marcatili's Analytical Solution 154
5.3.4 The Knox and Toulios Solution (Effective Index Method) 156

5.4 Techniques for Studying Slab and Stripe Optical Waveguide 158

5.4.1 Introduction 158
5.4.2 The Prism Coupler Technique 159
5.4.3 The End-Fire Coupling Technique 163

5.5 Ti:$LiNbO_3$ Slab Waveguide Measurements 164

5.6 Measurements on Slab Waveguides Formed by Proton-Exchange using Concentrated Benzoic Acid Melts 166

5.6.1 Measurement at λ= 632.8 nm (for X- and Z-cut Waveguides) 166
5.6.2 Measurement at λ= 1150 nm (for X-cut Waveguides) 169
5.6.3 Propagation Loss Measurements 169
5.6.3.1 Introduction 169
5.6.3.2 Intermodal Scattering 171
5.6.3.3 Out-of-Plane Scattering 172

5.6.3.4 In-Plane Scattering 174

5.7 Measurements on Slab Waveguides Formed by Proton-Exchange using Diluted Benzoic Acid Melts 175

5.7.1 Waveguide Refractive Index Measurements 175
5.7.2 Waveguide Stability Study 177
5.7.3 Propagation Loss Measurements 177
5.7.4 Optical Damage Effects 178
5.7.5 Annealing Experiments 179
5.7.6 In-Plane and Intermodal Scattering Measurements 179
5.7.7 Electro-Optic Activity Study using Mach-Zehnder Interferometers 180

5.8 Summary 182

References 185

CHAPTER 5

THEORETICAL ANALYSIS AND EXPERIMENTAL EVALUATION OF SLAB AND STRIPE OPTICAL WAVEGUIDES WITH STUDIES OF ELECTRO-OPTIC ACTIVITY

5.1 Introduction

The experimental results of the optical characterization of slab PE (concentrated and diluted) waveguides in X- and Z-cut $LiNbO_3$ are presented and in addition measurements of the effective refractive index (n_{eff}) values of Y-cut Ti:$LiNbO_3$ slab waveguide samples used as controls are also presented. The theoretical analysis of the slab PE waveguides was based the methods given by Kogelnik and Ramaswamy [5.1] and the IWKB technique [5.2, 5.3]. The two methods are described in Section 5.2.

However, to realise the full potential of integrated optics technology, stripe (2-Dimensional) optical waveguides are required. The theoretical analysis of the stripe waveguides is based on the approaches of Marcatili [5.4] and Knox and Toulios [5.5] {commonly known as the Effective Index Technique (EIT)} and results from these studies were used to design and realise single-mode PE stripe waveguides.

The prism-coupling technique [5.6, 5.7, 5.8] was used to measure the modal properties of the slab PE waveguides. The propagation loss (or out-of-plane scattering) and the in-plane scattering of the slab waveguides were measured using a vidicon camera system and a scanning photodetector unit respectively, while the stripe waveguides were evaluated by the use of an end-fire coupling setup [5.9, 5.10]. Descriptions of the prism-coupling and the end-fire coupling techniques are given in Section 5.4.

5.2 Theory of Planar Dielectric Optical Waveguides

5.2.1 Introduction

The theory of the propagation of light in planar optical waveguides is of fundamental importance in the understanding of slab PE optical waveguides in X- and Z-cut $LiNbO_3$. There are two well established techniques in the evaluation of planar optical waveguides. The first technique to be described is the ray-optics approach [5.11] and the second method involves a solution using only Maxwell's equations [5.12, 5.13, 5.14]. Although most of the important features of planar optical waveguides can be understood using the ray-optics approach, Maxwell's equations must be used in situations where information such as modal field energy and power flow are needed.

Figure 5.1 illustrates a typical step-index planar optical waveguide structure. The step-index model was found convenient for description of properties of experimental proton-exchange waveguides (to quite a good approximation). The waveguide consists of a single waveguiding layer of thickness h and refractive index n_f. It is bounded by a substrate and waveguide media of refractive indices n_s and n_g respectively. All the waveguide media are assumed to be homogeneous. It is convenient and sufficient for present purposes to derive the waveguide characteristic equations using a ray-optics approach.

5.2.2 Step Index Waveguides

5.2.2.1 Ray Optics Treatment of Optical Waveguides

To develop an understanding of waveguide phenomena, it is convenient to start with a ray optics point of view and consider a waveguide mode to consist of a ray of light trapped within the slab waveguide by total

internal reflection (TIR), as illustrated by Figure 5.2. For TIR to occur at the waveguide-substrate and waveguide-superstrate interfaces, Snell's Law requires that the refractive index of the waveguide n_g must be larger than those of the substrate and the cover i.e. $n_s < n_g > n_c$. Also the angle θ_1 shown in Figure 5.2 must exceed the critical angle at each interface. Therefore, the allowed values of θ_1 must satisfy the relationship:

$$n_s/n_g \leq \sin\ \theta_1 \geq n_c/n_g \tag{5.1}$$

The condition $\sin\ \theta_1 \geq n_s/n_g$ applies to the slab optical waveguides studied in this thesis.

When the light has undergone TIR, the phase-change on reflection for infinite beam is counterpart of Goos-Hanchen shift for finite-beamwidth [5.15], as illustrated in Figure 5.3. Let Φ_{gs} and Φ_{gc} be the phase changes on reflection at the waveguide-substrate and waveguide-superstrate interfaces respectively. From [5.11] the phase changes on reflection are:

$$\Phi_{gs} = \tan^{-1} \{ \sqrt{[(n_g)^2\sin^2\theta_1 - (n_s)^2]}/(n_g \cos\ \theta_1) \} \tag{5.2}$$

$$\Phi_{gc} = \tan^{-1} \{ \sqrt{[(n_g)^2\sin^2\theta_1 - (n_c)^2]}/(n_g \cos\ \theta_1) \} \tag{5.3}$$

for TE modes, and

$$\Phi_{gs} = \tan^{-1} \{ (n_g)^2\sqrt{[(n_g)^2\sin^2\theta_1 - (n_s)^2]}/[(n_s)^2(n_g \cos\ \theta_1)] \} \tag{5.4}$$

$$\Phi_{gc} = \tan^{-1} \{ (n_g)^2\sqrt{[(n_g)^2\sin^2\theta_1 - (n_c)^2]}/[(n_c)^2(n_g \cos\ \theta_1)] \} \tag{5.5}$$

for TM modes.

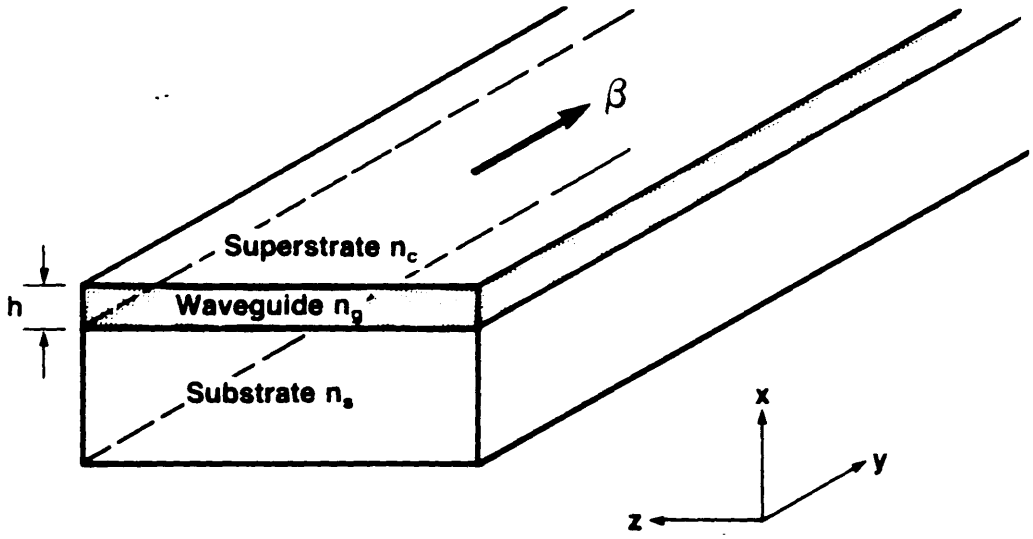

Figure 5.1 A Typical Step-Index Planar Optical Waveguide

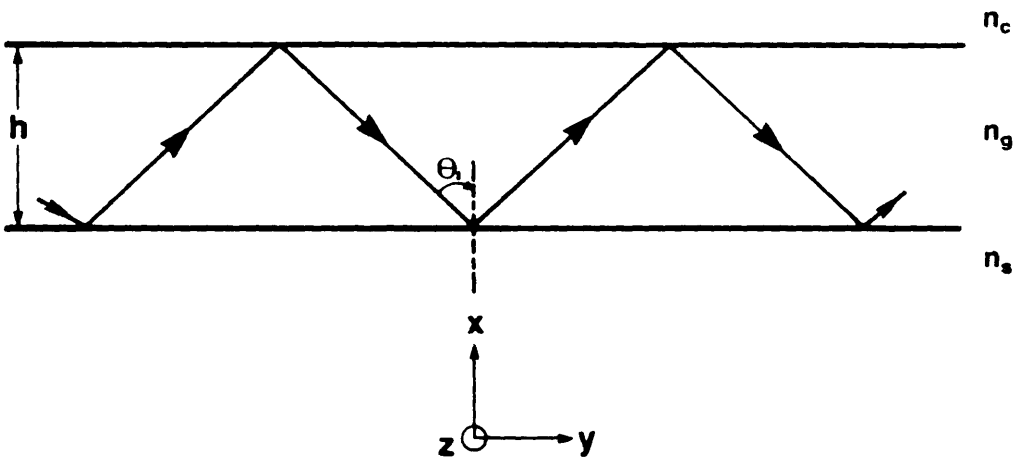

Figure 5.2 Schematic Showing A Ray Of Light Trapped Within The Slab Waveguide By TIR

The propagation constant β is defined as,

$$\beta = k_o n_g \sin\theta_1 \qquad (5.6)$$

and the phase velocity V as,

$$V = C\,(k_o/\beta) \qquad (5.7)$$

where $k_o = 2\pi/\lambda_o$ is the wave number.

For the guided-wave modes to interfere constructively, the total phase-change for one round trip within the slab waveguide must be an integral multiple of 2π. The above condition yields the equation,

$$2\,k_o n_g h\cos\theta_1 - 2\phi_{gc} - 2\phi_{gs} = 2\,M\pi \qquad (5.8)$$

where M is an integer = 0, 1, 2, 3, ..., known as the mode number. It is also convenient to use an "effective refractive index" defined as:

$$n_{eff} = \beta/k_o = n_g \sin\theta_1$$

which is bounded by

$$n_s < n_{eff} < n_g$$

Therefore, using Equations (5.2 and 5.3), Equation 5.8 can be rewritten as:

$$k_o h\sqrt{[(n_g)^2-(n_{eff})^2]} = M\pi + \tan^{-1}\{\sqrt{[(n_{eff})^2-(n_s)^2]}/\sqrt{[(n_g)^2-(n_{eff})^2]}\} + \tan^{-1}\{\sqrt{[(n_{eff})^2-(n_c)^2]}/\sqrt{[(n_g)^2-(n_{eff})^2]}\} \qquad (5.9)$$

for TE modes, and using Equations (5.4 and 5.5), Equation 5.8 can be rewritten as:

$$k_o h\sqrt{[(n_g)^2-(n_{eff})^2]} = M\pi + \tan^{-1}[(n_g)^2/(n_s)^2]\{\sqrt{[(n_{eff})^2-(n_s)^2]}/\sqrt{[(n_g)^2-(n_{eff})^2]}\} + \tan^{-1}[(n_g)^2/(n_c)^2]\{\sqrt{[(n_{eff})^2-(n_c)^2]}/\sqrt{[(n_g)^2-(n_{eff})^2]}\} \quad (5.10)$$

for TM modes.

Equations (5.9) and (5.10) are the characteristic optical waveguide equations used to determine β for the homogeneous planar waveguide system illustrated in Figure 5.1. However, neither of the above two equations can be solved directly to yield β. Accurate specific solutions of β can be easily obtained by numerical interpolation using a mainframe computer system or a personal computer.

5.2.2.2 Electromagnetic Theory Treatment of Optical Waveguides

Alternatively, electromagnetic field theory can be employed to derive Equations (5.9) and (5.10). For non-magnetic, isotropic, homogeneous, charge free media, Maxwell's equations can be expressed as the following:

$$\underline{\nabla} \times \underline{E} = -\mu_o(\partial \underline{H}/\partial t) \quad (5.11)$$

$$\underline{\nabla} \times \underline{H} = \varepsilon_o n^2(\partial \underline{E}/\partial t) \quad (5.12)$$

$$\underline{\nabla} \bullet \underline{E} = 0 \quad (5.13)$$

$$\underline{\nabla} \bullet \underline{H} = 0 \quad (5.14)$$

and yield the following wave equations:

$$\underline{\nabla}^2 \underline{E} = \mu_0 \varepsilon_0 n^2(\partial^2 \underline{E}/\partial t^2) \quad (5.15)$$

$$\nabla^2 \underline{H} = \mu_0 \varepsilon_0 n^2 (\partial^2 \underline{H} / \partial t^2) \qquad (5.16)$$

for the coordinate system shown in Figure 5.1. By formulating suitable time-harmonic solutions in each region and by using the appropriate boundary conditions to Equations (5.15) and (5.16), the characteristic optical waveguide Equations (5.9) and (5.10) can be derived. In these considerations, the TE solutions have field components E_y, H_x and H_z, while the TM solution have field components H_y, E_x and E_z.

5.2.2.3 Comments on Step Index Waveguide Analysis

For each of the exterior regions there exists a field that decays exponentially with distance. This field is called the evanescent field. The proportion of the modal optical energy carried in this evanescent field is very much dependent on the refractive index difference between the waveguide and its substrate and air and the waveguide thickness. It is important to ensure, when designing optical waveguides for active electro-optical devices, that the power in the evanescent field is relatively small because the optical device can experience high optical losses at the metallic boundaries associated with electrodes.

Finally, from Equations (5.9) and (5.10) it is possible to derive the cut-off condition (i.e. the minimum thickness of a waveguide formed from a given combination of refractive indices that will support a guided mode) for the waveguide system illustrated in Figure 5.1. This happens when $n_{eff} = n_c$ or n_s . In all the waveguides reported in this thesis, $n_c = 1$ and n_s is either the extraordinary or the ordinary refractive index of $LiNbO_3$. Therefore, when $n_{eff} = n_s$, the cut-off thickness of TE modes is obtained from:

$$h_{cut\text{-}off} = \{M\pi + \tan^{-1}[\sqrt{\{(n_s)^2-(n_c)^2\}}/\sqrt{\{(n_g)^2-(n_s)^2\}}]/[k_0\sqrt{\{(n_g)^2-(n_s)^2\}}] \quad (5.17)$$

and the cut-off thickness of TM modes is obtained from:

$$h_{cut\text{-}off} = \{M\pi + \tan^{-1}[(n_g)^2\sqrt{\{(n_s)^2-(n_c)^2\}}/(n_c)^2\sqrt{\{(n_g)^2-(n_s)^2\}}]/ [k_0\sqrt{\{(n_g)^2-(n_s)^2\}}] \quad (5.18)$$

In these situations, the evanescent fields penetrate deeper into the substrate.

On the other hand, as the optical waveguide thickness increases at a fixed wavelength, the number of guided modes supported will increase. This implies that the n_{eff} value will approach that of n_g. For this other extreme condition, the power carried by the evanescent fields is minimal and most of the optical power is carried by the waveguide.

From the above, it is always desirable to fabricate optical waveguides (slab or stripe) away from the cut-off but not multimoded since all phase modulators used in the experiments reported in this thesis must support a single guided optical mode for efficient device operation.

5.2.3 Treatment of Normalised Waveguide Dispersion Equations by Kogelnik and Ramaswamy

Kogelnik and Ramaswamy [5.1] have shown that by introducing a set of three normalised variables V, b, and **a** to describe a step-index, single layer, dielectric optical waveguide, the guided modes of any step-index, single layer optical waveguide can be determined from the universal curves generated from Equations (5.9) and (5.10). The parameters V, b, and **a** are the normalised waveguide thickness, normalised effective mode index, and the

asymmetry parameter of the waveguide and its surrounding media respectively. The equations defining the three normalised parameters are:

$$V = \{2\pi h\sqrt{[(n_g)^2-(n_s)^2]}\}/\lambda_0, \tag{5.19}$$

$$b = [(n_{eff})^2-(n_s)^2]/[(n_g)^2-(n_s)^2], \text{ and} \tag{5.20}$$

$$a_{TE} = [(n_s)^2-(n_c)^2]/[(n_g)^2-(n_s)^2] \tag{5.20}$$

for TE modes, or

$$a_{TM} = [(n_g/n_c)^4][(n_s)^2-(n_c)^2]/[(n_g)^2-(n_s)^2]$$

for TM modes. (5.21)

Therefore the characteristic optical waveguide Equations (5.9) and (5.10) can be written as:

$$V\sqrt{(1-b)} = M\pi + \tan^{-1}\sqrt{[b/(1-b)]} + \tan^{-1}\sqrt{[(a_{TE}+b)/(1-b)]} \tag{5.22a}$$

$$V\sqrt{(1-b)} = M\pi + \tan^{-1}\sqrt{[b/(1-b)]} + \tan^{-1}\sqrt{[(a_{TM}+b)/(1-b)]} \tag{5.22b}$$

A computer program based on the above technique was used to find the waveguide thicknesses and refractive indices (n_g) in the PE slab waveguide work. In this program the inputs to the computer program were the measured mode effective indices. By knowing the number of modes which the PE waveguide supported, an appropriately restricted range of values for V was determined. Within this range a computer scan was carried out to obtain an estimate of n_g for each mode, given an initial estimate of the asymmetry parameter a_{TE} or a_{TM}. With the initial choice of V, b values were

obtained from the theoretical plots. Together with the knowledge of the various n_{eff} from the prism-coupling measurements, sets of estimated n_g values could then be obtained. V was then adjusted (and also the set of b values) until the standard deviation over a set of n_g values was small (i.e. 10^{-4} for PE waveguides that supported several modes). The value for the asymmetry parameter **a** was also adjusted at the same time. Once an estimate of n_g was obtained with its corresponding value of V, the depth of the optical waveguide h could be calculated using Equation 5.19. This program was used exclusively in analysing data from the work on concentrated PE waveguides realised in Z-cut $LiNbO_3$.

5.2.4 The IWKB Method of Waveguide Refractive Index Profile Determination

Many researchers have described the calculation of the modal indices of an optical waveguide with a given refractive index profile [5.16, 5.17, 5.18] using the WKB approximation [5.19]. White and Heidrich [5.2] first described in detail a technique whereby, for a given set of measured modal indices n_m, with m=1, 2, 3, ...M, the refractive index profile n(x) could be obtained, where x is the direction perpendicular to the surfaces of the planar optical waveguides. This technique of slab waveguide analysis has become known as the inverse WKB (IWKB) method. It should be noted that a continuous function for n(x) cannot be predicted exactly since the amount of information from the prism-coupling measurements is finite. Instead, certain functions such as step, Gaussian, exponential or complementary error maybe used to give a 'best-fit' to the individual calculated points. The IWKB technique for waveguide mode analysis is, therefore, more accurate for optical waveguides with many modes. This method was used to analyse planar waveguides formed in $LiNbO_3$ by both the concentrated and dilute melt proton exchange techniques.

According to the IWKB method, n(x) appears in the form of a piecewise linear function given by:

$$n(x) = n_k + [(n_{k-1}-n_k)(x_k-x)/(x_k-x_{k-1})] \qquad (5.23)$$

for $x_{k-1} < x \leq x_k$, where x_k denotes the turning points of the waveguide modes with effective refractive index n_k. Having substituted (5.23) into the waveguide characteristic equation:

$$k_0 \int_0^{x_m} \sqrt{[n^2(x)-(n_m)^2]}\, dx = \pi(m-3/4) + \tan^{-1} \varphi\sqrt{\{[(n_m)^2-1]/[(n_g)^2-(n_m)^2]\}} \qquad (5.24)$$

where

m=1, 2, 3, ..., M (M is the number of guided modes in the waveguide being evaluated),

k_0 is the light wave number in vacuum,

n_g is the surface refractive index of the waveguide being evaluated,

$\varphi = 1$ for TE modes or $\varphi = (n_g)^2$ for TM modes, and

x_m are the turning points of the measured modes defined by the equation, $n(x_m) = n_m$,

the following recurrent equation for x_m was obtained:

$$x_m = x_{m-1} + (3\lambda_0/4\pi)\ [(n_{m-1}+3n_m)(n_{m-1}-n_m)/2]^{-1/2} * \{\pi(m-3/4) + \tan^{-1} \varphi \sqrt{\{[(n_m)^2-1]/[(n_g)^2-(n_m)^2]\}}\} - 4\pi/3\lambda_0 \sum_{k=1}^{m-1} [(n_{k-1} + n_k)/2 + n_m]^{1/2}\ [(x_k-x_{k-1})/(n_{k-1}-n_k)]$$

$$* \; [(n_{k-1}-n_k)^{3/2} - (n_k-n_m)^{3/2}]\}, \text{ and}$$

$$x_1 = (3\lambda_0/4\pi) \; [(n_g+3n_1)(n_g-n_1)/2]^{-1/2}$$

$$* \left\{ \pi/4 + \tan^{-1} \varphi \sqrt{\{[(n_1)^2-1]/[(n_g)^2-(n_1)^2]\}} \right\} \qquad (5.25)$$

for m = 2, 3, ..., M, where λ_0 is the wavelength of light in vacuum.

In order to calculate the first turning point x_1, the value of n_g has to be determined. This was achieved by making use of the fact that changes in the value of n_g cause significant changes in the refractive index profile curvature n(x). To evaluate the curvature in this case, the field sum of triangles with the following vertices were used:

$$(x_k, n_k), (x_{k+1}, n_{k+1}), \text{ and } (x_{k+2}, n_{k+2}),$$

where k = 0, 1, 2, ..., M-2. Computations were carried out to obtain a value of n_g for which the field sum would assume the least possible value.

Using Equation 5.25, the turning points x_m of the TE and TM modes were evaluated. The data sets (n_m, x_m) obtained could be used to find the analytical form of n(x). However for all the related work reported in this thesis, the complementary error function, exponential, Gauusian, and step functions were used to fit the data sets and the method of least mean-square error was used to calculate the error of the fit in all cases. The Gaussian and exponential functions chosen can be described as:

Exponential function,

$$n(x) = n_s + \Delta n_0 \; [\exp-(x/d)], \text{ and} \qquad (5.26)$$

Gaussian function,

$$n(x) = n_s + \Delta n_0 \ [\exp-(x/d)^2]. \qquad (5.27)$$

where

$\Delta n_0 = (n_g - n_s)$, and

d is the depth of the waveguide.

Examples of slab waveguide analysis using IWKB are given in Sections 5.5, 5.6, and 5.7 of this chapter.

5.3 Theory of Stripe (Two Dimensional) Dielectric Optical Waveguides

5.3.1 Introduction

Stripe waveguides (also known as two dimensional waveguides) enable optical radiation to be confined in both directions perpendicular to the direction of light propagation. For integrated optics technology to be used successfully in optical communication systems, optical sensor systems and some advanced signal processing circuits, it is essential to have low loss single-mode stripe optical waveguides.

The analysis of a stripe dielectric optical waveguide is more complex than that of the planar optical waveguide described in Section 5.2. Due to the fact that the electric and magnetic fields even of a homogeneous rectangular stripe waveguide cannot be expressed exactly by separable functions of the rectangular coordinates, more-or-less complex numerical analyses are employed to obtain precise solutions.

5.3.2 Summary of Published Analyses used in this Thesis

Two waveguide analysis methods were used to generate the dispersion curves for proton-exchanged stripe optical waveguides in $LiNbO_3$. The two

techniques were proposed and described repectively by Marcatili [5.4] and by Knox and Toulios [5.5]. It is noted that the two methods are quite similar. The Knox and Toulios method of waveguide analysis maybe regarded as a natural extension/modification to Marcatili's method. Neither of the two methods of waveguide analysis is rigorous or a true numerical approach. On a physically reasonable and intuitive basis, the two methods are used quite often to estimate waveguide properties.

Gallagher [5.20] has used the technique described by Knox and Toulios (also commonly known as the effective index method) for analysing ion-exchanged waveguides in soda-lime glass substrates. Reasonable results were generated eventhough the ion-exchanged waveguides have a graded index profile. Miller [5.21] has used Marcatili's theory to analyse high aspect ratio sandwich ribbon fibres with success.

5.3.3 Marcatili's Analytical Solution

In this method, an approximate 'analytical' solution in closed form was formulated using simple sinusoidal and exponential functions. The rectangular dielectric waveguide configuration under consideration is shown in Figure 5.4. In this analysis, the fields in the shaded areas are neglected due to the difficulties of matching the tangential fields over those boundaries.

The analysis assumes that most of the guided-wave power is travelling in region 1, with very little in regions 2, 3, 4 and 5, and with a negligible amount in the shaded regions. Since the optical waveguide modes are assumed to be well guided, their electric fields decay exponentially in regions 2, 3, 4, and 5. Hence, due to the above assumptions, only a small error should be introduced into the solution for guided modes that are far away from cut-off. By assuming simple electric field distributions, the field matching along the four sides of region 1 can be accomplished. The guided

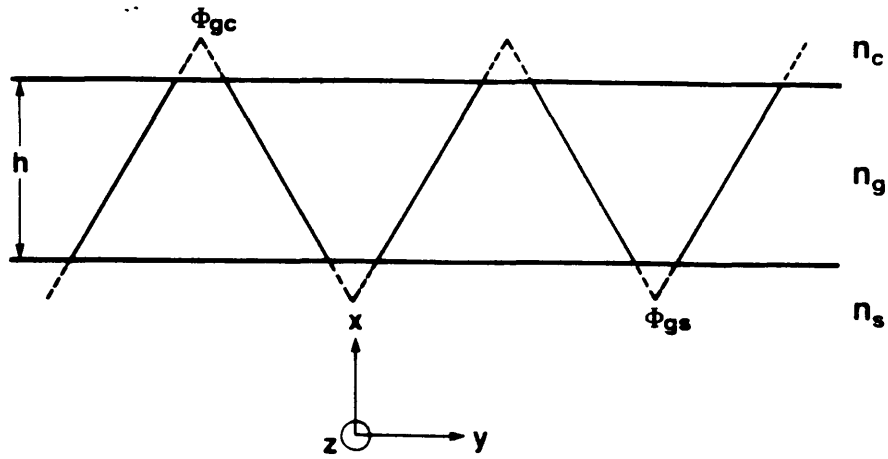

Figure 5.3 Phase Change On Reflection Represented By The Goos-Haenchen Shift

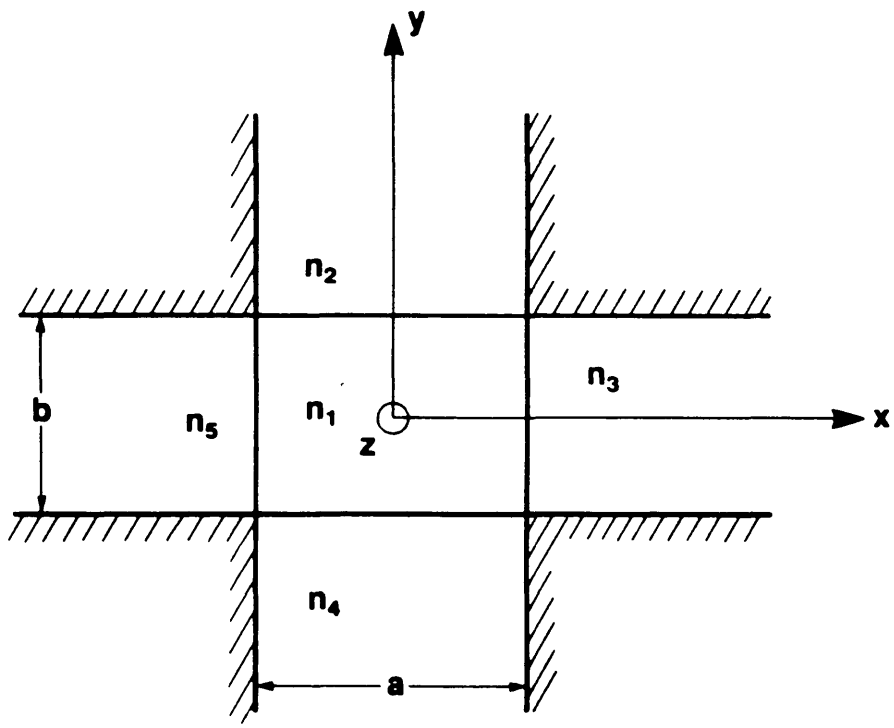

Figure 5.4 Rectangular Waveguide Geometry

modes are essentially of the T.E.M. type and they can be grouped into two types namely $(E_{pq})^x$ and $(E_{pq})^y$. The largest field components are found to be perpendicular to the axis of propagation and the main field components of the members of the first type are E_x and H_y, while those of the second type are E_y and H_x. The subindices p and q represent the number of nodes in the x and y directions respectively. The longitudinal propagation coefficient β_z may be expressed as:

$$k_z = \beta_z = \sqrt{[(k_1)^2 - (k_x)^2 - (k_y)^2]} \tag{5.28}$$

where $k_1 = n_1 k_0 = n_1 2\pi/\lambda_0$, and k_x and k_y are the propagation coefficients in the x- and y- directions respectively, being the solutions of the following transcendental equations.

$$k_x\, a = p\pi - \tan^{-1} k_x\, \xi_3 - \tan^{-1} k_x\, \xi_5 \tag{5.29}$$

$$k_y\, b = q\pi - \tan^{-1} (n_2/n_1)^2\, k_y\, \zeta_2 - \tan^{-1}(n_4/n_1)^2\, k_y\, \zeta_4 \tag{5.30}$$

for $(E_{pq})^y$ modes, and

$$k_x\, a = p\pi - \tan^{-1} (n_3/n_1)^2\, k_x\, \xi_3 - \tan^{-1}(n_5/n_1)^2\, k_x\, \xi_5 \tag{5.31}$$

$$k_y\, b = q\pi - \tan^{-1} k_y\, \zeta_2 - \tan^{-1} k_y\, \zeta_4 \tag{5.32}$$

for $(E_{pq})^x$ modes, where:

$$\xi_i = 1/(|k_{xi}|) = 1/\sqrt{[(\pi/A_i)^2 - (k_x)^2]} \qquad i = 3, 5 \tag{5.33}$$

$$\zeta_i = 1/(|k_{yi}|) = 1/\sqrt{[(\pi/A_i)^2 - (k_y)^2]} \qquad i = 2, 4 \tag{5.34}$$

$$A_i = \lambda/\{2\sqrt{[(n_1)^2-(n_i)^2]}\} \qquad i = 2, 3, 4, 5, \text{ and} \tag{5.35}$$

$$k_i = 2\pi n_i/\lambda = k_0 n_i \qquad i = 1, 2, 3, 4, 5 \qquad (5.36)$$

The constants ξ_i and ζ_i in the above equations are the inverse measures of the distance the evanescent field penetrates into regions 2, 3, 4 and 5 since it was assumed that the field components in these regions decay in an exponential form. As the guided mode tends towards cut-off, the discrepancy between Marcatili's analytical solutions and Goell's computer solutions [5.22] becomes greater since the fields in the shaded regions of Figure 5.4 are now more significant because they carry more optical power. The above equations apply, therefore, only to situations where the guided modes are fairly far away from cut-off.

For stripe proton-exchange waveguides in $LiNbO_3$, where the refractive index difference between the waveguide and the surrounding areas is large (i.e. $\Delta n = 0.12$) and the stripe waveguide has a large aspect ratio (i.e. a >> b), then the $(E_{pq})^x$ and $(E_{pq})^y$ modes tend to those of the TE_m and TM_m modes of a planar waveguide with m = q-1. The two eigenvalue equations 5.30 and 5.32, as $a \rightarrow \infty$, $k_x \rightarrow 0$, reduce to those equations that are used to describe planar waveguides which support TE and TM modes.

5.3.4 The Knox and Toulios Solution (Effective Index Method)

In 1970 Knox and Toulios proposed an alternative technique for analysing rectangular dielectric waveguide which generated results that were in close agreement with those produced by the circular harmonic computer analysis of Goell [5.22] for optical modes that were close to cut-off. This method of waveguide analysis became commonly known as the effective index method. It has been used extensively by various workers to calculate dispersion curves for various stripe optical waveguide structures in soda-lime glass, $LiNbO_3$ and III-V type waveguides [5.20, 5.23, 5.24].

The effective index method basically derives an effective index value which serves to couple the two planar optical waveguides that approximate the original stripe geometry illustrated in Figure 5.5. From the papers describing this method, there appears to be no rigorous mathematical justification for the effective index technique although it clearly has features in accord with physical intuition. This method predicts for stripe waveguides that are close to cut-off, propagation constants which are closer to those generated by Goell than those produced by Marcatili's solutions. Again in this method the optical field penetration into the shaded regions as shown in Figure 5.4 is not considered in the analysis.

The procedure of Knox and Toulios is firstly to allow the stripe dielectric waveguide width a go to infinity, as shown in Figure 5.5. This reduces the stripe waveguide structure to an asymmetrical planar dielectric waveguide of thickness b with a normalised propagation constant of $n_e = \beta/k_0$, which can be calculated as already described in Section 5.2. This calculated value n_e is then used to calculate a new value of propagation constant $n'_e = \beta'/k_0$ where n'_e is the normalised propagation constant for the stripe dielectric waveguide structure of width a and thickness b.

When using this technique to calculate the propagation constant, one must ensure that there is polarisation continuity. As an example, if the $(E_{pq})^x$ modes (quasi planar TE_{q-1} mode) are considered; the asymmetric planar dielectric waveguide of thickness b must support a TE_{q-1} mode, whilst the asymmetric planar dielectric waveguide of width a must now support a TM_{p-1} mode. On the other hand, if one now is considering the calculation of the $(E_{pq})^y$ modes, the above described TE and TM conventions are reversed. This means that TM_{q-1} and TE_{p-1} modes will be involved instead.

The other approach for analysis of a stripe optical dielectric waveguide using the effective index technique is to consider firstly the asymmetrical planar waveguide of width a and then consider the

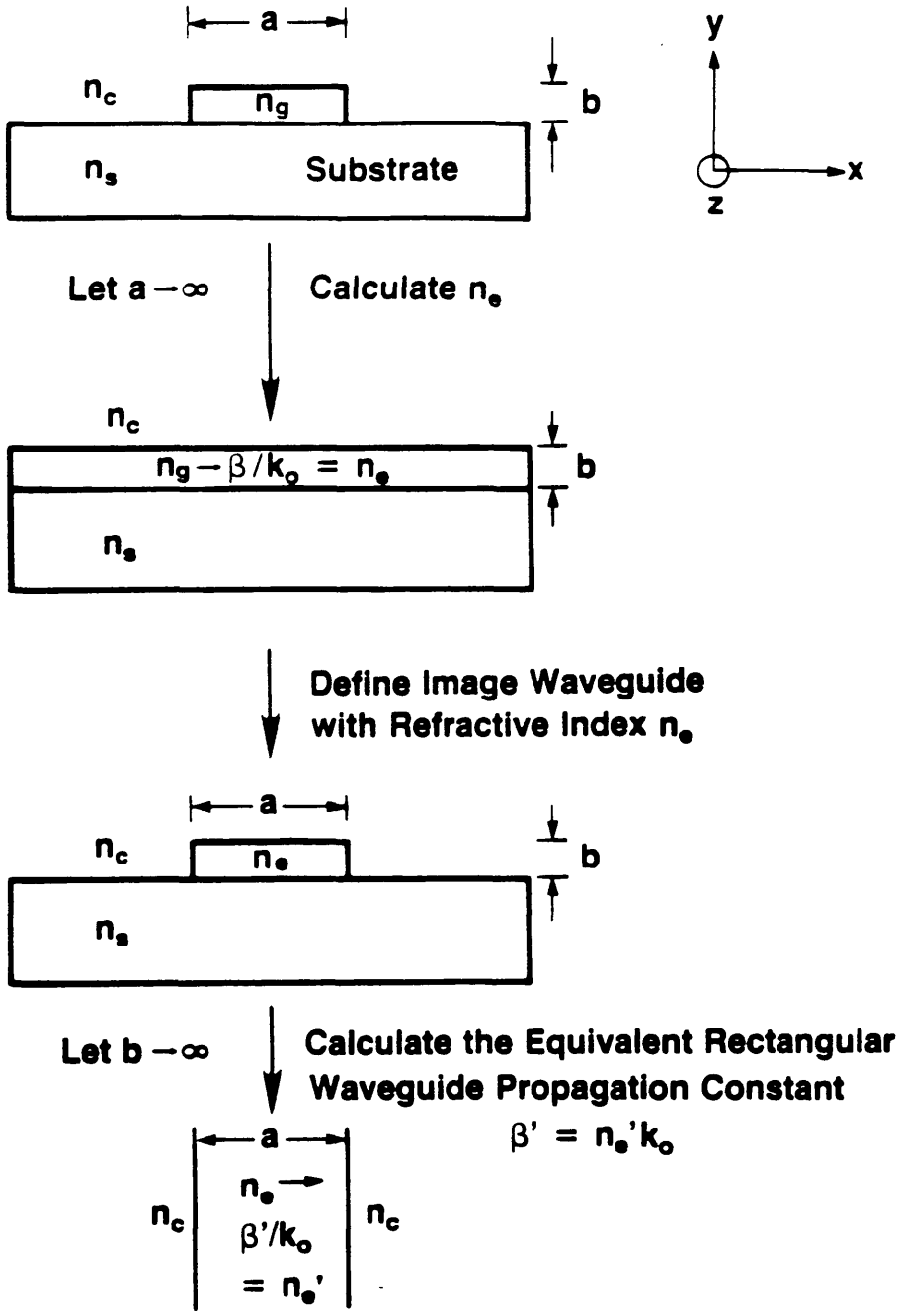

Figure 5.5 Calculation Of Rectangular Waveguide Propagation Constant Using The Effective Index Method (EIM)

asymmetrical planar waveguide of thickness b. With reference to Figure 5.6, let b go to infinity and then the value of n_e for the asymmetrical planar waveguide of width a can be calculated. As before, the equivalent rectangular normalised propagation constant $\beta_z = k_0 n'_e$ is calculated using the calculated n_e value and by defining an asymmetrical planar waveguide of thickness b.

In general it would appear that both ways of calculating the effective refractive index are equally valid, especially for stripe optical dielectric waveguides with small Δn change. However, for larger Δn changes and a greater degree of asymmetry, it appears that the order of calculating the effective refractive index is important. MacFadyen [5.24] showed that there could be at least a 10% variation between the effective refractive index values calculated by approaching the calculation using the two alternate ways. Thus, for the stripe PE waveguides in $LiNbO_3$ reported in this thesis, it was decided to calculate the slab with the smaller confinement (i.e. the transverse slab) first since this was more sensitive to Δn changes and waveguide dimensions.

The calculations for the stripe waveguides in proton-exchange $LiNbO_3$ are reported in Chapter 6. In the calculations both Marcatili's method and the Knox and Toulios methods were used.

5.4 Techniques for Studying Slab and Stripe Optical Waveguides

5.4.1 Introduction

There are three common methods for coupling laser radiation into optical waveguides. They are prism-coupling [5.6, 5.7, 5.8], grating couplers [5.25], and end-fire coupling [5.9, 5.10]. Of these three methods, the most widely used for evaluating slab and stripe optical waveguides are prism-

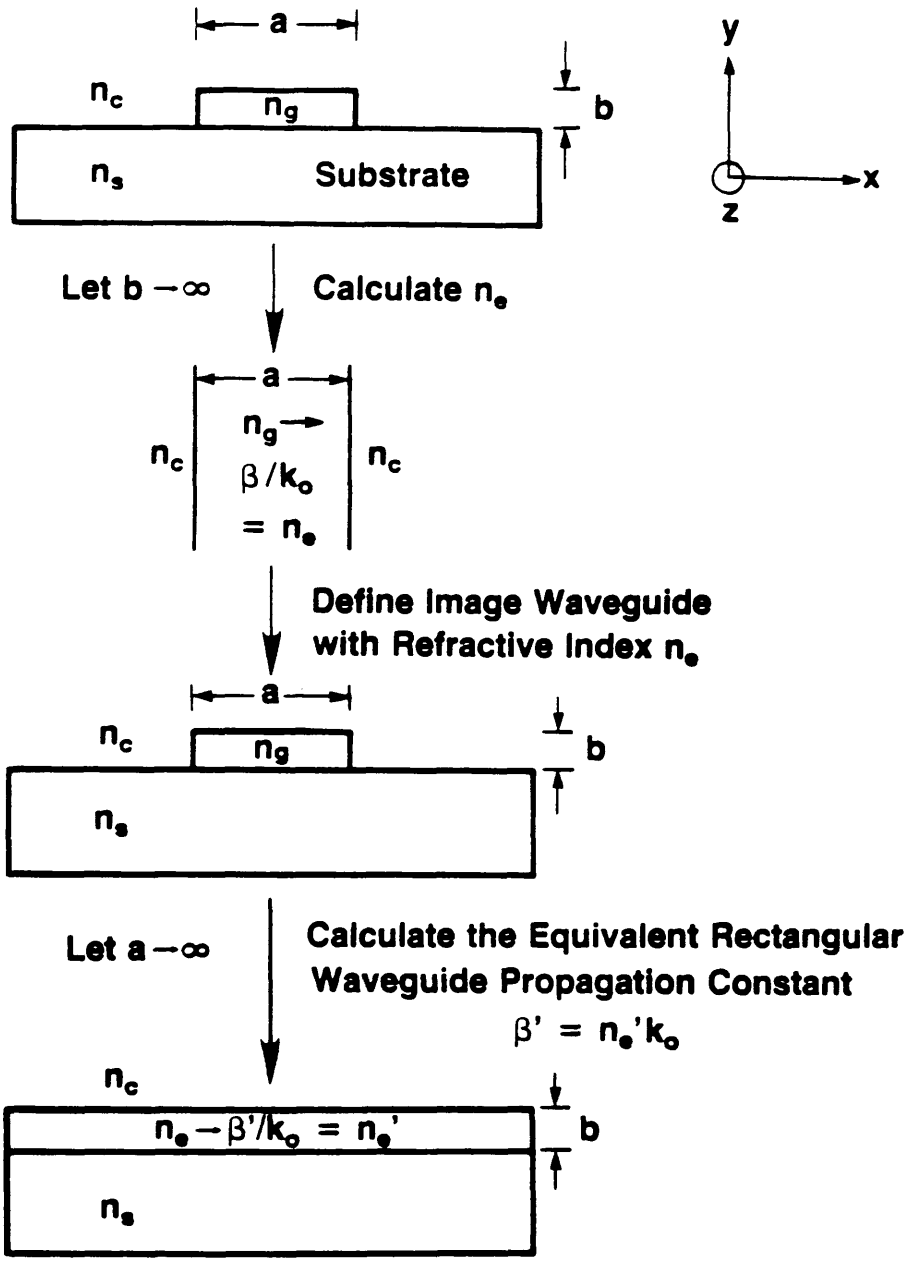

Figure 5.6 Calculation Of Rectangular Waveguide Propagation Constant Using The Effective Index Method (EIM)

coupling and end-fire coupling respectively. Both of these techniques were extensively used in this work.

5.4.2 The Prism Coupler Technique

It was Tien et al [5.6] who first proposed this method for coupling laser light into and out of optical waveguides. The prism-coupling method has since been used extensively by researchers, as a convenient way to measure the effective refractive indices of a wide range of optical waveguide systems. The advantages of prism-coupling are:

(a) the waveguide sample can be tested without any special preparation such as end-polishing of the sample edges or formation of gratings,

(b) as mentioned earlier, individual waveguide modes can be excited and their effective refractive indices can be measured and

(c) the coupling efficiency that can be achieved can be very high. It has been shown that the theoretical coupling efficiency could be as high as 100% if a tapered air gap is used. To date, a maximum coupling efficiency of 94% has been reported by Sarid [5.26].

Figure 5.7 shows a schematic diagram of the input and output prism couplers on a waveguide. The method involves clamping a prism with a refractive index (n_p) higher than the refractive index of the optical waveguide (n_g) which is to be measured. The input and output prisms are separated from the waveguide by a small air gap. From now on, the discussions will only be on the input prism coupler. The output prism is used as a convenient way to decouple the guided light in the waveguide so that each individual mode can readily be identified.

Laser radiation that is incident upon the lower face of the input prism at an angle θ will be totally internally reflected if:

$$\theta > \sin^{-1} (1/n_p) \qquad (5.37)$$

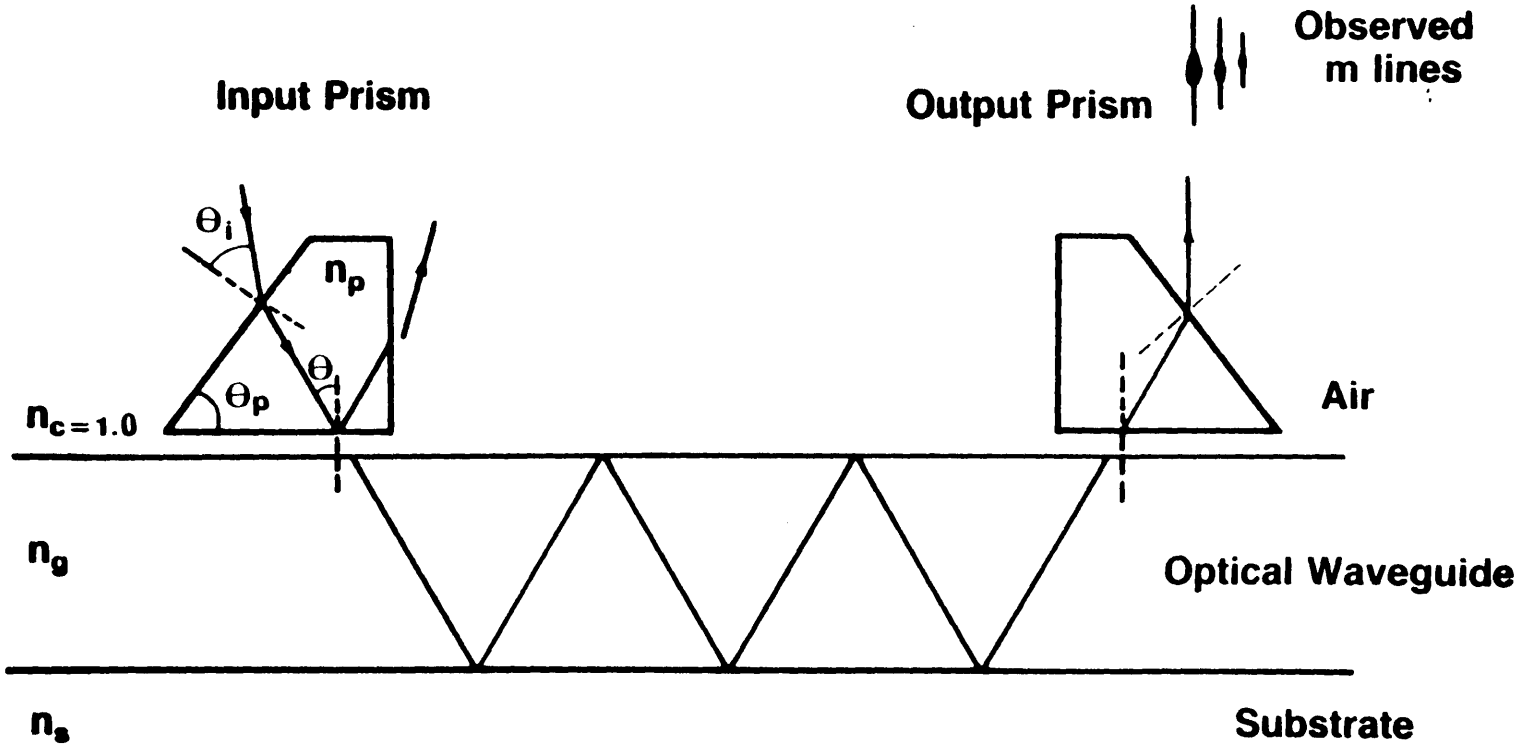

Figure 5.7 Schematic Diagram Of The Input And Output Prism Couplers On A Waveguide

However also set up in the same region of the prism is an evanescent field in the air gap which propagates parallel to the optical waveguide surface with a propagation constant:

$$\beta_e = k_0 n_p \sin\theta \tag{5.38}$$

where $k_0 = 2\pi/\lambda_0$ is the wavenumber in free space. When this is phase-matched to a guided-mode in the waveguide, optical power will be transferred into the waveguide and at this condition, $\beta_e = \beta$ where β is the propagation constant of the guided-mode. The incident angle of the input beam can be changed to satisfy the conditions for propagation of other modes. Hence the general equation that satisfies the above situation is:

$$\beta_e = \beta = k_0 n_p \sin\theta \tag{5.39}$$

Therefore the effective refractive index, n_{eff} of the waveguide mode for each value of θ can be calculated from:

$$n_{eff} = \beta/k_0 = n_p \sin\theta \tag{5.40}$$

From the prism geometry and the use of Snell's Law:

$$\theta = \theta_p + \sin^{-1}[\sin(\theta_i)/n_p] \tag{5.41}$$

where θ_i is the coupling angle between the incident laser beam and the normal to the sloping prism face and θ_p is the prism angle, as indicated in Figure 5.7.

The angle θ_i is known as the synchronous or mode-angle and forms the foundation for all the measurements and calculations of the mode effective

refractive index of any optical waveguides. After substituting θ from Equation 5.40 into Equation 5.41, the value of n_{eff} is given by:

$$n_{eff} = n_p \sin \{\theta_p + \sin^{-1}[\sin(\theta_i)/n_p]\} \qquad (5.42)$$

In the prism-coupling system used to measure the mode angles of the optical waveguides, no special optimization was taken to maximise the coupling efficiency. The reason for this was that the intensity of the coupled modes did not have a major impact on any measurements to be taken using the system except maybe the in-plane scattering study. In all cases, the output power measurements were normalised relative to an initial value. In general the coupling efficiency in most experiments was found to be between 40% to 64%.

The prisms used in all the experiments described in this thesis were made from rutile (TiO_2). The extraordinary (n_e) and ordinary (n_o) refractive indices of TiO_2 at 632.8 nm and 1150 nm are:

(a) $n_e = 2.8719$, $n_o = 2.5837$, and

(b) $n_e = 2.7323$, $n_o = 2.4717$

respectively [5.27].

It was found from a substantial number of mode-angle measurements that there was a significant variation in the substrate refractive indices of X-cut and Z-cut $LiNbO_3$. This variation is discussed in the Section 5.5 of this chapter.

In order to determine accurately the Δn_{eff} values of the measured optical waveguides, the following procedures were taken:

(a) accurate alignment of the reflected laser beam from the input face of the rutile prism and the incident laser beam,

(b) use of rotation stage with an accuracy to ± 0.01°,

(c) a silicon photodetector and oscilloscope measuring system was used to maximise the signal of the measured m-lines, and

(d) the input prism apex angle (θ_p) was determined by reflecting the laser beam back on itself first from the substrate surface and then from the prism input face. In both cases, a beam splitter and the silicon photodetector and oscilloscope system was used to ensure as near perfect back reflection as possible.

It was deduced that the largest error in the evaluation of n_{eff} came from the prism. Since all mode-angle measurements were made with the same input rutile prism, it was possible to eliminate the errors due to the prism by taking:

$$\Delta n_{eff} = n_{eff} - n_e \text{ (or } n_o) \qquad (5.43)$$

Errors due to prism misalignment with respect to the direction of propagation were ignored. However, the substrates of waveguides to be tested were always located by double sided tape onto a microscope slide. This was to ensure that the input coupling prism could be positioned accurately on the sample. The biggest error in measuring the mode-angle was that due to the rotation stage, i.e. $\pm$ 0.01°.

Figure 5.8 shows a schematic of the experimental arrangement used to take mode-angle measurements on optical waveguides. The sample to be tested was held on a microscope slide with double sided tape. The microscope slide was then placed in a holder held in a precision goniometer with X, Y and Z linear movements, rotational and tilt movements. As mentioned earlier, the rotational movement about the Z-axis was measured electronically to an accuracy of 0.01°. Waveguide TE or TM modes were excited by a vertically or horizontally polarised He-Ne laser beam at wavelengths of 632.8 nm and 1150 nm. A chopper unit, to intensity modulate

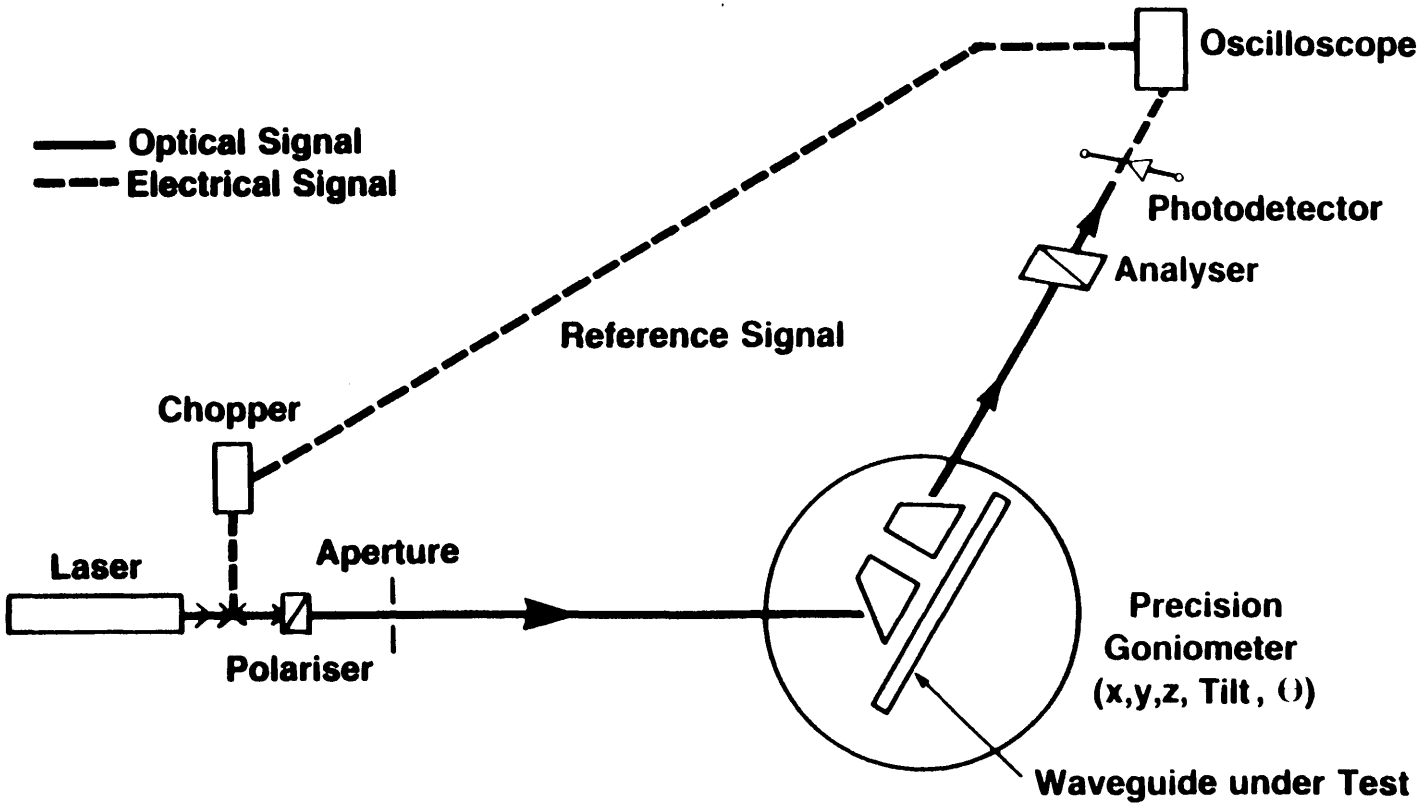

Figure 5.8 Schematic Of The Experimental Arrangement Used To Take Mode Angle Measurements On Optical Waveguides

the laser light at about 1 kHz was used in conjuction with a variable biased a.c. coupled silicon photodetector and an oscilloscope to perform accurate measurements. Figure 5.9 illustrates the precision goniometer with the sample holder used in all the mode angle measurement experiments.

5.4.3 The End-Fire Coupling Technique

The end-fire coupling technique is the most common method for stripe optical waveguide excitation. With this method, it is not possible to derive any effective refractive index values for the stripe waveguides. However, other researchers have employed a hybrid arrangement whereby the laser light was end-fired into the stripe waveguide and towards the other end of the stripe waveguide, a prism coupler was employed to couple out the mode lines. By measuring the angle between the mode line(s) and the perpendicular to the sloping face of the prism, it is possible to derive the n_{eff} values [5.28]. However, in all the stripe waveguide studies reported in this thesis, only the end-fire coupling system was used. Figure 5.10 shows the actual end-fire coupling system used in all the stripe waveguide study.

Ideally the laser beam, of operating wavelength λ_0, entering the input microscope objective should be expanded and collimated to a parallel beam. For minimum spot size at the focus of a particular microscope objective, the input laser beam diameter d should just fill the aperture of the objective. However, in practice it was sufficient to direct the laser beam from the HeNe laser straight into the X40 microscope objective. The focused spot diameter of the laser beam S_d using a microscope objective with a numerical aperture NA is given approximately by [5.29, 5.30]:

$$S_d = \{2\lambda_0 D[1-(NA)^2]^{1/2}\} / [\pi d(NA)] \qquad (5.44)$$

where D is the objective pupil diameter.

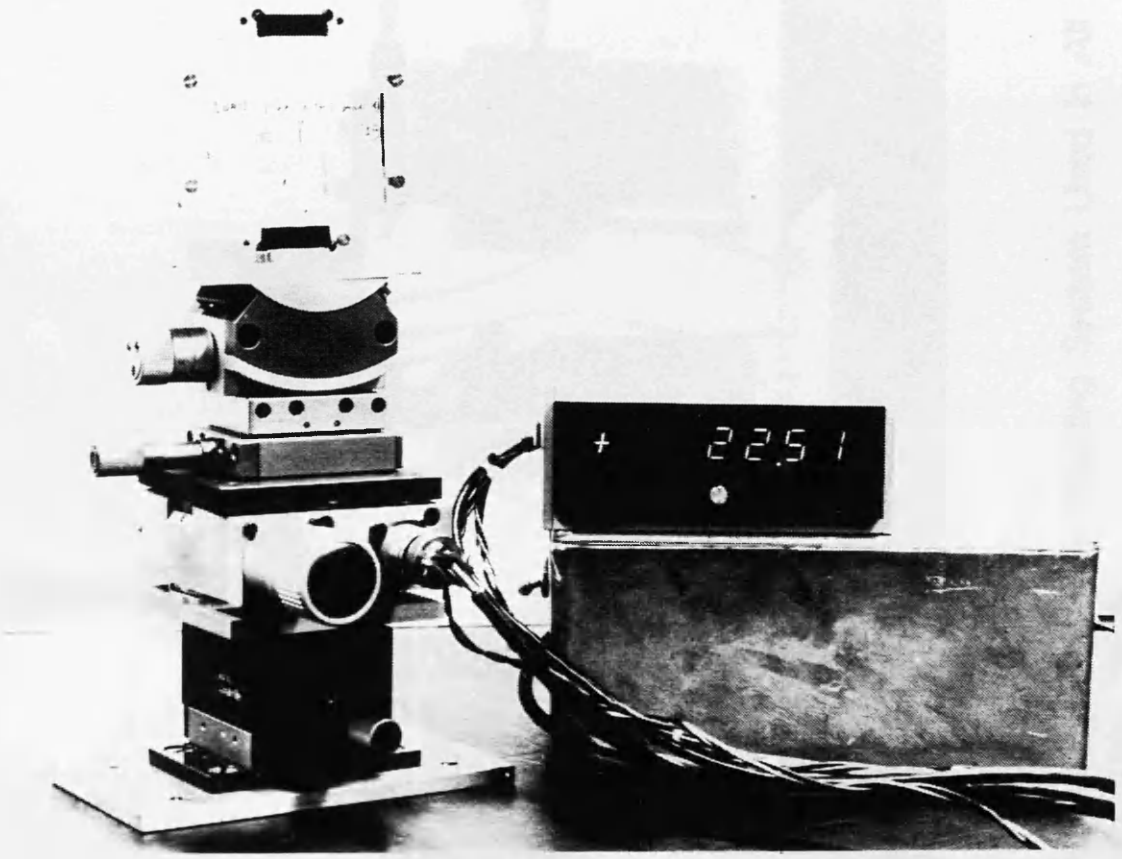

Figure 5.9 The Actual Precision Prism Coupling System Used For Mode Angle Measurements

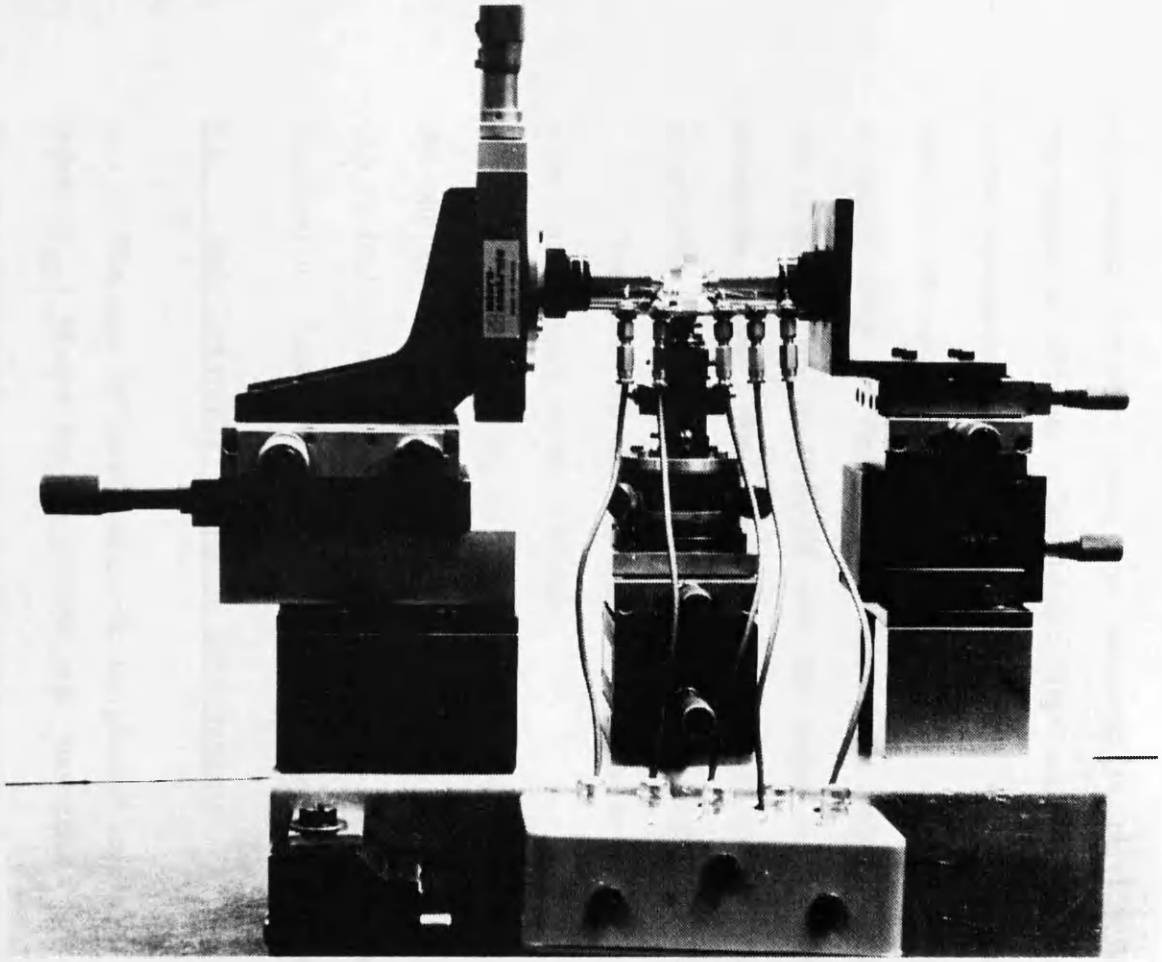

Figure 5.10 The Actual End–Fire Coupling System Used In All The Stripe Waveguide Study

From Equation 5.44, the minimum spot size for a 1.5 mm wide input HeNe laser beam, at λ_0 = 633 nm for a X40, 5 mm microscope objective with a numerical aperture of 0.65 was estimated to be 1.6 μm. In the discussions of beam diameter, spot size and mode profiles of optical waveguides in this chapter, the 1/e value of the optical field amplitudes will be used.

In general, it was found that the insertion loss due to the two X40 microscope objectives alone was measured to be 1.1 dB at the operating wavelength of 633 nm. Due to the large mismatch between the 4 or 5 μm stripe waveguides and the focussed output from the microscope objectives used in the optical frequency translator work, the total insertion loss measured using the same pair of microscope objectives was found to lie in the range 5.5 dB to 18.5 dB with the larger values measured in PE stripe waveguide devices. The complete set of results for the insertion loss study on Ti:$LiNbO_3$ and PE stripe waveguide devices is reported in Chapter 6.

Therefore for the end-fire coupling to be effective and efficient, two main criteria have to be achieved:-

(a) efficient matching of the input focussed laser spot and the mode(s) of the optical waveguide under test, and

(b) high quality optical end faces, i.e. they have to be polished (as described in Chapter 4) and be free of chips at the edges of the waveguides.

5.5 Slab Ti:$LiNbO_3$ Waveguide Measurements

The aim of this section is to present measured effective refractive index (n_{eff}) results for the control slab waveguides that were fabricated at the same time as the stripe optical waveguides. The main aim was to monitor the variation of Δn_{eff} for samples with varying titanium thicknesses. In addition, the measurements provided a check on the titanium deposition process. This was to ensure that when the stripe waveguide results were compared the exact fabrication conditions were well established. As stated in

Chapter 4, the following titanium thicknesses and diffusion conditions were adhered to for the fabrication of all the Y-cut $LiNbO_3$ phase modulators:

(1) Titianium Thickness: Between 250 Å and 550 Å, and

(2) Diffusion Conditions: 8 hours at 1000°C, in a closed alumina tube with congruent $LiNbO_3$ flakes.

The reason for the above choice of fabrication conditions was to utilise the stripe waveguide study results that were obtained by McLachlan [5.28].

The prism-coupling technique as described in Section 5.4.2 of this chapter was used to evaluate the control slab waveguides. Table 5.1 shows the measured results (Δn_{eff}) of a typical batch of control samples (with varying initial titanium thicknesses) obtained from a number of titanium deposition runs. As can be seen from the above table, a number of samples with similar titanium thicknesses were included. The results indicated that there might be variations in the titanium thicknesses. However, the measured variations in Δn_{eff} were not large enough to merit any concern in this particular study. In addition, an experimental plot of Δn_{eff} versus initial titanium thickness was made (Figure 5.11). The purpose of this particular plot was to provide a standard reference check to all similar future fabrication experiments. The results from Table 5.1 indicate that the titanium deposition process was repeatable. Extreme care was required for each deposition run with initial titanium film thickness calibration graph obtained for each run. The Δn_{eff} values obtained for an initial titanium film thickness of 380 Å in this thesis were found to be comparable to those results (for an initial titanium film thickness of 375 Å) reported by McLachlan [5.28]. In both cases the same diffusion conditions were used.

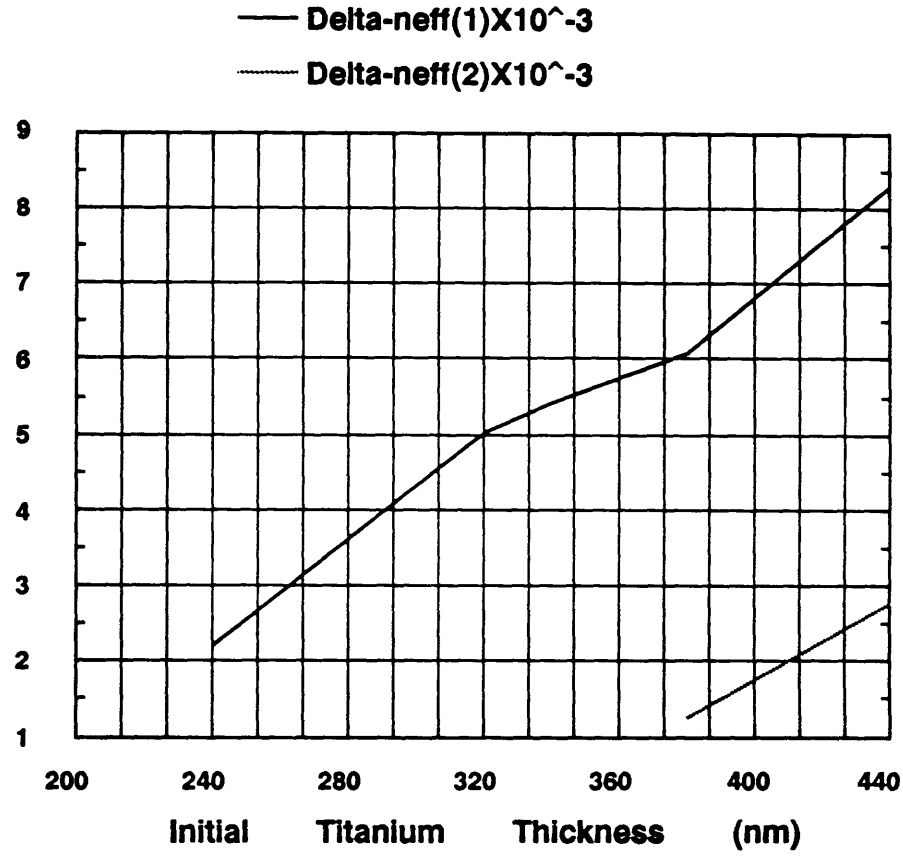

Figure 5.11 Plot Of Δn_{eff} Versus Initial Titanium Film Thickness

	t = 240 Å			t = 320 Å			t = 340 Å			t = 380 Å			t = 440 Å		
	R1	R2	R3	R1	R2	R3	R1	R2	R3	R1	R2	R3	R1	R2	R3
Δn_{eff1} X10^{-3}	2.1	2.3	2.2	4.9	5.1	5.1	5.6	5.3	5.4	6.2	5.9	6.1	8.3	8.5	8.1
Δn_{eff2} X10^{-3}	-	-	-	-	-	-	-	-	-	1.3	1.2	1.3	2.8	2.9	2.6

Note: t is the initial titanium thickness and R is the deposition run number

Table 5.1 Results Of Measured Δn_{eff} For Control Samples With Varying Titanium Thicknesses

5.6 Measurements on Slab Waveguides Formed by Proton-Exchange using Concentrated Benzoic Acid Melts

The prism-coupling technique with single-crystal rutile prisms was used to evaluate the optical characteristics of the waveguides formed. All measurements were carried out at a wavelength of 632.8 nm, unless otherwise stated. It was confirmed experimentally that only TE and TM modes were excited in PE waveguides fabricated in X- and Z-cut $LiNbO_3$ respectively, along the chosen direction of propagation.- along the Y-direction (for X-cut $LiNbO_3$) and along the X-direction (for Z-cut $LiNbO_3$).

The effective refractive index (n_{eff}) of each measured TE or TM mode was calculated from the measured mode-angle (Using Equation 5.42). These values were then used as data input for a computer program based on the normalized step index equations, as described by Kogelnik and Ramaswamy (Section 5.2). The program calculated the surface refractive index and waveguide depth for the given input wavelength on the assumption of a step index change in the slab waveguide.

5.6.1 Measurements at λ = 632.8 nm (for X- and Z-cut Waveguides)

It was found that the n_{eff} of freshly fabricated PE optical waveguides in both X- and Z-cut $LiNbO_3$ decreased with time. This behaviour is similar to that reported by Nutt [5.31]. The result was however in contrast to that reported by Yi-Yan [5.32] where a periodic variation of n_{eff} with time was observed. It is possible that the method of fabricating the PE waveguides in the $LiNbO_3$ substrates contributed to this observed difference in results. The waveguides fabricated for this work and those fabricated by Nutt were exchanged in a stainless steel beaker with a Pyrex cover. The PE waveguides used by Yi-Yan were fabricated in sealed ampoules. In all three fabrications, molten benzoic acid was used as the protonic source. Figures

5.12(a) and 5.12(b) illustrate plots of the relaxation of Δn_{eff} (i.e. the difference between n_{eff} and the substrate refractive index of X- or Z-cut $LiNbO_3$) versus time in days after the PE fabrication process. The X- and Z-cut waveguide measured were both PE at 200°C for one hour. Due to the relaxation of the measured n_{eff} values, all measurements presented in this section were obtained six months after fabrication. This was to avoid any measurable decrease in the n_{eff} values of the PE waveguides and thus provide a stable set of results.

Figures 5.13(a) and 5.13(b) show plots of diffusion depth versus $(time)^{0.5}$ for X- and Z-cut PE waveguides. The results were obtained for waveguides fabricated in benzoic acid melts of various temperatures, i.e. from 160°C to 220°C. Assuming that the proton source concentration did not vary during the exchange process, values for the diffusion coefficient D(T) were calculated from the gradients of the curves. The values of the diffusion coefficient at various exchange temperatures for X- and Z-cut PE waveguides are given in Tables 5.2(a) and 5.2(b) respectively. These values were calculated assuming that the diffusion depth (d) varied as follows [5.33]:

$$d_i = 2\sqrt{[t \times D_i(T)]} \qquad (5.45)$$

where t is the exchange time in hours and $D_i(T)$ the diffusion coefficient in $\mu m^2/h$ for the PE process in X-cut (i = x) and Z-cut (i = z) $LiNbO_3$. In Equation 5.45, the dependence of $D_i(T)$ on temperature T in degrees Kelvin, is given by the Arrhenius Law:

$$D_i(T) = D_{0i} \times \exp[(-Q_i)/(R_0 T)] \qquad (5.46)$$

where D_{0i} is a constant and Q_i is the activation energy for the PE process with i= x and z for X- and Z-cut $LiNbO_3$ respectively, and where R_0 is the universal gas constant, with a value of 8.314 J/Kmol. Figures 5.14(a) and

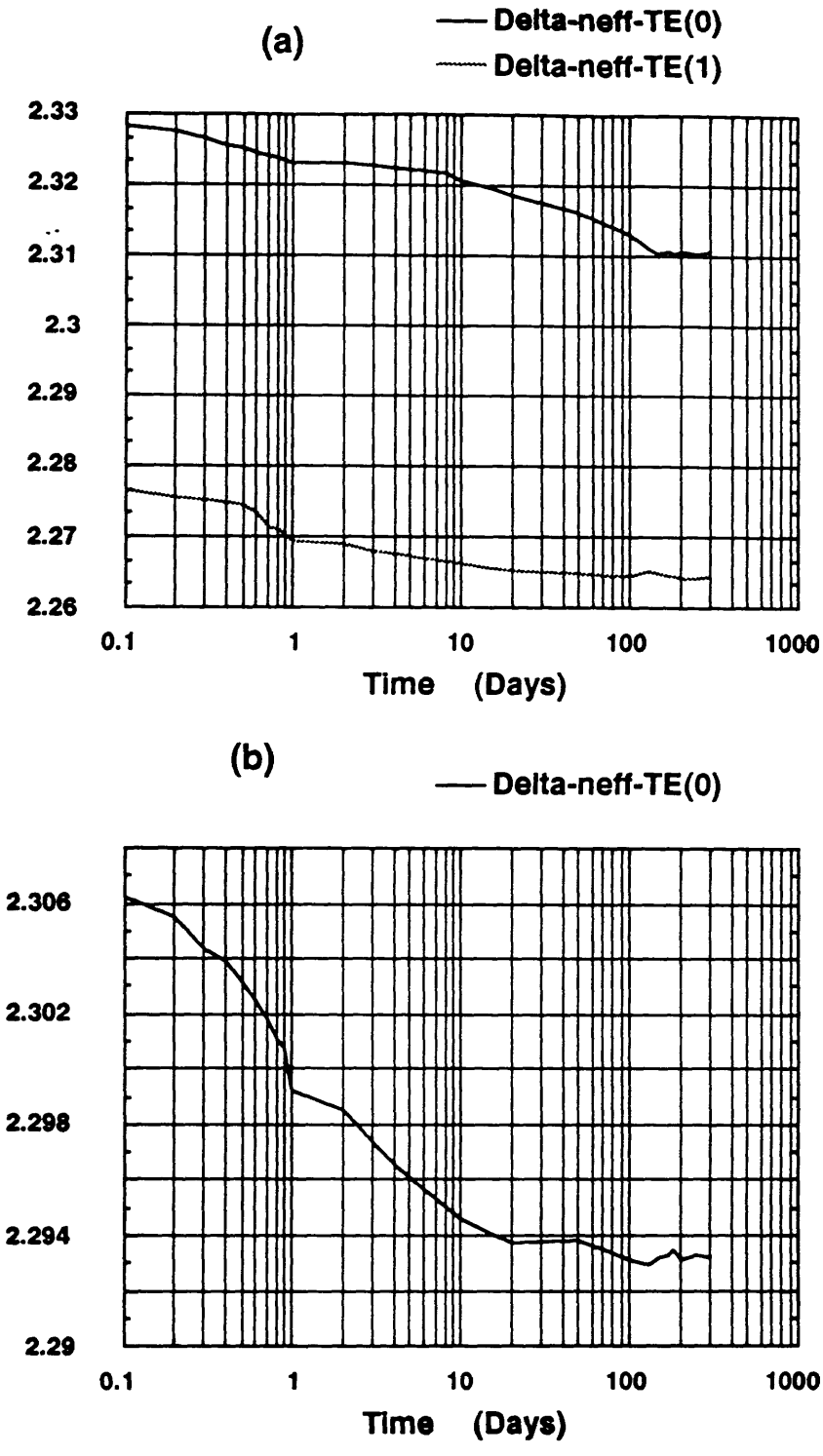

Figure 5.12 Plot Of The Relaxation Of Δn_{eff} Over A Time Period Of 200 Days For:
(a) PE X-Cut $LiNbO_3$
(b) PE Z-Cut $LiNbO_3$

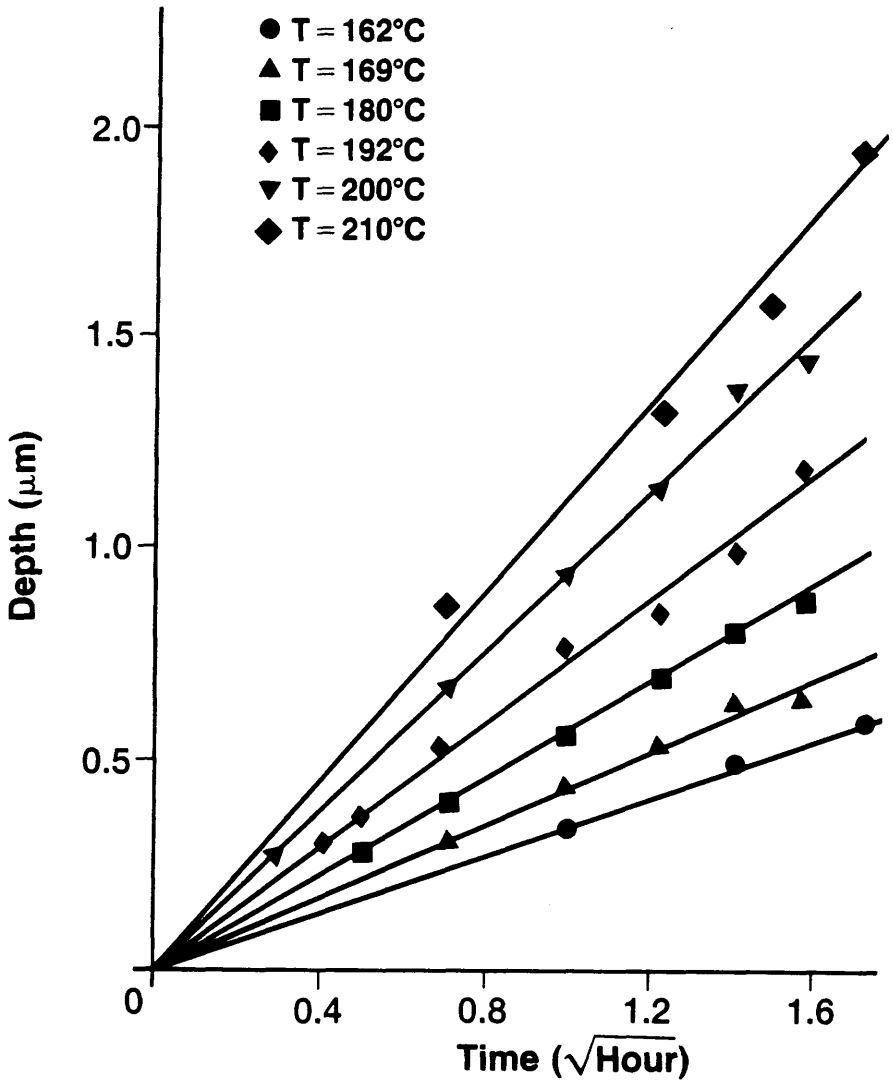

Figure 5.13(a) **Plots Of Diffusion Depth Versus √(Time) For PE X-Cut $LiNbO_3$**

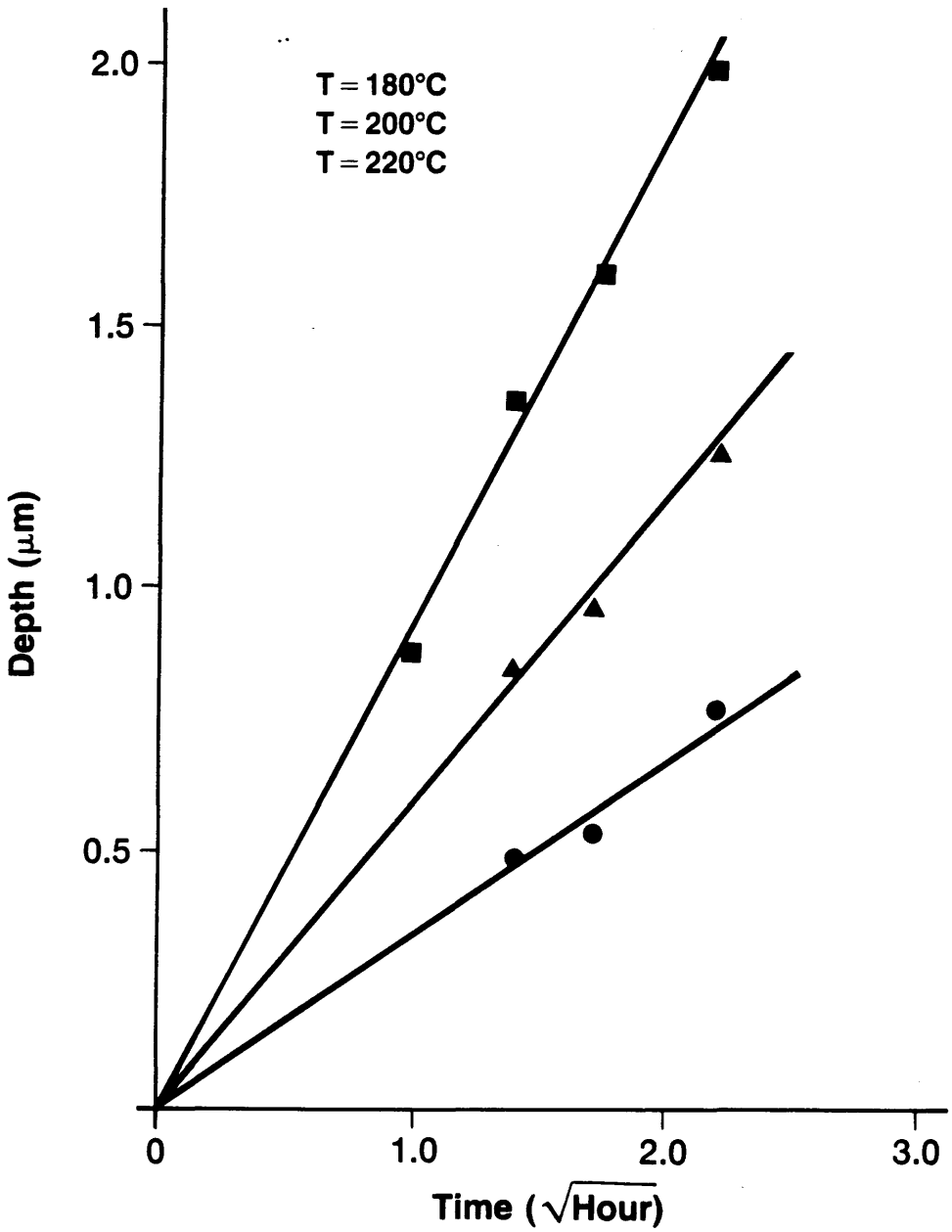

Figure 5.13(b) Piots Of Diffusion Depth Versus √(Time) For PE Z-Cut $LiNbO_3$

T°C [K]	D(T), $\mu m^2/h$
162 [435]	0.029
169 [442]	0.047
180 [453]	0.081
192 [465]	0.136
200 [473]	0.220
210 [483]	0.291

(a)

T°C [K]	D(T), $\mu m^2/h$
180 [453]	0.027
200 [473]	0.081
220 [493]	0.207

(b)

Table 5.2 **Table Of Diffusion Coefficients At Various Temperatures**
(a) For PE X-Cut $LiNbO_3$
(b) For PE Z-Cut $LiNbO_3$

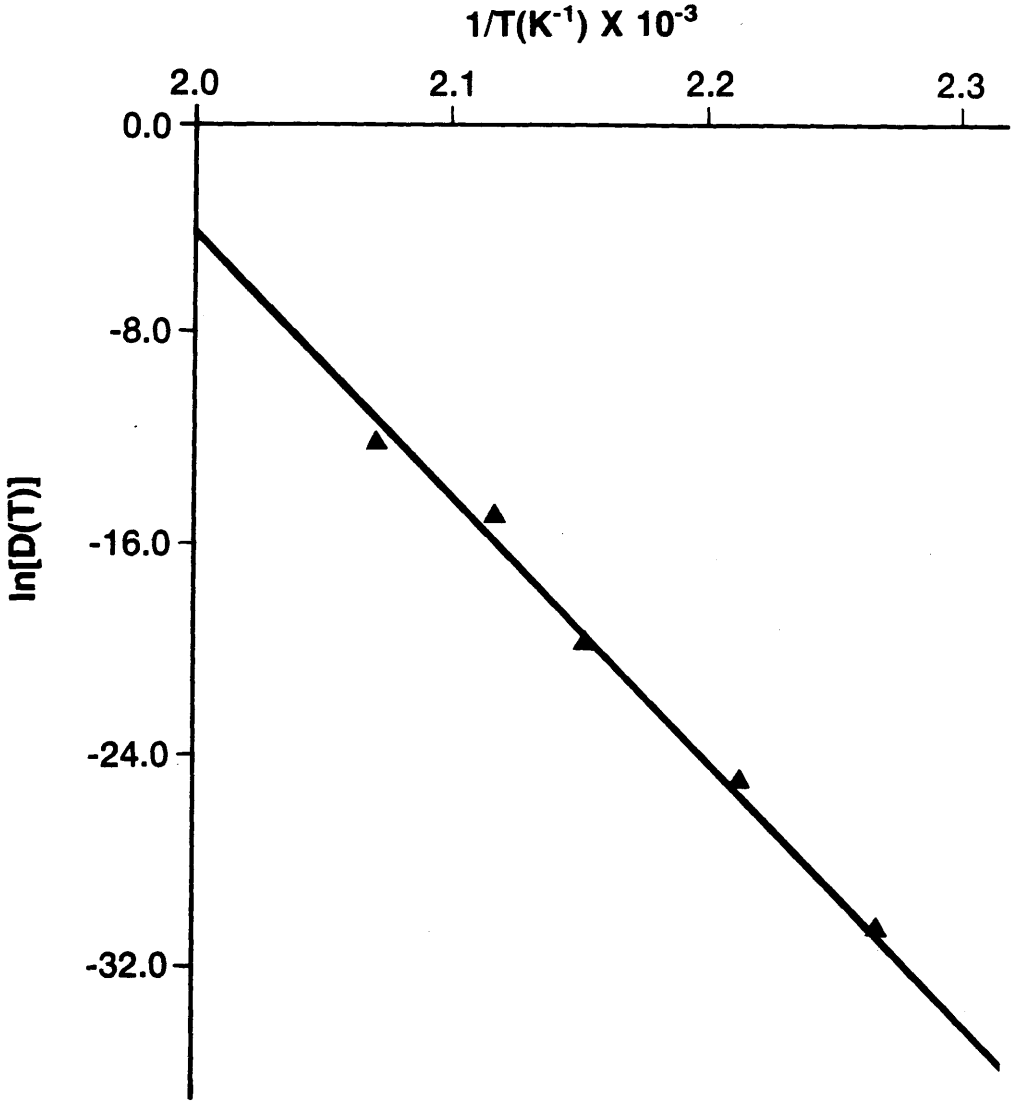

Figure 5.14(a) Plot Of ln D(T) Versus 1/T (Gradient= Q/R) For PE X-cut $LiNbO_3$

5.14(b) illustrate the relationship between 1/T and ln D(T). From this plot, values of Q_i and D_{oi} have been obtained:

$$Q_x = 84 \text{ kJ/mole}, \qquad Q_z = 94 \text{ kJ/mole}$$

$$D_{ox} = 4.326 \times 10^8 \ \mu m^2/h, \qquad D_{oz} = 1.84 \times 10^9 \ \mu m^2/h.$$

Equation 5.45 can, therefore, be written as follows:

$$d_x = 4.169 \times 10^4 \ (t)^{0.5} \times \exp(-5.052 \times 10^3/T) \ \mu m \qquad (5.47)$$

$$d_z = 8.580 \times 10^4 \ (t)^{0.5} \times \exp(-5.650 \times 10^3/T) \ \mu m \qquad (5.48)$$

Using Figures 5.14(a) and 5.14(b), the value of any diffusion coefficient within the working range of benzoic acid (i.e. 160°C to 249°C) can be read off conveniently.

After having studied and defined the diffusion properties of the PE process, the optical properties for the slab waveguides were investigated at the various diffusion conditions. Figures 5.15(a) and 5.15(b) show sets of dispersion curves obtained theoretically (Section 5.2), together with the experimental results for PE X- and Z-cut waveguides respectively. As can be seen from the plots, the theoretically derived and experimentally measured results are in excellent agreement with each other. From these dispersion plots, the cutoff depth for each waveguide mode was obtained. The cutoff depths for modes in the range TE_0 to TE_5 and TM_0 to TM_5 are tabulated in Tables 5.3(a) and 5.3(b) respectively.

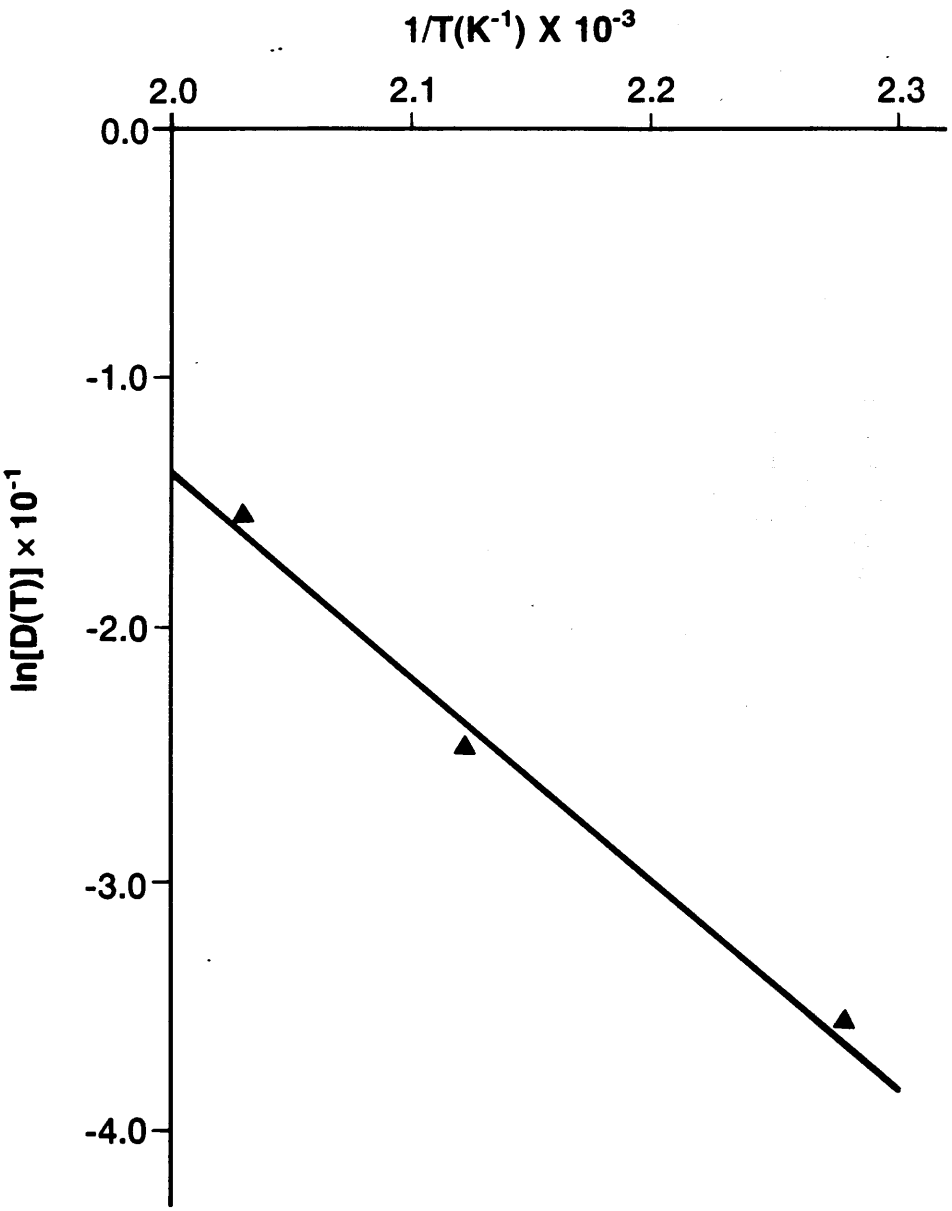

Figure 5.14(b) Plot Of ln D(T) Versus 1/T (Gradient= Q/R) For PE Z-cut $LiNbO_3$

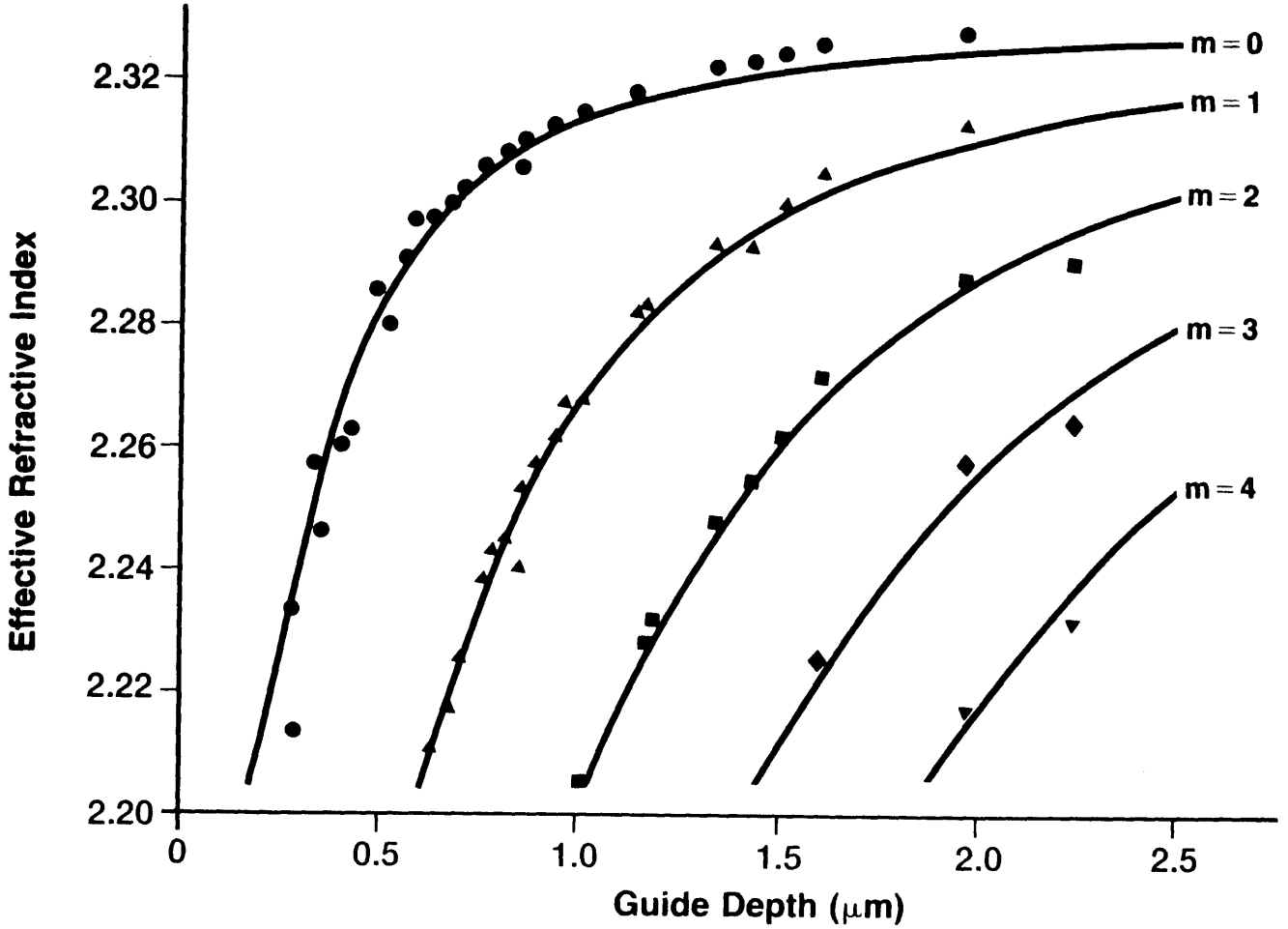

Figure 5.15 (a) Plot Of Theoretical And Experimental n_{eff} Values Against Depth Of Waveguide For PE X–cut $LiNbO_3$

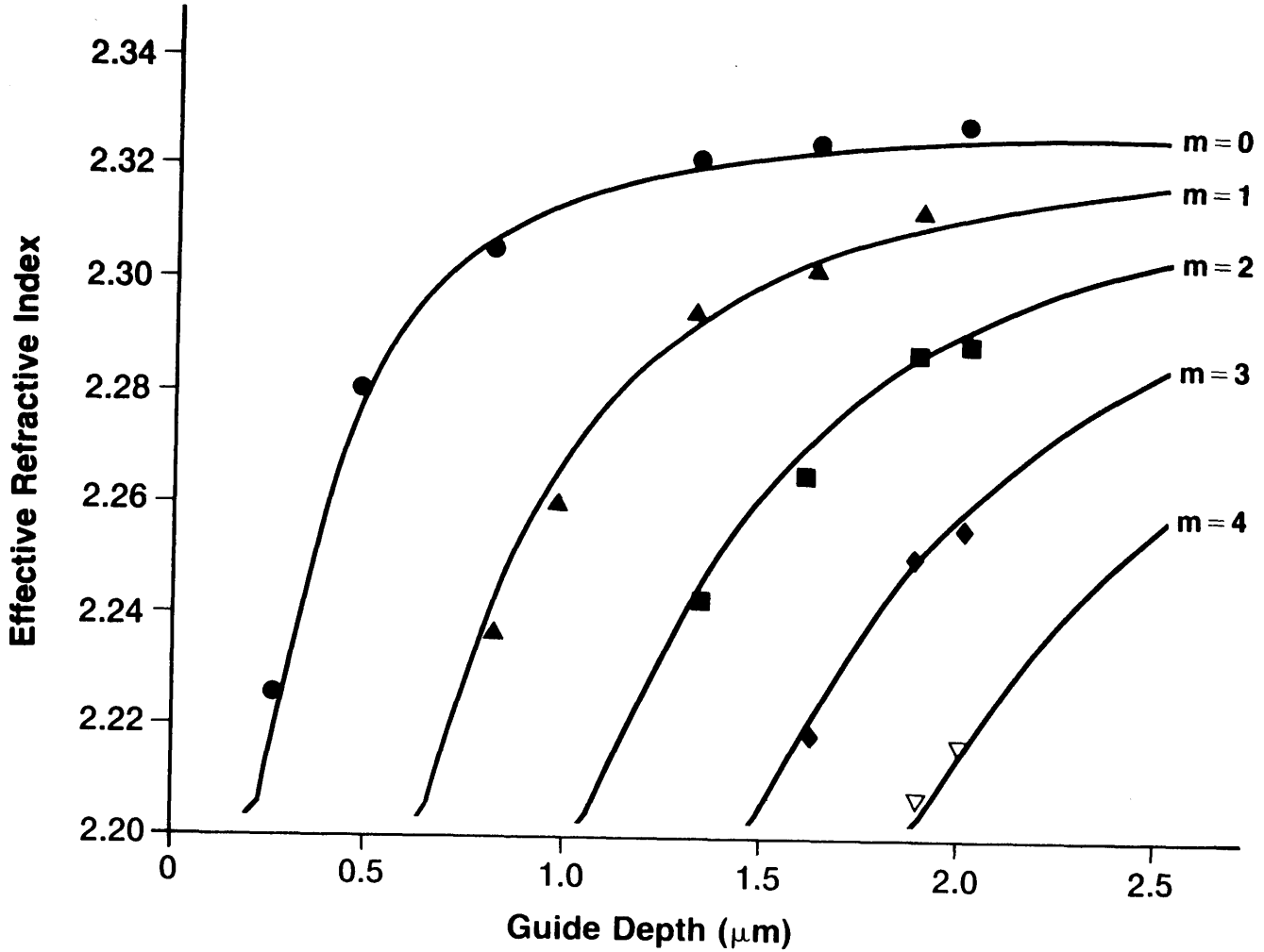

Figure 5.15(b) Plot Of Theoretical And Experimental n_{eff} Values Against Depth Of Waveguide For PE Z–cut $LiNbO_3$

Mode Number	Cutoff Depth (μm)
0	0.15
1	0.57
2	1.00
3	1.42
4	1.82
5	2.25

(a)

Mode Number	Cutoff Depth (μm)
0	0.18
1	0.62
2	1.03
3	1.46
4	1.88
5	2.30

(b)

Table 5.3 Table Of Cutoff Depth For Each TE/TM Mode
(a) For X-Cut $LiNbO_3$ (TE)
(b) For Z-Cut $LiNbO_3$ (TM)

5.6.2 Measurements at λ = 1150 nm (for X-cut Waveguides)

All the X-cut PE samples used in the above measurements of Section 5.6.1 were then remeasured at a longer wavelength. It was found that most of the Z-cut PE samples were not thick enough to support any TM modes. In view of this and the secondary importance of Z-cut PE samples for the work in this thesis, no more Z-cut samples were fabricated.

It was found experimentally that the majority of the X-cut PE waveguides supported only the fundamental TE mode. For purposes of comparison, it was convenient to use three multimoded waveguides fabricated respectively at 193°C, 202°C and 211°C and exchanged for 2.5 hours, 2.0 hours and 3.0 hours respectively. Using the prism-coupling technique, mode-angles for each guided mode were measured and the corresponding effective refractive indices were calculated. Finally, applying the computer program based on the normalized step index equations of Kogelnik and Ramaswamy, values of the surface refractive index and waveguide depth were calculated for each sample. Table 5.4 shows a summary of the measurements and calculated results at λ= 1150 nm. The values in the brackets were measured at λ= 632.8 nm. From this study, it can be deduced that the average Δn change at λ= 1150 nm is 0.096. The aim of this short piece of experimental work was to obtain an indication of the dispersion of Δn for PE waveguides.

5.6.3 Propagation Loss Measurements

5.6.3.1 Introduction

In order to identify a waveguide fabrication technology that can realise high quality waveguide devices, it is important to measure the scattering of laser light by imperfections in the waveguides. This property

Sample number	Temperature C	Time hours	Surface index n_f	Film thickness, t_f, μm	Δn^*
D2	193	2.5	2.2477 (2.3290)	1.3258 (1.3017)	0.0960 (0.1265)
F4	202	2.0	2.2477 (2.3319)	1.3915 (1.3731)	0.0960 (0.1294)
H3	211	3.0	2.2471 (2.3313)	1.9356 (1.9603)	0.0954 (0.1288)

*$n_{substrate}$ at λ = 632.8 nm = 2.2025
*$n_{substrate}$ at λ = 1150 nm = 2.1517

Table 5.4 Summary Of Measured Waveguide Properties At λ_o = 1150 nm With Bracketed Values Measured At λ_o = 632.8 nm For Comparison

will play an important role in the ultimate performance level that can be achieved in integrated optical systems.

Optical energy that is guided in an ideal waveguide will remain trapped in the bound mode and the guided-wave will propagate unattenuated along the length of the waveguide. In reality, it is impossible to fabricate a perfect waveguide. In fact, all fabricated waveguides contain some form of imperfection and these can be divided into two broad categories, namely:

(a) refractive index variations due e.g. to compositional fluctuations within the volume of the waveguide, and

(b) dimensional fluctuations associated with variations in the width and height of the waveguides (i.e. depending on whether it is a slab or a stripe waveguide).

Other potential scattering centres that are due to dust particles on the surface of the waveguides during fabrication can generally be substantially avoided by careful cleaning and fabrication techniques as described in Section 4.2. The fundamental loss mechanisms that are difficult to avoid will be treated in the following sections. They are scattering (in-plane and out-of-plane), absorption, and intermodal scattering. Measurements of in-plane, out-of-plane, and intermodal scattering are presented in the following three sections.

Absorption losses can be practically ignored in optical devices in large bandgap ferroelectric materials such as $LiNbO_3$ and $LiTaO_3$ and this loss mechanism generally manifests itself more in semiconductor waveguides. Various researchers have attempted to measure absorption losses in Ti:$LiNbO_3$ waveguides and found the figures to be very low, less than 0.1 db/cm [5.34, 5.35]. Therefore for all the PE waveguides fabricated, it was assumed that the absorption loss was very low and hence could be ignored.

5.6.3.2 Intermodal Scattering

Intermodal scattering can be defined as the scattering of light from one guided mode into another. For example, light that is scattered out of the TE_0 (or TM_0) mode into the TE_1 (or TM_1) mode of a planar waveguide. Physically, the scattering mechanisms must satisfy the following condition: part of the optical energy must match to the second or higher order modes and

For all the multimoded PE slab waveguides tested, it was observed that some intermodal scattering was present. Measurements of the intermodal scattering consisted of focusing the modal lines, commonly known as m-lines, using a cylindrical lens of focal length 4 cm on to a silicon photodetector system (Complete description of the photodetector system can be found in Section 6.3.2.3). Table 5.5 summarizes the measurements taken for various PE X- and Z-cut $LiNbO_3$. The results did not compare favourably with those obtained for Ti:$LiNbO_3$. The conclusion that can be drawn from the measurements is that intermodal scattering is more serious in the case of PE slab waveguides fabricated using concentrated benzoic acid melts. Figure 5.16(a) to (d) show a number of m-lines and the intermodal scattering seen in multimoded PE X- and Z-cut slab waveguides fabricated by concentrated benzoic acid melts. The slab PE waveguides evaluated were not thermally annealed. It is expected the intermodal scatterings of the slab PE waveguides can be reduced by suitable thermal annealing. However, intermodal scattering can be easily eliminated by using single-moded waveguide. Since most guided-wave optic devices to be used in systems applications are single-moded, this problem can in principle be eliminated.

Single-moded slab waveguides in general can support either the TE_0 or TM_0 modes. In the case of PE X- and Z-cut slab waveguides, only the TE_0 and the TM_0 modes respectively are supported. However, it was noticed in

Excited Mode	Intermodal Scattering Level (dB)		
	Mode 0	Mode 1	Mode2
0	0	-12.2	-9.2
1	-11.2	0	-12.2
2	-9.9	-11.1	0

(a) 2.5H, 200°C

Excited Mode	Intermodal Scattering Level (dB)		
	Mode 0	Mode 1	Mode2
0	0	-10.3	-8.8
1	-9.2	0	-10.3
2	-7.0	-8.8	0

(b) 8H, 200°C

Table 5.5 Summary Of Measured Intermodal Scattering Levels (Conc. Melts)
(a) For PE X-Cut $LiNbO_3$
(b) For PE Z-Cut $LiNbO_3$

Figure 5.16a Photograph Of Inter-Modal Scattering For PE X-Cut $LiNbO_3$ (1 H, 245°C) - TE_0

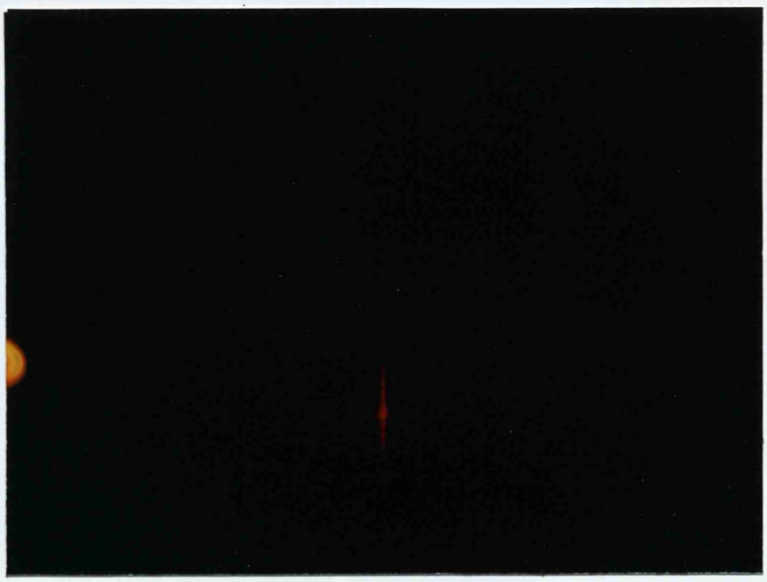

Figure 5.16b Photograph Of Inter-Modal Scattering For PE X-Cut $LiNbO_3$ (1 H, 245°C) - TE_2

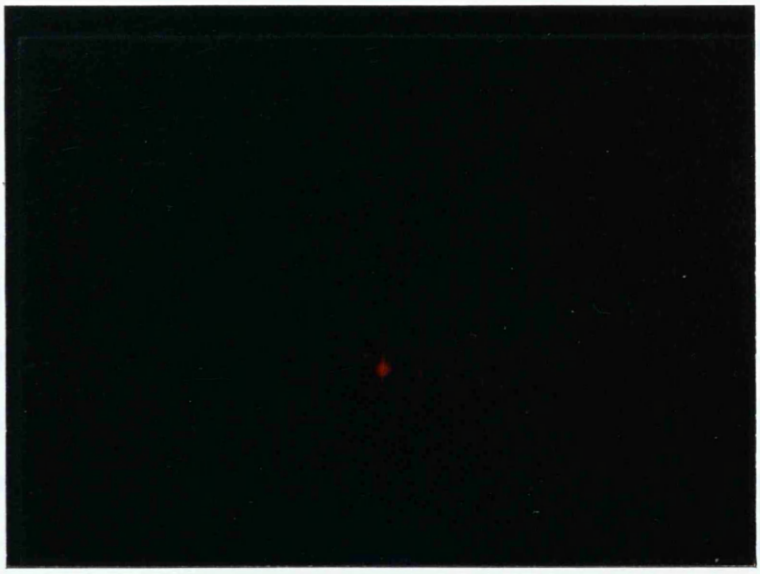

Figure 5.16c Photograph Of Inter-Modal Scattering For PE Z-Cut $LiNbO_3$ (3 H, 235°C) - TM_0

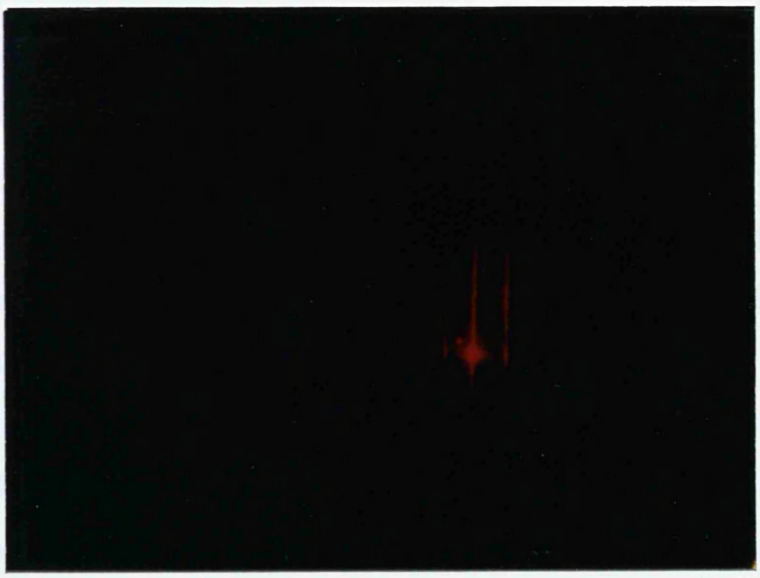

Figure 5.16d Photograph Of Inter-Modal Scattering For PE Z-Cut $LiNbO_3$ (3 H, 235°C) - TM_2

some PE slab waveguide measurements that a second faint set of m-lines was observed along with the regular m-line pattern. At first it was thought that the faint second m-line pattern was a reflection of the main m-line pattern. On checking the polarisation of the faint m-line pattern, it was found that they were of the opposite polarisation to that of the main m-line pattern. The presence of the faint second m-line pattern was discovered to be strongly affected by the pressure applied to the input- and output-coupling rutile prisms. The difference in intensity of the actual and faint m-line patterns generally ranged from 25 dB to 35 dB. By very careful coupling of the prisms, it was possible to eliminate the 'ghost' m-line pattern altogether.

5.6.3.3 Out-of-Plane Scattering

Out-of-plane scattering can be thought of as a process which involves intermodal scattering between guided and radiation modes. However, in this case, scattering takes place between a guided mode and an unguided or radiation mode. The fact that it is possible to see, at visible wavelengths, a guided-wave as a streak of light in the waveguide is direct evidence that the waveguide is losing optical energy by radiation. By making the assumption that the power of the scattered light is proportional to the optical power of the guided light, it is possible to measure the contribution of out-of-plane scattering to propagation loss using a vidicon camera/monitor system.

To make the out-of-plane scattering measurement, first of all, the guided mode was optimised by careful adjustment of the sychronous angle with the assistance of a photodetector and oscilloscope as described in Section 5.4.2. The scattered light streak on the substrate was then imaged on a monitor using a Hamamatsu vidicon camera. The light intensity at any point along the streak could be monitored with the aid of the line scan option available on the Hamamatsu C1000 controller unit. This technique has also

been extensively used by other researchers to measure out-of-plane scattering losses in ion-exchanged waveguides in soda-lime glass waveguides [5.36].

A vidicon camera system was used to measure propagation losses of a number of single-moded PE slab waveguides. The results from such a study are summarized in Tables 5.6(a) and (b). It can be seen from the results that no clear relationship between propagation loss and fabrication conditions could be identified for measurements at λ= 632.8 nm and λ= 1150 nm. The measured propagation losses for single-moded X- and Z-cut PE waveguides were between 1.3 dB/cm and 2.8 dB/cm and between 2.4 dB/cm and 4.8 dB/cm respectively. This maybe compared to the value of 0.5 dB/cm for X-cut PE $LiNbO_3$ waveguides quoted by other researchers [5.37, 5.38, 5.39] where thermally annealing was employed by two research groups to realise the PE waveguides used in the reported studies [5.38, 5.39].

Other methods of measuring propagation losses include the two and the three prism-coupling techniques [5.40, 5.41]. Using either of the methods mentioned, the individual mode scattering and intermodal scattering losses can, in principle, be routinely measured. However due to the requirement for the two prism-coupling technique that the coupling efficiency of the output prism has to be maintained at the same level for each measurement during movement of the output prism with respect to the input prism, a third prism is introduced in the three prism method to eliminate this problem.

Propagation loss measurements using the two prism-coupling method were also made in the present work. An input prism was used to couple light into the waveguide to be measured and an output prism was then used to couple light out from the waveguide. The output prism was located as far from the input prism as possible. The exact distance between the two prisms was then measured. A cylindrical lens with a focal length of 4 cm was then

Fabrication Conditions	Measured Propagation Loss (dB/cm)
7 minutes, 160°C	2.2
5 minutes, 165°C	1.9
5 minutes, 170°C	1.3
3 minutes, 175°C	2.5
3 minutes, 180°C	2.8

(a)

Fabrication Conditions	Measured Propagation Loss (dB/cm)
20 minutes, 160°C	3.3
17 minutes, 165°C	2.4
15 minutes, 170°C	4.2
14 minutes, 175°C	4.0
13 minutes, 180°C	2.5

(b)

Table 5.6 Summary Of Out-Of-Plane Loss Measurements (Conc. Melts)
(a) For PE X-Cut $LiNbO_3$
(b) For PE Z-Cut $LiNbO_3$

used to focus the optical energy of individual m-lines on to a silicon photodetector system. The same experimental arrangement as described in Section 5.6.3.2 was used to perform this measurement. In order to establish the propagation losses, the output rutile prism was moved successively towards the input prism, in small steps, and the separation and the optical power level measurements were recorded each time. Figure 5.17(a) and (b) show a typical plot of such a measurement for an X-cut and a Z-cut PE sample respectively. From the plot of measured guided-wave power (normalised against the maximum power value) as a function of prism-separation (cm), the waveguide propagation losses could be determined. Propagation loss values obtained by the two prism-coupling method were in general higher (between 2.0 dB/cm to 5.0 dB/cm higher) when compared to those values obtained using the Hamamatsu camera/monitor system. This can be easily attributed to the variations in the coupling efficiency of the output prisms or the possibility of inaccurate estimation of background for substraction using the vidicon camera system. No attempts were made to use the three prism-coupling method.

5.6.3.4 In-Plane Scattering

In-plane scattering occurs in planar optical waveguides [5.42, 5.43, 5.44, 5.45]. It is typically caused by the following:

(a) refractive index fluctuations and

(b) surface roughness.

The measurement of in-plane scattering levels in a slab waveguide was based on the assumption that the scattered laser light and the unscattered light could both be collected by the output rutile prism coupler. To perform a fair comparison of the in-plane scattering levels of slab waveguides fabricated by titanium indiffusion, PE and DMPE, the distance between the input and

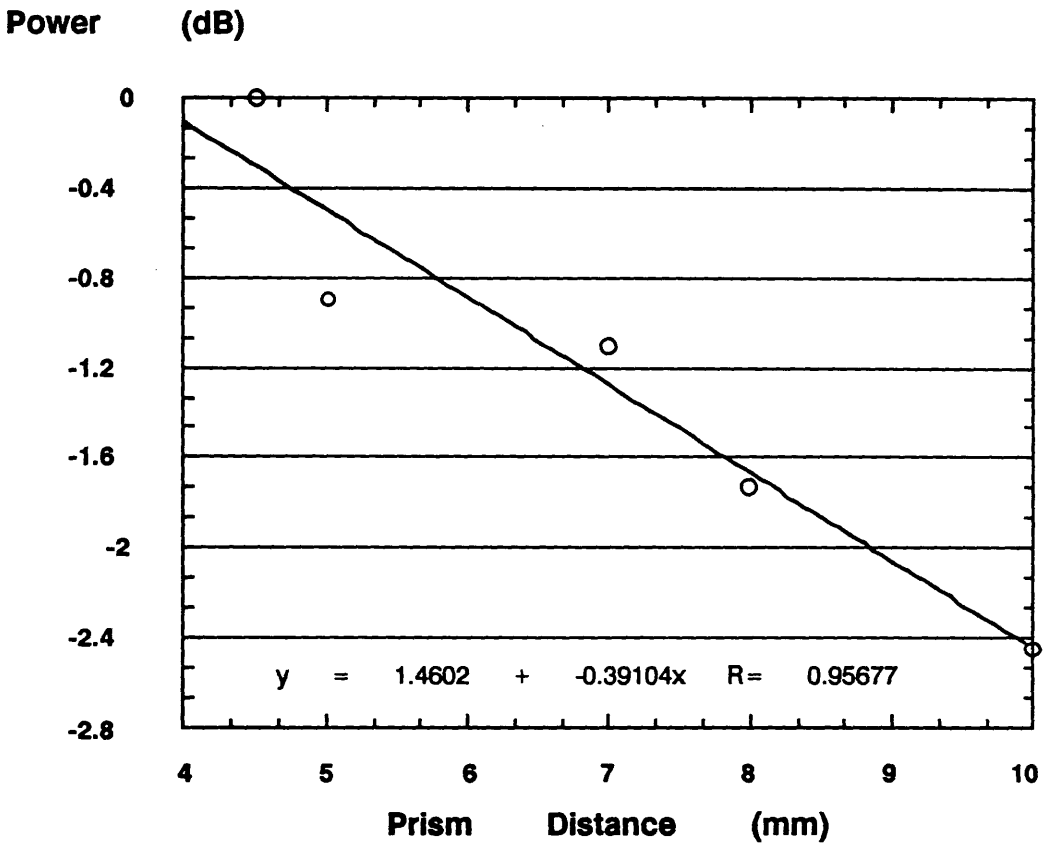

Figure 5.17a Plot Of Propagation Loss Measurement For PE X-Cut $LiNbO_3$ Sample (0.5 H, 200°C)

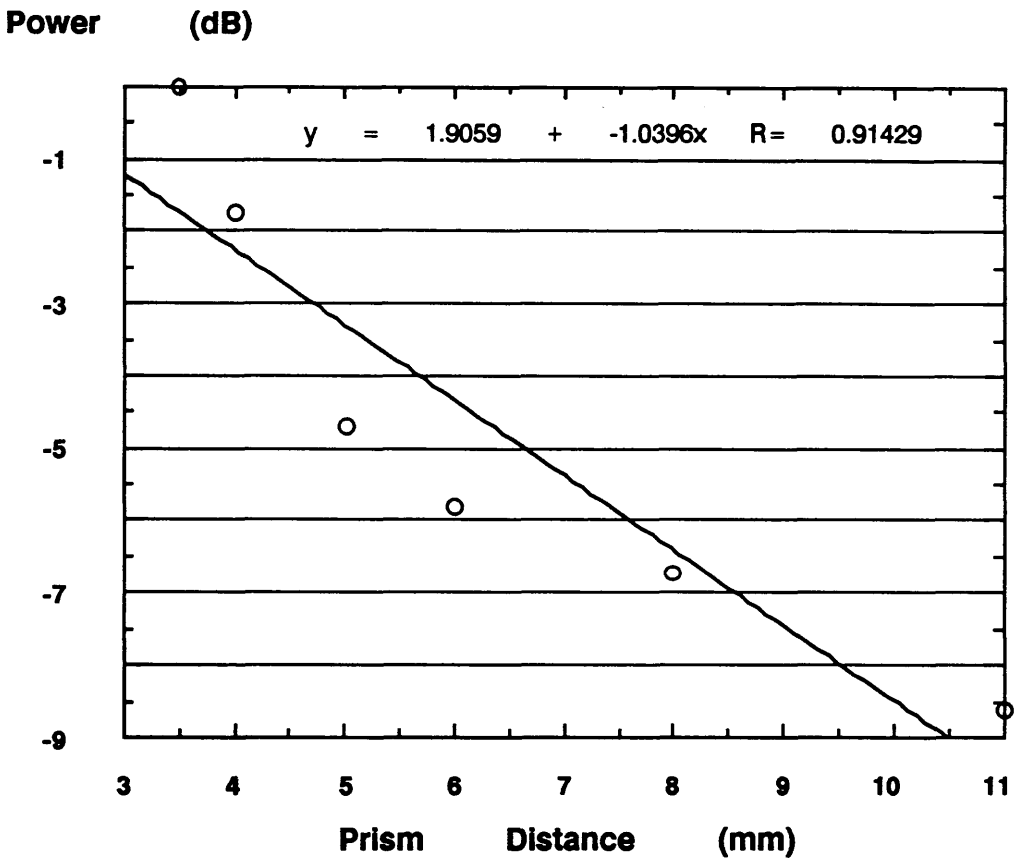

Figure 5.17b Plot Of Propagation Loss Measurement For PE Z-Cut $LiNbO_3$ Sample (0.8 H, 200°C)

output prisms was always kept constant, i.e. 10 mm in all measurements reported in this thesis.

The equipment used to measure the in-plane scattering levels of the waveguides includes a scanning silicon photodetector with a 5 μm slit in the front of the active detector area, an EG&G lock-in amplifier and an HP 9816 computer. The distance between the output prism and the scanning photodetector was always kept at a constant distance of 40 mm. This was again to ensure that all the results could be compared fairly.

Results obtained by measuring waveguides under different fabrication conditions (temperature of bath ranging from 160°C to 235°C, and immersion times in molten benzoic acid ranging from 0.5 hour to 5 hours) indicated that the in-plane scattering intensity levels were generally between 10 dB and 17 dB for a scattering angle of 0.5° in the waveguides. Table 5.7 summarizes all the in-plane scatter results. As can be seen from the table, the results gave no regular trend. Figure 5.18(a) and (b) show typical m-line scans for X-cut and Z-cut PE $LiNbO_3$ samples, respectively. The in-plane scatter results indicate that the slab PE waveguides fabricated using concentrated benzoic acid melts in both X- and Z-cut $LiNbO_3$ were at best comparable to those reported for slab Ti:$LiNbO_3$ waveguides [5.42, 5.43, 5.45]. Therefore PE waveguides (without thermal annealing) are not suitable for applications such as for use in the integrated optical spectrum analyser [5.44].

5.7 Measurements on Slab Waveguides Formed by Proton-Exchange using Diluted Benzoic Acid Melts

5.7.1 Waveguide Refractive Index Measurements

The prism-coupling technique was again employed to evaluate the optical characteristics of the waveguides formed. All measurements were

Exchange Time, Hours	TE_0, dB	TE_1, dB	TE_2, dB	TE_3, dB
0.5	10	12	9	8
0.75	14	11	13	15
1.0	12	14	11	7

(a)

Exchange Time, Hours	TM_0, dB	TM_1, dB	TM_2, dB	TM_3, dB
1.0	13	14	11	-
1.5	12	11	9	10
2.0	11	12	11	14

(b)

Table 5.7 Summary Of In-Plane Scattering Results (For An In-Plane Angle Of 0.5°)
(a) X-Cut, 235°C, λ = 632.8 nm
(b) Z-Cut, 235°C, λ = 632.8 nm

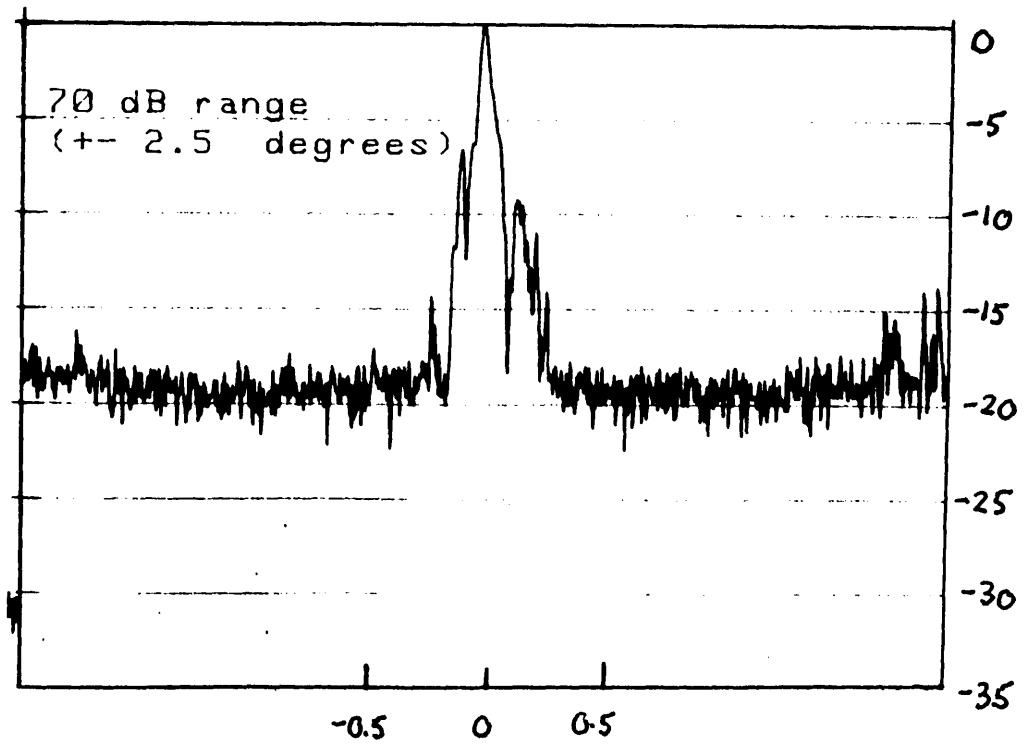

Figure 5.18a Plot Of A Typical m–Line Scan For PE X–Cut $LiNbO_3$ Sample (0.5 H, 200°C)

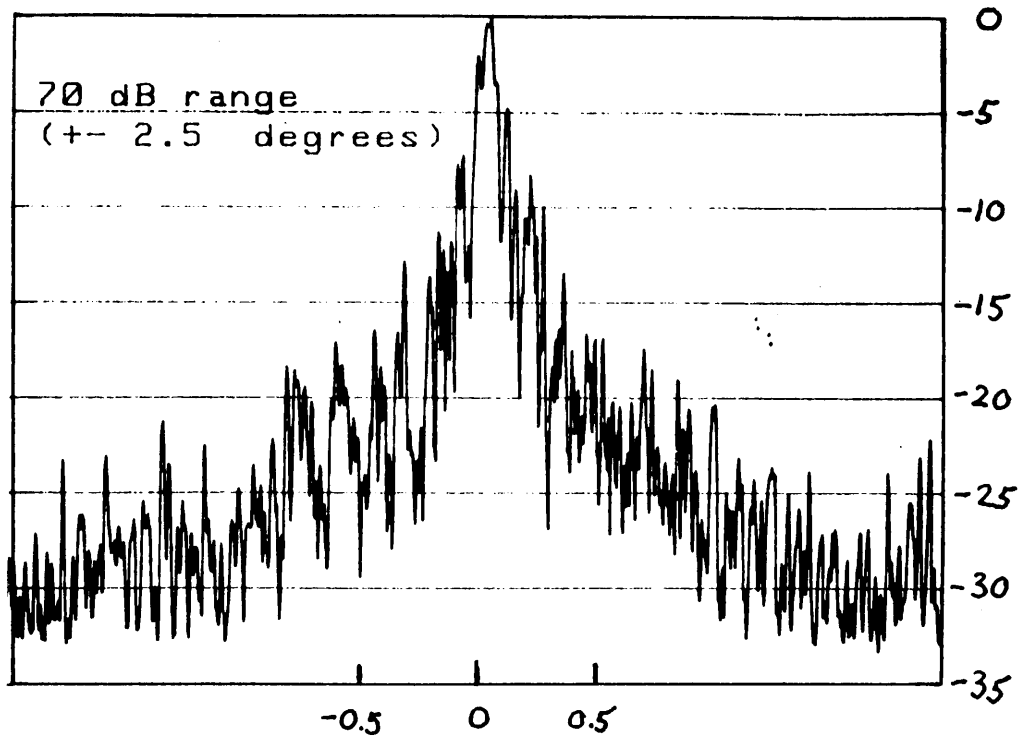

Figure 5.18b Plot Of A Typical m–Line Scan For PE Z–Cut $LiNbO_3$ Sample (0.8 H, 200°C)

carried out at a wavelength of 632.8 nm. It was again confirmed experimentally that only TE or TM modes were excited in DMPE waveguides formed in X- and Z-cut $LiNbO_3$ respectively. The choice of propagation direction for the X-cut and the Z-cut $LiNbO_3$ substrates were along the Y-direction and the X-direction respectively.

Again the effective refractive index (n_{eff}) of each measured TE or TM mode was calculated from the measured mode-angle values. These values were then used as data input for a computer program based on the WKB approximation which estimates the shape of the refractive index profile of the measured waveguide. This technique is commonly known as IWKB technique [5.2, 5.3] and has been discussed in Section 5.2. The program calculates the surface refractive index and the waveguide depth at which the n_{eff} value becomes equal to the local refractive index.

Figures 5.19 and 5.20 show the step-like refractive index profiles (Δn = 0.12) of DMPE waveguides fabricated in X- and Z-cut $LiNbO_3$ respectively. The fabrication conditions for these waveguides are given in the two figures. In general, all the waveguides formed with 0.5% or 1.0% dilution at temperature 235°C or 245°C were found to have step-index profiles and a Δn of 0.12.

Figure 5.21 shows a plot of the optically estimated diffusion depth versus $(time)^{0.5}$ for X- and Z-cut $LiNbO_3$ with dilutions of 0.5% and 1.0%, at a temperature of 235°C. Assuming that the proton source concentration did not vary during the exchange process, the diffusion coefficient D(T), evaluated at T=235°C, can be calculated from the gradient of the four curves. The values of the diffusion coefficients, at the two given dilutions and for X- and Z-cut samples, are given in Table 5.8. In addition, these values were compared to diffusion coefficients obtained by pure benzoic acid exchanges. These values were derived from Equations 5.47 and 5.48 at the appropriate temperature. The results indicated that for X-cut $LiNbO_3$, when the PE was performed using

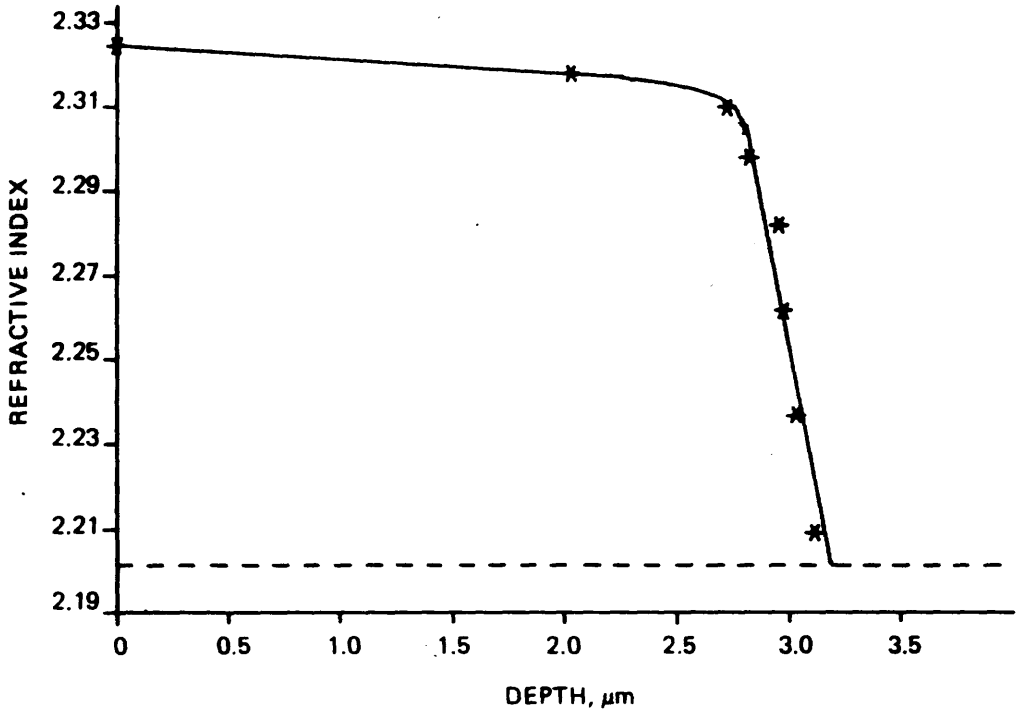

Figure 5.19 Refractive Index Profiles For An X-Cut Sample Exchanged For 18 Hours At 235°C (1% Dilution)

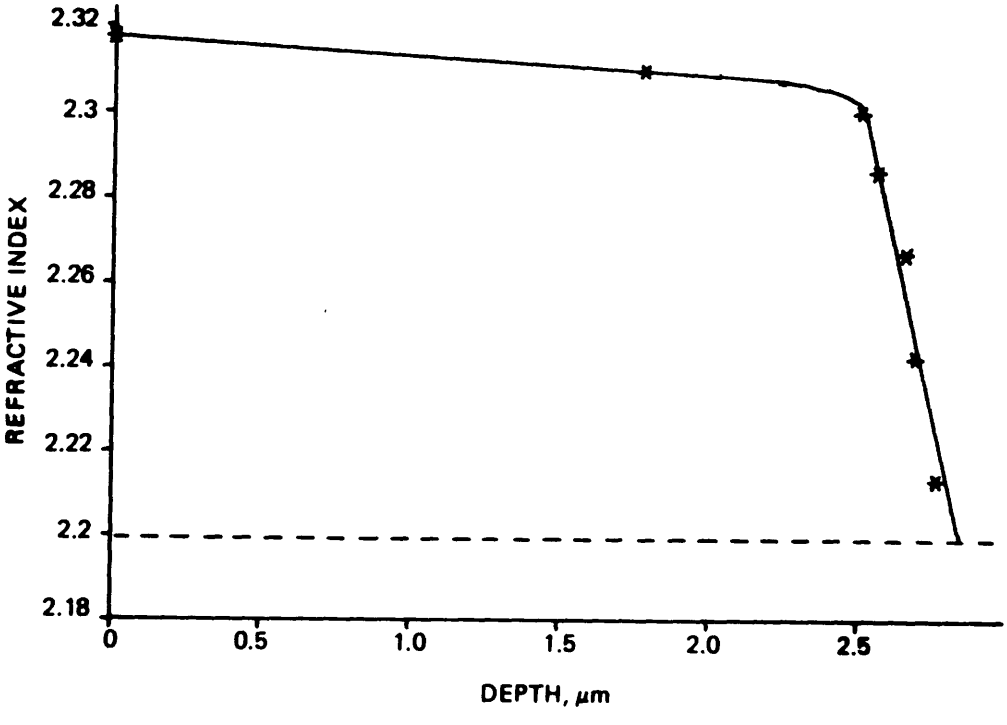

Figure 5.20 Refractive Index Profiles For A Z-Cut Sample Exchanged For 17.5 Hours At 235°C (0.5% Dilution)

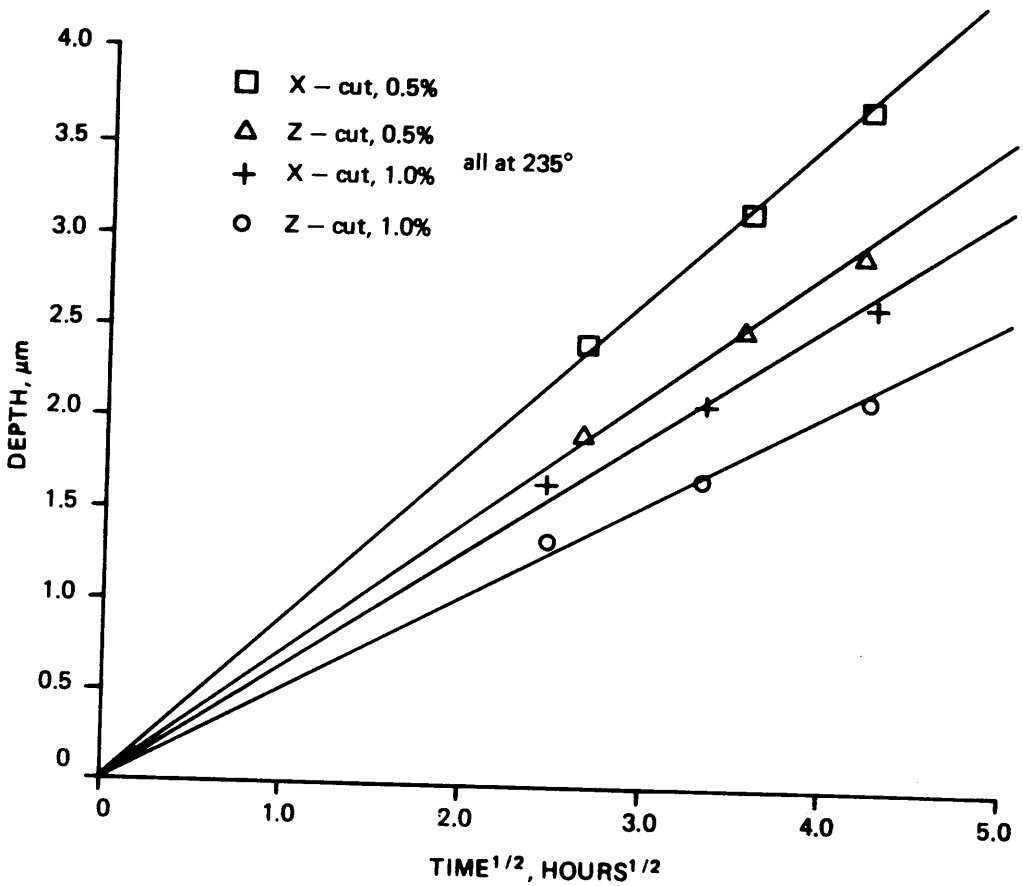

Figure 5.21 **Plots Of Diffusion Depth Versus √(Time)**

$LiNbO_3$ cut	Dilution %	D_c, μm^2/ hour (235°C– dilute melt)	D_d, μm^2/ hour (235°C– conc. melt)	$R = \frac{D_c}{D_d}$
X	0.5	0.201	0.997	4.96
	1.0	0.103	0.997	9.68
Z	0.5	0.129	0.397	3.08
	1.0	0.067	0.397	5.93

Table 5.8 Diffusion Coefficients Under Different Fabrication Conditions

a melt dilution of 0.5% and 1%, the process was slowed by 5 and 10 times respectively. As for PE waveguides formed in Z-cut $LiNbO_3$ using a melt dilution of 0.5% and 1.0%, the process was slowed by 3 and 6 times respectively. The above results implied that by proper dilution of the benzoic acid, there would be a better control over the optical characteristics of the fabricated waveguides.

After studying the diffusion properties of the DMPE process, the optical properties of the waveguides with a dilution of 0.5% were investigated, with exchange times between 1 and 18 hours and a temperature of 235°C. Figures 5.22 and 5.23 show sets of dispersion curves obtained theoretically (assuming a step index profile) and experimentally for both X- and Z-cut samples respectively. From these plots, the various cutoff depths for each waveguide mode in the range TE_0-TE_6 and TM_0-TM_5 can be estimated and are given in Table 5.9.

5.7.2 Waveguide Stability Study

The stability of measured n_{eff} versus time was studied, since previously discussed results on waveguides fabricated by pure benzoic acid indicate that a relaxation of n_{eff} occurs after fabrication. Figures 5.24 and 5.25 show the results of such a study, lasting about 10 months, for dilute melt X-cut and Z-cut $LiNbO_3$ waveguide samples respectively. As can be seen from the plots, there appears to be no measurable aging of n_{eff} with time. Thus, it can be deduced that the dilute melt process produces more stable waveguides when compared to the waveguides fabricated by concentrated benzoic acid melts (without thermal annealing).

5.7.3 Propagation Loss Measurements

Propagation loss measurements were made on various single-moded X-cut and Z-cut samples fabricated at different dilutions and temperatures.

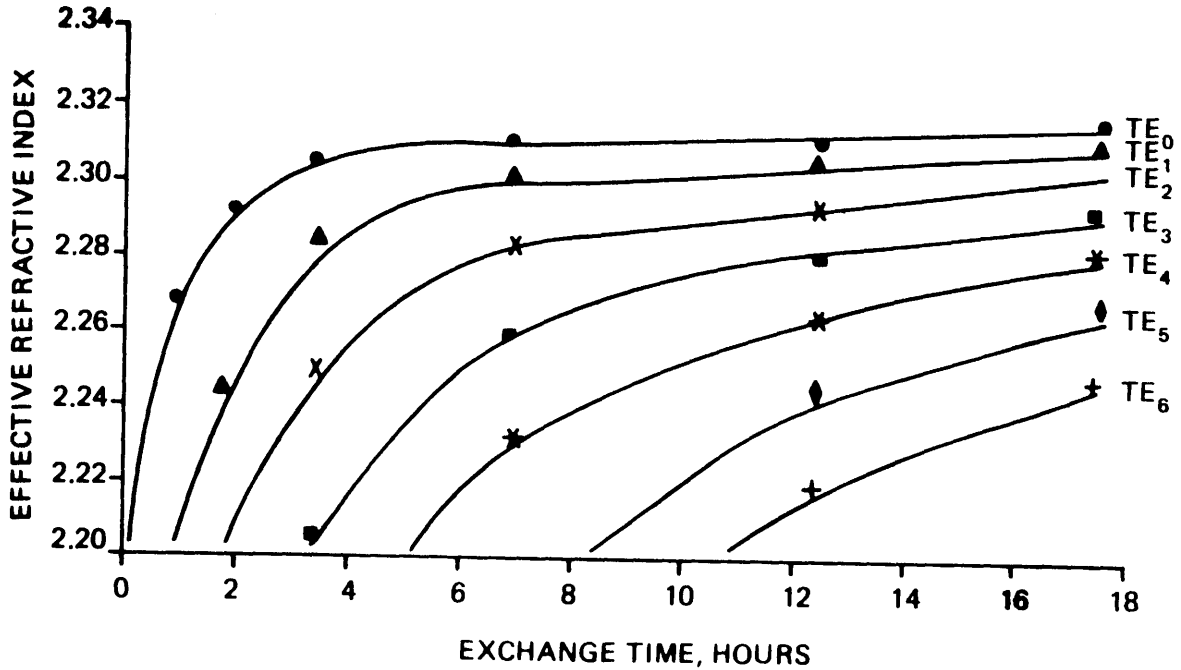

Figure 5.22 Plot Of Theoretical And Experimental TE Mode Spectra Of DMPE Slab Waveguides in X–Cut $LiNbO_3$ (0.5%,235°C)

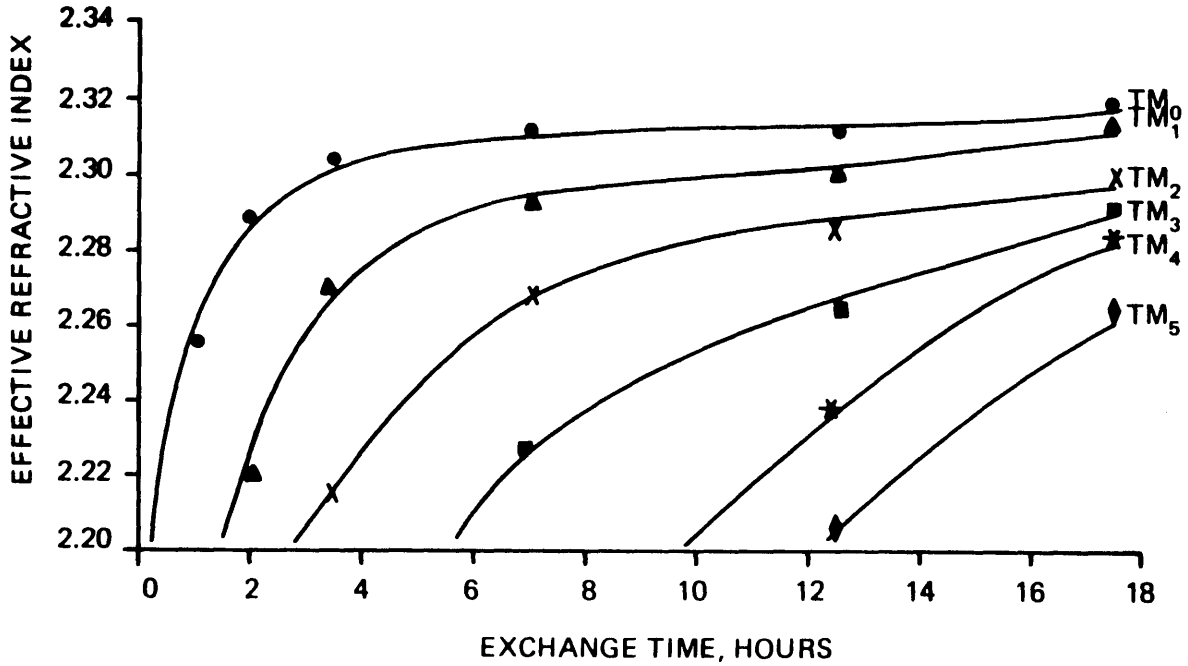

Figure 5.23 Plot Of Theoretical And Experimental TM Mode Spectra Of DMPE Slab Waveguides in Z–Cut $LiNbO_3$ (0.5%, 235°C)

ModeNumber	Cutoff Depth (μm)
0	0.40
1	0.87
2	1.23
3	1.64
4	2.04
5	2.60
6	2.96

(a)

ModeNumber	Cutoff Depth (μm)
0	0.34
1	0..88
2	1.20
3	1.71
4	2.26
5	2.54

(b)

Table 5.9 Table Of Cutoff Depth For Each TE/TM Mode
(a) For X-Cut DMPE $LiNbO_3$ (TE)
(b) For Z-Cut DMPE $LiNbO_3$ (TM)

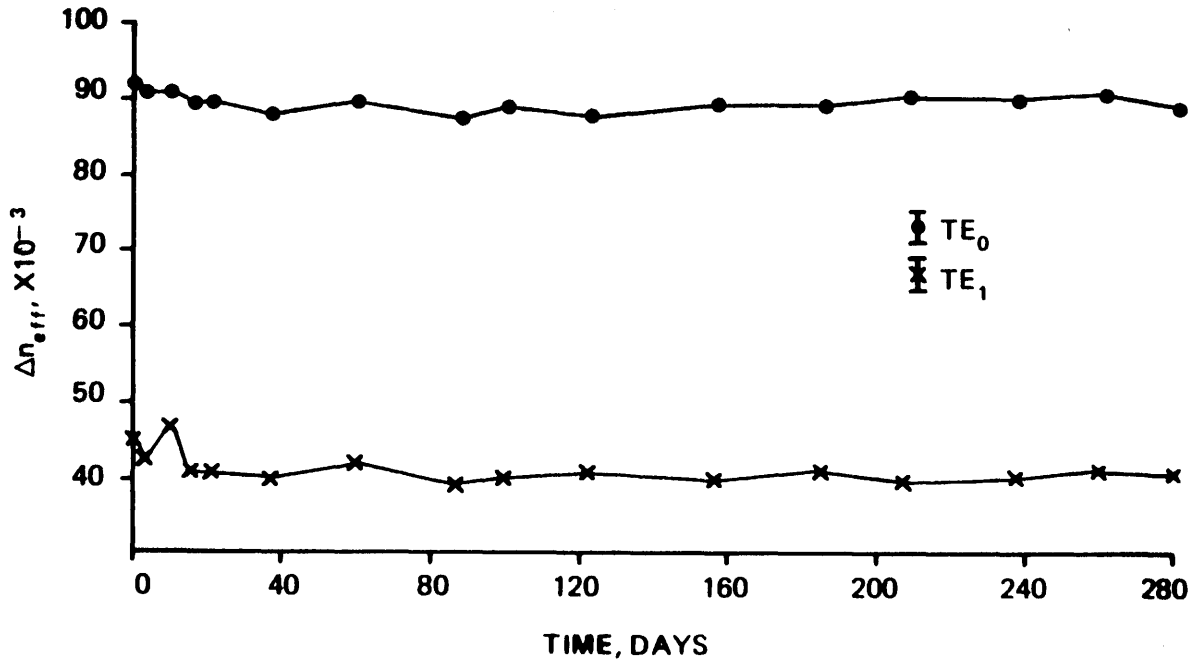

Figure 5.24 Long–Term Refractive Index Stability Of A Dilute Melt Proton Exchange Waveguide In X–Cut $LiNbO_3$ (10 months) (1% Dilution, 235°C, 2 Hours)

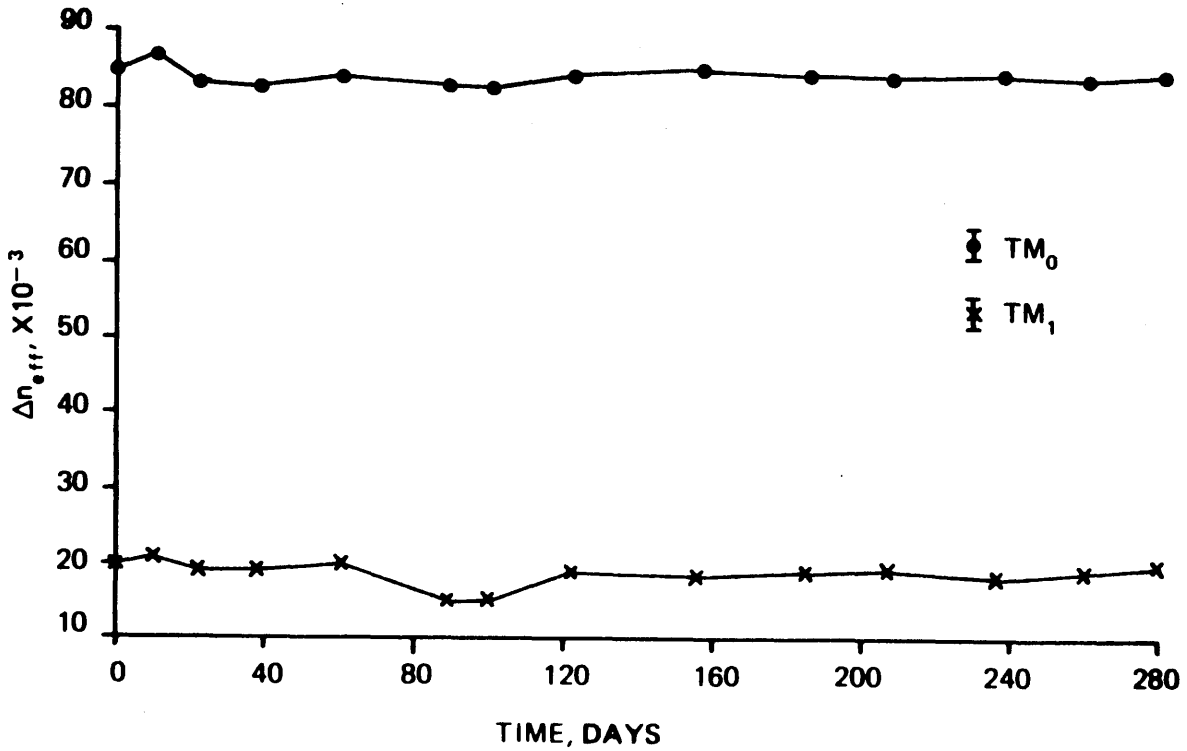

Figure 5.25 Long–Term Refractive Index Stability Of A Dilute Melt Proton Exchange Waveguide In Z–Cut $LiNbO_3$ (10 months) (1% Dilution, 235°C, 2 Hours)

As in Section 5.6.3, the absorption loss was assumed to be negligible, and hence the propagation loss was attributed completely to scattering loss. These measurements were obtained as described in Section 5.6.3, i.e. using the two prism-coupling technique and by imaging the scattered light of the propagating fundamental waveguide mode on a visible wavelength vidicon camera unit (Hamamatsu with C1000 control unit) and displaying the scattered light signal on a TV monitor.

It was found that the measured propagation losses range between 0.5 dB/cm and 1.0 db/cm at 632.8 nm, although these figures are of the same order as the measurement accuracy. The losses measured using the two prism-coupling technique in general were found to be slightly higher than those measured using the vidicon imaging system. Also, in general, the out-of-plane scatter losses of DMPE waveguides were low. This was experienced directly when, in some situations, it was impossible to monitor the scattered laser light streak. In these cases, it is believed that the losses were definitely less than 0.5 dB/cm. However, no clear relationship between propagation and fabrication conditions could be established. The only conclusion that could be drawn from this study was that the measured losses for the X-cut samples appeared to be slightly lower than for the Z-cut samples (Table 5.10). Hence to properly measure propagation losses of DMPE waveguides, more accurate loss measurement techniques will have to be devised. Due to limitation in research time, no attempts were made in this area.

5.7.4 Optical Damage Effects

No optical damage effects were observed in dilute melt PE X-cut $LiNbO_3$ slab waveguides using a 5 mW HeNe laser operating at 632.8 nm. The estimated maximum optical power density propagated by the above waveguides (typical depth of waveguides are in the range 0.85 μm to .94 μm) at 632.8 nm was about 40 kW/cm^2. Similar optical damage studies were

Fabrication Conditions	Measured Propagation Loss (dB/cm)
5 minutes, 0.5%	1.0
6 minutes, 0.5%	0.7
7 minutes, 0.5%	0.9
10 minutes, 1.0%	0.8
12 minutes, 1.0%	0.8
14 minutes, 1.0%	0.5

(a) 235°C

Fabrication Conditions	Measured Propagation Loss (dB/cm)
7 minutes, 0.5%	1.8
9 minutes, 0.5%	1.5
11 minutes, 0.5%	0.8
18 minutes, 1.0%	1.5
20 minutes, 1.0%	1.2
22 minutes, 1.0%	0.9

(b) 235°C

Table 5.10 Summary Of Out-Of-Plane Loss Measurements
(a) For DMPE X-Cut $LiNbO_3$
(b) For DMPE Z-Cut $LiNbO_3$

carried out in X-cut Ti:LiNbO3 slab waveguides and they were found to damage easily at the same optical power density of 40 kW/cm^2. Further experiments using an argon-ion laser operating at 514.5 nm were carried out using the same waveguides that were studied at 633 nm. It was found again that no optical damage effects were observed up to a power density of 35.2 kW/cm^2 (Figure 5.26). In both experiments, the same laser beam width was used (1.5 mm). Also, a lock-in amplifier was employed to reduce possible effects caused by external perturbation on the photodetector. The results obtained here were comparable to those reported by Jackel et al [5.46], who reported no optical damage effects at average optical power densities of 10 kW/cm^2 at a wavelength of 620 nm.

5.7.5 Annealing Experiments

Some annealing experiments were carried out for both X- and Z-cut samples. As an example of this study, the mode angles of the two DMPE samples were measured prior to annealing for 5 hours, at each of 100°C, 200°C, and 280°C. The mode angles were remeasured for each case and the results are summarized in Table 5.11. The results indicate that the waveguides fabricated were unaffected by annealing temperatures of less than 200°C. The general conclusion of this study is that the refractive index of DMPE waveguides is not significantly modified provided that they are not placed in an environment with a temperature greater than the fabrication melt temperature.

5.7.6 In-Plane and Intermodal Scattering Measurements

The in-plane scattering of the DMPE waveguides was again studied using a scanning photodetector and a lock-in amplifier arrangement [5.42]. For all the mode line scans, the photodetector (with a 5 μm slit) was placed at a distance of 40 cm away from the output rutile prism. The distance between

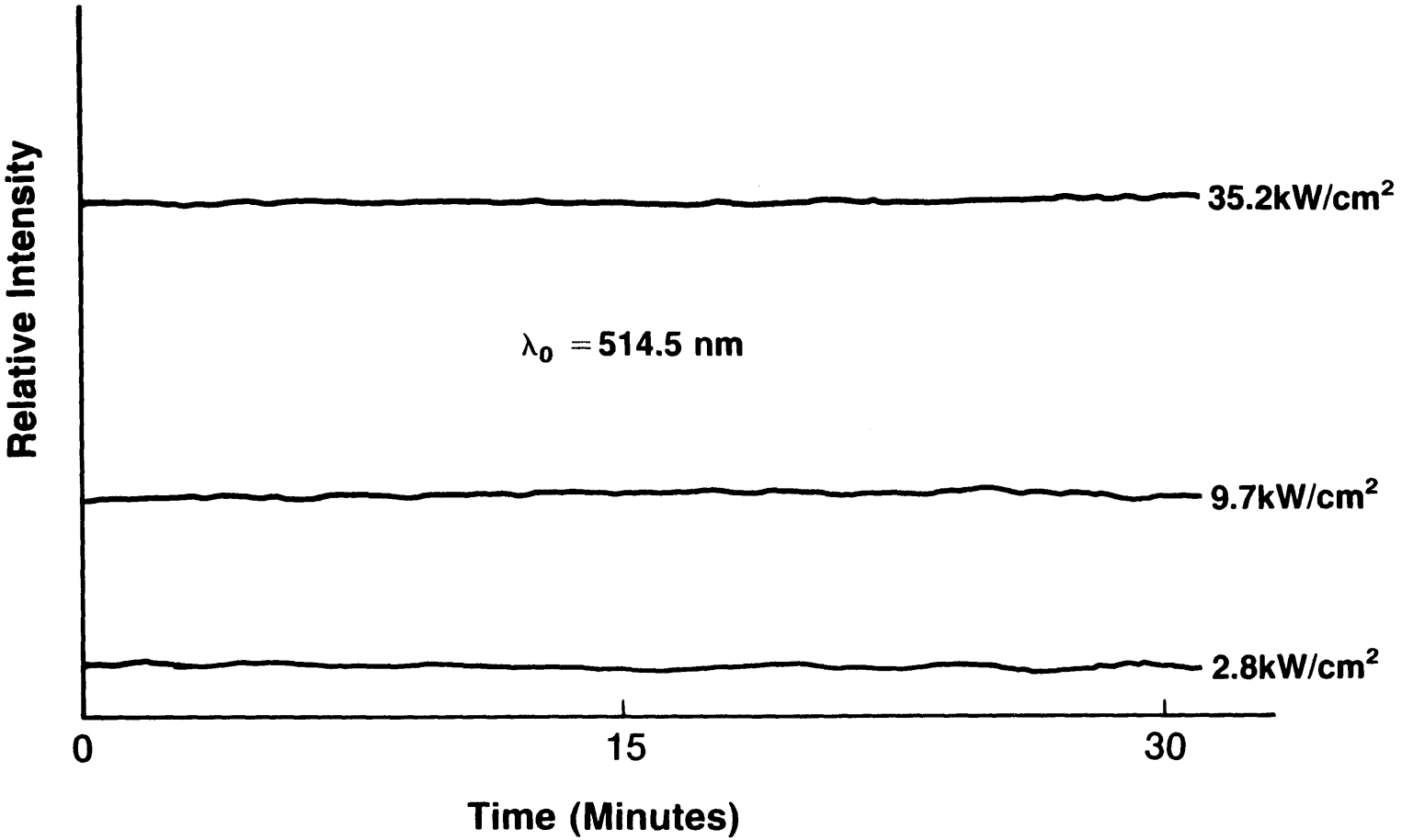

Figure 5.26 Optical Damage Study Of A Dilute Melt Proton Exchange Waveguide in X–Cut $LiNbO_3$ At $\lambda = 514.5$ nm

		Annealing Experiments			
Sample	Mode	Initial ^{n}eff	5 hours @ 100°C	5 hours @ 200°C	5 hours @ 280°C
ANX1 (X-cut) 4.5 hours @ 240°C	TE_0	2.292	2.290	2.291	2.286
	TE_1	2.244	2.242	2.243	-
ANZ1 (Z-cut) 4.5 hours @ 245°C	TM_0	2.262	2.262	2.261	2.202
	TM_1	2.202	2.202	2.202	-

Table 5.11 Annealing Effects On X– And Z–Cut DMPE $LiNbO_3$ Samples

the input and output prisms was always 10 mm. Results obtained by measuring waveguides formed under different fabrication conditions (i.e., 0.5% or 1.0% dilution and 235°C or 245°C) indicated that the scattering intensity levels were generally between 23 dB and 30 dB for a scattering angle of 0.5° in the waveguides. The best measured in-plane scatter value to date is lower than -35 dB at 0.5° and this is shown in Figure 5.27. Figures 5.28(a) to (d) illustrate four plots of each of the mode-lines of a typical waveguide fabricated in X-cut $LiNbO_3$ for 6 hours at 235°C with a dilution of 1.0%. In general, there is no observed improvement in the measured in-plane scatter loss values with changes in the percentage dilution and temperature of fabrication. This is best described by Table 5.12 and Table 5.13 which show measured in-plane scatter levels of X-cut and Z-cut substrate fabricated in a 1.0% diluted melt bath at 235°C. Here the only variation is the time of exchange.

In the case of intermodal scattering levels obtained on DMPE waveguides, it was found that in general the waveguides have between 10 and 18 dB lower levels than those obtained for waveguides made by CMPE. In a number of cases, especially DMPE waveguides formed on X-cut substrates, the output m-lines, as seen by the human eye, consisted of just a very bright central m-line spot for a single-moded DMPE waveguide. This therefore again indicates the high quality of the DMPE waveguides.

5.7.7 Electro-Optic Activity Study using Mach-Zehnder Interferometers

A number of Mach-Zehnder interferometers (MZI) were fabricated in X-cut $LiNbO_3$ using dilute (1.0%) benzoic acid melts at 235°C for exchange times ranging from 15 minutes to 45 minutes. The detailed fabrication procedure for the device has been described in Section 4.3.4. The Mach-Zehnder interferometers had a waveguide width of 4 μm and an active interaction length of 8 mm. Figure 5.29 shows the MZI used in this study.

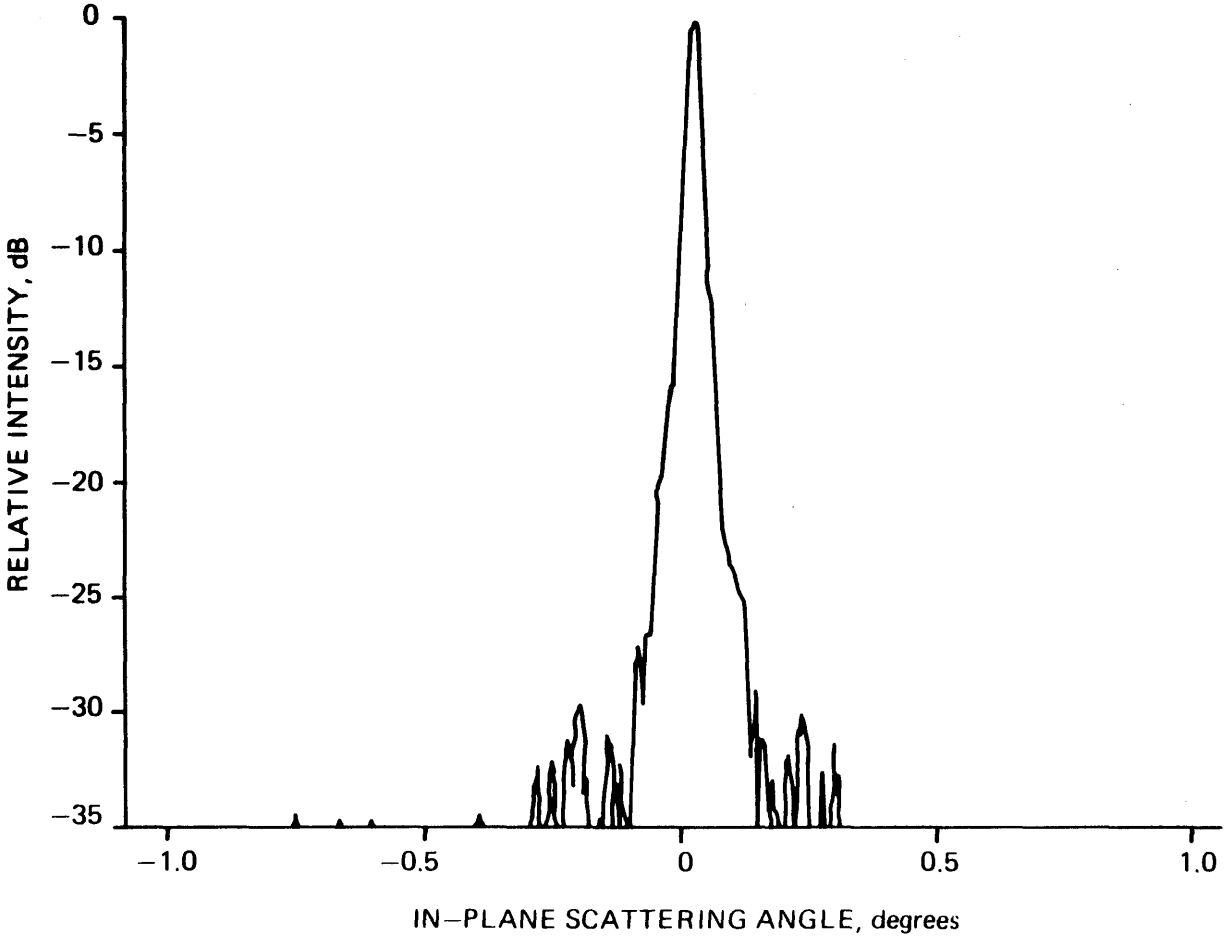

Figure 5.27 **In–Plane Scatter Plot Of A X–Cut DMPE Slab Optical Waveguide (At λ_o= 632.8 nm, 1% Dilution, 4 Hours At 245°C)**

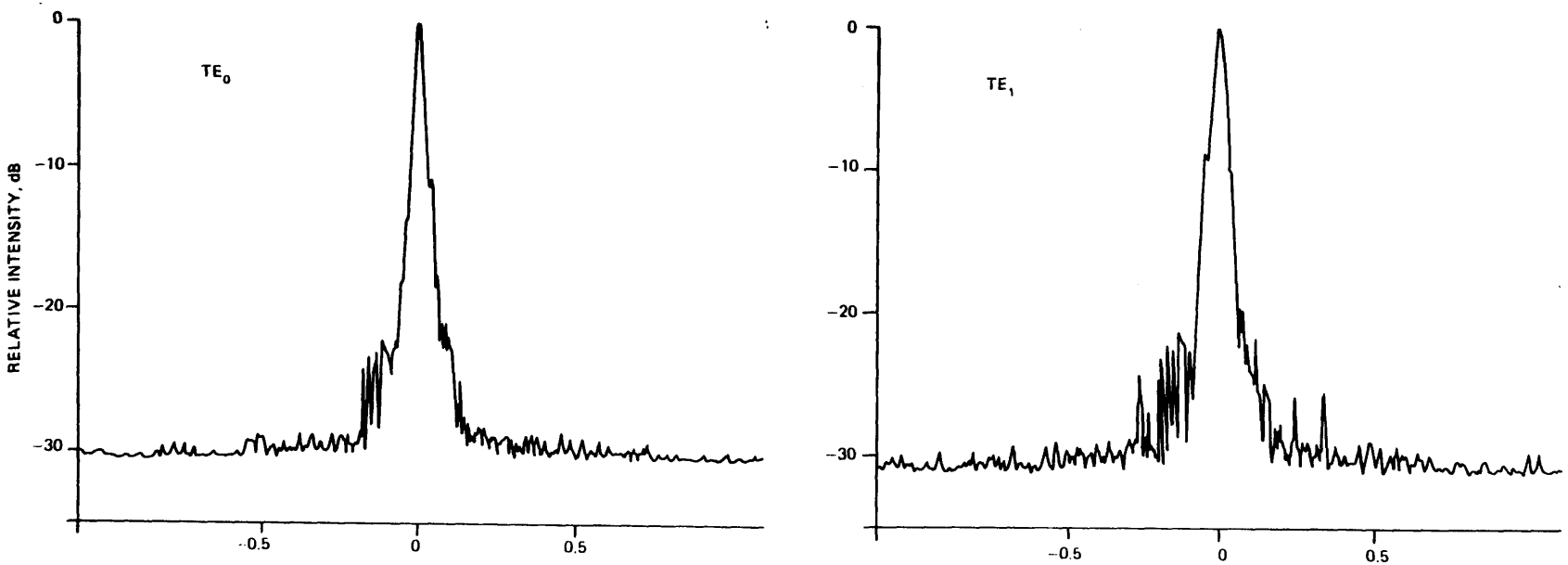

Figure 5.28 (a)–(b) Typical In–Plane Scatter Plots Of A DMPE Slab Waveguide at λ_o= 632.8 nm (1.5%, 6 Hours At 235°C)

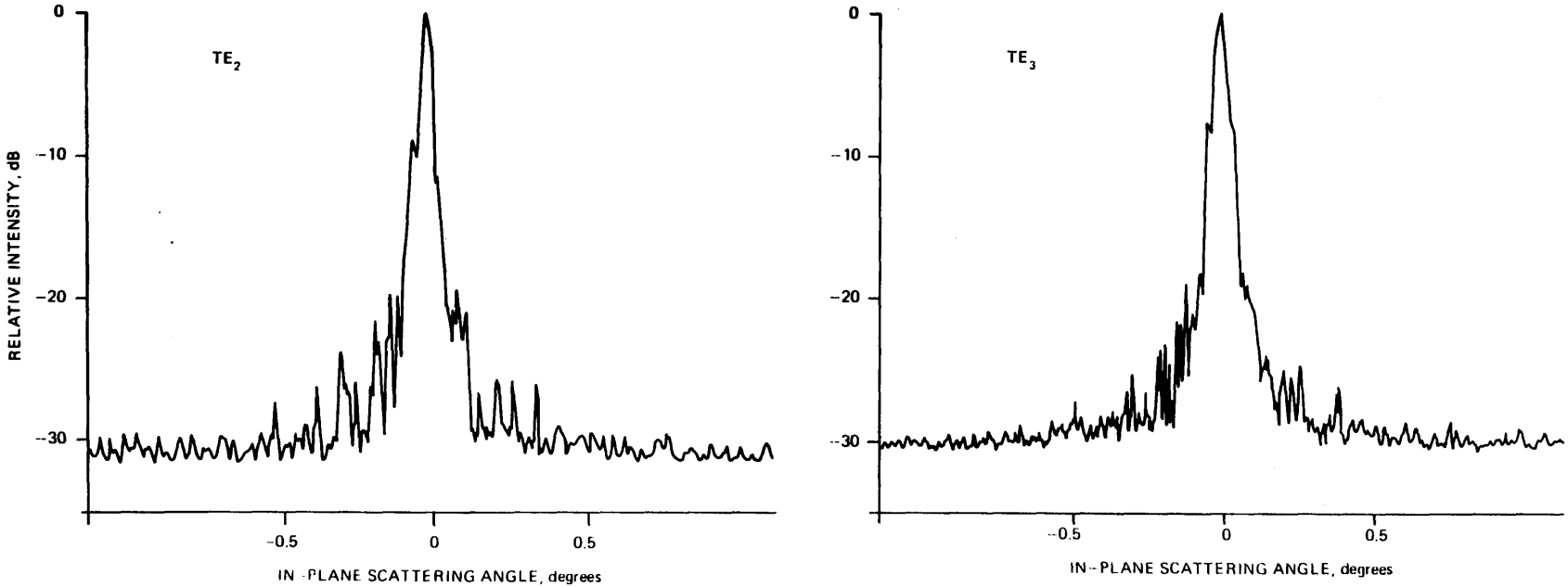

Figure 5.28 **(c)–(d) Typical In–Plane Scatter Plots Of A DMPE Slab Waveguide at λ_0= 632.8 nm (1.5%, 6 Hours At 235°C)**

Exchange time, hours	TE_0, dB	TE_1, dB	TE_2, dB	TE_3, dB	TE_4, dB	TE_5, dB
18.0	22	21	23	29	26	25
11.0	30	30	29	29	27	–
6.0	29	29	28	28	–	–

Table 5.12 Measured In-Plane Scattering Levels Of X-Cut DMPE Waveguides (In-Plane Angle= 0.5°, 235°C, λ = 632.8 nm)

Exchange time, hours	TM_0, dB	TM_1, dB	TM_2, dB	TM_3, dB	TM_4, dB
18.0	28	27	23	21	18
11.0	21	27	28	30	–
6.0	27	24	27	–	–

Table 5.13 Measure In-Plane Scattering Levels Of Z-Cut DMPE Waveguides (In-Plane Angle= 0.5°, 235°C, λ = 632.8 nm)

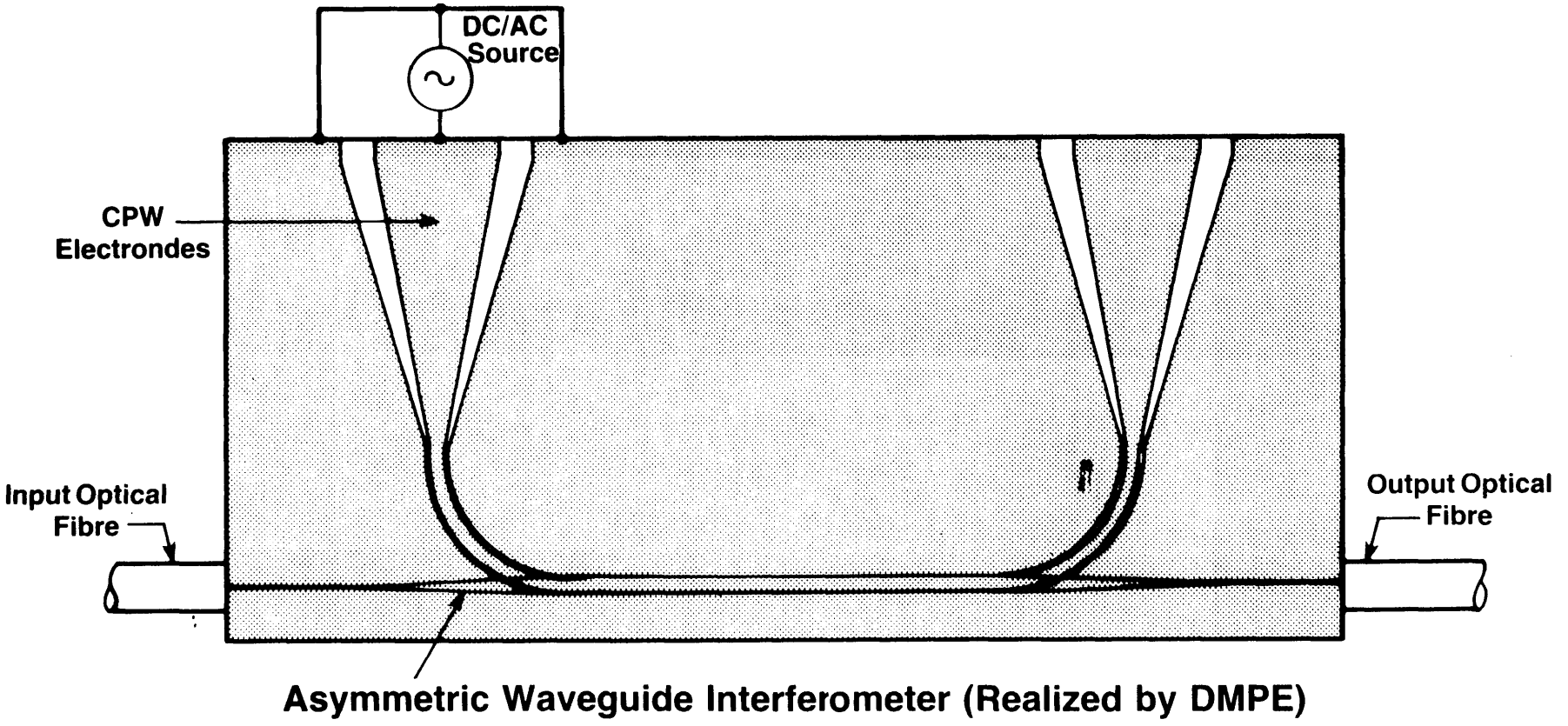

Figure 5.29 Schematic Of The PE IO Mach–Zehnder Interferometer

The design of the travelling-wave device was carried out by Parsons [5.47]. Previous devices made from this mask with titanium indiffused waveguides were found to have a measured V_π voltage requirement of 1.8 volts at λ_0= 830 nm [5.48].

Figure 5.30 shows a schematic of the experimental arrangement used to measure the V_π of the fabricated DMPE MZI. The dilute melt proton exchange devices were tested and the measured V_π voltages were between 1.7 volts and 2.5 volts. Figure 5.31 shows an oscillogram of such a result. These results suggested that the electro-optic activity in dilute devices was preserved almost completely. The reason for the variations in the measured V_π voltages in some MZI devices was found to be due to misalignment of the electrode patterns with respect to the MZ waveguide patterns due to the difficulty in the alignment process with a buffer layer over the waveguide. Some unintentional annealing of the waveguides was almost certainly performed, since in the process of realising the dilute melt devices they underwent a stage which involved the deposition of SiO_2 by a pyrolitic chemical vapour deposition (CVD) technique. The temperature of the CVD process was 400°C and the samples were in the reaction chamber for 15 minutes. This resulted in a 200 nm thick SiO_2 buffer layer. Inevitably, this stage was bound to have some effect on the waveguide mode structure. In view of this, linear optical field intensity plots were obtained using a computer interfaced vidicon camera system. The measured 1/e width and depth of the MZI was found to be 5.3 μm and 3.4 μm respectively (Figure 5.32) which indicated that the CVD process had a significant effect on the mode profiles of the fabricated stripe waveguides. The above measured values were similar to those obtained for the titanium indiffused MZI [5.48].

Hence by using the DMPE process of waveguide formation and the pyrolitic CVD technique of SiO_2 deposition, electrooptically active devices in $LiNbO_3$ with good performance can be successfully realised. However it must

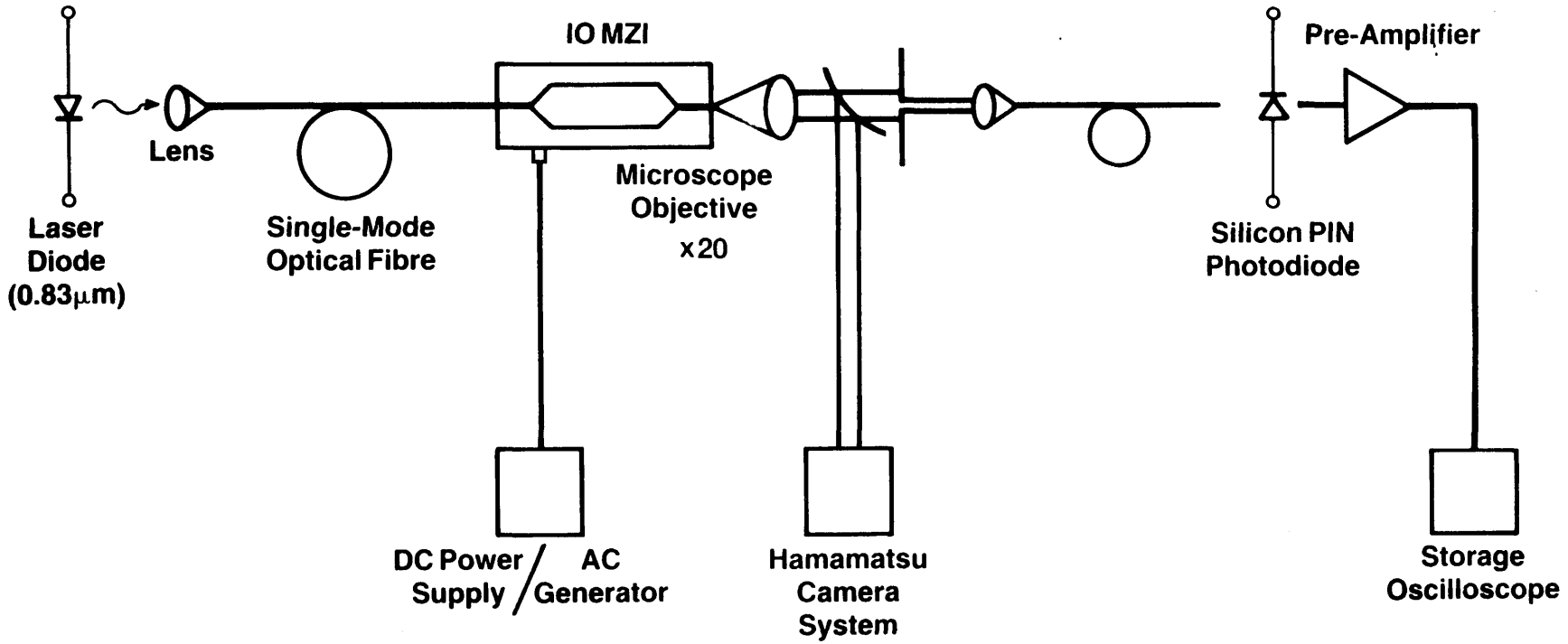

Figure 5.30 Experimental Arrangement For Evaluating The IO Mach–Zehnder Interferometers

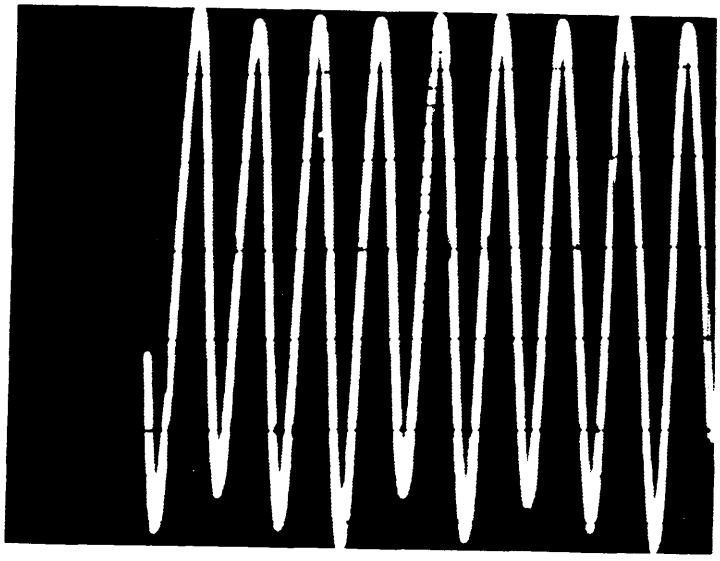

Figure 5.31 DC Response (Y-axis: 0-100%) Plotted Against Applied Voltage (X-Axis) For An IO MZI Realised By DMPE (1% Dilution, 0.75 Hours At 245°C) Measured V_{π} = 1.7 Volts At λ = 830 nm

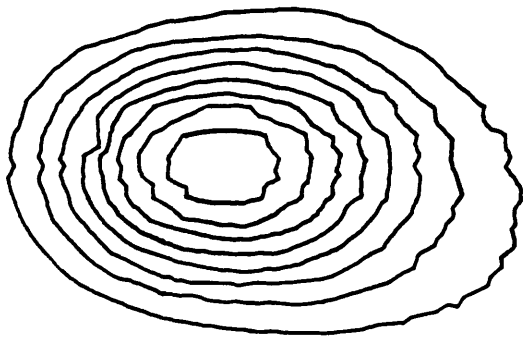

Measured $^{1}/_{e}$ width = 5.3 μm
Measured $^{1}/_{e}$ depth = 3.4 μm

Figure 5.32 Linear Field Intensity Plot For An IO MZI Realised By DMPE (1% Dilution, 0.75 Hours At 245°C) Measured V_{π} = 1.7 Volts At λ = 830 nm

be pointed out that due to the large Δn change after annealing at 400° C for 15 minutes in the CVD reactor, it was found that the repeatable realisation of single-moded stripe waveguides was very difficult. In view of this the author has embarked on the realisation of PE MZI devices using $LiTaO_3$ [5.49]. It was found that the realisation of single-moded waveguides in PE X-cut $LiTaO_3$ at the same temperature of 235°C was easier to achieve since Δn was equal to 0.02. This activity is not reported here since it is beyond the main aim of this thesis.

5.8 Summary

Results of the measured slab Ti:$LiNbO_3$ waveguides, used as control samples in all titanium deposition runs for the eventual realisation of optical phase modulators, indicated that there were small variations in the runs with the same measured initial titanium thicknesses. However the 3-9% variations in the Δn_{eff} results did not merit any further investigations.

The experimental results for the slab PE waveguides realised by using concentrated benzoic acid melts in X- and Z-cut $LiNbO_3$ can be summarised by the following points:-

(1) The refractive index profiles of all the PE waveguides fabricated were step-like,

(2) The measured n_{eff} values were found to decrease with time (over a period of 7 months),

(3) The Δn was found to be about 0.12 and 0.096 at 632.8 nm and 1150 nm respectively for both cuts,

(4) The general relationship of diffusion depth with $(time)^{0.5}$ and temperature was established to be linear (Equations 5.47 and 5.48),

(5) Intermodal scattering was observed and measured for the PE waveguides and found to be at best comparable to the results reported for Ti:$LiNbO_3$,

(6) The measured propagation losses for single-moded X-cut and Z-cut PE waveguides were between 1.3 and 2.8 dB/cm and between 2.4 and 4.8 dB/cm respectively, and

(7) In-plane scattering levels of 10-17 dB for a scattering angle of 0.5° in the waveguides were measured. These results indicated that the PE waveguides were no better than those formed by titanium indiffusion for similar crystal cut.

The results from the optical properties of proton exchange waveguides fabricated by dilute (0.5% or 1.0%) benzoic acid melts indicated the following:

(1) The refractive index profile was still found to be step like with a Δn of 0.12 measured at 632.8 nm for both cuts,

(2) The n_{eff} values were measured to be stable over a period of 10 months (i.e. the monitoring period),

(3) The diffusion coefficients for the DMPE process were three to nine times smaller than those for the concentrated PE process depending on the cut of the crystal (i.e. X- or Z-cut),

(3) Annealing experiments suggested that the waveguides were unaffected by temperatures as high as 200° C over a period of 10 hours,

(4) The measured propagation losses of the DMPE waveguides were between 0.5 dB and 1.0 dB and in some waveguides, especially those realised in X-cut substrates, the propagation losses were so low as to be impossible to measure with the present equipment,

(5) In-plane scattering results were obtained and the measured values indicated that there was a 10 dB to 20 dB improvement over those realised by concentrated PE,

(6) The intermodal scattering levels were about 10-18 dB lower than those measured for CMPE waveguides. In some single-moded DMPE

waveguides, especially in X-cut substrates, only a bright spot was visible as the output m-line.

As can be seen from the above comparisons of waveguides formed by concentrated PE (CMPE) and DMPE, it is definitely desirable to have waveguides realised by DMPE. However, due to the limitation in time and effort, no optical phase modulators were realised by DMPE.

REFERENCES

[5.1] H. Kogelnik and V. Ramaswamy, "Scaling Rules For Thin Film Optical Waveguides", Appl. Opt., Vol. 13, No. 8, pp 1325-1350, August 1974.

[5.2] J.M. White and P.F. Heidrich, "Optical Waveguide Refractive Index Profiles Determined From Measurement of Mode Indices: A Simple Analysis", Appl. Opt., Vol. 15, No. 1, pp151-155, January 1976.

[5.3] J. Finak, H. Jerominek, Z. Opilski, and K. Wojtala, "Planar Diffusion Glass Waveguides Obtained By Immersing in Molten KNO_3", Optica Applicata, Vol. XII, No. 1, pp 11-17, 1982.

[5.4] E.A.J. Marcatili, "Dielectric Rectangular Waveguide and Directional Coupler for Integrated Optics", B.S.T.J., Vol. 48, No. 7, pp 2071-2102, September 1969.

[5.5] R.M. Knox and P.P. Toulios, "Integrated Circuits For The Millimetre Through Optical Frequency Range", in J. Fox (Ed.) "Proc. of the MRI Symposium on Submillimetre Waves", Polytech Press, Brooklyn, NY, pp 497-516, 1970.

[5.6] P.K. Tien, R. Ulrich, and R.J. Martin, "Modes of Propagating Light Waves in Thin Deposited Semiconductor Films", Appl. Phys. Lett., Vol. 14, No. 9, pp 291-294, 1 May 1969.

[5.7] P.K. Tien and R. Ulrich, "Theory of Prism-Film Coupler and Thin-Film Light Guides", J. Opt. Soc. Amer., Vol. 60, No. 10, pp 1325-1337, October 1970.

[5.8] W. Sohler and H. Suche, "Efficient Prism-Coupling into Titanium Diffused Lithium Niobate Optical Waveguides", Wave Electron., Vol. 3, pp 269-275, 1979.

[5.9] W.K. Burns and G.B. Hocker, "Endfire Coupling Between Optical Fibres and Diffused Channel Waveguides", Appl. Opt., Vol. 16, No. 8, pp 2048-2050, August 1977.

[5.10] H.P. Hsu, A.F. Milton, and W.K. Burns, "Multiple Fibre End Fire Coupling with Single-Mode Channel Waveguides", Appl. Phys. Lett., Vol. 33, No. 7, pp 603-605, 1 October 1978.

[5.11] P.K. Tien, "Light Waves in Thin Films and Integrated Optics", Appl. Opt., Vol. 10, No. 11, pp 2395-2413, November 1971.

[5.12] D. Marcuse, "Theory of Dielectric Optical Waveguides", Academic Press, NY, 1974.

[5.13] M.K. Barnoski (Ed.), "Introduction to Integrated Optics", Plenum Press, NY, 1974.

[5.14] M.J. Adams, "An Introduction to Optical Waveguides", John Wiley & Sons, Chichester, 1981.

[5.15] H.K.V.Lotsch, "Reflection and Refraction of a Beam of Light at a Plane Interface", J. Opt. Soc. Amer., Vol. 58, No. 4, pp 551-561, April 1968.

[5.16] E.M. Conwell, "Modes in Optical Waveguides Formed by Diffusion", Appl. Phys. Lett., Vol. 23, No. 6, pp 328-329, 15 September 1973.

[5.17] P.K. Tien, S. Riva-Sanseverino, R.J. Martin, A.A. Ballman, and H. Brown, "Optical Waveguide Modes in Single-Crystalline $LiNbO_3$-$LiTaO_3$ Solid-Solution Films", Appl. Phys. Lett., Vol. 24, No. 10, pp 503-506, 15 May 1974.

[5.18] E.M. Conwell, "Modes in Anisotropic Optical Waveguides Formed by Diffusion", IEEE J. Quantum Electron., Vol. QE-10, No. 8, pp 608-612, August 1974.

[5.19] D. Marcuse, "TE Modes of Graded-Index Slab Waveguides", IEEE J. Quantum Electron., Vol. QE-9, No. 10, pp 1000-1006, October 1973.

[5.20] J.G. Gallagher, "Silver Ion-Exchanged Waveguides for Integrated Optics", PhD Thesis, University of Glasgow, Dept. of Electronics & Electrical Engineering, 1977.

[5.21] C.A. Millar, "Evanescent Field Coupling of Thin Film and Fibre Optical Waveguides", PhD Thesis, University of Glasgow, Dept. of Electronics & Electrical Engineering, October 1976.

[5.22] J.E. Goell, "A Circular-Harmonic Computer Analysis of Rectangular Dielectric Waveguides", BSTJ, Vol. 48, No. 7, pp 2133-2160, September 1969.

[5.23] G.B. Hocker and W.K. Burns, "Mode Dispersion in Diffused Channel Waveguides by the Effective Index Method", Appl. Opt., Vol. 16, No. 1, pp 113-118, January 1977.

[5.24] D.N. MacFadyen, "Components for Gallium Arsenide Integrated Optics Fabricated By Wet Chemical Etching", PhD Thesis, University of Glasgow, Dept. of Electronics & Electrical Engineering, December 1980.

[5.25] M.L. Dakss, L. Kuhn, P.F. Heidrich, and B.A. Scott, "Grating Coupler for Efficient Excitation of Optical Guided Waves in Thin Films", Appl. Phys. Lett., Vol. 16, No. 12, pp 523-525, 15 June 1970.

[5.26] D. Sarid, "High Efficiency Input-Output Prism Waveguide Coupler: An Analysis", Appl. Opt., Vol. 18, No. 17, pp 2921-2926, 1 September 1979.

[5.27] M.W. Ribarsky, "Titanium Dioxide (TiO_2) (Rutile)", in Handbook of Optical Constants of Solids, E. D. Palik (Ed.), pp 795-804, Academic Press, Inc., 1985.

[5.28] A.D. McLachlan, "Theoretical and Experimental Investigations of Titanium Diffused Lithium Niobate Optical Waveguides", PhD Thesis, University of Glasgow, Dept. of Electronics & Electrical Engineering, January 1981.

[5.29] I.P. Kaminow and L.W. Stulz, "Loss Measurements in Diffused $LiNbO_3$ Waveguides", Presented in Topical Meeting on Integrated & Guided-Wave Optics, pp WA1-1 to WA1-4, January 1978.

[5.30] I.P. Kaminow and L.W. Stulz, "Loss in Cleaved Ti-Diffused $LiNbO_3$ Waveguides", Appl. Phys. Lett., Vol. 33, No. 1, pp 62-64, 1 July 1978.

[5.31] A.C.G. Nutt, "Techniques for Fabricating Integrated Optical Components on Lithium Niobate", PhD Thesis, University of Glasgow, Dept. of Electronics & Electrical Engineering, October 1985.

[5.32] A. Yi-Yan, "Index Instabilities in Proton-Exchanged $LiNbO_3$ Waveguides", Appl. Phys. Lett., Vol. 42, No. 8, pp 633-635, 15 April 1983.

[5.33] J. Crank, "The Mathematics of Diffusion", Second Edition, Clarendon Press, Oxford, 1979.

[5.34] K.H. Haegele and R. Ulrich, "Pyroelectric Loss Measurement in $LiNbO_3$:Ti Guides", Opt. Lett., Vol. 4, No. 2, pp 60-62, February 1979.

[5.35] S.D. Allen, E. Garmire, M. Bass, and B. Packer, "Calorimetric Measurement of $LiNbO_3$ Waveguide Absorption Losses", Appl. Phys. Lett., Vol. 34, No. 7, pp 435-437, 1 April 1979.

[5.36] Y. Okamura, S. Yoshinaka, and S. Yamamoto, "Measuring Mode Propagation Losses of Integrated Optical Waveguides: A Simple Method", Appl. Opt., Vol. 22, No. 23, pp 3892-3894, 1 December 1983.

[5.37] J.L. Jackel, C.E. Rice, and J.J. Veselka, "Proton Exchange For High-Index Waveguides in $LiNbO_3$", Appl. Phys. Lett., Vol. 41, No. 7, pp 607-608, 1 October 1982.

[5.38] A. Loni, R.M. De La Rue, and J.M. Winfield, "Very Low-Loss Proton-Exchanged $LiNbO_3$ Waveguides With A Substantially Restored Electro-Optic Effect", Presented in IGWO'88, Santa Fe, pp MD3-1 to MD3-4, 28-30 March 1988.

[5.39] P.G. Suchoski, M.M. Abou el leil, T.K. Findakly, and F.J. Leonberger, "Low-Loss Proton-Exchanged $LiNbO_3$ Waveguides With No Electrooptic Degradation", Presented in IGWO'88, Santa Fe, pp MD4-1 to MD4-4, 28-30 March 1988.

[5.40] H.P. Weber, F.A. Dunn, and W.N. Leibolt, " Loss Measurements in Thin-Film Optical Waveguides", Appl. Opt.., Vol. 12, No. 4, pp 755-757, April 1973.

[5.41] Y.H. Won, P.C. Jaussaud, and G.H. Chartier, "Three-Prism Loss Measurements of Optical Waveguides", Appl. Phys. Lett., Vol. 37, No. 3, pp 269-271, 1 August 1980.

[5.42] M.N. Armenise, M. De Sario, C. Canali, P. Franzosi, J. Singh, R.H. Hutchins, and R.M. De La Rue, "In-Plane Scattering in Titanium-Diffused $LiNbO_3$ Optical Waveguides", Appl. Phys. Lett., Vol. 45, No. 4, pp 326-328, 15 August 1984.

[5.43] M.N. Armenise, C. Canali, M. De Sario, P. Franzosi, J. Singh, R.H. Hutchins, and R.M. De La Rue, "Dependence of In-Plane Scattering Levels in Ti:$LiNbO_3$ Optical Waveguides on Diffusion Time", IEE Proc., Vol. 131, Pt. H, No. 5, pp 295-298, October 1984.

[5.44] M.K. Barnoski, B.U. Chen, T.R. Joseph, J.Y.M. Lee, and O.G. Ramer, "Integrated-Optic Spectrum Analyzer", IEEE Trans. on Circuits and Systems, Vol. CAS-26, No. 12, pp 1113-1124, December 1979.

[5.45] J. Singh, "Studies Concerning The Dynamic Range of The Integrated Optic Spectrum Analyzer", PhD Thesis, University of Glasgow, Dept. of Electronics & Electrical Engineering, March 1983.

[5.46] J.L. Jackel, A.M. Glass, G.E. Peterson, C.E. Rice, D.H. Olson, and J.J. Veselka, "Damage-Resistant $LiNbO_3$ Waveguides", J. Appl. Phys., Vol. 55, No. 1, pp 269-270, 1 January 1984.

[5.47] N.J. Parsons, Private Communication, GEC Research Ltd., Marconi Research Centre, 1985.

[5.48] A.C. O'Donnell, K.K. Wong, and N.J. Parsons, "Efficient and Wideband Integrated Optical Modulators With High Damage Threshold", Presented in IEE Colloquium on "Optical Control & Generation of Microwave Signals", London, 14 January 1986.

[5.49] K.K. Wong, A.C. O'Donnell, I.A. Wood, and N.J. Parsons, "Integrated Optical Mach-Zehnder Interferometers in $LiTaO_3$ Fabricated By Proton Exchange", Proc. of the Fourth European Conf. on Integrated Optics, Glasgow, Scotland, pp 123-126, 11-13 May 1987.

CHAPTER 6 EXPERIMENTAL RESULTS OF THE OPTICAL SERRODYNE FREQUENCY-TRANSLATORS

6.1 Introduction 189

6.2 Design of the Optical Phase-Modulators 189

6.2.1 Introduction 189
6.2.2 The Electro-Optic Effect 190
6.2.3 Theoretical Performance of q Lumped Electrode Type Optical Phase-Modulator 194
6.2.3.1 Phase-Modulator Voltage Requirements 194
6.2.3.2 Design of Lumped Electrodes for Phase-Modulator 196
6.2.4 Choice of Single-Mode Stripe Optical Waveguides 199
6.2.5 Design of Electrode Structures 200

6.3 Test Equipment and Experimental Techniques 202

6.3.1 Introduction 202
6.3.2 Self Heterodyne Experimental Arrangement 202
6.3.2.1 Main Experimental Setup 202
6.3.2.2 RF Radiation Problems 203
6.3.2.3 Optical Detectors and Detection Principles 204
6.3.3 Theoretical Calculation of the Self Heterodyne Detection Process 205

6.4 Evaluation of Optical Serrodyne Frequency-Translators 207

6.4.1 Introduction 207
6.4.2 Optical Evaluations of Phase-Modulators 207
6.4.2.1 Ti:$LiNbO_3$ Phase-Modulators 207
6.4.2.2 Proton Exchange $LiNbO_3$ Phase-Modulators 209
6.4.3 Electrical Frequency Response of Phase-Modulators 213
6.4.4 Experimental Results for Titanium-Indiffused Phase-Modulators Driven by Sawtooth Electrical Waveforms 213
6.4.4.1 Determination of $V_{2\pi}$ Values 213
6.4.4.2 Effect of Non-Zero Flyback/Fall-Time 215
6.4.4.3 Effect of Non-Optimum Sawtooth Amplitude 217
6.4.4.4 Effect of Non-Optimum Operation Over a Band/Range of Frequencies using a Constant Sawtooth 218

Amplitude
6.4.4.5 Presence of Amplitude Modulation in an Electro-Optic Phase-Modulator and its Effects 219
6.4.5 Experimental Results for Proton-Exchange Phase-Modulators Driven by Sawtooth Electrical Waveforms 221
6.4.5.1 Determination of $V_{2\pi}$ Values 221
6.4.5.2 Effect of Non-Zero Flyback/Fall-Time 223
6.4.5.3 Effect of Non-Optimum Sawtooth Amplitude 224
6.4.5.4 Effect of Non-Optimum Operation Over a Band/Range of Frequencies using a Constant Sawtooth Amplitude 225
6.4.5.5 Presence of Amplitude Modulation in an Electro-Optic Phase-Modulator and its Effects 226

6.5 Summary 227

Appendix 6.1 230

Appendix 6.2 232

A6.2.1 Background Theory 232
A6.2.2 Example of a Calculation to Obtain the Value of k 232

References 234

CHAPTER 6

EXPERIMENTAL RESULTS OF THE OPTICAL SERRODYNE FREQUENCY-TRANSLATORS

6.1 Introduction

The key component for the optical frequency translation experiments is the optical phase-modulator. The design of the phase-modulator is described in detail in Section 6.2. The choice of the optical waveguide widths and the types of electrode structure are highlighted.

The experimental arrangement used to evaluate the stripe optical waveguides and eventually the phase-modulators is described in Section 6.3. A Mach-Zehnder interferometer configuration incorporating a Bragg-cell to give heterodyne measurements was chosen to ensure that positive and negative sidebands generated by the optical frequency translation process could be studied effectively. The heterodyne detection process using PIN silicon photodiodes and/or avalanche silicon photodiodes was also studied.

Results of optical phase-modulators realised mainly in Y-cut $LiNbO_3$, together with some results for modulators realised in Z-cut Ti:$LiNbO_3$ and X-cut PE $LiNbO_3$, are presented in Section 6.4. In all the experiments the wavelength of operation was 632.8 nm. The electrical and optical properties of the phase-modulators are also presented. Finally the results of the serrodyne experiments are presented in detail for all the above devices.

6.2 Design of the Optical Phase-Modulators

6.2.1 Introduction

In this section, the procedures employed to design the optical phase-modulators are described in detail. Phase modulation is a fundamental electrooptic property which is widely used in electrooptic devices, such as IO

Mach-Zehnder interferometers and optical directional coupler switches. In order to understand this effect better, the electrooptic effect in $LiNbO_3$ is described in the next section. Next, the theoretical performance of an optical phase-modulator is calculated. Finally. the correct choice of optical waveguide widths for single mode operation at the operating wavelength of 633 nm and the corresponding electrode pattern are described.

6.2.2 The Electro-Optic Effect

The linear electro-optic effect (or Pockel's effect) is a fundamental property of non-centrosymmetric crystals in which an electric field applied across the crystal will change the refractive index of the crystal proportionately [6.1]. This property forms the basis for controlling the phase of an optical beam in the $LiNbO_3$ devices reported in this thesis.

The refractive indices of a general crystalline material can be represented by the indicatrix or index ellipsoid [6.2]:

$$(X/n_x)^2 + (Y/n_y)^2 + (Z/n_z)^2 = 1, \qquad (6.1)$$

where n_x, n_y, and n_z are the refractive indices for the principal x, y, and z axes of the crystal respectively. For a uniaxial crystal such as $LiNbO_3$, it can be described by an ellipsoid, as illustrated in Figure 6.1, and can be expressed as:

$$(X/n_o)^2 + (Y/n_o)^2 + (Z/n_e)^2 = 1, \qquad (6.2)$$

using Equation 6.1. By definition, the optic axis is parallel to the Z-axis.

With electric field components E_x, E_y, and E_z applied to the crystal, the index ellipsoid can be described in the form:

$$(X/n_o)^2 + (Y/n_o)^2 + (Z/n_e)^2 + (X/n_{xx})^2 + (Y/n_{yy})^2 + (Z/n_{zz})^2 +$$

$$+ 2[1/(n_{yz})^2]YZ + 2[1/(n_{xz})^2]XZ + 2[1/(n_{xy})^2]XY = 1 \qquad (6.3)$$

Equation 6.3 can be expressed in matrix form as:

$$\begin{pmatrix} 1/(n_{xx})^2 \\ 1/(n_{yy})^2 \\ 1/(n_{zz})^2 \\ 1/(n_{yz})^2 \\ 1/(n_{xz})^2 \\ 1/(n_{xy})^2 \end{pmatrix} = \begin{pmatrix} r_{11} & r_{12} & r_{13} \\ r_{21} & r_{22} & r_{23} \\ r_{31} & r_{32} & r_{33} \\ r_{41} & r_{42} & r_{43} \\ r_{51} & r_{52} & r_{53} \\ r_{61} & r_{62} & r_{63} \end{pmatrix} \begin{pmatrix} E_x \\ E_y \\ E_z \end{pmatrix} \qquad (6.4)$$

The above 6 x 3 matrix in r_{ij} , the electrooptic coefficients, is known as the electrooptic tensor, where i is between 1 and 6 and j is between 1 and 3. Since $LiNbO_3$ has 3m symmetry, the electrooptic tensor in matrix form is [6.3]:

$$\begin{pmatrix} 0 & -r_{22} & r_{13} \\ 0 & r_{22} & r_{13} \\ 0 & 0 & r_{33} \\ 0 & r_{51} & 0 \\ r_{51} & 0 & 0 \\ -r_{22} & 0 & 0 \end{pmatrix}$$

It is important to distinguish between "free" electrooptic coefficients $(r_{ij})^T$ i.e. measured under constant stress or at low frequencies and "clamped" electrooptic coefficients $(r_{ij})^S$ i.e. measured under constant strain or at high frequencies. Below the acoustic resonance frequencies there is a large

contribution from the photoelastic effect which may be of the same order of magnitude as the electrooptic effect. Researchers have found that the upper frequency for the photoinduced or photoelastic effect is appproximately 50 MHz [6.4].

Table 6.1 shows the electrooptic coefficients for $LiNbO_3$ in units of pm/V at λ= 633 nm and at room temperature. The low and high frequency electrooptic coefficients were measured by Bernal [6.5] and Turner [6.6] respectively.

The basic equations that are required to predict the effect of applied electric fields in $LiNbO_3$ are now available. The work reported in this thesis employed the following crystal cuts, directions of propagation, and choice of TE or TM modes:

(a) X-cut, Y-propagating, TE modes,

(b) Y-cut, X-propagating, TE modes, and

(c) Z-cut, Y-propagating, TM modes.

In order to calculate the refractive index change when an electric field is applied, the numerical values of the electrooptic tensor of $LiNbO_3$ were substituted in Equation 6.4. In all the experiments reported in this thesis, predominantly E_z electric fields were applied to the above crystal cuts. Therefore the following equations applied:

$$1/(n_{xx})^2 = r_{13}\, E_z \tag{6.5}$$

$$1/(n_{yy})^2 = r_{13}\, E_z \tag{6.6}$$

$$1/(n_{zz})^2 = r_{33}\, E_z \tag{6.7}$$

$$1/(n_{yz})^2 = 0 \tag{6.8}$$

Electrooptic Coefficients of $LiNbO_3$ at $\lambda_o = 633$ nm			
$(r_{33})^S = 30.8$	$(r_{13})^S = 8.6$	$(r_{22})^S = 3.4$	$(r_{51})^S = 28$
$(r_{33})^T = 30.9$	$(r_{13})^T = 9.6$	$(r_{22})^T = 6.8$	$(r_{51})^T = 32.6$

Table 6.1 The Electrooptic Coefficients Of $LiNbO_3$ (Units In 10^{-12} m/V, $\lambda_o = 633$ nm, Room Temperature)

$$1/(n_{xz})^2 = 0 \tag{6.9}$$

$$1/(n_{xy})^2 = 0 \tag{6.10}$$

By substituting Equations 6.5 to 6.10 into Equation 6.3, the new index ellipsoid is:

$$(X/n_o)^2 + (Y/n_o)^2 + (Z/n_e)^2 + (X)^2 r_{13} E_z +$$

$$(Y)^2 r_{13} E_z + (Z)^2 r_{33} E_z = 1 \tag{6.11}$$

For Cases (a) and (c), the X-Z cross-section of the index ellipsoid (described by Equation 6.11) only is considered. Therefore in this situation, Y=0, to give the ellipse in the X-Z plane as:

$$(X/n_o)^2 + (Z/n_e)^2 + (X)^2 r_{13} E_z + (Z)^2 r_{33} E_z = 1 \tag{6.12}$$

For Case (b), the Y-Z cross-section of the index ellipsoid (described by Equation 6.11) only is considered. Therefore, in this case, X=0, to give the ellipse in the Y-Z plane as:

$$(Y/n_o)^2 + (Z/n_e)^2 + (Y)^2 r_{13} E_z + (Z)^2 r_{33} E_z = 1 \tag{6.13}$$

Equations 6.12 and 6.13 can be rewritten to describe the indices seen by TE and TM modes for the above three cases (a), (b), and (c) as:

$$(X)^2 (1/n_{TM})^2 + (Z)^2 (1/n_{TE})^2 = 1, \text{ and} \tag{6.14}$$

where $(1/n_{TM})^2 = [(1/n_o)^2 + r_{13} E_z]$ and $(1/n_{TE})^2 = [(1/n_e)^2 + r_{33} E_z]$

$$(Y)^2 (1/n_{TE})^2 + (Z)^2 (1/n_{TM})^2 = 1, \text{ and} \tag{6.15}$$

where $(1/n_{TE})^2 = [(1/n_o)^2 + r_{13} E_z]$ and $(1/n_{TM})^2 = [(1/n_e)^2 + r_{33} E_z]$

Therefore the change in the refractive index due to the applied electric field E_z in the cases of (a) and (b) is:

$n_{TE} = n_e - (1/2)n_e^3 r_{33} E_z$, using the binomial theorem.

$$\therefore \Delta n_{TE} = - (1/2)n_e^3 r_{33} E_z \qquad (6.16)$$

Therefore the change in the refractive index due to the applied electric field E_z in the case of (c) is:

$n_{TM} = n_e - (1/2)n_e^3 r_{33} E_z$, using the binomial theorem.

$$\therefore \Delta n_{TM} = - (1/2)n_e^3 r_{33} E_z \qquad (6.17)$$

6.2.3 Theoretical Performance of a Lumped Electrode Type Optical Phase Modulator

6.2.3.1 Phase Modulator Voltage Requirements

An integrated optic phase-modulator [6.7] consists, in its simplest form, of a stripe waveguide (titanium-indiffused or proton-exchanged) which supports a single mode of effective refractive index n_{eff}. On either side of the waveguide are located the parallel electrodes of length L separated by a distance G, as shown in Figure 6.2. Applying a voltage V to the electrodes causes a change in the waveguide refractive index via the electrooptic effect. The electrooptically induced change in the effective refractive index Δn_{eff} [From Equations 6.16 or 6.17] is:

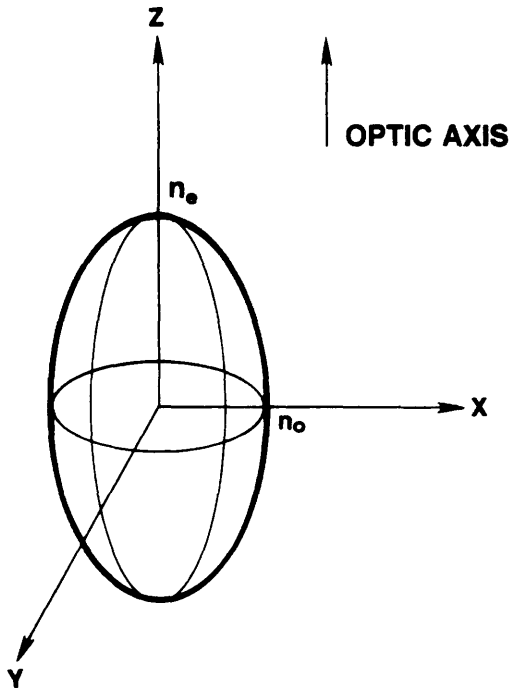

Figure 6.1 Index Ellipsoid For A Uniaxial Crystal

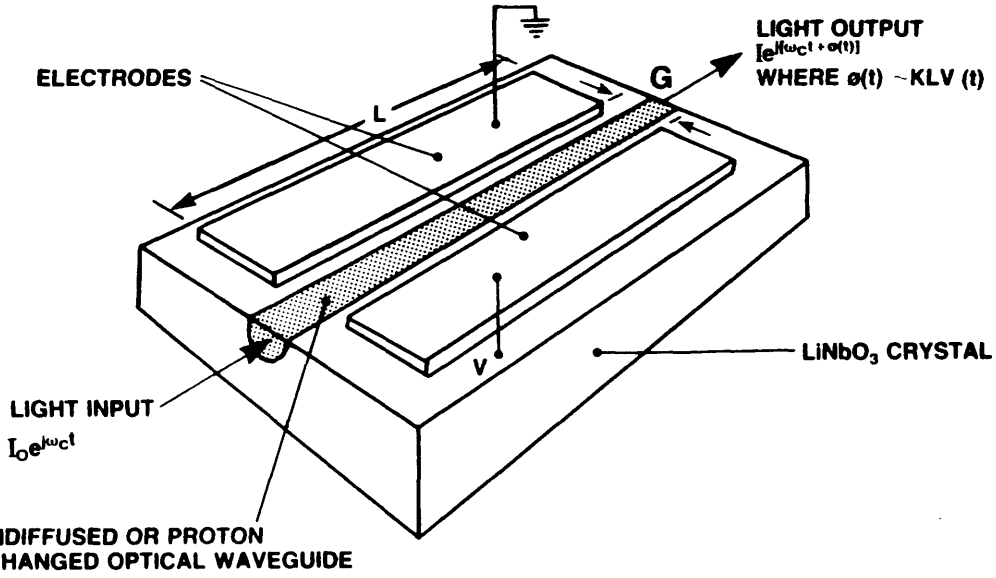

Figure 6.2 Schematic Of The Integrated Optical Phase Modulator

$$\Delta n_{eff} = - (1/2) \Gamma (n_{eff})^3 r_{ij} (V/G) \quad (6.18)$$

where Γ is the overlap integral of the electric field with the waveguide optical mode and r_{ij} is the relevant electrooptic coefficient which depends upon the $LiNbO_3$ crystal orientation and the direction of the applied electric field. All the phase-modulators described in this thesis utilised the largest diagonal electrooptic coefficient i.e. r_{33}. The total phase modulation $\Delta\phi$ for this device is given by:

$$\Delta\phi = \Delta\beta L = 2\pi \Delta n_{eff} L/\lambda \quad (6.19)$$

By substituting Equations 6.18 into 6.19, the phase modulation induced is given by:

$$\Delta\phi = - [\pi \Gamma (n_{eff})^3 r_{ij}] (V/G) (L/\lambda) \quad (6.20)$$

Therefore from Equation 6.20, the voltage required to produce a 2π phase change is given by:

$$V_{2\pi} = - (2 G \lambda)/[\Gamma (n_{eff})^3 r_{ij} L] \quad (6.21)$$

The above equation was then employed to determine the design of the phase-modulator used in all the serrodyne experiments. Figure 6.3 shows a general plot of $V_{2\pi}$ versus electrode gap for optical/electric fields overlap values of 0.25, 0.30, 0.35 and 0.40. Figure 6.4 illustrates a plot of $V_{2\pi}$ versus the overlap factor for electrode gaps of 9.0 μm, 10.0 μm and 11.0 μm. For both the phase modulator design plots shown in Figures 6.3 and 6.4, the following values were used: λ= 632.8 nm, n_{eff}= 2.2125, r_{33}= 30.8 pm/V and L= 10 mm. The actual phase modulators used in all the serrodyne experiments had the following typical dimensions: G= 10.0 μm, L= 10 mm and optical waveguide widths= 4.0

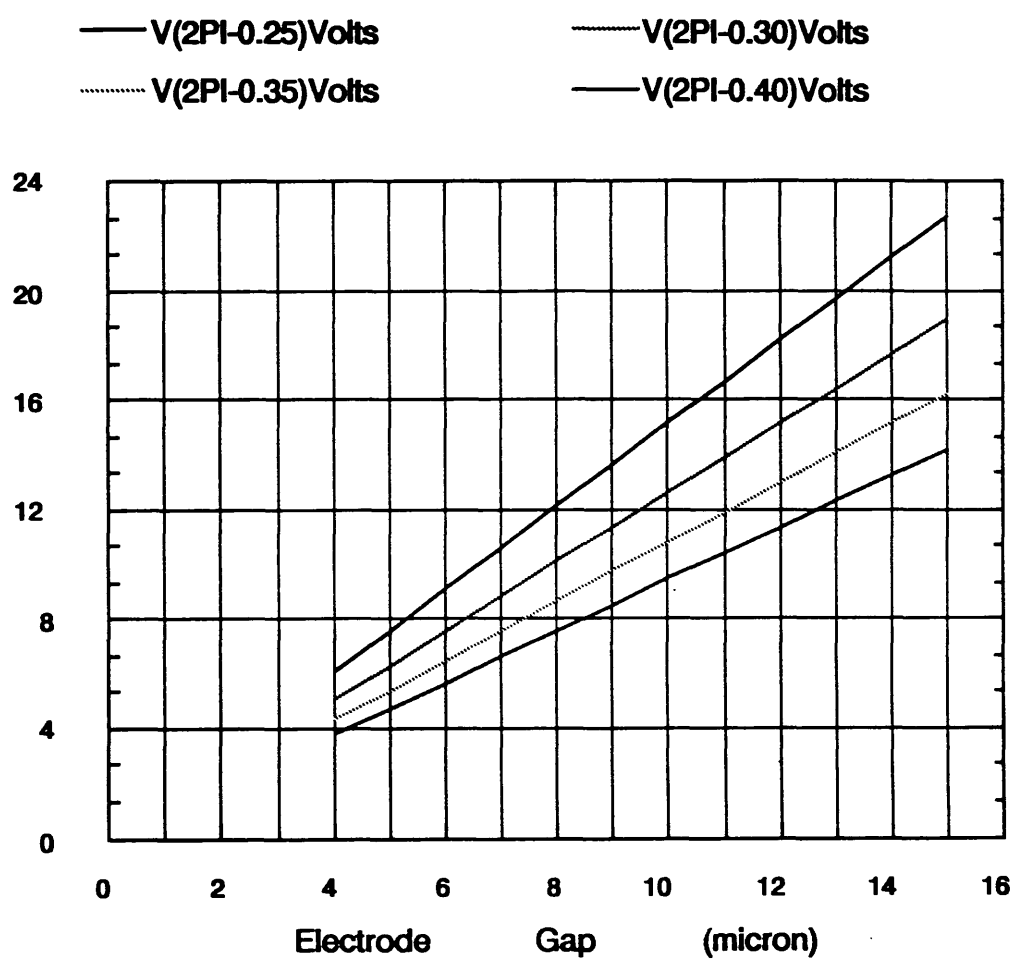

Figure 6.3 Phase Modulator Design Plot: $V_{2\pi}$ Versus Electrode Gap (For Overlap Factor Values Of 0.25, 0.30, 0.35, 0.40)

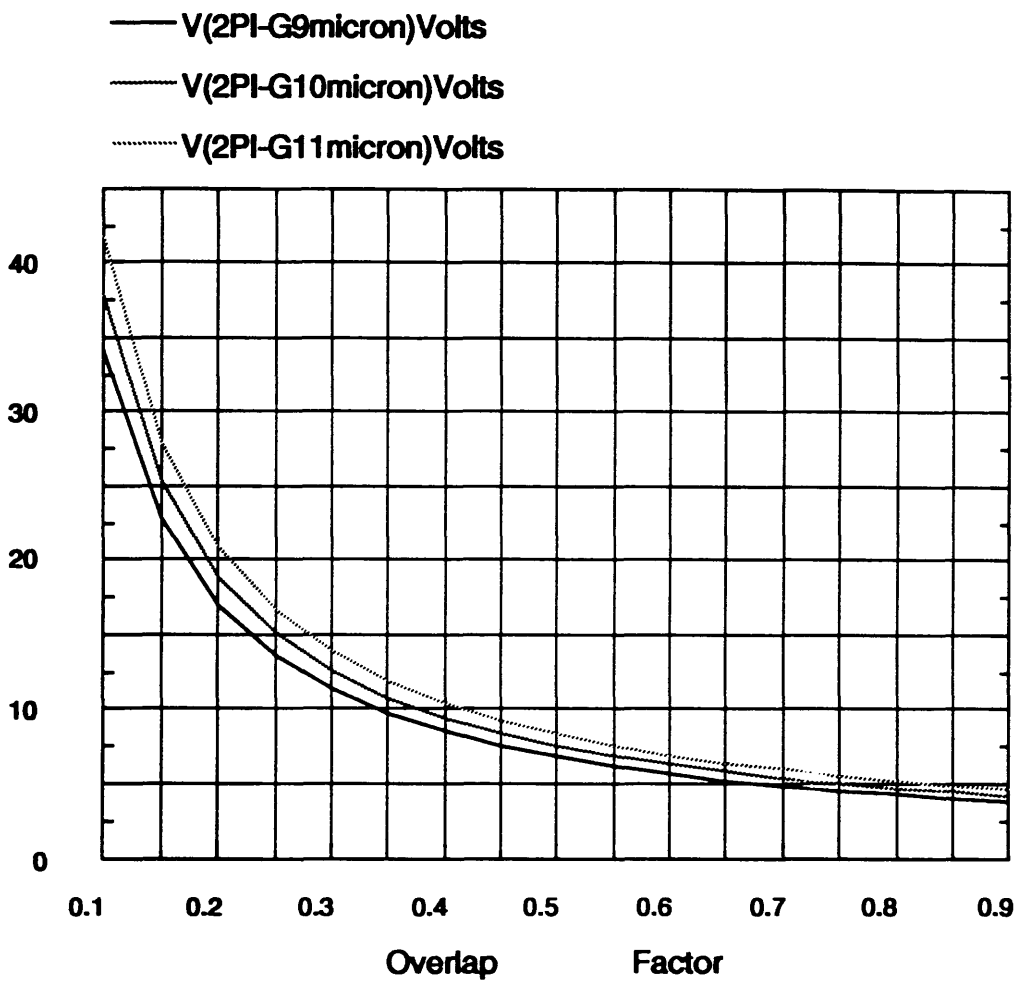

Figure 6.4 Phase Modulator Design Plot: $V_{2\pi}$ Versus Overlap Factor (For Electrode Gaps Of 9.0 μm, 10.0 μm, 11.0 μm)

μm and 5.0 μm. Therefore from the phase modulator design plots the voltage required for a 2π phase change can range from 9 to 15 volts.

In addition the voltage-length product required for a 2π phase modulation is given by:

$$|V_{2\pi} L| = (2 G \lambda)/[\Gamma (n_{eff})^3 r_{ij}] \qquad (6.22)$$

6.2.3.2 Design of Lumped Electrodes for Phase Modulator

The maximum frequency at which the serrodyne experiments were carried out was limited by the limits of commercially available sawtooth generators, i.e. the highest sawtooth frequency was around 5 MHz. Therefore lumped electrode modulators were selected, since the use of travelling-wave electrodes would involve extra and unnecessary fabrication procedures such as the fabrication of thick gold electrodes.

The capacitance per unit length, C/L, for the coplanar, parallel electrodes on $LiNbO_3$, illustrated in Figure 6.2, is given by [6.8]:

$$C/L = (\varepsilon_{eff}/\pi)\ln(4W/G) \qquad (6.23)$$

where W is the electrode width, $\varepsilon_{eff} = (\varepsilon_o)(1 + \varepsilon_s)$, ε_o is the permittivity of vacuum with a value of 8.854×10^{-12} F/m, and $\varepsilon_s = (\varepsilon_x \varepsilon_y)^{(1/2)}$ with $\varepsilon_x = 28$ and $\varepsilon_y = 44$ for modulation frequencies below 50 MHz (ε_x and ε_y are the relative permittivities for $LiNbO_3$).

As noted in the earlier part of this chapter, $LiNbO_3$ has two sets of permittivity constants, namely "free" and "clamped" constants [6.9]. The transition from "free" to "clamped" occurs at around 50 MHz. In the "clamped" situation, ε_x is 29 and ε_y is 84 [6.4]. However, since all the modulation experiments performed in this work were below 50 MHz, only the values for the "free" permittivity values were used.

The phase-modulator 3 dB bandwidth is given by:

$$\Delta f = 1/(\pi RC) \qquad (6.24)$$

for a given termination resistance R across the lumped electrodes. Figure 6.5 shows a lumped electrode design plot of phase modulator bandwidth versus ratio of electrode width to electrode gap for electrode lengths of 10 mm, 15 mm and 20 mm and a termination resistance of 50 Ω. For the designed phase modulator used in the serrodyne experiments, the capacitance limited bandwidth is 2.7 GHz.

Another limitation to the bandwidth of the phase-modulator with lumped electrodes is the electrical transit time τ_{elec} which is given by the expression:

$$\tau_{elec} = [(\varepsilon_s^{1/2}.L)]/c \qquad (6.25)$$

where c = 3.0 X 10^8 m/s is the speed of light in a vacuum, and ε_s = 35 for $LiNbO_3$.

The electrical transit time limited bandwidth Δf of the phase-modulator is therefore given by [6.10]:

$$\Delta f = 1/(\pi\, \tau_{elec}) \qquad (6.26)$$

i.e. $$\Delta f = c/[(\pi)\ (\varepsilon_s^{1/2}.L)] \qquad (6.27)$$

From Equation 6.27, it can be calculated that a $LiNbO_3$ phase-modulator with a lumped electrode has a transit time limited bandwidth-length product of 1.6 GHz-cm. Therefore for the designed phase modulator used in the serrodyne experiments the transit time limited bandwidth is 1.6 GHz.

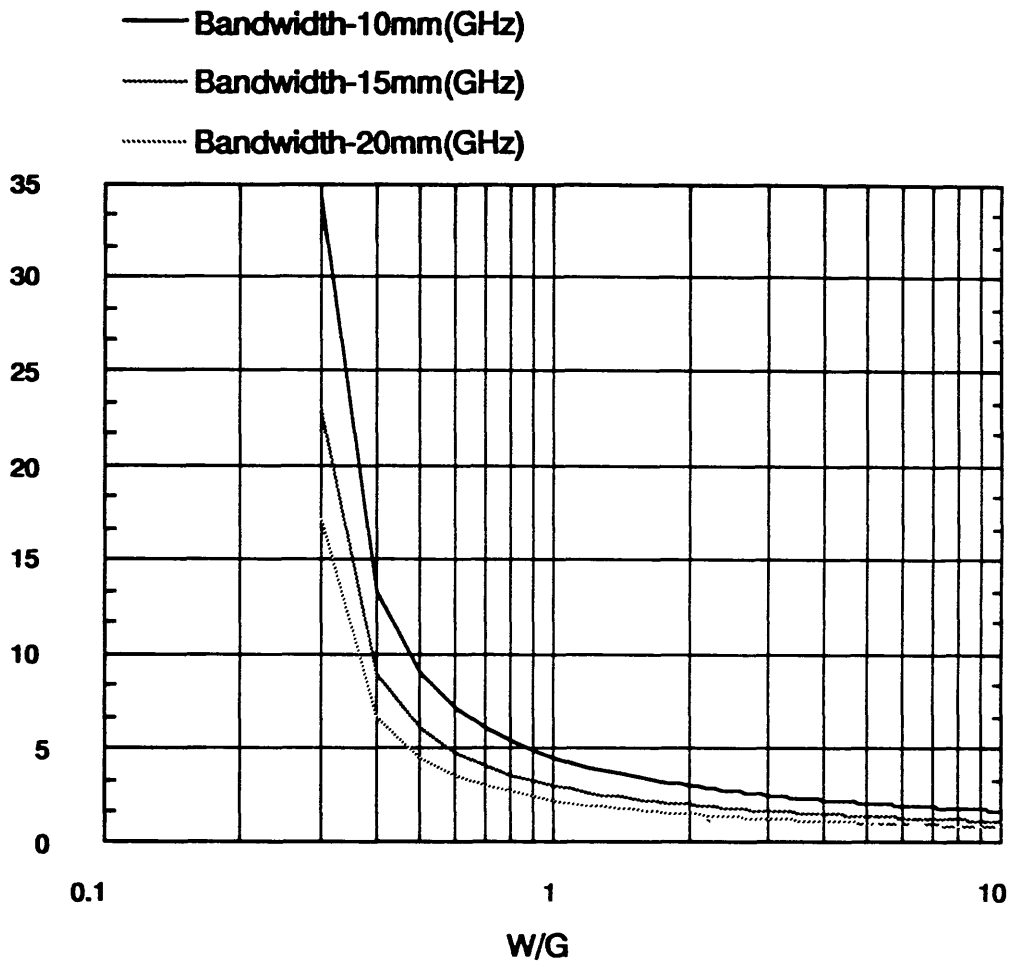

Figure 6.5 Lumped Electrode Design Plot: Bandwidth Versus W/G (For Electrode Lengths Of 10 mm, 15 mm, 20 mm)

The voltage/bandwidth ratio (assuming the capacitance limit) for a 2π phase modulation can be derived by considering Equations 6.22, 6.23, and 6.24:

$$V_{2\pi}/\Delta f = \{(2\ R\ G\ \lambda\ \varepsilon_{eff})\ [\ln(4W/G)]\}/[\Gamma\ (n_{eff})^3\ r_{ij}] \qquad (6.28)$$

Figure 6.6 illustrates a plot of $V_{2\pi}/\Delta f$ against the overlap factor for an optical phase modulator at an operating wavelength of 632.8 nm with the following characteristics: R= 50 Ω, W/G= 1.0, 2.5 and 5.0, n_{eff}= 2.2125 and r_{33}= 30.8 pm/V. For a typical phase modulator used in the serrodyne experiments with a typical overlap factor value of 0.35, the voltage(2π)/bandwidth ratio (assuming capacitance limited case) is about 4 volts/GHz.

Finally, Auracher has pointed out that the ohmic resistance R_e of the electrodes can limit the modulation bandwidth of an electrooptic device [6.11]. It was found that there can be a substantial reduction in bandwidth if $R_e \geq 5\ \Omega$/mm. However, for $R_e \leq 2\ \Omega$/cm, the modulation bandwidth reduction due to distributed resistance was estimated to be ≤ 20% even for an electrode length of 10 mm. It can be deduced from Equation 6.25 that as (W/G) decreases, the capacitance decreases, and hence the RC limited modulation bandwidth of the device increases as the width of the electrode is decreased for a given electrode gap G. Assuming that the electrode thickness is constant, R_e/L is increased as W decreases. This relation can be deduced from Equation 6.29. The theoretical ohmic resistance per unit length R_e/L is given by:

$$R_e/L = \rho/(W\ T_e) \qquad (6.29)$$

where ρ is the resistivity of the metal used to form the electrode pattern and T_e is the thickness of the metal. Typically for a 2000 Å thick aluminium electrode and assuming a bulk resistivity value of $2.61 \times 10^{-8}\ \Omega$ m, the

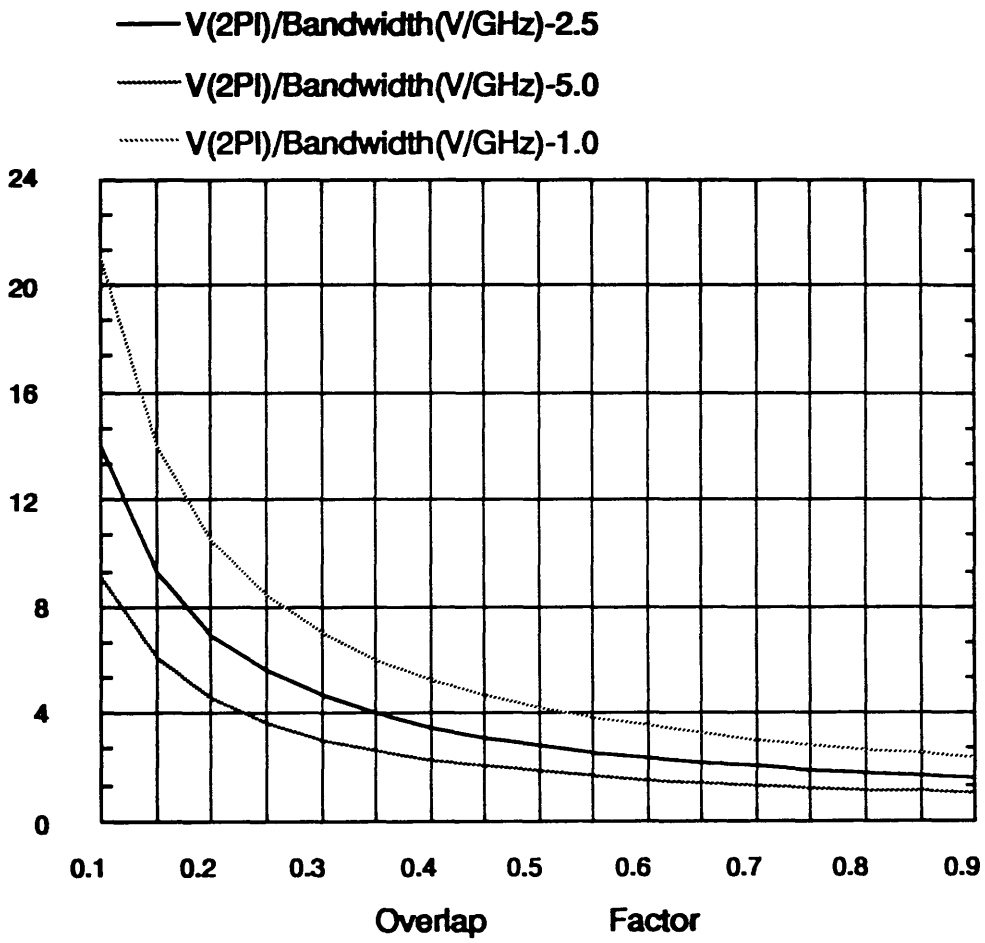

Figure 6.6 Phase Modulator Figure of Merit Plot: $V_{2\pi}/\Delta f$ Versus Overlap Factor (For W/G Values Of 1.0, 2.5, 5.0)

calculated value of R_e/L is 5.2 Ω/mm for a 25 μm wide electrode. If gold was used instead of aluminium and assuming a bulk resistivity value of 2.01×10^{-8} Ωm, the calculated R_e/L value for the same electrode is 4.02 Ω/mm. However all the phase-modulators used in the serrodyne experiments had aluminium electrodes.

6.2.4 Choice of Single-Mode Stripe Optical Waveguides

The stripe optical waveguides used in the serrodyne optical frequency-translators had to be single moded to ensure proper operation of the devices at the wavelength of 633 nm. In choosing the waveguide parameters for the optical phase-modulators, fabricated by titanium indiffusion or proton-exchange, the following factors were considered:

(1) the cut of $LiNbO_3$ to be used, the direction of propagation, and hence the correct polarisation of the propagating guided optical mode to ensure the use of the largest electrooptic coefficient,

(2) the initial waveguide width,

(3) initial titanium thickness,

(4) the diffusion (exchange) time,

(5) the diffusion (exchange) temperature, and

(6) the diffusion atmosphere and conditions.

The choice of the cut of $LiNbO_3$ was based on the easy availability of the crystal substrates. At the start of this work, the choice was made to use Y-cut $LiNbO_3$ substrates but in the later stages of this work, both Z- and X-cut $LiNbO_3$ substrates were employed to realise PE slab and stripe waveguides. As indicated in Chapter 4, Y- and Z-cut Ti:$LiNbO_3$ phase-modulators were used for the serrodyne experiments. After the detailed optical characterization of PE waveguides in X- and Z-cut $LiNbO_3$, as described in Chapter 5, only X-cut PE

phase-modulators were realised due to the limited time available to complete the work.

The selection of the waveguide widths was based on the results of previous researchers [6.12, 6.13] in the Electronics and Electrical Department at Glasgow University, from literature studies [6.14, 6.15, 6.16], the ease with which the waveguide mask could be made and, last but not least, the success rate in fabrication of single mode waveguides. The selection was made from work performed by McLachlan [6.12] and during the course of this work there was exchange of information with fellow researchers Andonovic [6.17] and Bjortorp [6.13]. It was decided to select 4 μm and 5 μm wide optical waveguides for all the work reported in this thesis. All the fabricated devices were evaluated at λ = 632.8 nm. Figure 6.7 illustrates the number of optical waveguide modes that can be supported as a function of waveguide width and titanium thickness for operation at 633 nm. A large number of the experimental points (for 4 μm and 5 μm) shown in Figure 6.7 were the a result of waveguide evaluations of the phase-modulators used for the serrodyne study. A detailed report of these results can be found in Section 6.4.2.1 of this chapter.

The selection of the waveguide widths based on Figure 6.7 implied that the diffusion time and temperature should be 8 hours and 1000°C respectively.

As indicated in Chapter 4, the diffusion conditions developed by Esdaile [6.18] were used throughout the experiments reported in this thesis. It was found that it was important to properly ensure that the same weight of congruent $LiNbO_3$ was used for each titanium diffusion run and also that the two tubes were properly held together by the springs. Otherwise, it was observed in a number of samples that the problem of outdiffusion was serious due to bad sealing.

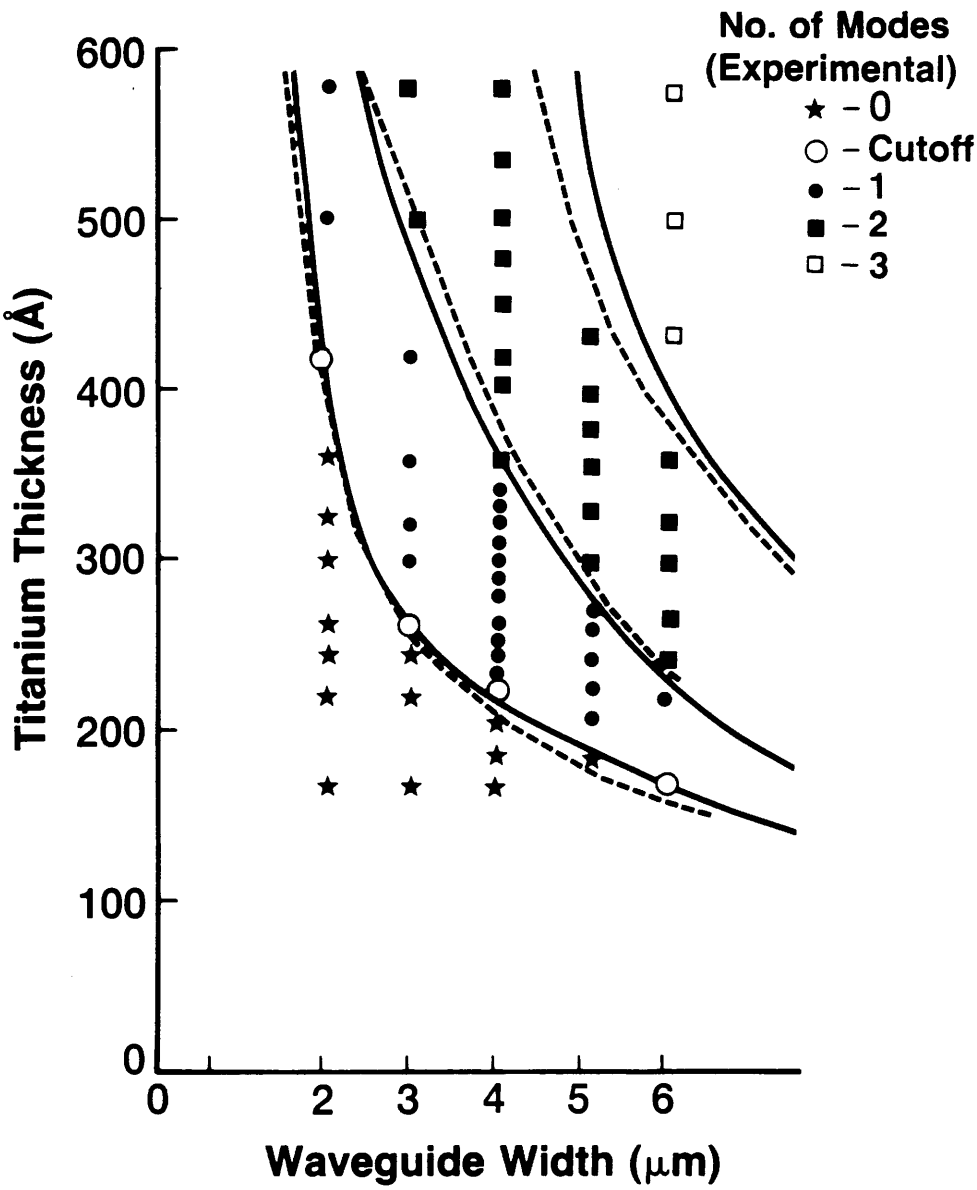

Figure 6.7 **Plot Of Number Of Waveguide Modes As A Function Of Titanium Thickness And Waveguide Width**
Experimental Points For λ_0 = 633 nm, Diffusion Time = 8 Hours, Diffusion Temperature = 1000°C - With Experimental Results For 4 μm & 5 μm From This Thesis (Reference: McLachlan And Bjortorp)

The PE stripe waveguides were realised using the same waveguide mask as described above. The exchange time and temperature of the oil bath were selected on the basis of dispersion curves generated by using the method of Marcatili and the Effective Index method, as described in Chapter 5. Figures 6.8(a) and (b) and 6.9(a) and (b) illustrate such dispersion curves based on Δn values of 0.10 and 0.12 respectively for both 4 μm wide and 5 μm wide stripe optical waveguides. The dispersion curves were used as an approximate guide in fabricating single-moded PE stripe optical waveguides. The validity of the generated dispersion curves is discussed in Section 6.4.2.2.

6.2.5 Design of Electrode Structures

After the selection of the waveguide widths, the electrode gap G, the electrode length L, and the width of the electrode W were chosen on the basis of the theory of lumped electrodes described in Section 6.2.3.2. The electrode pattern mask was designed to have parallel electrode geometry as illustrated in Figure 6.2. The length and the width of the electrodes were 10 mm and 25 μm respectively except for the requirement of 50 μm pads (located centrally along the side of the electrodes) for wire bonding purposes. The electrode gaps were varied from 6 μm to 10 μm in order to establish experimentally the most effective optical phase-modulator for the serrodyne experiments. Using Equations 6.22, 6.23, 6.24, and 6.29 and assuming a 50 Ω resistor connected to the coplanar electrode pattern, the $V_{2\pi}$ (with a typical overlap factor of 0.35), C, electrical bandwidth, and the static resistance (for an aluminium electrode pattern) of the phase-modulator were calculated. In the calculation of R_e, values of $\rho = 2.61 \times 10^{-8}$ Ωm and thickness $T_e = 0.2$ μm were used. Table 6.2 summarizes the calculated values and the results imply that the devices designed had the necessary bandwidth for serrodyne operation. The phase-modulators were driven with sawtooth waveforms of frequencies up to 7 MHz.

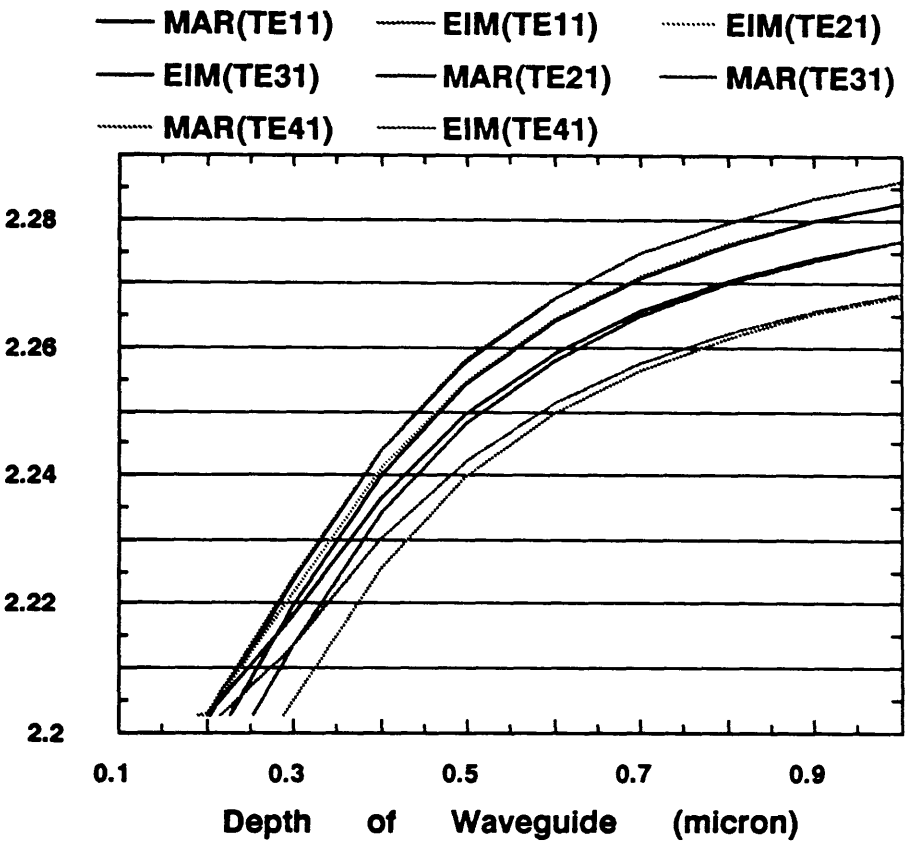

Mode Number	Cut-off Depth, μm (Marcatili)	Cut-off Depth, μm (Effective Index)
TE_{11}	0.204	0.189
TE_{21}	0.226	0.194
TE_{31}	0.253	0.202
TE_{41}	0.289	0.215

Figure 6.8a Dispersion Curves For A 4 μm Wide Stripe Waveguide ($\Delta n = 0.10$) With Values Of Cutoff Depth (By Marcatili And Effective Index Methods)

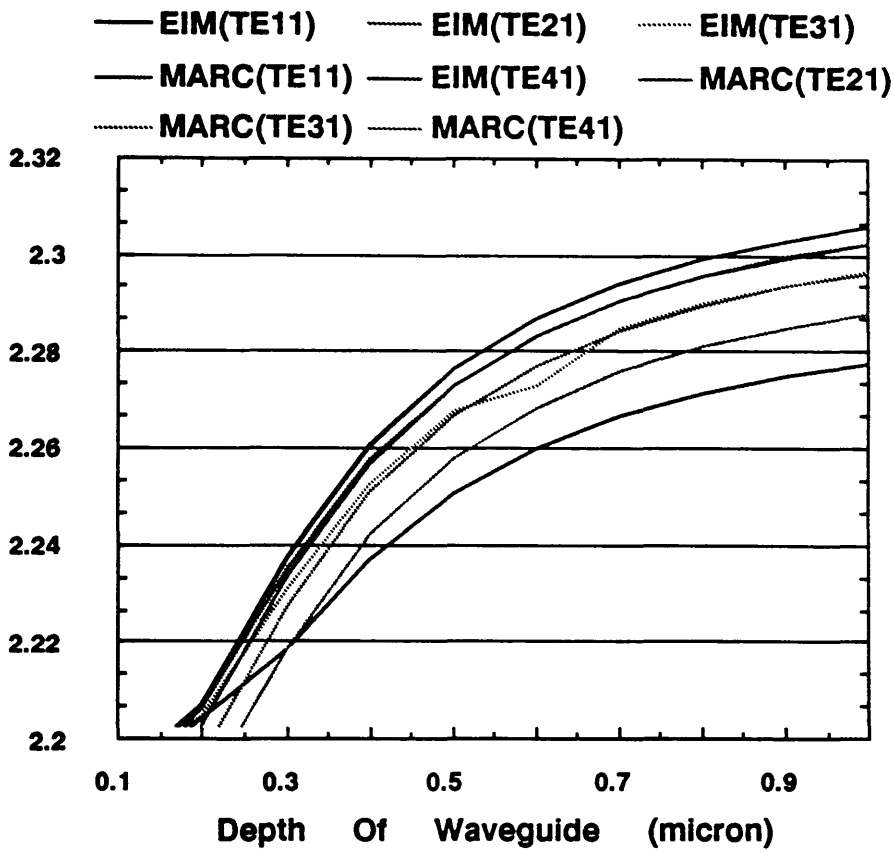

Mode Number	Cut-off Depth, μm (Marcatili)	Cut-off Depth, μm (Effective Index)
TE_{11}	0.180	0.168
TE_{21}	0.198	0.172
TE_{31}	0.220	0.178
TE_{41}	0.247	0.187

Figure 6.8b Dispersion Curves For A 4 μm Wide Stripe Waveguide ($\Delta n = 0.12$) With Values Of Cutoff Depth (By Marcatili And Effective Index Methods)

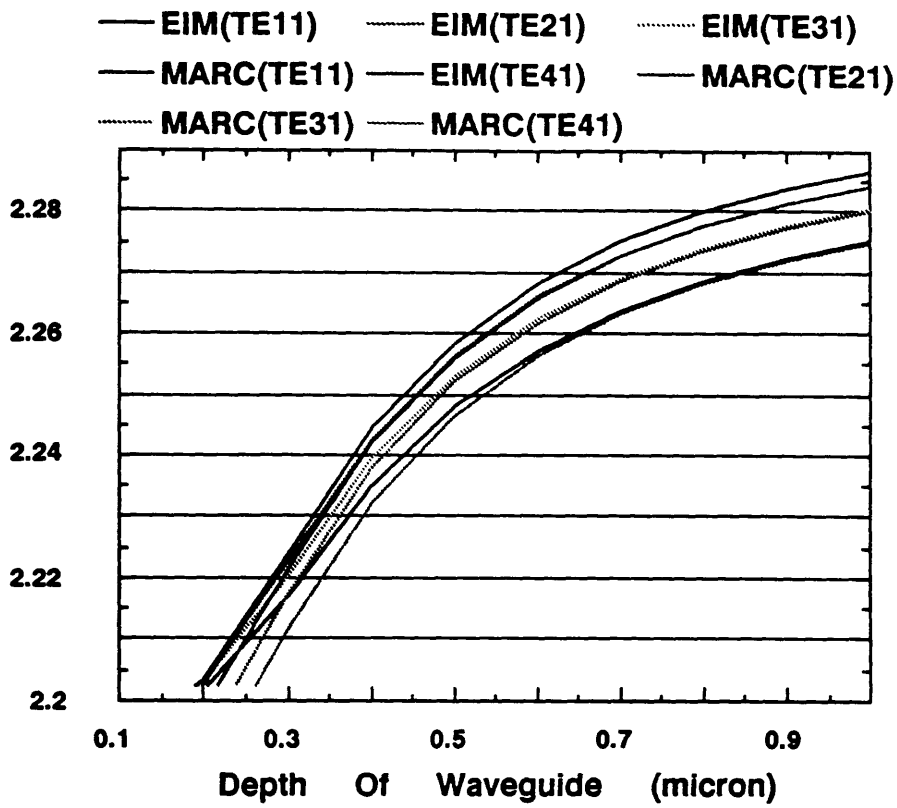

Mode Number	Cut-off Depth, μm (Marcatili)	Cut-off Depth, μm (Effective Index)
TE_{11}	0.200	0.189
TE_{21}	0.217	0.192
TE_{31}	0.237	0.197
TE_{41}	0.261	0.204

Figure 6.9a Dispersion Curves For A 5 μm Wide Stripe Waveguide ($\Delta n = 0.10$) With Values Of Cutoff Depth (By Marcatili And Effective Index Methods)

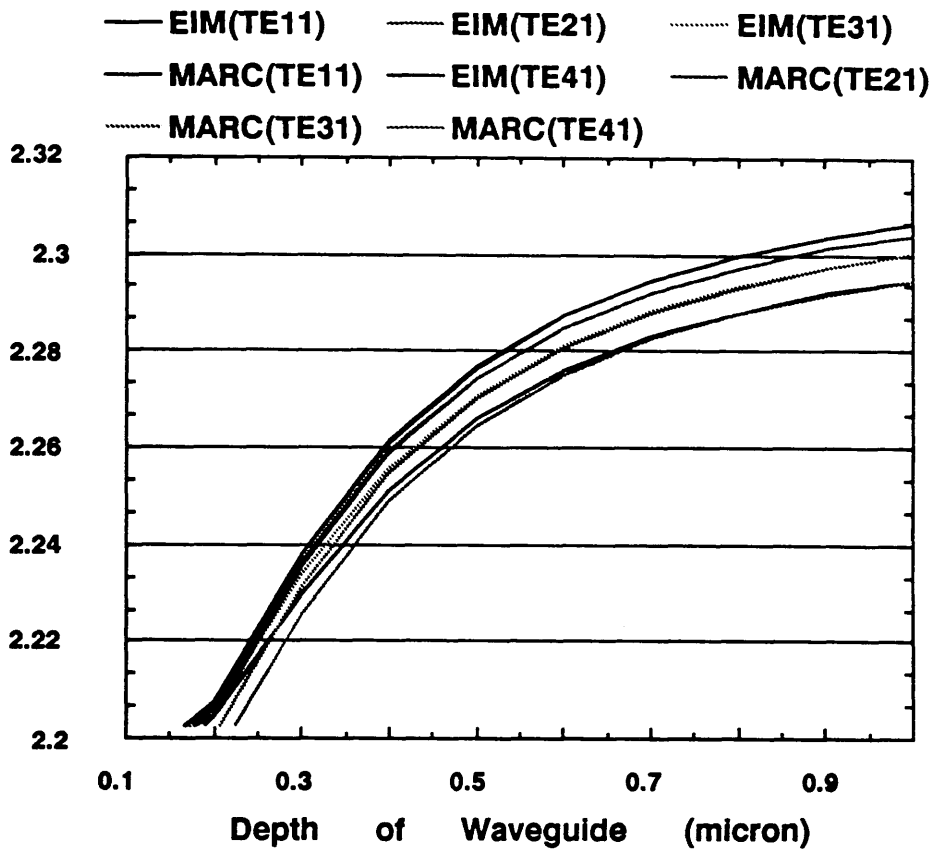

Mode Number	Cut-off Depth, μm (Marcatili)	Cut-off Depth, μm (Effective Index)
TE_{11}	0.178	0.168
TE_{21}	0.191	0.170
TE_{31}	0.207	0.174
TE_{41}	0.226	0.179

Figure 6.9b Dispersion Curves For A 5 μm Wide Stripe Waveguide ($\Delta n = 0.12$) With Values Of Cutoff Depth (By Marcatili And Effective Index Methods)

$V_{2\pi}$ (Volts)	Capacitance (pF)	Δf_c (GHz) (capacitance limited)	Δf_e (GHz) (electrical transit time limited)	Ohmic Resistance Ω
10.83	2.3	2.7	1.6	52

Table 6.2 Calculated Electrical Properties Of The Phase Modulator Configuration Used In All The Serrodyne Experiments

6.3 Test Equipment and Experimental Techniques

6.3.1 Introduction

In this section the basic experimental arrangement employed to evaluate the phase-modulators is described. The instruments used for this evaluation are described in Appendix 6.1.

The self heterodyne method was used exclusively in the evaluation of the phase-modulators as serrodyne optical frequency-translators. In order to understand this method better, the theoretical aspects of the process are presented in Section 6.3.3.

6.3.2 Self Heterodyne Experimental Arrangement

6.3.2.1 Main Experimental Setup

The main experimental arrangement used to evaluate the optical phase-modulators was a 'bulk' Mach-Zehnder interferometer. In this situation, since both the local oscillator beam and the signal beam were derived from the same laser source and such a setup is also known as a self heterodyne arrangement (SHA). The word heterodyne is used because a known frequency shift was imposed in one arm of the Mach-Zehnder interferometer using a Bragg cell.

The experimental SHA is shown schematically in Figure 6.10. The laser source that was used exclusively for all the serrodyne test experiments was a Spectra Physics 120 HeNe laser operating at 633 nm. The laser beam was divided into two beams at BS1. The optical phase-modulator to be tested was placed on the endfire coupling system (described in Chapter 5), in one arm of the interferometer. In all the experiments carried out using the endfire coupling system, coupling into and out of the optical phase-

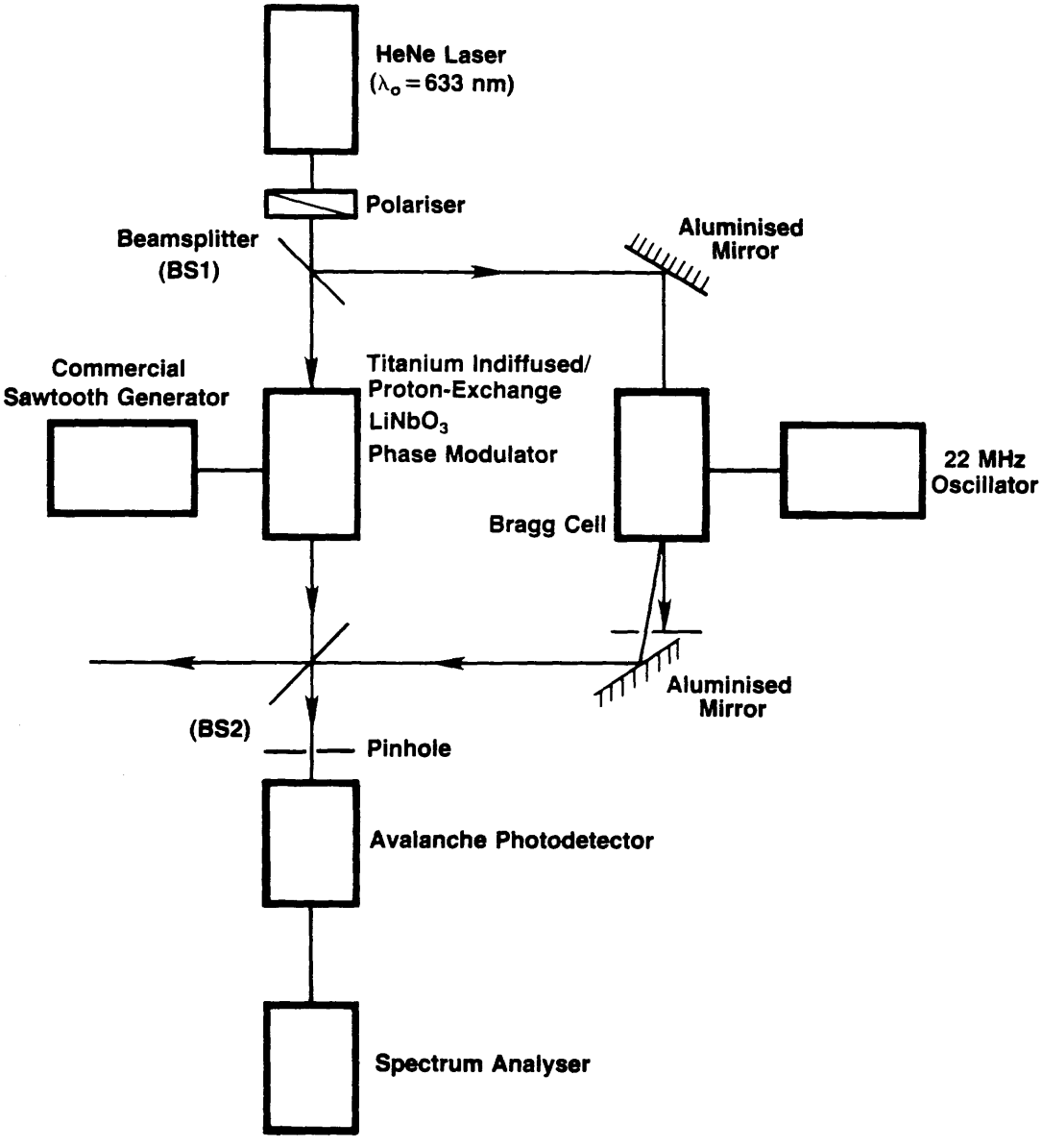

Figure 6.10 Schematic Of The Self Heterodyne Arrangement Used To Evaluate The Phase Modulators As Optical Serrodyne Translators

modulator was achieved using Olympus microscope objectives (usually X40 and sometimes, for output coupling, X20). On the other arm of the Mach-Zehnder interferometer, the laser beam was passed through a water filled acousto-optic Bragg cell operating at 22.2 MHz. The first-order diffracted beam, shifted in frequency by this amount, was then combined with the device output on BS2. The two optical beams were then directed on to a reverse biased HP 4207 silicon PIN photodiode or an AEG BPW 28 silicon avalanche photodiode. The heterodyned product of the two laser beams was then observed on a HP 8553B spectrum analyzer. The purpose of the Bragg cell was to simplify the interpretation of the serrodyne device output spectrum. It translated the observed spectrum from dc to 22.2 MHz, so that positive and negative frequency components resulting from the serrodyne action could be distinguished. Figure 6.11 illustrates the actual experimental setup used for the serrodyne frequency translation experiments. The list of instruments used in the above experiment is given in Appendix 6.1.

6.3.2.2 RF Radiation Problems

In performing the above experimental work, it was found that there was a problem with RF radiation from the power amplifiers and the Bragg cell at 22.2 MHz. This was observed as a spurious signal on the spectrum analyzer at 22.2 MHz when there was no input optical signal to the photodiode. The level of this spurious signal was between 10 and 15 dB above the noise level of the spectrum analyzer.

This problem was solved by shielding the power amplifiers completely and the Bragg cell partially during the actual serrodyne modulation measurements. The location of the power amplifier with respect to the optical table was adjusted to ensure minimum pickup by the photodiode unit, and, in addition, where possible, double shielded cables were used, especially for the cable connection between the Bragg cell and the power

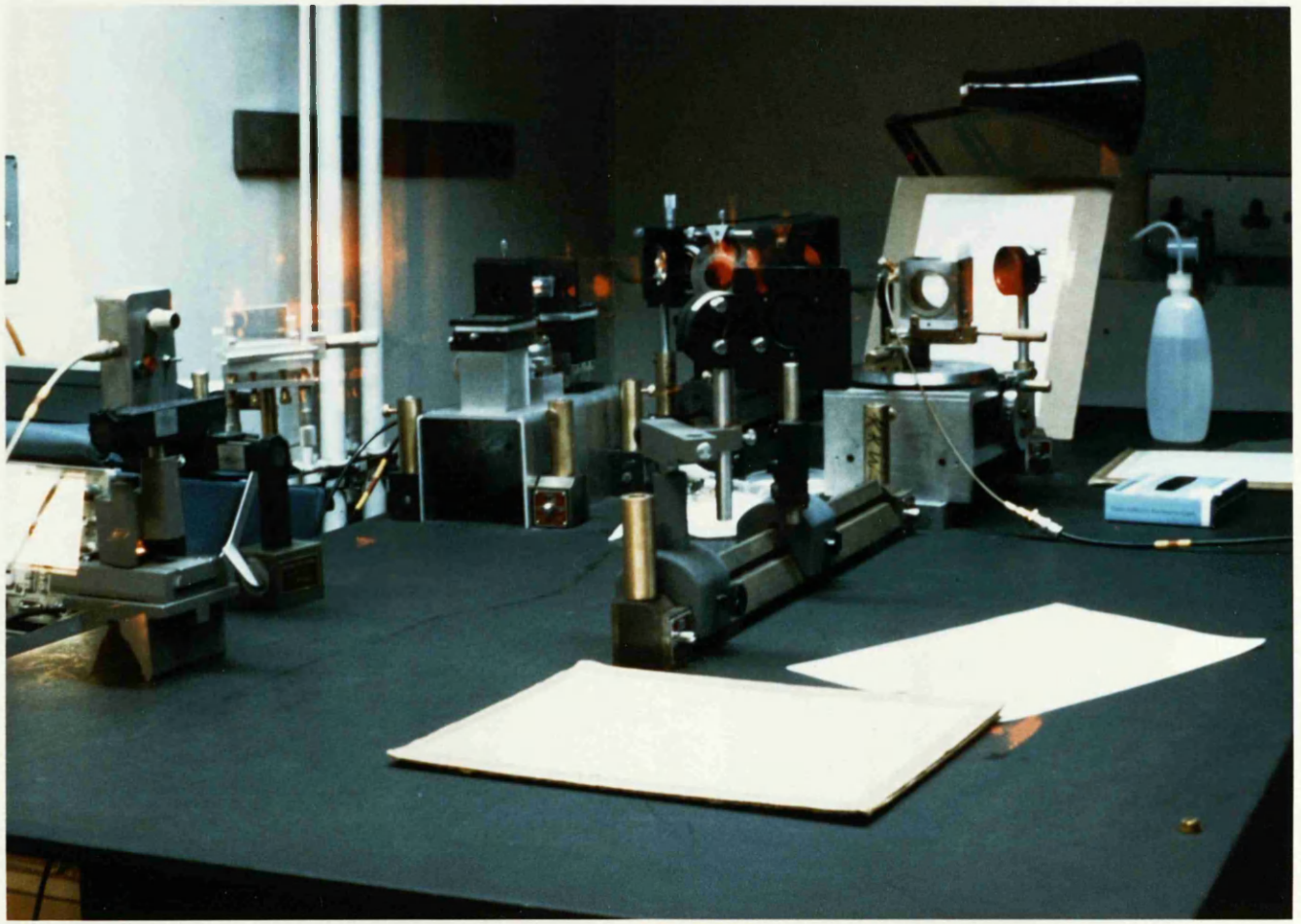

Figure 6.11 Photograph Of The Actual Self Heterodyne Arrangement Experimental Setup

amplifier. Also, the endfire coupling setup was partially shielded. The above procedures did help to eliminate the spurious radiation observed on the spectrum analyzer. With careful shielding of the various equipment it was possible to reduce the spurious pickup signal by 10 dB.

6.3.2.3 Optical Detectors and Detection Principles

As mentioned in Section 6.3.2.1, two types of photodiode were used in the serrodyne modulation experiments. The first kind was the silicon PIN photodiode. In order to fully utilise the potential performance of the silicon PIN photodiode, the DC coupled electrical bias circuit shown in Figure 6.12 was used. In the silicon PIN photodiode unit constructed, the reverse bias voltage V_b applied was 18 volts (supplied by two PP9 batteries) and the load resistors were 47 Ω, 100 Ω, 1KΩ, 10 KΩ, and 100 KΩ.

In some optical measurements where the heterodyned optical signals were too low to be measured by the silicon PIN photodetector unit, a silicon avalanche photodiode (APD) was used. In this case a self-regulating bias circuit as shown in Figure 6.13 was used. Since the silicon APD needed a fairly large DC bias voltage, the photodiode unit was AC coupled. This was achieved by having a 5 nF capacitor between the photodiode and the output BNC connector. This created a high pass filter system. It was noted that there is a non-linear variation of the multiplication factor M_{apd} with the applied bias voltage to the APD. This voltage dependent M_{apd} is defined as the ratio of the photocurrent $I_{apd}(t)$ at a particular reverse bias voltage V_b to the photocurrent at a set bias voltage of 10 volts. Figure 6.14 illustrates the multiplication factor as a function of reverse bias voltage for the APD used in the experiments reported in the thesis. A reverse bias voltage of -140 volts was used in all the experiments. This provided a photocurrent gain of about 10. Care was taken to ensure that this value was not exceeded because of the increase in the noise level of the APD detection setup.

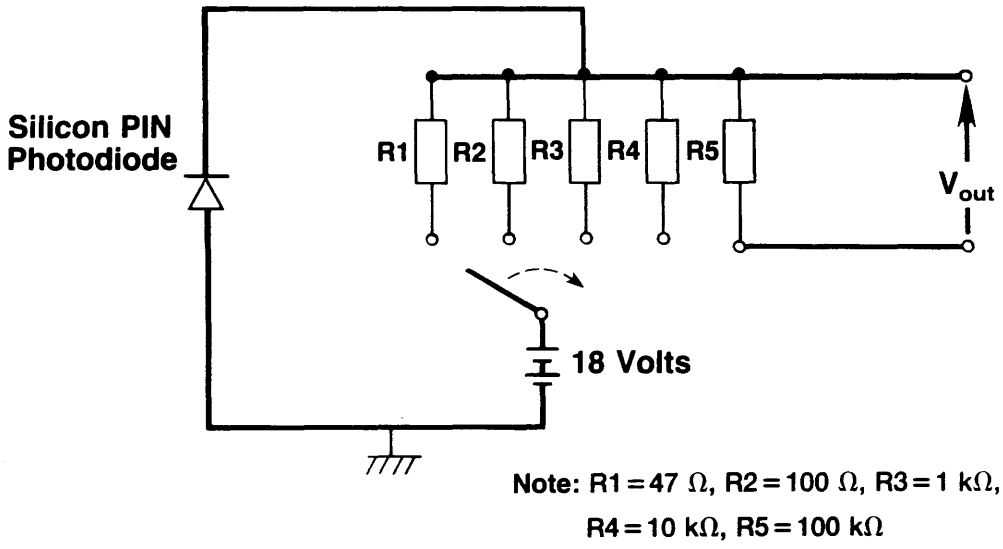

Figure 6.12 Schematic Of The DC Coupled Electrical Bias Circuit For The Silicon PIN Photodetectors

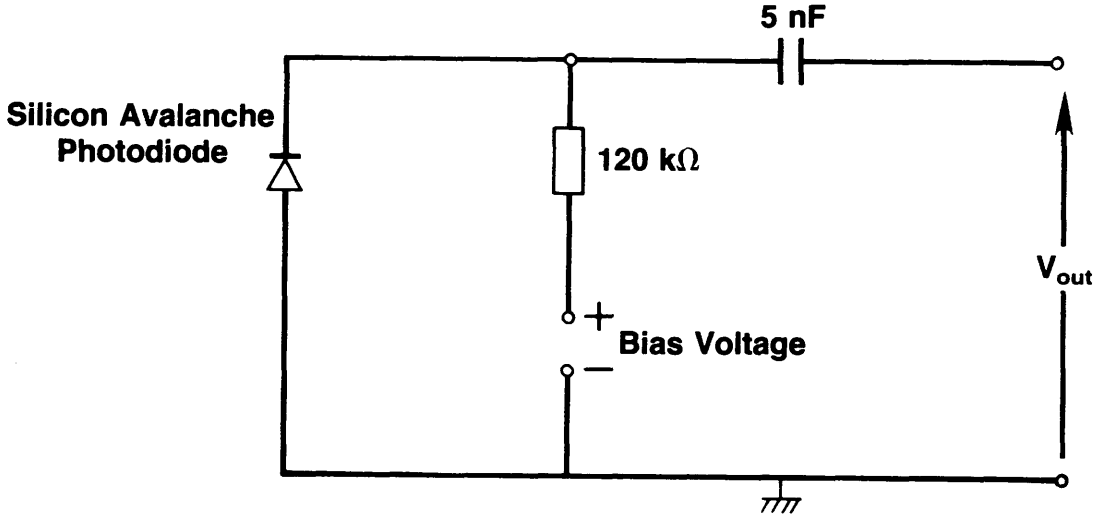

Figure 6.13 Schematic Of The Self Regulating Bias AC Coupled Circuit For The Silicon Avalanche Photodetector

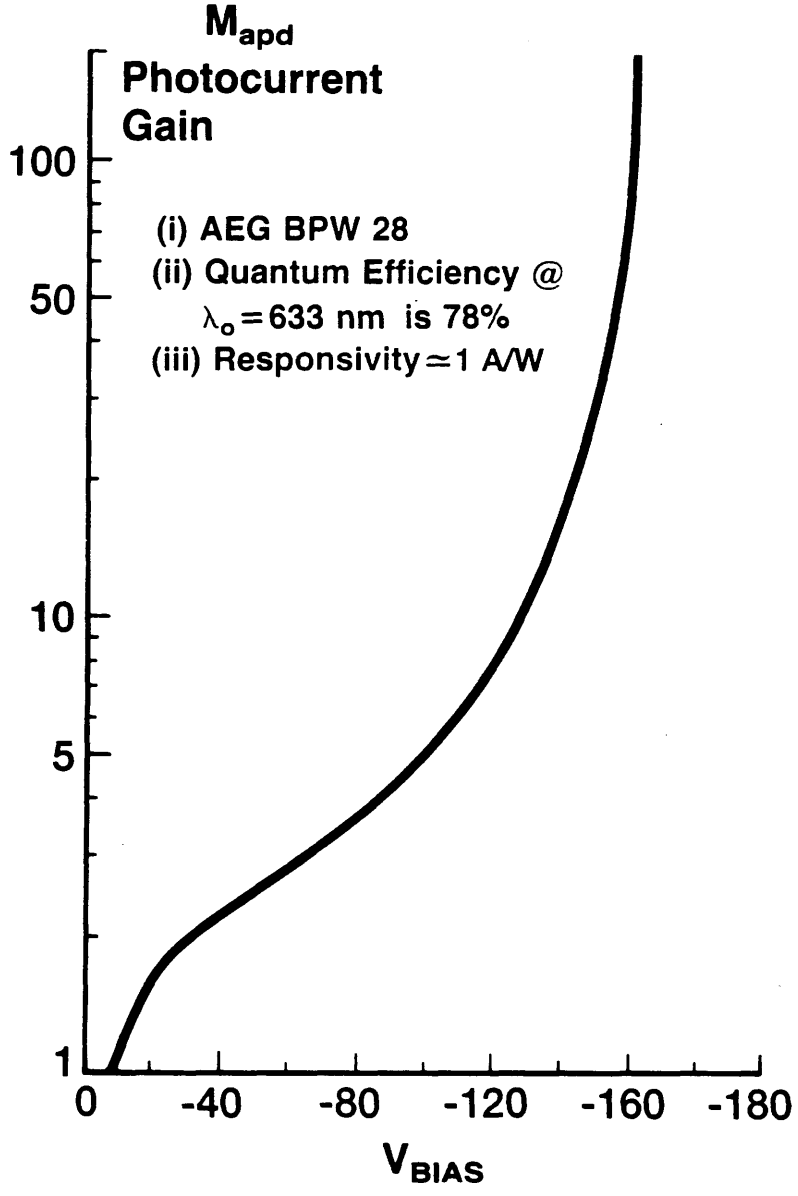

Figure 6.14 Plot Of The Multiplication Factor Versus Reverse Bias Voltage (BPW 28)

6.3.3 Theoretical Calculation of the Self Heterodyne Detection Process

As stated in the previous section of this chapter, the optical test arrangement used to evaluate the optical serrodyne frequency-translators was a bulk Mach-Zehnder interferometer arrangement (Figure 6.10). In this situation, only one laser source was used in the experiment.

In this self heterodyne mode of optical detection, the so called 'local oscillator' optical field $E_x(t) = E_{lo} \cos[(\omega_c+\omega_{lo})t]$, representing the Mach-Zehnder interferometer arm with the Bragg cell in it, was combined on the photodiode with the optical frequency shifted signal (other arm of the Mach-Zehnder interferometer) to be detected i.e $E_y(t) = E_{mod} \cos[(\omega_c+\omega_{mod})t]$. In all the work reported in this thesis, the optical frequency shifted signal ω_{mod} is very much smaller than the optical frequency of the HeNe laser radiation ω_c, i.e. $\omega_c >> \omega_{mod}$. Therefore the total heterodyned optical field $E_z(t)$ on the photodiode is given by the expression:

$$E_z(t) = E_{lo} \cos[(\omega_c+\omega_{lo})t] + E_{mod} \cos[(\omega_c+\omega_{mod})t] \qquad (6.30)$$

Since the photodiode is a square law device, the current $I_{pc}(t)$ generated by the detector as a result of the above heterodyning of the two optical fields is proportional to the square of the total optical field $E_z(t)$ and this can be expressed as:

$$I_{pc}(t) \propto [E_z(t)]^2$$

$$= 1/2[(E_{lo})^2+(E_{mod})^2] + 1/2(E_{lo})^2\cos[2(\omega_c+\omega_{lo})t]$$

$$+ 1/2(E_{mod})^2\cos[2(\omega_c+\omega_{mod})t]$$

$$+ E_{lo}E_{mod}\cos[(2\omega_c+\omega_{lo}+\omega_{mod})t]$$

$$+ E_{lo}E_{mod}\cos[(\omega_{lo}-\omega_{mod})t] \qquad (6.31)$$

where $\omega_{lo} > \omega_{mod}$ in all the experiments reported in this chapter.

In actual practice, the photodetector unit used in the experiments cannot follow the instantaneous intensity at the optical frequency of the laser source ω_c, due to the limitation of the rise time. The photodetector will be able to respond and detect the first and last terms of Equation 6.31. Therefore, the output from the photodiode unit due to the two incident optical fields $E_x(t)$ and $E_y(t)$ is given by the expression:

$$I_{pc}(t) = \beta\{1/2[(E_{lo})^2+(E_{mod})^2] + E_{lo}E_{mod}\cos[(\omega_{lo}-\omega_{mod})t]\}$$

$$= I_{dc} + I_{if}(t) \qquad (6.32)$$

where β is the photodiode conversion factor. This factor is dependent on the quantum efficiency, η, of the photodiode and the photon energy $h\upsilon$. In general, $\beta = \eta q/h\upsilon$, where q is the charge of an electron, h is Planck's constant, and υ is the frequency of the incident optical radiation.

In all the self heterodyne experiments reported in this chapter, the amount of optical power that was coupled through an optical phase-modulator was kept at a minimal ($\leq$ 1 mW) power level to avoid optical damage effects [6.19, 6.20, 6.21]. Most of the optical power from the laser was diverted by the beam splitter BS1 (Figure 6.10) to the arm with the Bragg cell. In this situation, it can be assumed that the amplitude of the modulated signal E_{mod} is much less than the amplitude of the local oscillator (Bragg cell) E_{lo}, i.e. $E_{lo} >> E_{mod}$. Therefore the output current of the photodiode $I_{pc}(t)$ can be rewritten as:

$$I_{pc}(t) = \beta P_{lo} \{1 + 2 \sqrt{[P_{mod}/P_{lo}]} \cos(\omega_{lo}-\omega_{mod})t\} \quad (6.33)$$

where P_{mod} and P_{lo} are the average optical powers of the incident modulated signal and the local oscillator signal respectively.

6.4 Evaluation of Optical Serrodyne Frequency-Translators

6.4.1 Introduction

In this section, the complete optical evaluation of titanium-indiffused and proton-exchanged phase-modulators is presented in Section 6.4.2. The results obtained experimentally are compared to the theoretical predictions described in Chapter 5 and elsewhere in this chapter. In addition, the electrical characteristics of the mounted phase-modulators are described and their implications for device performance are discussed in Section 6.4.3. Finally, the optical phase-modulators were operated as frequency-translators by the application of suitable sawtooth waveforms. The results of this study are presented in detail in Sections 6.4.4 and 6.4.5.

6.4.2 Optical Evaluations of Phase-Modulators

6.4.2.1 Ti:$LiNbO_3$ Phase-Modulators

As described in the earlier sections of this thesis, the stripe optical waveguides of the Ti:$LiNbO_3$ phase-modulators realised were both 4 μm and 5 μm wide. The main parameters checked were the initial thicknesses of the deposited titanium films and the number of waveguide modes supported by the stripe waveguides after fabrication using the standard diffusion conditions adapted in this thesis i.e. diffusion at 1000°C for 8 hours in a closed alumina tube with $LiNbO_3$ flakes of congruent composition. The wavelength of operation for all the active devices tested was 633 nm.

During the course of this work, stripe optical waveguides with initial titanium thicknesses ranging from 250 Å to 550 Å were fabricated. After the devices were prepared as outlined in Chapter 4, the end-fire coupling method was used exclusively to excite the waveguide modes. In so doing, a table of the number of optical waveguide modes observed as a function of titanium thickness and waveguide widths was drawn up (Table 6.3). In addition, following the work of McLachlan [6.12] and Bjortorp [6.13], the results from this work were added to the so called mode boundary curves. Figure 6.7 illustrates such a curve with the previously obtained theoretical and experimentally obtained results. In most cases, the results obtained in this work fitted well with their results. However in a few cases, especially for initial titanium thicknesses close to the cutoff mode lines, the results were either below the cutoff or more waveguide modes were observed. This may be attributed to the errors in the measurement of the titanium films and variation in the $LiNbO_3$ substrates.

In addition to the above results for Y-cut $LiNbO_3$, a number of stripe waveguides of similar width were realised in Z-cut $LiNbO_3$ by titanium indiffusion. The fabrication conditions used for Z-cut $LiNbO_3$ were similar to those adapted for Y-cut $LiNbO_3$, except for the method used for the control of outdiffusion. The technique adopted was the use of wet flowing oxygen during the full diffusion period i.e. including the ramp up and cool down periods. This was found to suppress any outdiffusion successfully. Figures 6.15a and 6.15b show photographs of the outputs from a 4 μm and a 5 μm stripe waveguide with an initial titanium thickness of 370 Å. From the titanium indiffusion experiments in Z-cut $LiNbO_3$, it was found that the titanium films have to be deposited on the negative Z-face of the crystal. If the titanium film was deposited on the positive Z-face of the $LiNbO_3$, some parts of the titanium stripe lines were found to be missing after the diffusion process. This may be due to the strong pyroelectric effects associated with

Titanium Thickness Å	Width Of Optical Waveguide 4 μm	5 μm
265	1	1
272	1	1
280	1	1
294	1	1 (2)
315	1	2
330	1	2
354	1 (2)	2
375	2	2
390	2	2
405	2	2
430	2	2
475	2	2
500	2	2 (3)
534	2	3

Table 6.3 Number Of Optical Waveguide Quasi-TE Modes Supported As A Function Of Titanium Thickness And Waveguide Width (Y-Cut $LiNbO_3$, 1000°C, 8 Hours, Closed Tube, λ_o= 633 nm)

Figure 6.15a Photograph Of The Observed Output Quasi-TM Mode From A 4 μm Stripe Waveguide
(370 Å Of Initial Titanium Thickness,
1000 °C, 8 Hours, Flowing Wet Oxygen)

Figure 6.15b Photograph Of The Observed Output Quasi-TM Mode From A 5 μm Stripe Guide
(370 Å Of Initial Titanium Thickness,
1000 °C, 8 Hours, Flowing Wet Oxygen)

this cut of the $LiNbO_3$. Table 6.4 summarises the results of the stripe optical waveguide measurements (number of quasi-TM modes) for titanium thicknesses ranging from 270 Å to 480 Å. Due to the limited number of samples and titanium range used for the Z-cut $LiNbO_3$ experiments, it was not possible to construct a mode boundary curves plot as described previously.

Next, the overall optical insertion losses for the Y- and Z-cut $Ti:LiNbO_3$ stripe waveguides (waveguide losses and modal mismatch loss between the microscope objective focal spot and the waveguide mode) were measured using end-fire coupling. The results are summarised in Table 6.5. In general the fairly high losses of 4 to 11 dB can be attributed to the mismatch between the waveguide modal distribution and the microscope objectives and to Fresnel reflection losses, with the higher loss values attributed to slight imperfections within the stripe waveguides; such as parts of the initial titanium lines were missing especially for stripe waveguides in Z-cut $LiNbO_3$. The solution to the modal mismatch problem is to use optical fibres with equivalent mode sizes to the stripe waveguides under tests. Unfortunately, at the time when this work was carried out no such single-mode optical fibres were commercially available at 633 nm.

Finally, the phase-modulators were fabricated (as described in Chapter 4) using the above tested stripe optical waveguides. In the case of Z-cut $LiNbO_3$ phase-modulators, before the electrode pattern was formed a thin layer of SiO_2 was deposited by pyrolitic chemical vapour deposition in Edinburgh University. This was to ensure that the electrode which was directly above the waveguide did not cause serious optical losses.

6.4.2.2 Proton Exchange $LiNbO_3$ Phase-Modulators

This section describes a similar optical waveguide study to that described in Section 6.4.2.1. However in this case no previously obtained results were available and therefore the study to be described was the first to

Titanium Thickness Å	Width Of Optical Waveguide 4 μm	5 μm
275	1	1
300	1	1
340	1	1
390	1	1 (2)
430	1 (2)	2
470	2	2

Table 6.4 Number Of Optical Waveguide Quasi-TM Modes Supported As A Function Of Titanium Thickness And Waveguide Width (Z-Cut $LiNbO_3$, 1000°C, 8 Hours, Flowing Wet O_2, λ_o= 633 nm)

Waveguide Width μm	Measured Optical Insertion Loss (dB) (Initial Titanium Thickness)		
	265 Å	294 Å	354 Å
4	9.8	8.8	6.2
5	7.5	8.0	5.6

Table 6.5a Measured Optical Insertion Losses For Ti:$LiNbO_3$ Stripe Guides (Y-Cut)
[Input & Output Microscope Objectives: X40]

Waveguide Width μm	Measured Optical Insertion Loss (dB) (Initial Titanium Thickness)		
	275 Å	300 Å	430 Å
4	8.8	7.7	4.4
5	8.0	11.0	10.8

Table 6.5b Measured Optical Insertion Losses For Ti:$LiNbO_3$ Stripe Guides (Z-Cut)
[Input & Output Microscope Objectives: X40]

be performed in the Department of Electronics and Electrical Engineering at Glasgow University.

The dispersion curves shown in Figures 6.8 and 6.9 (based on the theory by Marcatili and the effective index method) were used to provide initial guidance as to the required depth for optical waveguiding for 4 and 5 μm wide waveguides at the operating wavelength of 633 nm. To recap, the Δn values used for generating the dispersion curves were 0.10 and 0.12.

All the PE stripe optical waveguide devices were fabricated in X-cut $LiNbO_3$ using concentrated benzoic acid melts. Due to the lack of time available, no devices were realised in Z-cut $LiNbO_3$ and also no phase-modulators were fabricated using the dilute melt process as described in Chapter 4. An important assumption that was made in fabricating the stripe waveguides was that the optical characterisation results of the slab waveguides reported in Chapter 5 could be used to design stripe waveguides. Hence Equation 5.47 was used exclusively to calculate the depth for stripe waveguides at a particular exchange temperature.

In order to produce the necessary mode boundary curves, further computations using Marcatili's method and the Effective Index method were carried out to generate cutoff depths for optical waveguides with stripe widths of 2.0 μm, 7 μm, and 9.0 μm for Δn values of 0.10 and 0.12. The cutoff depths are shown in Tables 6.6, 6.7 and 6.8 respectively. In this work, only exchange temperatures of around 162°C, 181°C, and 200°C were used. The main reason for this choice of temperatures was that if higher temperatures were used, the diffusion coefficient would be larger and therefore it would be more difficult to realise single mode PE stripe waveguides since the time required for the exchange process would become excessively short.

The theoretical mode boundary curves were plotted for the above three selected exchange temperatures. These are illustrated in Figures 6.16(a-d), 6.17(a-d), and 6.18(a-d). From all these theoretical analyses, it was

Mode Number	Cut-off Depth, μm (Marcatili)	Cut-off Depth, μm (Effective Index)
TE_{11}	0.222	0.193
TE_{21}	0.279	0.211
TE_{31}	0.375	0.251
TE_{41}	0.590	0.353

(a) $\Delta n = 0.10$

Mode Number	Cut-off Depth, μm (Marcatili)	Cut-off Depth, μm (Effective Index)
TE_{11}	0.196	0.171
TE_{21}	0.241	0.184
TE_{31}	0.312	0.213
TE_{41}	0.451	0.277

(b) $\Delta n = 0.12$

Table 6.6 Values Of Cut-off Depths For A 2 μm Wide Stripe Waveguide With $\Delta n = 0.10$ And $\Delta n = 0.12$ (By Marcatili And Effective Index Methods)

Mode Number	Cut-off Depth, μm (Marcatili)	Cut-off Depth, μm (Effective Index)
TE_{11}	0.196	0.188
TE_{21}	0.207	0.190
TE_{31}	0.220	0.192
TE_{41}	0.235	0.196

(a) $\Delta n = 0.10$

Mode Number	Cut-off Depth, μm (Marcatili)	Cut-off Depth, μm (Effective Index)
TE_{11}	0.173	0.167
TE_{21}	0.183	0.169
TE_{31}	0.193	0.171
TE_{41}	0.205	0.173

(b) $\Delta n = 0.12$

Table 6.7 Values Of Cut-off Depths For A 7 μm Wide Stripe Waveguide With $\Delta n = 0.10$ And $\Delta n = 0.12$ (By Marcatili And Effective Index Methods)

Mode Number	Cut-off Depth, μm (Marcatili)	Cut-off Depth, μm (Effective Index)
TE_{11}	0.194	0.188
TE_{21}	0.202	0.189
TE_{31}	0.212	0.191
TE_{41}	0.222	0.193

(a) $\Delta n = 0.10$

Mode Number	Cut-off Depth, μm (Marcatili)	Cut-off Depth, μm (Effective Index)
TE_{11}	0.172	0.169
TE_{21}	0.179	0.171
TE_{31}	0.187	0.173
TE_{41}	0.195	0.176

(b) $\Delta n = 0.12$

Table 6.8 Values Of Cut-off Depths For A 9 μm Wide Stripe Waveguide With $\Delta n = 0.10$ And $\Delta n = 0.12$ (By Marcatili And Effective Index Methods)

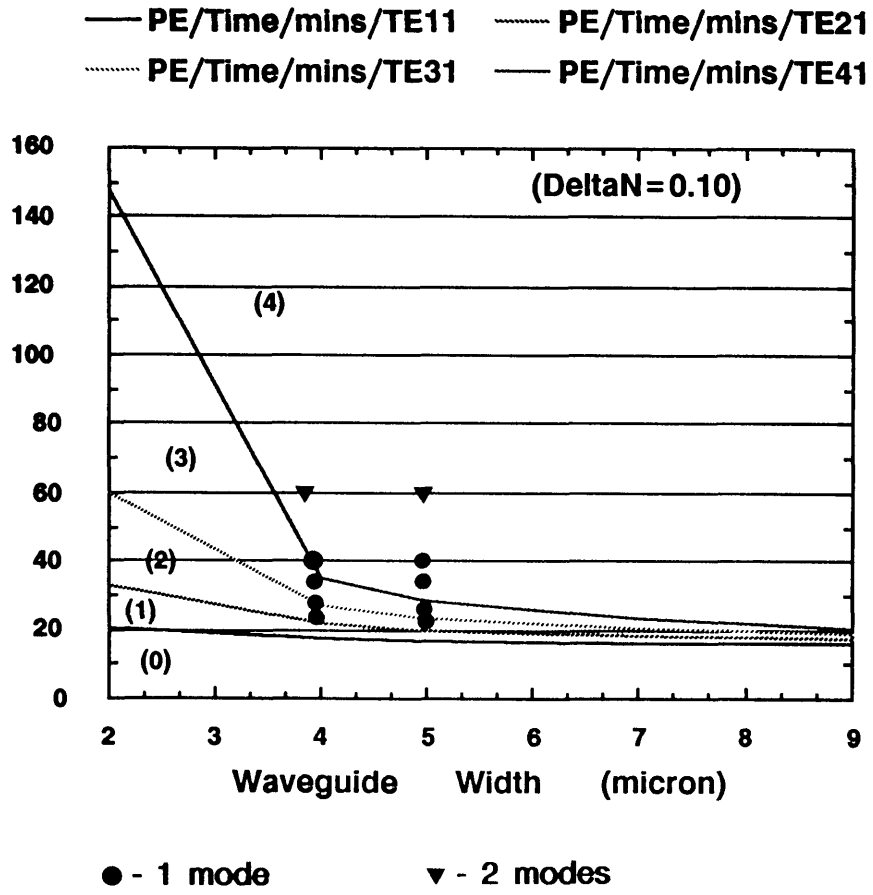

Figure 6.16a Number Of Quasi–TE Modes Supported As A Function Of Waveguide Width (in μm) And Exchange Time (in minutes) For X–Cut $LiNbO_3$ – Marcatili's Method (Exchange Temperature= 162°C, Δn=0.10)

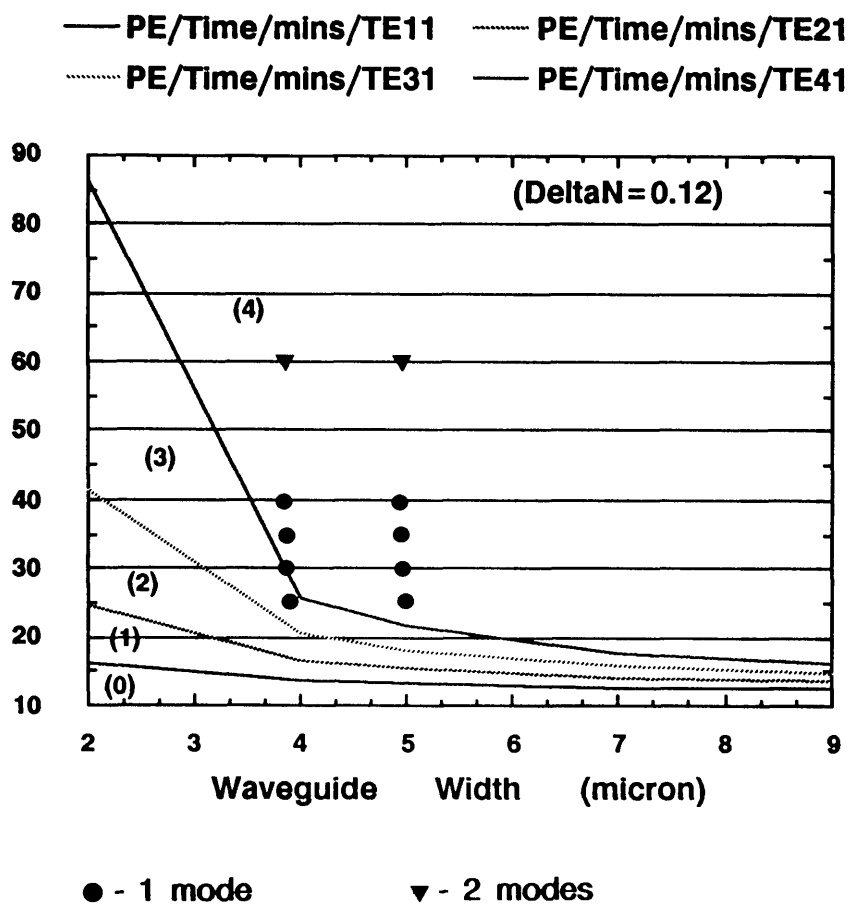

Figure 6.16b Number Of Quasi–TE Modes Supported As A Function Of Waveguide Width (in μm) And Exchange Time (in minutes) For X–Cut $LiNbO_3$ – Marcatili's Method (Exchange Temperature= 162°C, Δn=0.12)

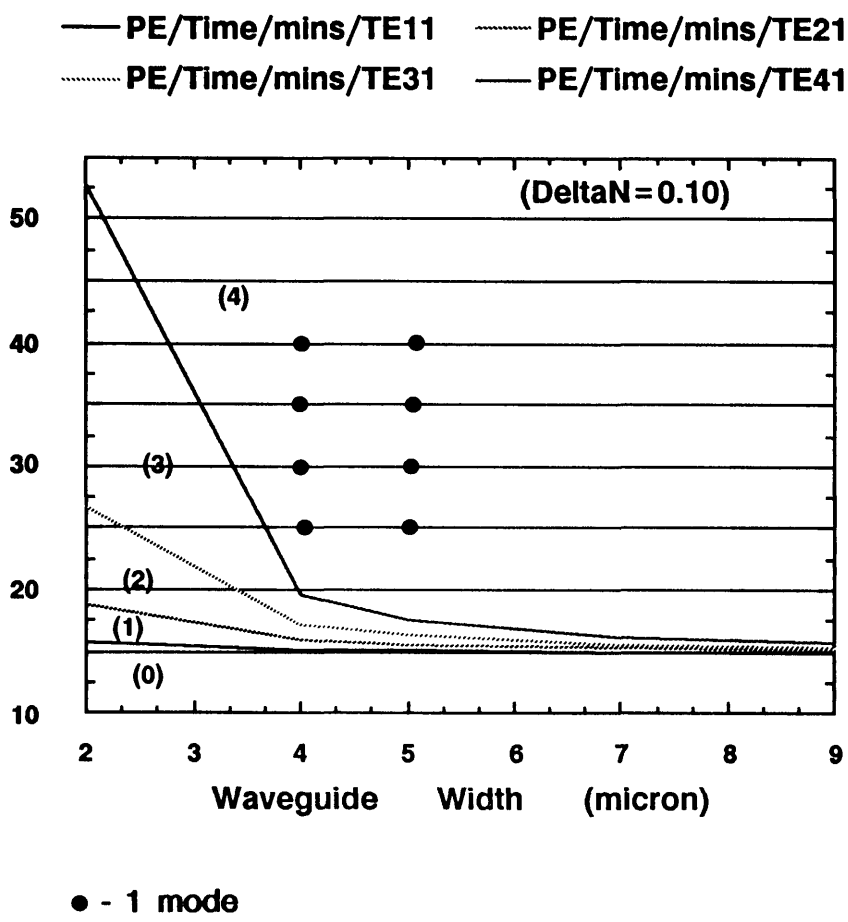

Figure 6.16c Number Of Quasi–TE Modes Supported As A Function Of Waveguide Width (in μm) And Exchange Time (in minutes) For X–Cut $LiNbO_3$ – Effective Index Method (Exchange Temperature= 162°C, Δn=0.10)

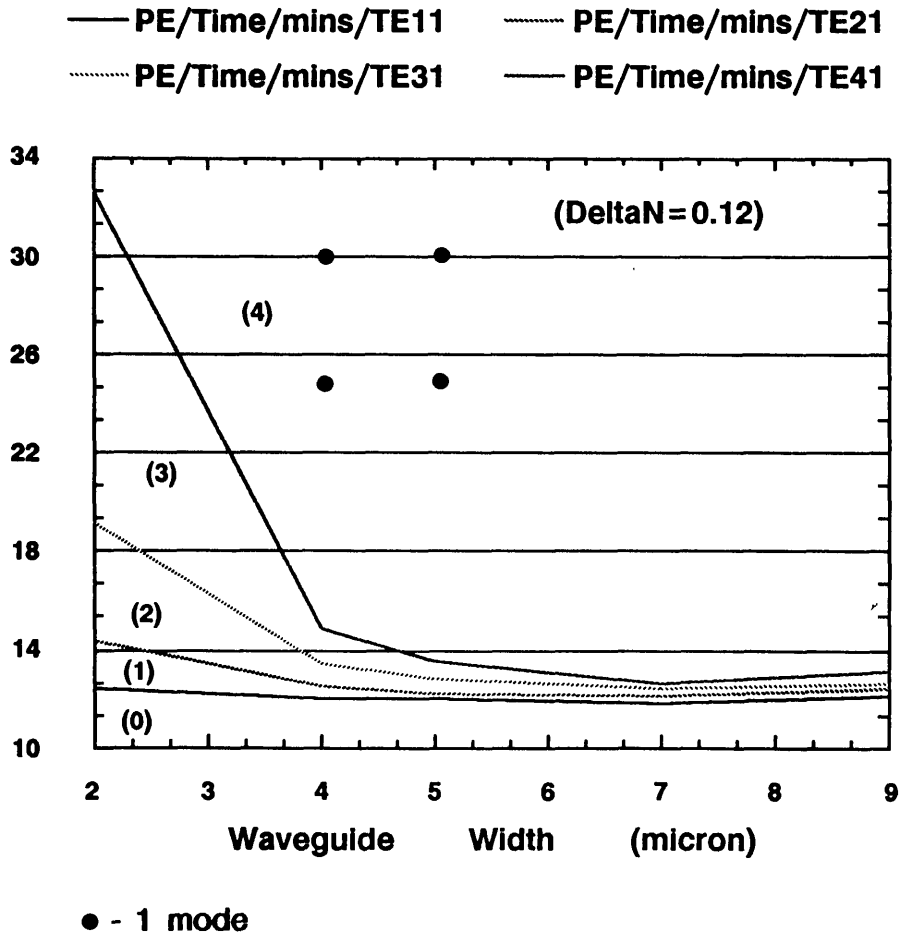

Figure 6.16d Number Of Quasi–TE Modes Supported As A Function Of Waveguide Width (in μm) And Exchange Time (in minutes) For X–Cut $LiNbO_3$ – Effective Index Method (Exchange Temperature= 162°C, Δn=0.12)

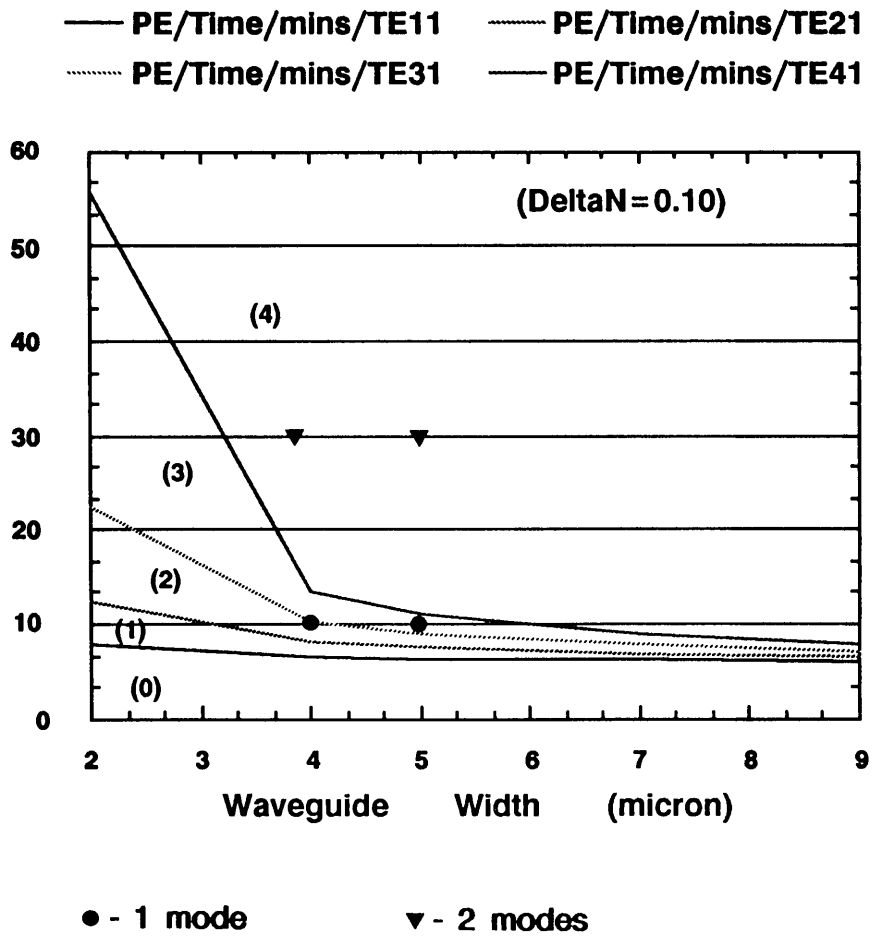

Figure 6.17a Number Of Quasi–TE Modes Supported As A Function Of Waveguide Width (in μm) And Exchange Time (in minutes) For X–Cut $LiNbO_3$ – Marcatili's Method (Exchange Temperature= 181°C, Δn=0.10)

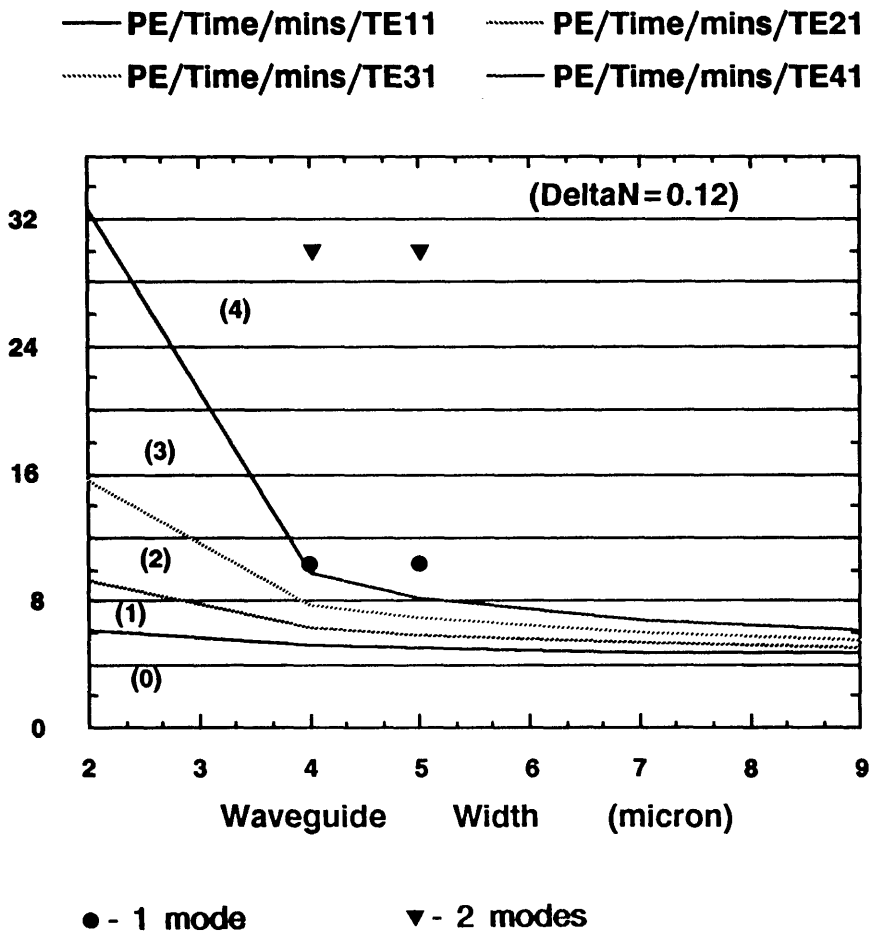

Figure 6.17b Number Of Quasi–TE Modes Supported As A Function Of Waveguide Width (in μm) And Exchange Time (in minutes) For X–Cut $LiNbO_3$ – Marcatili's Method (Exchange Temperature= 181°C, Δn=0.12)

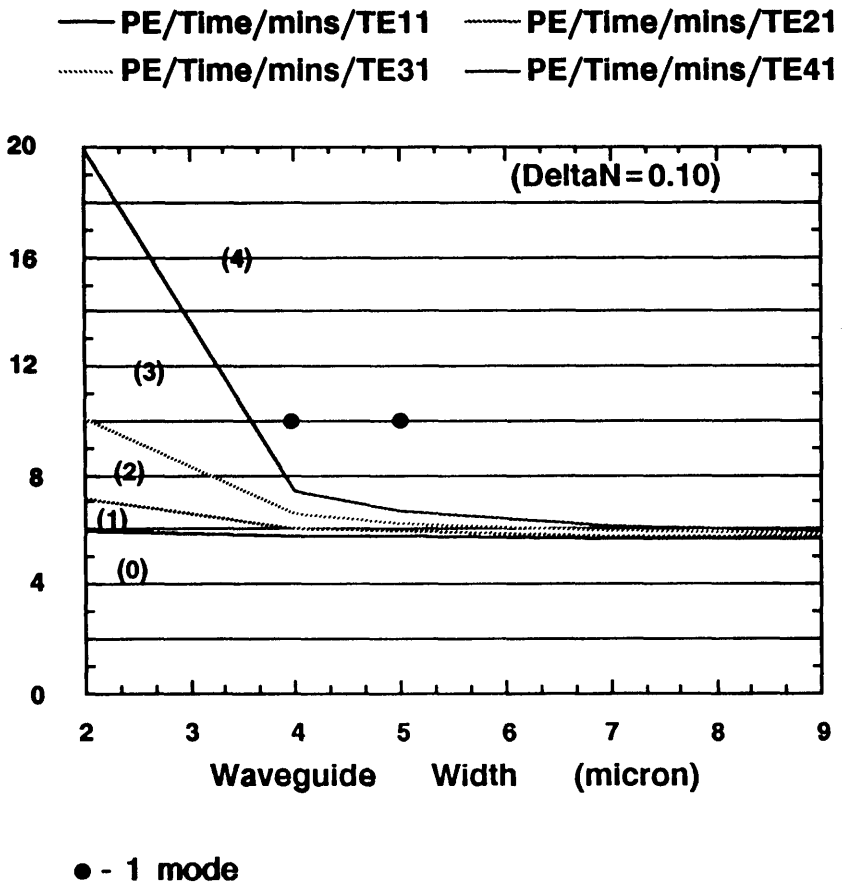

Figure 6.17c Number Of Quasi–TE Modes Supported As A Function Of Waveguide Width (in μm) And Exchange Time (in minutes) For X–Cut $LiNbO_3$ – Effective Index Method (Exchange Temperature= 181°C, Δn=0.10)

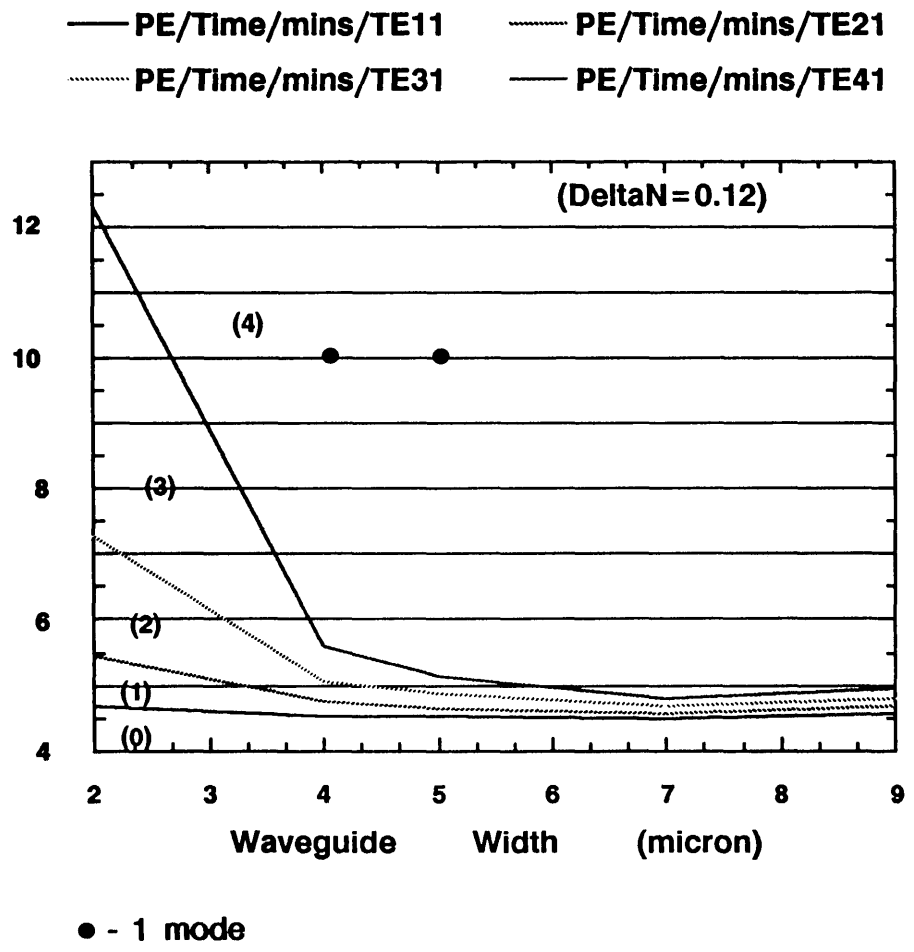

Figure 6.17d Number Of Quasi–TE Modes Supported As A Function Of Waveguide Width (in μm) And Exchange Time (in minutes) For X–Cut $LiNbO_3$ – Effective Index Method (Exchange Temperature= 181°C, Δn=0.12)

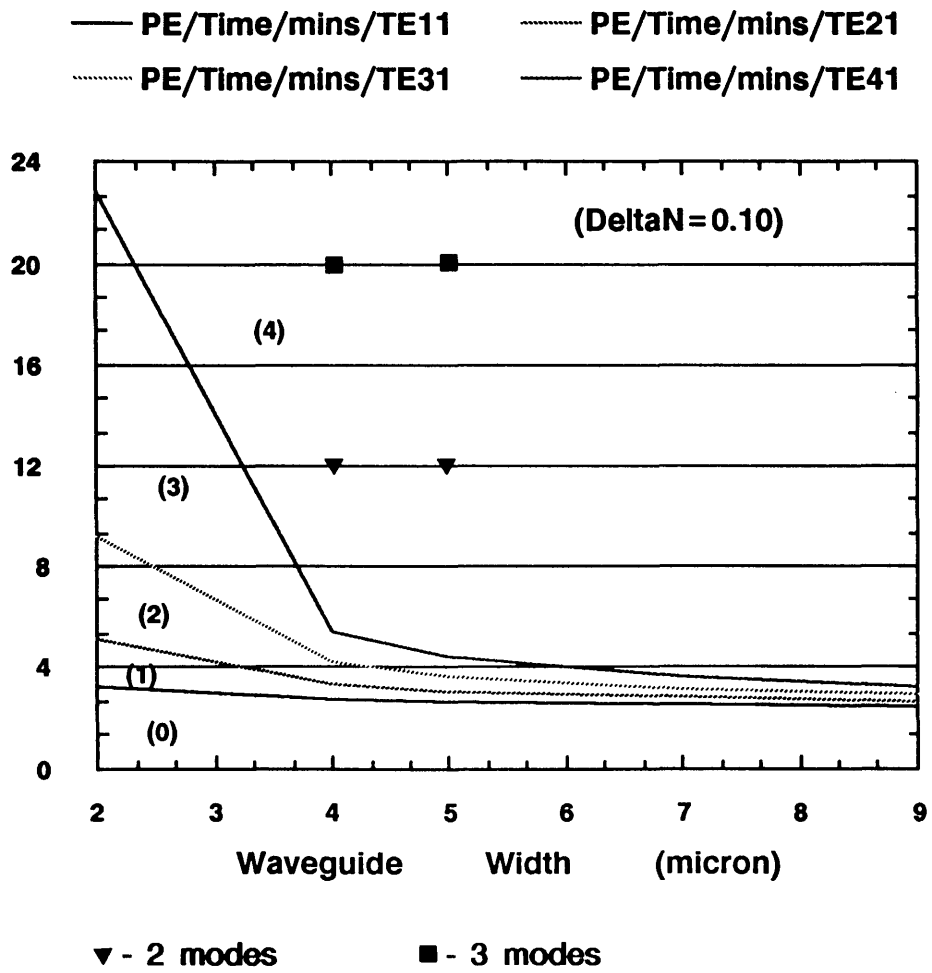

Figure 6.18a Number Of Quasi–TE Modes Supported As A Function Of Waveguide Width (in μm) And Exchange Time (in minutes) For X–Cut $LiNbO_3$ – Marcatili's Method (Exchange Temperature= 200°C, Δn=0.10)

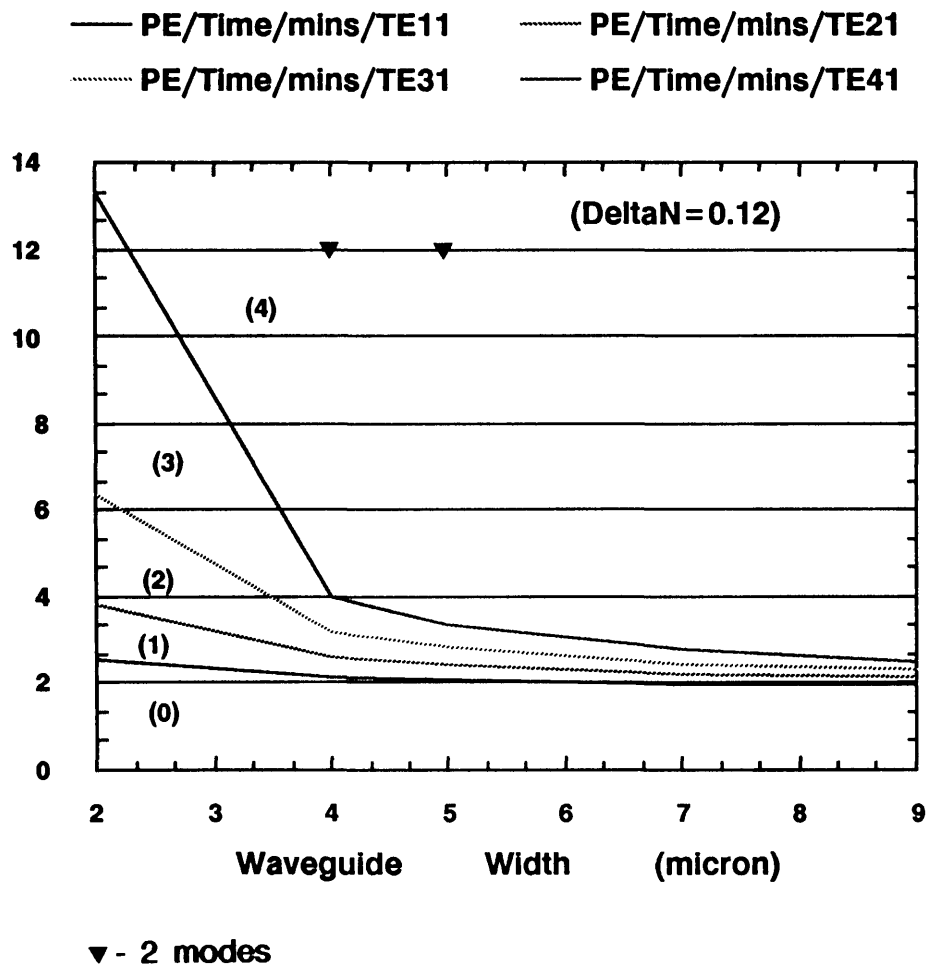

Figure 6.18b Number Of Quasi–TE Modes Supported As A Function Of Waveguide Width (in μm) And Exchange Time (in minutes) For X–Cut $LiNbO_3$ – Marcatili's Method (Exchange Temperature= 200°C, Δn=0.12)

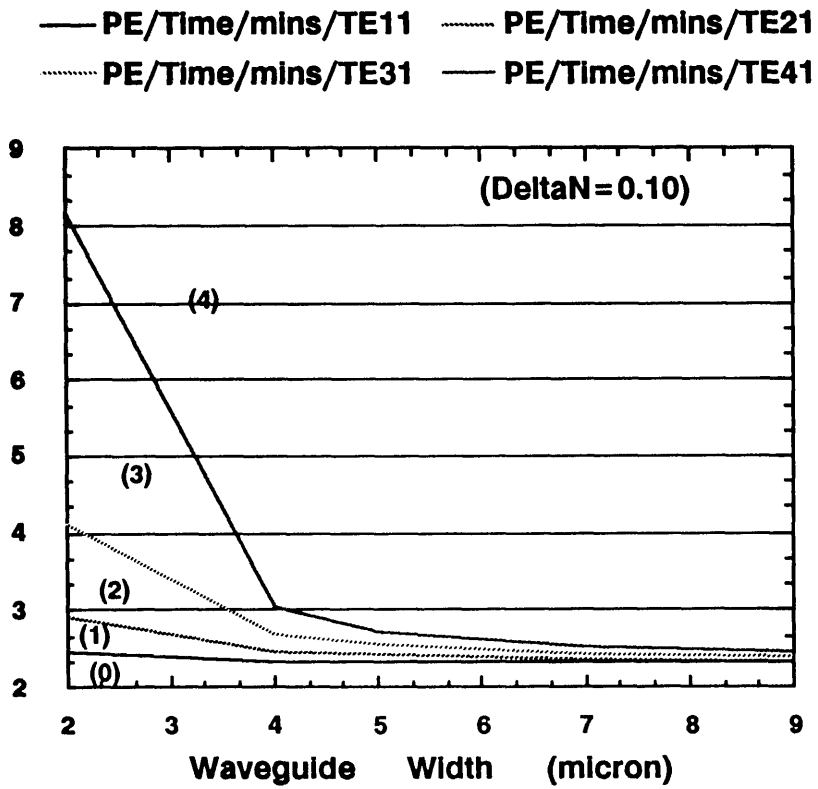

Figure 6.18c Number Of Quasi–TE Modes Supported As A Function Of Waveguide Width (in μm) And Exchange Time (in minutes) For X–Cut $LiNbO_3$ – Effective Index Method (Exchange Temperature= 200°C, Δn=0.10)

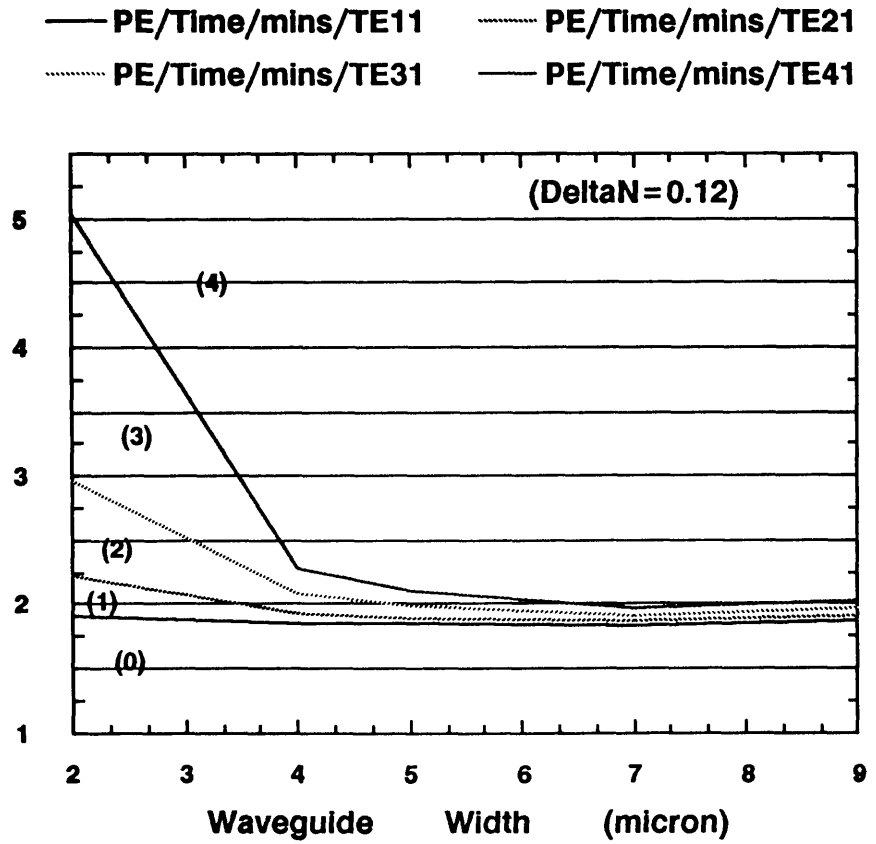

Figure 6.18d Number Of Quasi–TE Modes Supported As A Function Of Waveguide Width (in μm) And Exchange Time (in minutes) For X–Cut $LiNbO_3$ – Effective Index Method (Exchange Temperature= 200°C, Δn=0.12)

decided to concentrate on using an exchange temperature of around 162°C for stripe waveguide fabrication. A number of stripe waveguides were also fabricated at the other two selected exchange temperatures.

The PE stripe waveguides were evaluated using the end-fire coupling method. The number of modes supported by the 4 μm and the 5 μm wide stripe waveguides were noted in each case and plotted in the respective mode boundary curves (Figures 6.16, 6.17, and 6.18). From these results, it was obvious that the cutoff for the fundamental quasi-TE mode predicted by the above procedure was incorrect. This may be attributed to two main factors. They are:-

(a) The use of the aluminium mask could have slowed the exchange process by the presence of an electric potential across the diffusion aperture [6.22], and

(b) The assumed Δn values of 0.10 and 0.12 for the fabricated stripe waveguide may be incorrect.

Recently, Sanford et al [6.23] investigated the above problems by using secondary-ion mass spectroscopy to characterise the lithium depletion of the fabricated PE stripe optical waveguides. Their studies indicated that the depletion of lithium from the stripe waveguide regions was dependant on the width of the waveguide (i.e. the width of the diffusion aperture) and the diffusion time. As an example of their work, a stripe waveguide formed by diffusing through a 6 μm wide metallic aperture for 10 minutes at 249°C apparently suffered 60% less lithium depletion near its surface than one formed by diffusing through a 12 μm aperture for the same time.

Walker et al [6.24, 6.25, 6.26] reported that by anodising the aluminium diffusion patterns to Al_2O_3, it was possible to eliminate the problem due to metallic diffusion masks. Again due to lack of available time, no research work was performed in this area.

The overall insertion losses of the fabricated PE stripe waveguides were measured as described in Section 6.4.2.1 above. Table 6.9 shows a summary of the measured losses as a function of the selected fabrication conditions for the 4 μm and 5 μm wide single-mode stripe waveguides. As can be seen from the table, the insertion losses for PE stripe waveguides were much higher than for the stripe Ti:$LiNbO_3$ waveguides, i.e. 10 to 20 dB higher. Most of these losses could be attributed to the distribution mismatch between the focussed input laser beam and the stripe waveguide mode. Figures 6.19a and 6.19b illustrate the modal width and depth intensity plots for a typical PE and a typical titanium-indiffused stripe waveguide (4 μm wide) in X-cut and Y-cut $LiNbO_3$ respectively. The modal plots were obtained using a computer controlled Hamamatsu C1000 visible camera system. The software was provided by Hamamatsu of Japan. For the PE stripe waveguide, the measured $1/e^2$ modal width and depth were 5.0 μm and 1.5 μm respectively. The calculated asymmetry, i.e. width divided by depth is 3.33. The measured $1/e^2$ modal width and depth for the titanium indiffused stripe waveguide were 8.4 mm and 5.8 mm respectively with a calculated asymmetry value of 1.45. The ratio of the asymmetry values between the stripe PE waveguide and the titanium indiffused waveguide is 2.3. The asymmetry between the width and depth optical mode is most probably the main contributing factor to the measured higher optical insertion loss values for the PE stripe waveguides. The solution to the problem of excessive modal confinement in PE stripe waveguides maybe to anneal them. Recently, insertion losses of around 1 db have been achieved by annealing stripe optical waveguides [6.27-6.30]. Therefore the problem of high insertion losses in stripe PE waveguides can be solved with ease. However, by annealing the PE waveguides, it has been shown that the refractive index profile of the waveguides changed from a step-like to a Gaussian shape. Also the Δn was reduced from 0.12 to as low as 0.01 [6.31, 6.32].

PE Fabrication Conditions	Measured Optical Insertion Loss (dB)
25 mins., 162°C	31dB
30 mins., 162°C	28dB
35 mins., 162°C	28dB
40 mins., 162°C	23dB
10 mins., 181°C	22dB

(a) 4 μm

PE Fabrication Conditions	Measured Optical Insertion Loss (dB)
25 mins., 162°C	30dB
30 mins., 162°C	28dB
35 mins., 162°C	23dB
40 mins., 162°C	17dB
10 mins., 181°C	20dB

(b) 5 μm

Table 6.9 Measured Optical Insertion Losses For PE Stripe Guides In X-Cut $LiNbO_3$ (a) 4 μm And (b) 5 μm [Input & Output Microscope Objectives: X40]

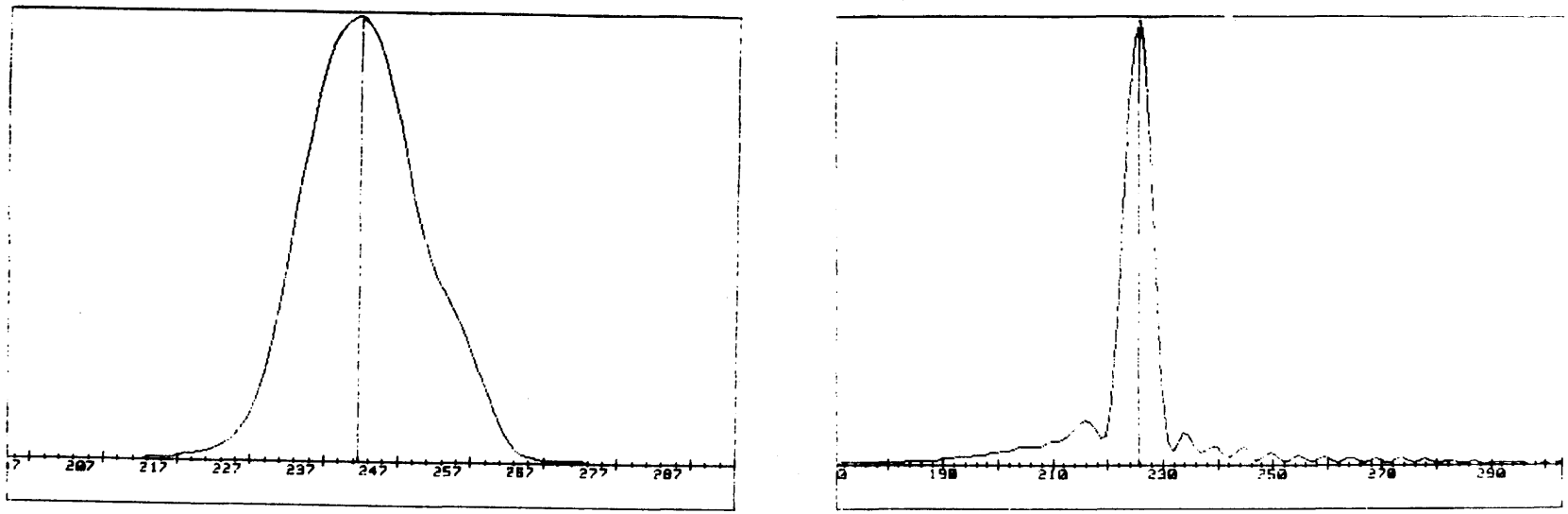

(a) (b)

Figure 6.19a Linear Optical Field Intensity Plots For A 4 μm Wide Proton–Exchange X–Cut $LiNbO_3$ Stripe Waveguide
[(a) $1/e^2$ Width= 5 μm, (b) $1/e^2$ Depth= 1.5 μm]

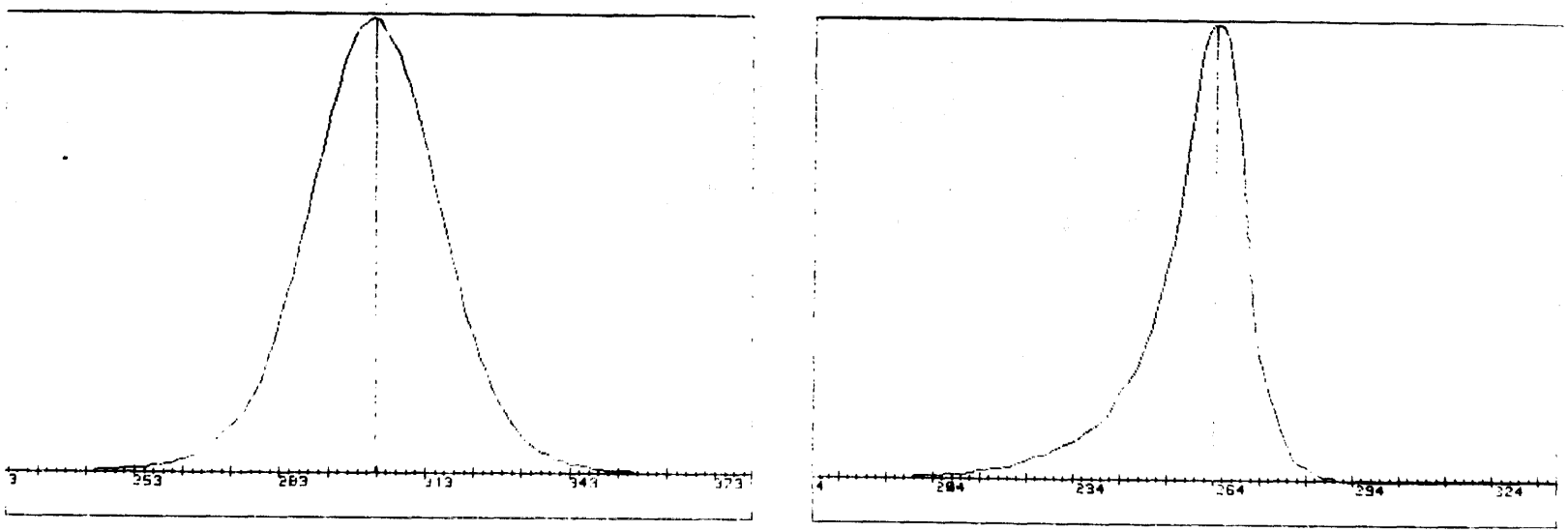

(a) (b)

Figure 6.19b Linear Optical Field Intensity Plots For A 4 μm Titanium Indiffused Y–Cut $LiNbO_3$ Stripe Waveguide
[(a) $1/e^2$ Width= 8.4 μm, (b) $1/e^2$ Depth= 5.8 μm]

After all the above waveguide studies, the stripe waveguides were then used to realise phase-modulators. These devices were then evaluated as optical frequency-translators using suitable sawtooth waveforms.

6.4.3 Electrical Frequency Response of Phase-Modulators

The electrical frequency response of the optical phase modulator was measured using the self heterodyne test arrangement shown in Figure 6.10 except that in this case the Bragg cell was not in use. The reference laser beam was combined with the laser beam from the phase modulator under evaluation using a beam splitter and the two beams were heterodyned on a fast silicon avalanche photodiode (Appendix 6.1). The input signal to the phase modulator was adjusted to be 10 dBm for a termination resistance of 47 Ω. Figures 6.20 and 6.21 show typical normalised frequency response plots for a Y-cut Ti:$LiNbO_3$ and a PE X-cut $LiNbO_3$ phase modulator respectively. The devices were found to have a 3 dB bandwidth of about 1.1 GHz. The calculated capacitance limited 3 dB bandwidth was 2.7 GHz (Table 6.2). The discrepancies in the calculated and measured 3 dB bandwidth may be attributed to the presence of the bonding pads which were not considered in the capacitance limited bandwidth calculations. Therefore the results implied that the optical phase-modulators were suitable for serrodyne frequency translation studies.

6.4.4 Experimental Results for Titanium-Indiffused Phase-Modulators Driven by Sawtooth Electrical Waveforms

6.4.4.1 Determination of $V_{2\pi}$ Values

After the successful optical characterization of the stripe waveguides and the determination of the electrical 3 dB bandwidth of the optical phase-modulators, the devices were ready for serrodyne frequency translation

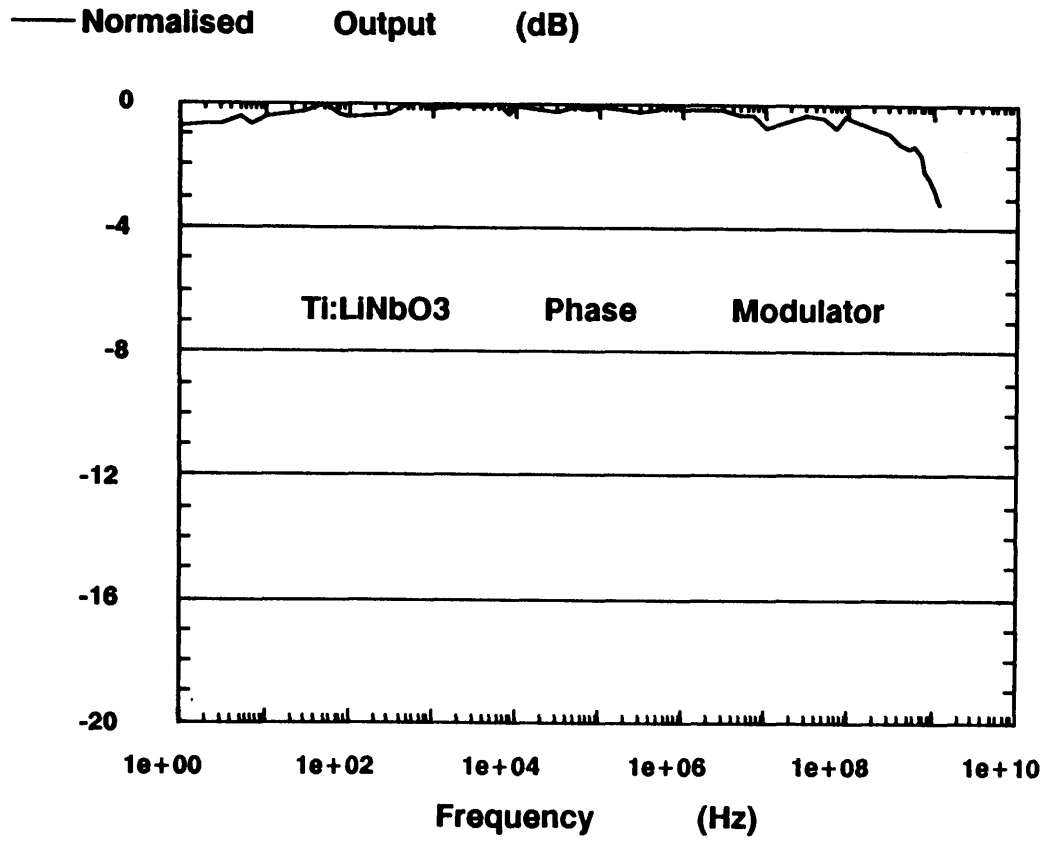

Figure 6.20 Normalised Frequency Response For A Ti:$LiNbO_3$ (Y–Cut) Optical Phase Modulator (λ= 633 nm, Initial Titanium Thickness= 330 Å, Width of Waveguide= 4 μm)

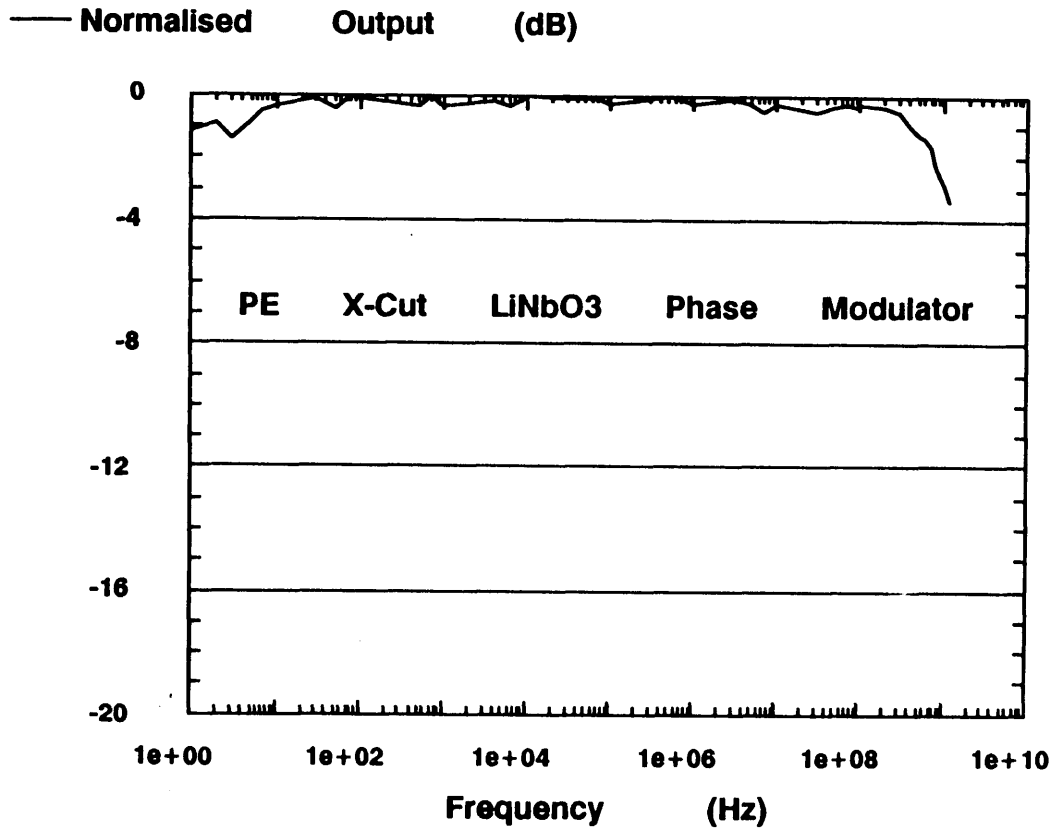

Figure 6.21 Normalised Frequency Response For A Proton–Exchange $LiNbO_3$ (X–Cut) Optical Phase Modulator (λ= 633 nm, Exchange Time= 25 minutes, Exchange Temperature= 162°C, Width of Waveguide= 4 μm)

experiments. The devices (both Y-cut and Z-cut) to be tested were placed in the bulk Mach-Zehnder interferometer arrangement described previously (Figure 6.10).

The first test involved the determination of the voltage required for generating a 2π phase change. This was accomplished by driving the phase-modulator with a variable (0 to 30 volts) dc signal. The Bragg cell was not used in this part of the experiment. The optical beams from both the arms of the bulk Mach-Zehnder interferometer were heterodyned on a dc coupled photodetector unit. The output from the photodetector was used to drive the Y-axis of the plotter with the X-axis driven by the variable dc signal. The $V_{2\pi}$ voltage requirement for each of the phase-modulators under evaluation was determined by measuring the voltage needed to move from one maximum to another maximum or from one minimum to another minimum. Tables 6.10(a, b) and 6.11(a, b) show the measured $V_{2\pi}$ values of the tested Y-cut and Z-cut $Ti:LiNbO_3$ phase-modulators (4 μm and 5 μm wide) respectively. From Tables 6.10a and 6.10b (for Y-cut $Ti:LiNbO_3$ devices) it can be seen that the measured $V_{2\pi}$ voltage values ranged from 9.5 volts to 15.0 volts. The reason for this variation is mainly due to the different active device lengths i.e. 7.7 mm to 10 mm. This was due to the non-uniform trimming of the ends of the devices prior to end-polishing. Another possible contributing factor to the variations in the measured $V_{2\pi}$ values is the slight variation in the overlap factor (0.29 to 0.40) since the initial titanium thickness ranged from 240 Å to 400 Å. The results in Tables 6.10a and 6.10b also indicated that the calculated overlap factor was slightly higher for the 5 μm wide phase modulators when compared to the 4 μm wide devices. The reason for this maybe due to the slightly higher n_{eff} values (see Equation 6.21). For Z-cut $Ti:LiNbO_3$ phase-modulators, the results indicated slightly higher measured $V_{2\pi}$ (12.5 volts to 15.8 volts) values for devices with the same active lengths. A possible reason for this maybe due to the presence of the SiO_2 buffer layer which can affect

Modulator Number	Active Length (mm)	Initial Titanium Thickness (Å)	Measured $V_{2\pi}$ Value (Volts)	Calculated Overlap Factor Value
SSB1	9.0	240	14.0	0.30
ST12	10.0	265	12.5	0.30
SSB3	9.5	272	13.8	0.29
ST2	7.7	315	15.0	0.33
ST5	8.9	330	12.2	0.35
ST7	10.0	354	9.5	0.40
ST8	9.0	375	10.8	0.39

Table 6.10a $V_{2\pi}$ Voltage Requirements For Tested 4 μm Wide Y–Cut $LiNbO_3$ Phase Modulators (With 10 μm Electrode Gap)

Modulator Number	Active Length (mm)	Initial Titanium Thickness (Å)	Measured $V_{2\pi}$ Value (Volts)	Calculated Overlap Factor Value
SSB1	9.0	240	13.5	0.31
ST12	10.0	265	12.0	0.32
SSB3	9.5	272	11.5	0.35
ST2	7.7	315	14.4	0.34
ST5	8.9	330	Not Evaluated	Not Evaluated
ST7	10.0	354	Not Evaluated	Not Evaluated
ST8	9.0	375	Not Evaluated	Not Evaluated

Table 6.10b $V_{2\pi}$ Voltage Requirements For Tested 5 μm Wide Y–Cut $LiNbO_3$ Phase Modulators (With 10 μm Electrode Gap)

Modulator Number	Active Length (mm)	Initial Titanium Thickness (Å)	Measured $V_{2\pi}$ Value (Volts)	Calculated Overlap Factor Value
SZ2	10.0	275	14.3	0.27
SZ7	9.0	340	13.6	0.31
SZ9	10.0	390	12.5	0.30
SZ10	8.0	430	15.8	0.30

Table 6.11a $V_{2\pi}$ Voltage Requirements For Tested 4 μm Wide Z–Cut $LiNbO_3$ Phase Modulators (With 10 μm Electrode Gap)

Modulator Number	Active Length (mm)	Initial Titanium Thickness (Å)	Measured $V_{2\pi}$ Value (Volts)	Calculated Overlap Factor Value
SZ2	10.0	275	13.5	0.28
SZ7	9.0	340	13.6	0.31
SZ9	10.0	390	12.6	0.30
SZ10	8.0	430	Not Evaluated	Not Evaluated

Table 6.11b $V_{2\pi}$ Voltage Requirements For Tested 5 μm Wide Z–Cut $LiNbO_3$ Phase Modulators (With 10 μm Electrode Gap)

the applied electric fields and hence the overlap factor (0.27 to 0.31). The phase modulators were then used for the serrodyne experiments.

6.4.4.2 Effect of Non-Zero Flyback/Fall-Time

In this section, studies of the effect of finite fall-time (T_f) on the sawtooth driven Y- and Z-cut Ti:$LiNbO_3$ phase modulators are reported. Commercial function generators were employed throughout the serrodyne frequency translation experiments. One of the features that makes such function generators attractive is the ability to change the fall-time of the sawtooth signals. Again the Mach-Zehnder interferometer setup was used to perform this study. Only upshift frequency translations are reported. The generated sideband results from the experiments were compared to the theoretically predicted sideband levels as discussed in Section 3.4.2 of Chapter 3.

Figure 6.22 shows a typical spectrum plot (dc to 110 MHz) with the entire frequency translation beat spectrum shifted to an intermediate frequency of 22 MHz as observed on the spectrum anlayzer. In this case, the device used was a 4 μm wide Y-cut Ti:$LiNbO_3$ phase modulator with an initial titanium thickness of 315 Å (device ST2 in Table 6.10a). As can be seen from the above beat spectrum only the 0th, 1st-(lower and upper), 2nd-(lower and upper), and 3rd-(lower and upper) order sidebands were significant and hence for all remaining results reported in this thesis only the above mentioned sideband levels were considered.

By applying multiple integer (i.e. 2, 3, ...) values of $V_{\equiv 2\pi}$ to the phase modulators, it is possible to achieve higher multiple ($2*f_m$, $3*f_m$, ...) frequency translations using one single serrodyne frequency value (f_m). As an example, Figures 6.23a and 6.23b illustrate the serrodyne frequency translation spectrum plots for a 4 μm wide Y-cut Ti:$LiNbO_3$ driven with $V_{\equiv 2\pi}$ and $V_{\equiv 4\pi}$ (= $2*V_{\equiv 2\pi}$) values and the resultant corresponding frequency shifts

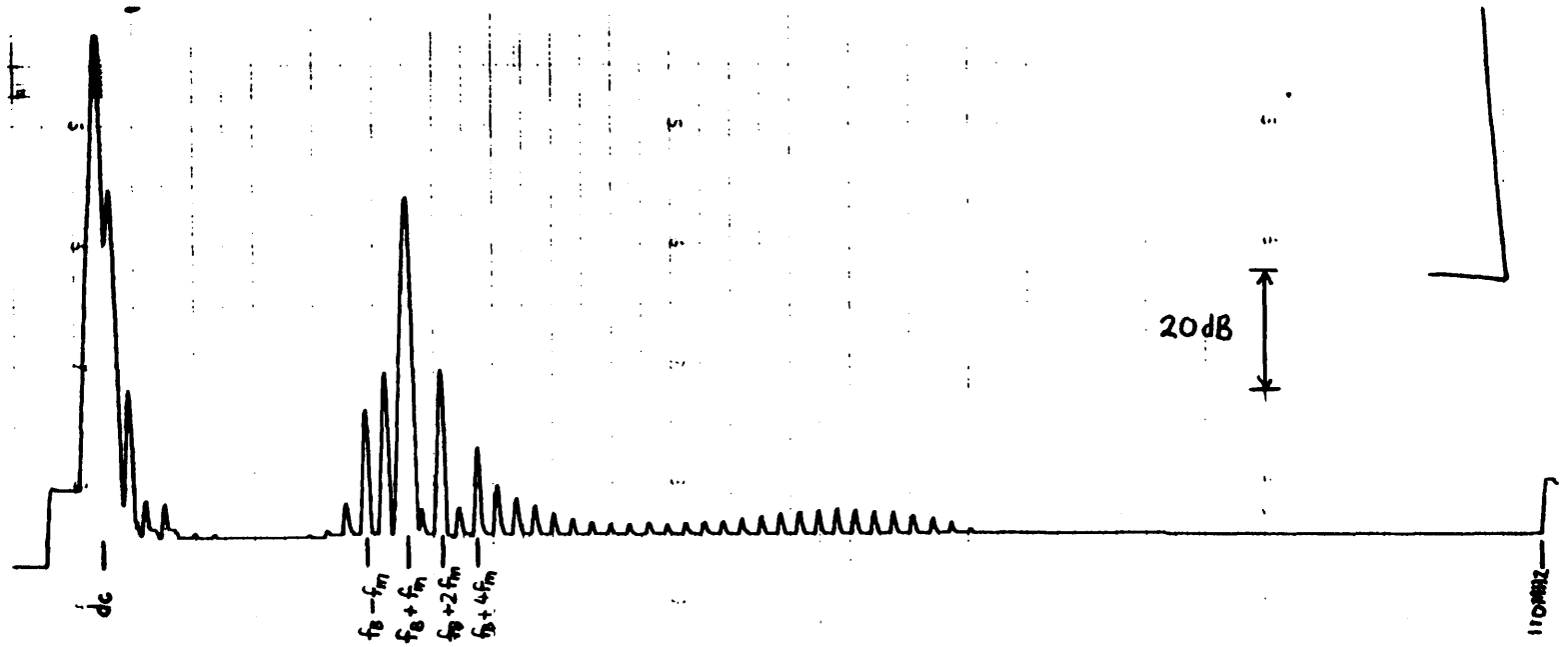

Figure 6.22 A Typical Complete Spectrum Plot (dc to 110 MHz) Illustrating The Frequency Translation Spectrum About The Bragg Frequency For A Serrodyne Driven 4 μm Wide Y–Cut Ti:$LiNbO_3$ Phase Modulator (f_B = 22 MHz, f_m = 1 MHz, $V_{\cong 2\pi}$ = 15.0 Volts)

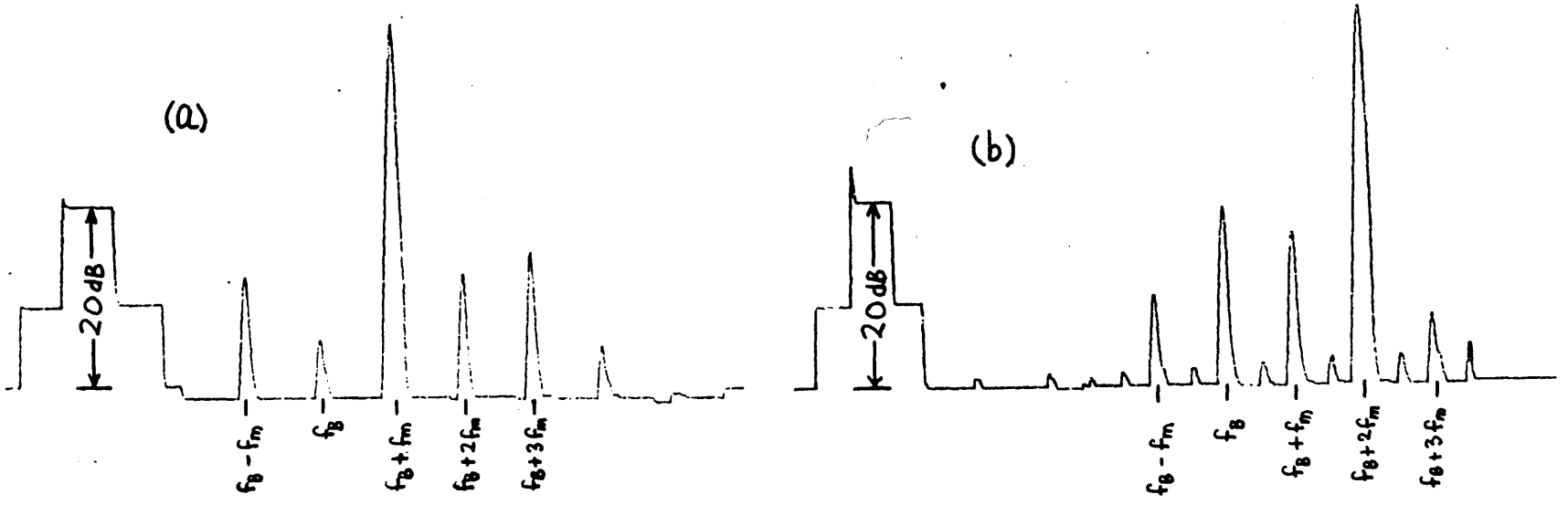

Figure 6.23 Examples Of Serrodyne Frequency Translation Plots Involving $V_{2\pi}$ And $V_{4\pi}$ Drive Signal Levels On A Y–Cut Ti:$LiNbO_3$ Phase Modulator
(a) Fundamental Shift, $f_m = 1$ MHz, $f_B = 22$ MHz, $V_{\cong 2\pi} = 12.0$ Volts
(b) 2nd Order Shift, $f_m = 2$ MHz, $f_B = 22$ MHz, , $V_{\cong 4\pi} = 24.0$ Volts

of 1 MHz and 2 MHz respectively. The above results indicated that the overall suppression values were 26.3 dB and 21.0 dB for the 1 MHz and 2 MHz frequency translations respectively. The reduced overall suppression value for the higher serrodyne frequency translation can be explained as follows. The measured fall-time (T_f) of the serrodyne signal in the above experiment was 40 ns. Therefore from Equation 3.12 of Chapter 3, the theoretical overall suppression (S_o) of spurious sidebands relative to the required sideband was calculated to be 28.0 dB for the 1 MHz frequency shift. In the case of the 2 MHz frequency shift with the same 1 MHz serrodyne signal, the calculated value of S_o was 22 dB. As can be seen from above the calculated and experimental results are in close agreement. Table 6.12 shows a summary of theoretical and experimental values of S_o for two Y-cut and two Z-cut Ti:$LiNbO_3$ phase modulators under multiple $V_{\cong 2\pi}$ studies. The conclusion from this short study is that it is not desirable to achieve multiple frequency translations using higher serrodyne amplitudes and a specific single frequency signal because of the reduction in the value of S_o with multiple $V_{\cong 2\pi}$ values. In all the serrodyne frequency translations reported in the remaining part of this section and in Section 6.4.5.2, no multiple $V_{\cong 2\pi}$ studies were carried out.

The ratio of the finite fall-time to the period of the sawtooth signal (T_f/T) and its effects on the various sideband levels were studied. The serrodyne modulators evaluated were realised with initial titanium thicknesses ranging from 240 Å to 430 Å in both Y- and Z-cut $LiNbO_3$. It was found from these experiments that the initial titanium thickness contributed in part to the realisation of high performance serrodyne devices. It was observed that for devices with initial titanium thicknesses of less than 280 Å, high levels of amplitude modulation were measured. These results are discussed in detail in Section 6.4.4.5.

Modulator Number	Active Length (mm)	Initial Titanium Thickness (Å)	Measured $V_{\pi 2\pi}$ Value (Volts) *	Experimental S_o Value - For $V_{\pi 2\pi}$ (dB) **	Experimental S_o Value - For $V_{\pi 4\pi}$ (dB) ***
ST5 (4 μm)	8.9	330	11.5	25.9	21.2
ST2 (5 μm)	7.7	315	14.2	27.3	20.8
SZ9 (4 μm)	10.0	390	11.8	26.6	21.6
SZ9 (5 μm)	10.0	390	12.3	27.5	22.0

* Here $V_{\pi 2\pi}$ Is Related To The Fact That $\phi_{\pi 2\pi} = 2\pi(1\text{-}0.04) = 1.92\pi$ (Equation 3.9 Of Chapter 3)

** Theoretical Value Of S_o = 28 dB (For A 1 MHz Frequency Translation With T_f = 40 ns)

*** Theoretical Value Of S_o = 22 dB (For A 2 MHz Frequency Translation With T_f = 40 ns)

Table 6.12 Summary Of Experimental S_o Values For Tested 4 μm And 5 μm Wide X– And Z–Cut Ti:$LiNbO_3$ Phase Modulators (With 10 μm Electrode Gap)

The serrodyne frequency chosen for the study of variations in fall-time was 1 MHz. The exact $V_{2\pi}$ value was used to drive each of the devices under evaluation. Studies of serrodyne frequency translations with respect to changes in non-optimum $V_{2\pi}$ and modulation frequency values are described in detail in Sections 6.4.4.3 and 6.4.4.4 respectively. The fall-time T_f of the sawtooth signal from the function generator was adjusted to one of the following values, i.e. 20 ns, 35 ns, 50 ns, 100 ns, 150 ns, 280 ns, and 400 ns. Table 6.13 gives the theoretical sideband levels of C_{-2}, C_{-1}, C_0, C_2 and C_3; the sideband values generated using Equation 3.10 of Chapter 3.

Three Y-cut phase modulators (ST5 - 4 μm wide, ST8 - 4 μm wide, ST2 - 5 μm wide) and two Z-cut phase modulators (SZ9 - 4 μm wide, SZ9 - 5 μm wide) were selected for the fall-time studies and the results are tabulated in Tables 6.14, 6.15, 6.16, 6.17, and 6.18 respectively. The results indicated that there is close agreement between the theoretical and experimental sideband levels with the exception of the carrier sideband C_0. Theoretically its value should be 0 but however because of RF pickup by the device from the signal generator that drove the Bragg cell, the value of C_0 fluctuated between -26 dB to -38 dB, the actual value depending on the drive level of the generator.

Therefore, from the above experimental results, it can be deduced that the serrodyne frequency translators are very dependant on the fall-time of the sawtooth signal. To improve any further on the sideband suppression levels to better than 60 dB, it is essential to procure a function generator with faster fall-time i.e. < 1ns at a serrodyne modulation frequency of 1 MHz.

6.4.4.3 Effect of Non-Optimum Sawtooth Amplitude

The requirement for a proper sawtooth signal level was critical in the demonstration of serrodyne devices with high overall suppression of spurious sideband levels. Tables 6.19 and 6.20 summarize the effect of non-

T_f/T	C_{-2} (dB)	C_{-1} (dB)	C_0 (dB)	C_2 (dB)	C_3 (dB)
0.020	–37.5	–40.0	∞	–28.0	–30.5
0.035	–32.6	–35.1	∞	–23.1	–25.6
0.050	–29.5	–32.0	∞	–20.0	–22.5
0.100	–23.5	–26.0	∞	–14.0	–16.5
0.150	–20.0	–22.5	∞	–10.5	–13.0
0.280	–14.6	–17.1	∞	–05.0	–07.5
0.400	–11.5	–14.0	∞	–02.0	–04.4

Table 6.13 Theoretical Values Of C_n where n = –2, –1, 0, 2, 3 . In This Case, T= 1 μs And C_1 = 1 (0 dB)

T_f/T	C_{-2} (dB)	C_{-1} (dB)	C_0 (dB)	C_2 (dB)	C_3 (dB)
0.020	-35	-36	-26	-24	-25
0.035	-29	-33	-26	-23	-24
0.050	-31	-28	-26	-19	-22
0.100	-25	-22	-27	-15	-15
0.150	-19	-23	-29	-09	-14
0.280	-11	-15	-26	-07	-09
0.400	-10	-14	-27	-03	-06

Note: T = 1 μs and C_1 = 1 (0 dB)

Table 6.14 Summary Of Experimental Sideband C_n Values (n = –2, –1, 0, 2, 3) With Respect To Different Fall–Times For A 4 μm Wide Y–Cut Ti:$LiNbO_3$ Phase Modulator (Device: ST5)

T_f/T	C_{-2} (dB)	C_{-1} (dB)	C_0 (dB)	C_2 (dB)	C_3 (dB)
0.020	-33	-36	-29	-27	-27
0.035	-28	-34	-29	-21	-23
0.050	-29	-29	-29	-19	-22
0.100	-23	-25	-30	-14	-14
0.150	-21	-23	-29	-10	-11
0.280	-12	-14	-29	-06	-08
0.400	-14	-17	-29	-03	-04

Note: T = 1 μs and C_1 = 1 (0 dB)

Table 6.15 Summary Of Experimental Sideband C_n Values (n = –2, –1, 0, 2, 3) With Respect To Different Fall–Times For A 4 μm Wide Y–Cut Ti:$LiNbO_3$ Phase Modulator (Device: ST8)

T_f/T	C_{-2} (dB)	C_{-1} (dB)	C_0 (dB)	C_2 (dB)	C_3 (dB)
0.020	-33	-37	-32	-25	-28
0.035	-29	-34	-34	-22	-23
0.050	-25	-29	-34	-17	-18
0.100	-22	-27	-33	-11	-14
0.150	-22	-24	-34	-11	-12
0.280	-13	-17	-35	-04	-06
0.400	-12	-15	-31	-02	-05

Note: T = 1 μs and C_1 = 1 (0 dB)

Table 6.16 Summary Of Experimental Sideband C_n Values (n = −2, −1, 0, 2, 3) With Respect To Different Fall–Times For A 5 μm Wide Y–Cut Ti:$LiNbO_3$ Phase Modulator (Device: ST2)

T_f/T	C_{-2} (dB)	C_{-1} (dB)	C_0 (dB)	C_2 (dB)	C_3 (dB)
0.020	-35	-35	-35	-26	-29
0.035	-33	-33	-35	-24	-27
0.050	-27	-28	-35	-18	-19
0.100	-24	-29	-33	-10	-16
0.150	-19	-20	-35	-09	-11
0.280	-11	-15	-36	-06	-08
0.400	-09	-11	-35	-04	-06

Note: T = 1 μs and C_1 = 1 (0 dB)

Table 6.17 Summary Of Experimental Sideband C_n Values (n = –2, –1, 0, 2, 3) With Respect To Different Fall–Times For A 4 μm Wide Z–Cut Ti:$LiNbO_3$ Phase Modulator (Device: SZ9)

T_f/T	C_{-2} (dB)	C_{-1} (dB)	C_0 (dB)	C_2 (dB)	C_3 (dB)
0.020	-38	-38	-38	-27	-25
0.035	-29	-29	-38	-26	-29
0.050	-25	-28	-38	-21	-22
0.100	-21	-23	-37	-13	-17
0.150	-23	-21	-38	-12	-12
0.280	-09	-11	-37	-07	-09
0.400	-11	-13	-37	-05	-05

Note: T = 1 μs and C_1 = 1 (0 dB)

Table 6.18 Summary Of Experimental Sideband C_n Values (n = −2, −1, 0, 2, 3) With Respect To Different Fall–Times For A 5 μm Wide Z–Cut Ti:$LiNbO_3$ Phase Modulator (Device: SZ9)

d	Phase ϕ	Applied Voltage (Volts)	Theoretical Value Of S_{or} (dB)	Experimental Value Of S_{or} (dB)
-0.02	6.16	10.6	34	33
0	6.28	10.8	28	27
0.02	6.41	11.0	24	22
-0.04	6.03	10.4	28	26
0.04	6.53	11.2	22	23
-0.06	5.91	10.2	24	22
0.06	6.66	11.5	20	19

Note: Theoretical results were calculated using the details described in Table 3.1 (Device: ST8, T_f = 20 ns, T = 1 μs, C_1 = 1)

Table 6.19 Summary Of Theoretical And Experimental Overall Sideband Suppression Values, S_{0r} . With Respect To Variations In Serrodyne Voltage Levels For A 4 μm Wide Y–Cut Ti:$LiNbO_3$ Phase Modulator (Device: ST8, $V_{2\pi}$= 10.8 V)

d	Phase ϕ	Applied Voltage (Volts)	Theoretical Value Of S_{or} (dB)	Experimental Value Of S_{or} (dB)
-0.02	6.16	12.3	34	33
0	6.28	12.5	28	26
0.02	6.41	12.8	24	22
-0.04	6.03	12.0	28	27
0.04	6.53	13.0	22	19
-0.06	5.91	11.8	24	26
0.06	6.66	13.3	20	18

Note: Theoretical results were calculated using the details described in Table 3.1 (Device: SZ9, T_f = 20 ns, T = 1 μs, C_1 = 1)

Table 6.20 Summary Of Theoretical And Experimental Overall Sideband Suppression Values, S_{0r} , With Respect To Variations In Serrodyne Voltage Levels For A 4 μm Wide Z–Cut Ti:$LiNbO_3$ Phase Modulator (Device: SZ9, $V_{2\pi}$= 12.5 V)

optimum sawtooth amplitude on serrodyne device performance for two $Ti:LiNbO_3$ phase modulators with the theoretical predictions for overall sideband level suppression calculated using the results found in Table 3.1 of Chapter 3. It was noted again that the contribution from C_0 (about 29 dB and 34 dB) which was due to RF pickup was ignored in the experiments summarized in the above tables. Figures 6.24 and 6.25 show plots of the overall sideband level suppression against the applied serrodyne voltage for the 4 μm wide Y-cut and 4 μm wide Z-cut devices. From the results above it can be concluded that the performance of the serrodyne frequency translator is sensitive to applied voltage variations and it can be stated that the optimum overall serrodyne sideband suppressions occured as predicted by theory in Section 3.4.3 of Chapter 3, i.e. $\phi_o = \phi_p\ [1-(T_f/T)]$ (Equation 3.14). It was calculated from Tables 6.19 and 6.20 that the voltage variation should not be larger than 0.5% to ensure stable serrodyne operation at the optimum voltage signal level. In general this was not a serious problem in the laboratory study of serrodyne devices. However in practical implementations of serrodyne frequency-translators it will be essential to maintain the stability of the required serrodyne signal level. This can be achieved possibly by using some form of electrical/optical feedback system.

6.4.4.4 Effect of Non-Optimum Operation Over a Band/Range of Frequencies using a Constant Sawtooth Amplitude

The electrical frequency responses of the phase modulators were measured prior to serrodyne testing as described in Section 6.4.3. Table 6.21 gives a summary of the electrical 3 dB bandwidth of the tested devices. It can be concluded that the devices for the frequency translation studies have the required bandwidth (i.e. 0.8 GHz to 1.1 GHz) for proper serrodyne operation.

Using Equations 3.17 and 3.19 of Chapter 3, a table of delayed reset times T_{nf} and the resultant degradation in the overall spurious suppression

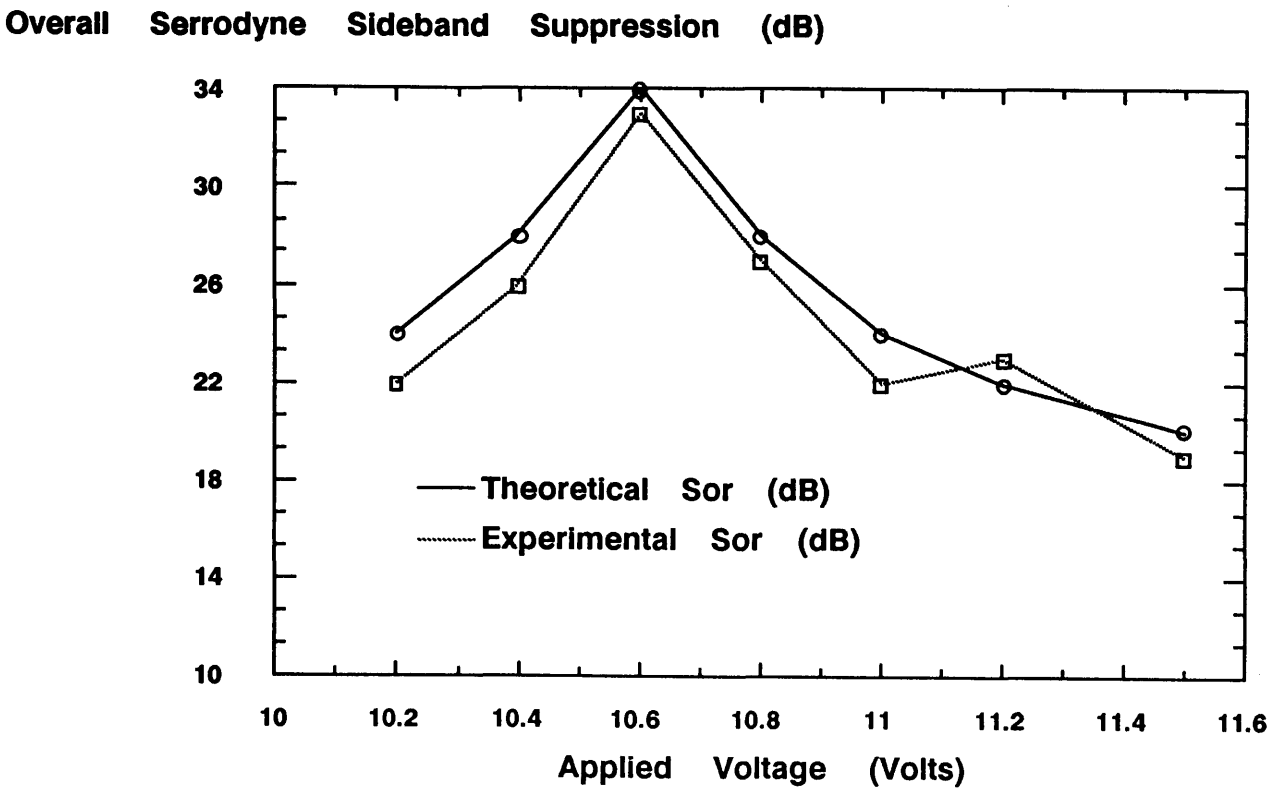

Figure 6.24 Plots Of Theoretical And Experimental Overall Serrodyne Suppression With Respect To Applied Voltage On A 4 μm Wide Y–Cut Ti:$LiNbO_3$ Phase Modulator (Device: ST8)
[f_m = 1 MHz, f_B = 22 MHz, $V_{2\pi}$ = 10.8 Volts]

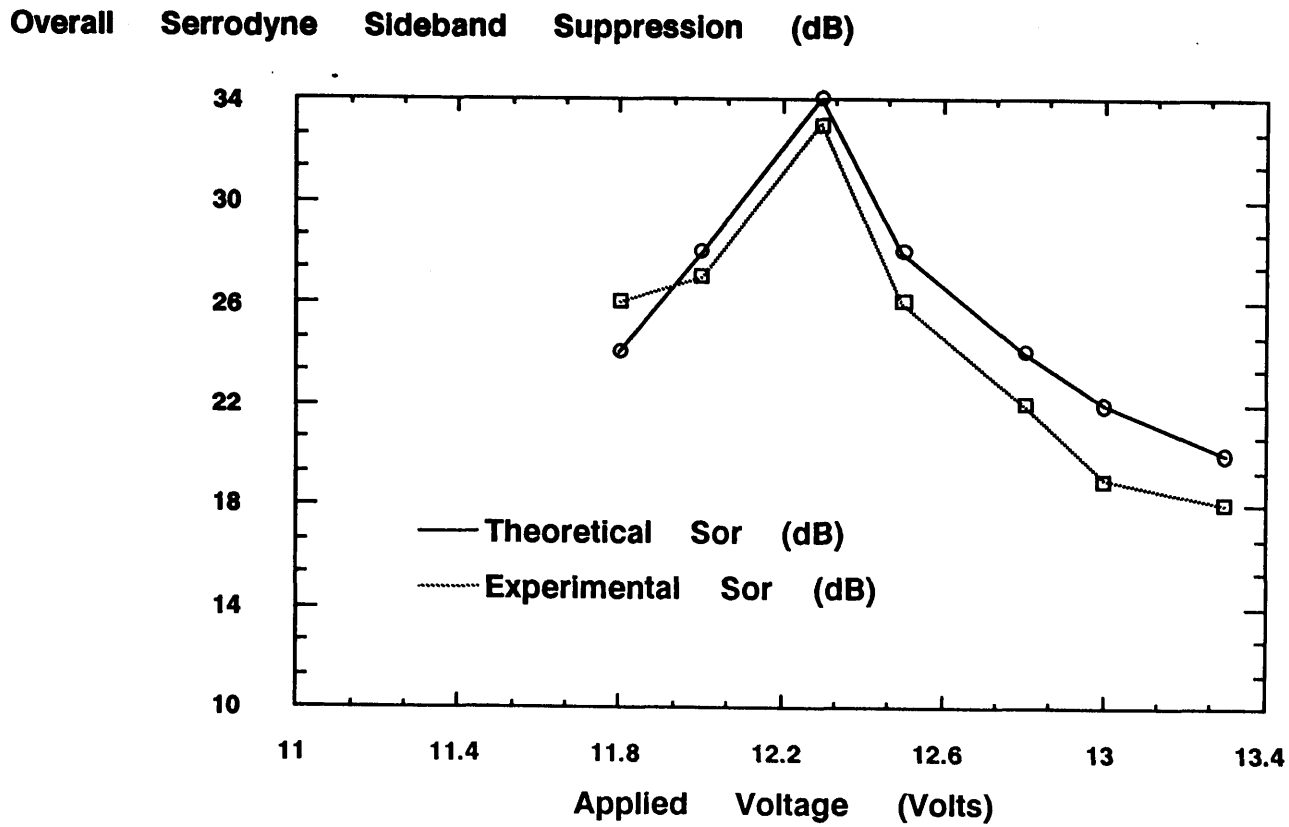

Figure 6.25 Plots Of Theoretical And Experimental Overall Serrodyne Suppression With Respect To Applied Voltage On A 4 μm Wide Z–Cut Ti:$LiNbO_3$ Phase Modulator (Device: SZ9)
[f_m = 1 MHz, f_B = 22 MHz, $V_{2\pi}$ = 12.6 Volts]

Modulator Number*	3 dB Electrical Bandwidth (GHz)
SSB1	0.96
SSB3	1.0
ST2	1.0
ST5	1.1
ST8	0.88
SZ2	0.9
SZ9	1.0

* Note: Details of the above phase modulators can be found in Tables 6.10 and 6.11.

Table 6.21 Summary Of 3 dB Electrical Bandwidth Of Ti:$LiNbO_3$ Phase Modulators

of sidebands S_{do} were calculated for serrodyne modulation frequencies in the range between 300 kHz and 7 MHz for device ST5 (Table 6.22). The 3dB electrical bandwidth of the device was measured to be 1.1 GHz which implied that it had a capacitance of 6.16 pF for a 47 Ω termination resistance. From Table 6.22 it can be concluded that the values of S_{do} are small, i.e. they range from 0.11 dB to 0.83 dB, and therefore the effect of T_{nf} can be ignored for the phase modulators in this study. Figure 6.26 illustrates the theoretically predicted and the experimentally measured overall sideband suppressions for the serrodyne modulation frequency range of 300 kHz to 7 MHz. The plot indicates clearly that the performance of the serrodyne frequency translator was limited by the fall-time of the function generator. Similar plots were obtained for devices ST8 (Figure 6.27) and SZ9 (Figure 6.28), all indicating fall-time limited performance especially at the higher serrodyne frequency of 7 MHz.

6.4.4.5 Presence of Amplitude Modulation in an Electro-Optic Phase Modulator and its Effects

As described in Section 6.4.4.2 the serrodyne devices with an initial titanium film thickness of less than 272 Å were found to have poor image sideband suppression values. This was eventually identified to be due to the presence of amplitude modulation effects. The magnitude of the amplitude modulation was measured directly using a photodiode unit and an osciloscope.

Figure 6.29 shows the measured amplitude modulation levels for such a serrodyne device (SSB1) with an initial titanium thickness of 240 Å. The width of the optical waveguide in this case was 4 μm. The applied voltage did not have an offset value. It can be deduced that for an applied voltage of 14 volts ($V_{2\pi}$) the measured amplitude modulation was 13.7%. This meant that the suppression of the image sideband compared to the frequency translated signal was calculated to be 17.2 dB. By applying a voltage with a positive dc

Serrodyne Frequency (MHz)	T_f (ns)	T_{nf} (ns)**	Theoretical Overall Sideband Suppression S_o (dB)	Experimental Overall Sideband Suppression S_o (dB)	S_{no} (dB)
0.3	84	85	32	30	0.11
0.5	50	51	32	31	0.18
0.7	32	33	33	31	0.29
1.0	20	21	34	33	0.48
2.0	11	12	33	30	0.83
3.0	10	11	30	27	0.83
4.0	10	11	28	25	0.83
5.0	10	11	26	23	0.71
6.0	10	11	25	20	0.67
7.0	10	11	23	21	0.62

** Note: C = 6.16 pF, R = 47 Ω.

Table 6.22 Study Of Serrodyne Frequency Response From 300 kHz To 7 MHz For Device ST5 (4 μm Wide, Y–Cut, Ti:$LiNbO_3$, Δf = 1.1 GHz)

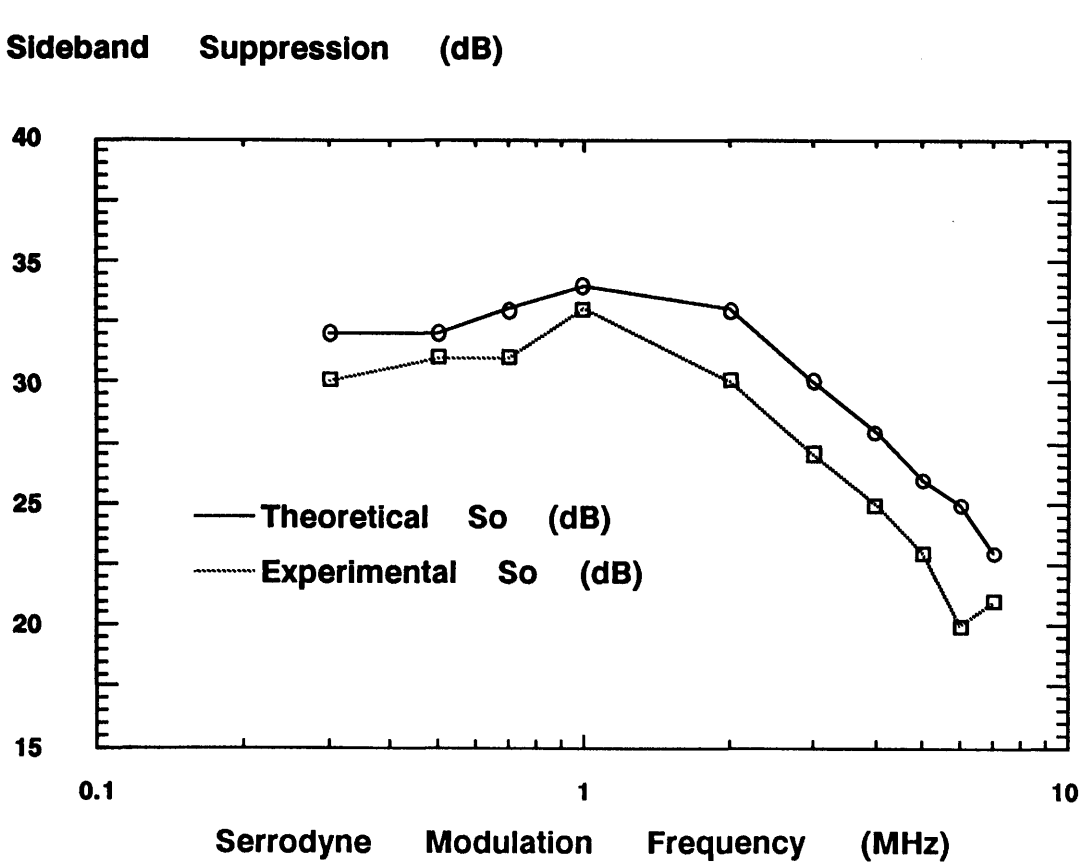

Figure 6.26 Plot Of Serrodyne Frequency Response From 300 kHz To 7 MHz For Device ST5 (4 μm Wide, Y–Cut, Ti:$LiNbO_3$, Δf = 1.1 GHz)

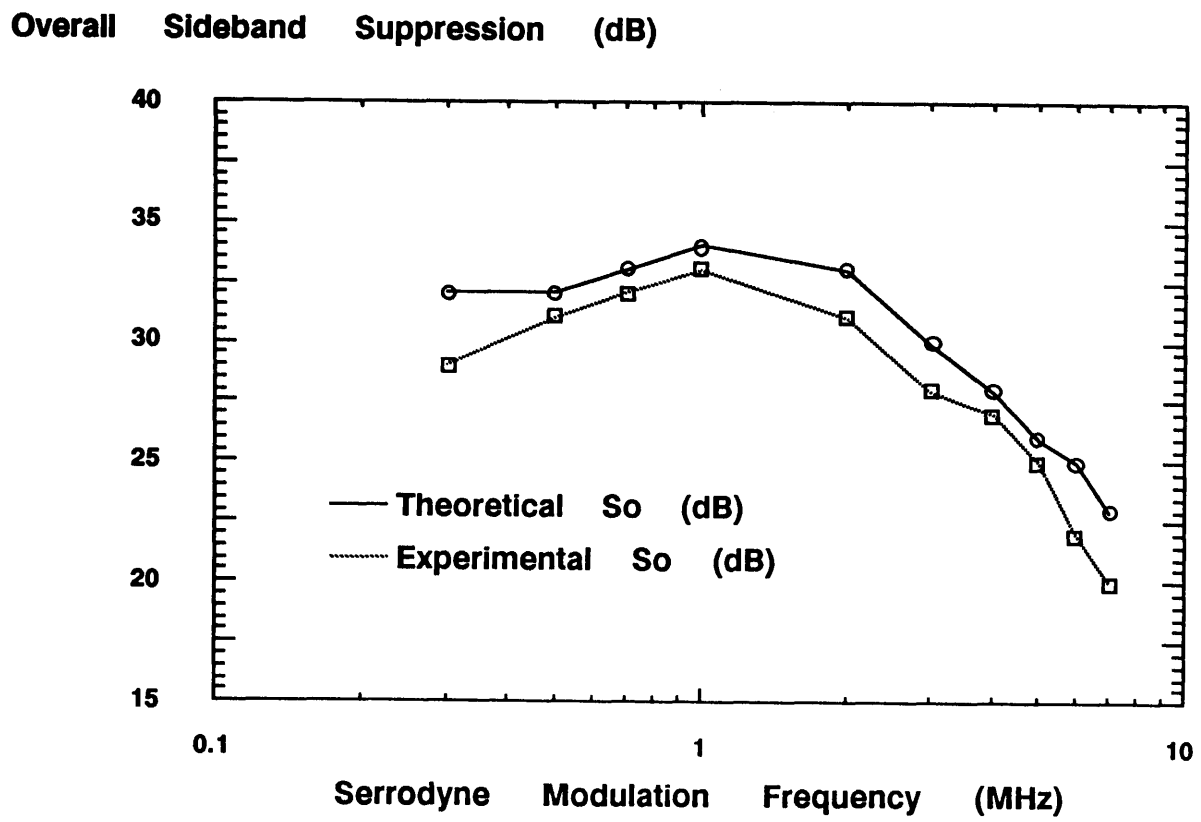

Figure 6.27 Plot Of Serrodyne Frequency Response From 300 kHz To 7 MHz For Device ST8 (4 μm Wide, Y–Cut, Ti:$LiNbO_3$, $\Delta f = 0.88$ GHz)

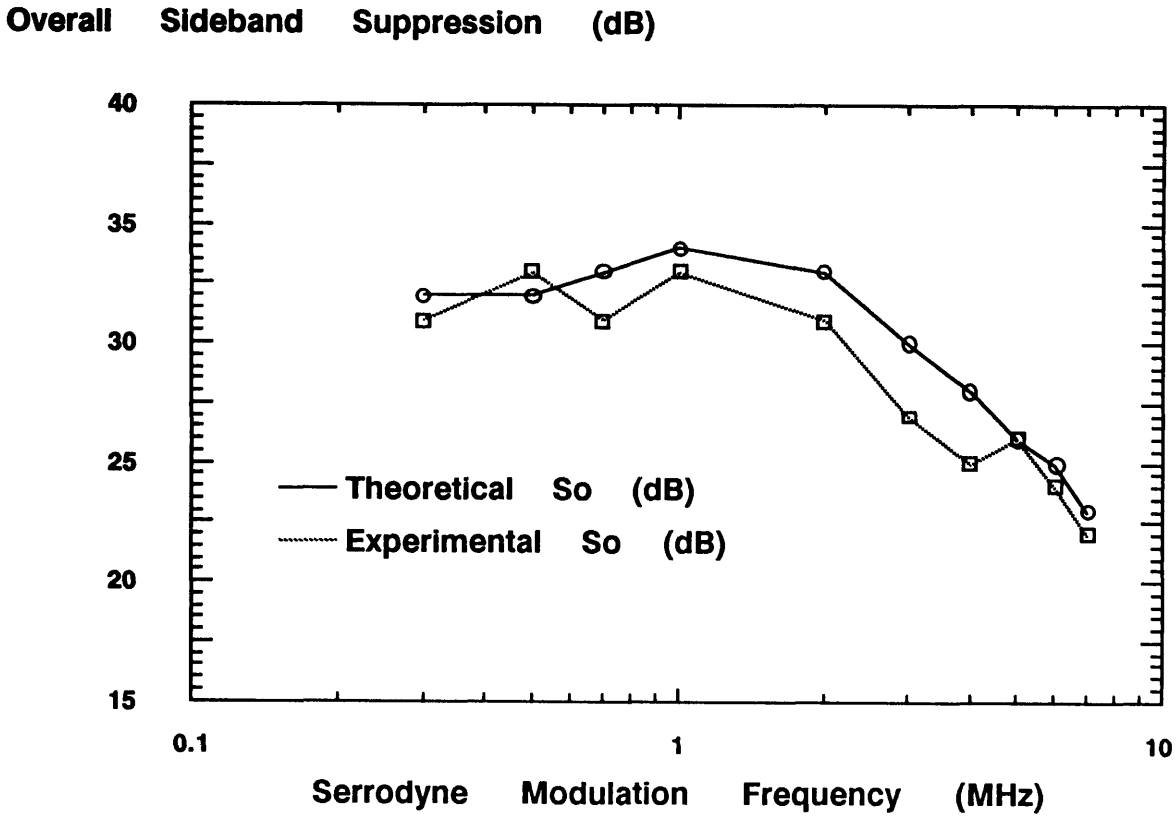

Figure 6.28 Plot Of Serrodyne Frequency Response From 300 kHz To 7 MHz For Device SZ9 (4 μm Wide, Z–Cut, Ti:$LiNbO_3$, Δf = 1.0 GHz)

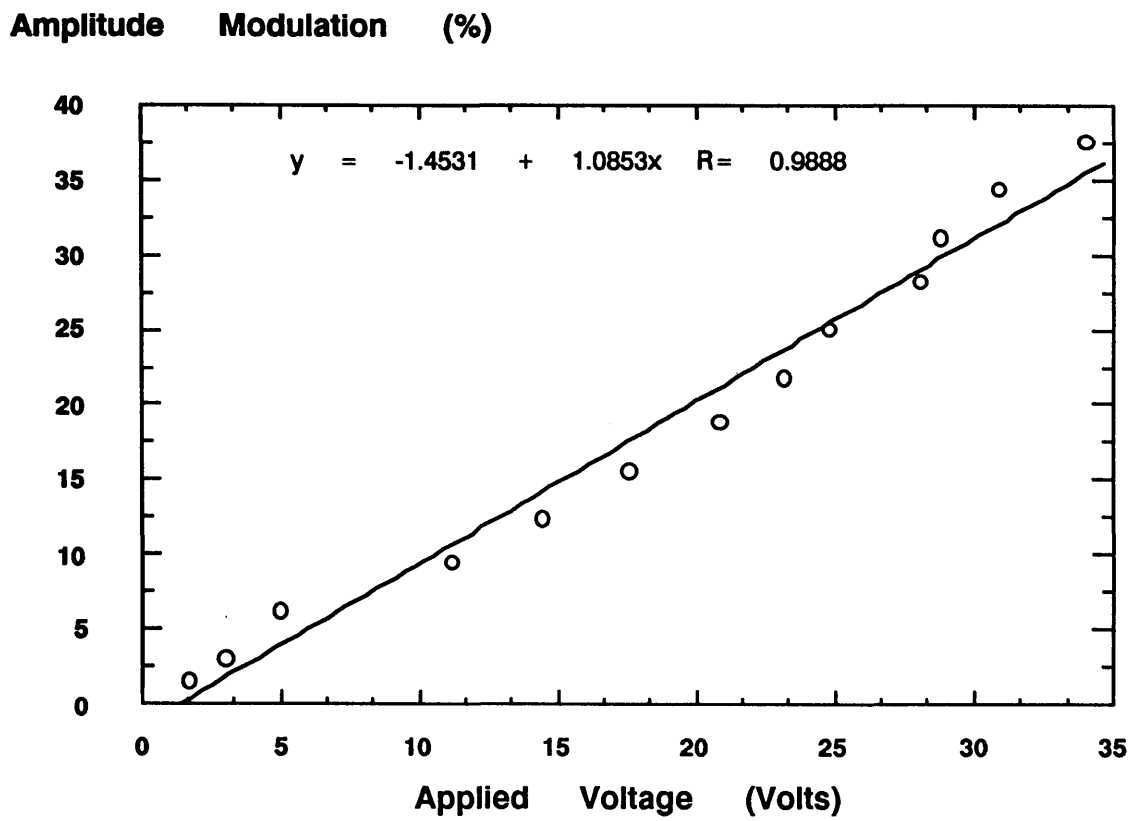

Figure 6.29 Plot Of Amplitude Modulation Level Versus Applied Voltage For Device SSB1 (DC Offset = 0 V, 4 μm Wide, Y–Cut, Ti:$LiNbO_3$, $V_{2\pi}$ = 14.0 Volts, Initial Titanium Thickness = 240 Å)

offset of 7.6 volts to the same device (SSB1), it was measured that the amplitude modulation levels were reduced as can be seen in Figure 6.30. Now for a $V_{2\pi}$ voltage of 14 volts, the measured amplitude modulation was 8.6% which gave a calculated suppression of the image sideband to frequency translated signal of 21.3 dB. However, if a voltage with a negative dc offset of 8.0 volts was applied to the same device (SSB1), the measured amplitude modulation levels were found to be higher than those reported above (Figure 6.31). The measured amplitude modulation with the applied voltage of 14 volts was found to be 55.7%. This implied that the suppression of the image sideband to frequency translated signal was calculated to be 5.1 dB. In this situation, with the application of 35 volts to the device, a cut-off or amplitude modulator was demonstrated. A cut-off ratio of about 19 dB was measured. The above changes in measured amplitude modulation levels can be explained as follows. The device SSB1 with an initial titanium thickness of 240 Å is close to cutoff (Figure 6.7). By applying a drive signal with an offset value to the device SSB1, it is possible to move the stripe optical waveguide closer to cutoff (with negative offset voltage) or away from cutoff (with positive offset voltage).

Table 6.23 summarizes the amplitude modulation studies for the following phase modulators: (a) SSB1, (b) ST12 - initial titanium thickness of 265 Å and (c) SSB3 - initial titanium thickness of 272 Å. The results clearly indicate that the initial titanium thickness of the optical waveguide plays an important role in the minimisation of amplitude modulation effects. As the initial titanium thickness was increased from 240 Å to 272 Å, the level of amplitude modulation drops significantly from 13.7% to 2.1% for a $V_{2\pi}$ signal without any dc offset.

In summary, to avoid the presence of measurable amplitude modulation (i.e. > 0.5%) in phase-modulators, it is important to realise strongly guiding single-moded devices. Other sources of amplitude

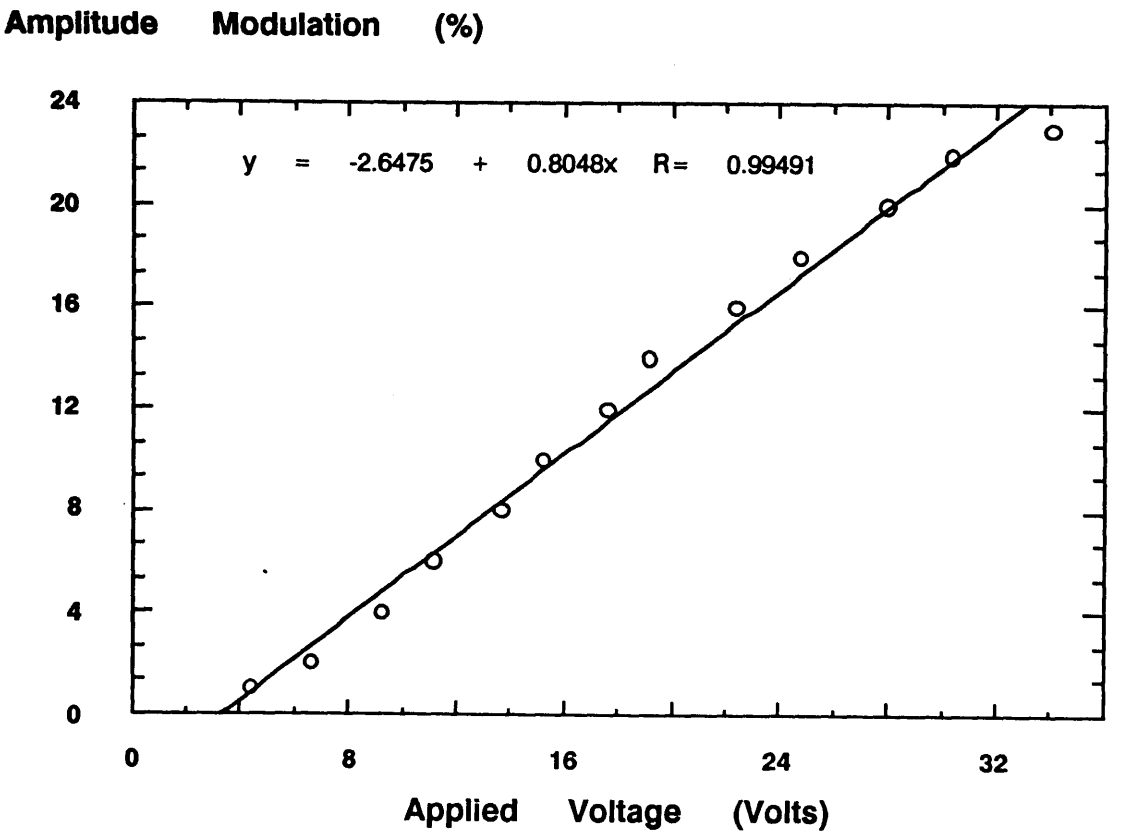

Figure 6.30 Plot Of Amplitude Modulation Level Versus Applied Voltage For Device SSB1 (DC Offset = +7.6 V, 4 μm Wide, Y–Cut, Ti:$LiNbO_3$, $V_{2\pi}$ = 14.0 Volts, Initial Titanium Thickness = 240 Å)

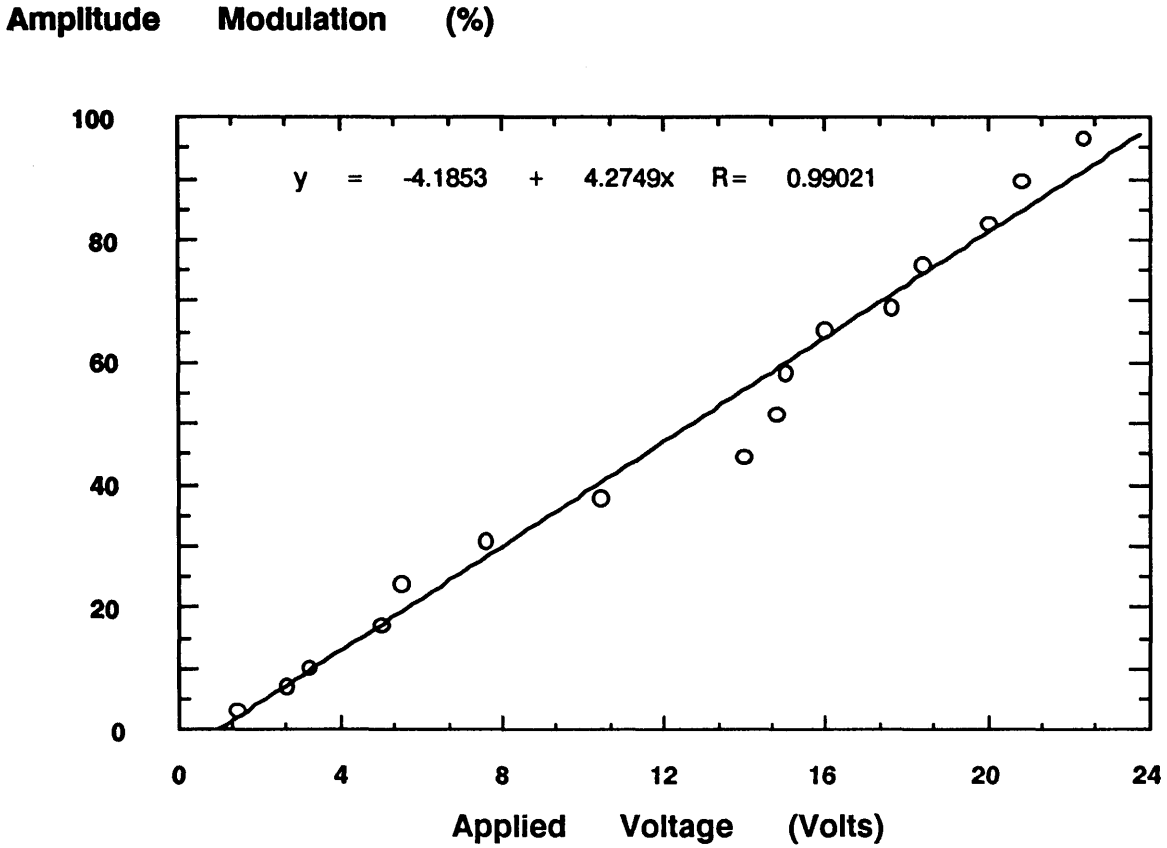

Figure 6.31 Plot Of Amplitude Modulation Level Versus Applied Voltage For Device SSB1 (DC Offset = –8.0 V, 4 μm Wide, Y–Cut, Ti:$LiNbO_3$, $V_{2\pi}$ = 14.0 Volts, Initial Titanium Thickness = 240 Å)

Modulator Number	Initial Titanium Thickness (Å)	Measured Amplitude Modulation (%)* With DC Offset Value (Volts)			Theoretical S_{im}/S_m Value**			Experimental S_{im}/S_m Value**		
		(a) 0	(b) +7.6	(c) -8.0	(a)	(b)	(c)	(a)	(b)	(c)
SSB1	240	13.7	8.6	55.7	17.3	21.3	5.1	16	22	4
ST12	265	5.6	3.7	12.1	25.0	28.6	18.3	23	31	17
SSB3	272	2.1	1.2	4.6	33.6	38.4	26.7	32	35	27

* Note: For an applied voltage equivalent to $V_{2\pi}$.

** Note: $T_f/T = 0.02$.

Table 6.23 Summary Of The Effects Of Amplitude Modulation On The Suppression Of The Image Sideband (S_{im}) Compared To The Serrodyne Frequency Translated Signal (S_m) For The Following Y–Cut Ti:$LiNbO_3$ Phase Modulators: (a) SSB1, (b) ST12, And (c) SSB3 [4 μm Wide Waveguides]

modulation due to Fabry Perot effects were not observed, presumably because of unintentional non-parallel polishing of the phase-modulator end-faces. Therefore this was not a problem in all the reported serrodyne experiments.

6.4.5 Experimental Results for Proton-Exchange Phase-Modulators Driven by Sawtooth Electrical Waveforms

6.4.5.1 Determination of $V_{2\pi}$ Values

The determination of the $V_{2\pi}$ voltage requirements for the PE X-cut $LiNbO_3$ phase modulators was more complex. The reason is that not all the fabricated devices performed as designed, i.e. there seemed to be two main problems. The first was that with PE devices that operated, there was an observed effect called the dc extinction problem. In brief, if dc voltages were applied to the PE phase modulators fabricated at 162°C, the output light levels of the single-moded devices were slowly reduced. This dc extinction problem is discussed in detail in Section 6.4.5.5.

The second problem is that all the single-moded PE phase modulators that were fabricated at a higher temperature of 181°C exhibited a reduction in electro-optic activity. Single-moded PE phase modulators were not fabricated at 200°C and therefore no electro-optic measurements were carried out at 200°C.

In view of the dc extinction effect, another technique was used to estimate the $V_{2\pi}$ values of the PE phase modulators fabricated at 162°C and 181°C. The technique involved the use of the self heterodyne arrangement shown in Figure 6.10. The optical signal from the PE phase modulator under evaluation was combined and mixed with the frequency shifted signal from the Bragg cell on an ac coupled photodetector unit. The output from the photodetector was displayed on a spectrum anlayzer which showed a beat signal at 22 MHz. The PE phase modulator was then driven with a sinusiodal

signal at 1 MHz whereby the familiar Bessel sidebands were generated about 22 MHz. By careful adjustment of the level of the sinusoidal signal, the 0th order of the spectrum can be suppressed to a minimum and hence the required estimated $V_{2\pi}$ value was determined. Figures 6.32 and 6.33 show typical spectra with optimally suppressed 0th order Bessel sidebands for PE phase modulators fabricated at 162°C with an exchange time of 25 minutes and at 181°C with an exchange time of 10 minutes respectively. Tables 6.24(a, b) summarize the complete study of the $V_{2\pi}$ determination of the PE phase modulators fabricated at 162°C and 181°C for 4 μm and 5 μm wide optical waveguides respectively. The results indicated that all the PE phase modulators fabricated at 162°C were more efficient than their Ti:$LiNbO_3$ counterparts with the same device geometries i.e. with an active length of 10 mm and an electrode gap of 10 μm. The possible reason for this lower $V_{2\pi}$ requirement is the increased efficiency in the overlap of the electrical and optical fields (0.51 to 0.55). This can be seen from the higher calculated overlap factor values shown in Tables 6.24(a, b) when compared to similar results for Ti:$LiNbO_3$ phase modulators summarized in Tables 6.10 and 6.11. As for the devices fabricated at 181°C, the $V_{2\pi}$ values were estimated to be 35 volts. This most likely implied that the electro-optic coefficient (r_{33}) was reduced. Assuming a similar overlap factor value of 0.50 (for a similar PE phase modulator fabricated at 162°C) the calculated r_{33} electro-optic coefficient value was 5.9 pm/V, indicating a five times reduction in the normal r_{33} bulk value.

The experimentally estimated $V_{2\pi}$ values were then compared to those derived theoretically using the standard table of Bessel functions of the first kind. Table 6.25(a, b) shows a complete comparison of the experimentally obtained and the theoretically calculated $V_{2\pi}$ values for 4 μm and 5 μm wide PE X-cut $LiNbO_3$ phase modulators respectively. The results indicated that

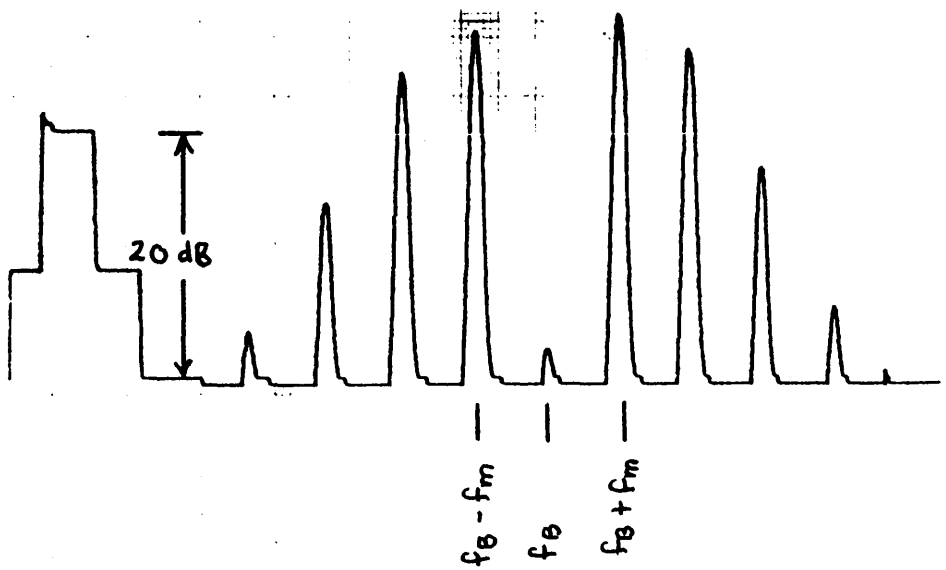

Figure 6.32 Output Beat Spectrum Showing The Optimum Suppression Of The 0th Order Bessel Sideband For A Proton–Exchange X–Cut $LiNbO_3$ Phase Modulator (Exchange Temperature= 162°C, Exchange Time= 25 minutes, Waveguide Width= 4 μm, f_B= 22 MHz, f_m= 1 MHz, $V_{2\pi}$= 6.5 Volts)

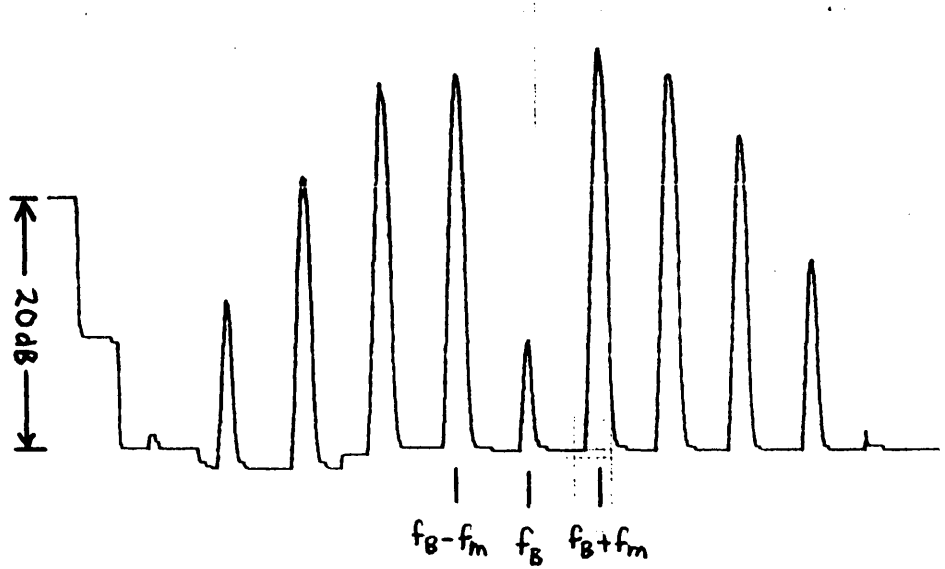

Figure 6.33 Output Beat Spectrum Showing The Optimum Suppression Of The 0th Order Bessel Sideband For A Proton–Exchange X–Cut $LiNbO_3$ Phase Modulator (Exchange Temperature= 181°C, Exchange Time= 10 minutes, Waveguide Width= 4 μm, f_B= 22 MHz, f_m= 1 MHz, $V_{2\pi}$= 35 Volts)

Modulator Number	Active Length (mm)	Proton-Exchange Conditions (°C, Minutes)	Measured $V_{2\pi}$ Value (Volts)	Calculated Overlap Factor Value
PEX3	10.0	162, 25	6.5	0.52
PEX5	8.7	162, 30	7.4	0.52
PEX6	9.9	162, 35	6.7	0.51
PEX11	10.0	162, 40	6.5	0.52
PELX4*	10.0	181, 10	35.0	0.50 **

* Calculated r_{33} = 5.9 pm/V
** Assumed Overlap Factor Value

Table 6.24a Summary Of $V_{2\pi}$ Voltage Requirements For Tested 4 μm Wide X–Cut Proton–Exchange $LiNbO_3$ Phase Modulator (With 10 μm Electrode Gap)

Modulator Number	Active Length (mm)	Proton-Exchange Conditions (°C, Minutes)	Measured $V_{2\pi}$ Value (Volts)	Calculated Overlap Factor Value
PEX3	10.0	162, 25	6.5	0.52
PEX5	8.7	162, 30	7.0	0.55
PEX6	9.9	162, 35	6.6	0.52
PEX11	10.0	162, 40	6.5	0.52
PELX4*	10.0	181, 10	35.0	0.50 **

* Calculated r_{33} = 5.9 pm/V
** Assumed Overlap Factor Value

Table 6.24b Summary Of $V_{2\pi}$ Voltage Requirements For Tested 5 μm Wide X–Cut Proton–Exchange $LiNbO_3$ Phase Modulator (With 10 μm Electrode Gap)

Modulator Number	Active Length (mm)	Proton-Exchange Conditions (°C, Minutes)	Measured $V_{2\pi}$ Value (Volts)	Theoretical $V_{2\pi}$ Value (Volts)
PEX3	10.0	162, 25	6.5	7.3
PEX5	8.7	162, 30	7.4	7.7
PEX6	9.9	162, 35	6.7	7.1
PEX11	10.0	162, 40	6.5	7.0

Table 6.25a Comparisons Of Experimentally Obtained And Theoretically Calculated $V_{2\pi}$ Values For 4 μm Wide Proton–Exchange X–Cut $LiNbO_3$ Phase Modulators

Modulator Number	Active Length (mm)	Proton-Exchange Conditions (°C, Minutes)	Measured $V_{2\pi}$ Value (Volts)	Theoretical $V_{2\pi}$ Value (Volts)
PEX3	10.0	162, 25	6.5	7.0
PEX5	8.7	162, 30	7.0	7.7
PEX6	9.9	162, 35	6.6	7.1
PEX11	10.0	162, 40	6.5	7.2

Table 6.25b Comparisons Of Experimentally Obtained And Theoretically Calculated $V_{2\pi}$ Values For 5 μm Wide Proton–Exchange X–Cut $LiNbO_3$ Phase Modulators

they are in close agreement as expected. The calculation for a typical theoretical $V_{2\pi}$ value is described in detail in Appendix 6.2.

6.4.5.2 Effect of Non-Zero Flyback/Fall-Time

The effect of a serrodyne signal with finite fall-time on proton-exchange X-cut $LiNbO_3$ phase modulators fabricated at 162°C with exchange times that ranged from 25 to 40 minutes, using concentrated benzoic acid melts, was studied. Commercial sawtooth signal generators with variable fall-time T_f were used throughout the above study. Only upshifts in frequency are reported. The experimentally generated sidebands due to the serrodyne process were compared to the theoretically predicted sideband levels calculated from the analysis of effects due to finite fall-time found in Section 3.4.2 of Chapter 3.

An example of a complete spectrum plot from dc to 110 MHz with the entire serrodyne frequency translation beat spectrum shifted to an intermediate frequency of 22 MHz can be seen in Figure 6.34a. For the above evaluation, the frequency of the serrodyne signal was 1.5 MHz and the device tested was a 4 μm wide X-cut PE $LiNbO_3$ phase modulator fabricated at 162°C with an exchange time of 35 minutes (Device no: PEX6 of Table 6.24a). The presence of a spectrum (Figure 6.34a) about the dc signal was found to be due to RF pickup by the photodetector unit. This was confirmed by observing the photodetector signal without any incident laser light using the spectrum analyzer (Figure 6.34b). Problems with RF pickup occurred occasionally with high drive signals to the Bragg cell and therefore were taken into account when they were photodetected.

The sawtooth frequency chosen for the study of effects of variations in the finite fall-time on serrodyne frequency translation experiments was 1 MHz. The exact $V_{2\pi}$ voltage value was used to drive each of the PE phase modulator under evaluation. Studies of the effects of non-optimum $V_{2\pi}$

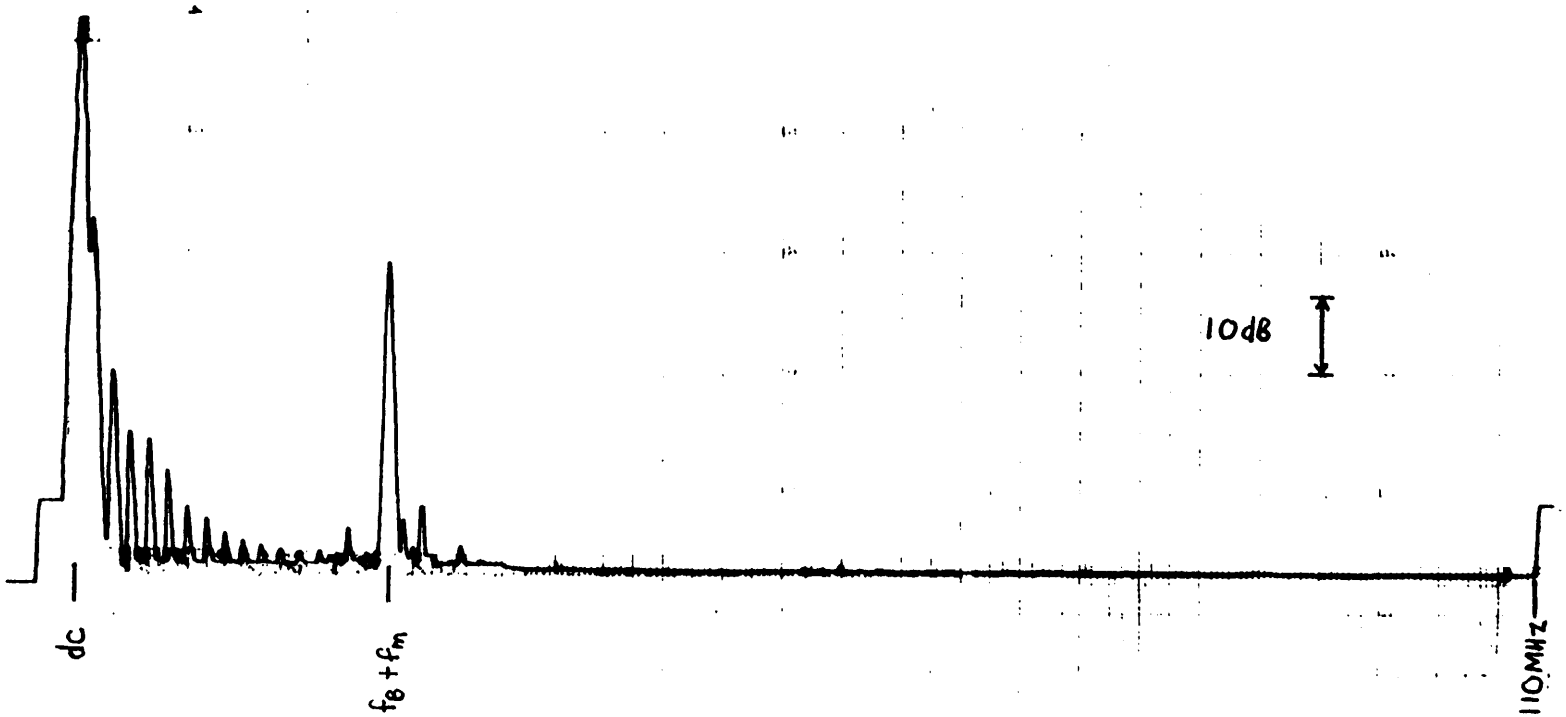

Figure 6.34a A Typical Complete Spectrum Plot (dc to 110 MHz) Illustrating The Frequency Translation Spectrum About The Bragg Frequency For A Serrodyne Driven 4 μm Wide X–Cut PE $LiNbO_3$ Phase Modulator (f_B = 22 MHz, f_m = 1.5 MHz, $V_{2\pi}$ = 6.6 Volts, T_f/T = 0.02)

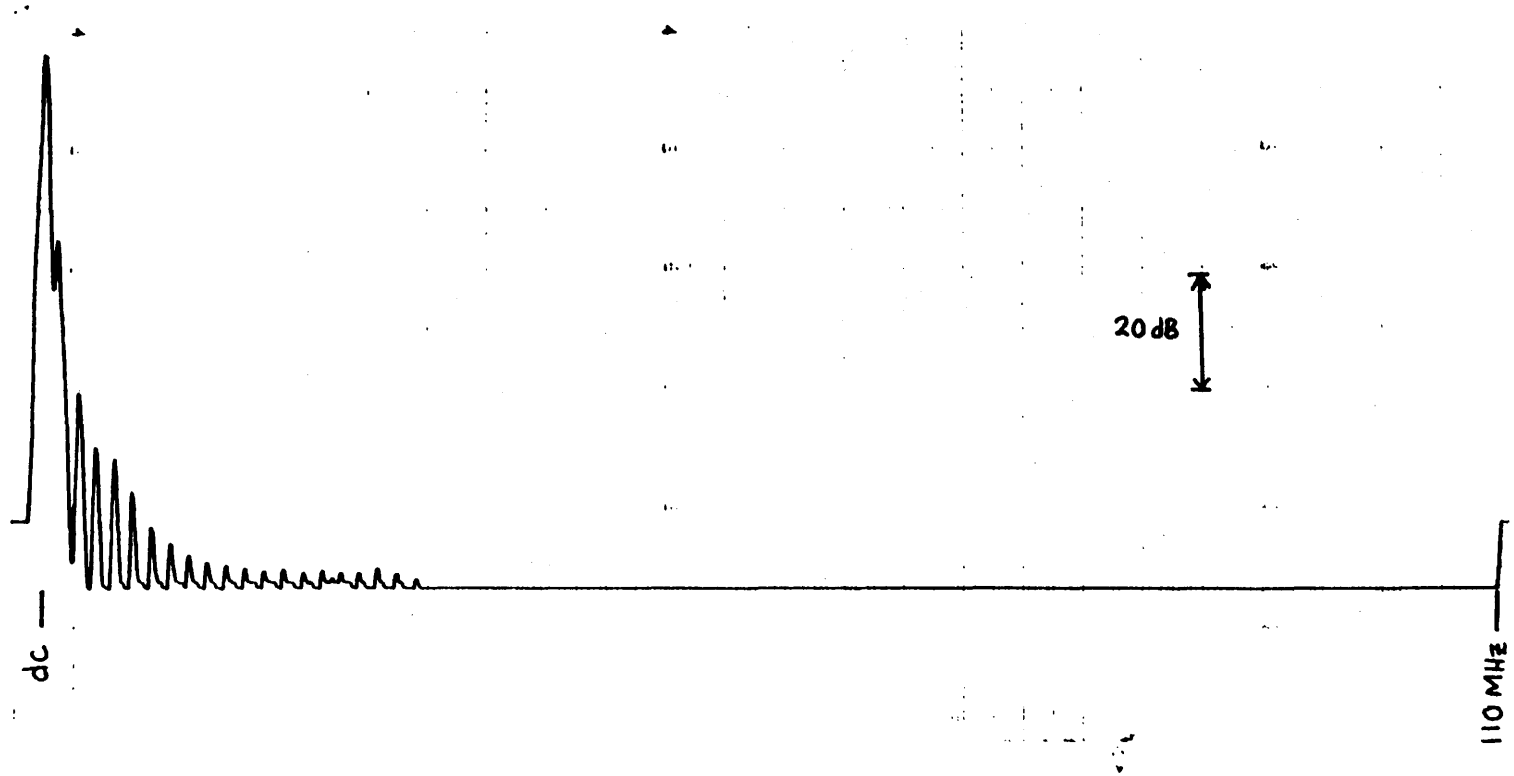

Figure 6.34b A Complete Spectrum Plot (dc to 110 MHz) Illustrating The RF Pickup By The Photodiode Unit (Without Any Laser Beam Incident On The Photodetector)

values and variations in modulation frequency values on serrodyne performances are described in Sections 6.4.5.3 and 6.4.5.4 respectively. The fall-time of the serrodyne modulation frequency was carefully adjusted to one of the following values, i.e. 20 ns, 35 ns, 50 ns, 100 ns, 150 ns, 280 ns, and 400 ns. The experimentally measured sideband levels for C_{-2}, C_{-1}, C_0, C_2 and C_3 were compared to similar theoretical sideband levels shown in Table 6.13.

All the 4 μm and 5 μm wide X-cut PE $LiNbO_3$ phase modulators were evaluated and the results are tabulated in Tables 6.26 to 6.29. The results indicated that there is fairly good agreement between the theoretical and experimental sideband levels. However devices PEX5 and PEX6 appeared to perform better than PEX3 and PEX11. A possible reason for the slightly poorer performances measured using devices PEX3 and PEX11 may be due to the fact that one is near to the cutoff and the other is near to the boundary of the 2nd order mode. No detailed investigation of these possible explanations were carried out due to the lack of time. In addition, the value of C_0 varied between -15 dB and -34 dB, the actual value depending on the RF drive level to the Bragg cell. The property in which PE devices are superior to Ti:$LiNbO_3$ devices is the requirement of lower $V_{2\pi}$ voltages; otherwise the results from both types of device are fairly comparable.

It can be concluded that the performance of the PE serrodyne modulators is very dependant on the value of the finite fall-time of the sawtooth signal. In order to make such devices useful in specific applications, such as the fibre-optic gyroscope, the fall-time has to be well below 1 ns for a serrodyne frequency of 1 MHz to ensure a dynamic range of 60 dB.

6.4.5.3 Effect of Non-Optimum Sawtooth Amplitude

The effects of non-optimum sawtooth amplitude on overall sideband suppression for all the X-cut PE $LiNbO_3$ phase modulators fabricated at

T_f/T	C_{-2} (dB)	C_{-1} (dB)	C_0 (dB)	C_2 (dB)	C_3 (dB)
0.020	-30 (-31)	-32 (-31)	-15 (-16)	-22 (-21)	-20 (-22)
0.035	-26 (-27)	-25 (-26)	-16 (-16)	-20 (-22)	-21 (-22)
0.050	-25 (-26)	-26 (-26)	-16 (-16)	-18 (-17)	-19 (-21)
0.100	-23 (-22)	-25 (-26)	-15 (-16)	-11 (-13)	-14 (-15)
0.150	-21 (-21)	-20 (-21)	-16 (-15)	-07 (-08)	-11 (-12)
0.280	-12 (-12)	-14 (-15)	-15 (-15)	-06 (-06)	-07 (-08)
0.400	-09 (-10)	-12 (-12)	-15 (-15)	-02 (-02)	-05 (-05)

Note 1: The results for the 5 μm devices are in the brackets
Note 2: T = 1 μs and C_1 = 1 (0 dB)

Table 6.26 Summary Of Experimental Sideband C_n Values (n = –2, –1, 0, 2, 3) With Respect To Different Fall–Times For A 4 μm And a 5 μm Wide X–Cut PE $LiNbO_3$ Phase Modulator (Device: PEX3, Exchange Temperature = 162°C, Exchange Time = 25 minutes)

T_f/T	C_{-2} (dB)	C_{-1} (dB)	C_0 (dB)	C_2 (dB)	C_3 (dB)
0.020	-34 (-34)	-35 (-35)	-26 (-26)	-26 (-26)	-27 (-27)
0.035	-30 (-30)	-31 (-31)	-26 (-26)	-21 (-22)	-22 (-24)
0.050	-29 (-28)	-28 (-29)	-25 (-26)	-18 (-19)	-19 (-20)
0.100	-22 (-23)	-24 (-24)	-25 (-25)	-12 (-12)	-17 (-17)
0.150	-19 (-21)	-20 (-18)	-26 (-25)	-08 (-08)	-13 (-14)
0.280	-13 (-12)	-17 (-14)	-26 (-25)	-05 (-06)	-08 (-08)
0.400	-11 (-13)	-13 (-15)	-26 (-26)	-01 (-02)	-04 (-03)

Note 1: The results for the 5 μm devices are in the brackets
Note 2: T = 1 μs and C_1 = 1 (0 dB)

Table 6.27 Summary Of Experimental Sideband C_n Values (n = –2, –1, 0, 2, 3) With Respect To Different Fall–Times For A 4 μm And a 5 μm Wide X–Cut PE $LiNbO_3$ Phase Modulator (Device: PEX5, Exchange Temperature = 162°C, Exchange Time = 30 minutes)

T_f/T	C_{-2} (dB)	C_{-1} (dB)	C_0 (dB)	C_2 (dB)	C_3 (dB)
0.020	-34 (-35)	-35 (-38)	-34 (-34)	-31 (-30)	-29 (-30)
0.035	-30 (-30)	-31 (-33)	-34 (-34)	-21 (-22)	-22 (-24)
0.050	-31 (-29)	-30 (-30)	-33 (-34)	-19 (-19)	-20 (-21)
0.100	-24 (-23)	-25 (-24)	-33 (-33)	-14 (-14)	-15 (-16)
0.150	-19 (-21)	-23 (-19)	-34 (-33)	-09 (-09)	-12 (-12)
0.280	-15 (-14)	-18 (-17)	-34 (-34)	-05 (-05)	-07 (-08)
0.400	-11 (-12)	-13 (-13)	-34 (-34)	-02 (-03)	-04 (-04)

Note 1: The results for the 5 μm devices are in the brackets
Note 2: T = 1 μs and C_1 = 1 (0 dB)

Table 6.28 Summary Of Experimental Sideband C_n Values (n = –2, –1, 0, 2, 3) With Respect To Different Fall–Times For A 4 μm And a 5 μm Wide X–Cut PE $LiNbO_3$ Phase Modulator (Device: PEX6, Exchange Temperature = 162°C, Exchange Time = 35 minutes)

T_f/T	C_{-2} (dB)	C_{-1} (dB)	C_0 (dB)	C_2 (dB)	C_3 (dB)
0.020	-32 (-32)	-30 (-32)	-31 (-30)	-26 (-26)	-26 (-25)
0.035	-28 (-29)	-30 (-31)	-31 (-31)	-20 (-22)	-22 (-23)
0.050	-27 (-27)	-29 (-31)	-30 (-30)	-16 (-15)	-17 (-16)
0.100	-21 (-20)	-22 (-22)	-30 (-30)	-12 (-11)	-13 (-13)
0.150	-15 (-16)	-18 (-20)	-30 (-30)	-08 (-07)	-11 (-11)
0.280	-13 (-12)	-14 (-14)	-30 (-30)	-04 (-04)	-05 (-05)
0.400	-06 (-05)	-10 (-11)	-30 (-30)	-03 (-02)	-03 (-02)

Note 1: The results for the 5 μm devices are in the brackets
Note 2: T = 1 μs and C_1 = 1 (0 dB)

Table 6.29 Summary Of Experimental Sideband C_n Values (n = –2, –1, 0, 2, 3) With Respect To Different Fall–Times For A 4 μm And a 5 μm Wide X–Cut PE $LiNbO_3$ Phase Modulator (Device: PEX11, Exchange Temperature = 162°C, Exchange Time = 40 minutes)

temperatures of 162°C are summarized in Tables 6.30 to 6.33, with the theoretical results calculated using the information in Table 3.1 of Chapter 3. Due to the RF pickup problem, the contribution of C_0 was not included in the analysis of the experimental sideband levels. It can be deduced from the results found in Tables 6.30 to 6.33 that the devices that performed well are those fabricated with exchange times of 30 and 35 minutes. This again suggests that the devices fabricated with exchange times of 25 and 40 minutes respectively are possibly close to cutoff or to the multimode regime of the waveguides. Figures 6.35 to 6.38 illustrate graphically the results of Tables 6.30 to 6.33 respectively, i.e. for devices PEX3, PEX5, PEX6, and PEX11. From the results above, it can be stated that the optimum overall serrodyne sideband suppressions occured as predicted by the theory described in Section 3.4.3 of Chapter 3, i.e. $\phi_o = \phi_p\ [1-(T_f/T)]$ (Equation 3.14). Again the results indicate that the performance of the PE serrodyne devices is as good as and in some cases better than those devices fabricated using titanium-indiffusion. The problem of maintaining a very stable serrodyne modulation signal is again noted to be an important parameter to be considered for any future use of serrodyne devices for fibre-optic sensor systems.

6.4.5.4 Effect of Non-Optimum Operation Over a Band/Range Of Frequencies using a Constant Sawtooth Amplitude

The 3 dB electrical bandwidth of device PEX3 was found to be 1.1 GHz (Section 6.4.3). Due to the lack of time no further experiments were carried out to establish the bandwidth of the remaining PE exchange devices, i.e. PEX5, PEX6, and PEX11. It seems likely that the remaining devices would have similar characteristics to device PEX3 and the titanium-indiffused phase modulators. The basis of this assumption was that the same device assembly procedures and connection between devices and signal sources were used.

d	Phase ϕ	Applied Voltage (Volts)	Theoretical Value Of S_{or} (dB)	Experimental Value Of S_{or} (dB)
-0.02	6.16	6.4	34	30 (31)
0	6.28	6.5	28	25 (25)
0.02	6.41	6.6	24	23 (23)
-0.04	6.03	6.2	28	25 (25)
0.04	6.53	6.8	22	21 (21)
-0.06	5.91	6.1	24	20 (21)
0.06	6.66	6.9	20	21 (20)

Note: (1) Theoretical results were calculated using the details described in Table 3.1 (Device: PEX3, T_f = 20 ns, T = 1 μs, C_1 = 1)
(2) The results for the 5 μm devices are shown in the brackets

Table 6.30 Summary Of Theoretical And Experimental Overall Sideband Suppression Values, S_{0r} , With Respect To Variations In Serrodyne Voltage Levels For A 4 And A 5 μm Wide X–Cut PE $LiNbO_3$ Phase Modulator (Device: PEX3, $V_{2\pi}$= 6.5 V)

d	Phase ϕ	Applied Voltage (Volts)	Theoretical Value Of S_{or} (dB)	Experimental Value Of S_{or} (dB)
-0.02	6.16	7.3	34	32 (32)
0	6.28	7.4	28	26 (28)
0.02	6.41	7.6	24	22 (22)
-0.04	6.03	7.1	28	27 (25)
0.04	6.53	7.7	22	23 (22)
-0.06	5.91	7.0	24	22 (22)
0.06	6.66	7.8	20	18 (17)

Note: (1) Theoretical results were calculated using the details described in Table 3.1 (Device: PEX5, T_f = 20 ns, T = 1 μs, C_1 = 1)
(2) The results for the 5 μm devices are shown in the brackets

Table 6.31 Summary Of Theoretical And Experimental Overall Sideband Suppression Values, S_{0r} , With Respect To Variations In Serrodyne Voltage Levels For A 4 And A 5 μm Wide X–Cut PE $LiNbO_3$ Phase Modulator (Device: PEX5, $V_{2\pi}$= 7.4 V)

d	Phase ϕ	Applied Voltage (Volts)	Theoretical Value Of S_{or} (dB)	Experimental Value Of S_{or} (dB)
-0.02	6.16	6.6	34	35 (34)
0	6.28	6.7	28	26 (27)
0.02	6.41	6.8	24	25 (24)
-0.04	6.03	6.4	28	26 (27)
0.04	6.53	7.0	22	21 (21)
-0.06	5.91	6.3	24	23 (21)
0.06	6.66	7.1	20	19 (19)

Note: (1) Theoretical results were calculated using the details described in Table 3.1 (Device: PEX6, T_f = 20 ns, T = 1 μs, C_1 = 1)
(2) The results for the 5 μm devices are shown in the brackets

Table 6.32 Summary Of Theoretical And Experimental Overall Sideband Suppression Values, S_{0r} , With Respect To Variations In Serrodyne Voltage Levels For A 4 And A 5 μm Wide X–Cut PE $LiNbO_3$ Phase Modulator (Device: PEX6, $V_{2\pi}$= 6.7 V)

d	Phase ϕ	Applied Voltage (Volts)	Theoretical Value Of S_{or} (dB)	Experimental Value Of S_{or} (dB)
-0.02	6.16	6.4	34	30 (30)
0	6.28	6.5	28	23 (24)
0.02	6.41	6.6	24	21 (21)
-0.04	6.03	6.2	28	24 (24)
0.04	6.53	6.8	22	18 (19)
-0.06	5.91	6.1	24	20 (19)
0.06	6.66	6.9	20	17 (18)

Note: (1) Theoretical results were calculated using the details described in Table 3.1 (Device: PEX11, T_f = 20 ns, T = 1 μs, C_1 = 1)
(2) The results for the 5 μm devices are shown in the brackets

Table 6.33 Summary Of Theoretical And Experimental Overall Sideband Suppression Values, S_{0r} . With Respect To Variations In Serrodyne Voltage Levels For A 4 And A 5 μm Wide X–Cut PE $LiNbO_3$ Phase Modulator (Device: PEX11, $V_{2\pi}$= 6.5 V)

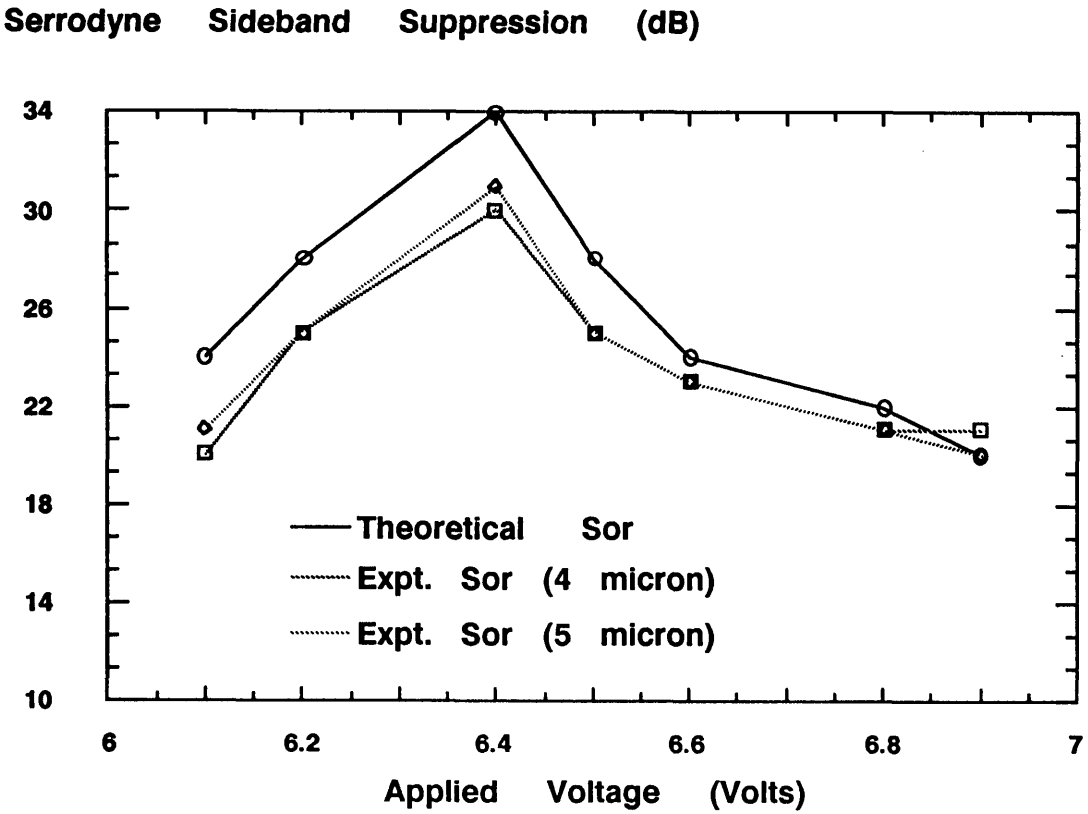

Figure 6.35 Plots Of Theoretical And Experimental Overall Serrodyne Suppression With Respect To Applied Voltage On A 4 μm And 5 μm Wide X–Cut PE $LiNbO_3$ Phase Modulator (Device: PEX3)
[f_m = 1 MHz, f_B = 22 MHz, $V_{2\pi}$ = 6.5 Volts]

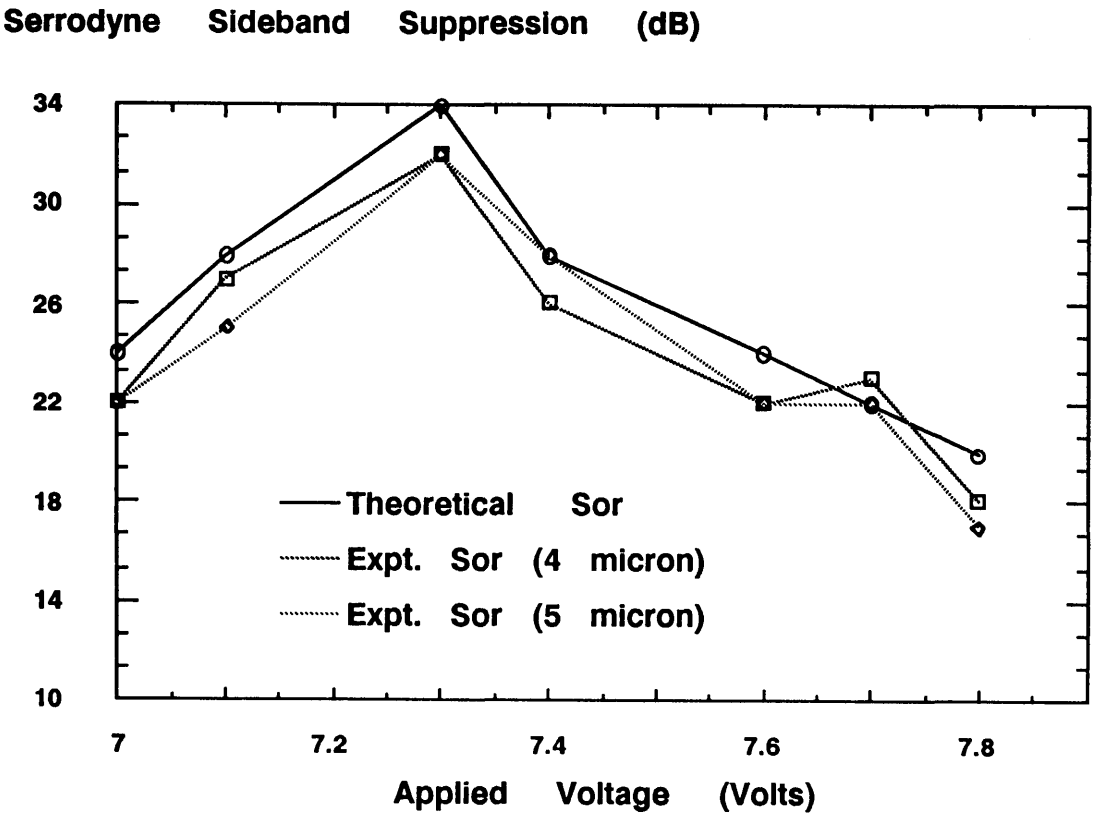

Figure 6.36 Plots Of Theoretical And Experimental Overall Serrodyne Suppression With Respect To Applied Voltage On A 4 μm And 5 μm Wide X–Cut PE $LiNbO_3$ Phase Modulator (Device: PEX5)
[f_m = 1 MHz, f_B = 22 MHz, $V_{2\pi}$ = 7.4 Volts]

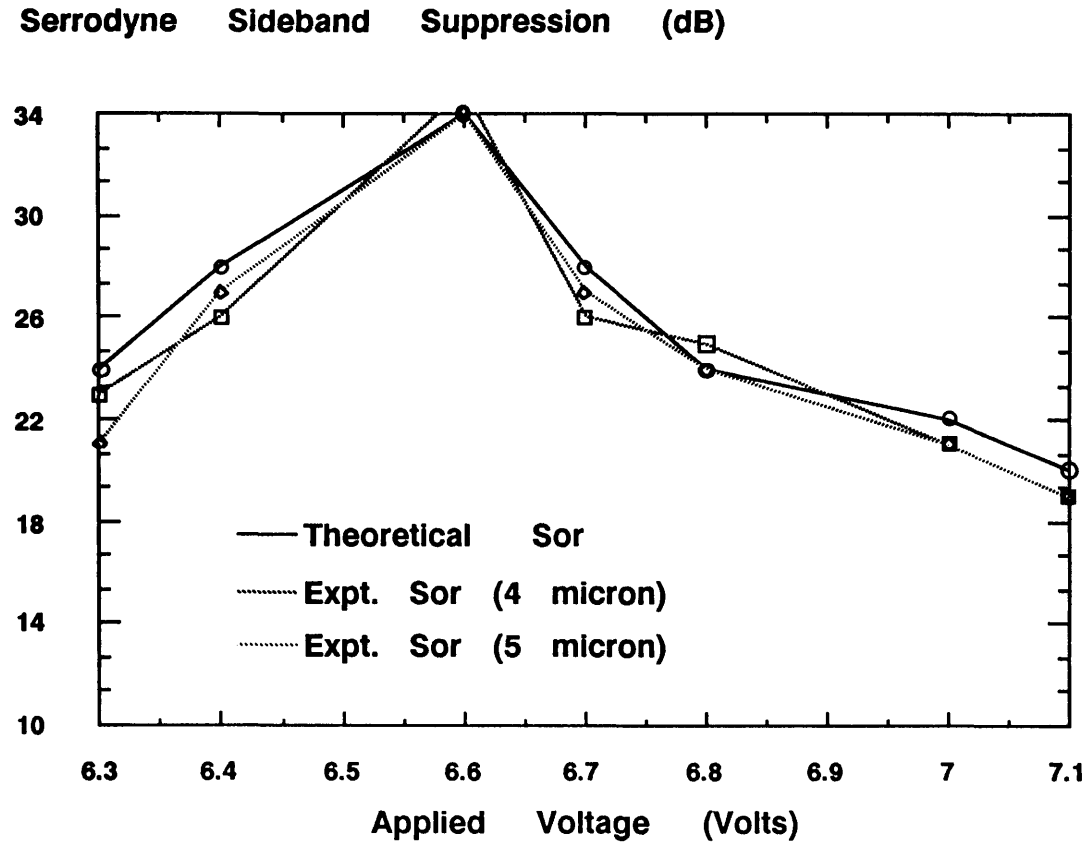

Figure 6.37 Plots Of Theoretical And Experimental Overall Serrodyne Suppression With Respect To Applied Voltage On A 4 μm And 5 μm Wide X–Cut PE $LiNbO_3$ Phase Modulator (Device: PEX6)
[f_m = 1 MHz, f_B = 22 MHz, $V_{2\pi}$ = 6.7 Volts]

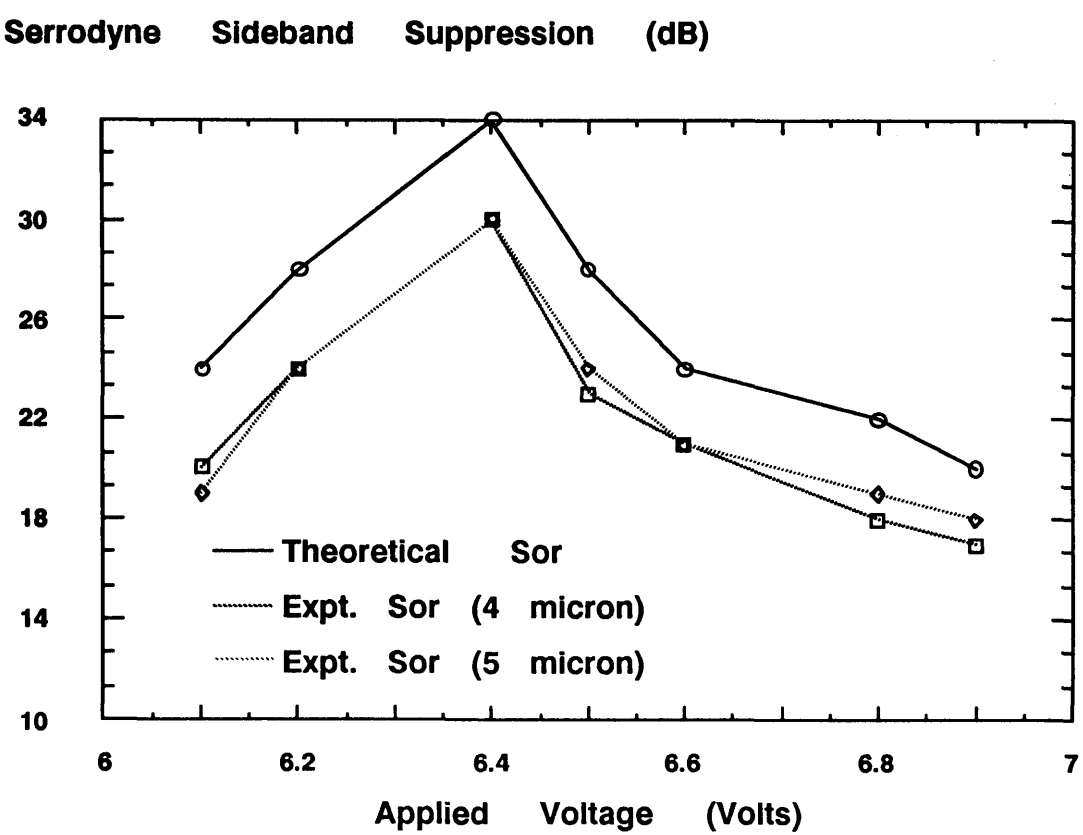

Figure 6.38 Plots Of Theoretical And Experimental Overall Serrodyne Suppression With Respect To Applied Voltage On A 4 μm And 5 μm Wide X–Cut PE $LiNbO_3$ Phase Modulator (Device: PEX11)
[f_m = 1 MHz, f_B = 22 MHz, $V_{2\pi}$ = 6.5 Volts]

The overall serrodyne sideband suppression levels for the four PE X-cut $LiNbO_3$ devices (i.e. PEX3, PEX5, PEX6, and PEX11) tested in the frequency range from 300 kHz to 7 MHz were measured (Table 6.34). The theoretical calculations from Table 6.22 of Section 6.4.4.4 was used to generate Figure 6.39 which included the experimental frequency response curves for the four PE devices. The conclusion from this study based on results shown in Figure 6.39 indicated that the performance of the serrodyne devices were limited by the fall-time of the function generator i.e. 11 ns at the highest sawtooth frequency of 7 MHz.

6.4.5.5 Presence of Amplitude Modulation in an Electro-Optic Phase Modulator and its Effects

It was not possible to measure the amplitude modulation levels for the X-cut PE $LiNbO_3$ serrodyne devices due an effect known as the dc extinction effect. By applying voltages greater than 5 volts to any of the four devices fabricated at 162°C, the light output from the devices could be slowly reduced from 100% to 10% with time constants ranging from about 80 seconds to as high as 900 seconds. Figure 6.40 shows an example of such a sequence of optical extinction effects due to the application of a dc signal of +5 volts and then +15 volts to device PEX3. The output of the PE stripe waveguide was intentionally defocussed to ensure that it could be easily observed. The optical extinction in this case was measured to be around 19 dB. A number of dc bias voltages were then applied to the devices and the corresponding optical extinctions were recorded. The data were then plotted as shown in Figure 6.41. It can be deduced from that figure that there was no systematic pattern to voltage dependence in the dc extinction effect. In fact the plot suggests that the dc extinction effect is random in nature. One possible explanation for this observed effect is the movement of lithium ions and proton in the PE waveguide regions under the influence of static electric

Serrodyne Frequency (MHz)	Theoretical Overall Sideband Suppression S_o (dB)	Experimental Overall Sideband Suppression S_o (dB)			
		PEX3	PEX5	PEX6	PEX11
0.3	32	31	32	31	32
0.5	32	31	33	30	31
0.7	33	30	31	32	31
1.0	34	30	32	35	30
2.0	33	31	32	32	30
3.0	30	29	29	31	27
4.0	28	26	27	27	25
5.0	26	24	23	26	23
6.0	25	23	24	25	21
7.0	23	22	23	22	20

Note: C = 6.16 pF, R = 47 Ω.

Table 6.34 Study Of Serrodyne Frequency Responses From 300 kHz To 7 MHz For Devices PEX3, PEX5, PEX6, And PEX11 (Only 4 μm Wide Devices Are Evaluated, X–Cut, PE $LiNbO_3$, For Device PEX3: Δf = 1.1 GHz)

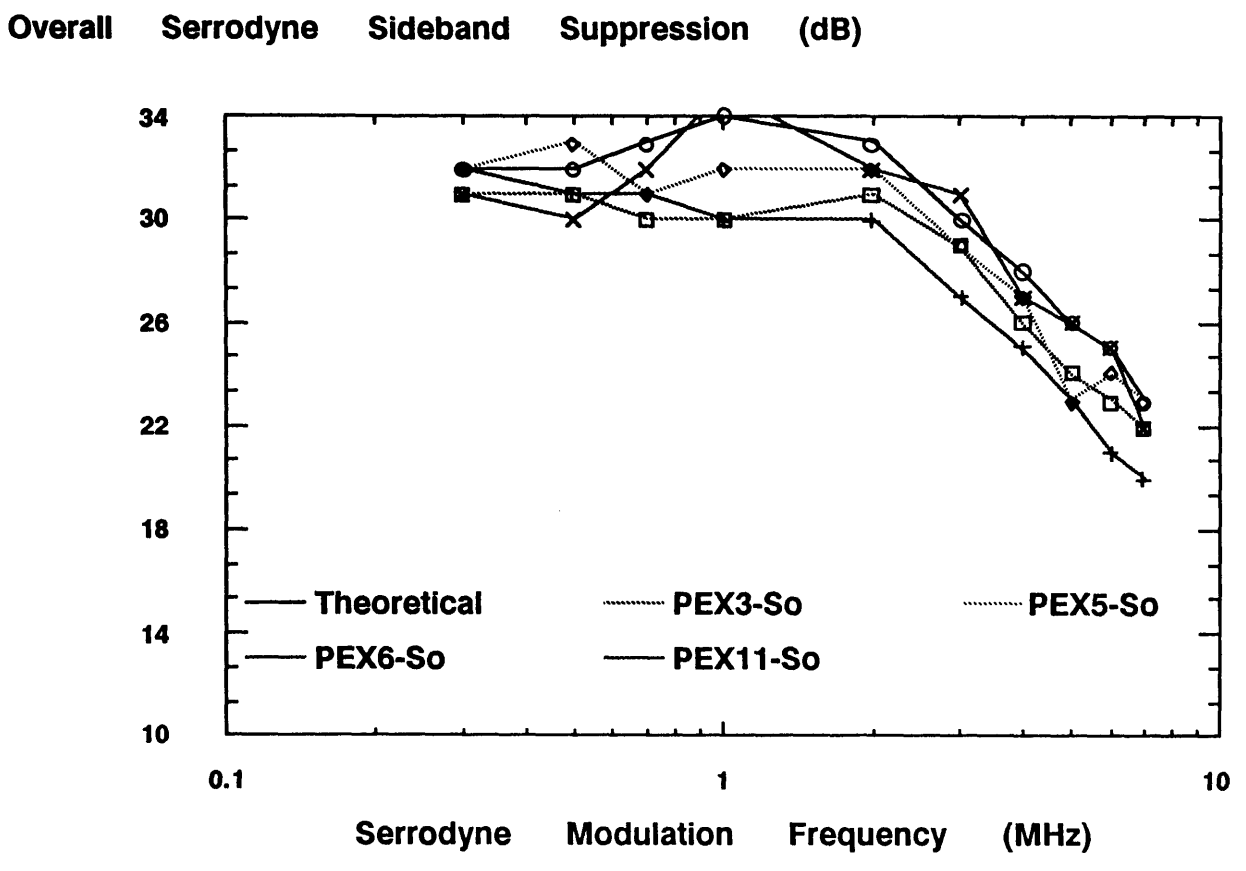

Figure 6.39 Plot Of Serrodyne Frequency Responses From 300 kHz To 7 MHz For Devices PEX3, PEX5, PEX6, And PEX11 (4 μm Wide Guides, X–Cut, PE $LiNbO_3$, For Device PEX3: $\Delta f = 1.1$ GHz)

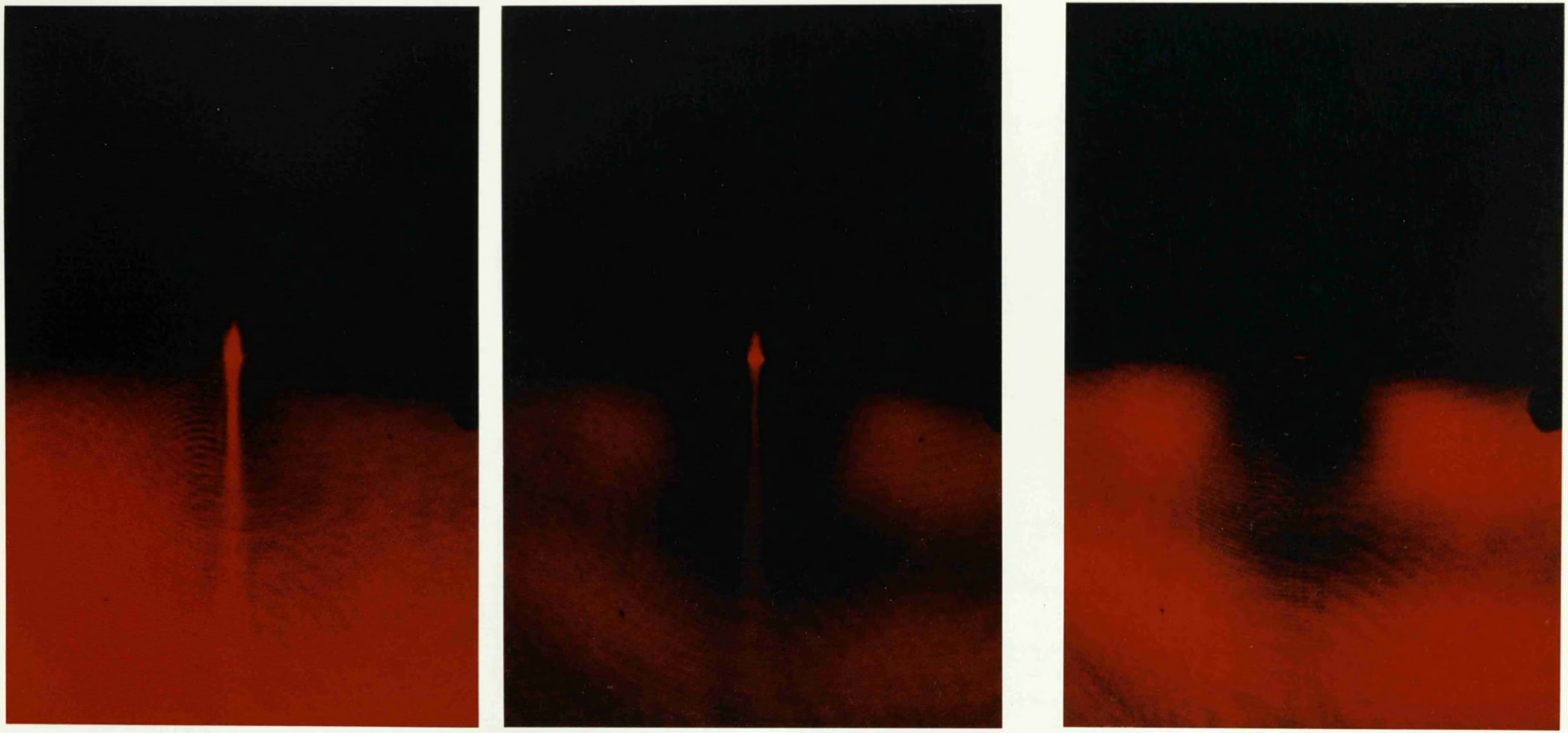

(a) (b) (c)

Figure 6.40 Sequence Of Three Photographs Illustrating The DC Extinction Effect For Device PEX3 (4 μm Wide Guides, X–Cut, PE $LiNbO_3$) (a) Without DC Voltage, (b) With A DC Voltage Of +5 Volts, And (c) With A DC Voltage Of +15 Volts

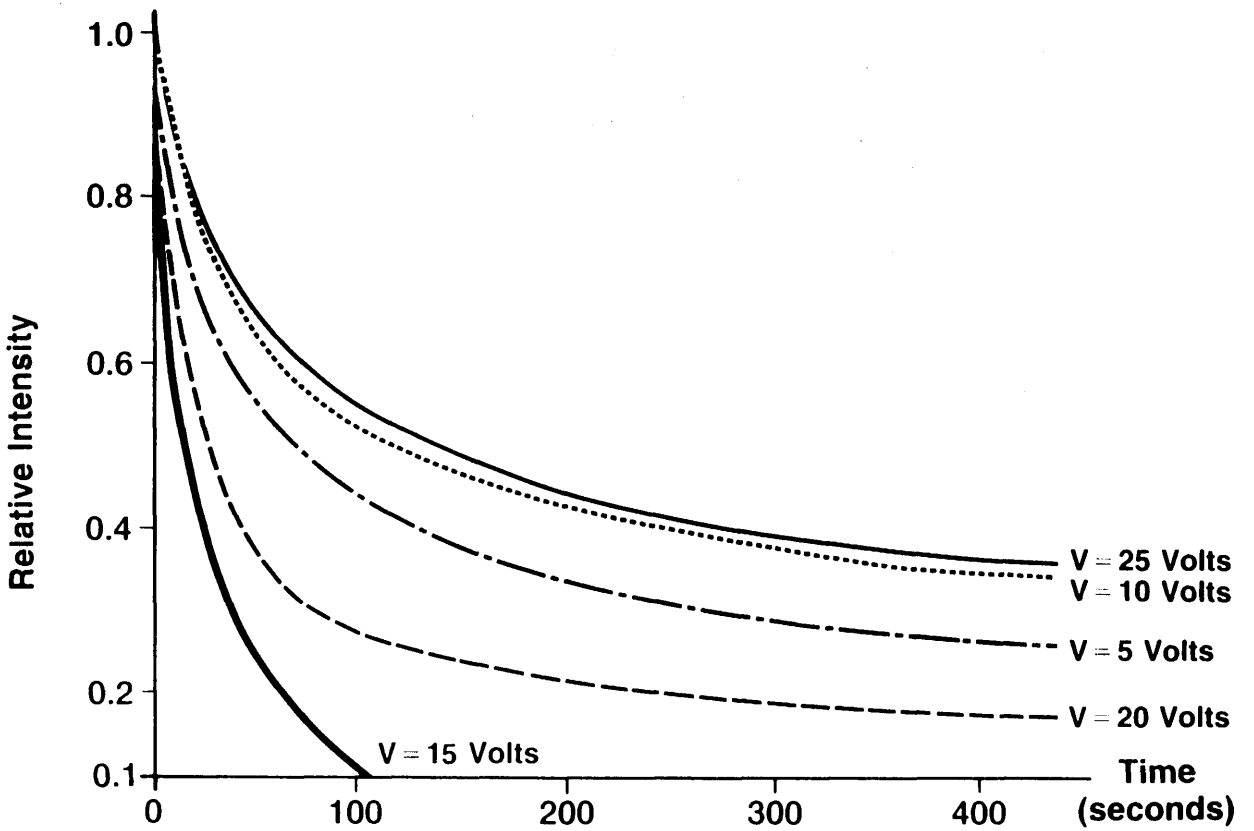

Figure 6.41 Effect Of Various DC Bias Levels On The Output Intensity Of Device Number PEX3 ($\Delta n = 0.12$, $\lambda = 633$ nm, 4 μm Wide Guides, X–Cut PE $LiNbO_3$ Phase Modulator)

fields. The movement of lithium ions may be the cause of the possible reduction in the refractive index of the waveguide areas and hence the amplitude modulation effect. However, more studies have to be carried out using material analysis techniques to discover what is the mechanism that is causing the dc extinction effect. It is clear that the dc extinction effect briefly reported in this section is not desirable for high performance serrodyne frequency translators and is by no means well understood.

6.5 Summary

The complete design procedures for optical phase-modulators in $LiNbO_3$ have been outlined. All the test equipment and experimental procedures that were employed to evaluate the serrodyne frequency-translators were described in detail. The use of the bulk Mach-Zehnder interferometer, with an acousto-optic Bragg cell on the reference arm, was used exclusively to study the sideband levels associated with the optical translation process. This technique was valuable since it facilitated the study of both positive and negative spurious sideband levels about a centre frequency determined by the Bragg cell. In all the experiments, the intermediate frequency was 22 MHz.

The optical phase-modulators were evaluated optically and electrically. This was to ensure that the optical waveguides of the fabricated devices were single-moded. The 3 dB electrical frequency responses of the fabricated Ti:$LiNbO_3$ and PE phase modulators were in the range from 0.8 GHz to 1.1 GHz. Therefore this was not a limiting factor for all the serrodyne experiments reported in this thesis. Finally the phase-modulators were operated as serrodyne frequency-translators by using the proper driving sawtooth signals obtained from commercial function generators. Optical frequency translation was demonstrated over the range from 300 kHz to 7 MHz.

The serrodyne results indicated that the performance of the $Ti:LiNbO_3$ serrodyne frequency-translators was limited by the finite fall-time of the commercial function generators. Overall sideband suppressions of up to a value of 33 dB have been measured. Also it was found that the serrodyne process is very sensitive to small voltage changes. It was concluded from the study that the serrodyne voltage has to be stable to within 0.5% of the $V_{2\pi}$ value. The other factor that limited the performance of some of the $Ti:LiNbO_3$ devices was the weakly confined waveguide modes of a number of devices. With these devices, the measured amplitude modulation levels were generally high, i.e. between 1% and 55%. By applying a dc bias voltage to such devices, the measured level of amplitude modulation varied appropriately, again indicating the weakly confined nature of the optical waveguides under test.

For the first time, electro-optical waveguide phase-modulators operated as serrodyne frequency-translators were demonstrated with proton-exchange (PE) waveguides. However, it was found that not all the fabricated PE phase-modulators worked. This was attributed to the reduction in the electro-optic activity in some of the devices. The key to realising operational devices appears to be to fabricate them at a low exchange temperature i.e. exchange temperatures of 162°C with exchange times of 25, 30, 35, and 40 minutes. However with the PE devices that operated efficiently as serrodyne modulators, the intensities of the guided modes were dramatically reduced by the application of dc bias voltages (as low as +5 volts). As serrodyne frequency-translators, these phase-modulators were found to operate more efficiently than the $Ti:LiNbO_3$ devices, i.e. they required lower $V_{2\pi}$ voltages. The required voltages for 2π phase change were reduced by approximately 30%. This implies a better electrical/optical overlap between the guided modes and the electric fields (around 0.5 for PE devices compared to 0.3 for titanium-indiffused devices). The rest of the

performance of the PE serrodyne frequency-translators was comparable to that of Ti:$LiNbO_3$ devices.

APPENDIX 6.1

TEST EQUIPMENT

(I) Laser

(a) Spectra Physics Model 120 HeNe Laser Lasing at 633 nm.

(II) Signal Generators

(a) Tektronix FG 504 40 MHz Function Generator.

(b) Tektronix Type 191 Constant Amplitude Signal Generator.

(c) HP 1900A Pulse Generator.

(d) Wavetek Sweep Oscillator (0-1400 MHz)

(III) RF Amplifiers

(a) EIN Model 601L RF Power Amplifier 1.2 Watts Linear (37 dB/0.8-1000 MHz).

(b) HP 230 Power Amplifier (10-500 MHz).

(IV) Photodiode Detectors

(a) AEG BPW 28 Silicon Avalanche Photodiode:-

Gain-Bandwidth Product Of > 200 GHz

Quantum Efficiency Of 75% At λ_o= 633 nm

Diameter Of Photosensitive Area Is 0.2 mm

(b) HP 4207 PIN Silicon Photodiode:-

Quantum Efficiency Of 78% At λ_o= 633 nm

Diameter Of Photosensitive Area Is 1.0 mm

(c) HP5082-4205 PIN Silicon Photodiode:-

Responsivity of 0.35A/W At λ_o= 633 nm.

Diameter Of Photosensitive Area Is 0.6 mm

Speed Of Response Is < 1 nanosecond

Mounted On A Conhex Connector

(V) Display Instruments

(a) HP Spectrum Analyzer (0-110 MHz) With RF Section (HP 8553B), IF Section (HP 8552B), And Display Section (HP 140T).

(b) HP Spectrum Analyzer (0-1250MHz) With RF Section (HP 8554L), IF Section (HP 8552A), And Display Section (HP 141T).

(c) Tektronix Oscilloscope 475 A.

(d) Tektronix Oscilloscope 7904 (Maximum Frequency: 1 GHz).

(VI) Preamplifier

(a) HP10855A Preamplifier:-

Frequency Range:	2 MHz - 1300 MHz
3 dB Bandwidth:	1MHz - 1400 MHz
Gain:	24 dB
Noise Figure:	< 8.5 dB

(VII) Recorder

(a) JJ Instruments Chart Recorder CR 500.

(b) HP Plotter 7044A X-Y Recorder.

(VIII) DC Stabilised Power Supply

Advance Electronics - Dual DC Stabilised Power Supply PP11A.

(IX) Optical Power Meter

(a) Photodyne 44XL Optical Power Meter With Large Area Photodiode Head For λ_0= 633 nm.

(X) Mode Profiling Equipment

(a) Hamamatsu Camera System With C1000 Camera Controller.

APPENDIX 6.2

THEORETICAL CALCULATION OF VALUES

A6.2.1 Background Theory

The total phase modulation ϕ derived from a phase modulator driven with a voltage V is given by the relationship:

$$\phi = k*V \qquad \text{(A6.2.1.1)}$$

where k is known as the modulator constant in radians/volt.

The following relationship for the 1st order of the Bessel functions of the first kind is true for small values of x:

$$J_1(x) \cong A*x \qquad \text{(A6.2.1.2)}$$

and therefore,

$$J_1(k*V) \cong A*k*V \qquad \text{(A6.2.1.3)}$$

By plotting $J_1(x)$ against x, the value of A can be deduced from the slope of the line. Similarly by plotting $10*\log[J_1{}^2(k*V)]$ versus $10*\log[V^2]$, the value of k can be obtained since A is known from Equation A6.2.1.2.

A6.2.2 Example of a Calculation to Obtain the Value of k

The first step as described in Section A6.2.1 is to plot $J_1(x)$ against x, where x is small. The values of $J_1(x)$ were obtained from a standard table of Bessel functions of the first kind [6.33]. Figure 6.42 shows such a plot. Therefore the value A was found to be 0.46.

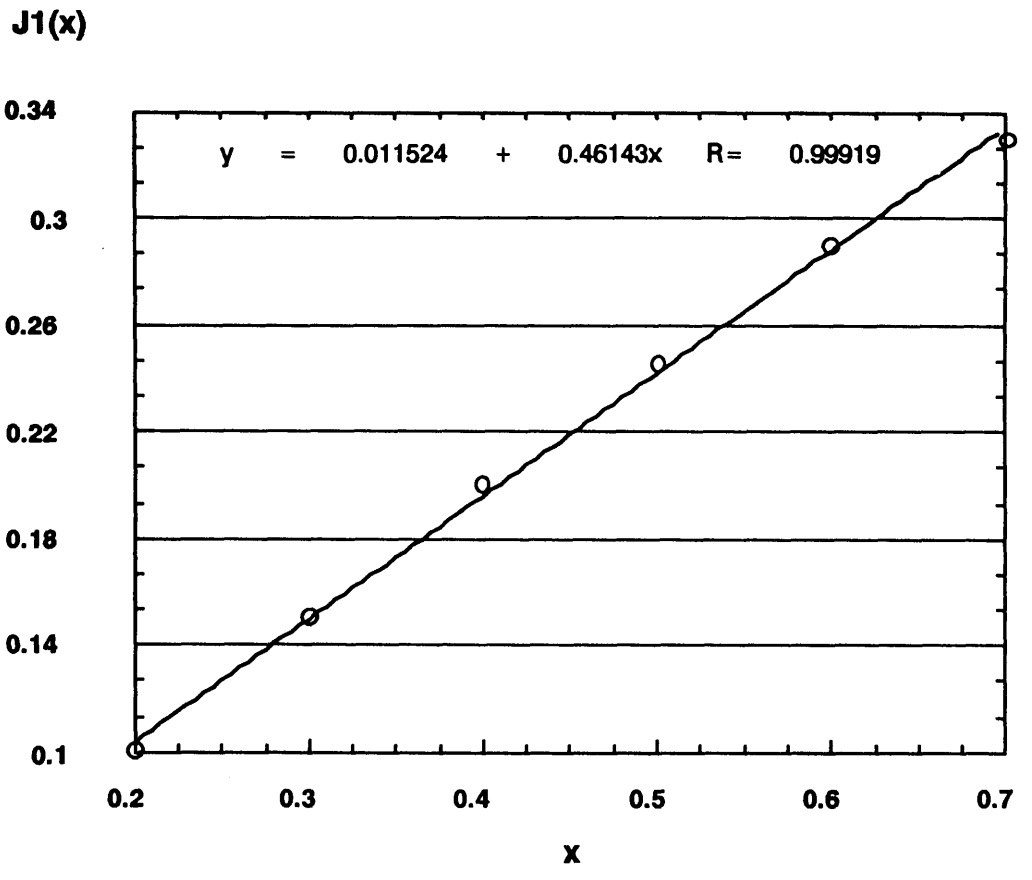

Figure 6.42 Plot Of Theoretical $J_1(x)$ Values Versus x

As an example, the results from a sinusoidally (1 MHz) driven PE X-cut $LiNbO_3$ phase modulator fabricated at 162°C with an exchange time of 25 minutes, tabulated in Table 6.35, were used to derive the value of k. A plot of $10*\log[J_1^2(k*V)]$ versus $10*\log[V^2]$ was carried out (Figure 6.43). From this plot, the intercept was found to be:

$$10*\log(A^2*k^2) = -16.5 \text{ dB} \qquad \text{(A6.2.2.1)}$$

Therefore the experimentally derived value of k is 0.33.

From the table of Bessel functions of the first kind [6.33], the 0th order goes to zero at a value of 2.4048. Substituting the values of ϕ= 2.4048 and k= 0.33 into Equation A6.2.1.1, therefore the calculated value of $V_{2\pi}$ was 7.3 volts. The experimentally obtained value of $V_{2\pi}$ was 6.5 volts. The above procedures were used in all the remaining calculations of $V_{2\pi}$ for the PE phase modulators under sinusoidal evaluations as shown in Tables 6.25a and 6.25b.

Sinusoidal Voltage (Volts)	Sinusoidal Voltage (dB)	1st Sideband Level -Experimental (dB)
1.0	0.00	-17
2.0	6.02	-11
3.0	9.54	-7
4.0	12.04	-6
5.0	13.98	-4
6.0	15.56	-5

Table 6.35 Summary Of 1st Sideband Level Results For A Sinusoidally Driven Proton–Exchange X–Cut $LiNbO_3$ Phase Modulator (Exchange Temperature= 162°C, Exchange Time= 25 minutes)

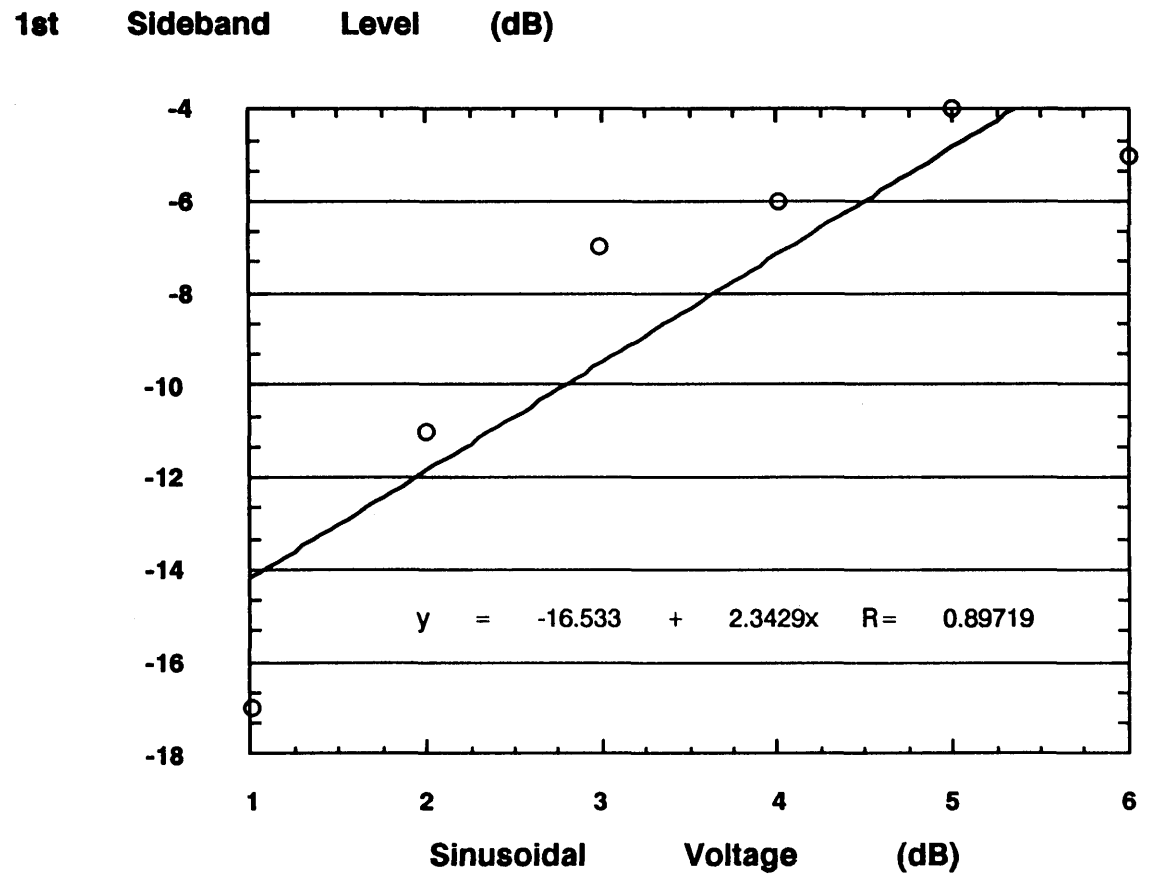

Figure 6.43 Plot Of Experimentally Obtained $10*\text{Log}[J_1^2(k*v)]$ Against $10*\text{Log}[V^2]$

REFERENCES

[6.1] I.P. Kaminow, "An Introduction to Electrooptic Devices", Academic Press, New York and London, 1974.

[6.2] J.F. Nye, "Physical Properties of Crystals - Their Representations By Tensors and Matrices", Clarendon Press, Oxford, 1976.

[6.3] A. Yariv, "Introduction to Optical Electronics", Second Edition, Holt, Rinehart, and Winston, New York, 1976.

[6.4] A. Rauber, "Chemistry and Physics of Lithium Niobate", Chapter 7 in Current Topics in Materials Science", Vol. 1, E. Kaldis (Ed.), North Holland, Oxford, 1978.

[6.5] E. Bernal, G.D. Chen, and T.C. Lee, "Low Frequency Electro-Optic and Dielectric Constants of Lithium Niobate", Phys. Lett., Vol. 21, No. 3, pp 259-260, 15 May 1967.

[6.6] E.H. Turner, "High Frequency Electro-Optic Coefficients of Lithium Niobate", Appl. Phys. Lett., Vol. 8, No. 11, pp 303-304, 1 June 1966.

[6.7] I.P. Kaminow, J.R. Carruthers, E.H. Turner, and L.W. Stulz, "Thin-Film $LiNbO_3$ Electro-Optic Light Modulator", Appl. Phys. Lett., Vol. 22, No. 10, pp 540-542, 15 May 1973.

[6.8] I.P. Kaminow, L.W. Stulz, and E.H. Turner, "Efficient Strip-Waveguide Modulator", Appl. Phys. Lett., Vol. 27, No. 10, pp 555-557, 15 November 1975.

[6.9] R.T. Smith and F.S. Welsh, "Temperature Dependence of the Elastic, Piezoelectric, and Dielectric Constants of Lithium Tantalate and Lithium Niobate", J. Appl. Phys., Vol. 42, No. 6, pp2219-2230, May 1971.

[6.10] P.S. Cross and R.V. Schmidt, "A 1 Gbit/s Integrated Optical Modulator", IEEE J. Quantum Electron., Vol. QE-15, No. 12, pp 1415-1418, December1979.

[6.11] F. Auracher and R. Keil, "Design Considerations and Performance of Mach-Zehnder Waveguide Modulators", Wave Electronics, Vol. 4, pp 129-140, 1980.

[6.12] A.D. McLachlan, "Theoretical and Experimental Investigations of Titanium Diffused Lithium Niobate Optical Waveguides", PhD Thesis, Dept. of Electronic & Electrical Engineering, University of Glasgow, January 1981.

[6.13] B. Bjortorp, "Active and Passive Devices in Lithium Niobate By Single and Double Diffusion of Titanium", PhD Thesis, Dept. of Electronic & Electrical Engineering, University of Glasgow, August 1983.

[6.14] W.K. Burns, P.H. Klein, E.J. West, and L.E. Plew, "Ti Diffusion in Ti:$LiNbO_3$ Planar and Channel Optical Waveguides", J. Appl. Phys., Vol. 50, No. 10, October 1979.

[6.15] M. Minakata, S. Saito, and M. Shibata, "Two-Dimensional Distribution of Refractive-Index Changes in Ti-Diffused $LiNbO_3$ Strip Waveguides", J. Appl. Phys., Vol. 50, No. 5, pp 3063-3067, May 1979.

[6.16] M. Fukuma, J. Noda, and H. Iwasaki, "Optical Properties in Titanium-Diffused $LiNbO_3$ Strip Waveguides", J. Appl. Phys., Vol. 49, No. 7, pp 3693-3698, July 1978.

[6.17] I. Andonovic, "Optical Waveguide Devices in Lithium Niobate", PhD Thesis, Dept. of Electronic & Electrical Engineering, University of Strathclyde, December 1983.

[6.18] R.J. Esdaile, "Titanium Doped Lithium Niobate For Electro-Optic Devices", PhD Thesis, Dept. of Electronic & Electrical Engineering, University of Glasgow, April 1979.

[6.19] A.M. Glass, "The Photorefractive Effect", Opt. Enging., Vol. 17, No. 5, pp 470-479, September-October 1978.

[6.20] A.M. Glass, I.P. Kaminow, A.A. Ballman, and D.H. Olson, "Absorption Loss and Photorefractive-Index Changes in $Ti:LiNbO_3$ Crystals and Waveguides", Appl. Opt., Vol. 19, No. 2, pp 276-281, 15 January 1980.

[6.21] R.A. Becker and R.C. Williamson, "Photorefractive Effects in $LiNbO_3$ Channel Waveguides: Model and Experimental Verification", Appl. Phys. Lett., Vol. 47, No. 10, pp 1024-1026, 15 November 1985.

[6.22] C.D.W. Wilkinson and R.G. Walker, "The Diffusion Profile Of Stripe Optical Waveguides Formed By Ion Exchange", Electron. Lett., Vol. 14, No. 18, pp 599-600, 31st August 1978.

[6.23] N.A. Sanford and W.C. Robinson, "Secondary-Ion Mass Spectroscopy Characterisation Of Proton-Exchanged $LiNbO_3$ Waveguides", Opt. Lett., Vol. 10, No. 4, pp 190-192, April 1985.

[6.24] R.G. Walker and C.D.W. Wilkinson, "Integrated Optical Ring Resonators Made By Silver Ion-Exchange In Glass", Appl. Opt., Vol. 22, No. 7, pp 1029-1035, 1 April 1983.

[6.25] R.G. Walker, C.D.W. Wilkinson, and J.A.H. Wilkinson, "Integrated Optical Waveguiding Structures Made By Silver Ion-Exchange In Glass: 1. The Propagation Characteristics Of Stripe Ion-Exchanged Waveguides; A Theoretical And Experimental Investigation", Appl. Opt., Vol. 22, No. 12, pp 1923-1928, 15 June 1983.

[6.26] R.G. Walker and C.D.W. Wilkinson, "Integrated Optical Waveguiding Structures Made By Silver Ion-Exchange In Glass: 2. Directional Couplers And Bends", Appl. Opt., Vol. 22, No. 12, pp 1929-1936, 15 June 1983.

[6.27] J.J. Veselka and G.A. Bogert, "Low-Loss TM-pass Polariser Fabricated By Proton Exchange For Z-cut $Ti:LiNbO_3$ Waveguides", Electron. Lett., Vol. 23, No. 1, pp 29-31, 2 January 1987.

[6.28] P.G. Suchoski, T.K. Findakly, and F.J. Leonberger, "Low-Loss High-Extinction Polarizers Fabricated in $LiNbO_3$ By Proton Exchange", Opt. Lett., Vol. 13, No. 2, pp 172-174, February 1988.

[6.29] A. Loni, R.M. De La Rue, and J.M. Winfield, "Very Low-Loss Proton-Exchanged $LiNbO_3$ Waveguides With A Substantially Restored Electro-Optic Effect", Presented in IGWO'88, Santa Fe, pp MD3-1 to MD3-4, 28-30 March 1988.

[6.30] P.G. Suchoski, M.M. Abou el leil, T.K. Findakly, and F.J. Leonberger, "Low-Loss Proton-Exchanged $LiNbO_3$ Waveguides With No Electrooptic Degradation", Presented in IGWO'88, Santa Fe, pp MD4-1 to MD4-4, 28-30 March 1988.

[6.31] S.M. Al-Shukri, A. Dawar, R.M. De La Rue, A.C.G. Nutt, M.R.S. Taylor, J.R. Tobin, G. Mazzi, A. Carnera, and C. Summonte, "Analysis of Annealed Proton-Exchanged Waveguides on Lithium Niobate by Optical Waveguide Measurements and Microanalytical Techniques", Seventh Topical Meeting on Integrated and Guided-Wave Optics, Post-Deadline Papers, pp PD7-1 to PD7-4, 24-26 April 1984.

[6.32] K.K. Wong, "Integrated Optical Waveguides And Devices Fabricated By Proton Exchange: A Review", SPIE Vol. 993, Integrated Optical Circuit Engineering VI, pp 13-25, 1988.

[6.33] G.A. Korn and T.M. Korn, "Mathematical Handbook for Scientists and Engineers", McGraw-Hill Book Company, pp 1037-1042, 1968.

CHAPTER 7 CONCLUSIONS AND RECOMMENDATIONS

7.1 Introduction 237

7.2 The Use of Integrated Optics Technology for Fibre-Optic Communication and Fibre-Optic Sensor Systems 238

7.3 Optical Frequency-Translators and Their Potential Use in Fibre-Optic Sensors 239

7.4 The Serrodyne Method of Frequency Translation 240

7.5 Optical Waveguide Fabrication Techniques 241

7.6 Optical Waveguide Analysis and Evaluations 243

7.7 Optical Serrodyne Frequency-Translators 247

7.8 Proposals for Future Work 251

7.8.1 Improvements to the Fabrication of Serrodyne Frequency-Translators 251

7.8.2 Improvements to the Evaluation Techniques for the Serrodyne Frequency-Translators 252

7.8.3 A Proposal for an Optical Frequency-Translator 253

7.9 Concluding Remarks 254

References 255

CHAPTER 7

CONCLUSIONS AND RECOMMENDATIONS

7.1 Introduction

The work reported in this thesis encompasses the study and the use of the serrodyne (sawtooth) phase modulation technique for optical frequency translation. This was accomplished by the use of optical phase modulators driven by commercially available function generators. The phase modulators were realised by titanium indiffusion and for the first time by proton exchange in $LiNbO_3$. A number of problems were identified with optical waveguides and devices realised by using concentrated benzoic acid as the protonic source. The solution to many of the problems was to fabricate optical waveguides and devices by using diluted molten benzoic acid melts (with lithium benzoate).

Chapter 1 described the progress of active lithium niobate devices and their use in fibre and integrated optical sensor systems. A summary of frequency translation methods using microwave, bulk optics, fibre and integrated optical components was presented in Chapter 2. The serrodyne phase modulation method for frequency translation was demonstrated for the first time using integrated optical phase modulators. The analysis of various non-ideal situations using sawtooth modulation signals and phase modulators was described in Chapter 3.

In order to realise phase modulators successfully in $LiNbO_3$, the complete waveguide/device fabrication procedures using titanium indiffusion and proton exchange techniques were described in Chapter 4. Chapter 5 outlined the theoretical treatment of slab and stripe optical waveguides with particular emphasis given to both slab and stripe step index waveguides.

Chapter 6 described in detail the complete design procedure of an optical phase modulator in $LiNbO_3$. In addition the experimental procedures and the evaluation setup used for the testing of the serrodyne phase modulators were discussed. The experimental results of the serrodyne phase modulators were presented as a function of the non-ideal waveform and device conditions.

The thesis ends with the conclusions summarised in this chapter. Proposals for future work in this area are made: in particular, suggestions on improvements to the fabrication of high performance serrodyne frequency-translators, improvements to the evaluation techniques for the serrodyne devices and on a possible implementation of an optical frequency-translator.

7.2 The Use of Integrated Optics Technology for Fibre-Optic Communication and Fibre-Optic Sensor Systems

The main thrust in the advancement of integrated optical components over the last few years has been from the designers of single mode optical communication systems. This push has led to some spectacular state-of-the art components both in $LiNbO_3$ and III-V material systems. However due to the relative simplicity and ease in the realisation of devices in $LiNbO_3$ compared with those fabricated using III-V semiconductor materials, it was decided that all the devices reported in this thesis would be of the former material. This point has been explored in Chapter 1.

The first optical waveguides in $LiNbO_3$ were realised by outdiffusion of lithium in the form of Li_2O. However the most commonly and successfully used method of waveguide realisation has been titanium-indiffusion. The progress of active optical devices fabricated by titanium indiffusion in $LiNbO_3$ was also described in Chapter 1.

Recently other areas of application for integrated optical devices have been identified. The need for such components in single mode fibre-

optic sensors became apparent. In signal processing schemes where heterodyne detection is adopted, the component that is at the heart of this technique is the optical frequency-translator.

7.3 Optical Frequency-Translators and Their Potential Use in Fibre-Optic Sensors

A comprehensive review of frequency translation techniques using microwave and optical methods was given in Chapter 2. A large number of research groups have demonstrated optical frequency-translators in $LiNbO_3$. The translators demonstrated were classed into two main types; those using acousto-optic interactions and others using electro-optic effects.

The review concluded that translators using the electro-optic effect are the preferred and better choice. The main reason is that the device configurations are more readily compatible with the rest of the integrated optical circuit. Of all the proposed and demonstrated electro-optic frequency-translators, the two kinds that are most useful are those using the quadrature and the serrodyne methods.

Optical frequency-translators realised by the former method are in general more complex, i.e. requiring a number of basic integrated optical devices (phase modulators and Y-junction splitters and combiners) to form the device configuration. In addition these devices generally require complex phase adjustments to ensure reasonable performance. These components are however useful for heterodyne detection schemes for optical communication systems since they have the inherent capability of optical frequency shifting from a few Herz to the GigaHerz region. The serrodyne frequency-translator is simple and can be readily implemented using an optical phase modulator. It can be operated from a few Hz to tens of MHz but its performance is limited by the drive electronics.

7.4 The Serrodyne Method of Frequency Translation

The serrodyne method was originally used for frequency translation in microwave systems. This technique has been used for the first time for achieving optical frequency translation using integrated optical phase modulators in the work described in this thesis. The method involves driving an optical phase modulator with a sawtooth signal. If a perfect phase modulator is driven with a perfect sawtooth with zero fall-time or flyback time, then ideal frequency translation is accomplished. Chapter 3 analysed the effects of the use of non-ideal phase modulators and non-ideal sawtooth waveforms. A number of non-ideal sawtooth waveform conditions were identified. These included non-zero flyback/fall-time, non-optimum sawtooth amplitude, non-linear sawtooth phase variation, and non-optimum operation over a band/range of frequencies using a constant sawtooth amplitude. For the phase modulator the presence of amplitude modulation is an important factor in determining the frequency translation performance of the device. Theoretical plots of various sideband suppressions for all the above non-ideal situations were presented in Chapter 3.

The serrodyne optical frequency-translator is a simple and efficient device. It can be integrated easily into any optical sensor signal processing circuit. However, the requirement of a high quality sawtooth waveform for the frequency translation process is the major disadvantage. This implies that in general the frequency translation range is from a few Herz to tens of MegaHerz, i.e. limited by the drive electronics.

The serrodyne frequency-translator has been proposed and used in a number of fibre-optic sensor systems. Three examples of their use in integrated optics based fibre-optic sensor systems were presented at the end of Chapter 3. This included the use of the device in an integrated optical/fibre laser doppler velocimeter, in the fibre-optic hydrophone and

more recently in the fibre-optic gyroscope. The last application is considered to be one of the most important because a number of establishments (both manufacturers and users) are considering the use of heterodyne systems in processing rotation rates. The commercial significance in this case is great. Potentially the fibre-optic gyroscope can replace most mechanical and all ring laser gyroscopes. Hence this may be the second most important application of integrated optical devices with the optical communication area possibly remaining as the major application.

7.5 Optical Waveguide Fabrication Techniques

In order to realise high performance integrated optical devices with repeatable characteristics it is of utmost importance to have close control over the fabrication procedures of the devices. Chapter 4 discussed the complete fabrication procedures for phase modulators in $LiNbO_3$ by titanium indiffusion and a relatively new process known as proton exchange (PE).

The complete procedures that were used for fabricating the integrated optical phase modulators included mask making, substrate preparation (an important foundation stage), waveguide pattern formation, waveguide realisation by titanium indiffusion or proton exchange, end polishing and finally mounting the devices for testing.

Substrate preparation was found to be one of the most important and critical process steps. The degreasing of the $LiNbO_3$ surfaces was found to be important in the eventual success of the optical waveguide pattern definations. A number of organic solvents in conjunction with ultrasonic cleaning were used in all stages of cleaning.

The titanium films were deposited by the electron beam evaporation method. The thicknesses of deposited films were monitored using a crystal thickness monitor setup. The accuracy of this system was $\pm$ 20 Å.

The photolithographic process was extensively used in this project. Positive photoresist was used throughout this process stage. Using the appropriate mask patterns and UV exposures, device patterns were defined.

The diffusion conditions for the fabrication of Ti:$LiNbO_3$ waveguides were a diffusion temperature of 1000°C and a closed alumina tube with congruent $LiNbO_3$ flakes for outdiffusion suppression, in the case of devices using Y-cut crystals. In the case of Z-cut devices, the outdiffusion suppression recipe was to flow wet oxygen through the diffusion tube with congruent $LiNbO_3$ flakes placed in the alumina diffusion boats. Experiments indicated that it is essential to diffuse the titanium only on the -Z face of the crystal. When this was not adhered to portions of the titanium pattern were lost in a number of diffusions.

A review of the proton exchange method for waveguide formation in $LiNbO_3$ was presented. The review included discussions of what is proton exchange, possible mechanisms of the process, a list of realised passive and active devices and, most important of all, the problems observed in this work and by other researchers using concentrated melts. The protonic source used in all the PE experiments was molten benzoic acid. The reasons for its use are that it melts at a fairly low temperature and that it is not toxic.

The apparatus used for the fabrication of PE waveguides in $LiNbO_3$ was a high temperature oil bath. At the start of this work, it seemed to be the best choice. However, the use of alternative equipment such as vertical furnaces and fluidized alumina baths are definitely worth some consideration since at high fabrication temperatures ($\cong$ 245°C) the oil can react with the benzoic acid (from stainless steel containers) and eventually the oil can lose its viscosity. Also long term exposure of the oil with the atmosphere could cause degradation in the viscosity.

Another important parameter that has to be monitored with extreme care in the PE process is the temperature of the molten protonic source. It is

also very critical to take into consideration the warmup time i.e. the time needed by the protonic bath to recover its original stabilised temperature after the substrates with the holders are immersed in the bath. This is especially critical in the realisation of single mode stripe optical waveguides by using concentrated benzoic acid melts.

The use of diluted molten benzoic acid (with lithium benzoate) was also employed to fabricate optical devices. The results of the optical evaluations of PE waveguides formed by concentrated and diluted benzoic acid melts were reported in Chapter 5.

In order to evaluate and eventually use the phase modulators the ends of the devices were polished. A polishing technique was developed and the criterion for successful polishing was to ensure chip-free top surface and end-face under a magnification of 400 times.

Finally the phase modulators were realised by photolithographically patterning the aluminium electrodes. The devices were then ready for optical and electrical evaluation.

7.6 Optical Waveguide Analysis and Evaluation

The theoretical analysis of slab and stripe optical waveguides formed by proton exchange (PE) in $LiNbO_3$ has been presented in Chapter 5. In addition the experimental evaluations of slab optical waveguides formed in X- and Z-cut $LiNbO_3$ by concentrated and diluted (with lithium benzoate) benzoic acid melts were also presented in the same chapter.

The theoretical analysis of slab and stripe optical waveguides with step-like refractive index profiles was dealt with exclusively. The reason is that all slab waveguides formed by diluted and concentrated benzoic acid melts were found experimentally to have step-like refractive index profiles. Two methods were used to analyse the fabricated slab optical waveguides. The first was the treatment of normalised waveguide dispersion equations for

step-index structures, as described by Kogelnik and Ramaswamy. The second technique was the IWKB method of determining the waveguide refractive index profiles. In both cases, the main inputs to the computer programs were the measured mode angles of the waveguides under evaluations. The above two methods were found to be suitable for analysing the PE waveguides.

The next step was to determine theoretically the dispersion curves of PE stripe optical waveguides for various waveguide widths-in particular 4 μm and 5 μm. For this analysis the two techniques used were Marcatili's analytical solution method and the Effective Index method first described by Knox and Toulious. A number of general assumptions were made when using the above two methods. They were:-

(1) The optical waveguides formed have step-like refractive index profiles, and

(2) The Δn of the fabricated stripe waveguides were assumed to have the values 0.10 and 0.12. These values of Δn were obtained from the slab waveguide studies.

The results of the theoretical analysis for stripe waveguides were presented in Chapter 6.

Two optical waveguide evaluation methods were used to study the properties of the waveguides formed by titanium indiffusion and PE. The prism coupling technique was used extensively to evaluate the slab waveguides formed. The measured mode angles were then used as the input for the above described slab waveguide analysis programs. The final results obtained from the calculations were the calculated surface refractive index values and the waveguide depths for the evaluated slab waveguides.

The end-fire coupling method was used in the study of the optical properties and to assist in the evaluation of the serrodyne modulation properties of the stripe waveguides and the fabricated phase-modulators

respectively. These results were reported in Chapter 6. Unfortunately, this method of waveguide evaluation does not generate effective refractive index values; it does however provide a convenient means of stripe waveguide mode excitation. Hence this method is extremely useful to verify the number of quasi-TE or quasi-TM modes supported by a stripe waveguide with a known waveguide width.

A minimum amount of study on Ti:$LiNbO_3$ slab and stripe waveguides was needed since a number of previous researchers (in particular McLachlan and Bjortorp) in the department had performed excellent related waveguide studies. However in order to ensure that their results were applicable to this work, control slab waveguides were always fabricated simultaneously with the stripe waveguides which were used for the eventual realisation of phase modulators. The slab waveguides were measured and compared with results obtained by the previous researchers. The widths of the stripe waveguides used in this study were 4 μm and 5 μm. The titanium-indiffused waveguides were realised mostly in Y-cut $LiNbO_3$ with a few realised in Z-cut $LiNbO_3$.

A more detailed optical waveguide characterization of slab waveguides formed by PE in X- and Z-cut $LiNbO_3$ was carried out because of the relative novelty of this waveguide technology. The slab waveguides formed by concentrated benzoic acid melts were evaluated for two laser wavelengths i.e. 633 nm and 1150 nm. The results from these studies indicated that the Δn values were 0.12 and 0.09 respectively. The initial interest for the waveguide study at the longer laser wavelength was to study the dispersion properties of the PE waveguides. It is possible to realise second harmonic generators using this dispersion property for the required phase matching condition.

Other parameters measured were intermodal scattering levels, out-of-plane scattering losses and in-plane scattering levels. These measurements

were systematically obtained for slab waveguides realised by concentrated and diluted benzoic acid melts. The main conclusions were that the optical performance of waveguides realised by diluted benzoic acid melts was superior in all of the above three properties. The measured propagation losses of waveguides fabricated by dilute melts were 1 to 3 dB lower than those fabricated by concentrated melts. In-plane scattering results of DMPE waveguides indicated that there was a 10 dB to 20 dB improvement over those realised by concentrated melts for a scattering angle of 0.5° in the waveguides. The intermodal scattering levels of DMPE waveguides were about 10-18 dB lower than those measured for concentrated PE waveguides.

As mentioned earlier a number of problems were identified with optical waveguides formed by concentrated benzoic acid melts. This included effective refractive index variations with time (after fabrication), dc extinction effects in active devices, reduced electro-optic activity, reduced acousto-optic interaction efficiency and fairly high waveguide propagation losses (a few dB/cm).

A possible solution to the above mentioned problems is to use diluted molten benzoic acid melts, using lithium benzoate as the dilutant (0.5% and 1%). The results of measured waveguides and devices (using Mach-Zehnder interferometers) confirmed that stable and low-loss waveguides can be made by this method. In addition the waveguides were found to have low in-plane scatter levels and a high optical damage threshold. The optical qualities of these waveguides are of higher quality than those realised by titanium indiffusion.

In addition the measurement of the voltage required to cause a π phase change in a Mach-Zehnder interferometer suggested that the electro-optic activity was preserved. These results were comparable to those obtained by evaluating devices formed by titanium indiffusion. These results were presented at the end of Chapter 5.

The slab waveguide studies also generated the diffusion coefficients of the proton exchange process at various exchange temperatures. A better control over the time of exchange was achieved by fabricating the slab waveguides using diluted benzoic acid melts since the diffusion coefficients were smaller (3 to 10 times) compared to those fabricated using concentrated benzoic acid melts, at the same melt temperatures. The Δn of all the waveguides was found to be 0.12 at 633 nm, i.e. the Δn values were not dependent on the concentration of the benzoic acid melts used in all the PE experiments.

7.7 Optical Serrodyne Frequency-Translators

The heart of the serrodyne frequency-translator work was the successful realisation of optical phase modulators. Therefore the design for an integrated optical phase modulator was outlined in Chapter 6. In the design model, only lumped electrodes were considered since the bandwidth required for the serrodyne frequency-translators was to be around a few hundred MegaHerz. The voltages required for a 2π phase change for a number of electrode gaps were calculated. These results were then used for the design of the electrode pattern for the phase modulator. The designed phase modulator has a calculated 3 dB bandwidth of 2.7 GHz and a $V_{2\pi}/\Delta f$ value of 4 volts/GHz for a 0.35 overlap factor between electrical and optical fields.

The experimental arrangement that was used to evaluate the serrodyne optical frequency-translators was a bulk Mach-Zehnder interferometer (MZI) with an acousto-optic Bragg cell in the path of one of the arms. The phase modulator was placed in the other arm of the MZI. The purpose of the Bragg cell was to shift the spectrum from dc to an intermediate frequency where the observation of the positive and negative

sidebands due to the serrodyne modulation process could be studied conveniently.

A large number of phase modulators in $LiNbO_3$ realised by titanium indiffusion and proton exchange were evaluated optically. The results were compared to the theoretical plots (number of waveguide modes supported in relation to the width of the waveguides) of McLachlan and Bjortorp (for titanium indiffused stripe waveguides) and the plots obtained from Marcatili and the Effective Index waveguide analysis (for PE stripe waveguides). It was found that the number of modes supported by titanium indiffused stripe waveguides was in good agreement with that predicted by McLachlan and Bjortorp. However for PE stripe waveguides, the results were in disagreement, with the worst cases predicted by the Effective Index method for stripe waveguide analysis. One possible reason for this discrepancy is that the depth of the stripe waveguide predicted from the slab waveguide results may not be applicable. Here the use of a metallic aluminium diffusion mask for fabricating the stripe waveguides may be the problem. Other researchers have reported on this type of problem in ion-exchanged waveguides and their effects on the depth of the fabricated stripe waveguides.

After the optical properties of the device waveguides were established, the next step was to evaluate the frequency response of the assembled devices. The 3 dB electrical bandwidths of the titanium-indiffused and proton-exchanged $LiNbO_3$ phase modulators were measured to be in the range from 0.8 GHz to 1.1 GHz. The bandwidth requirements in all the reported serrodyne experiments were well within this range. Hence bandwidth limitation was not a limiting factor in the performance of the serrodyne devices tested.

The performances of both the Ti:$LiNbO_3$ and PE $LiNbO_3$ serrodyne devices were limited by the fall-time of the sawtooth waveforms generated

from commercial function generators. This limited the overall suppression of spurious sidebands to 33 dB when compared to the translated signal. In order to overcome this limitation, it would be desirable to design a sawtooth generator with fall-times as fast as 1 ns for an operating frequency of 1 MHz. This would imply an overall spurious sideband suppression of 60 dB. For the serrodyne frequency-translators to be useful for example in a phase nulling fibre-optic gyroscope, an overall suppression of better than 50 dB is essential.

Another serious limitation in the performance of the Ti:$LiNbO_3$ serrodyne frequency-translators was the weakly guided waveguide modes of a number of serrodyne devices. With these devices, the measured amplitude modulation levels were generally high, i.e. between 1% to 55%. This limited the suppression of image and other spurious sidebands to 40 dB and to 5 dB respectively. By applying a dc bias voltage to such devices, the measured level of amplitude modulation varied appropriately. In the case where the applied bias dc voltage increases the effective refractive indices of the optical waveguides, the measured level of amplitude modulation decreased from 14% to 9%. However, if the applied bias was reversed, i.e. reducing the effective refractive index even further, the measured levels of amplitude modulation were dramatically increased from 14% to the total cut-off condition, with an extinction ratio of 19 dB. Fortunately, this problem seemed to occur for optical waveguides realised with initial titanium thicknesses of below 272 Å.

Serrodyne frequency-translators were demonstrated with proton exchange (PE) waveguides for the first time. Unfortunately, it was found that not all the fabricated PE phase modulators worked. This could be attributed to the possible reduction in the electro-optic activity in some of the devices that were fabricated. It was found that the r_{33} electro-optic coefficient for PE devices fabricated at 181°C was five times lower than the

bulk value (30.8 pm/V). The key to the successful realisation of operational serrodyne devices appears to be to fabricate them at a low exchange temperature (e.g. 162°C). However, even with the PE devices that did work, a dc extinction phenomenon was observed, as described in Chapter 6. This problem was observed with applied dc voltages as low as +5 volts. The PE serrodyne modulators were nevertheless found to operate more efficiently than the Ti:$LiNbO_3$ devices, i.e. requiring lower $V_{2\pi}$ voltages. The required voltages for 2π phase change for PE devices were reduced by approximately 30% when compared to titanium indiffused devices. This implies a better electrical/optical overlap between the guided modes and the electric fields i.e. an overlap factor of 0.5 for PE devices compared to an overlap factor of 0.3 for titanium indiffused devices. However, due to the fact that the depth of the PE waveguides was typically around 0.5 μm, the measured total insertion losses for these devices were of the order of 17 to 31 dB.

The serrodyne frequency translation process was found to be very sensitive to voltage changes. It was concluded from this study that the voltage variations should not be larger than 0.5% of the applied $V_{2\pi}$ voltage level, otherwise this will have serious consequences in the suppression of unwanted sidebands.

In conclusion, the serrodyne principle of optical frequency translation is extremely attractive for present day fibre and integrated optical heterodyne sensor systems as long as the maximum frequency of translation required is of the order of a few MHz. Special function generators which are capable of producing very fast fall-time (< 1 ns) and very stable voltage signals have to be realised to obtain the performance required for systems applications. Phase modulators with large electrical bandwidths (up to 1 GHz) and negligible amplitude modulation (less than 0.1%) when driven by function generators with fall-times of less than 1

nanosecond could yield high performance serrodyne frequency-translation with overall sideband suppression of better than 60 dB.

7.8 Proposals for Future Work

7.8.1 Improvements to the Fabrication of Serrodyne Frequency Translators

The optical properties of serrodyne frequency-translators fabricated by titanium indiffusion in $LiNbO_3$ may be improved by the use of X-cut crystal instead of Y-cut crystal. The areas of improvement include reduction of the lateral diffusion of the titanium ions and more reproducible suppression of outdiffusion, resulting in phase modulators with better optical mode compatibility with optical fibres. In addition, the overlap of the optical field with the electrical field in an optical phase modulator could possibly be improved by fabricating a PE stripe waveguide of narrower width dimension within a previously fabricated titanium indiffused stripe waveguide (Figure 7.1). The PE waveguide serves the purpose of translating the optical mode nearer to the surface of the device.

Various dielectric materials should be investigated for possible use as masks for the fabrication of stripe waveguide devices by the proton-exchange method. It has been reported by a number of researchers that a metallic mask may not be suitable for ion-exchange based waveguide formation processes. The prime dielectric candidate is silicon dioxide (SiO_2). However a number of methods used for depositing SiO_2 have been reported such as pyrolitic chemical vapour deposition, plasma enhanced chemical vapour deposition and sputtering. Therefore it is crucial to identify the most suitable method of SiO_2 deposition based on the density and the porosity of the deposited films. Another method for fabricating a dielectric mask is to anodise an aluminium film, whereby Al_2O_3 is formed.

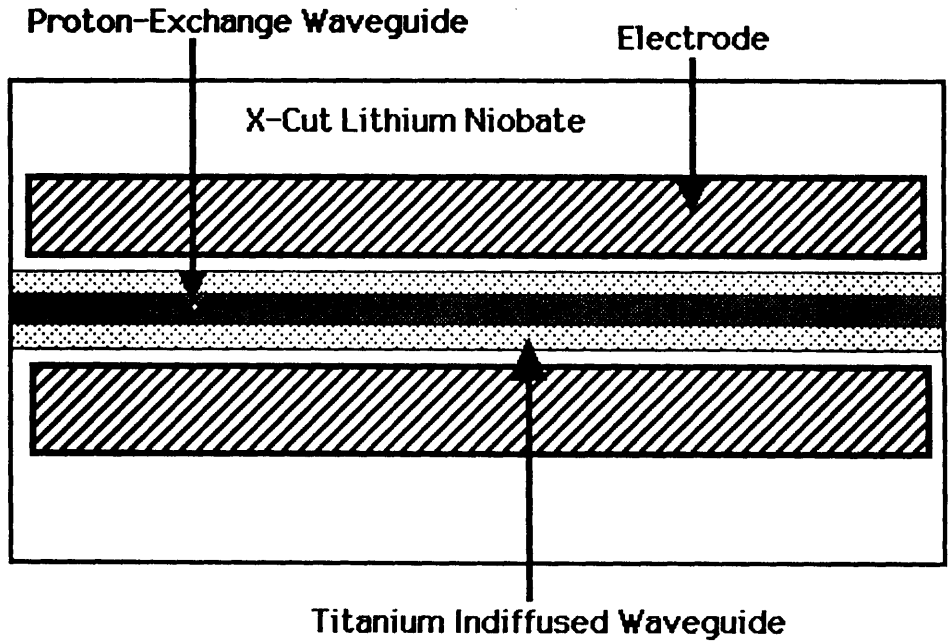

Figure 7.1 An Improved Ti:$LiNbO_3$ Optical Phase Modulator Using An Extra Proton-Exchange Stripe Waveguide

7.8.2 Improvements To The Evaluation Techniques For The Serrodyne Frequency-translators

The bulk Mach-Zehnder interferometer (MZI) test arrangement shown in Figure 6.6 of Chapter 6 can be improved by the use of polarisation preserving optical fibres. The two beam splitters can be replaced by two 3 dB fibre couplers. Figure 7.2 illustrates the all fibre based bulk MZI. The practical wavelengths of operation for serrodyne frequency-translators are 830 nm and 1300 nm for applications like the fibre-optic gyroscopes. Therefore the implementation of the above arrangement will not be a problem since polarisation preserving fibres operating at the above two wavelengths are readily available. In addition, polarisers and analysers are placed before and after the phase modulators and the acousto-optic modulator. This is needed to ensure maximum serrodyne frequency translation performance as reported by Johnson and Cox[7.1].

A more robust and easy to implement test arrangement was reported by Johnson and Cox[7.1]. The experimental structure used for the evaluation of serrodyne frequency translation is shown in Figure 7.3. The device was a Ti:$LiNbO_3$ MZI with two independent phase modulators. Each of these phase modulators was used as a serrodyne frequency-translator. The two phase modulators were driven with sawtooth signals of frequencies f_1 and f_2 as illustrated where $f_1 \gg f_2$. Using this configuration it was possible to observe both the upper and lower sidebands due to the frequency translation signal f_2 since all the sidebands were translated to f_1 from dc. In the reported experiments, f_1 was obtained directly from a commercially available function generator and the other translation signal f_2 was generated by a high performance sawtooth drive circuit. The above integrated optical circuit is a superior test vehicle to the bulk MZI (used in this thesis) or the all fibre-optic MZI.

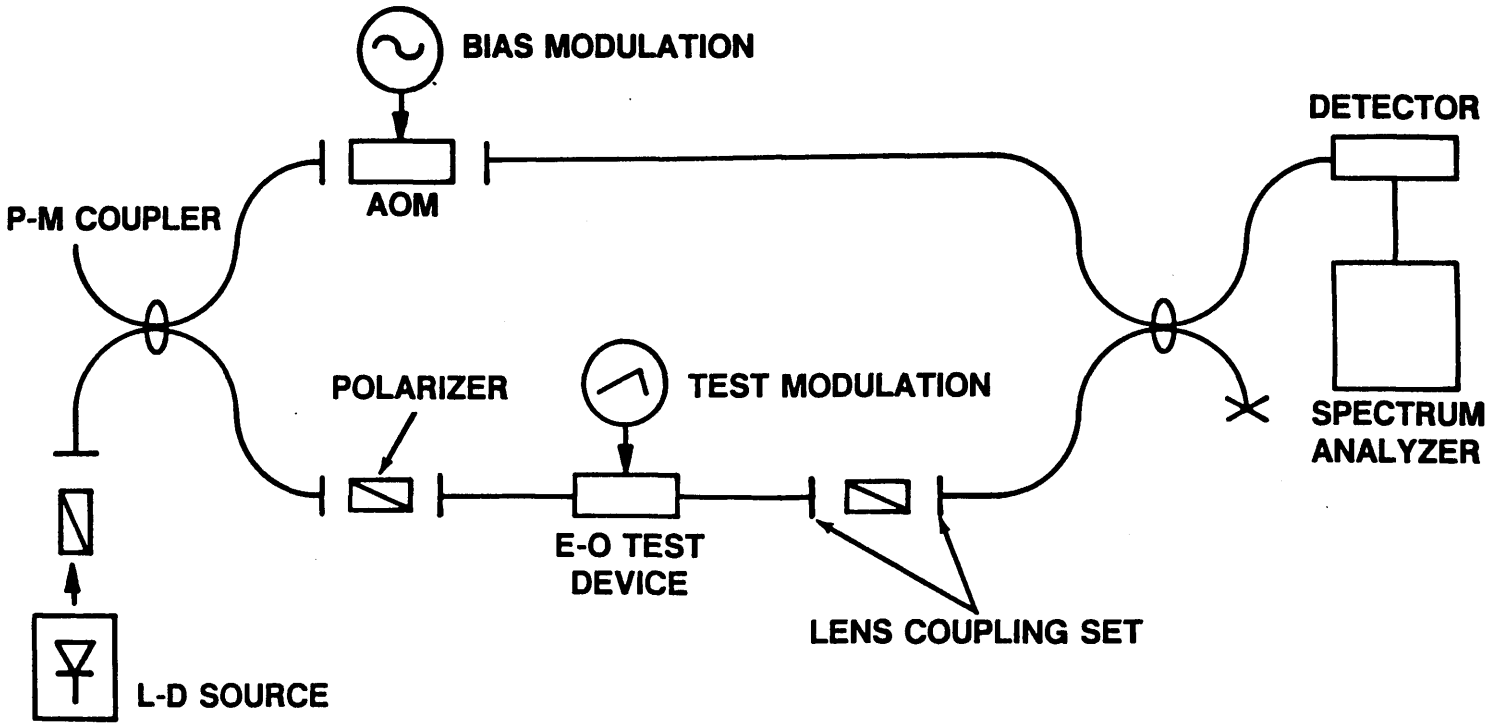

Figure 7.2 Schematic Of The All Fibre–Optic Bulk Mach–Zehnder Interferometer

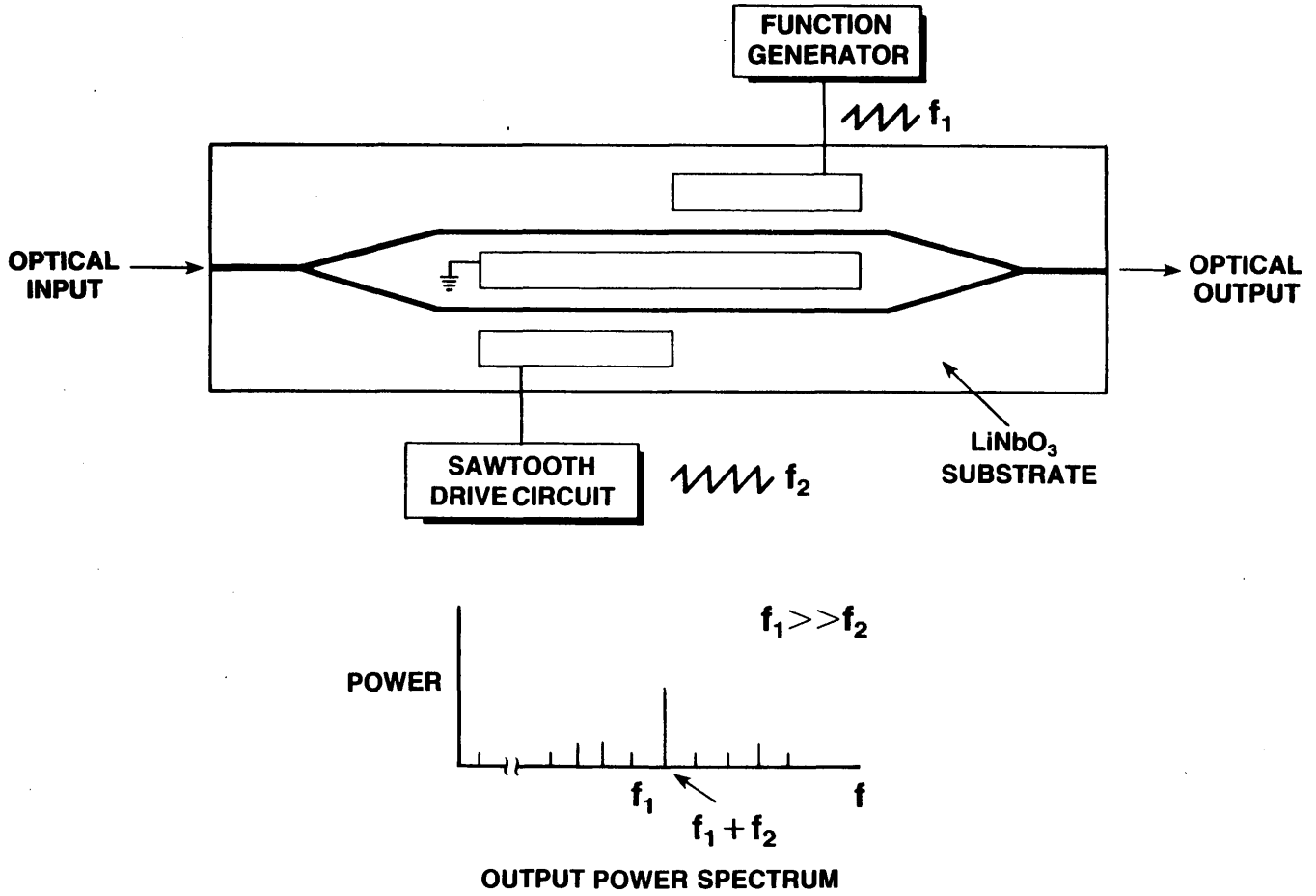

Figure 7.3 **Schematic Of The Integrated Optical Mach–Zehnder Interferometer For Evaluating Serrodyne Frequency Translation** (Sawtooth Signals Of Frequencies f_1 And f_2 Are Applied To The Phase Modulator. The Resulting Output Power Spectrum Is Illustrated)

Johnson and Cox have experimentally verified that polarisation effects can reduce the performance of the serrodyne frequency-translators. By equally exciting the TE and TM modes of the phase modulator, the overall sideband suppression was degraded by a few dB. From the PE waveguide study of this thesis, it is found that the stripe waveguides formed were polarisation selective. Therefore, by incorporating sections of PE stripe waveguides in the input and output of the MZI, it is possible to reduce any waveguide depolarisation effects and therefore maximum sideband suppression can be achieved.

7.8.3 A Proposal For An Optical Frequency-Translator

In this section the 'staircase' approximation for the sawtooth waveform is proposed for optical frequency-translation. The simplest optical frequency-translator will be realised again using an optical phase modulator in $LiNbO_3$ driven by a multiple step sawtooth function. The analysis of a phase modulator driven by such a staircase waveform was carried out in Chapter 3. The advantage in using such an approximation to the continuous phase change function is that the spurious sidebands are spaced away from the shifted signal by an integral number of the steps used in the approximation of the staircase. Therefore the greater the number of steps in the stepped waveform, the further away the spurious sidebands will be found. These results are clearly demonstrated in Appendix 3.1.

It may then be possible to realise a digitally driven optical phase-modulator, as shown in Figure 7.4. The proposed frequency-translator consists of a multiple set of electrodes with the physical lengths appropriately determined by the number of steps in the staircase approximation of the continuous phase function. In this proposed device, the number of steps is sixteen. By applying a clock signal of $16f_m$, where f_m is the frequency of the shift required, to the binary divider units, the device

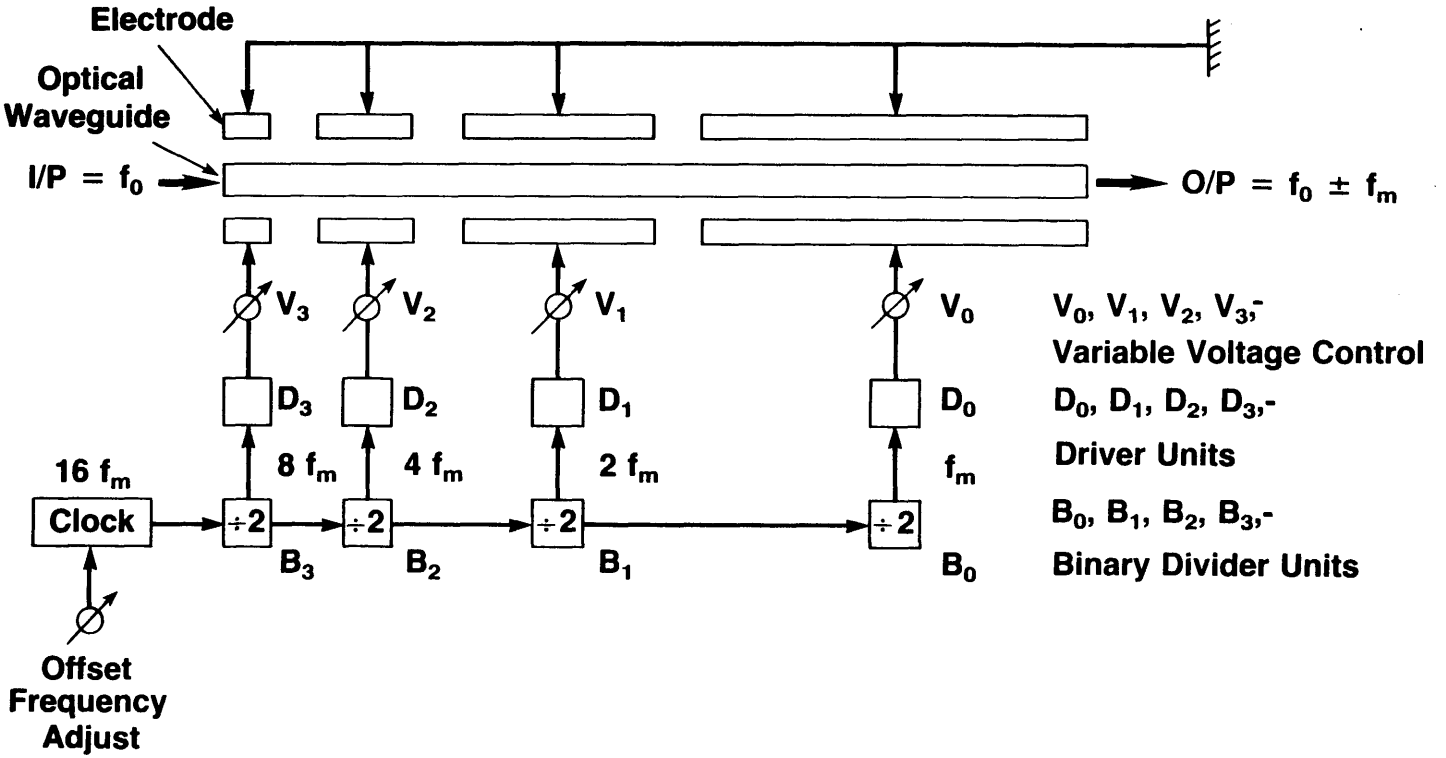

Figure 7.4 Schematic Of The Proposed Digital Optical Frequency Translator Implemented In Lithium Niobate

operation can be implemented. Such a device has been realised in the microwave regime [7.2] and found to operate with a performance similar to that of both the microwave and the optical serrodyne frequency modulators driven by the conventional sawtooth waveforms.

7.9 Concluding Remarks

In conclusion the use of optical phase modulators as serrodyne frequency translators was shown to be a simple and useful technique for frequency translation in the range from a few Herz to a few MegaHerz. Optical phase modulators fabricated by titanium indiffusion and proton-exchange were found to perform equally well. The proton-exchange method was used for the first time to realise electro-optic active devices. Not all the proton-exchanged phase modulators worked. With those that worked, a dc extinction phenomenon was observed and measured. It is predicted by the author that the serrodyne frequency translator will be used in many heterodyne fibre sensor systems especially the fibre-optic gyroscope.

REFERENCES

[7.1] L.M. Johnson and C.H. Cox III, "Lithium Niobate Serrodyne Frequency Translator For Fibre-Optic Gyroscopes", SPIE Vol. 719 Fiber Optic Gyros: 10th Anniversary Conference, pp 141-145, 1986.

[7.2] G. Klein and L. Dubrowsky, "The Digilator, A New Broadband Microwave Frequency Translator", IEEE Transactions on Microwave Theory and Techniques, Vol. MTT-15, No. 3, pp 172-179, March 1967.

LIST OF PUBLICATIONS

(1) K.K. Wong and S. Wright, "An Optical Serrodyne Frequency Translator", Proc. of a NATO Advanced Study Institute on Integrated Optics: Physics and Applications, Erice, Italy, pp 409-410, 17-30 August 1981.

(2) K.K. Wong and S. Wright, "An Optical Serrodyne Frequency Translator", First European Conference on Integrated Optics, London, IEE Conf. No. 201, pp 63-65, 14-15 September 1981.

(3) K.K. Wong, S. Wright, and R.M. De La Rue, "Performance of a Serrodyne Optical Frequency Translator", Topical Meeting on Integrated and Guided-Wave Optics, pp WA5-1 to WA5-4, 6-8 January 1982.

(4) E.Y.B. Pun, K.K. Wong, I. Andonovic, P.J.R. Laybourn, and R.M. De La Rue, "Efficient Waveguide Bragg-Deflection Grating on Lithium Niobate", Electron. Lett., Vol. 18, No. 17, pp 740-742, 19 August 1982.

(5) K.K. Wong, R.M. De La Rue, and S. Wright, "Electro-Optic-Waveguide Frequency Translator in Lithium Niobate Fabricated By Proton Exchange", Opt. Lett., Vol. 7, No. 11, pp 546-548, November 1982.

(6) K.K. Wong and R.M. De La Rue, "An Improved Electro-Optic Waveguide Serrodyne Frequency Translator in X-cut Lithium Niobate Using Proton Exchange", First International Conf. on Optical Fibre Sensors, London, IEE Conf. Proc. No. 221, pp 72-74, 26-28 April 1983.

(7) A.C.G. Nutt, K.K. Wong, D.F. Clark, P.J.R. Laybourn, and R.M. De La Rue, "Proton-Exchange Lithium Niobate Slab and Stripe Waveguides: Characterization and Comparisons", Second European Conf. on Integrated Optics, Florence, IEE Conf. No. 227, pp 53-56, 17-18 October 1983.

(8) D.F. Clark, A.C.G. Nutt, K.K. Wong, P.J.R. Laybourn, and R.M. De La Rue, "Characterization of Proton-Exchange Slab Optical Waveguides in Z-cut Lithium Niobate", J. Appl. Phys., Vol. 54, No. 11, pp 6218-6220, November 1983.

(9) K.K. Wong, "Integrated Optical Device Fabrication By Proton Exchange in Lithium Niobate (Invited Talk)", IERE Colloquium on Integrated Optics, London, 12 June 1984.

(10) K.K. Wong, N.J. Parsons, A.R. Oldroyd, and A.C. O'Donnell, "High Quality Optical Waveguides in Lithium Niobate By Dilute Melt Proton-Exchange", IOOC/ECOC'85, Venice, Italy, Vol. 1, pp 59-62, 1-4 October 1985.

(11) K.K. Wong, "An Experimental Study of Dilute Melt Proton Exchange Waveguides in X- and Z-cut Lithium Niobate", GEC J. Research, Vol. 3, No. 4, pp 243-250, 1985.

(12) N.J. Parsons, K.K. Wong, and A.C. O'Donnell, "Efficient Proton Exchange Travelling Wave Modulator in $LiNbO_3$", Topical Meeting in Integrated and Guided-Wave Optics, Post-Deadline Paper, Atlanta, 26-28 February 1986.

(13) K.K. Wong, A.C.G. Nutt, D.F. Clark, J. Winfield, P.J.R. Laybourn, and R.M. De La Rue, "Characterization of Proton-Exchange Slab Optical Waveguides in X-cut Lithium Niobate", IEE Proc. Part J, Vol. 133, No. 2, pp 113-117, April 1986.

(14) K.K. Wong, "Proton Exchange Techniques For Lithium Niobate Optical Waveguides (Invited Talk)", American Ceramic Society - 39th Pacific Coast Regional Meeting, Seattle, 22-24 October 1986.

(15) K.K. Wong, A.C. O'Donnell, I.A. Wood, and N.J. Parsons, "Integrated Optical Mach-Zehnder Interferometers in $LiTaO_3$ Fabricated By Proton Exchange", Proc. of the Fourth European Conference on Integrated Optics, ECIO 87, Glasgow, Scotland, pp 123-126, 11-13 May 1987.

(16) K.K. Wong, "Integrated Optical Waveguides And Devices Fabricated By Proton Exchange: A Review", SPIE Vol. 993, Integrated Optical Circuit Engineering VI, pp 13-25, 1988.